

Multi-Century Simulations of LGM and Present Day Climate Using
an Accelerated Coupled GCM Carrying Water Isotope Tracers, With
Comparisons to Ocean Sediment/Ice Cores and Observations

Duane Ethan Thresher

Submitted in partial fulfillment of the
requirements for the degree
of Doctor of Philosophy
in the Graduate School of Arts and Sciences

COLUMBIA UNIVERSITY
2004

©2004
Duane Ethan Thresher
All Rights Reserved

ABSTRACT

Multi-Century Simulations of LGM and Present Day Climate Using an Accelerated Coupled GCM Carrying Water Isotope Tracers, With Comparisons to Ocean Sediment/Ice Cores and Observations

Duane Ethan Thresher

440 and 540-year climate simulations of the Last Glacial Maximum (21 kyBP) and Present Day were done with a 5 x 4 degree Coupled General Circulation Model (13-level ocean, 9-level atmosphere), without flux corrections and fully carrying Oxygen 18 as water isotope tracer. To run the CGCM to near-equilibrium in reasonable time, CGCM acceleration schemes were implemented and tested: Reduced Gravity, Distorted Physics, program parallelization, and starting from another equilibrium. Up-to-date era-appropriate boundary conditions were prepared for the CGCM: insolation, greenhouse gases, and, as a function of sea level, land/ocean mask, straits, land/glacier elevations, ocean depths, and mean ocean O18 and salt concentrations.

Testing “forward modelling” of climate proxies, CGCM ocean results were input into a model of foraminifera O18 ratio and the results compared to a database of ocean sediment core foraminifera O18, compiled as part of this research. CGCM precipitation O18 ratio results were compared directly to an also-compiled ice core O18 database. For PD, CGCM results were compared to gathered observations.

Parallelization was found to be the least-problematic acceleration scheme; use of the others possibly affecting the equilibrium reached. Forward modelling of foraminifera O18 was found to be a useful technique. It was determined that the LGM to PD change (LGM–PD) in mean ocean O18 was -1.0 permil, although LGM–PD deep ocean O18 from core pore water was found not to match well the CGCM’s. LGM–PD mean tropical SST was determined to be 3.6 C, significantly greater than CLIMAP’s. LGM–PD SST from alkenones and foraminifera Mg/Ca were found not to match well the CGCM’s or CLIMAP’s, regardless of month. Terrestrial temperature proxies, which contradict CLIMAP, were found to match well the CGCM. Contrary to its proxies, North Atlantic meridional overturning circulation was found to be stronger

at the LGM than PD. Consistent with ice core borehole paleothermometry, the spatial relationship of surface air temperature versus snow O18 was found to be significantly different from the temporal one at a location.

Table of Contents

Table of Contents	i
List of Figures	v
List of Tables	xiii
Acknowledgements	xvii
Dedication	xviii
1 Introduction	1
2 Water Isotopes	5
2.1 H ₂ O	5
2.1.1 Oxygen and Hydrogen Isotopes	5
2.1.2 Fractionation	6
2.1.3 Global Isotopic Variation	8
2.1.4 In GCMs	9
2.2 Proxies	12
2.2.1 Foraminifera and $\delta^{18}\text{O}_c$ Model	13
2.2.2 Other Ocean Water Proxies	15
2.2.3 Ice	16
2.2.4 Other Precipitation Proxies	17
3 Quest for Equilibrium	19
3.1 Equilibrium	19
3.2 OGCM Acceleration	21

3.2.1	OGCM Description	21
3.2.2	Starting From Another OGCM Equilibrium	23
3.2.3	Reduced Gravity	24
3.2.4	Distorted Physics	28
3.2.5	Program Parallelization	32
3.3	CGCM	35
3.3.1	CGCM Description	35
3.3.2	OGCM Streamfunction	37
3.3.3	CGCM/OGCM Leapfrog Acceleration Scheme	42
3.3.4	Non-Equilibrium OGCM Initial Conditions	44
4	CGCM Boundary Conditions	47
4.1	Greenhouse Gases	47
4.2	Aerosols	50
4.3	Insolation	51
4.4	Topography	59
4.5	Land Surface	73
5	Ocean Sediment and Ice Core $\delta^{18}\text{O}$ Data	79
5.1	Downcore $\delta^{18}\text{O}$ Time Series	79
5.2	Coretop $\delta^{18}\text{O}$	82
6	Comparisons of Simulations, Observations, and Ocean Sediment and Ice Core $\delta^{18}\text{O}$ Data	86
6.1	Time of Simulation Averages and Proximity to Equilibrium	86
6.2	Outline of Comparisons	91
6.2.1	Variables and Eras	91
6.2.2	Methods: Maps, Plots, and Means	94
6.3	Present Day (PD) Simulation Compared to Observations	99
6.3.1	Maps	99
6.3.2	Plots	119
6.3.3	Means	119
6.4	PD Simulation Compared to Ocean Sediment and Ice Coretop $\delta^{18}\text{O}$ Data	128

6.4.1	Maps	128
6.4.2	Plots	139
6.4.3	Means	139
6.5	LGM – PD of Simulations Compared to Ocean Sediment and Ice Core $\delta^{18}\text{O}$ Data	150
6.5.1	Means	150
6.5.2	Maps	155
6.5.3	Plots	155
6.6	LGM Simulation Compared to Ocean Sediment and Ice Core $\delta^{18}\text{O}$ Data	165
6.6.1	Maps	165
6.6.2	Plots	166
6.6.3	Means	166
6.7	LGM – PD of Simulations	179
7	Addressing Questions of the LGM	190
7.1	Mean Ocean $\delta^{18}\text{O}_w$	190
7.2	CLIMAP Tropical SSTs	195
7.2.1	Comparison to CGCM Results	196
7.2.2	Comparison to $U_{37}^{K'}$ SST Results	200
7.2.3	Comparison to Mg/Ca SST Results	202
7.2.4	From Terrestrial Temperature Proxy Data	209
7.3	North Atlantic Meridional Overturning Circulation	213
7.4	Temporal and Spatial Relationships of Surface Air Temperature Versus Precipitation $\delta^{18}\text{O}$	225
8	Conclusions and Future Work	232
8.1	Conclusions	232
8.2	Future Work	234
	References	241
A	Downcore $\delta^{18}\text{O}$ Time Series Core Information	261

B	Downcore $\delta^{18}\text{O}$ Time Series Plots	311
B.1	Downcore $\delta^{18}\text{O}$ Time Series Plots for <i>Cibicidoides wuellerstorfi</i>	311
B.2	Downcore $\delta^{18}\text{O}$ Time Series Plots for <i>Globigerinoides sacculifer</i> . . .	319
B.3	Downcore $\delta^{18}\text{O}$ Time Series Plots for <i>Globigerinoides ruber</i> (white) .	323
B.4	Downcore $\delta^{18}\text{O}$ Time Series Plots for <i>Globigerinoides ruber</i> (pink) . .	328
B.5	Downcore $\delta^{18}\text{O}$ Time Series Plots for <i>Globigerina bulloides</i>	331
B.6	Downcore $\delta^{18}\text{O}$ Time Series Plots for <i>Neogloboquadrina pachyderma</i> (sinistral)	335
B.7	Downcore $\delta^{18}\text{O}$ Time Series Plots for <i>Neogloboquadrina pachyderma</i> (dextral)	339
B.8	Downcore $\delta^{18}\text{O}$ Time Series Plots for Glacier Ice H_2O	341
C	Downcore $\text{U}_{37}^{K'}$ SST Time Series Core Information	344
D	Downcore $\text{U}_{37}^{K'}$ SST Time Series Plots	350
D.1	Downcore $\text{U}_{37}^{K'}$ SST Time Series Plots for the Southern Extra-Tropics	350
D.2	Downcore $\text{U}_{37}^{K'}$ SST Time Series Plots for the Tropics	352
D.3	Downcore $\text{U}_{37}^{K'}$ SST Time Series Plots for the Northern Extra-Tropics	355
E	Downcore Mg/Ca SST Time Series Core Information	357
F	Downcore Mg/Ca SST Time Series Plots	359
F.1	Downcore Mg/Ca SST Time Series Plots for <i>Globigerina bulloides</i> . .	359
F.2	Downcore Mg/Ca SST Time Series Plots for <i>Globigerinoides sacculifer</i>	361
F.3	Downcore Mg/Ca SST Time Series Plots for <i>Neogloboquadrina pachy-</i> <i>derma</i> (sinistral)	363
F.4	Downcore Mg/Ca SST Time Series Plots for <i>Globigerinoides ruber</i> (white)	365

List of Figures

3.1	Mean (global, annual, first decade of each century) ocean potential temperature at selected OGCM levels	26
3.2	Mean (global, annual, first decade of each century) ocean salinity at selected OGCM levels	27
3.3	Annual NAMOC streamfunction value at OGCM grid box lat# 35, level 10 versus model years for various OGCM and CGCM runs . . .	39
4.1	Fig. 1 from Monnin et al. 2001 showing the atmospheric CO ₂ and CH ₄ record from the Dome C, Antarctica ice core	49
4.2	Differences from PD of zonally-averaged monthly-mean top-of-atmosphere insolation for LGM and suggested Deglaciation eras: Dec–May . . .	57
4.3	Differences from PD of zonally-averaged monthly-mean top-of-atmosphere insolation for LGM and suggested Deglaciation eras: Jun–Nov	58
4.4	CGCM grid box maps for PD of land/ocean, land elevation, and ocean depth	63
4.5	CGCM grid box maps for PD of glacier extent, glacier thickness, and non-glaciated non-lake ground	64
4.6	CGCM grid box maps for LGM of land/ocean, land elevation, and ocean depth	66
4.7	CGCM grid box maps for LGM of glacier extent, glacier thickness, and non-glaciated non-lake ground	67
4.8	CGCM grid box maps for LGM – PD of land/ocean, land elevation, and ocean depth	69
4.9	CGCM grid box maps for LGM – PD of glacier extent, glacier thickness, and non-glaciated non-lake ground	70

4.10	CGCM grid box maps for PD of lake fraction, lake thickness, and river direction	74
4.11	CGCM grid box maps for LGM of lake fraction, lake thickness, and river direction	76
6.1	Mean global/annual OGCM potential temperature versus model years at selected OGCM levels for PD and LGM runs	88
6.2	Mean global/annual salinity versus model years at selected OGCM levels for PD and LGM runs	89
6.3	Mean global/annual OGCM $\delta^{18}\text{O}_w$ versus model years at selected OGCM levels for PD and LGM runs	90
6.4	Annual NAMOC streamfunction value at OGCM grid box lat# 35, level 10 versus model years for PD and LGM runs	92
6.5	CGCM grid box maps of PD annual bottom ocean $\delta^{18}\text{O}_w$ for OGCM, observations, and OGCM minus observations	101
6.6	CGCM grid box maps of PD annual bottom ocean in situ temperature for OGCM, observations, and OGCM minus observations	103
6.7	CGCM grid box lon# 30 sections of PD annual ocean $\delta^{18}\text{O}_w$ for OGCM, observations, and OGCM minus observations	105
6.8	CGCM grid box lon# 30 sections of PD annual ocean in situ temperature for OGCM, observations, and OGCM minus observations	106
6.9	Grid box lon# 30 sections of PD annual salinity for OGCM, observations, and OGCM minus observations	107
6.10	CGCM grid box maps of PD annual surface ocean $\delta^{18}\text{O}_w$ for OGCM, observations, and OGCM minus observations	109
6.11	CGCM grid box maps of PD annual P – E for AGCM, observations, and AGCM minus observations	111
6.12	CGCM grid box maps of PD annual sea ice concentration for OGCM, observations, and OGCM minus observations	113
6.13	CGCM grid box maps of PD annual surface salinity for OGCM, observations, and OGCM minus observations	114

6.14	CGCM grid box maps of PD annual surface ocean in situ temperature for OGCM, observations, and OGCM minus observations	116
6.15	CGCM grid box maps of PD annual precipitation $\delta^{18}\text{O}$ for AGCM, observations, and AGCM minus observations	117
6.16	CGCM grid box maps of PD annual precipitation rate for AGCM, observations, and AGCM minus observations	118
6.17	PD annual surface OGCM $\delta^{18}\text{O}_w$ versus observed surface ocean $\delta^{18}\text{O}_w$ and PD annual bottom OGCM $\delta^{18}\text{O}_w$ versus observed bottom ocean $\delta^{18}\text{O}_w$	120
6.18	PD annual OGCM $\delta^{18}\text{O}_w$ versus observed ocean $\delta^{18}\text{O}_w$ and PD annual OGCM in situ temperature versus observed ocean in situ temperature	121
6.19	PD annual surface OGCM in situ temperature versus observed surface ocean in situ temperature and PD annual bottom OGCM in situ temperature versus observed bottom ocean in situ temperature . . .	122
6.20	PD annual AGCM precipitation $\delta^{18}\text{O}$ versus observed precipitation $\delta^{18}\text{O}$	123
6.21	CGCM grid box maps of PD annual $\delta^{18}\text{O}_c$ of benthic foraminifera <i>C. wuellerstorfi</i> in OGCM/foraminifera model, coretops, and OGCM/foraminifera model minus coretops	130
6.22	CGCM grid box maps of PD annual $\delta^{18}\text{O}_c$ of planktonic foraminifera <i>G. sacculifer</i> in OGCM/foraminifera model, coretops, and OGCM/foraminifera model minus coretops	132
6.23	CGCM grid box maps of PD annual $\delta^{18}\text{O}_c$ of planktonic foraminifera <i>G. ruber</i> (white) in OGCM/foraminifera model, coretops, and OGCM/foraminifera model minus coretops	133
6.24	CGCM grid box maps of PD annual $\delta^{18}\text{O}_c$ of planktonic foraminifera <i>G. ruber</i> (pink) in OGCM/foraminifera model, coretops, and OGCM/foraminifera model minus coretops	134
6.25	CGCM grid box maps of PD annual $\delta^{18}\text{O}_c$ of planktonic foraminifera <i>G. bulloides</i> in OGCM/foraminifera model, coretops, and OGCM/foraminifera model minus coretops	136

6.26	CGCM grid box maps of PD annual $\delta^{18}\text{O}_c$ of planktonic foraminifera <i>N. pachyderma</i> (sinistral) in OGCM/foraminifera model, coretops, and OGCM/foraminifera model minus coretops	137
6.27	CGCM grid box maps of PD annual $\delta^{18}\text{O}_c$ of planktonic foraminifera <i>N. pachyderma</i> (dextral) in OGCM/foraminifera model, coretops, and OGCM/foraminifera model minus coretops	138
6.28	CGCM grid box maps of PD annual $\delta^{18}\text{O}$ of AGCM precipitation, ice coretop H_2O , and AGCM precipitation minus ice coretop H_2O	140
6.29	PD OGCM/foraminifera model annual $\delta^{18}\text{O}_c$ versus ocean sediment coretop foraminifera $\delta^{18}\text{O}_c$ and PD AGCM annual snow $\delta^{18}\text{O}_i$ versus ice coretop H_2O $\delta^{18}\text{O}_i$	141
6.30	CGCM grid box maps of LGM – PD annual $\delta^{18}\text{O}_c$ of benthic foraminifera <i>C. wuellerstorfi</i> in OGCM/foraminifera model, cores, and OGCM/foraminifera model minus cores	156
6.31	CGCM grid box maps of LGM – PD annual $\delta^{18}\text{O}_c$ of planktonic foraminifera <i>G. sacculifer</i> in OGCM/foraminifera model, cores, and OGCM/foraminifera model minus cores	157
6.32	CGCM grid box maps of LGM – PD annual $\delta^{18}\text{O}_c$ of planktonic foraminifera <i>G. ruber</i> (white) in OGCM/foraminifera model, cores, and OGCM/foraminifera model minus cores	158
6.33	CGCM grid box maps of LGM – PD annual $\delta^{18}\text{O}_c$ of planktonic foraminifera <i>G. ruber</i> (pink) in OGCM/foraminifera model, cores, and OGCM/foraminifera model minus cores	159
6.34	CGCM grid box maps of LGM – PD annual $\delta^{18}\text{O}_c$ of planktonic foraminifera <i>G. bulloides</i> in OGCM/foraminifera model, cores, and OGCM/foraminifera model minus cores	160
6.35	CGCM grid box maps of LGM – PD annual $\delta^{18}\text{O}_c$ of planktonic foraminifera <i>N. pachyderma</i> (sinistral) in OGCM/foraminifera model, cores, and OGCM/foraminifera model minus cores	161
6.36	CGCM grid box maps of LGM – PD annual $\delta^{18}\text{O}_c$ of planktonic foraminifera <i>N. pachyderma</i> (dextral) in OGCM/foraminifera model, cores, and OGCM/foraminifera model minus cores	162

6.37	CGCM grid box maps of LGM – PD annual $\delta^{18}\text{O}$ of AGCM precipitation, ice core H_2O , and AGCM precipitation minus ice core H_2O . .	163
6.38	LGM – PD OGCM/foraminifera model annual $\delta^{18}\text{O}_c$ versus ocean sediment core foraminifera $\delta^{18}\text{O}_c$ and LGM – PD AGCM annual snow $\delta^{18}\text{O}_i$ versus ice core H_2O $\delta^{18}\text{O}$	164
6.39	CGCM grid box maps of LGM annual $\delta^{18}\text{O}_c$ of benthic foraminifera <i>C. wuellerstorfi</i> in OGCM/foraminifera model, cores, and OGCM/foraminifera model minus cores	167
6.40	CGCM grid box maps of LGM annual $\delta^{18}\text{O}_c$ of planktonic foraminifera <i>G. sacculifer</i> in OGCM/foraminifera model, cores, and OGCM/foraminifera model minus cores	168
6.41	CGCM grid box maps of LGM annual $\delta^{18}\text{O}_c$ of planktonic foraminifera <i>G. ruber</i> (white) in OGCM/foraminifera model, cores, and OGCM/foraminifera model minus cores	169
6.42	CGCM grid box maps of LGM annual $\delta^{18}\text{O}_c$ of planktonic foraminifera <i>G. ruber</i> (pink) in OGCM/foraminifera model, cores, and OGCM/foraminifera model minus cores	170
6.43	CGCM grid box maps of LGM annual $\delta^{18}\text{O}_c$ of planktonic foraminifera <i>G. bulloides</i> in OGCM/foraminifera model, cores, and OGCM/foraminifera model minus cores	171
6.44	CGCM grid box maps of LGM annual $\delta^{18}\text{O}_c$ of planktonic foraminifera <i>N. pachyderma</i> (sinistral) in OGCM/foraminifera model, cores, and OGCM/foraminifera model minus cores	172
6.45	CGCM grid box maps of LGM annual $\delta^{18}\text{O}_c$ of planktonic foraminifera <i>N. pachyderma</i> (dextral) in OGCM/foraminifera model, cores, and OGCM/foraminifera model minus cores	173
6.46	CGCM grid box maps of LGM annual $\delta^{18}\text{O}$ of AGCM precipitation, ice core H_2O , and AGCM precipitation minus ice core H_2O	174
6.47	LGM OGCM/foraminifera model annual $\delta^{18}\text{O}_c$ versus ocean sediment core foraminifera $\delta^{18}\text{O}_c$ and LGM AGCM annual snow $\delta^{18}\text{O}_i$ versus ice core H_2O $\delta^{18}\text{O}$	175

6.48	CGCM grid box maps of annual bottom OGCM $\delta^{18}\text{O}_w$ for LGM, PD, and LGM – PD	180
6.49	CGCM grid box maps of annual bottom OGCM in situ temperature for LGM, PD, and LGM – PD	182
6.50	CGCM grid box maps of annual surface OGCM $\delta^{18}\text{O}_w$ for LGM, PD, and LGM – PD	183
6.51	CGCM grid box maps of annual surface OGCM in situ temperature for LGM, PD, and LGM – PD	184
6.52	CGCM grid box maps of annual surface OGCM salinity for LGM, PD, and LGM – PD	185
6.53	CGCM grid box maps of annual OGCM sea ice concentration for LGM, PD, and LGM – PD	186
6.54	CGCM grid box maps of annual AGCM precipitation $\delta^{18}\text{O}$ for LGM, PD, and LGM – PD	187
6.55	CGCM grid box maps of annual AGCM precipitation rate for LGM, PD, and LGM – PD	189
7.1	CGCM grid box maps of LGM – PD annual bottom ocean $\delta^{18}\text{O}_w$ for OGCM, pore water and OGCM minus pore water	193
7.2	LGM – PD annual bottom OGCM $\delta^{18}\text{O}_w$ versus ocean sediment core pore water $\delta^{18}\text{O}$	194
7.3	CGCM grid box maps of LGM – PD August SSTs for OGCM, CLIMAP, and OGCM minus CLIMAP	197
7.4	CGCM grid box maps of LGM – PD February SSTs for OGCM, CLIMAP, and OGCM minus CLIMAP	198
7.5	CGCM grid box maps of $U_{37}^{K'}$ LGM – PD SSTs and CLIMAP minus $U_{37}^{K'}$ LGM – PD SSTs for August and February	203
7.6	LGM – PD CLIMAP SSTs versus $U_{37}^{K'}$ SSTs and LGM – PD OGCM SSTs versus $U_{37}^{K'}$ SSTs	204
7.7	CGCM grid box maps of OGCM minus $U_{37}^{K'}$ LGM – PD SSTs for annual, August, and February	205

7.8	CGCM grid box maps of Mg/Ca LGM – PD SSTs and CLIMAP minus Mg/Ca LGM – PD SSTs for August and February	207
7.9	LGM – PD CLIMAP SSTs versus Mg/Ca SSTs and LGM – PD OGCM SSTs versus Mg/Ca SSTs	208
7.10	CGCM grid box maps of OGCM minus Mg/Ca LGM – PD SSTs for annual, August, and February	210
7.11	CGCM grid box maps of CLIMAP August SSTs for LGM and PD .	214
7.12	CGCM grid box maps of CLIMAP February SSTs for LGM and PD	215
7.13	CGCM grid box maps of OGCM August sea ice concentration for LGM and PD	216
7.14	CGCM grid box maps of OGCM February sea ice concentration for LGM and PD	217
7.15	Depth-latitude sections of annual Atlantic OGCM meridional overturning circulation streamfunction for LGM and PD	219
7.16	CGCM grid box maps of annual AGCM precipitation minus evaporation for LGM, PD and LGM – PD	221
7.17	CGCM grid box maps of annual surface OGCM current speeds and vectors for LGM, PD and LGM – PD	222
7.18	CGCM grid box maps of annual surface AGCM wind speeds and vectors for LGM, PD and LGM – PD	223
7.19	CGCM grid box maps of annual surface AGCM temperature for LGM, PD and LGM – PD	226
7.20	CGCM grid box maps of annual surface OGCM heat flux for LGM, PD and LGM – PD	227
7.21	Plot, with linear regressions, of 100-year mean annual AGCM precipitation $\delta^{18}\text{O}_i$ versus 100-year mean annual surface AGCM temperature in PD and LGM Greenland grid boxes and of annual AGCM precipitation $\delta^{18}\text{O}_i$ versus annual surface AGCM temperature in grid box [29,42] for each of the 100 sampled years of the LGM and PD simulations .	231
8.1	Latest mean global/annual OGCM potential temperature versus model years at selected OGCM levels for PD and LGM runs	235

8.2	Latest mean global/annual salinity versus model years at selected OGCM levels for PD and LGM runs	236
8.3	Latest mean global/annual OGCM $\delta^{18}\text{O}_w$ versus model years at selected OGCM levels for PD and LGM runs	237
8.4	Latest annual NAMOC streamfunction value at OGCM grid box lat# 35, level 10 versus model years for PD and LGM runs	238

List of Tables

2.1	Summary of the effects on $\delta^{18}\text{O}$ of fractionation at the water phase change interfaces of the hydrological system	7
4.1	Atmospheric concentrations of the most important non-water-vapor greenhouse gases for PD, LGM and deglaciation eras	48
4.2	Orbital parameters of obliquity, eccentricity, and longitude of perihelion relative to the moving vernal equinox for PD, LGM, and suggested Deglaciation eras	53
4.3	Amplitudes, rates, phases, and corresponding periods of largest amplitude terms in series expansion for obliquity	54
4.4	Amplitudes, rates, phases, and corresponding periods of largest amplitude terms in series expansion for eccentricity	55
4.5	Amplitudes, rates, phases, and corresponding periods of largest amplitude terms in series expansion for longitude of perihelion relative to the moving vernal equinox	56
4.6	CGCM metagrid straits characteristics for PD topography	65
4.7	CGCM metagrid straits characteristics of the LGM topography	71
6.1	Calculation of PD mass-weighted mean ocean $\delta^{18}\text{O}_w$ bias of OGCM compared to observations	124
6.2	Estimate of locational bias and numerical error using PD mean OGCM $\delta^{18}\text{O}_w$ from mass-weighted averaging all grid boxes	124
6.3	Calculation of PD mass-weighted mean surface ocean $\delta^{18}\text{O}_w$ bias of OGCM compared to observations	124

6.4	Calculation of PD mass-weighted mean bottom ocean $\delta^{18}\text{O}_w$ bias of OGCM compared to observations	125
6.5	Calculation of PD mass-weighted mean surface ocean in situ temperature bias of OGCM compared to observations	126
6.6	Calculation of PD mass-weighted mean bottom ocean in situ temperature bias of OGCM compared to observations	126
6.7	Calculation of PD mass-weighted mean ocean in situ temperature bias of OGCM compared to observations	127
6.8	Calculation of PD mass-weighted mean precipitation $\delta^{18}\text{O}$ bias of AGCM compared to observations	127
6.9	Calculation of PD mass-weighted mean <i>C. wuellerstorfi</i> $\delta^{18}\text{O}_c$ mismatch of OGCM/foraminifera model compared to ocean sediment coretops	142
6.10	Calculation of PD mass-weighted mean <i>G. sacculifer</i> $\delta^{18}\text{O}_c$ mismatch of OGCM/foraminifera model compared to ocean sediment coretops	143
6.11	Calculation of PD mass-weighted mean <i>G. ruber</i> (white) $\delta^{18}\text{O}_c$ mismatch of OGCM/foraminifera model compared to ocean sediment coretops	143
6.12	Calculation of PD mass-weighted mean <i>G. ruber</i> (pink) $\delta^{18}\text{O}_c$ mismatch of OGCM/foraminifera model compared to ocean sediment coretops	144
6.13	Calculation of PD mass-weighted mean <i>G. bulloides</i> $\delta^{18}\text{O}_c$ mismatch of OGCM/foraminifera model compared to ocean sediment coretops	144
6.14	Calculation of PD mass-weighted mean <i>N. pachyderma</i> (sinistral) $\delta^{18}\text{O}_c$ mismatch of OGCM/foraminifera model compared to ocean sediment coretops	145
6.15	Calculation of PD mass-weighted mean <i>N. pachyderma</i> (dextral) $\delta^{18}\text{O}_c$ mismatch of OGCM/foraminifera model compared to ocean sediment coretops	145
6.16	Analysis of possible reduced model/data PD mass-weighted mean <i>G. sacculifer</i> $\delta^{18}\text{O}_c$ mismatch due to foraminifera model bias	147

6.17	Analysis of possible reduced model/data PD mass-weighted mean <i>G. ruber</i> (white) $\delta^{18}\text{O}_c$ mismatch due to foraminifera model bias	147
6.18	Analysis of possible reduced model/data PD mass-weighted mean <i>G. ruber</i> (pink) $\delta^{18}\text{O}_c$ mismatch due to foraminifera model bias	148
6.19	Analysis of possible reduced model/data PD mass-weighted mean <i>G. bulloides</i> $\delta^{18}\text{O}_c$ mismatch due to foraminifera model bias	148
6.20	Analysis of possible reduced model/data PD mass-weighted mean <i>N. pachyderma</i> (sinistral) $\delta^{18}\text{O}_c$ mismatch due to foraminifera model bias . . .	149
6.21	Analysis of possible reduced model/data PD mass-weighted mean <i>N. pachyderma</i> (dextral) $\delta^{18}\text{O}_c$ mismatch due to foraminifera model bias . . .	149
6.22	Calculation of PD mass-weighted mean snow/ice $\delta^{18}\text{O}_i$ mismatch of AGCM compared to ice coretops	150
6.23	Calculation of real LGM mass-weighted mean ocean $\delta^{18}\text{O}_w$ from <i>C. wuellerstorfi</i> $\delta^{18}\text{O}_c$	151
6.24	Calculation of real LGM mass-weighted mean ocean $\delta^{18}\text{O}_w$ from <i>G. sacculifer</i> $\delta^{18}\text{O}_c$	152
6.25	Calculation of real LGM mass-weighted mean ocean $\delta^{18}\text{O}_w$ from <i>G. ruber</i> (white) $\delta^{18}\text{O}_c$	152
6.26	Calculation of real LGM mass-weighted mean ocean $\delta^{18}\text{O}_w$ from <i>G. ruber</i> (pink) $\delta^{18}\text{O}_c$	153
6.27	Calculation of real LGM mass-weighted mean ocean $\delta^{18}\text{O}_w$ from <i>G. bulloides</i> $\delta^{18}\text{O}_c$	153
6.28	Calculation of real LGM mass-weighted mean ocean $\delta^{18}\text{O}_w$ from <i>N. pachyderma</i> (sinistral) $\delta^{18}\text{O}$	154
6.29	Calculation of real LGM mass-weighted mean ocean $\delta^{18}\text{O}_w$ from snow/ice $\delta^{18}\text{O}_i$	154
6.30	Estimate of numerical error using LGM mean OGCM $\delta^{18}\text{O}_w$ from mass-weighted averaging all grid boxes	176
6.31	Calculation of LGM mass-weighted mean <i>C. wuellerstorfi</i> $\delta^{18}\text{O}_c$ mismatch of OGCM/foraminifera model compared to ocean sediment cores	176
6.32	Calculation of LGM mass-weighted mean <i>G. sacculifer</i> $\delta^{18}\text{O}_c$ mismatch of OGCM/foraminifera model compared to ocean sediment cores . .	177

6.33	Calculation of LGM mass-weighted mean <i>G. ruber</i> (white) $\delta^{18}\text{O}_c$ mismatch of OGCM/foraminifera model compared to ocean sediment cores	177
6.34	Calculation of LGM mass-weighted mean <i>G. ruber</i> (pink) $\delta^{18}\text{O}_c$ mismatch of OGCM/foraminifera model compared to ocean sediment cores	177
6.35	Calculation of LGM mass-weighted mean <i>G. bulloides</i> $\delta^{18}\text{O}_c$ mismatch of OGCM/foraminifera model compared to ocean sediment cores . .	178
6.36	Calculation of LGM mass-weighted mean <i>N. pachyderma</i> (sinistral) $\delta^{18}\text{O}_c$ mismatch of OGCM/foraminifera model compared to ocean sediment cores	178
6.37	Calculation of LGM mass-weighted mean <i>N. pachyderma</i> (dextral) $\delta^{18}\text{O}_c$ mismatch of OGCM/foraminifera model compared to ocean sediment cores	178
6.38	Calculation of LGM mass-weighted mean snow/ice $\delta^{18}\text{O}_i$ mismatch of AGCM compared to ice cores	179
7.1	August, February and annual LGM – PD average temperatures/standard deviations of tropical American surface AGCM grid boxes at available elevations, of surrounding tropical Pacific/Atlantic surface OGCM grid boxes, and of CLIMAP surrounding sea surface	212
7.2	Single-value North Atlantic meridional overturning streamfunction for existing CGCM simulations of LGM and PD	224

Acknowledgements

First and foremost I would like to thank the members of my committee: David Rind (advisor), Gavin Schmidt and Jean Lynch-Stieglitz. In particular, Gavin has provided significant help in many areas over several years. I would also like to thank those who created, maintain, and contribute to PANGAEA, whose online database and help made the compiling of my ocean sediment core $\delta^{18}\text{O}$ database much easier. Thanks too to Wally Broecker and Rick Fairbanks for courses and talks that informed and spurred my thinking about paleoclimate. Finally, thanks to Stan Jacobs for my research cruise experience, which made climate and research a lot more real for me.

Dedication

To my parents, for having been very understanding about my interest in things they say they don't much understand, and to my grandmother, for making me walk a million miles to the library.

Chapter 1

Introduction

Over the past several hundred thousand years the world has experienced alternating eras of cold glacial and warm interglacial climates, as indicated by numerous climate proxy records. These have occurred in major cycles of approximately 100,000 years and have been correlated with Milankovitch cycles (see for example Berger et al. 1984), which are variations in insolation due to changes over millennia in the Earth's orbital characteristics of eccentricity, obliquity and precession. Despite the oft-cited correlation with Milankovitch cycles, the causes and characteristics of the glacial-interglacial cycles are still not well understood. An understanding is important because these involve large, relatively-rapid climate changes and if they are not comprehended little confidence can be placed in present day predictions of anthropogenic climate change, which indeed will occur on a background of these glacial-interglacial cycles. Past climate transitions, the change from one relatively stable climate state to another, are often difficult to study, precisely because they were in transition. As a start then, the transition's stable beginning and ending states must be understood as much as possible, particularly in comparison to each other. Further, in paleoclimate research the more recent the better with respect to the availability of climate proxy data for studying a past climate era. Thus, as stable end states of the most recent glacial-interglacial transition (the Deglaciation), research into the Last Glacial Maximum (LGM, 21,000 calendar years before present, 21 kyBP) in comparison to the Holocene (as represented by present day, PD, 1978 A.D.) is the best choice to study glacial-interglacial cycles.

From previous studies of the LGM compared to PD several important larger questions have arisen and persisted, to be addressed again and again as new paleoclimate techniques develop, as is the case with this research.

- 1) How much did mean ocean $\delta^{18}\text{O}$ change from the LGM to PD?
- 2) Are the LGM to PD changes in tropical SSTs determined by CLIMAP consistent with other proxies and models?
- 3) How did the North Atlantic meridional overturning circulation change from the LGM to PD?
- 4) Are the temporal and spatial relationships of surface air temperature versus precipitation $\delta^{18}\text{O}$ the same?

These are “larger” questions in the sense that they involve several different proxies, climate variables, and/or subquestions. Addressing them, as was done in this work, is a useful way to approach studying the climate of the LGM compared to PD. The background of these important questions will be discussed later but briefly, the first and fourth questions relate to how much temperature and glacier ice volume change with climate change; the second, to the role of the tropics in climate change; and the third, to changes in the thermohaline circulation with climate change. They are thus all very topical with regards to current concerns about global warming.

The relative recentness of the LGM still does not mean there is enough climate proxy data to understand it well. It is a global climate state and given the expense, physical difficulty, and time involved in gathering climate proxy data from even a single site there never will be enough. Furthermore, the climate system involves many factors and the climate proxies that there are address only a few. Worse, most likely each climate proxy was actually affected by several climate factors in an unknown combination. Drawing global paleoclimate inferences from climate proxy data from just a few sites, addressing just a few, but mixed, factors is problematic at best. General circulation models (GCMs) can include the many climate factors in a physically-consistent way over the entire globe. While their boundary conditions can be realistic, their simulation results still need to be compared to (verified with) the real world. For paleoclimate simulations this means climate proxy data. Typically, the climate inferences from proxy data are what is compared to the GCM results but as described this is problematic. A better new technique, the central one of this research,

is to develop models of how the proxies are affected by all the relevant climate factors and input the GCM climate simulation results into these climate proxy models, then compare the proxy model results directly to the climate proxy data, i.e., “forward modelling”. This is a more powerful and physically-consistent way of drawing global paleoclimate inferences from climate proxy data from just a few sites. This technique can also be used for PD, in addition to verifying with PD observational climate data.

One strength of this technique is that many different proxies can be modelled and brought together in a common physically-consistent framework. In this work though, as a first step, just the $\delta^{18}\text{O}$ of ocean sediment core foraminifera shell CaCO_3 and ice core H_2O were used. These will be described in detail in later chapters but it should be noted here that one major reason they were chosen was because they are the most widespread and abundant of the proxies (thus also the most influential). This is important because even with this technique it is best to have for comparison as much and as geographically diverse climate proxy data as possible and a necessary, large part of this work was the compilation of this ocean sediment and ice core $\delta^{18}\text{O}$ data.

A proxy model of $\delta^{18}\text{O}$ of foraminifera shell CaCO_3 must have the $\delta^{18}\text{O}$ of the GCM ocean water as one of its inputs from the GCM. Similarly, for comparison to the $\delta^{18}\text{O}$ of ice H_2O the $\delta^{18}\text{O}$ of GCM precipitation must be available. This means that the GCM must have both an ocean and atmosphere and that ^{18}O must be carried as a water tracer in both. A coupled ocean-atmosphere GCM fully carrying ^{18}O as a water tracer was recently developed and used in this research.

Inclusion of an ocean GCM (OGCM) with an atmospheric GCM (AGCM) into a coupled GCM (CGCM) adds severe computational burdens. Unlike an AGCM, which will run to equilibrium within a few model years, an OGCM may take hundreds or even thousands of model years to run to equilibrium. For credibility, especially for questions related to the deep ocean, the OGCM must be run to equilibrium. This applies to both paleo and PD simulations. Given the prohibitive computer time normally necessary to run for hundreds or thousands of model years, running the OGCM to equilibrium requires the use of acceleration techniques. A major part of this work then was implementing and testing acceleration techniques for the CGCM.

Researching and implementing realistic LGM and PD boundary conditions for

the CGCM was also a major task of this work. Compared to PD, at the LGM sea level was about 120 m lower. This meant different land/ocean boundaries then (i.e., more land), including the closing of straits. The water from the reduced sea level was locked up in increased continental glaciers then, which changed the land topography and surface characteristics. Recent research into sea level change, isostasy and past histories of inland seas provided for realistic reconstruction of these CGCM boundary conditions. Changes in insolation with changes in the Earth's orbit over millenia — the Milankovitch cycles — are accurately known and were implemented as CGCM boundary conditions appropriately for the LGM and PD. The concentrations of the most important non-water greenhouse gases (carbon dioxide, chlorofluorocarbons, methane and nitrous oxide) were lower at the LGM compared to PD. These concentrations have been well-determined from recent ice core research and could thus be accurately set in the CGCM for the LGM and PD. Not nearly as well-determined as any of the preceding are the non-glacier land surface changes (e.g., vegetation) and the atmospheric aerosols changes, so for the LGM these were essentially left the same as PD in the CGCM.

The preceding — the science questions addressed and the research done to address them — outlines this dissertation (along the way, information for possible future work will also be given). Given its importance in this work, following first is a discussion of water isotopes, of which ^{18}O is the primary one.

Chapter 2

Water Isotopes

2.1 H₂O

2.1.1 Oxygen and Hydrogen Isotopes

“Water isotopes” refer to the isotopes of oxygen and hydrogen in H₂O (“water”) in its liquid, gas or solid phases (i.e., water, vapor or ice) in the Earth’s hydrological system. There are three natural stable isotopes of oxygen. ¹⁶O is the lightest and by far the most abundant at about 99.76% of oxygen found in nature (all abundances from Bradley 1985). ¹⁸O is the heaviest oxygen isotope, rare at about 0.2% of oxygen found in nature, and is the primary isotope of interest here. ¹⁷O is the middleweight oxygen isotope but rarest at about 0.04% of oxygen found in nature. While ¹⁷O is of interest for atmospheric O₂ research (e.g., see Luz et al. 1999), it is little used in water isotope research since it tends just to parallel ¹⁸O in the hydrological system but being lighter and less abundant has less detectable effects. It is thus not included in this work. For oxygen then, the two water isotopes of interest here are H₂¹⁶O and H₂¹⁸O. ¹⁸O (i.e., H₂¹⁸O) is measured in proportion to ¹⁶O (i.e., H₂¹⁶O) due to the nature of mass spectrometers, with which it is usually measured. Further, for comparisons this ratio/concentration is usually in reference to a standard ratio, that of Standard Mean Ocean Water (SMOW). Finally, since H₂¹⁶O is far more abundant than H₂¹⁸O, to avoid very small numbers a factor of 1000 is included so that ¹⁸O in H₂O is measured

in units of permil (‰) as:

$$\delta^{18}O_{H_2O} = \left[\frac{\left(\frac{^{18}O}{^{16}O} \right)_{H_2O}}{\left(\frac{^{18}O}{^{16}O} \right)_{SMOW}} - 1 \right] \times 1000$$

A positive $\delta^{18}O_{H_2O}$ means more ^{18}O (“enriched”, “heavier”) compared to SMOW and a negative $\delta^{18}O_{H_2O}$ means less ^{18}O (“depleted”, “lighter”) compared to SMOW. SMOW itself, which based on samples from the deep ocean is assumed to be that of average water of the PD ocean, has $\delta^{18}O_w = 0‰$.

There are two natural stable isotopes of hydrogen and one radioactive one. 1H , which is stable, is the lightest and by far the most abundant of the three at about 99.984% of hydrogen found in nature. 2H , which is also stable, is usually referred to as deuterium and thus written symbolically as D instead of 2H . At 0.016% of hydrogen found in nature, this middleweight hydrogen isotope is quite rare. It and 1H are the hydrogen isotopes of interest here. 3H , usually referred to as tritium (T), is the heaviest of the hydrogen isotopes but is radioactive with a half-life of only 12.45 years. This makes it unsuitable for paleoclimate research. For hydrogen then, the two water isotopes of interest here are 1H_2O and 1HDO . Similarly to ^{18}O and ^{16}O , D in H_2O (i.e., 1HDO) is measured in proportion to H (i.e., 1H_2O) in units of permil (‰) as:

$$\delta D_{H_2O} = \left[\frac{\left(\frac{^1HDO}{^1H_2O} \right)_{H_2O}}{\left(\frac{^1HDO}{^1H_2O} \right)_{SMOW}} - 1 \right] \times 1000$$

Because combinations in H_2O of the rare isotopes of oxygen and hydrogen are even rarer, they are not of concern. Thus the water isotopes considered in this work are $^1H_2^{16}O$, $^1H_2^{18}O$, and $^1HD^{16}O$.

2.1.2 Fractionation

As they compose the water itself, water isotopes can be used as tracers throughout the Earth’s complete hydrological system: ocean, atmosphere, land water and glaciers/sea ice. However, to do so there must be some way of using them to figure out where the water has travelled from. Unlike “transient tracers” like CFCs, which are added to the system at a particular place and time, the stable water isotopes are “steady-state tracers” like salt, which are always in the system (the radioactive water isotope

Phase Change	Hydrological System Occurrence	Resulting Relative $\delta^{18}\text{O}$	In Other Words
liquid \rightarrow gas	ocean \rightarrow atmo evaporation land \rightarrow atmo evaporation	$\delta^{18}\text{O}_w > \delta^{18}\text{O}_v$	Vapor depleted compared to water
gas \rightarrow liquid	condensation of rain	$\delta^{18}\text{O}_v < \delta^{18}\text{O}_w$	Rain enriched compared to vapor
gas \rightarrow solid	condensation of snow	$\delta^{18}\text{O}_v < \delta^{18}\text{O}_i$	Snow enriched compared to vapor
liquid \rightarrow solid	sea ice formation	$\delta^{18}\text{O}_w < \delta^{18}\text{O}_i$	Ice enriched compared to water
solid \rightarrow gas	glacier/sea ice sublimation	$\delta^{18}\text{O}_i > \delta^{18}\text{O}_v$	Vapor depleted compared to ice
solid \rightarrow liquid	glacier/sea ice melting	$\delta^{18}\text{O}_i = \delta^{18}\text{O}_w$	No fractionation ¹

Table 2.1: Summary of the effects on $\delta^{18}\text{O}$ (same for δD) of fractionation at the water phase change interfaces of the hydrological system

with tritium would be a transient tracer). Like salt, the stable water isotopes are used by means of their changing concentrations to trace water from its phase change interfaces in the system. Unlike salt, whose changing concentration at these interfaces is generally just a matter of being completely left behind in the liquid water, the water isotopes are in all water phases of the hydrological system. Further, their changing non-zero concentrations on each side of the water phase change interfaces are due to the preferential exchange of one water isotope over another at the interfaces, i.e., fractionation. The preference is that the heavier water isotopes, $^1\text{H}_2^{18}\text{O}$ and $^1\text{HD}^{16}\text{O}$, tend more toward the lower energy water phase than the lighter water isotope $^1\text{H}_2^{16}\text{O}$.

For the details of the theory of the effects of fractionation at the water phase change interfaces of the hydrological system see for example Gat 1996 and references therein but Table 2.1 is a summary of the effects for $\delta^{18}\text{O}$; for δD it is the same. The ordering of Table 2.1 is roughly from most (top) to least (bottom) important in the hydrological system. Particularly for the top three phase changes, it is very important to note that the fractionation effects are inversely and strongly temperature dependent, with colder temperatures resulting in increased fractionation. Note also that ocean to atmosphere evaporation tends to affect salinity in the same way as it affects $\delta^{18}\text{O}_w$.

¹Due to the very low rate of isotopic diffusion in the solid (ice).

2.1.3 Global Isotopic Variation

While the details of precipitation formation from water vapor are complicated, the preceding is enough to understand the resulting general global isotopic variation of atmospheric water vapor and precipitation. First, there is a “latitude effect” where, from vapor-depleting evaporation over ocean/land water at lower latitudes², there is a net vapor transport to high latitudes, with the vapor becoming increasingly depleted as it precipitates as it gets colder with latitude. Precipitation is more enriched than its source vapor but since the source vapor is getting more depleted so is the precipitation. At high latitudes where thick glaciers lie this depletion is enhanced by the “altitude effect” wherein adiabatic cooling with altitude has a similar depleting effect. Also similarly, in that it is strongly related to temperature, there is a “continental effect” whereby depletion increases with increasing downwind distance inland (since, for example, given continental versus maritime climates it is generally colder farther from the ocean in winter). Given the temperature control there is of course also a seasonal effect. Finally, and also related to temperature, there is an “amount (or rate) effect” in precipitation whereby the more precipitation falls at a location the more depleted it is. Many of these effects on precipitation $\delta^{18}\text{O}$ can be seen in Figure 6.15.

The general global isotopic variation of ocean water is less (although ultimately) due directly to fractionation at water phase change interfaces than is atmospheric water vapor and precipitation. Instead there are large effects from mixing with waters of different $\delta^{18}\text{O}$ and δD . First, as discussed, precipitation, falling in a well-known general pattern over the ocean, will tend to be depleted compared to ocean water. Second, since it stems from precipitation falling over land, river water flowing into the ocean at well-known locations will also tend to be depleted compared to ocean water. Third, as glaciers are accumulations of precipitation that fell over land, glacial (and iceberg) meltwater flowing into the ocean at high-latitudes will tend to be depleted compared to ocean water. Finally, these waters and waters with different $\delta^{18}\text{O}$ (and δD) more directly due to fractionation at phase change interfaces will be moved and mixed throughout the ocean by well-known currents, convection and upwelling. Some of these effects on surface ocean water $\delta^{18}\text{O}$ can be seen in Figure 6.10. Note again

²At latitudes as low as those of the Hadley Cell there is a net vapor transport equatorward.

that all this will also tend to affect salinity in the same way as it affects ocean water $\delta^{18}\text{O}$ and δD .

Over millennia, fractionation from evaporation over the ocean and mixing throughout the ocean can increase the mean ocean $\delta^{18}\text{O}_w$ and δD_w if precipitation tends to accumulate in continental glaciers and be removed from the ocean. Conversely, if the glaciers melt, the mean ocean $\delta^{18}\text{O}_w$ and δD_w decreases. The latter is the case for the Deglaciation. The former is the case for the Last Glacial Maximum and is the case of interest in this work. Going into the LGM the continental glaciers had grown several kilometers thicker than PD and sea level had fallen ≈ 120 m lower than PD (Fairbanks 1989), which made the mean ocean $\delta^{18}\text{O}_w = 1.25\text{‰}$ (an estimate stated in Guilderson et al. 1994 based on a figure in Fairbanks 1989), compared to 0.00‰ for PD. The LGM mean ocean δD_w is estimated to have been 10‰ , based on the generally observed 8X relationship between $\delta^{18}\text{O}$ and δD in the hydrological system³. With the source ocean water enriched at the LGM, it might seem that on average the snow falling on the glaciers then must also have been enriched compared to PD. However, the LGM was generally colder than PD and this meant increased fractionation effects during ocean/land water evaporation, which is most important. The result was that LGM precipitation was on average depleted compared to PD (this further enhanced LGM ocean water enrichment). Finally, note again, but for the LGM case, that there must have been a similar effect on salinity as on ocean water $\delta^{18}\text{O}$ and δD and the removal of ocean water with all its salt left behind implies an increased mean ocean salinity at the LGM.

2.1.4 In GCMs

While the global isotopic variation can be generally understood, at any particular place or time there are numerous effects combined in an unknown way so that the reasons a sample of precipitation or ocean water at a particular location at a particular time has the exact $\delta^{18}\text{O}$ or δD it has is far from obvious. A coupled GCM carrying water isotopes as tracers, with the described important water isotope fractionations,

³From the “meteoric water line”. The difference from an exact 8X relationship is known as the “deuterium excess” and is of interest in water isotope research but not in this work because there is relatively little deuterium proxy data.

can help sort out all the factors. Water isotopes then, were added to the OGCM and AGCM of the CGCM used here (see Chapter 3 for GCM descriptions); for implementation details, primarily for the OGCM, see Schmidt 1999. $^1\text{H}_2^{16}\text{O}$, $^1\text{H}_2^{18}\text{O}$, and $^1\text{HD}^{16}\text{O}$ were all added and were run in the PD and LGM simulations. However, for deuterium (i.e., $^1\text{HD}^{16}\text{O}$) there is little observed or proxy data to compare with (as will be seen in the next section, it is not even in some important types of proxies) so it is not considered much in this work.

As can be seen in the following brief history of water isotope tracers in GCMs, the work here is quite unique in using water isotope tracers in a coupled GCM of moderately-high horizontal resolution (5° longitude x 4° latitude; see Section 3.3.1) to do full PD and LGM simulations run to near-equilibrium and compared to observations and ocean sediment/ice core $\delta^{18}\text{O}$ data.

Joussaume et al. 1984 pioneered the use of water isotope tracers in GCMs using a coarse resolution ($\approx 11.25^\circ$ x 7.5°) atmospheric GCM (Laboratoire de Météorologie Dynamique; LMD) simulating a perpetual PD January. Jouzel et al. 1987 used a similarly coarse (10° x 8°) atmospheric GCM (Goddard Institute for Space Studies; GISS) with water isotope tracers but simulated a full PD seasonal cycle. Experiments to test the sensitivity of the water isotope results to changes in the parameterizations of hydrological processes in this GISS AGCM were then done in Jouzel et al. 1991 for a perpetual PD July. All three works used comparisons to PD observations and established the viability of using water isotope tracers in AGCMs for PD simulations.

As a start at simulating changed climates using GCMs with water isotope tracers, in Cole et al. 1993 the mentioned GISS AGCM was given specified SSTs from contrasting extreme ENSO phases during the 20th-century and perpetual January and July simulations were compared to observations. A number of papers then showed the paleoclimatic possibilities of using GCMs with water isotope tracers by doing LGM simulations (usually in conjunction with a PD control simulation). Joussaume and Jouzel 1993 did perpetual February and August LGM simulations using an $\approx 5.6^\circ$ x 3.6° version of the LMD AGCM of the mentioned Joussaume et al. 1984 and, anticipating this work, compared them to ice core data. Jouzel et al. 1994 did an LGM simulation using the coarse GISS AGCM of the mentioned Jouzel et al. 1987 and compared it to ice core data. With an emphasis on the Greenland ice core

record, Charles et al. 1994 did an LGM simulation using a $5^\circ \times 4^\circ$ version of the GISS AGCM. With an emphasis on the Asian monsoon, Hoffmann and Heimann 1997 did an LGM simulation using a $2.8^\circ \times 2.8^\circ$ AGCM (ECHAM3) carrying water isotope tracers.

While Hoffmann and Heimann 1997 used a higher resolution GCM than in this work, it was still an atmosphere-only GCM. Water isotope tracers in ocean GCMs began with Schmidt 1998, which used a $5^\circ \times 4^\circ$ OGCM (the direct ancestor of the GISS OGCM used in this work) carrying water isotope tracers to do a PD simulation and compared it to observations. However, the simulation only ran 60 model years so was almost certainly not equilibrated (equilibrium discussed in Chapter 3). Paul et al. 1999 did a PD simulation compared to observations using an $\approx 3.6^\circ \times 1.8^\circ$ OGCM (MOM) run to equilibrium using a variable time step acceleration technique. Anticipating this work, they also compared their results to ocean proxy data (the $\delta^{18}\text{O}$ of shell CaCO_3 of benthic foraminifera from ocean sediment coretops). Delaygue et al. 2000 did a PD simulation compared to observations by first running an $\approx 8^\circ \times 4.6^\circ$ OGCM with water isotope tracers for 2000 model years and then from the end of this presumably equilibrated run, running an $\approx 4^\circ \times 2.3^\circ$ version of the OGCM for 200 more model years. Wadley et al. 2002 used a “variable resolution” OGCM to do both PD and LGM simulations by first running both for 2000 model years to quasi-equilibrium, then adding the water isotope tracers and running for another 2500 model years to isotopic quasi-equilibrium. The PD simulation was then compared to observations.

While this work using ocean-only isotopic GCMs was being done, work using atmosphere-only isotopic GCMs continued. Using the mentioned ECHAM3 AGCM of Hoffmann and Heimann 1997 at resolutions of both $2.8^\circ \times 2.8^\circ$ and $5.6^\circ \times 5.6^\circ$, Hoffmann et al. 1998 did PD simulations and compared to observations. Cole et al. 1999 expanded on the mentioned Cole et al. 1993 by doing full seasonal cycle simulations. Using both the mentioned GISS and ECHAM isotopic AGCMs, Jouzel et al. 2000 did PD and 6 kyBP simulations. Charles et al. 2001 did LGM simulations as in Charles et al. 1994 but tested different specified tropical SSTs. Characterizing a newly isotopic AGCM, Mathieu et al. 2002 did a PD simulation with an $\approx 3.75^\circ \times 3.75^\circ$ AGCM (GENESIS) and compared to observations. Examining the correlations between mod-

eled isotopic signal, temperature and precipitation in a newly isotopic AGCM, Noone and Simmonds 2002 did a PD simulation with an $\approx 5.63^\circ \times 3.25^\circ$ AGCM (MUGCM) and compared to observations.

The uniqueness of the work here is summarized in Jouzel et al. 2000: “... the full coupling of the atmospheric and oceanic isotopic models ... represents a new and exciting challenge for our scientific community.”

2.2 Proxies

While there are direct water isotope observations for PD, for comparisons with LGM and other paleoclimate simulations using CGCMs carrying water isotope tracers, paleowater proxy records are necessary. These can be grouped into ocean water proxies and precipitation proxies. For the purposes of the “forward modelling” technique central to this work — inputting CGCM climate simulation results into a climate proxy model and then comparing the proxy model results directly to the climate proxy data — one ocean water proxy, foraminifera, and one precipitation proxy, ice, are most immediately suitable and are used in this work, although the latter doesn’t require a proxy model. There are other ocean water and precipitation proxies worth mentioning here as well: corals, pore water, speleothems, tree cellulose. Some of these are candidates for future work; some don’t require proxy models and will thus be compared to briefly in this work.

Two ocean water proxies, foraminifera and corals, and one precipitation proxy, speleothems, record their ^{18}O signal in calcium carbonate (CaCO_3). Measurement of ^{18}O in CaCO_3 is similar to that in H_2O but with reference to a different standard ratio, that of PDB:

$$\delta^{18}\text{O}_{\text{CaCO}_3} = \left[\frac{\left(\frac{^{18}\text{O}}{^{16}\text{O}} \right)_{\text{CaCO}_3}}{\left(\frac{^{18}\text{O}}{^{16}\text{O}} \right)_{\text{PDB}}} - 1 \right] \times 1000$$

PDB is an acronym for PeeDee Belemnite and refers to the shell CaCO_3 of belemnites (marine mollusks) from the Pee Dee geological formation in South Carolina. The

relationship between PDB (‰) and SMOW (‰) used in this work is (Hut 1987)⁴:

$$\text{PDB} = \text{SMOW} - 0.27\text{‰}$$

2.2.1 Foraminifera and $\delta^{18}\text{O}_c$ Model

Foraminifera are shell-forming 100- μm -scale marine organisms. Foraminifera species can be either benthic or planktonic. Benthic species are ocean bottom dwellers and thus in a position to provide vital deep water information. *Cibicidoides wuellerstorfi* is the important example in this work. Planktonic species live at near-surface depths and the important examples in this work are *Globigerinoides sacculifer*, *Globigerinoides ruber* (both white and pink varieties), *Globigerina bulloides*, and *Neogloboquadrina pachyderma* (both sinistral and dextral varieties). Planktonic foraminifera have complex ecologies that vary between species and one facet of this is their habitat depth. This may be anywhere from the top of the mixed layer down through the thermocline and may depend on one or more of temperature, salinity, nutrients or light levels. The first two factors may thus imply a dependence on density and all of them may imply a seasonal dependence. Furthermore, their habitat depth may change through their life cycle. Shell formation may occur during one or more stages of their life cycles and thus at one or more habitat depths.

Foraminifera build their shells of calcium carbonate (CaCO_3) using oxygen (O) from the ocean water (H_2O). The $\delta^{18}\text{O}_c$ of their shell thus reflects the $\delta^{18}\text{O}_w$ of the ocean water they were in at the time(s) the shell was formed. Just as important, during this shell formation there is also a temperature-dependent fractionation, with colder water resulting in shell CaCO_3 more enriched in ^{18}O than warmer water, i.e., resulting in a higher $\delta^{18}\text{O}_c$. Thus, as foraminifera die, sink and accumulate as ocean sediment, a record of $\delta^{18}\text{O}$ that is an unknown combination of these two factors is created. On millennial time scales though, the source ocean water $\delta^{18}\text{O}_w$ and temperature dependence tend in most cases to reinforce each other in the $\delta^{18}\text{O}_c$ record. For example, compared to PD, LGM ocean water was on average enriched in ^{18}O , due the described glacier increase/sea level decrease, and was also on average

⁴Actually, $\delta^{18}\text{O}_{\text{PDB}}$ is quite different from $\delta^{18}\text{O}_{\text{SMOW}}$ but paleotemperature equations are based on this conversion (Jean Lynch-Stieglitz, personal communication).

colder, increasing fractionation and the percentage of ^{18}O going into foraminifera shell CaCO_3 .

Foraminifera from ocean sediment cores are the ocean water proxy concentrated on in this work, which includes a significant compilation of the available foraminifera $\delta^{18}\text{O}_c$ records (see Chapter 5 and related appendices). As part of the forward modelling technique of this work these records are for comparison to the results of the proxy model, i.e. the foraminifera $\delta^{18}\text{O}_c$ model, into which are fed the LGM and PD simulation results from the CGCM. As discussed, a CGCM carrying water isotope tracers can help sort out all the factors (see Section 2.1.3) affecting ocean water $\delta^{18}\text{O}_w$ and temperature, and thus foraminifera $\delta^{18}\text{O}_c$, at a particular location at a particular time. A foraminifera $\delta^{18}\text{O}_c$ model needs to be species-specific because the fractionation (e.g., see Bemis et al. 1998) and ecology are. It is important for a foraminifera $\delta^{18}\text{O}_c$ model to account for a foraminifera’s species-specific ecology because, as a critical example, its habitat depth may vary through its life cycle and the depth-dependent $\delta^{18}\text{O}_w$ and temperature of the water it is in when its shell forms affects its $\delta^{18}\text{O}_c$.

For the mentioned six planktonic foraminifera species, an ecological foraminifera model was developed in Schmidt 1999, “Forward modeling of carbonate proxy data from planktonic foraminifera using oxygen isotope tracers in a global ocean model”, and, more fully, Schmidt and Mulitza 2002, “Global calibration of ecological models for planktic foraminifera from coretop carbonate oxygen-18”. To do this they first defined some important ecological parameters (e.g., temperature optimum and range) and put together an observed PD ocean $\delta^{18}\text{O}_w$ database, observed PD ocean temperature and salinity climatologies, and several suggested foraminifera $\delta^{18}\text{O}_c = f(T, \delta^{18}\text{O}_w)$ equations. They then used a Monte Carlo technique to find the parameters and equation that resulted in the $\delta^{18}\text{O}_c$ predicted from them best fitting a species-specific ocean sediment coretop foraminifera $\delta^{18}\text{O}_c$ database (coretop so as to be representative of PD). The foraminifera model then consisted of the $\delta^{18}\text{O}_c$ predicted with these optimum ecological parameters and equation. It was adapted here in this work to take as input a GCM year’s worth of monthly mean ocean water temperature, $\delta^{18}\text{O}_w$, and salinity output from the CGCM and calculate which grid boxes a foraminifera species could live in and its annual $\delta^{18}\text{O}_c$ if it did.

For the mentioned one benthic foraminifera species, the ecology is relatively simple — it spends its life on the ocean bottom — and only a straightforward $\delta^{18}\text{O}_c = f(T, \delta^{18}\text{O}_w)$ relationship was necessary in the foraminifera model. This relationship was developed in this work in consultation with Jean Lynch-Stieglitz. Based on Duplessy et al. 2002, at water temperatures less than or equal to 4°C the $\delta^{18}\text{O}_c$ (‰ PDB) of *C. wuellerstorfi* shell is related to the water temperature (T_w) and $\delta^{18}\text{O}_w$ (‰ SMOW) by

$$\delta^{18}\text{O}_c = 4.225 - 0.64 - 0.28 * T_w + [\delta^{18}\text{O}_w - 0.27]$$

and based on Lynch-Stieglitz et al. 1999a, at water temperatures greater than 4°C

$$\delta^{18}\text{O}_c = 3.38 - 0.21 * T_w + [\delta^{18}\text{O}_w - 0.27]$$

In both equations the brackets enclose the mentioned conversion from the SMOW standard of $\delta^{18}\text{O}_w$ to the PDB standard of $\delta^{18}\text{O}_c$.

2.2.2 Other Ocean Water Proxies

Corals are much like foraminifera in building their aragonite structure of calcium carbonate using oxygen from the ocean water they are in, so that their $\delta^{18}\text{O}_c$ reflects the $\delta^{18}\text{O}_w$ and temperature (via fractionation) of the water at the time of structure formation. They create a $\delta^{18}\text{O}$ record in annual layers. There are species-specific fractionation and ecological factors to consider, so a proxy model would be in order, but there is not the concern about changing habitat depth since at the time of structure formation corals are fixed in one near-surface location (e.g., a reef). The global distribution of corals is more limited than for foraminifera and long $\delta^{18}\text{O}$ records are scarcer so they are not considered further in this initial work but they might be worth modelling in future work. Note too that corals were the basis of the cited Fairbanks 1989, whose results were important in this work.

Water in the pores of ocean sediment can record changes in the $\delta^{18}\text{O}_w$ (also salinity, δD_w) of the overlying ocean water and thus be used as a (deep) ocean water proxy record. Other researchers have already developed and applied a pore water model, although only for a few ocean sediment cores, and the results from it will be compared to this work's CGCM simulation results in Section 7.1, where a brief description of the technique will also be given.

2.2.3 Ice

As they are samples through the annual snowfall layers accumulated in glaciers, ice cores are frozen precipitation proxy records. Since the ice is H_2O , both $\delta^{18}\text{O}_i$ and $\delta^{18}\text{D}_i$ are available. Further, the $\delta^{18}\text{O}$ of the ice H_2O should not be confused with the $\delta^{18}\text{O}$ of the atmospheric O_2 gas trapped in the ice, which is of interest in other research (e.g., the Dole Effect; see Bender et al. 1994) but not in this work (hence the distinction made in this work of “ice H_2O $\delta^{18}\text{O}$ ”). Because the ice in a core is, to enough accuracy for this work, the original frozen precipitation, a proxy model for it is not necessary — its $\delta^{18}\text{O}$ can be compared directly. However, it should be noted that there are actually some effects (e.g., diffusion, sublimation) that can indeed alter the $\delta^{18}\text{O}$ of the original precipitation a little once it is in/on the glacier.

Ice cores are probably the most popularly-known paleowater proxy and are the precipitation proxy considered in this work, which includes a significant compilation of the available records (see Chapter 5 and related appendices). However, while they are at least roughly globally distributed, there are not many ice cores whose $\delta^{18}\text{O}_i$ record reaches back through the LGM. Further, while the upper, recent parts of ice cores typically have annual resolution via layer counting, down in the ice core as far back as the LGM, individualized glacier flow models are usually necessary for dating and so the ages become much more uncertain.

Ice H_2O $\delta^{18}\text{O}$ is typically used as a surface air temperature proxy, given the described dependence. However (and again), there are many other climate factors that can affect it and if these change over time so does the ice core $\delta^{18}\text{O}_i$ record, without any direct relationship to changes in surface air temperature. For example, the precipitation’s source ocean water $\delta^{18}\text{O}$ could change over time due to ocean or atmospheric circulation changes. As another example, annual $\delta^{18}\text{O}_i$ is the mean of precipitation falling in different amounts with different $\delta^{18}\text{O}$ at different times of the year and changes in this seasonality over time may cause non-temperature-dependent changes in the ice core $\delta^{18}\text{O}_i$ record. The known PD spatial $T = f(\delta^{18}\text{O})$ relationship is often used as a substitute for the unknown temporal $T = f(\delta^{18}\text{O})$ relationship to find paleotemperatures from ice core $\delta^{18}\text{O}_i$ records and this seasonality effect is implicated in the reason this substitution may not be valid, an important invalidity which will be shown in this work (see Section 7.4 and references therein). As a final

example, if an ice core is located along a steep spatial gradient of precipitation $\delta^{18}\text{O}$, a small movement in this gradient over time, due perhaps to a change in the mean atmospheric circulation, may also cause a non-temperature-dependent change in the ice core $\delta^{18}\text{O}_i$ record. Again, a CGCM carrying water isotope tracers can help sort out all the factors affecting precipitation $\delta^{18}\text{O}$ at a particular location at a particular time. All this is similarly true for the following other precipitation proxies.

2.2.4 Other Precipitation Proxies

Speleothems are calcitic structures in limestone caves, the major examples being stalagmites, stalagtites and flowstone slabs (for a speleothem overview see Bradley 1985). They are formed by the non-biological precipitation of CaCO_3 out of groundwater that has percolated through the overlying host rock and soil, where it acquired dissolved CaCO_3 and CO_2 from decaying organic matter. In most cases CaCO_3 precipitation is triggered by the degassing of the groundwater's CO_2 in the cave and the resulting groundwater CaCO_3 supersaturation. During this speleothem CaCO_3 precipitation, there is a temperature-dependent fractionation of the O isotopes going into the CaCO_3 , with colder cave temperatures resulting in precipitated CaCO_3 more enriched in ^{18}O , i.e., with a higher $\delta^{18}\text{O}_c$. While speleothems are generally more enriched than their source groundwater (i.e., $\delta^{18}\text{O}_c > \delta^{18}\text{O}_w$), speleothem $\delta^{18}\text{O}_c$ also varies with the $\delta^{18}\text{O}_w$ of the source groundwater, which being from atmospheric precipitation (rain or melted snow) varies as described (for a controversial example see Winograd et al. 1988). Speleothem layers (often annual) are dated using U/Th dating, since uranium also gets precipitated in speleothems in small amounts, and there are samples from the LGM. There are few speleothem $\delta^{18}\text{O}_c$ records so they are not considered further in this initial work but in future work they might be worth compiling, and the speleothems modelled, since they can begin to tie land water $\delta^{18}\text{O}$ records to those of the ocean and glaciers.

The last precipitation proxy record worth mentioning here is tree-ring cellulose (see the recent Robertson et al. 2001 and references therein). Cellulose in tree wood contains O and H isotopes derived primarily from precipitation H_2O , via root-absorbed groundwater from rain or melted snow. There is temperature-dependent fractionation involved in cellulose formation and its $\delta^{18}\text{O}$ (or δD) also reflects that

of its source precipitation. There are no tree-ring chronologies that go back to the LGM so the famed absolute annual dating via tree-rings is not available for that era. However, less-accurate radiocarbon dating is possible. Again, there are few cellulose $\delta^{18}\text{O}$ records so they are not considered further in this initial work but in future work they might be worth compiling, and the cellulose modelled, since they can begin to tie land water $\delta^{18}\text{O}$ to that of the ocean and glaciers.

Chapter 3

Quest for Equilibrium

3.1 Equilibrium

Typically in paleoclimate modelling, and as done in this work, a single experiment consists of two simulations: a PD “control” simulation and a paleosimulation, which has different boundary conditions from the PD simulation and is considered a perturbation to it. The results of the PD simulation are then subtracted from the paleosimulation to hopefully remove any biases that are inherent in the model, i.e., that exist regardless of what era it is simulating. These biases are one reason the results from a PD or paleosimulation may not directly match observations or proxies, respectively, from that era. A better match should be the paleo minus PD simulation compared to the (paleo) proxies minus observations. This differencing is equivalent to assuming linear changes. This may not be a valid assumption but this differencing is the best attempt at correction that can be made and is typically done for climate forecasting experiments as well.

However, if a simulation with a GCM has not reached its equilibrium there will be a drift towards that equilibrium. For example, the mean annual global deep ocean temperature should at equilibrium be at a fairly constant value over years but may take hundreds of years to reach this value as the effects of deep convection, heat diffusion, and advection compete. This drift is not necessarily at the same rate or even in the same direction at the same time for all fields in all simulations. The mentioned differencing will thus not remove its effect and the true (equilibrium) effect of a past

era’s non-PD boundary conditions will be difficult to distinguish from drift effect.

Unfortunately, running a simulation with a GCM to full equilibrium to eliminate this problem can take an impractically large amount of time — model time (e.g., years of the era simulated), CPU time (i.e., computer processor cycles used), and real time (i.e., time on a wall clock or calendar). Again though, just as in the real world, different parts of a GCM’s climate system equilibrate at different rates. The ocean part of a coupled ocean-atmosphere GCM (the OGCM of the CGCM), while generally requiring less CPU time to run the same model time than does the atmosphere part of the coupled GCM (the AGCM of the CGCM), takes much more model time to equilibrate. This more than negates the OGCM’s CPU time per model time advantage and makes it the seriously problematic part of the CGCM reaching equilibrium. Specifically, the deepest part of the OGCM takes the most model time to equilibrate. A longstanding rule of thumb is that the AGCM equilibrates in a model year but the deepest part of the OGCM takes on the order of 1000 model years (e.g., see Bryan 1984). Without some kind of acceleration of the simulation with the CGCM, 1000 model years can equate to years of CPU and real time, which is impractical in most cases.

To avoid this impracticality, shorter simulations are in practice the norm and analysis is limited to those parts of the CGCM climate system — atmosphere and upper ocean — that equilibrate fastest and are thus nearest their equilibrium by the end of the run. Conclusions about these are then (most) clearly and credibly drawn. Still, since it allows drawing credible conclusions about the entire CGCM climate system, including the not-well-understood deep ocean, full equilibrium is the gold standard (and holy grail, given its elusiveness) for simulations with CGCMs. The change in the state of the deep ocean from LGM to PD is of considerable paleoclimatic interest so it was very important in this work to be able to address it credibly. With the OGCM the problematic part of reaching equilibrium, before the PD and LGM simulations were done with the CGCM considerable research was first done towards accelerating simulations with the OGCM by itself, with unexpected and mixed results. The successful results were then applied to the CGCM.

Before telling the story of this OGCM acceleration work, a practical definition/measure of full equilibrium should be given. There does not seem to be one that is com-

monly cited. Even though full equilibrium is such a touchstone, this is perhaps not too surprising: given how long it is thought to take to reach full equilibrium, in many cases it is just assumed that simulations have not reached it and so it may never be explicitly checked for. The definition of full equilibrium used here is based on that stated in Wood 1995 where an ocean “model is deemed to have reached equilibrium when the global mean temperature at each model level is changing by less than 0.01°C per century, and the salinity by 0.004 psu per century”. In practice this is quantitatively modified a little and, given the discussed variable equilibration rates, is primarily applied to the deepest OGCM level. Similarly, it is assumed to apply to the entire CGCM since the AGCM equilibrates so much faster than the OGCM.

3.2 OGCM Acceleration

3.2.1 OGCM Description

The ocean GCM used in the acceleration research is a primitive equation OGCM with a horizontal resolution of 5° longitude by 4° latitude such that there are 72 by 46 grid boxes with grid box edges at longitudes -180° , -175° , -170° , \dots , 170° , 175° , 180° and latitudes -90° , -88° , -84° , -80° , \dots , 80° , 84° , 88° , 90° (the pole boxes are only 2° in latitude, which is why there are 46 grid boxes in latitude and not 45). In the vertical, at each ocean horizontal grid box location there are, depending on bathymetry (see Section 4.4), from 1 to 13 discrete levels (L) of grid boxes with tops at depths (calculated from $24(1.5^L - 1)$ m) of about: 0, 12, 30, 57, 98, 158, 249, 386, 591, 899, 1360, 2052, and 3090 m; deepest bottom at 4647 m.

At this resolution, if there were only representation by the grid boxes, there would be quite a few important straits that would have to be considered land and thus be blocked. To address this problem there is a parameterization in the OGCM consisting of metagrid straits, whereby two non-adjacent ocean grid boxes are specified to be connected by a strait with specified realistic characteristics (see Section 4.4). These straits are subject to most of the same physics (e.g., convection) that ocean grid boxes are but the water in them is non-divergent and accelerated only by the pressure gradient between the two connected ocean grid boxes. Because of these limitations

and for simplicity, it is desirable in the OGCM to be able to represent real world straits by standard $5^\circ \times 4^\circ$ ocean grid boxes where feasible, but where not, the metagrid straits are used.

The OGCM was developed coupled to an AGCM as part of a CGCM but had been modified by Gavin Schmidt for ocean-only use. In its essentials it was the same during the OGCM acceleration research as when used in the CGCM of this work (see Section 3.3). However, a few important likenesses and differences compared to when used in the CGCM should be noted here. First, it had the KPP vertical mixing scheme (Large et al. 1994) as when used in the CGCM. However, it did not yet have the Gent-McWilliams (GM) isopycnal mixing scheme (Gent and McWilliams 1990, Gent et al. 1995). Further, there were no water isotope or other tracers¹ included during the OGCM acceleration work because they use a large share of CPU time and were not clearly necessary. Also, there was no salinity gradient limiting done² (Thresher 1999). Additionally, the topography used, primarily the land/ocean mask, was closer to the standard PD topography than that used in the CGCM in this work (see Section 4.4). Finally though, the OGCM had the same thermodynamic/dynamic sea ice model (Russell 1999) as when used in the CGCM.

As it was not coupled to an AGCM, atmospheric boundary conditions of surface pressure, temperature, specific humidity, incoming longwave/shortwave radiation, and precipitation were supplied to the OGCM from seasonally-varying PD observational climatologies. The original observational surface wind climatology was deemed unrealistically weak in the polar regions so that from a 10-year CGCM run was used. Similarly, river runoff was from a CGCM run due to a lack of a global observational climatology.³ Conservative surface salinity restoring on a 60-day time

¹My Oral's research was adding and using CFCs as tracers in the OGCM, as discussed in Thresher 1999. Similarly, I later added some "ideal" tracers to the OGCM.

²Salinity and tracers (as well as temperature) in the OGCM have gradients calculated for them in each grid box. If these are allowed to become too steep it can result in negative concentrations. This is a rare situation but necessary to prevent so the gradients are limited.

³It might have made more sense to have all the atmospheric boundary conditions for the OGCM come from an AGCM, since ultimately the goal was equilibrium within a CGCM. However, all of the other researchers' OGCM experience, which was vital in this work, was from using it with the observational climatologies.

scale to an annual PD observational ocean climatology was used (see Thresher 1999). Ocean initial conditions were also adapted from this PD observational ocean climatology, which was from Levitus et al. 1994.

The preceding is most of what will be important here to know about the OGCM. For more information about the OGCM essentials see Russell et al. 1995. Finally however, for the OGCM acceleration discussion it is very important to also know a little about the timestepping scheme. The OGCM uses two timesteps: an “ocean dynamics” timestep, DTO, and a “source” timestep, DTS. The OGCM’s momentum primitive equation is integrated (using a staggered leapfrog scheme) on the dynamics timestep and this occurs several integral times within a source timestep so that $\text{DTO} * \text{NDYNO} = \text{DTS}$, where NDYNO is an integer. Generally speaking, the OGCM’s “physics” are calculated on the source timestep and actually consist of everything besides the momentum calculations; for example, advection and convection of heat, salt and tracers. Roughly, the dynamics and source calculations each take about 50% of the total CPU time required by the OGCM. Due to stability constraints, normally the largest timesteps possible, and thus the fastest the OGCM can be run, are $\text{DTO} = 7.5$ minutes and $\text{DTS} = 1$ hour, with $\text{NDYNO} = 8$. At these settings, a model year takes about 265 CPU minutes on an SGI Origin 2000, which is the computer used throughout this OGCM acceleration research.

3.2.2 Starting From Another OGCM Equilibrium

Since it is used in conjunction with the other acceleration schemes discussed ahead, the first OGCM acceleration scheme that should be discussed is that of starting the OGCM from another OGCM equilibrium (or near-equilibrium). That is, to use the final ocean state (e.g., temperature, salinity, velocity, at each grid box) of another long OGCM run as the OGCM’s initial condition instead of the state adapted from a PD observational climatology. Another OGCM equilibrium could possibly be different from the equilibrium sought because it will have been from a different OGCM, i.e., one with modified code or boundary conditions (obviously, if it was an equilibrium from the exact same OGCM, the sought-after equilibrium would already exist). The modifications might even have been to implement another OGCM acceleration scheme, given how long it takes to get to any equilibrium.

The simple idea is that one way to get to equilibrium faster is to start closer to it, decreasing the model time, and thus CPU and real time, necessary to reach it. Wood 1995 points out the efficacy of this idea in OGCMs in stating “The model is deemed to have reached equilibrium when ... (this typically takes between 400 and 1600 years, depending on how close the initial conditions are to the final solution).” Even if the equilibrium reached by a modified OGCM is different from the equilibrium sought it may still help since another OGCM equilibrium need only be closer to the sought-after equilibrium than the PD observational climatology to speed up equilibration.

However, while unlikely, it’s not certain that another OGCM equilibrium isn’t further from the equilibrium sought. It’s “unlikely” because a modified OGCM is probably inherently more related to the OGCM than is the PD observational climatology. Additionally, while it is thought less likely than the other OGCM acceleration schemes discussed ahead to have an effect on equilibrium, given chaos and sensitive dependence on initial conditions, it is also not known for certain whether different initial conditions — another OGCM equilibrium instead of a PD observational climatology — lead to significantly different equilibriums in the OGCM. This muddies the picture a bit. In any case, starting from another OGCM equilibrium is such a simple scheme and acceleration to equilibrium is so important, that it is used repeatedly ahead, where it’s muddying effects should be kept in mind in the comparisons.

3.2.3 Reduced Gravity

In the Reduced Gravity OGCM acceleration scheme the basic idea is to slow down the fastest ocean waves in order to stably allow a larger timestep, while hoping this fast-wave deceleration has a negligible effect in the long term, i.e., on the equilibrium. A larger timestep allows running the OGCM to equilibrium faster in CPU and real time; model time to equilibrium should be unaffected. The target fast waves are external (shallow water) gravity waves and their deceleration is accomplished by changing the surface air pressure boundary condition by assuming an atmospheric density that is a much larger fraction (0.75 was used) of the density of sea water than in reality. This scheme had already been implemented in the OGCM (in the pressure gradient code; see Schmidt 1997) by Gavin Schmidt and allowed stably using $DTO = 15$ minutes and $DTS = 3$ hours, with $NDYNO = 12$, so that a model year took about 110

CPU minutes, less than half that for the unaccelerated OGCM. However, a test of the hoped-small long-term effects of the Reduced Gravity scheme in the OGCM had never been made.

A 5600-model-year PD run of the OGCM with Reduced Gravity was done⁴, starting from PD observational climatology. Even with this acceleration scheme, this run took about 16 months of real time (including occasional brief computer downtimes). As can be seen in Figures 3.1 and 3.2 and approximately within the given definition of equilibrium, the run of the OGCM with Reduced Gravity reached equilibrium after about 2500 model years; this took about 7 months of real time. Note as discussed, and most clearly in the ocean potential temperature (rather than salinity) figures, that the upper OGCM levels reached their equilibrium values faster than the deeper levels, in particular the deepest.

Testing the effects of an acceleration scheme on the equilibrium requires as reference the equilibrium of the unaccelerated OGCM and the whole point of acceleration is that this reference takes impractically long to run to. For this reason the discussed OGCM acceleration scheme of starting from another OGCM equilibrium was employed to hopefully get to the reference quicker. In this case, the other OGCM equilibrium was from the 5600-model-year PD run of the OGCM with Reduced Gravity.⁵

The unaccelerated OGCM was thus started from the ocean state at the end of this very long run and run until it apparently reached equilibrium, all as seen in Figures 3.1 and 3.2 (note in the upper levels that it does not look like the unaccelerated OGCM run was started from the end of the OGCM with Reduced Gravity run because the

⁴It was believed at the time that the Reduced Gravity scheme would have no effect on equilibrium, so this run was actually not started as part of a test of that, although it became one. Rather, this run stemmed from the observation that the time *not* doing anything to run an OGCM to equilibrium due to the perceived obstacles, or the time to develop a better acceleration scheme and then run with it to equilibrium, might be more than the time just to run an existing slow OGCM to equilibrium. However, long runs require non-negligible maintenance so are perhaps not to be attempted lightly.

⁵Again, this run was not actually started as part of a test of the effect of the Reduced Gravity scheme on equilibrium. If it had been known to be that, the unaccelerated OGCM might have been started at the same time, from PD observational climatology, and, given the run speed, might have gotten to equilibrium in under the 16 real months the OGCM with Reduced Gravity was run.

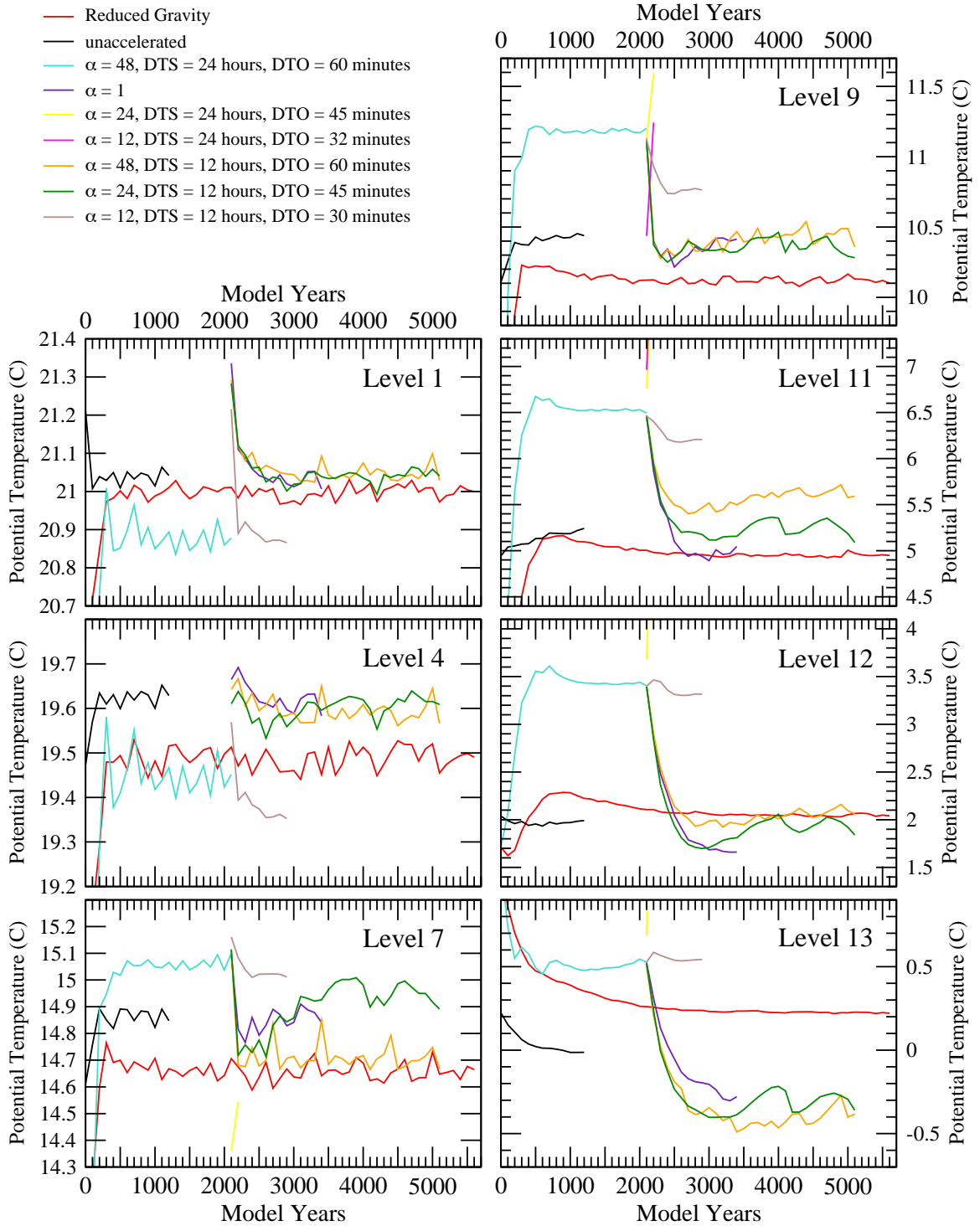


Figure 3.1: Mean (global, annual, first decade of each century) ocean potential temperature (C) at selected OGCM levels. All runs starting from the end of other runs are shown that way (the length of their runs in model years thus calculated as a subtraction) except for the unaccelerated OGCM run, which because it was started from the end of the very long OGCM with Reduced Gravity run is, for compactness, shown starting from 0 model years. Note the changes in y-axis scales between levels.

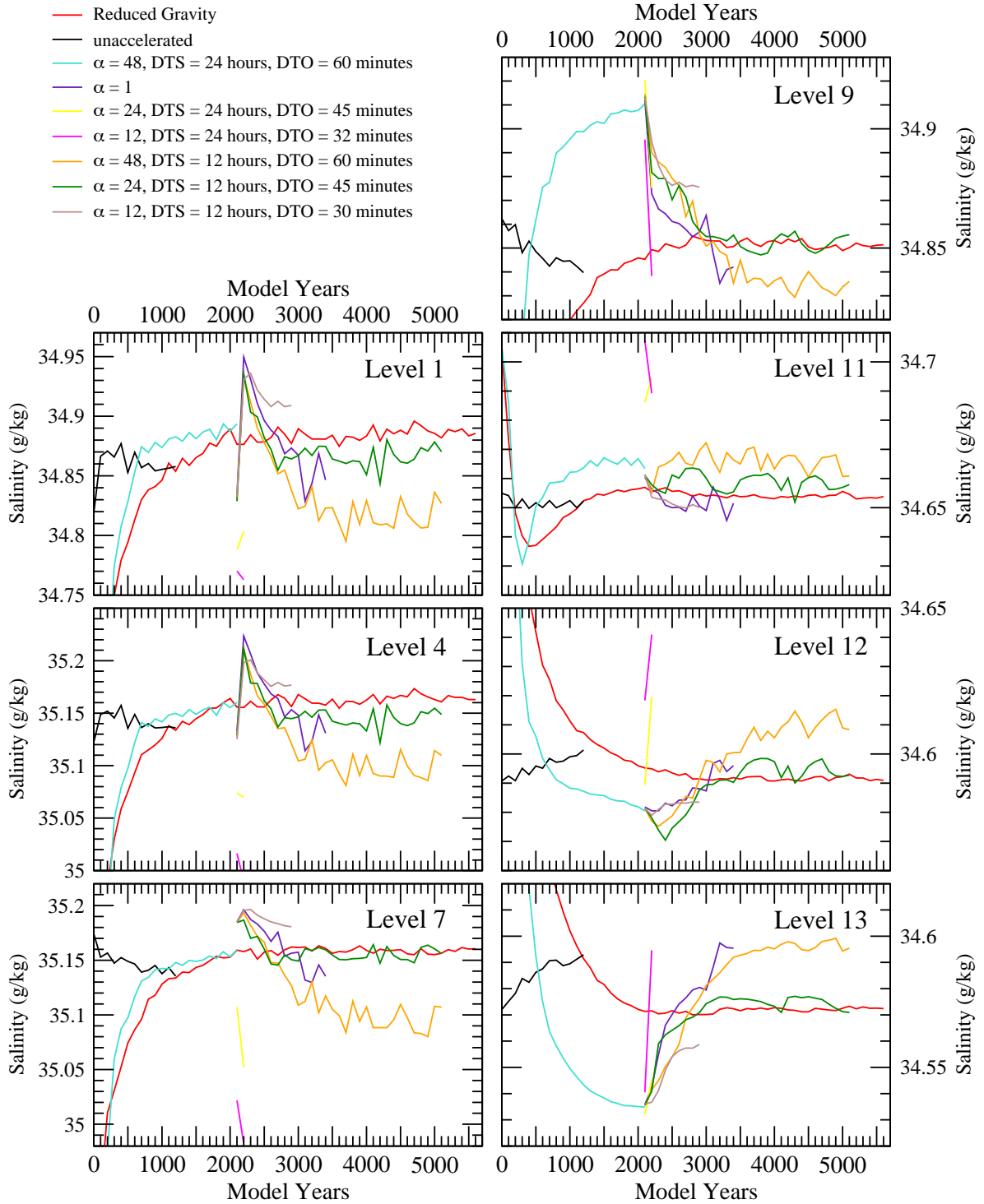


Figure 3.2: Mean (global, annual, first decade of each century) ocean salinity (g/kg) at selected OGCM levels. All runs starting from the end of other runs are shown that way (the length of their runs in model years thus calculated as a subtraction) except for the unaccelerated OGCM run, which because it was started from the end of the very long OGCM with Reduced Gravity run is, for compactness, shown starting from 0 model years. Note the changes in y-axis scales between levels.

adjustment in those levels is so fast, i.e., less than the 100-year sampling interval). This took about 1200 model years and about 9 real months. The former is in contrast to the 2500 model years for the OGCM with Reduced Gravity to equilibrate, so one conclusion drawn from this test is that the scheme of starting from another OGCM equilibrium seems to have accelerated the “unaccelerated” OGCM’s equilibration. This conclusion is muddled though, as discussed, by the possibility of different initial conditions leading to different, possibly closer, equilibriums.

As can be seen in the figures, the unaccelerated OGCM’s equilibrium is significantly different from that of the OGCM with Reduced Gravity. While this effect is also muddled by the possibility of different initial conditions leading to different equilibriums, it is thought that the different equilibrium is indeed due to use of the Reduced Gravity acceleration scheme. As will be emphasized in the next section, OGCMs are very complicated and it should perhaps not be expected that an acceleration scheme will not affect the equilibrium; it certainly cannot be known without testing. In any case, it was thus concluded that the Reduced Gravity OGCM acceleration scheme should not be used. Note that it really couldn’t have been used directly in the CGCM, where atmospheric density can’t be so easily set, but could have been used indirectly as part of the CGCM/OGCM leapfrog acceleration scheme discussed in Section 3.3.3 ahead.

3.2.4 Distorted Physics

As with the Reduced Gravity OGCM acceleration scheme, the basic idea of the Distorted Physics OGCM acceleration scheme is to slow down the fastest ocean waves in order to allow stably using a larger timestep, and thus run the OGCM faster in CPU and real time, while hoping this fast-wave deceleration has a negligible effect on the equilibrium (steady-state) solution. In the Distorted Physics scheme though, the target fast waves are not only external gravity waves but also internal gravity waves and Rossby waves (and perhaps others). The Distorted Physics scheme was also dramatically more difficult to implement but is simple in concept. Following Wood 1995 (also Wood 1998), if the OGCM’s momentum primitive equation is written simply as

$$\frac{\partial u}{\partial t} = (RHS)_u$$

then with the Distorted Physics scheme it becomes

$$\frac{\partial u}{\partial t} = \frac{1}{\alpha}(RHS)_u$$

As required, the fast waves are thus slowed down in the latter by a factor of α but the steady-state (equilibrium) solution

$$\frac{\partial u}{\partial t} \equiv 0$$

is the same in both

$$(RHS)_u = 0$$

The reason this was difficult and time-consuming to implement in the OGCM is that the OGCM's momentum primitive equations are actually spread throughout many of the OGCM program's subroutines and often intricately and obscurely intertwined with the similarly-complicated non-momentum "physics" calculations (see Section 3.2.1).

After many months of debugging and experimentation to get the OGCM with Distorted Physics to run stably with even a single combination of α , DTO, and DTS (again, $DTS = DTO * NDYNO$), it was realized that generally, increasing α increased the stability. Attempting to pick the largest value of α that was still unlikely to effect equilibrium, a value of $\alpha = 48$ was chosen, based on the Wood 1995's admittedly conservative choice of $\alpha = 24$. With $\alpha = 48$, the largest timesteps stably possible seemed empirically to be $DTO = 60$ minutes and $DTS = 24$ hours (from $NDYNO = 24$) so the first PD run to equilibrium of the OGCM with Distorted Physics was made with this fastest possible combination of parameters. Like the very long OGCM with Reduced Gravity run, it was started from PD observational climatology. The results are shown in Figures 3.1 and 3.2 alongside those from the unaccelerated OGCM and the OGCM with Reduced Gravity. There appears to be greater variability (cyclicity?) in the OGCM with Distorted Physics so it is harder to say when equilibrium is reached but it seems to have been reached by the end of the run at 2100 model years (which took about 40 real days) and arguably at 1200 model years. At about 25 CPU minutes per model year, this run of the OGCM with Distorted Physics gave a very desirable factor of 10+ speedup over the unaccelerated OGCM.

However, as can be seen in the figures, the equilibrium reached was significantly different from that of the unaccelerated OGCM, implying $\alpha = 48$ was too large. This was not the only possible cause though. As an inexact (see ahead) check of an alternate possibility — incorrect Distorted Physics modifications to the OGCM program — a run was started with $\alpha = 1$, DTO = 7.5 minutes and DTS = 1 hour (from NDYNO = 8), which theoretically should be the same as the unaccelerated OGCM. This run was going to take a lot of real time; at 336 CPU minutes per model year, even longer than the unaccelerated OGCM because of the overhead of the added Distorted Physics calculations, which even with $\alpha = 1$ are still performed. For this reason the discussed OGCM acceleration scheme of starting from another OGCM equilibrium was again employed. The other OGCM equilibrium used was the end of the first, fastest OGCM with Distorted Physics run ($\alpha = 48$, DTS = 24 hours, DTO = 60 minutes), which it was suspected would actually have an equilibrium closest to the sought-after equilibrium.

In the meantime, runs faster than the $\alpha = 1$ run but using α less than 48 were performed to test α 's effect on equilibrium. Even though they were faster, these runs were still slower than the first, fastest OGCM with Distorted Physics run ($\alpha = 48$, DTS = 24 hours, DTO = 60 minutes) so these too were started from the end of that run in the hopes of getting them to equilibrium faster. Two runs were performed with the same DTS = 24 hours, α successively halved (24 then 12), DTO decreased for stability (45 then 32 minutes, respectively) and NDYNO increased accordingly (32 then 45, respectively). As can be seen in Figures 3.1 and 3.2 these seemed to rapidly go off toward vastly different equilibriums and so were abandoned after only about 200 model years. To counter this, DTS was then decreased to 12 hours and three runs to apparent equilibrium were performed in which α was successively halved again starting from 48 (then 24 then 12), DTO was decreased for stability starting from 60 minutes (then 45 then 30 minutes, respectively), and NDYNO was increased accordingly starting from 12 (then 16 then 24, respectively). The speed of the runs was thus also decreasing. The results from these runs are also shown in the figures, along with the final results from the $\alpha = 1$ run, which took 10 real months to reach apparent equilibrium.

Given the extreme slowness of the $\alpha = 1$ run, deciding whether it had reached equi-

librium had to be done as soon as possible, perhaps prematurely and thus arguably so. Even at near-equilibrium though, it's equilibrium seems significantly different from that of the unaccelerated OGCM, which theoretically it should be the same as. As indicated, this might imply incorrect Distorted Physics modifications to the OGCM program. However, practically, the necessary Distorted Physics modifications to the OGCM program went well beyond the outlined theory. For example, for stability the sea ice and straits subroutines had to be reordered, made to use smaller timesteps, and put in loops so that they were done during the original source timestep. This sort of modification can significantly affect numerical outcomes, causing the OGCM to take a different “path” in the long-term. The OGCM with Distorted Physics actually had a “twin” without Distorted Physics but with most of these reorderings and the results from the twin closely matched those from the OGCM with Distorted Physics. However, these tests were only done for short runs. Thus, it can't be definitely said that the Distorted Physics modifications to the OGCM program were “incorrect”. Further, the fact that the $\alpha = 1$ run had as the initial condition the end of the first OGCM with Distorted Physics run ($\alpha = 48$, DTS = 24 hours, DTO = 60 minutes) and the unaccelerated OGCM run had the different initial condition of the end of the OGCM with Reduced Gravity run means the comparisons are further muddled, as discussed.

Even with the same initial condition, the end of the first OGCM with Distorted Physics run ($\alpha = 48$, DTS = 24 hours, DTO = 60 minutes), all of the post-first OGCM with Distorted Physics runs seem to have different equilibriums (at some level). Theoretically, as α is decreased, distortion should decrease and the equilibriums should approach the “true” equilibrium of $\alpha = 1$ but this does not seem to be the case. A good example is that the two runs with $\alpha = 48$ and 24, DTS = 12 hours, and DTO = 60 and 45 minutes, respectively, have equilibriums that seem closer to that of the $\alpha = 1$ run than does the equilibrium of the run with $\alpha = 12$, DTS = 12 hours, and DTO = 30 minutes. In fact, assuming that their different initial conditions are not a factor, note that the latter run has an equilibrium that is closest to the first OGCM with Distorted Physics run with $\alpha = 48$, DTS = 24 hours, and DTO = 60 minutes (note also that it reached this equilibrium, that is close to its initial condition, in fewer model years than runs that had more different equilibriums).

Despite too much time and effort it never became clear what the problem was. As discussed in Wood 1995, one possible problem is clearly a timestep sensitivity of equilibriums, i.e., using a different timestep results in a different equilibrium. Wood 1995 points out that the parts of an OGCM’s physics that act in a near-instantaneous way, i.e., switched on or off within a timestep, are the ones most likely to be the cause of this and that sea ice formation and vertical mixing tend to fall into this category. In fact, the vertical mixing scheme had to be modified against this in the OGCM of Wood 1995. Understandably perhaps, given the noted long run times involved, no research on the equilibrium timestep sensitivity of the OGCM here had previously been done but it really should have been a prerequisite for this equilibrium research. Equilibrium timestep sensitivity does seem to fit the symptoms well, including possibly even having been the problem in the OGCM with Reduced Gravity. Wood 1995 also suggests the possibilities of multiple valid equilibria and distortion of the limit cycle (i.e., due to seasonal, interannual and longer timescale inherent variability, equilibriums actually show cyclicity, as was apparently seen in this work, where it made it difficult to determine when a run had reached equilibrium).

In any case, as critical as acceleration is⁶, trying to use the Distorted Physics scheme in the OGCM had to be abandoned due to time constraints. Note that it really couldn’t have been used directly in the CGCM but could have been used indirectly as part of the CGCM/OGCM leapfrog acceleration scheme to be discussed in Section 3.3.3 ahead.

3.2.5 Program Parallelization

In the preceding sections a distinction has been made between CPU time and real time, as well as the more obviously different model time. Barring computer downtime, on one processor (CPU) of a computer CPU and real time should be about the same and this was the case in the runs of the preceding sections. However, if the OGCM program can be run on more than one processor such that parts of the program run *concurrently* then the real time necessary to run a given amount of model time can

⁶It was even tried in this work to use the Reduced Gravity scheme together with the Distorted Physics scheme to multiply the OGCM acceleration but they could not be made to work together stably.

be reduced. Total CPU time would be the same or (more) probably but would be split up among several processors running at the same time. This form of OGCM acceleration can be accomplished by “parallelizing” the OGCM program and running it on multiple processors of a multiprocessor computer such as the SGI Origin series supercomputers used throughout this work.

There are a number of different parallel programming paradigms and practical implementations of these.⁷ Due to the nature of the OGCM program, as well as the computer it was going to run on, it was decided to use OpenMP, a practical implementation of the shared memory paradigm. The OGCM program consists of “legacy” Fortran code, meaning that it is an existing hodgepodge of pieces written by a variety of people with a variety of programming styles/skills using various old Fortran versions (pre-Fortran 90). OpenMP (Open Multi Processing) is a set of compiler directives, library routines and environment variables and is the most amenable to being used (although it is still not easy) with such legacy Fortran code since, for example, it can be added incrementally. In contrast, MPI (Message Passing Interface), a practical implementation of the message passing paradigm, really requires inclusion throughout the program from the initial coding onwards. Programs with MPI though, can be run on centralized/distributed shared memory multiprocessor computers and multicomputers like Beowulf clusters. Programs with OpenMP can only be run on the former but the SGI Origin series supercomputer that the OGCM was run on was in this category and had an OpenMP-aware Fortran compiler available.

Using OpenMP, the focus of parallelization in the program code are the Fortran “DO” loops where much of the OGCM calculations are done. Usually these are loops through the latitude, longitude and/or level numbers of the OGCM grid boxes. The idea is that if each iteration of a loop is independent of the others then the order of the iterations is irrelevant — they can be executed backwards or, more importantly, concurrently on different processors and the result after all the iterations are done will be the same. For an iteration to be independent of the others it can’t change any variables that are read by them or read any variables that are changed by them.

⁷During July 2000 I attended the NASA High Performance Computational Earth and Space Sciences Summer School at Goddard Space Flight Center, Greenbelt, MD to learn about these and work on parallelizing the OGCM.

Parallelizing then, requires keeping careful track of variables, detecting dependencies, and modifying to remove these, while leaving the loop calculations mathematically unchanged. Loops are then actually parallelized by inserting a compiler directive just before them in the code. Unfortunately, keeping track of variables in the legacy Fortran code of the OGCM program was difficult due to its use of implicit typing and programming “tricks”. Further, even in theory finding dependencies can be difficult, as can modifications to remove them while leaving the loop calculations mathematically unchanged.

Given the large amount of effort required to parallelize, it was only worth parallelizing the most CPU-intensive subroutines of the OGCM program and even some of those could not be parallelized. The CPU-intensivity order of those that were parallelized varied due to factors like the OGCM version (for example, parallelization was actually first done on the version with Distorted Physics) and the length of model time looked at. Roughly though, based on tests with speed profiling software, it was, in decreasing order, those subroutines that calculated: momentum advection, convection, pressure gradient forces, mass fluxes, west-east heat/salt advection, zonal filtering, mass/momentum to density/velocity conversion, south-north heat/salt advection, vertical heat/salt advection, column mass, and sea ice velocity. Together these typically accounted for more than 65% of the total required CPU time.

Given the difficulties, it’s important to extensively test the parallelization of a program. On a single processor this can be done by changing (e.g., reversing) the order of iterations in the loop being tested. If the results are numerically identical with the iterations in any order, that is a good (but not absolute) indication the loop has been correctly parallelized. Then when multiple processors are available for testing, the parallelized program can be run on one, then multiple processors. If the one-vs-multiple results are numerically identical, that is also a good (but not absolute) indication the program has been correctly parallelized.

Note that the results from a correctly parallelized program and its unparallelized version (*not* just the correctly parallelized program run on one processor) may not be identical, especially for longer runs, because often the modifications necessary for parallelizing, while leaving the calculations mathematically unchanged, change things like order of operations, which in a computer can change numerical results.

For short runs the differences will usually be small but for longer runs there can be a cumulative effect and the “path” the OGCM follows can be altered, possibly affecting the equilibrium reached. Due to time constraints a long run to equilibrium with the parallelized OGCM was never done to test this but as with the Reduced Gravity and Distorted Physics OGCM acceleration schemes it really should have been, even if an equilibrium effect is thought much less likely with parallelization.

The resulting speedup from parallelizing a program depends on the number of processors the program is actually run on. A fundamental fact about this is that, due to increasing overhead when running parallelized, there is a diminishing speedup with increasing number of processors. For example, doubling the number of processors significantly less than doubles the speedup, especially for larger numbers of processors. Due to limited availability, usually only four processors were used in the short test runs of the parallelized OGCM and this gave a speedup of about a factor of 2 over the unparallelized OGCM. However, this was near the “sweet spot” in the speedup versus processors curve, with more processors providing significantly less speedup.

Thus, while parallelizing the OGCM program did not provide anything like the factor of 10 speedup seen with Distorted Physics, it was the OGCM acceleration scheme that seemed to be most robust and to pay off on the time invested in it, especially since it was then applied to the CGCM.

3.3 CGCM

3.3.1 CGCM Description

The coupled GCM is composed of an ocean GCM and an atmospheric GCM. As discussed in Section 3.2.1, the OGCM is essentially as used in the acceleration research but with the addition of the GM isopycnal mixing scheme, the inclusion of water isotope tracers, the limiting of salinity gradients, and topography changes. The AGCM is a primitive equation model (rather than spectral) and has the same $5^\circ \times 4^\circ$ horizontal resolution as the OGCM. In the vertical, the AGCM has terrain-following sigma coordinates in the lower atmosphere, constant pressure coordinates in the upper atmosphere, and a total of nine pressure levels: level bottoms at 984, 934, 854,

720, 550, 390, 255, 150, and 70 mb; with a top-of-atmosphere pressure of 10 mb. It has an advanced atmospheric radiation scheme (Lacis and Oinas 1991) capable of using greenhouse gas and aerosol concentrations set at the significantly-different levels of thousands of years before PD and of using insolutions significantly-different from PD due to millennial-scale orbital variations. The AGCM includes a land surface model that can account for glaciers, variously-vegetated ground, and lakes, including runoff/rivers in directions that can be specified. It has a timestep of 1 hour. For a more detailed description see Hansen et al. 2002 and the references therein.

Given the apparent benefit and with the experience of having done it for the OGCM by itself, the CGCM program too was parallelized using OpenMP. Since it is essentially the same as the OGCM by itself, the OGCM part of the CGCM program was more or less already parallelized. However, it did have the addition of the GM isopycnal mixing scheme. Its four subroutines were parallelized using OpenMP as well.⁸

The AGCM part of the CGCM program had to be parallelized more from scratch, with all the attendant problems discussed in Section 3.2.5. These were even worse in the AGCM though, to the point that some of the less CPU-intensive subroutines could not be successfully parallelized because of them. Still, the most CPU-intensive subroutines of the AGCM part of the CGCM program were parallelized with OpenMP. Roughly, in decreasing order of CPU-intensity, they are those subroutines that calculate: vertical moisture advection, vertical heat advection, condensation, west-east moisture advection, moist convection, south-north moisture advection, west-east heat advection, momentum advection, pressure gradient forces, combined heat advection, south-north heat advection, horizontal velocity noise filtering, mass fluxes, combined moisture convection, and integration of dynamic terms. As implied by the mentioned fact that the OGCM generally requires less CPU time to run the same model time than does the AGCM, in an ordered list of all the most CPU-intensive

⁸In the CPU-intensity list of Section 3.2.5, the GM subroutine that sums horizontal and vertical fluxes of heat/salt/tracers comes after convection. The other three GM subroutines, which calculate 1) density gradients and tracer operators for the isopycnal skew fluxes, 2) isopycnal slopes from density, and 3) horizontal/vertical density gradients come, in that order, after vertical heat/salt advection in the list.

CGCM subroutines, the AGCM subroutines tend to be more CPU-intensive than the OGCM subroutines. Note that coupling tends to change the order slightly even within just the AGCM or OGCM. Also note that, because they are incorporated into existing CGCM subroutines, the inclusion of water isotope tracers in the CGCM doesn't significantly affect which are the most CPU-intensive subroutines but does add significantly to the overall required CPU time.

Those subroutines of the CGCM program that were parallelized using OpenMP typically account for about 75% of the required CPU time. The CGCM program is run on only four CPUs of an SGI Origin 3000 supercomputer, due to limited availability (typically CPUs are allotted to users by the node and there are 4 CPUs per node), but on these the parallelization provided a speedup of a little more than a factor of 2. Finally, the bottom line is that it takes about one real day to run two model years.

3.3.2 OGCM Streamfunction

There is great interest in the differences from PD in the ocean's thermohaline circulation, particularly in the North Atlantic during the LGM and subsequent deglaciation. However, as aptly pointed out in Wunsch 2002, the term "thermohaline circulation" is used in the literature to mean several different, often inconsistent, things. This ambiguity means that how to measure it and its changes is also unclear and that comparing values is often meaningless. There does though seem to be general agreement that integrated zonally in the North Atlantic at PD, there is a rough meridional overturning circulation (MOC), with water mass within about a kilometer of the surface flowing north, sinking to greater depths in the north, and then flowing south at those depths. To view this meridional overturning circulation in the OGCM, a depth-latitude section of annual streamfunction is typically calculated, which essentially just shows magnitude and direction (i.e., along streamlines) of the zonally averaged mass flux; for example, see Figure 7.15. As a reasonable single-value measure of this in the North Atlantic, the value for CGCM grid box lat# 35 (44–48°N) in the Atlantic at OGCM level 10 (899–1360 m depth) is used. Getting a steady realistically large PD North Atlantic MOC (NAMOC) streamfunction in the OGCM part of the CGCM is important for the credibility of using the CGCM to address questions of changes in the ocean's thermohaline circulation and deep ocean state.

At a point before the CGCM was fully modified (e.g., parallelized) and the boundary conditions for the LGM and PD simulations (greenhouse gases, aerosols, insolation, topography, land surface; see Chapter 4 ahead) were complete, it was decided due to time constraints to put the quest for equilibrium aside and just do a short less-ambitious glacial meltwater sensitivity experiment with the CGCM carrying water isotope tracers. This experiment followed on the research of Rind et al. 2001 Part 1 and Rind et al. 2001 Part 2 and consisted of a PD Meltwater Control run and a Meltwater run that added 32 times the normal freshwater flow out of the St. Lawrence. Although this idea is associated with the Deglaciation, specifically the Younger Dryas, it could not be considered a simulation of that, both because the meltwater volume used was much larger than the estimates and because the boundary conditions were left the same as those of the PD control run, which are significantly inappropriate for a Deglaciation era like the Younger Dryas (see Chapter 4 ahead).

Figure 3.3 shows the single-value annual NAMOC streamfunction versus model years and as seen, during the PD Meltwater Control run its streamfunction plummeted.⁹ For the cited credibility reasons, this was unacceptable and it was attempted to determine the reasons for the streamfunction problem by comparing to previous runs (Section 3.2) with the OGCM alone.

Also shown in Figure 3.3 then, are the single-value NAMOC streamfunctions of three PD runs from the described OGCM (only) acceleration research; for run descriptions see Sections 3.2.3 and 3.2.4 and Figure 3.1. The streamfunction of the OGCM with Reduced Gravity run initially plummeted like that of the PD Meltwater Control run with the CGCM. However, it subsequently recovered to a weak but more reasonable value. The streamfunction of the unaccelerated OGCM run actually increased from the weak equilibrium value of the end of the Reduced Gravity run from which it was started. Finally, the streamfunction of the $\alpha = 1$ OGCM with Distorted

⁹Also shown in Figure 3.3 is the streamfunction of the Meltwater run itself, which as shown started from the ocean state of model year 22 of the Meltwater Control run. Clearly, the streamfunction of the Meltwater run plummets as well but it does so at an even faster rate than that of the Meltwater Control run. This would seem to indicate that the meltwater was having the hypothesized effect. However, given the dubious streamfunction of the Meltwater Control run, the Meltwater run was abandoned after that was discovered.

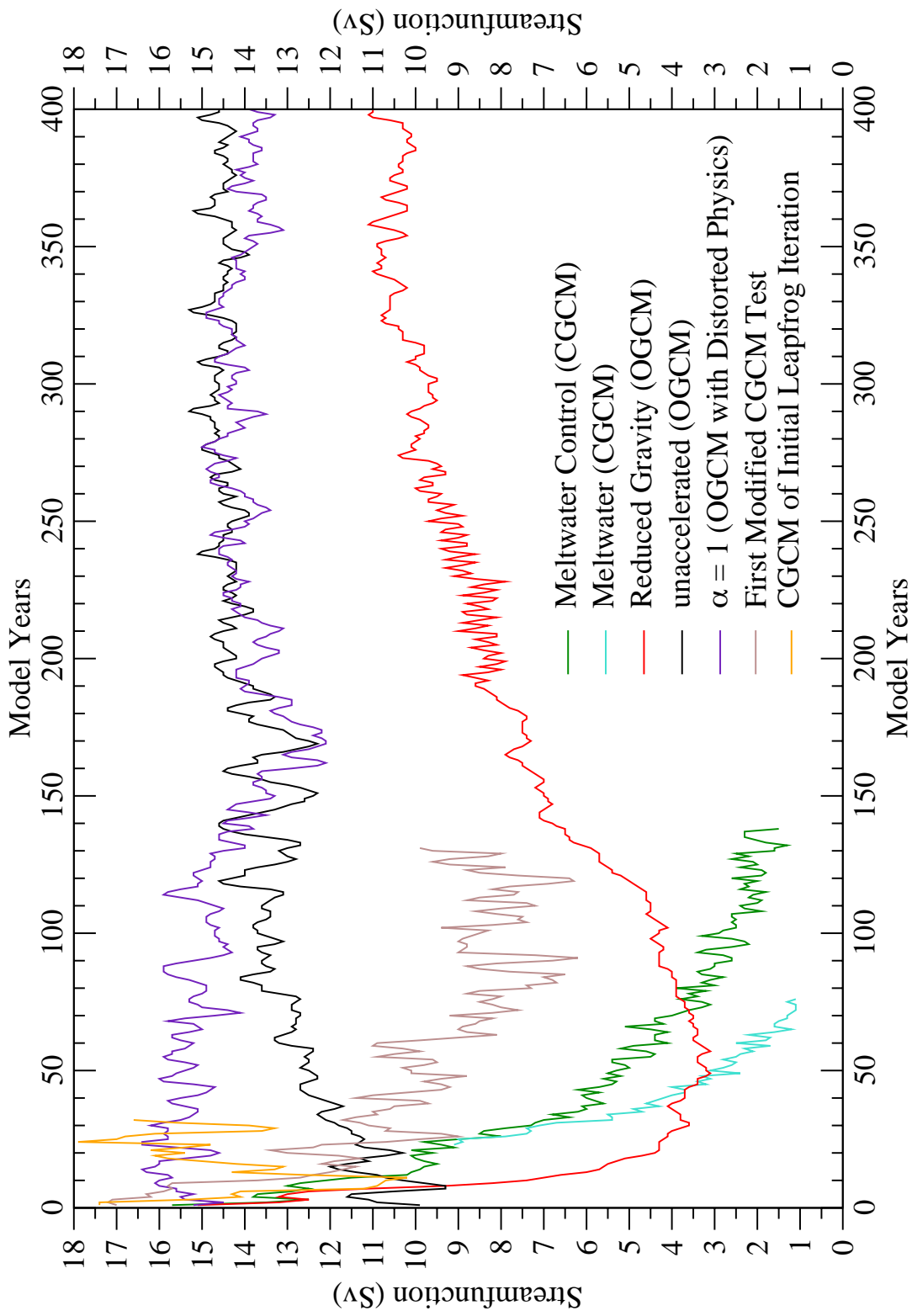


Figure 3.3: Annual NAMOC streamfunction value (Sv) at OGCM grid box lat# 35 (44–48°N), level 10 (899–1360 m depth) versus model years for various OGCM and CGCM runs. See text for descriptions of runs.

Physics run decreased, but not dramatically, from the reasonable equilibrium value of the end of the first ($\alpha = 48$, DTS = 24 hours, DTO = 60 minutes) OGCM with Distorted Physics run from which it was started (not shown in figure).

Unfortunately, there were a variety of differences between the OGCMs (alone and in the CGCM) of all the runs, making sorting out their effects on NAMOC streamfunction difficult. For example, between the OGCMs by themselves and the OGCM in the CGCM at the time there were the differences of the coupling itself, the acceleration scheme used, the velocity filter/viscosity subroutine¹⁰ used, the addition of the GM isopycnal mixing scheme, the salinity gradient limiting done, and in some cases use of different initial conditions. Just between the OGCMs by themselves there were the discussed differences of acceleration scheme and initial conditions used. The effect of all these differences on NAMOC streamfunction could not be sorted out in an easy or timely fashion. For example, it was thought to let the Meltwater Control run continue in order to see if its streamfunction recovered like that of the OGCM with Reduced Gravity run but an unrelated CGCM program bug caused the run to stop. As the CGCM was not yet parallelized anyway and thus might take a lot of real time to show if its streamfunction recovered, the Meltwater Control run was abandoned.

There were two things that seemed strongly implicated in getting a steady reasonably large NAMOC streamfunction value and thus worth acting on. First, it was considered telling that the two runs that were started from the PD observational ocean climatology, the Reduced Gravity and Meltwater Control runs, had streamfunctions that initially plummeted, while the two runs that were started from a previous OGCM equilibrium, the unaccelerated and $\alpha = 1$ runs, had streamfunctions that either initially increased or only fell a little, to still reasonably large values. It was thus decided that runs should be started from one of the previous OGCM equilibriums, including LGM simulation runs (there were no LGM OGCM equilibriums available and of course no LGM observational ocean climatology). Since the unaccelerated OGCM was probably most like the OGCM in the CGCM and had the best streamfunction it was decided to use the PD equilibrium ocean state at the end of its run as this initial condition.

Second, a close comparison of the timing of the equilibrations of the mentioned

¹⁰Removes noise near the pole.

OGCM runs in Figures 3.1 and 3.2 (primarily Level 13 potential temperature) with that of the timing of the NAMOC streamfunctions of the same runs in Figure 3.3 shows that there always seemed to be a less than 500-year initial period of the most rapid equilibration, after which the run could be described as “near-equilibrium”. During this period the streamfunction changed the most, only becoming acceptably “quasi-stable” afterwards. It was thus concluded that a run must be gotten to near-equilibrium to have a quasi-stable reasonably large streamfunction. This connection makes intuitive sense and is part of the reason for putting the OGCM streamfunction discussion in a chapter on the quest for equilibrium.

Additionally, it was decided to use in the OGCM of the CGCM the original velocity filter subroutine used in the OGCMs by themselves since all the runs with non-plummeting NAMOC streamfunctions had this in their OGCMs. Also, while it was in the OGCM of a run with a plummeting streamfunction, it was decided to still use the GM isopycnal mixing scheme because it was not thought to be the problem and had good effects in other areas. Similarly, salinity gradient limiting was done because it was required with the inclusion of water isotope tracers.

At this point in the story, the boundary conditions for the PD and LGM simulations were nearing completion (the topography and land surface still needed some finishing touches) and so the new CGCM runs were to be for these more ambitious simulations rather than the glacial meltwater sensitivity experiments.¹¹ As described, these simulations were to have the OGCM of the CGCM started from the equilibrium ocean state at the end of the unaccelerated OGCM run but still had to at least get through the initial most-rapid equilibration to get to near-equilibrium and a quasi-steady NAMOC streamfunction. To do this in a practical amount of real time, acceleration of the whole CGCM had to be addressed. The CGCM was thus parallelized as described previously in Section 3.3.1. However, with an OGCM and AGCM of a CGCM there was also the possibility of an additional acceleration scheme and this is discussed in the next section.

¹¹These could have been made to have realistic Younger Dryas boundary conditions and been compared to the ocean sediment and ice core $\delta^{18}\text{O}$ data. However, there were more problems preparing topography for the Younger Dryas than the LGM (see Section 4.4) and the ocean sediment and ice core $\delta^{18}\text{O}$ data is much more ambiguous for the Younger Dryas than the LGM (see Chapter 5).

First though, note that two short PD CGCM test runs with the aforementioned modifications were done. These also had the greenhouse gas concentrations and insolation of the PD simulation boundary conditions, which are slightly different from the standard PD ones normally used in the CGCM, but did not have the topography and land surface of the PD simulation boundary conditions (see Chapter 4 ahead), just the standard PD ones normally used in the CGCM. The difference between the two Modified CGCM Test runs was simply that the second did not include equilibrium sea ice initial conditions as part of the equilibrium ocean initial conditions; it just used the standard PD observational climatology sea ice initial conditions. The OGCM NAMOC streamfunction of the First Modified CGCM Test run is shown in Figure 3.3. Because it was so similar to the First Modified CGCM Test run (i.e., for clarity) and because it was never the case again, the second run, without the equilibrium sea ice initial conditions, is not shown (initially it's streamfunction was generally slightly smaller than that of the First Modified CGCM Test run but this difference disappeared as the runs progressed). Both streamfunctions did drop initially but, while quite variable, did not drop to the near-zero values of the Meltwater Control run and seemed to start to recover towards even more reasonable values. Note too, that the drops were from a value higher than that of the unaccelerated OGCM equilibrium ocean state from which they were started (this value was probably higher due to the AGCM being more variable than the PD observational climatology atmospheric boundary conditions of the unaccelerated OGCM) so they were thus not as precipitous initial drops as seemed at first glance. Thus, the streamfunction results of the Modified CGCM Test runs seemed to fit in with the ideas discussed above and were encouraging for doing the complete PD and LGM simulations with the CGCM.

3.3.3 CGCM/OGCM Leapfrog Acceleration Scheme

As mentioned, the AGCM equilibrates quickly to its boundary conditions but it (and thus the CGCM) takes a lot of CPU time per model time, while the OGCM (specifically it's deepest levels) equilibrates slowly to its boundary conditions but takes much less CPU time per model time than the AGCM. A possible scheme for accelerating the CGCM to equilibrium then, is to run the CGCM for the few model years necessary to get the AGCM to equilibrium, derive reasonable mean atmospheric

boundary conditions from it for the OGCM, and then to run the OGCM by itself with these mean atmospheric boundary conditions for the many more model years necessary to get it to near-equilibrium for them. Then using the resulting ocean state as initial conditions to the CGCM, the process is repeated. This CGCM/OGCM “leapfrog” acceleration scheme could bring the entire CGCM to near-equilibrium and a quasi-steady reasonably valued NAMOC streamfunction faster than by just running the CGCM, especially if for the CGCM run of the initial iteration a previous OGCM equilibrium was still used as the ocean initial condition as discussed and if the OGCM and CGCM were still run parallelized. This CGCM/OGCM leapfrog acceleration scheme has been used successfully elsewhere (for example, by the Geophysical Fluid Dynamics Laboratory).

A plan based on the preceding for both PD and LGM simulations was drawn up and started for the PD simulation, for which all the boundary conditions were finally completed. The initial CGCM run was to be for no more than 10 model years — greater than the year needed for the AGCM to equilibrate but before the OGCM NAMOC streamfunction dropped to a value where it probably would significantly affect the AGCM. From this, the best single year’s worth of monthly means of atmospheric boundary conditions for the OGCM (see Section 3.2.1) would then be derived; similarly for surface salinity for the conservative surface salinity restoring done by the OGCM by itself. The best single year’s data were to be used instead of a multi-year mean so as not to smooth out the extremes that are believed responsible for many deep convective events that contribute to a real streamfunction. In fact, for the same reason, it was thought to use daily means instead of monthly means but the program changes necessary for this were considered too burdensome given the time constraints. The single year of monthly means of atmospheric boundary conditions would then be repeated over and over (note that repeating more than a single year would introduce an unnatural periodicity) and the OGCM by itself run for around 100 model years. This CGCM/OGCM iteration would then be repeated at least once until a final CGCM run was done.

There was no guarantee this CGCM/OGCM leapfrog acceleration scheme would work but it turned out to be moot. The CGCM run of the initial leapfrog iteration was promising — as seen in Figure 3.3, after a brief initial dip its mean NAMOC stream-

function seemed to increase to a realistically large value. With an early realistically strong streamfunction, it was thus decided not to do the labor-intensive CGCM/OGCM leapfrog acceleration scheme, instead doing the LGM and PD simulations by just running the CGCM as far toward equilibrium as time permitted.

Compared to the Modified CGCM Test runs of Section 3.3.2, the CGCM run of the initial leapfrog iteration had topography and land surface differences, so these are thus implicated in the further improved NAMOC streamfunction. Moreover, there were a series of false starts for the now-just-CGCM PD simulation during which program bugs were fixed, sea ice advection in the metagrid straits was removed, the representation of the northern strait of the Sea of Japan was made more realistic, and small topography and land surface changes were made. During these short (≈ 60 model years) false start runs, their NAMOC streamfunctions (for clarity, not shown) were much the same as that of the CGCM run of the initial leapfrog iteration, as well as that of the final CGCM-only PD simulation, whose streamfunction continued to increase, so these false start changes seem to have had little effect on improving streamfunction. See Chapter 4 for descriptions of the larger changes in topography and land surface boundary conditions but note here that there are quite a few so a single one can't be pinpointed as the primary improver of the streamfunction. Clearly though, changes within the range still considered to be of a particular era can have a significant effect on streamfunction. The NAMOC streamfunctions and equilibrations of the final CGCM-only PD and LGM simulations are discussed in Section 6.1 ahead but note finally here that the LGM simulation's streamfunction even more steadily and rapidly increased initially so large boundary condition changes certainly have an effect on streamfunction.

3.3.4 Non-Equilibrium OGCM Initial Conditions

The ocean state that was used as the initial conditions for the OGCM part of the CGCM for the PD and LGM simulations had to have, for each grid box: the ocean water mass, its horizontal velocities, its heat and salt content, and the horizontal and vertical gradients of the heat and salt; the sea ice mass, heat content, pressure, horizontal velocities, fractional coverage, and horizontal gradients of fractional coverage; the equivalents of all the preceding in the straits. As the CGCM was also carrying

water isotope tracers, the masses and vertical gradients of these were also necessary. As indicated, this initial condition ocean state was largely that of the equilibrium at the end of the unaccelerated OGCM run described in Section 3.2.3. However, this was not able to provide all that was necessary and so the initial condition ocean state was not entirely that of an equilibrium.

First, water isotope tracers were not carried in the unaccelerated OGCM so the initial condition ocean state of these had to be derived from the end of an early short non-equilibrated CGCM run (similarly for the initial condition atmospheric state of the water isotope tracers).

Second, for water isotope tracers and all the other ocean variables, in CGCM grid boxes where the bathymetry (including land, which has a depth of 0 m) of the PD and LGM simulations differed from that of the standard PD bathymetry normally used in the unaccelerated OGCM, non-equilibrium adjustments had to be made. This was done in the same program written to calculate topography for the PD and LGM simulations (see Section 4.4). In grid boxes where there was new land or bottom compared to the standard PD bathymetry, the variables were just ignored but where there was new ocean, values for the variables had to be come up with. This was done simply by borrowing values from the nearest neighboring ocean grid box according to an algorithm already used in the topography program.¹²

Finally, for just the LGM simulation, the initial salt mass in each ocean grid box could not be from the equilibrium ocean state at the end of the unaccelerated OGCM run and the initial heavy water isotope mass in each ocean grid box could not even simply be from the mentioned non-equilibrated CGCM run. As discussed in Section 2.1.3, this is because the extra water in the continental glaciers at the expense of the ocean at the LGM compared to PD, resulting in the ≈ 120 m lower sea level at the LGM, did not have any of the salt or all of the heavy water isotope originally in that ocean water. Without an obvious mechanism for its removal, total ocean salt was assumed to have remained constant from the LGM to PD, implying an increased mean ocean salinity at the LGM of ≈ 1 g/kg. For the LGM simulation then, the

¹²Note that the OGCM part of the CGCM is on a “C grid” so that its velocities are defined on grid box edges. If a grid box is land, the velocities on all four edges must be zero. Borrowing velocity values can violate this rule so this had to be checked for and enforced in the topography program.

initial salt mass in each ocean grid box was calculated (in the mentioned topography program) by first summing the total (all grid boxes) salt in the unaccelerated OGCM equilibrium ocean adjusted for the PD simulation bathymetry, summing the total salt in the unaccelerated OGCM equilibrium ocean adjusted for the LGM simulation bathymetry, and taking the difference. Then for each ocean grid box in the unaccelerated OGCM equilibrium ocean adjusted for the LGM simulation bathymetry, a fraction of this difference equal to the fraction of the total salt the ocean grid box already has was added to the salt the ocean grid box already has. Given the non-linear dependence of water density on salinity this could very well have made the ocean non-equilibrium.

Since not all of a heavy water isotope is left behind in an ocean to glacier water transfer, the situation for a heavy water isotope is somewhat different from salt. Instead of keeping the total ocean heavy water isotope constant from LGM to PD, for the LGM simulation the mean ocean $\delta^{18}\text{O}$ and δD were set to the mentioned (Section 2.1.3) estimated LGM values of 1.25‰ and 10‰, respectively. Setting the mean ocean $\delta^{18}\text{O}$ and δD is already done in the CGCM when carrying water isotope tracers (0‰ for PD) and like salt involves proportionally distributing added water isotope. This setting of the total ocean salt and heavy water isotope might also be considered part of the CGCM boundary conditions, which are the subject of the next chapter.

Chapter 4

CGCM Boundary Conditions

4.1 Greenhouse Gases

The settings in the CGCM of the atmospheric concentrations of the radiatively-active “greenhouse” gases are important for the atmospheric radiation calculations (see Section 3.3.1 and references there), and thus for temperatures. After water vapor, which is variable in the real world and in the CGCM, the most important greenhouse gases for PD (1978 A.D.) are, in order of decreasing importance: carbon dioxide (CO_2), chlorofluorocarbons (CFCs), methane (CH_4) and nitrous oxide (N_2O); the two most important CFCs are CFC-12 (CCl_2F_2) and CFC-11 (CCl_3F). From Keeling and Whorf 2001, Khalil and Rasmussen 1994, Khalil et al. 2002, and Elkins et al. 1994, the atmospheric concentrations of CO_2 , CH_4 , N_2O , and the CFCs, respectively, were set in the CGCM for the PD simulation as given in Table 4.1 (see also Rasmussen and Khalil 1986 for an early compilation of the non- CO_2 greenhouse gas concentrations). These were from the latest reconstructions that include 1978 A.D. and vary somewhat from the standard “Present Day” values normally used in the CGCM.

Concentrations of all CFCs before 1930 A.D. were zero since they have no natural sources. The concentrations of the remaining important greenhouse gases for the LGM were taken from ice core records of trapped atmospheric gases. For CO_2 the best record for this is described in Monnin et al. 2001. “Best”, because it is from Dome Concordia, Antarctica, where compared to Greenland, ice core CO_2 records are thought to be less “compromised by the production of CO_2 by chemical reactions

		CO ₂	CH ₄	N ₂ O	CFC-12	CFC-11
Era	Year	(ppmv)	(ppbv)	(ppbv)	(pptv)	(pptv)
PD	1978 AD	336	1554	301	271	149
Holo	11 kyBP	265	675	270	0	0
YD	12 kyBP	245	470	245	0	0
BA	13 kyBP	236	645	265	0	0
PreB	15 kyBP	222	455	203	0	0
LGM	21 kyBP	185	355	190	0	0

Table 4.1: Atmospheric concentrations of the most important non-water-vapor greenhouse gases for PD, LGM and Deglaciation eras. Note differing units among gases.

between impurities in the ice”, and because, compared to other Antarctic ice core CO₂ records, its time resolution is much higher. From this same ice core and reference, and thus with no age offset, is a similarly-detailed CH₄ record. Figure 4.1 is Fig. 1 from Monnin et al. 2001 and shows the synchronous record of both of these gases. As both gases are very important forcings (and products) in the climate system and seem to go through similarly-timed stages, Figure 4.1 suggests Deglaciation time slices¹ to be simulated by the CGCM in future work: a pre-Bølling/Allerød (PreB) era at 15 kyBP; a Bølling/Allerød (BA) era at 13 kyBP; a Younger Dryas (YD) era at 12 kyBP; and a Holocene (Holo) era at 11 kyBP. In future work, simulations with glacial meltwater might also be added for each of these eras to see if that improves the simulation compared to available proxy climate data.

For N₂O during the LGM, the best most-recent measurements are from a Byrd, Antarctica ice core described in Leuenberger and Siegenthaler 1992. For N₂O during the Deglaciation, Flückiger et al. 1999 describes a high-resolution N₂O record from a Summit, Greenland ice core (GRIP), which reassuringly has a CH₄ record that is remarkably similar to the Dome C, Antarctica ice core CH₄ record (although about 500 years askew) and consistent with the Leuenberger and Siegenthaler 1992 LGM data.

For the LGM simulation, the atmospheric concentrations of the important greenhouse gases were thus set in the CGCM as given in Table 4.1. For future work, also given in the table are values for the mentioned Deglaciation eras.

¹At multiples of 1000 years due to paleotopography being available at that interval; see Section 4.4.

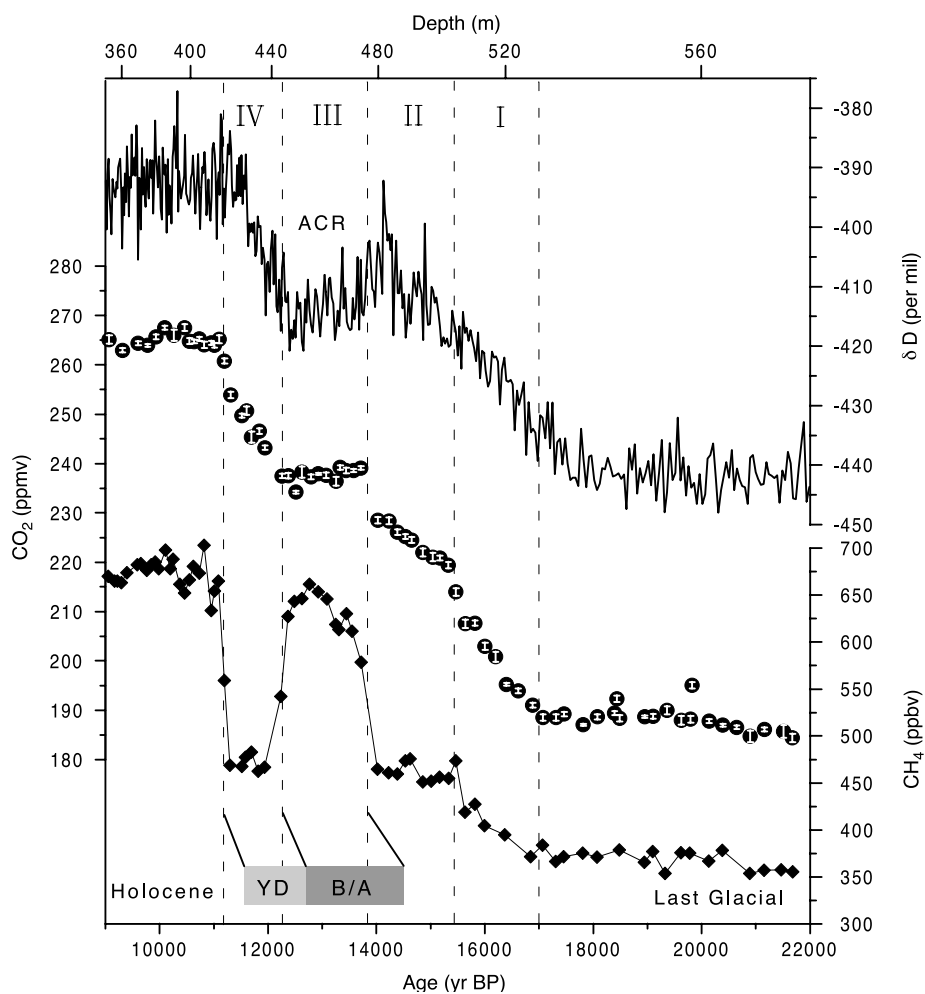


Figure 4.1: Fig. 1 from Monnin et al. 2001 showing the atmospheric CO₂ and CH₄ records, as well as δD, from the Dome C, Antarctica ice core. Circles are CO₂, diamonds are CH₄ and the solid curve is δD, which they interpret as temperature proxy.

4.2 Aerosols

The settings in the CGCM of the aerosols (e.g., dust, sulfates) are also important for the atmospheric radiation calculations, and thus for temperatures. For the PD simulation these were left at the standard PD concentrations/distributions normally used in the CGCM, which may be a bit out of date for “present day” but thus probably more appropriate for 1978 A.D. than newer data.

For the LGM there is considerable evidence in ice cores (e.g., Petit et al. 1999) and in sediments that there were generally increased dust and perhaps other aerosols then. However, globally quantifying this for realistic setting in a CGCM is a considerable task that has not yet been completed. With continued research into LGM dust provenance (e.g., Biscaye et al. 1997) for example, this may be possible for future work but was not available for the LGM simulation in this work. With one exception then, the aerosols in the CGCM for the LGM simulation are the same as those for the PD simulation. The one exception is that in the standard PD aerosols normally used in the CGCM there is an anthropogenic sulfates component but this was set to zero for the LGM simulation, since this clearly wouldn’t have existed at the LGM. While it might at first thought seem that this could have stood in for the increased LGM aerosols, it is probably of a quite different nature.

Unrealistic aerosols is an important but unavoidable deficiency in the LGM simulation. The effect of dust on radiative forcing/temperature at the LGM, and thus a measure of possible error in the LGM simulation, has been estimated in other research. For a review of these estimates and LGM dust in general, see Harrison et al. 2001. They indicate that energy balance models have suggested an additional cooling of 1–3°C due to dust at the LGM. Perhaps more applicable to an LGM simulation with a CGCM, the one estimate using a GCM (an AGCM), Overpeck et al. 1996, gives a global *warming* of 0.13–0.19°C due to dust but with regional warming of up to 5°C. There are many shortcomings with all these estimates but they do exemplify the uncertainty of the radiative forcing/temperature effect of aerosols at the LGM and in fact, this uncertainty is even the case for PD.

4.3 Insolation

Of more immediately obvious importance to the CGCM atmospheric radiation calculations is the insolation (**incoming solar radiation**). At each top-of-atmosphere (TOA) grid box the CGCM needs to calculate the TOA insolation, S , and this is a function of the solar “constant” (a.k.a. total solar irradiance), S_0 , the normalized Sun-Earth distance, ρ , and the solar declination, δ , along with the TOA grid box’s latitude, ϕ , and hour angle (i.e., local solar time), h . The equation is

$$S = \frac{S_0}{\rho^2} (\sin \phi \sin \delta + \cos \phi \cos \delta \cos h)$$

The standard PD solar constant normally used in the CGCM is 1367 W/m². Based on up-to-date satellite data and its analysis (e.g., Fröhlich 2002) this is about 1 W/m² higher than the actual mean total solar irradiance over the past 20 years but is within the variation around that mean. For consistency then, 1367 W/m² was used for the PD simulation of this work. For lack of paleo solar constant data this value was also used for the LGM simulation and so should also be used in any paleosimulations of the mentioned (Section 4.1) Deglaciation time slices of future work. Note though that given, for example, the oft-cited connection between the Little Ice Age and the Maunder Minimum in sunspots, which are thought to affect total solar irradiance, this unrealistic LGM solar constant could cause small but still significant errors. Research (e.g., Bard et al. 2000) on cosmogenic nuclides (¹⁰Be, ¹⁴C) may in the future provide better, and further in the past, estimates of paleo total solar irradiance.

The normalized Sun-Earth distance, ρ , is normalized by the semi-major axis of the Earth’s orbit and the solar declination, δ , is the latitude at which the Sun passes through the zenith at each day of the year. Both are functions of where Earth is in its orbit, i.e., the day of the year. The CGCM calculates ρ (specifically ρ^2) and δ (specifically $\sin \delta$ and $\cos \delta$) at the beginning of each day, which is midnight GMT.² An algorithm for these calculations that was more efficient and up-to-date than the standard one normally in the CGCM was adapted from Berger 1978a/Berger 1978b, tested and substituted into the CGCM. Eccentricity, e , is the ratio indicating how

²However, as representative averages for a day, the values of ρ and δ at noon are better, so their calculation at midnight in the CGCM was made in this work to have noon of the day as the time actually input to the calculation.

non-circular Earth's orbit is, obliquity, ϵ , is the angle of Earth's axis with respect to a perpendicular to the ecliptic plane, and longitude of perihelion relative to the moving vernal equinox, $\tilde{\omega}$, is the precession-dependent orbit angle from the vernal equinox to perihelion. With the time of year in the CGCM, D , going from 1.0 to 366.0 and V the time of year of the vernal equinox, the preliminary formulas of the algorithm are then (all angles in radians)

$$\begin{aligned}
 \beta &= \sqrt{1 - e^2} \\
 \lambda_{m0} &= 2 \left[\left(\frac{1}{2}e + \frac{1}{8}e^3 \right) (1 + \beta) \sin(\tilde{\omega} + \pi) - \frac{1}{4}e^2 \left(\frac{1}{2} + \beta \right) \sin 2(\tilde{\omega} + \pi) \right. \\
 &\quad \left. + \frac{1}{8}e^3 \left(\frac{1}{3} + \beta \right) \sin 3(\tilde{\omega} + \pi) \right] \\
 \lambda_m &= \lambda_{m0} + (D - V) \frac{2\pi}{365} \\
 \lambda &= \lambda_m + \left(2e - \frac{1}{4}e^3 \right) \sin(\lambda_m - (\tilde{\omega} + \pi)) + \frac{5}{4}e^2 \sin 2(\lambda_m - (\tilde{\omega} + \pi)) \\
 &\quad + \frac{13}{12}e^3 \sin 3(\lambda_m - (\tilde{\omega} + \pi))
 \end{aligned}$$

so that the normalized Sun-Earth distance, ρ , and the solar declination, δ , are finally

$$\begin{aligned}
 \rho &= \frac{1 - e^2}{1 + e \cos(\lambda - (\tilde{\omega} + \pi))} \\
 \delta &= \arcsin(\sin \epsilon \sin \lambda)
 \end{aligned}$$

Two points related to the vernal equinox should be noted. First, as indicated in the λ_m equation, the time of year of the vernal equinox, V , is the reference for the calculation of where Earth is in its orbit and without being able to perfectly match a calendar year to a sidereal year, which requires a leap year correction that the CGCM does not do, the choice of vernal equinox is somewhat arbitrary for both PD and paleo eras. For consistency and standardization, the vernal equinox was set in the PD and LGM simulations, and should be set in any other paleosimulations, as noon on March 21 ($V = 80.5$ in the CGCM) as specified by the Paleoclimate Modeling Intercomparison Project (see for example Joussaume and Taylor 1993). Second, as indicated in the formulas, the longitude of perihelion relative to the moving vernal equinox, $\tilde{\omega}$, is always used with π radians added to it. See Appendix B of Berger et al. 1993 for the heliocentric versus geocentric reasons for this.

As can be seen in the final formulas, the normalized Sun-Earth distance, ρ , and solar declination, δ , are functions of Earth's orbital parameters of obliquity, ϵ , eccen-

Era	Year	$\epsilon(^{\circ})$	e	$\tilde{\omega} + \pi (^{\circ})$
PD	-28 BP	23.44263077	0.01671259	282.51864624
Holo	11 kyBP	24.20120430	0.01952877	98.40795898
YD	12 kyBP	24.15218353	0.01960790	82.02331543
BA	13 kyBP	24.08047295	0.01965675	65.65399170
PreB	15 kyBP	23.87421227	0.01966412	32.92767334
LGM	21 kyBP	22.94902420	0.01899384	294.42498779

Table 4.2: Orbital parameters of obliquity, ϵ , eccentricity, e , and longitude of perihelion relative to the moving vernal equinox, $\tilde{\omega}$, for PD, LGM, and suggested Deglaciation eras. Note that the angles here are all in degrees and that, as when used, $\tilde{\omega}$ has 180° (π radians) added to it.

tricity, e , and longitude of perihelion relative to the moving vernal equinox, $\tilde{\omega}$. While over decades these orbital parameters are essentially unchanged, over millennia they change significantly (e.g., due to precession). These thus had to be set appropriately for the LGM simulation (as well as the PD simulation since they were of an algorithm new to the CGCM) and they would have to be set correctly for any other paleosimulations as well. They were calculated once before the start of each simulation using an algorithm (series expansions) adapted from Berger 1978b/Berger 1978a, which will be discussed next. The years before present (BP) of the specific year of a simulation’s era is used in the algorithm, with “present” being 1950 A.D. in this case (for everything else in the PD simulation, 1978 A.D. is “present day”). The resulting orbital parameters are given in Table 4.2 for the PD, LGM, and suggested Deglaciation eras (see Section 4.1).

These orbital parameters vary cyclically over millenia and thus so does insolation. Given the widespread influential practice of looking for the periods of these “Milankovitch cycles” in time series of climate proxy data, it is perhaps enlightening to explicitly see the series expansions for calculating these parameters, wherein lie their periods.

For obliquity, ϵ , with A_i the amplitudes in arc seconds, f_i the rates in arc seconds per year, t the years before (negative) or after (positive) 1950 A.D., and δ_i the phases (not declinations) in degrees, the series expansion is

$$\epsilon = 23.320556^{\circ} + \sum_{i=1}^{240} A_i \cos(f_i t + \delta_i)$$

i	A_i (")	f_i ("/yr)	δ_i (°)	Period (yrs)
1	-2462.2214466	31.609974	251.9025	41000
2	-857.3232075	32.620504	280.8325	39730
3	-629.3231835	24.172203	128.3057	53615
4	-414.2804924	31.983787	292.7252	40521
5	-311.7632587	44.828336	15.3747	28910
6	308.9408604	30.973257	263.7951	41843
7	-162.5533601	43.668246	308.4258	29678

Table 4.3: Amplitudes, rates, phases, and corresponding periods of largest amplitude terms in series expansion for obliquity, ϵ

The coefficients and corresponding periods ($= \frac{2\pi}{f_i} \frac{3600''}{1^\circ} \frac{360^\circ}{2\pi}$) of the largest/first seven terms are given in Table 4.3 (from the 47 given in Berger 1978a/Berger 1978b). While the period of the largest amplitude term is the well-known 41,000-year period attributed to obliquity, other large amplitude terms have significantly different periods.

For eccentricity, e , with E_i the amplitudes, λ_i the rates (not λ from above) in arc seconds per year, t the years before (negative) or after (positive) 1950 A.D., and ϕ_i the phases (not latitudes) in degrees, the series expansion is

$$e = 0.028707 + \sum_{i=1}^{1394+} E_i \cos(\lambda_i t + \phi_i)$$

The coefficients and corresponding periods ($= \frac{2\pi}{\lambda_i} \frac{3600''}{1^\circ} \frac{360^\circ}{2\pi}$) of the largest fifteen terms are given in Table 4.4 (from the 42 given in Berger 1978a or the 107 given in Berger 1978b). Clearly, many of the largest amplitude terms have periods quite different from the well-known 100,000-year period attributed to eccentricity.

It should be noted that, probably for historical computational limitations which are no longer the case, Berger 1978b/Berger 1978a actually calculates eccentricity with the more quickly convergent but still accurate series expansion (not the same β as above)

$$e = \left[\left(\sum_{i=1}^{19} M_i \sin(g_i t + \beta_i) \right)^2 + \left(\sum_{i=1}^{19} M_i \cos(g_i t + \beta_i) \right)^2 \right]^{\frac{1}{2}}$$

For convenience and consistency this is what was used in this work as well. As an approximation series its periods are no longer meaningful so are not shown but Berger

i	E_i	λ_i ("/yr)	ϕ_i (°)	Period (yrs)
1	0.01102940	3.138886	165.16	412885
2	-0.00873296	13.650058	279.68	94945
3	-0.00749255	10.511172	114.51	123297
4	0.00672394	13.013341	291.57	99590
5	0.00581229	9.874455	126.41	131248
6	-0.00470066	0.636717	348.10	2305441
7	-0.00254464	12.639528	250.75	102535
8	0.00231485	0.991874	58.57	1306618
9	-0.00221955	9.500642	85.58	136412
10	0.00201868	2.147012	106.59	603630
11	-0.00172371	0.373813	40.82	3466974
12	-0.00166112	12.658184	221.11	102384
13	0.00145096	1.010530	28.93	1282495
14	0.00131342	12.021467	233.00	107807
15	0.00101442	0.373813	40.82	3466974

Table 4.4: Amplitudes, rates, phases, and corresponding periods of largest amplitude terms in series expansion for eccentricity, e

1978a/Berger 1978b provides coefficients for 19 terms of this series expansion.

For the longitude of perihelion relative to the moving vernal equinox, $\tilde{\omega}$, with P_i the amplitudes, α_i the rates in arc seconds per year, t the years before (negative) or after (positive) 1950 A.D., and ζ_i the phases in degrees, the series expansion is

$$\tilde{\omega} = \arctan \left(\frac{\sum_{i=1}^{589} P_i \sin(\alpha_i t + \zeta_i)}{\sum_{i=1}^{589} P_i \cos(\alpha_i t + \zeta_i)} \right)$$

The coefficients and corresponding periods ($= \frac{2\pi}{\alpha_i} \frac{3600''}{1^\circ} \frac{360^\circ}{2\pi}$) of the largest nine terms are given in Table 4.5 (from the 46 given in Berger 1978a or the 117 given in Berger 1978b). The periods of the largest amplitude terms are not exactly the 19,000- and 23,000-year periods usually attributed to precession, of which the longitude of perihelion relative to the moving vernal equinox is a measure.

Again, it should be noted that, probably for historical computational limitations which are no longer the case, Berger 1978b/Berger 1978a actually calculates the longitude of perihelion relative to the moving vernal equinox, $\tilde{\omega}$, with an algorithm that uses more quickly convergent but still accurate series expansions:

$$\tilde{\omega} = \psi + \pi$$

				Period
i	P_i	α_i ("/yr)	ζ_i (°)	(yrs)
1	0.0186080	54.646484	32.01	23716
2	0.0162752	57.785370	197.18	22428
3	-0.0130066	68.296539	311.69	18976
4	0.0098883	67.659821	323.59	19155
5	-0.0033670	67.286011	282.76	19261
6	0.0033308	55.638351	90.58	23293
7	-0.0023540	68.670349	352.52	18873
8	0.0014002	76.656036	131.83	16907
9	0.0010070	56.798447	157.53	22818

Table 4.5: Amplitudes, rates, phases, and corresponding periods of largest amplitude terms in series expansion for longitude of perihelion relative to the moving vernal equinox, $\tilde{\omega}$

$$\psi = (50.439273''/\text{yr})t + 3.392506^\circ + \sum_{i=1}^{411} F_i \sin(f'_i t + \delta'_i)$$

$$\pi = \arctan\left(\frac{\sum_{i=1}^{19} M_i \sin(g_i t + \beta_i)}{\sum_{i=1}^{19} M_i \cos(g_i t + \beta_i)}\right)$$

where ψ is the general precession and π is the longitude of perihelion relative to the *fixed* vernal equinox. For convenience and consistency this is what was used in this work as well. As an approximation series its periods are no longer meaningful so are not shown but Berger 1978b provides coefficients for 78 terms for the ψ series expansion (Berger 1978a provides just 10). The coefficients for the series expansion for π are just those from the “quick-converge” series expansion for e above.

For the actual resulting insolation then, the differences from PD of the zonally-averaged monthly-mean top-of-atmosphere insolation for the LGM and suggested Deglaciation eras are shown in Figures 4.2 and 4.3 for all 12 months (since they are quite varied and the CGCM outputs monthly mean fields). A horizontal line at 0 W/m² would represent PD. Note how much closer to PD (1978 A.D.) the LGM (21 kyBP) insolation is compared to the more recent Deglaciation eras. Still, the LGM differences from PD are significant.

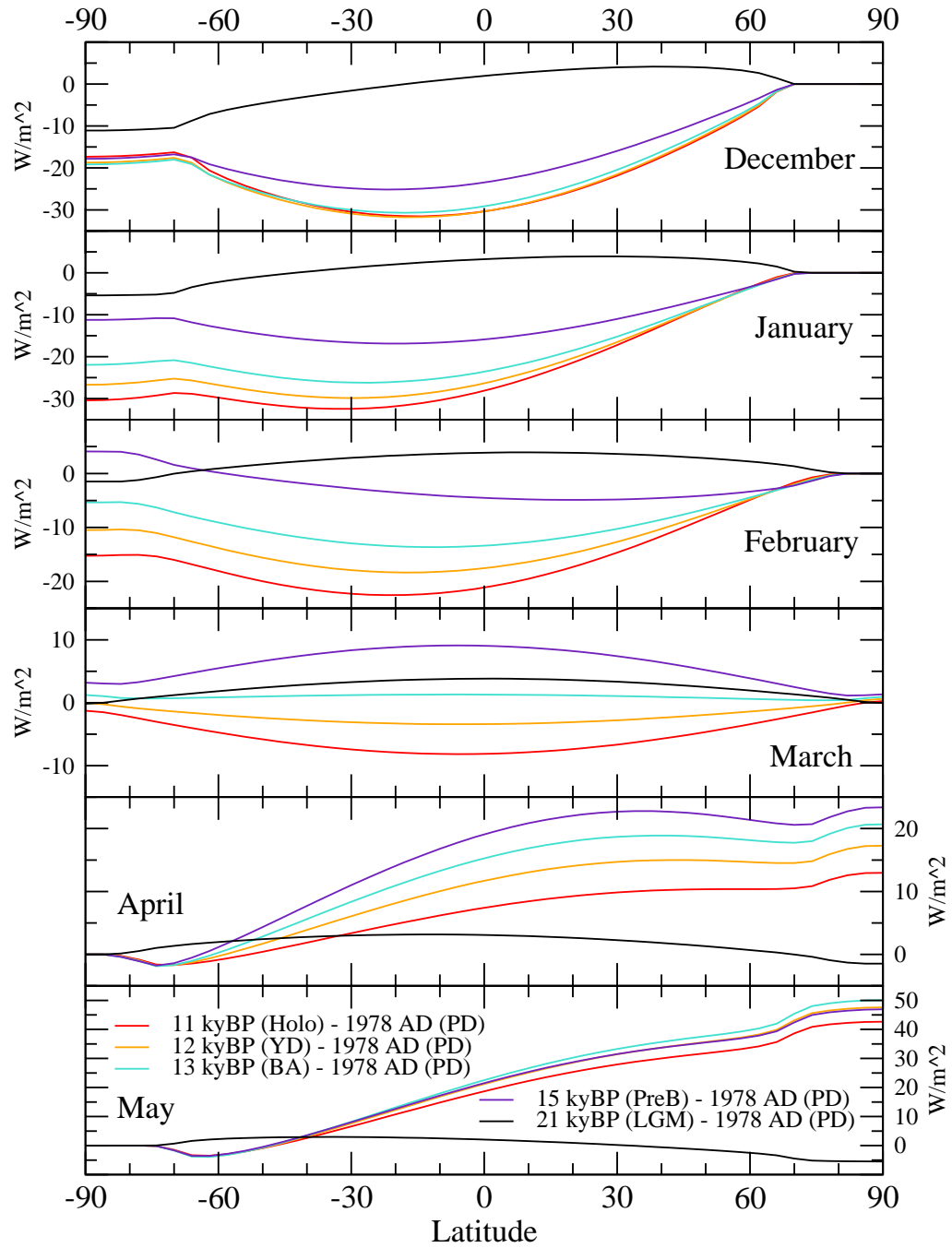


Figure 4.2: Differences from PD of zonally-averaged monthly-mean top-of-atmosphere insolation for LGM and suggested Deglaciation eras: Dec–May. Note that to most clearly show the differences between eras, each W/m^2 scale has been expanded as much as possible and thus might not be the same for each month.

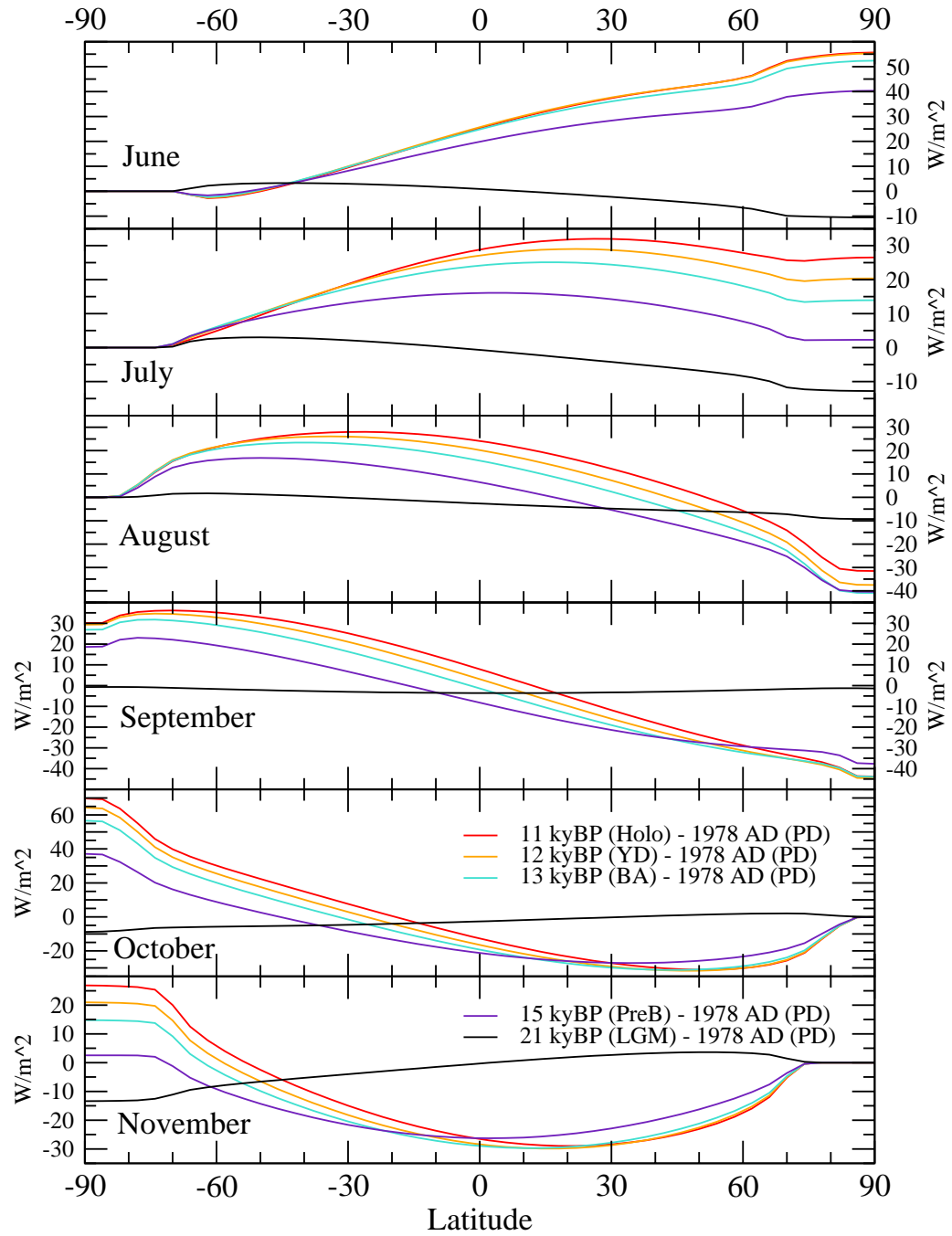


Figure 4.3: Differences from PD of zonally-averaged monthly-mean top-of-atmosphere insolation for LGM and suggested Deglaciation eras: Jun–Nov. Note that to most clearly show the differences between eras, each W/m^2 scale has been expanded as much as possible and thus might not be the same for each month.

4.4 Topography

The most extensive boundary condition difference of the LGM compared to PD is the topography: the increase in continental glacier thickness and extent, the resulting lower sea level, the resulting elevation/bathymetry changes, and the resulting land/ocean boundary and straits changes. This can be globally reconstructed using relative sea level histories from dated raised/submerged shorelines and a model of the viscoelastic Earth. Such a reconstruction was done in Peltier 1994, where a description of the theory can be found. The result was a global dataset of continental glacier extent and elevation/bathymetry relative to sea level at the time (again, LGM sea level was ≈ 120 m lower than PD; see Section 2.1.3). This dataset was called ICE-4G and was usable for making the topographies used in GCMs. Unfortunately, particularly for the Paleoclimate Model Intercomparison Project (PMIP; see Joussaume and Taylor 1994), which extensively used it, there was an oversight in the formulation of ICE-4G and it was in error, particularly in its underestimation of LGM glacier thickness in Hudson Bay and the Barents Sea. A correction to this oversight was given in Peltier 1998, where it was presented as the discovery of “implicit ice”. The corrected ICE-4G dataset (Peltier and Solheim 2001) was obtained for this work. At $1^\circ \times 1^\circ$ resolution and for 1000-year time slices from the LGM to PD, this dataset gives continental glacier thickness and elevation/bathymetry relative to sea level at the time.

While looking in this corrected ICE-4G dataset at the 12 kyBP time slice in preparation for a possible Younger Dryas simulation it was noted that the glacier in the Barents Sea had significant thickness but had an elevation significantly below sea level. This was found to be true in other large glacier areas as well. There is no logical way to interpret this and in fact, W. R. Peltier confirmed there is a problem (personal communication, August 2002). A resolution was promised but none was available at the time of this writing. This “submarine glacier” problem also exists in the dataset for the LGM (21 kyBP) and PD (0 kyBP) time slices of concern in this work but in those it generally occurs in isolated single $1^\circ \times 1^\circ$ boxes. If these isolated single problem boxes are ignored when doing the interpolation of the dataset up to the $5^\circ \times 4^\circ$ resolution (see Section 3.2.1) of the CGCM, the rest of the $1^\circ \times 1^\circ$ boxes in each

encompassing $5^\circ \times 4^\circ$ CGCM grid box produce a reasonable elevation/bathymetry and glacier thicknesses for that CGCM grid box. Thus, the dataset was usable for making the CGCM topographies for the LGM and PD simulations in this work but would not be for any of the Deglaciation era simulations suggested (see Section 4.1) for future work. However, even while the resulting LGM and PD topographies seem reasonable, they must be regarded with reduced confidence. To avoid confusion of what is “corrected”, the implicit-ice-corrected ICE-4G dataset will be referred to in this work as the “Implicit ICE-4G dataset”.

Using the Implicit ICE-4G dataset to make the LGM and PD topographies required writing a program to:

- 1) map the dataset’s $1^\circ \times 1^\circ$ grid boxes into the CGCM’s $5^\circ \times 4^\circ$ grid boxes
- 2) decide whether each CGCM box was land/ocean based on the fraction (threshold = .5) of dataset boxes within it whose elevations were greater/less than 0 (sea level)
- 3) custom set some CGCM boxes as land/ocean that would from the previous step otherwise undesirably be considered ocean/land
- 4) calculate the fraction of each CGCM land box covered by glacier (always 1 in Antarctica) based on the number of dataset boxes within it whose glacier thickness and elevation were greater than 0
- 5) calculate the elevation of each CGCM land box as the average of the greater-than-zero elevations of the dataset boxes within it (except if the CGCM land box was landlocked, in which case even the less-than-zero elevations were included in the average)
- 6) calculate the ocean thickness of each CGCM ocean box as the negative of the average of the less-than-zero elevations of the dataset boxes within it
- 7) custom set some CGCM ocean box thicknesses to account for important sub-grid ocean bottom ridges
- 8) calculate the glacier thickness of each glaciated CGCM box as the average of the greater-than-zero thicknesses of the glaciated dataset boxes within it (custom setting any Antarctic CGCM boxes that still needed a non-zero glacier thickness)
- 9) calculate the bathymetry of each CGCM ocean box as the negative of its ocean

thickness

10) take care of the pole boxes, which were often special cases in the preceding

From the resulting $5^\circ \times 4^\circ$ topography the CGCM itself calculates the actual discrete grid box levels used: in the AGCM of the CGCM, terrain-following sigma coordinates are used in the lower atmosphere (see Section 3.3.1); in the OGCM of the CGCM, each ocean grid box column has from 1 to 13 levels of grid boxes depending on what level the bathymetry reaches into there (see Section 3.2.1).

As discussed in Section 3.2.1, where not feasible in the OGCM to represent a real-world strait by a standard $5^\circ \times 4^\circ$ ocean grid box, there is a parameterization consisting of metagrid straits, whereby two non-adjacent ocean grid boxes are specified to be connected by a strait with specified realistic characteristics. The Implicit ICE-4G dataset provides no specific information on straits characteristics, so these had to be individually researched and custom set in the CGCM: the two non-adjacent ocean grid boxes to be connected, the strait-depth-corresponding number of discrete OGCM levels, the strait width, and the direction $((x,y) \text{ where } x^2 + y^2 = 1)$ of the strait from each connecting ocean grid box. Note in this work that for simplicity individual grid boxes are specified in the horizontal by $[\text{lon}\#, \text{lat}\#]$, where $\text{lon}\#$ is the CGCM grid box number in longitude (1–72) and $\text{lat}\#$ is the CGCM grid box number in latitude (1–46).

As indicated, the PD topography was also made from the Implicit ICE-4G dataset even though a standard PD topography already existed. This was done for consistency between the LGM and PD simulations but the resulting PD topography in this work differs quite a bit from the standard PD topography normally used in the CGCM. Besides differences due to the differing elevation/bathymetry and continental glacier data on which the ICE-4G dataset is based, the custom setting of CGCM grid boxes to land or ocean in the PD topography in this work was done with renewed attention to assuring that observed ocean currents (as given in Tomczak and Godfrey 1994) were at least possible in the CGCM. In particular, the representations of islands and continental coasts of several important regions were significantly modified: the Indonesia/Philippines/Southeast Asia/New Guinea region, the Gulf of Mexico, north/east Canada, and Japan. Additionally, several other islands that have a significant effect on ocean currents but that were not represented, were underrepresented,

or were incorrectly represented in the standard PD topography were modified in the PD topography in this work: New Zealand, Tasmania, Taiwan, Scotland, Spitsbergen, Franz Josef Land, North Land, and the New Siberian Islands. For the resulting PD topography in this work, the CGCM grid box maps of land/ocean, land elevation, and ocean depth are given in Figure 4.4 a, b, and c, respectively, and the maps of glacier extent and thickness are given in Figure 4.5 a and b, respectively.

In the standard PD topography normally used in the CGCM there are twelve metagrid straits specified. More recent research on the corresponding real-world straits indicated that the existing specified characteristics of eleven of these metagrid straits were accurate enough to not make it worth updating them. The twelfth metagrid strait though seemed clearly and significantly problematic. That strait is a representation of the Soya Strait from the northernmost Sea of Japan to the southernmost Sea of Okhotsk. The problem with it is that it is the only strait represented in that area so also seems to represent the Tsugaru Strait from the northeastern Sea of Japan to the Pacific Ocean. However, in reality the Tsugaru Strait is by far the more important strait (see for example Keigwin and Gorbarenko 1992), with a much larger current in a more critical direction (returning back out to the Pacific Ocean the warm salty waters flowing into the south Sea of Japan via the Korea/Tsushima Strait). The twelfth metagrid strait in the PD topography of this work was thus made a representation of the Tsugaru Strait (some custom land/ocean settings in the area were also made). The characteristics of the twelve specified CGCM metagrid straits of the PD topography of this work are given in Table 4.6.

Together the above PD modifications pointed out the need for a careful study of the effect of topography in the OGCM, which would be a large project in itself and was thus outside the scope of this work. Note though, that as discussed in Section 3.3.3, it was found that small changes in topography may have improved NAMOC streamfunction.

Since the LGM is less well-known than PD, to make the LGM topography there had to be less reliance on custom settings and more on the calculations of the program to make the topography from the Implicit ICE-4G dataset. However, given the ≈ 120 m lower sea level at the LGM and its critical effect on many straits, there is available

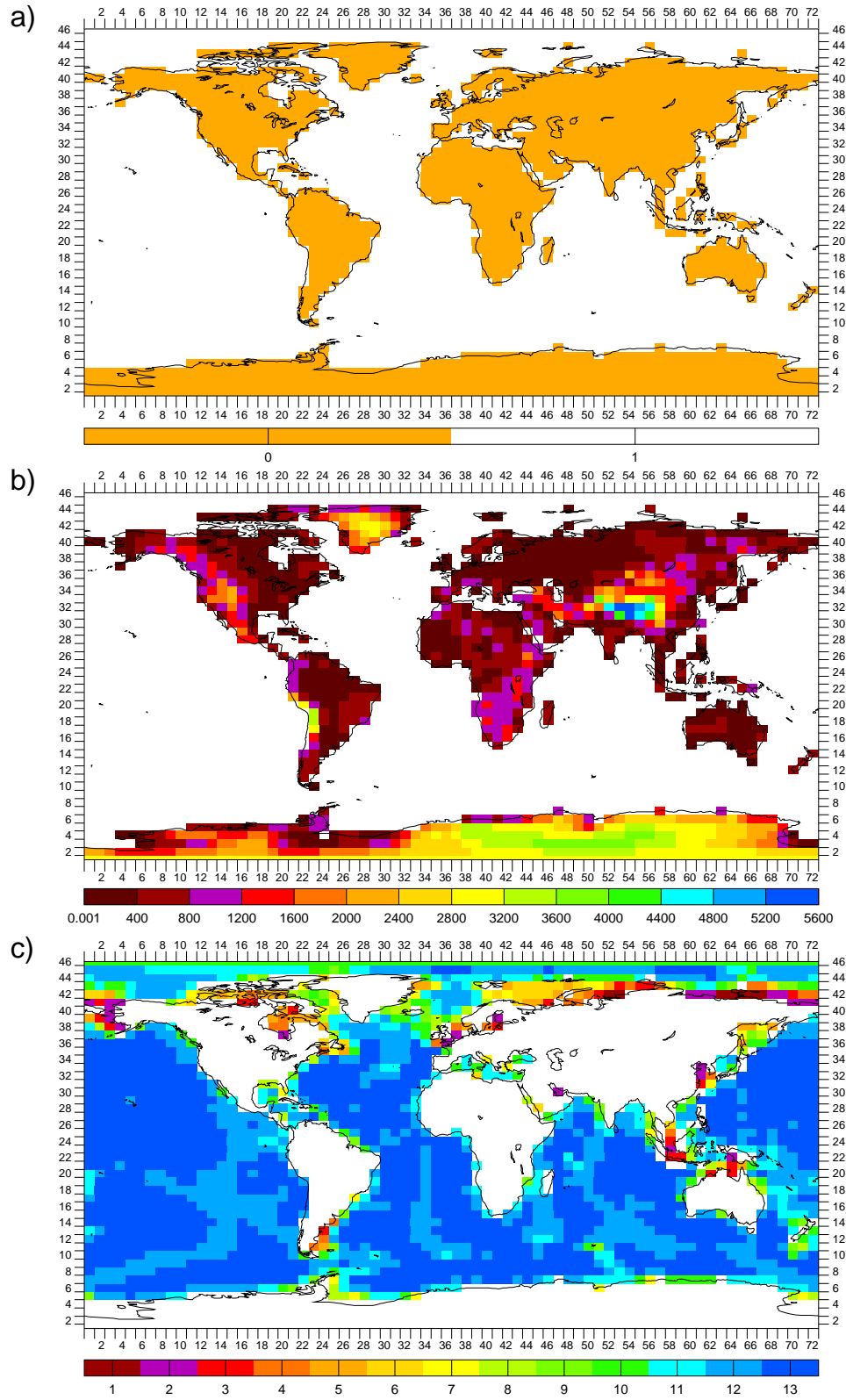


Figure 4.4: CGCM grid box maps for PD: a) land/ocean (0/1); b) land elevation (m); and c) ocean depth (OGCM level)

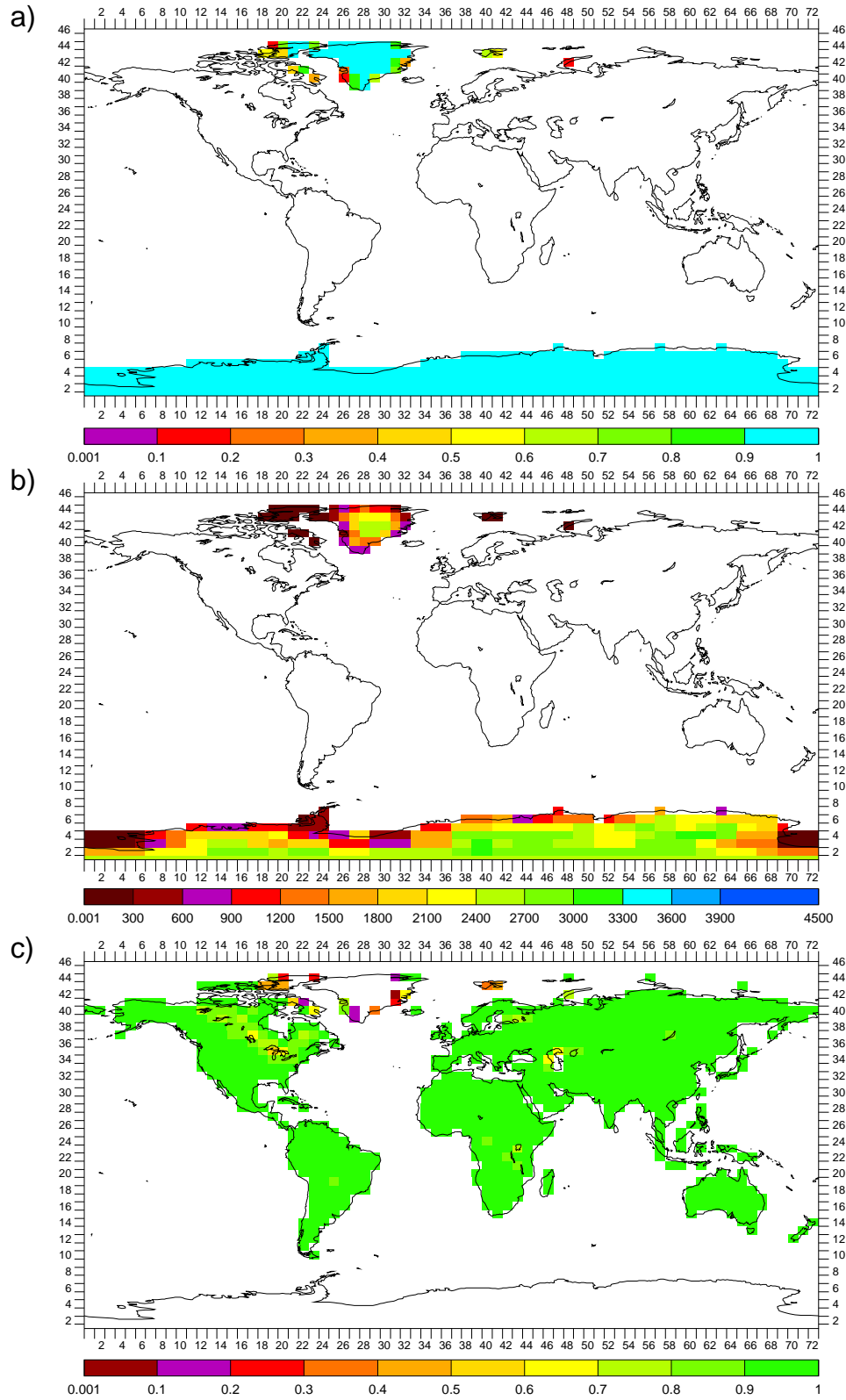


Figure 4.5: CGCM grid box maps for PD: a) glacier extent (fraction of box); b) glacier thickness (m); and c) non-glaciated non-lake ground (fraction of box)

#	Strait Name	Depth (OGCM level)	Width (km)	Connected ocean grid boxes [lon#,lat#]		Directions from ocean grid boxes (x,y)	
1	Fury & Hecla	2	20	[19,42]	[20,40]	(0,-1)	(0,1)
2	Nares	5	5	[22,43]	[24,44]	(.6,.8)	(-.8,-.6)
3	Gibraltar	5	25	[35,32]	[37,33]	(.6,.8)	(-.8,-.6)
4	English	2	35	[36,36]	[37,37]	(1,0)	(0,-1)
5	Kattegat	2	60	[38,38]	[40,38]	(1,0)	(-.6,-.8)
6	Bosphorous	2	6	[42,33]	[43,34]	(0,1)	(-.8,-.6)
7	Red Sea	6	250	[44,29]	[45,28]	(.6,-.8)	(-.8,.6)
8	Bab el Mandab	6	25	[45,28]	[46,27]	(.6,-.8)	(-1,0)
9	Hormuz	2	50	[47,30]	[49,29]	(1,0)	(-.7,.7)
10	Malacca	3	50	[56,25]	[58,24]	(.6,-.8)	(-1,0)
11	Korea	4	170	[62,32]	[63,33]	(0,1)	(-.6,-.8)
12	Tsugaru	4	20	[64,34]	[66,34]	(1,0)	(-1,0)

Table 4.6: CGCM metagrid straits characteristics for PD topography

published research about those straits at the LGM. This literature³ was consulted in making the LGM topography, for changes both in the specified characteristics of the CGCM metagrid straits and in straits represented by the usual CGCM ocean grid boxes. For the resulting LGM topography, the CGCM grid box maps of land/ocean, land elevation, and ocean depth are given in Figure 4.6 a, b, and c, respectively, and the maps of glacier extent and thickness are given in Figure 4.7 a and b, respectively.

The characteristics of the five specified CGCM metagrid straits of the LGM topography are given in Table 4.7. Given the ≈ 120 m lower sea level and the increased glacier extent at the LGM, many of the straits that exist at PD were closed by land or glaciers at the LGM. For direct LGM/PD comparison these closed straits are listed in the table as well, along with references that indicate their closure at the LGM. Of the five LGM metagrid straits, none at a different location from PD was used so the connected ocean grid boxes and directions from these ocean grid boxes were unchanged and thus not given again in Table 4.7. The lower LGM sea level did change the depths and widths of the remaining straits though, so these are given in the table,

³Interestingly, this includes serious consideration of several flood-related myths: see Collina-Girard 2001 for the Strait of Gibraltar and the myth of Atlantis; Aksu et al. 2002 and the references therein for the Strait of Bosphorus and the myth of Noah's Flood; and Teller et al. 2000 for the Straits of Hormuz and the myths of Noah's Flood and the Epic of Gilgamesh.

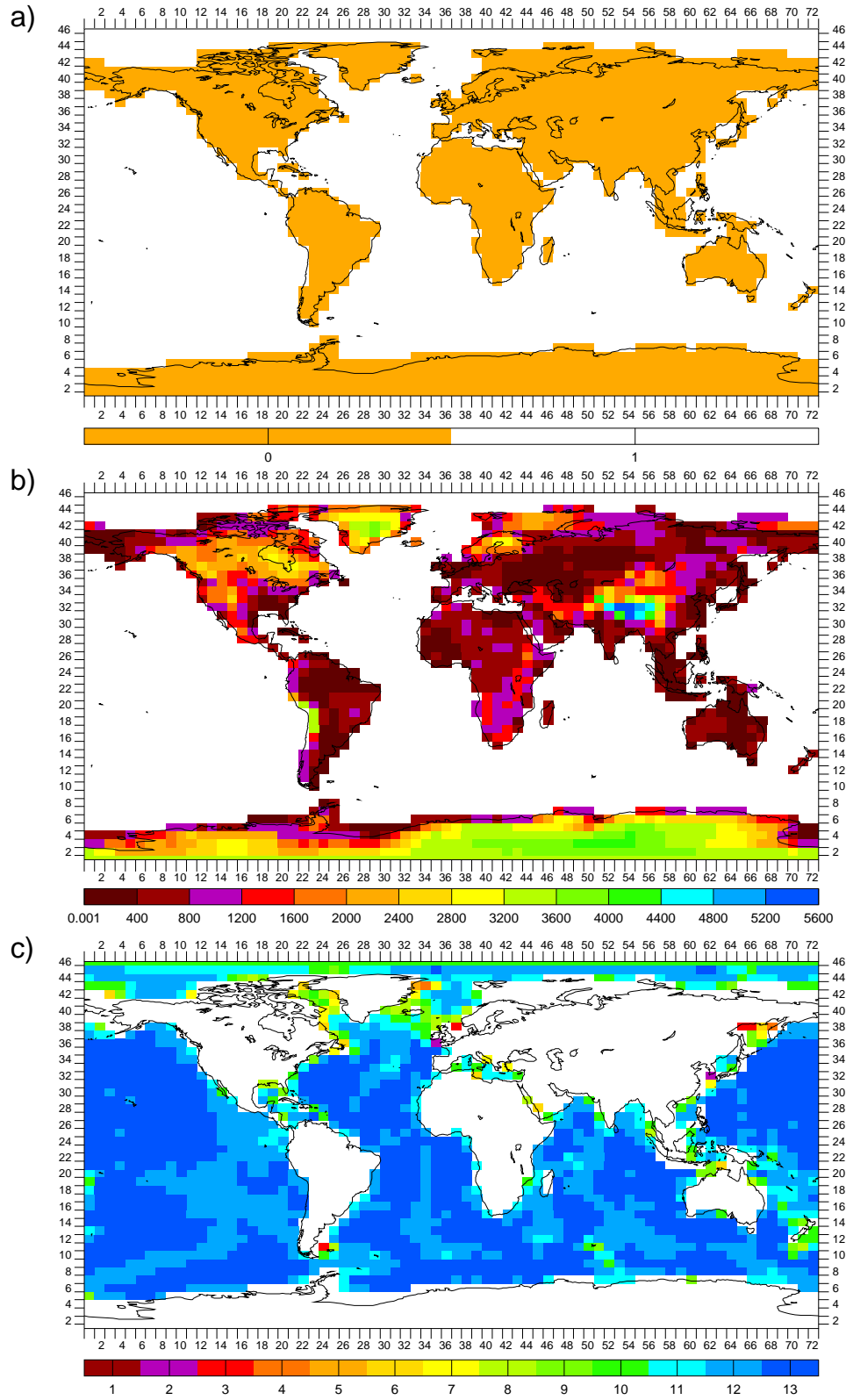


Figure 4.6: CGCM grid box maps for LGM: a) land/ocean (0/1); b) land elevation (m); and c) ocean depth (OGCM level)

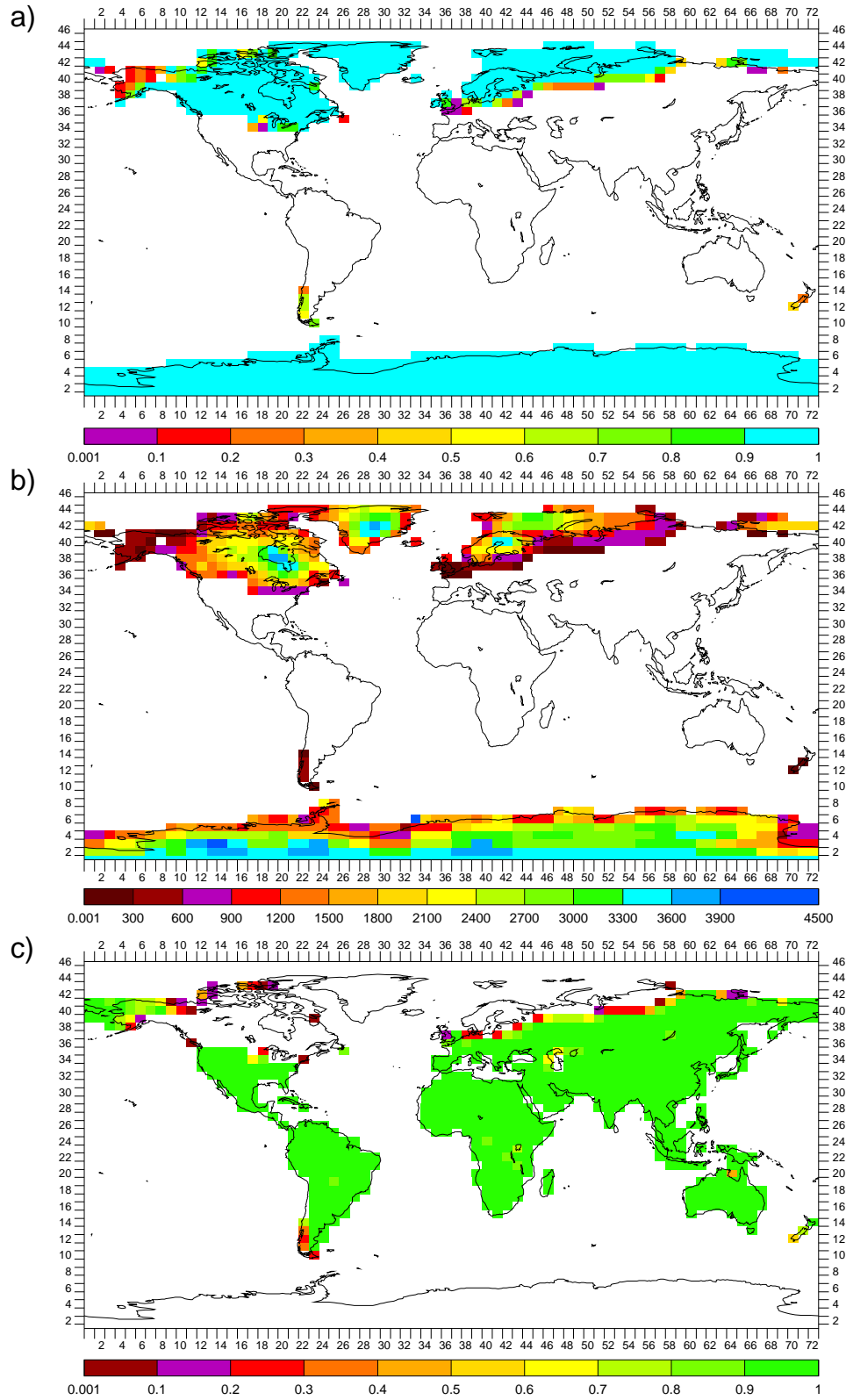


Figure 4.7: CGCM grid box maps for LGM: a) glacier extent (fraction of box); b) glacier thickness (m); and c) non-glaciated non-lake ground (fraction of box)

along with the references used to derive them. There are a couple of explicit notations that should be made about the two metagrid straits that connect the two isolated Red Sea ocean grid boxes to each other and an Indian ocean grid box. First, the Red Sea metagrid strait between the two Red Sea ocean grid boxes does not really represent a strait as usually defined by a sill. Instead it just represents the Red Sea at around midlength. Its depth then is just set as that of the southeastern Red Sea ocean grid box. Its width at PD is set at the characteristic Red Sea width of 250 km and at the LGM Rohling and Zachariasse 1996 states that the area of the Red Sea was reduced by 50% so its width then is set as 125 km. Second, for the Bab el Mandab metagrid strait at the LGM, the pertinent sill it is representing was 17 m ($137\text{ m} - 120\text{ m}$) deep then⁴ according to Rohling and Zachariasse 1996. While this is closer to the 12 m depth of OGCM level 1 than to the 30 m depth of OGCM level 2, the latter was used to allow for simulation of the “in at one level, out at another” flow that is characteristic of the single-opening Red Sea.

As discussed in Section 3.1 it is important in paleoclimate modelling to look at the differences between the paleosimulation and PD control simulation results. It is thus also important to explicitly note the differences in the input boundary conditions, such as topography. Figure 4.8 then, is the LGM – PD difference between the fields of Figures 4.6 and 4.4 and Figure 4.9 is the LGM – PD difference between the fields of Figures 4.7 and 4.5. The LGM – PD differences in the metagrid straits have already been noted.

Figure 4.8a clearly shows the increased land at the LGM compared to PD due to increased LGM continental glacier extent (Figure 4.9a) along the Antarctic coast, northern Eurasia and in Canada and due to lower LGM sea level along the mid and low latitude continental coasts and the Australasian region. Note the resulting closing of the Bering Strait, Northwest Passage, Hudson Strait, Sunda Shelf seas, and Arufa Sea, as well as the thinning of the Drake Passage, all of which are not represented by CGCM metagrid straits. Note also that the single ocean grid box Florida Strait is left unchanged between PD and LGM. This was a conscious decision (i.e., custom set): the Florida Strait was more restricted at the LGM but not closed and as it is represented

⁴137 m is often invoked as an upper limit on sea level lowering at the LGM since it is believed the Red Sea was still open to the ocean then.

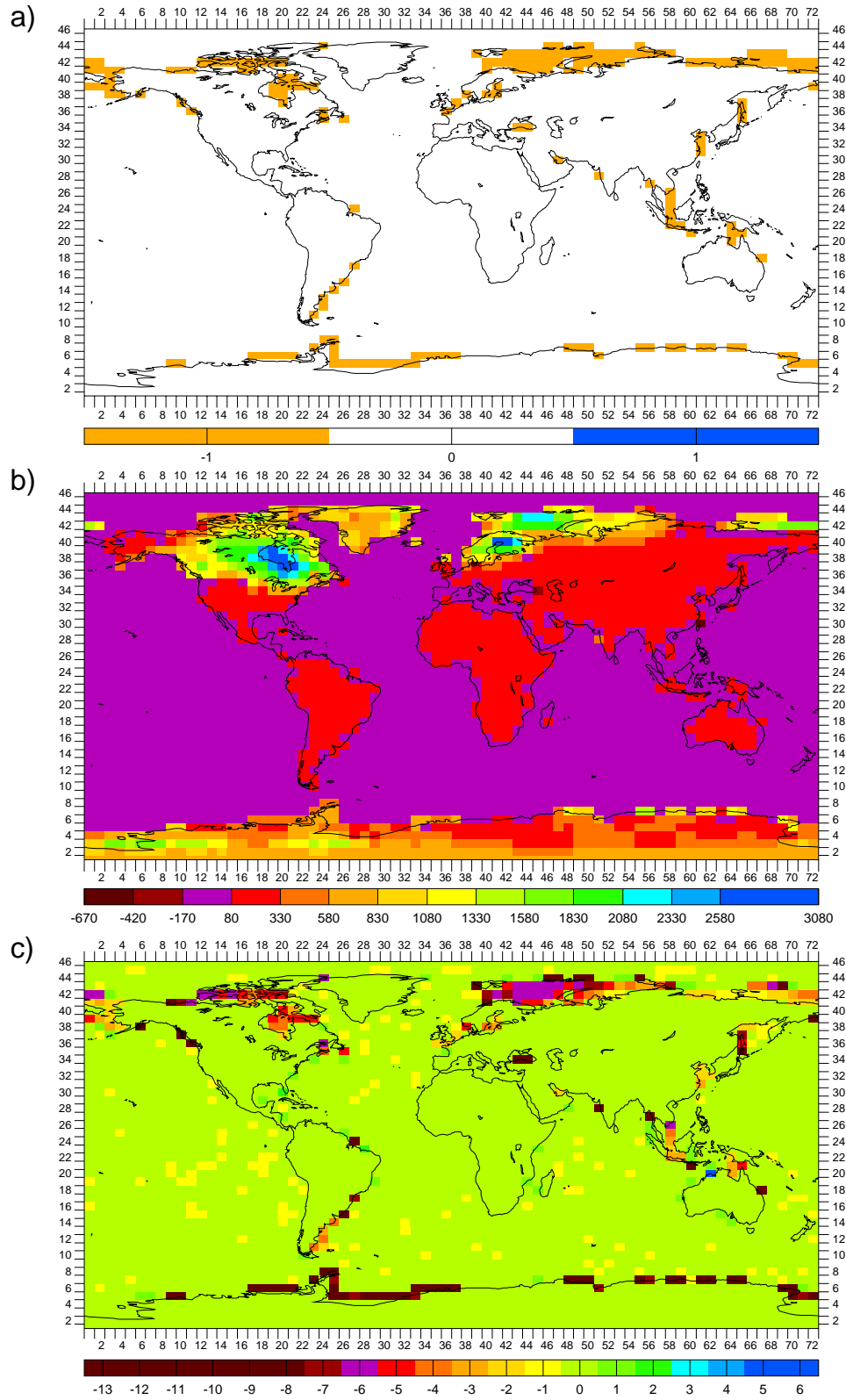


Figure 4.8: CGCM grid box maps for LGM – PD: a) land/ocean (0/1); b) land elevation (m); and c) ocean depth (OGCM level)

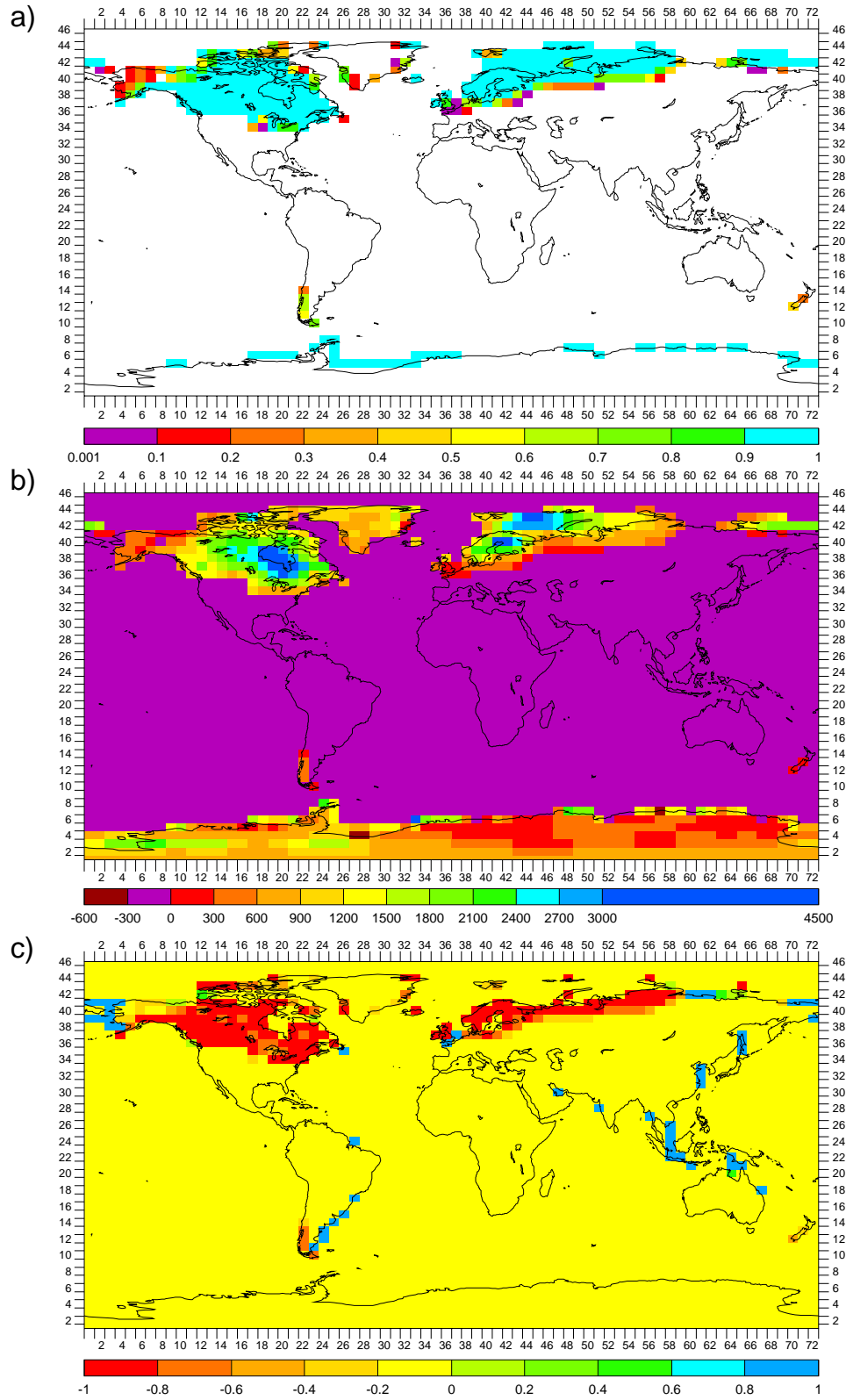


Figure 4.9: CGCM grid box maps for LGM – PD: a) glacier extent (fraction of box); b) glacier thickness (m); and c) non-glaciated non-lake ground (fraction of box)

#	Strait Name	Depth (OGCM level)	Width (km)	References
1	Fury & Hecla	Closed by glacier at LGM		Implicit ICE-4G dataset
	Nares	Closed by glacier at LGM		England 1999
	Gibraltar	3	10	Tsimplis and Bryden 2000, Collina-Girard 2001
	English	Closed by land at LGM		Lambeck 1997
	Kattegat	Closed by glacier at LGM		Implicit ICE-4G dataset
2	Bosphorous	Closed by land at LGM		Aksu et al. 2002
	Red Sea	6	125	Rohling and Zachariasse 1996
	Bab el Mandab	2	11	Rohling and Zachariasse 1996
3	Hormuz	Closed by land at LGM		Teller et al. 2000
	Malacca	Closed by land at LGM		Deckker et al. 2002
	Korea	1	15	Keigwin and Gorbarenko 1992, Ishiwatari et al. 2001, Crusius et al. 1999
5	Tsugaru	1	5	Keigwin and Gorbarenko 1992, Ishiwatari et al. 2001, Crusius et al. 1999

Table 4.7: CGCM metagrid straits characteristics of the LGM topography

by a too-wide single ocean grid box at PD it was left that way for the LGM. Given its criticality to ocean circulation, future work could include representing it as a more finely measured CGCM metagrid strait. Finally for land/ocean comparisons, the reasons the Black Sea and the Persian Gulf are considered land at the LGM will be discussed ahead.

Figure 4.8b shows the significantly increased land elevation at the LGM compared to PD due to increased LGM continental glacier thickness (Figure 4.9b) over Canada, Greenland, northern Eurasia and Antarctica. The (smaller) increased land elevation over most of the remaining unglaciated land is due to the lower LGM sea level and the fact that an era's sea level is used as the reference for elevation then (i.e., the LGM yardstick moved down). This increased LGM elevation is not the same over all remaining land or exactly the magnitude of the LGM sea level drop because the viscoelastic changes in the Earth's surface at the LGM are not spatially uniform, in magnitude or even direction.

Given the ≈ 120 m lower sea level at the LGM compared to PD, the sparsity

in Figure 4.8c of decreased LGM ocean depth in the open ocean may at first glance seem odd. However, these ocean depths are discrete OGCM levels that based on bathymetry are assigned (by the CGCM) from the surface down, with the deepest levels being non-linearly a couple orders of magnitude thicker than the shallowest levels, e.g., 12 m thickness for the surface level, 1, versus 1557 m thickness for the deepest possible level, 13. Unless an ocean grid box column had only a few OGCM levels at PD, in which case an ≈ 120 m lower sea level at the LGM was likely to just turn it into land (this is a lot of the coastal depth decreases seen in Figure 4.8c), or was near the cutoff depth for being assigned the next shallower OGCM level, then there was not a decrease in assigned OGCM level at the LGM. A more consistent scheme may be to take 120 m off the definition of the thickness of the deepest possible OGCM level or to proportionately reduce the thickness of all OGCM levels, making the sum of the reductions 120 m, but doing this in the CGCM is very problematic and it was thus not tried.

Note that the assigned OGCM levels of the Red Sea ocean grid boxes are also unchanged between the LGM and PD, but not for the preceding reason. In fact, the Red Sea depths (m) calculated from the Implicit ICE-4G dataset by the discussed interpolation program are somewhat *larger* at the LGM compared to PD, even with the ≈ 120 m lower sea level then. This is because the number of below-sea-level Implicit ICE-4G dataset $1^\circ \times 1^\circ$ boxes averaged for each Red Sea CGCM $5^\circ \times 4^\circ$ grid box decreases with the lower sea level at the LGM and the shallower $1^\circ \times 1^\circ$ grid boxes are the PD below-sea-level boxes that disappear, since going from shallow to deep near land usually consists of a relatively shallow shelf and then a plunge to the deep. This anomaly is acceptable because the dominant dynamic processes, rather than just volumes, are what is important and with the shallower areas gone, the dominant processes are those over the deep areas. Any concerns about unreal effects outside the Red Sea from the unchanged Red Sea water volume at the LGM are addressed by the more-restricted Bab el Mandab metagrid strait then (see Tables 4.7 and 4.6). All this is similarly true for other inland seas. Further, note in Figure 4.8c along coasts that for the same reason there are actually some *increases* in ocean depth at the LGM compared to PD.

4.5 Land Surface

There are three types of land surface defined in the CGCM: glacier, lake and ground. Each CGCM grid box that is land can have a fraction that is glacier, a fraction that is lake and a fraction that is ground, with the fractions having to add up to 1.0. These fractions and the characteristics specified for glacier, lake and ground are used by the CGCM to calculate the interaction of the land with the atmosphere and ocean. The specified characteristics of glacier, lake and ground are standard PD global datasets made for the CGCM from observations. A couple of the more important examples in this work are lake thickness and river direction, which is a lake characteristic since rivers/runoff are considered overflowing lakes. Other examples include vegetation types, which is a ground characteristic.

Clearly, the determination of topography as described in Section 4.4 is intertwined with the determination of glacier, lake and ground. And in fact this land surface determination was done in the same program written for making the topographies for the CGCM from the Implicit ICE-4G dataset. To begin with, which grid boxes were land at all was determined and then what fraction of each was covered by glacier. Lake fraction is a land surface characteristic specified in a PD global dataset and with the glacier fraction and lake fraction determined and a requirement that all three fractions sum to 1.0, the ground fraction is determined as a remainder. Figure 4.10a and Figure 4.5c are the CGCM grid box maps for PD of lake fraction and ground fraction, respectively.

Unfortunately, global datasets of land surface characteristics usable for the CGCM do not exist for the LGM and making them specially here was out of the question: the making of the standard PD set was apparently a large effort in itself and making them for the LGM is a far more ambitious project (one in fact being undertaken by a large group of researchers). It was decided then to just use the land surface characteristics of PD for the LGM too — where not superseded by increased glacier extent — as suggested by the Paleoclimate Model Intercomparison Project (see Joussaume and Taylor 1994). However, as shown, there was increased land at the LGM and even the PD topography has land in some CGCM grid boxes that the standard PD topography normally used in the CGCM, on which the global datasets of land

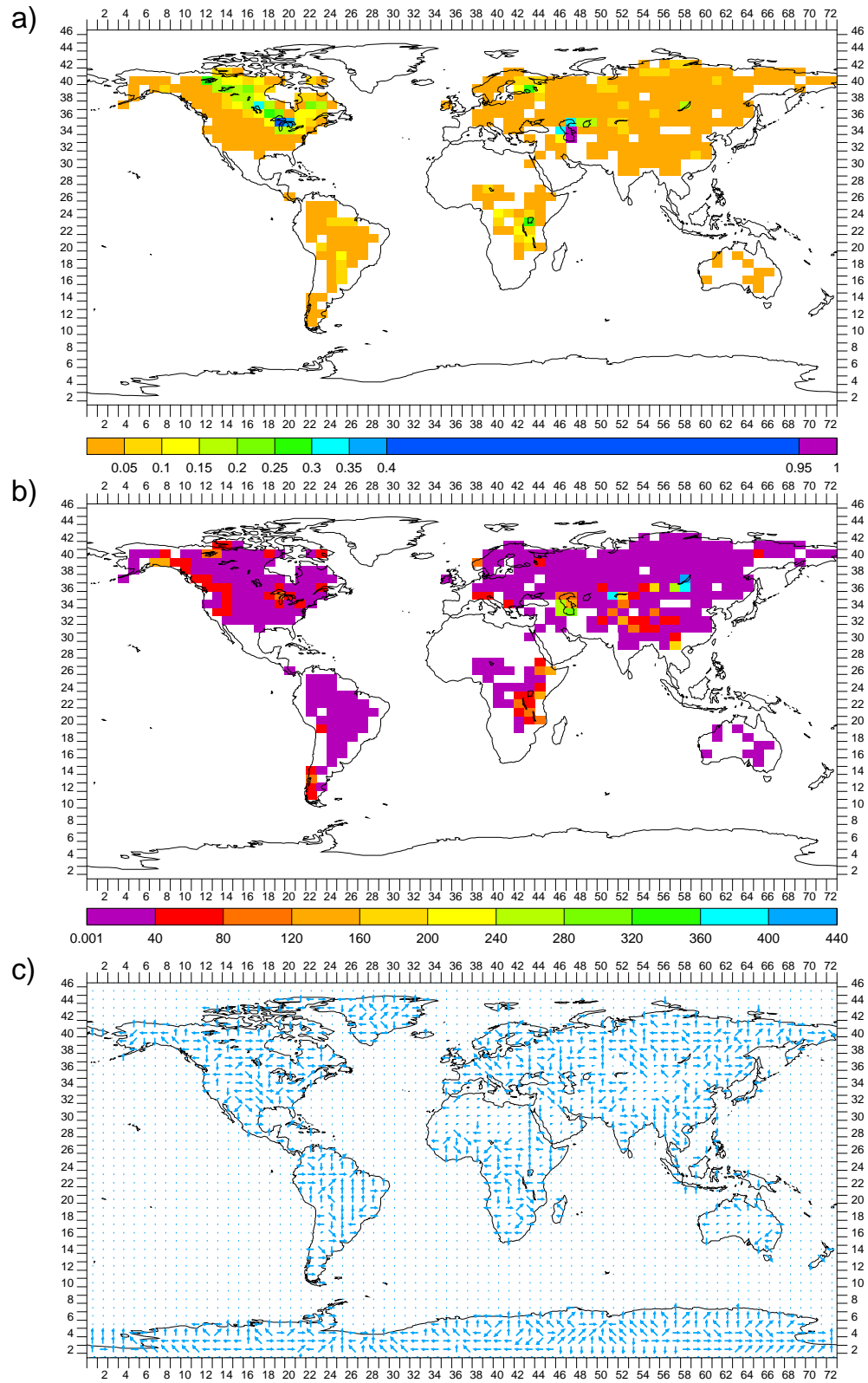


Figure 4.10: CGCM grid box maps for PD: a) lake (fraction of box); b) lake thickness (m); and c) river direction

surface characteristics are based, does not. For these “new” land grid boxes, the characteristics of a neighboring original PD land grid box were used (also as suggested by PMIP) in the following order of directional preference: W, E, S, N, SW, NW, SE, NE, and custom set from a non-neighboring original PD land grid box. Figure 4.11a for example then, is the CGCM grid box map for the LGM of lake fraction and Figure 4.7c is that for resulting ground fraction.

Even for land grid boxes covered at the LGM by glacier, which would seem to supersede the need for other land surface characteristics, or for new land grid boxes where a neighboring original PD land grid box was available, one land surface characteristic still had to be custom set: river direction (chosen from the eight compass points). This is because glaciated grid boxes still have a river direction associated with runoff from them and because taking a river direction from a neighboring grid box does not necessarily produce a sensible result. For new PD land grid boxes, maps showing rivers/topography were simply consulted for the appropriate river direction. For glaciated and new land grid boxes at the LGM, the higher resolution $1^\circ \times 1^\circ$ Implicit ICE-4G dataset was looked at for each of these CGCM $5^\circ \times 4^\circ$ grid boxes to get an idea of which direction water would most likely flow. Figure 4.10c and Figure 4.11c are the CGCM grid box maps for PD and LGM, respectively, of river direction.

For the LGM, characteristics associated with lake (e.g., lake fraction, lake thickness) were custom set for some land grid boxes, especially those along the perimeter of continental glaciers, where grid boxes were often partially glaciated. However, the most important custom setting of characteristics associated with lake, and another example of the determination of topography being intertwined with the determination of land surface, is the converting of inland sea ocean grid boxes to lake-covered land grid boxes. While it is easy to see how the closing of straits at the LGM might lead to this situation, the example that set the rule is from an inland sea that was never connected even by a strait to the world ocean: the Caspian Sea. In the standard PD topography normally used in the CGCM, the Caspian Sea is two neighboring ocean grid boxes with no connection to the world ocean. During early research with just the OGCM of the CGCM it was found that the water mass of these Caspian Sea ocean grid boxes grew ridiculously large because of the imbalance of prescribed

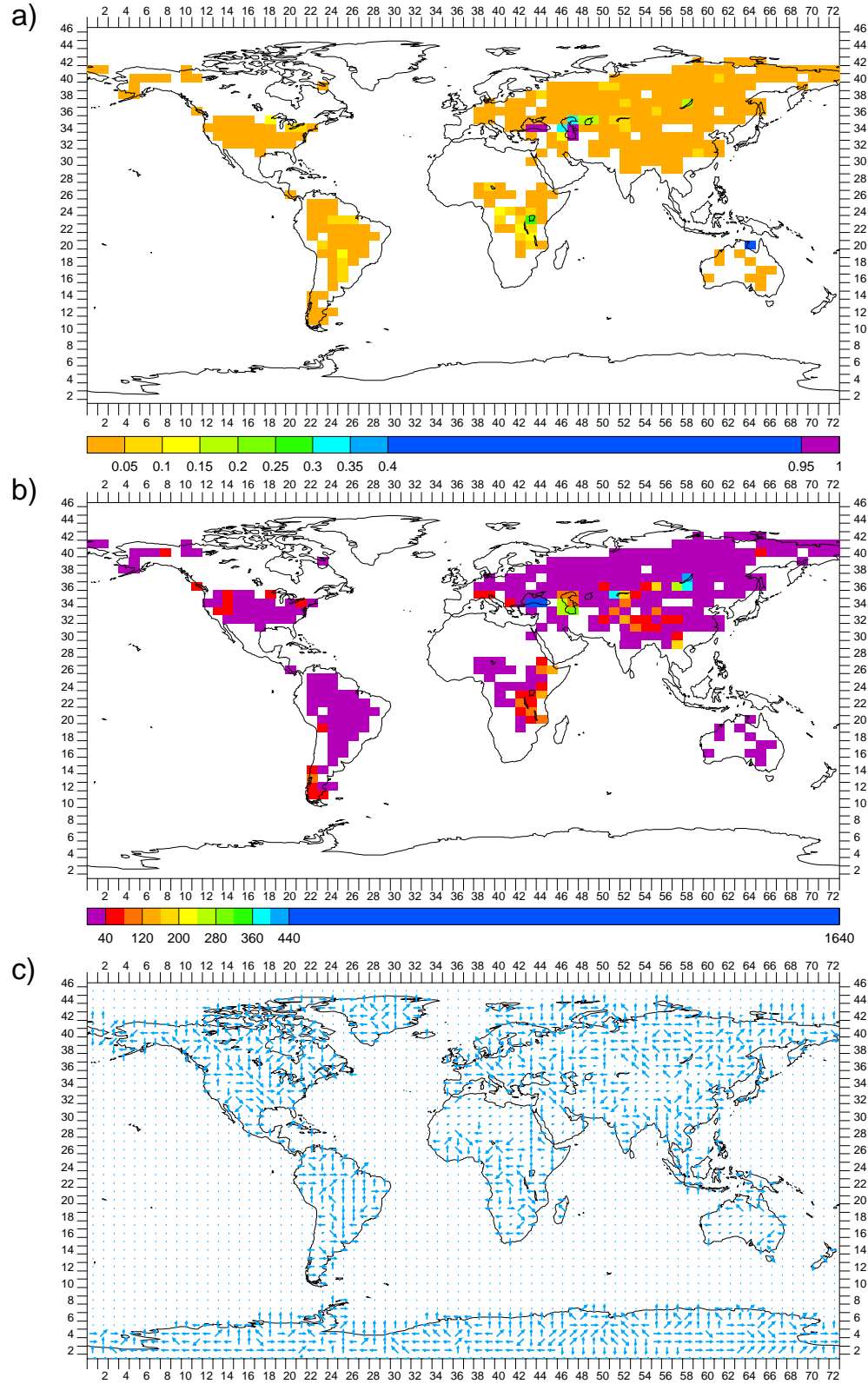


Figure 4.11: CGCM grid box maps for LGM: a) lake (fraction of box); b) lake thickness (m); and c) river direction

(from AGCM output) precipitation over evaporation there and the lack of an outlet. A rule was thus adopted that all ocean grid boxes should have a connection to the world ocean; otherwise, these isolated inland seas should just be set as land grid boxes with a high lake fraction and an appropriate lake thickness and, relatedly, elevation (since it is not necessarily sea level). Hence, another of the differences of the PD topography from the standard PD topography normally used in the CGCM is that in the former the Caspian Sea is two land boxes ([47,33] and [47,34]) with lake fractions of 1.0 and lake thicknesses set equal to the original ocean grid box thicknesses there (316.267 and 120.908 m, respectively); the elevations remained -30 m. For the LGM, the Caspian Sea is the same two land grid boxes with lake fractions of 1.0. However, according to Mamedov 1997, the Caspian Sea level at the LGM (during the Caspian Sea Yenotavian era) was about 50 m below PD global sea level and since at PD it is 30 m below, the Caspian Sea land grid box lake thicknesses at the LGM were set as the PD lake thicknesses minus 20 m minus the uplifts under the Caspian Sea. Those uplifts were -16.178 and -12.738 m, respectively, and were calculated from LGM – PD differences in the Implicit ICE-4G dataset, assuming a 120 m difference in global sea level. The resulting Caspian Sea land grid box lake thicknesses were thus set for the LGM to 312.445 and 113.646 m, respectively. The LGM elevations (relative to sea level then) of the two Caspian Sea land grid boxes were just set to 70 m: the -50 m LGM Caspian Sea level was relative to PD global sea level plus the 120 m PD global sea level is above that at the LGM.

In the PD topography, there is a CGCM metagrid Strait of Bosphorus connecting two Black Sea ocean grid boxes to the world ocean. As indicated though, at the LGM the Strait of Bosphorus was closed and the Black Sea was isolated from the world ocean. For the LGM then, the two Black Sea ocean grid boxes ([43,34] and [44,34]) were thus converted to two land grid boxes with lake fractions of 1.0. According to Aksu et al. 2002, the Black Sea level at the LGM was about 110 m below PD global sea level, so the Black Sea land grid box lake thicknesses were set as the PD ocean grid box thicknesses there (1632.62 and 1725.91 m, respectively) minus 110 m minus the uplifts under the Black Sea. Those uplifts were -12.712 and -15.311 m, respectively, and were calculated from LGM – PD differences in the Implicit ICE-4G dataset, assuming a 120 m difference in global sea level. The resulting Black Sea land

grid box lake thicknesses were thus set for the LGM to 1535.332 and 1631.221 m, respectively. The LGM elevations of the two Black Sea land grid boxes were then the sum of the lake thicknesses plus the calculated Implicit ICE-4G dataset bathymetry.

In the PD topography, there is a CGCM metagrid Straits of Hormuz connecting a Persian Gulf ocean grid box to the world ocean. As indicated though, at the LGM the Straits of Hormuz was closed. For the LGM, the Persian Gulf ocean grid box ([47,30]) was thus converted to a land grid box. However, Teller et al. 2000 indicates that the Persian Gulf completely dried up at the LGM so the lake fraction was left at its PD value of 0.0 (the lake fraction value of an ocean grid box).

The Gulf of Carpentaria, in north Australia, is an ocean grid box in the PD topography. According to Chivas et al. 2001 though, at the LGM it became closed off from the rest of the ocean, leaving a lake (Lake Carpentaria) covering about half its area to a depth of about 15 m. For the LGM then, the Carpentaria ocean grid box ([64,20]) was converted to a land grid box with a lake fraction of .5 and a lake thickness of 15 m.

There were probably other significant lake changes at the LGM (a field in itself), but the above implemented changes were the ones that stemmed directly from the implemented LGM topography changes. As indicated, in general the LGM lake characteristics were left as for PD; see Figure 4.10 a and b and Figure 4.11 a and b.

Chapter 5

Ocean Sediment and Ice Core $\delta^{18}\text{O}$ Data

As discussed (Chapter 1 and Section 2.2), the technique of forward modelling of $\delta^{18}\text{O}$ of ocean sediment core foraminifera shell CaCO_3 and ice core H_2O and comparing to their paleodata is central to this work. Even with this technique it is best to have as much and as geographically diverse of this ocean sediment and ice core $\delta^{18}\text{O}$ data for comparison as possible. One major reason these two proxies were chosen was because they are the most widespread and abundant of the climate proxies (thus also the most influential) and it was a necessary part of this work to make a compilation of their paleodata. While they are the most widespread and abundant of the proxies they are still globally quite sparse and limited in number, which is understandable given the expense, physical difficulty and time involved in even a single core. Further, gathering even just the published data can be problematic and contributed to the sparsity in this work.

5.1 Downcore $\delta^{18}\text{O}$ Time Series

Primarily during the 5 months from May through September 2001 as much ocean sediment and ice core $\delta^{18}\text{O}$ data as possible was gathered (future work could thus include adding data that became available after the end of September 2001). This was from published work because it was then easiest to know the necessary details of the

data, e.g., its age model (or even its existence). Individual researchers were contacted, particularly those with core data from strategic locations, but this was unsuccessful as often as not. Most of the data thus came from public databases. Probably the largest and best known paleoclimatic database in the United States is that of the NOAA Paleoclimatology Program of the National Climatic Data Center, located at the National Geophysical Data Center in Boulder, Colorado. This provided quite a bit of ice core $\delta^{18}\text{O}$ data but had limited ocean sediment core $\delta^{18}\text{O}$ data. The best source of ocean sediment core $\delta^{18}\text{O}$ data, without which even the limited compilation of this work would not have been possible, was the PANGAEA database of environmental data (www.pangaea.de). PANGAEA is operated by the Alfred Wegener Institute for Polar and Marine Research, Bremerhaven, Germany and the Center for Marine Environmental Sciences, University of Bremen, Bremen, Germany.

For comparisons with the PD and LGM simulations and the Deglaciation simulations suggested for future work, entire downcore $\delta^{18}\text{O}$ time series from PD back through the LGM were sought, although all of whatever was available covering any of this time span was collected. Given, for example, that early dating based on ^{14}C gave the time of the LGM as 18 kyBP but later knowledge of the skew between ^{14}C ages and calendar ages changed this to 21 kyBP (that used in this work), the use of many different cores made the age model of each core important. Most ocean sediment cores, and thus most of those used in this work, had age models that were variously based on SPECMAP (Imbrie et al. 1984 and/or Martinson et al. 1987), which, while using a couple of ^{14}C ages, is primarily from orbital tuning to Milankovitch cycles (see Section 4.3) and is thus more or less a calendar-age age model. The age models of the remaining ocean sediment cores used were based primarily on ^{14}C ages that had been converted to calendar ages (according to Stuiver and Reimer 1993 for example) by the researchers themselves; ages with and without reservoir corrections were included. Future work could include also using the previously-excluded ocean sediment cores that had age models based only on unconverted ^{14}C ages by converting these ages to calendar ages, using the CALIB 4.x program of Stuiver et al. 1998 for example. Given the age uncertainties in SPECMAP and in reservoir corrections this calendar age/ ^{14}C age distinction may not be critically important, especially as far back in time as the LGM or even the Deglaciation, but it is at least a reasonable start at control

of age model consistency. The ice core age models were typically based on annual layer counting, glacier flow modelling, comparison to other calendar-age-dated cores or known-age events (e.g., volcanic eruptions), or some combination thereof, and thus were more or less calendar-age age models.

Appendix A is a compilation of the information about the cores from which $\delta^{18}\text{O}$ time series were gathered: name, latitude, longitude, depth, $\delta^{18}\text{O}$ source, references, age model, notes, and dataset sources.

Often there was quite a variety of more than just $\delta^{18}\text{O}$ data in a core's obtained dataset so that even for datasets from PANGAEA, which were generally formatted quite logically, programs custom written for each were necessary to extract the $\delta^{18}\text{O}$ time series. Further processing was also often necessary. For example, many times only the ages at control points down the core were given and so the ages of $\delta^{18}\text{O}$ values between these had to be linearly interpolated. Further, often there were multiple $\delta^{18}\text{O}$ measurements per downcore depth/age. These were simply averaged to give one value per depth/age. This average $\delta^{18}\text{O}$ value per depth/age is what was used in all analyses in this work.

While only LGM and PD $\delta^{18}\text{O}$ values are necessary for the comparisons in this work, it is illuminating to see entire downcore $\delta^{18}\text{O}$ time series. The number of time series shown can be practically limited though. For the ocean sediment cores, $\delta^{18}\text{O}$ time series were collected for all available species of foraminifera, following the universally good advice of “get it when you see it” and in preparation for possible future work. However, as discussed in Section 2.2.1 there are foraminifera $\delta^{18}\text{O}$ models for just the seven foraminifera species *Cibicidoides wuellerstorfi*, *Globigerinoides sacculifer*, *Globigerinoides ruber* (white), *Globigerinoides ruber* (pink), *Globigerina bulloides*, *Neogloboquadrina pachyderma* (sinistral), *Neogloboquadrina pachyderma* (dextral). Additionally, glacier ice H_2O $\delta^{18}\text{O}$ data is also used in this work. Thus Appendices B.1 through B.8 contain the plots of the downcore $\delta^{18}\text{O}$ time series for just these eight “species” of interest (see the plot notes preceding the plots in Appendix B and note further that information about the cores in the plots can be looked up numerically and alphabetically by core name in Appendix A). The decrease in average $\delta^{18}\text{O}$ from the LGM to PD (Holocene) is clear in most of these plots, which is reassuring since as discussed (Section 3.1) this LGM – PD difference

is of primary interest. However, the generally rough time resolution is also apparent and this is compounded by the uncertainties of the age models and core vagaries like bioturbation and sedimentation rates. These factors should be kept in mind in the comparisons because an incorrect age may imply an incorrect $\delta^{18}\text{O}$ value.

Directly used in the comparisons in this work, specifically in the next chapter, the eight Figures 6.39b to 6.46b are the CGCM grid box maps showing the LGM values of the downcore $\delta^{18}\text{O}$ time series for the mentioned eight (respective) species of interest. These maps were made using a single LGM-representative $\delta^{18}\text{O}$ value per core and doing a simple average of these for all the cores in each CGCM grid box (for what cores are in what grid boxes see the plots of Appendix B). The single LGM-representative $\delta^{18}\text{O}$ value per core was a simple average of all the measured (rather than interpolated) values in a 3000-year interval centered at 21 kyBP. As mentioned, a measurement may itself have been a simple average of more than one measurement at that downcore depth/age. The 3000-year interval is somewhat arbitrary but on the order of the mentioned age errors. Given the typically rough time resolution of the cores, there are typically only a few measurements in the interval, often similarly valued.

Even remembering that foraminifera and glacier ice have, for various reasons, geographic ranges out of which they are unlikely ever to be found, for even the most densely populated of these maps the sparsity is obvious. It is made worse by the fact that the relatively few CGCM grid boxes that do have a core in them may have multiple cores, out of the relatively small number of total cores compiled to begin with. This is related to the fact that cores are often taken preferentially in a few small regions of “interest”. Thus even if core data available after September 2001 is added, or that with ^{14}C -based age models is converted to calendar ages and added, the sparsity may not be much alleviated. These additions would still be worth it though to improve the accuracy of the average $\delta^{18}\text{O}$ value in each grid box.

5.2 Coretop $\delta^{18}\text{O}$

$\delta^{18}\text{O}$ values for PD can be obtained from the coretops of the downcore $\delta^{18}\text{O}$ time series if the age models indicate the coretops are PD. Similarly but asymmetrically

to the described determination of a single representative $\delta^{18}\text{O}$ value per core for the LGM, a single representative $\delta^{18}\text{O}$ value per core for PD was arrived at as a simple average of all the measurements in a 3000-year interval extending back from 0 kyBP. Again, given the typically rough time resolution of the cores, there are typically only a few measurements in the interval, often similarly valued.

As can be seen in Appendix B, even with this criterion some downcore $\delta^{18}\text{O}$ time series still could not be considered to have PD $\delta^{18}\text{O}$ values, probably due to their cores having had significant coretop sediment loss and/or lack of recent sedimentation. For single-core CGCM grid boxes in the LGM – PD comparisons this is the same as also not having an LGM $\delta^{18}\text{O}$ value, i.e., the same as no value. However, quite a few of these PD-less downcore $\delta^{18}\text{O}$ time series can be “saved” and the PD comparisons greatly enhanced because there exists, and is compiled, quite a bit more coretop-only $\delta^{18}\text{O}$ data than downcore $\delta^{18}\text{O}$ time series. This makes sense because coretop data is easier to get than entire downcore time series: a long core may not have to be taken and dating may not be necessary. It is important to note though, that without dating, an assumption has to be made that coretop values represent PD, which may not be valid even for the stated criterion for consideration as PD. Still, given the absolute upcore age limit — it can’t go into the future — this is a better assumption than any made about where the LGM is in an undated core.

An already-compiled coretop $\delta^{18}\text{O}$ database was thus acquired. It was from the recent Mulitza 2001 so was probably the most current and complete available at the time and was yet another dataset gotten from PANGAEA (see Mulitza 2001 for the http address). The compilation was used in developing the ecological foraminifera model of Schmidt and Mulitza 2002 (see Section 2.2.1) and only includes coretop $\delta^{18}\text{O}$ data for the planktonic foraminifera *Globigerinoides sacculifer*, *Globigerinoides ruber* (white), *Globigerinoides ruber* (pink), *Globigerina bulloides*, *Neogloboquadrina pachyderma* (sinistral), and *Neogloboquadrina pachyderma* (dextral). The other foraminifera of interest in this work, the benthic *Cibicidoides wuellerstorfi*, was not in the compilation but this is the least serious foraminifera omission because *C. wuellerstorfi* already had the most PD data from the downcore $\delta^{18}\text{O}$ time series. For glacier ice H_2O , PD data was available from all the downcore $\delta^{18}\text{O}$ time series.

Since data in this compiled coretop $\delta^{18}\text{O}$ database was often taken from other,

independent compilations, which used some of the same sources, duplicates for some core data exist in the database and these had to be manually removed in this work. This was made difficult (and makes it understandable why duplicates were not previously removed from the database) by the variations in core name, latitude, longitude, and sometimes even the supposedly-same $\delta^{18}\text{O}$ measurement, often given for a single core by different authors/compiler in different references. For the downcore $\delta^{18}\text{O}$ time series cores, these variations are noted in the core information of Appendix A. Multiple coretop $\delta^{18}\text{O}$ measurements per core also exist in the database and as with the downcore $\delta^{18}\text{O}$ time series these were simply averaged to give one value per core. This average $\delta^{18}\text{O}$ value per core is what was used in all analyses in this work.

The $\delta^{18}\text{O}$ data for PD from the downcore $\delta^{18}\text{O}$ time series was then combined with that from this reduced coretop $\delta^{18}\text{O}$ database for the six foraminifera species the latter includes. Given that these two $\delta^{18}\text{O}$ databases were also independently compiled, this resulted in the same described problem of duplicates (although given how the $\delta^{18}\text{O}$ values for PD were calculated from the downcore time series, the $\delta^{18}\text{O}$ values for the same core from the two databases were never the same). These duplicates were manually eliminated by removing the data contributed by the downcore $\delta^{18}\text{O}$ time series, the logic being that since most of the data in this combined database was from the reduced coretop $\delta^{18}\text{O}$ database, it would be most consistent to prefer that over data from the downcore $\delta^{18}\text{O}$ time series. While examining these duplicates, it was noted in several instances that a downcore $\delta^{18}\text{O}$ time series showed that a reduced coretop $\delta^{18}\text{O}$ database entry, while still Holocene, was significantly older than the 3000 years considered PD for the downcore $\delta^{18}\text{O}$ time series, pointing out again that coretop does not necessarily mean PD. However, this is probably a rare occurrence and PD $\delta^{18}\text{O}$ values are often quite close to those of the rest of the Holocene so it is probably an acceptable error.

The eight Figures 6.21b to 6.28b then, are the resulting CGCM grid box maps of PD $\delta^{18}\text{O}$ for the mentioned (respective) eight species of interest (again, for *C. wuellerstorfi* and glacier ice H_2O there was no $\delta^{18}\text{O}$ data from the coretop $\delta^{18}\text{O}$ database). As in the making of the LGM maps, these PD maps were made using a single PD-representative $\delta^{18}\text{O}$ value per core and doing a simple average of these for all the cores in each CGCM grid box. Clearly, while the PD maps are still sparse

they are much denser than the LGM maps.

With both LGM and PD $\delta^{18}\text{O}$ data thus available, the eight Figures 6.30b to 6.37b are the resulting CGCM grid box maps of LGM – PD $\delta^{18}\text{O}$ for the mentioned (respective) eight species of interest.

Chapter 6

Comparisons of Simulations, Observations, and Ocean Sediment and Ice Core $\delta^{18}\text{O}$ Data

6.1 Time of Simulation Averages and Proximity to Equilibrium

For purposes of comparison to the ocean sediment and ice core $\delta^{18}\text{O}$ data, all variables looked at from the simulations are annual averages, rather than winter and summer month averages, because in most cases this data is an annual average at best. All variables looked at from the PD simulation are 100-year averages from years 441 to 540 of that run, which took more than 10 months of real time to reach. All variables looked at from the LGM simulation are 100-year averages from years 341 to 440 of that run, which took more than 9 months of real time to reach.

The proximity to equilibrium of each run at the time of these averages should be noted here since as discussed in Chapter 3 it is important for the credibility of conclusions drawn about the deep ocean. As described in Section 3.1, a practical measure of equilibrium is the change with time of the mean global/annual salinity and potential temperature at OGCM level 13 (3090–4647 m depth), the deepest possible level. These time series are thus shown in the right bottom boxes of Figures 6.2 and 6.1, respectively. Just from inspection it is apparent that neither the PD nor LGM

runs were in equilibrium at the time of the averages. The PD salinity and temperature changed by -0.002 g/kg and -0.1°C during the averaged century, respectively. Judged by the salinity change alone the PD run could be said to have been in equilibrium but in conjunction with the less-moderate temperature change it cannot. In the LGM run the mean global/annual salinity and potential temperature at OGCM level 13 changed by 0.015 g/kg and -0.26°C during the averaged century, respectively, and thus it was decidedly not in equilibrium (note that the LGM salinity in Figure 6.2 has 1.00 subtracted from it to put it on the same scale as that for PD; see Section 3.3.4).

Since ocean water $\delta^{18}\text{O}$ is a major concern in this work, particularly this chapter, its proximity to equilibrium is also of concern. Similarly to the potential temperature and salinity figures then, Figure 6.3 is that for ocean water $\delta^{18}\text{O}$ (note that the LGM OGCM $\delta^{18}\text{O}_w$ in Figure 6.2 has 1.25 subtracted from it to put it on the same scale as that for PD; see Section 3.3.4). Conclusions similar to those from salinity can be drawn from it.

However, that the salinity, potential temperature, and $\delta^{18}\text{O}_w$ of OGCM level 13 at the time of the averages do not indicate equilibrium does not at all discredit the simulations in their entirety. For the reasons discussed in Section 3.1 and as shown in the rest of Figures 6.1 to 6.3, the levels up from OGCM level 13 are increasingly and significantly closer to their equilibrium state. Additionally, since the concern here with the bottom of the ocean is that it is the environment of benthic (bottom-dwelling) foraminifera, “bottom” in this chapter is defined as the deepest OGCM level (1–13) at any location, whether or not it is the deepest possible OGCM level (13). Thus, the “bottom” of the OGCM actually also consists of other shallower levels (see Figures 4.4 and 4.6), not just OGCM level 13, which is just the deepest possible OGCM level. Moreover, the $\delta^{18}\text{O}$ of the calcium carbonate of benthic foraminifera shells changes by only 0.028‰ (see Section 2.2.1) for each 0.1°C change in the temperature of the ocean water they form in and by 0.1‰ for each 0.1‰ change in the $\delta^{18}\text{O}$ of the ocean water. If changes in foraminifera $\delta^{18}\text{O}_c$ of less than 0.1‰ are considered small then many of the changes seen in the figures are small in regards to this.

Finally, both the PD and LGM runs at the time of the averages are well past the earliest transients, which are usually the most extreme. An important example of this is the North Atlantic meridional overturning circulation (NAMOC) streamfunction.

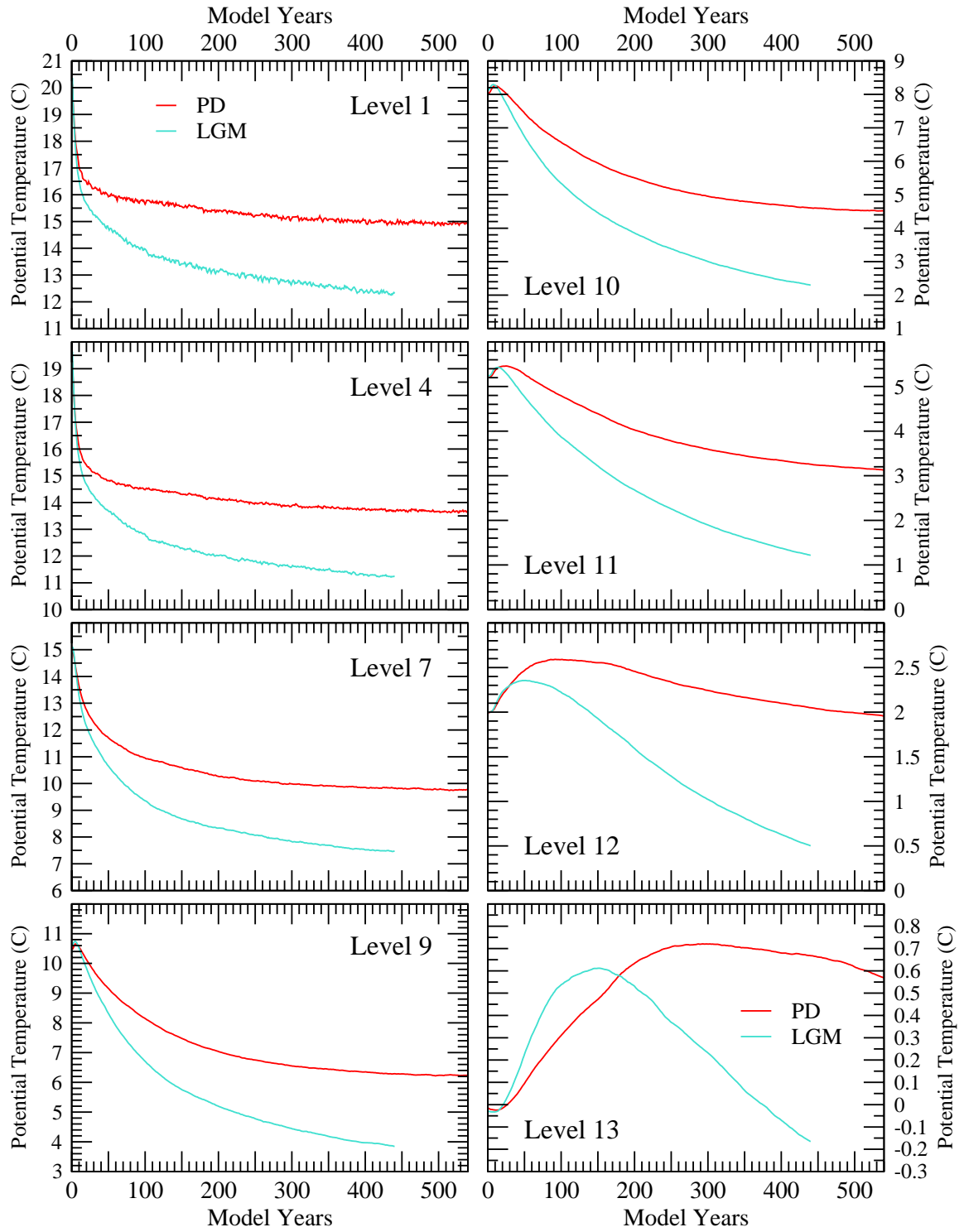


Figure 6.1: Mean global/annual OGCM potential temperature (C) versus model years at selected OGCM levels for PD and LGM runs.

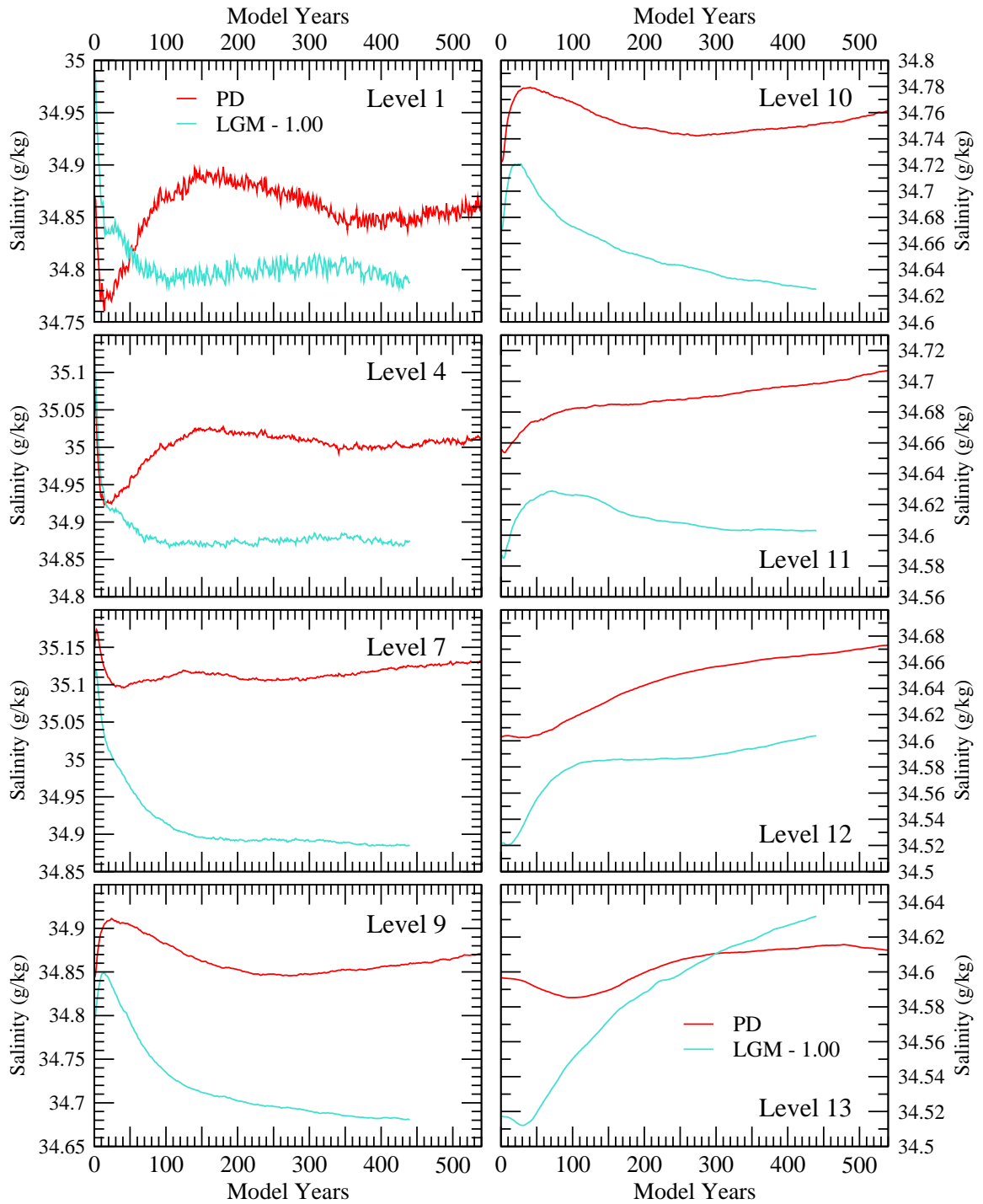


Figure 6.2: Mean global/annual salinity (g/kg; minus 1.00 for LGM) versus model years at selected OGCM levels for PD and LGM runs.

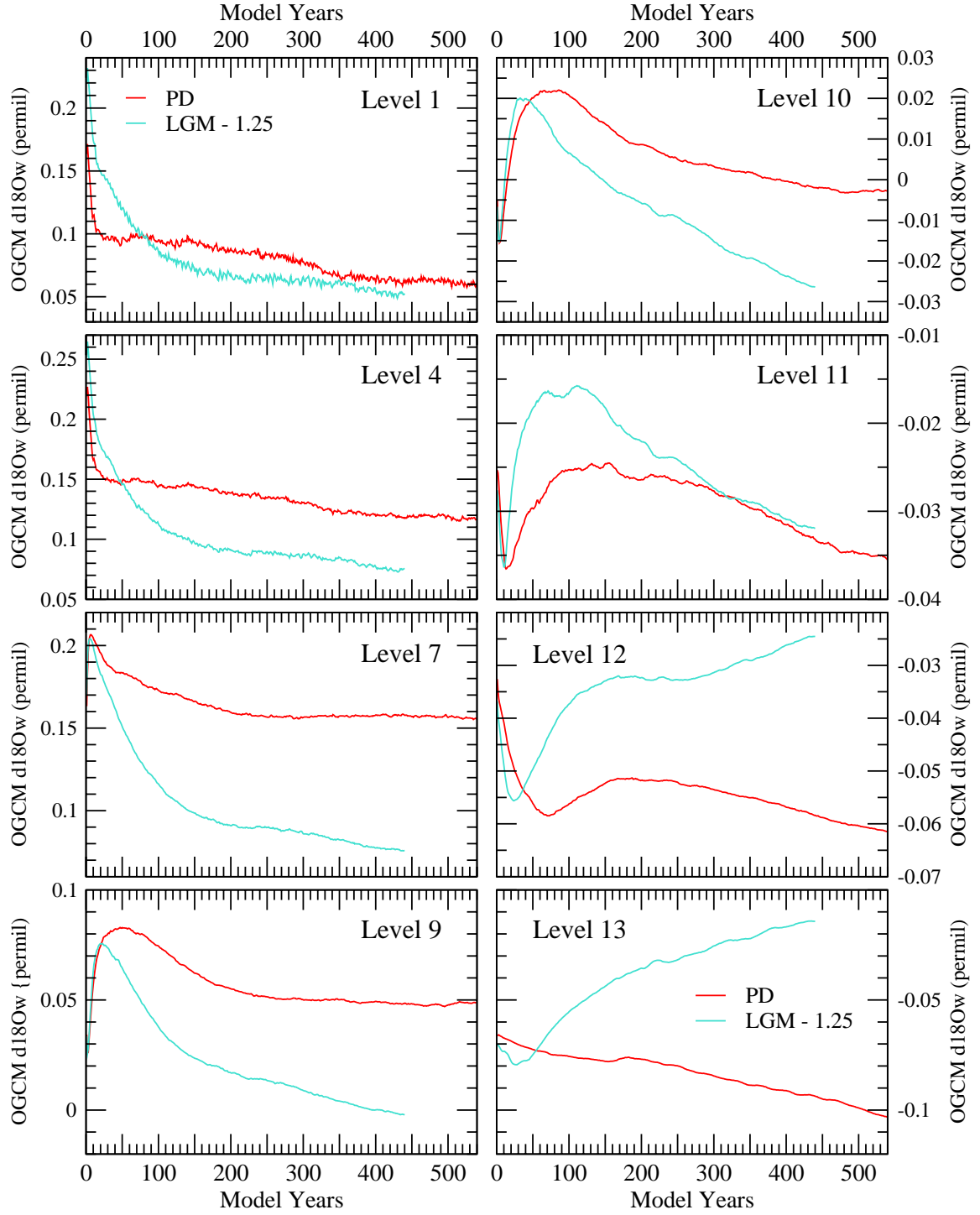


Figure 6.3: Mean global/annual OGCM $\delta^{18}\text{O}_w$ (‰ SMOW; minus 1.25 for LGM) versus model years at selected OGCM levels for PD and LGM runs.

As discussed in Section 3.3.2, the stability and strength of this is important for the credibility of conclusions drawn about the “thermohaline circulation”, and thus all ocean levels. The time series of the single-value measure of this is shown in Figure 6.4 and indicates that after early large spiky plateaus both the PD and LGM NAMOC streamfunctions had settled down to stable smaller, but still reasonable, values at the time of the averages.

6.2 Outline of Comparisons

6.2.1 Variables and Eras

To test the forward modelling technique that is central to this work (see Chapter 1 and Section 2.2), the ultimate variable comparisons are: the mismatch between OGCM/foraminifera model simulated foraminifera $\delta^{18}\text{O}_c$ and ocean sediment core foraminifera $\delta^{18}\text{O}_c$; and the mismatch between the AGCM simulated precipitation $\delta^{18}\text{O}_i$ and ice core H_2O $\delta^{18}\text{O}_i$. If these mismatches are relatively small it can provide confidence in the CGCM, simulations, proxy models¹ and core data. To remove any biases inherent in the model (see Section 3.1), the ultimate era comparison is LGM minus PD (LGM – PD), for whatever variables are looked at.

It is useful to also look at variables other than the mentioned $\delta^{18}\text{O}$ ones and to look at both PD and LGM separately. In particular for the variables, note that foraminifera $\delta^{18}\text{O}_c$ is a function (see Section 2.2.1) of ocean water $\delta^{18}\text{O}$ and in situ temperature² so these should be looked at in detail too. Ocean water $\delta^{18}\text{O}$ is in turn affected by (see Sections 2.1.2 and 2.1.3) the difference between precipitation and evaporation ($P - E$) and sea ice so these should also be looked at. Salinity too can affect the $\delta^{18}\text{O}_c$ of foraminifera³ and is also supposed to vary similarly (correlate)

¹A proxy model isn’t used for ice core H_2O $\delta^{18}\text{O}_i$ — it is directly compared to AGCM precipitation $\delta^{18}\text{O}_i$. See Section 2.2.3. Note that for notational brevity the subscript “i” is occasionally used to refer to non-ice precipitation (i.e., non-snow) as well.

²Temperature is “in situ” rather than “potential” because the point in the following sections of this chapter is the temperature foraminifera experience.

³This effect is largely through salinity’s effect on water density and primarily applies to planktonic foraminifera. That is, ocean water $\delta^{18}\text{O}$ and in situ temperature, thus foraminifera $\delta^{18}\text{O}_c$, may vary

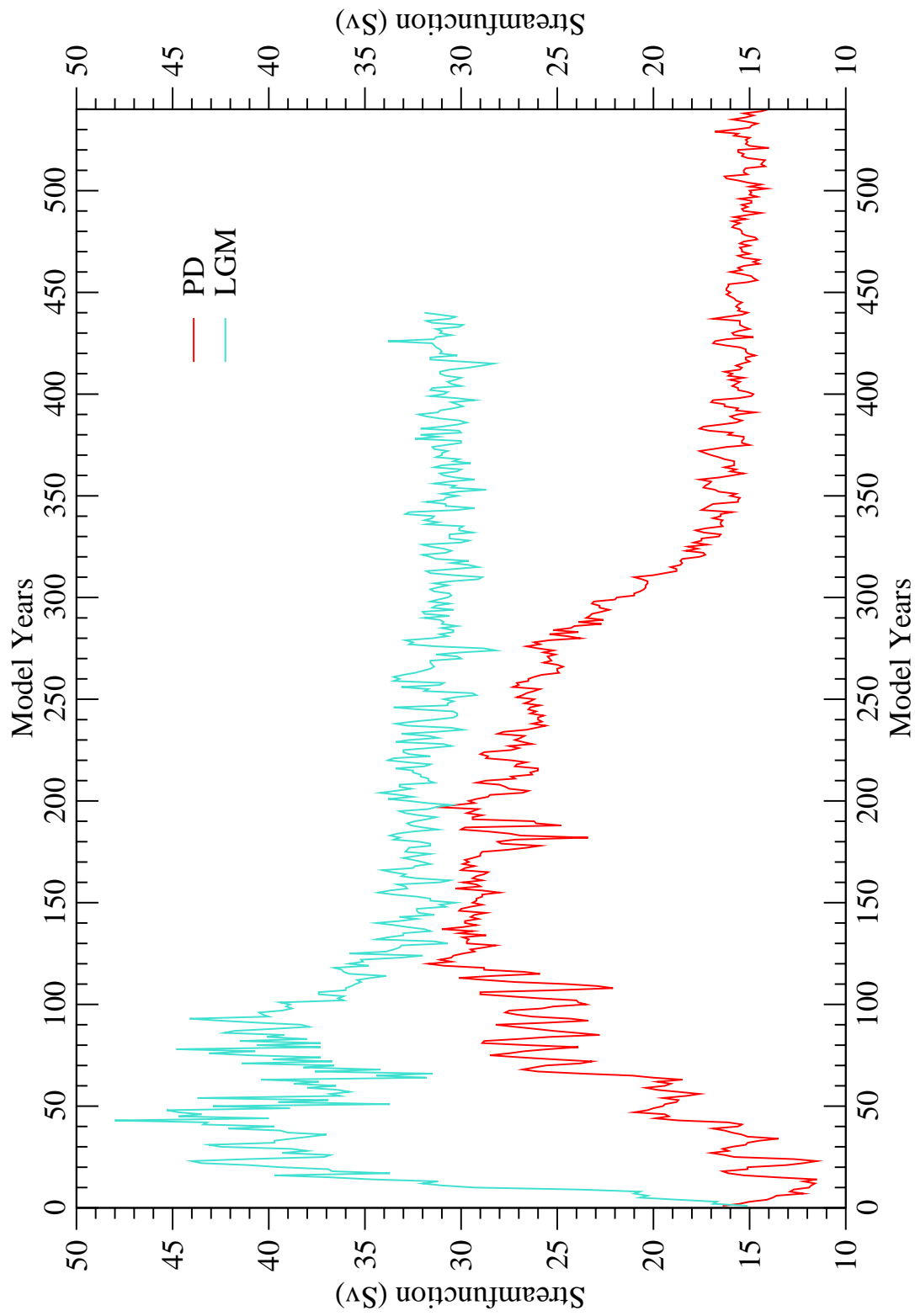


Figure 6.4: Annual NAMOC streamfunction value (Sv) at OGCM grid box lat# 35 (44–48°N), level 10 (899–1360 m depth) versus model years for PD and LGM runs.

to ocean water $\delta^{18}\text{O}$ (see Sections 2.1.2 and 2.1.3) so salinity should be looked at as well. Precipitation $\delta^{18}\text{O}$ is a function of precipitation rate (see Section 2.1.3) so precipitation rate too should be looked at.⁴ All of these variables are also of general climate interest apart from their affect on foraminifera $\delta^{18}\text{O}_c$ and precipitation $\delta^{18}\text{O}$, i.e., they are the reasons for doing the climate simulations in the first place.

In particular for eras other than LGM – PD, for all the mentioned variables the biases in the model should be noted, not just differenced out, and this can be done by doing PD comparisons. For the non- $\delta^{18}\text{O}_c$ variables, comparing to the PD real world means using observational data for them, which like the core data has its own caveats. A useful way to do these comparisons is to predict, where there are cores, what affect the biases will have on the PD OGCM/foraminifera model simulated foraminifera $\delta^{18}\text{O}_c$ and PD AGCM simulated precipitation $\delta^{18}\text{O}$ before looking at those. Since the non- $\delta^{18}\text{O}_c$ variables are of general climate interest, comparing them to observations also serves as a general evaluation of the PD simulation and the CGCM. For OGCM/foraminifera model simulated foraminifera $\delta^{18}\text{O}_c$ and AGCM simulated precipitation $\delta^{18}\text{O}$, PD comparisons to coretop $\delta^{18}\text{O}$ data are a good test of the forward modelling since PD has the the most and best data. However, seeing these comparisons for the LGM is also of interest.

Thus, the next sections of this chapter do the following comparisons. Section 6.3 compares for PD and to observations the CGCM simulated ocean water $\delta^{18}\text{O}$, ocean water in situ temperature, salinity, P – E, sea ice, precipitation $\delta^{18}\text{O}$, and precipitation rate. Since the concern is with benthic and planktonic foraminifera, the first three variables are done at the bottom OGCM level, as defined for benthic foraminifera in Section 6.1, and the surface OGCM level (1), as representative of the habitat of planktonic foraminifera. Sections 6.4, 6.5, and 6.6 compare, for PD, LGM – PD, and

with depth and for planktonic foraminifera, unlike benthic foraminifera, habitat depth may vary depending on water density. See Section 2.2.1.

⁴As indicated in Sections 2.1.2 and 2.1.3, precipitation $\delta^{18}\text{O}$ is also strongly a function of the temperature at which the precipitation formed. However, given the convolutions of precipitation formation it is not possible to know where to look at air temperatures such that they are reliably relevant to precipitation formation. $\delta^{18}\text{O}$ of ice core H_2O , thus precipitation, is often used as a proxy for surface air temperature but this correlation is in question so using it in reverse is also questionable.

LGM, respectively, the OGCM/foraminifera model simulated foraminifera $\delta^{18}\text{O}_c$ to ocean sediment core foraminifera $\delta^{18}\text{O}_c$ and the AGCM simulated precipitation $\delta^{18}\text{O}_i$ to ice core H_2O $\delta^{18}\text{O}_i$. Section 6.7 does LGM – PD comparisons for the aforementioned CGCM simulated variables of Section 6.3.⁵

6.2.2 Methods: Maps, Plots, and Means

Three methods are used to show the comparisons. The first uses CGCM grid box maps and is done for all the mentioned variables of a section. For each variable there is a “map comparison figure” with three maps: “a” (top), “b” (middle), and “c” (bottom). What these maps are varies with which of the described sections they are in. In Section 6.3, for each of its mentioned variables, the “a” map is the CGCM PD simulated variable, the “b” map is the observations, and the “c” map is “a” minus “b”. Small-magnitude values (i.e., near zero) in the grid boxes of the “c” maps indicate small CGCM biases. In Sections 6.4 to 6.6, for foraminifera $\delta^{18}\text{O}_c$ and precipitation $\delta^{18}\text{O}_i$, the “a” map is the CGCM/foraminifera model simulated variable, the “b” map is the core data, and the “c” map is “a” minus “b”. Small-magnitude values in the grid boxes of the “c” maps indicate a good match and some provide confidence in the CGCM, simulations, proxy models and core data. In Section 6.7, for each of its mentioned variables, the “a” map is the PD CGCM simulated variable, the “b” map is the LGM CGCM simulated variable, and the “c” map is “a” minus “b”, i.e., LGM – PD.

Map comparison figures provide a good spatial comparison and show how much and where the data is. However, it can be difficult with them to overall assess biases (using observations; Section 6.3) and goodness of match (using core $\delta^{18}\text{O}$ data; Sections 6.4 to 6.6), especially if the data is sparse. For the $\delta^{18}\text{O}$ -critical biases of ocean water $\delta^{18}\text{O}$, ocean water in situ temperature and precipitation $\delta^{18}\text{O}$ and for goodness of match of foraminifera $\delta^{18}\text{O}_c$ and of snow/ice $\delta^{18}\text{O}_i$, use is made of a second method, a “model/data plot”, which is essentially a reduction of the first method. A model/data plot consists of the CGCM/foraminifera model simulated variable on

⁵Except for the LGM – PD comparison of CGCM simulated P – E, which is done in Chapter 7 ahead.

the y-axis, the observed or core $\delta^{18}\text{O}$ data on the x-axis, and a line of slope 1.0 going through the origin. The points correspond to grid box values⁶ and many points on or near the line indicate an overall small bias or good match. This method is used in Section 6.3 for ocean water $\delta^{18}\text{O}$ and precipitation $\delta^{18}\text{O}$, both of which have limited observations, and in Sections 6.4 to 6.6, for foraminifera $\delta^{18}\text{O}_c$ and precipitation $\delta^{18}\text{O}_i$, both of which have sparse core data. This method is also used in Section 6.3 for ocean water in situ temperature, although there is a complete ocean observational dataset of that.

At the expense of spatial information, model/data plots allow for an easier general overall assessment of biases and goodness of match while still showing how much data there is. However, for a bottom-line quantitative assessment of the stated variables assessed with model/data plots there is the difference of the means of the variables being compared. Before discussing this, it is necessary to introduce some notation. The variables for which this is necessary are T, in situ temperature, or, more extensively, δ , which is $\delta^{18}\text{O}$ for any of the substances discussed. The variable symbols represent means over the set of grid boxes where there are values for both variables being compared. As previously in this work, the right-hand subscript of a variable symbol is the substance it is for: “c” for foraminifera shell calcium carbonate, “w” for ocean water, or “i” for snow/ice. The right-hand superscript is the “reality” of the variable: “M” for modelled, i.e., CGCM or foraminifera model output, or “R” for real world, i.e., observations or core $\delta^{18}\text{O}$ data. The left-hand superscript is the era of the variable: “L” for LGM or “P” for PD. Lack of a superscript or subscript means the variable symbol represents all choices. In this notation for means then, the ultimate comparisons stated at the beginning of Section 6.2.1 are:

$$\delta_c^M - \delta_c^R \quad (6.1)$$

$$\delta_i^M - \delta_i^R \quad (6.2)$$

$$({}^L\delta_c^M - {}^L\delta_c^R) - ({}^P\delta_c^M - {}^P\delta_c^R) \quad (6.3)$$

$$({}^L\delta_i^M - {}^L\delta_i^R) - ({}^P\delta_i^M - {}^P\delta_i^R) \quad (6.4)$$

⁶It’s thus often possible to locate plot points, especially outliers, on the corresponding CGCM grid box map.

Using means to assess biases (using observations; Section 6.3) can be done straightforwardly for ocean in situ temperature but a caveat is necessary for ocean water $\delta^{18}\text{O}$ and precipitation $\delta^{18}\text{O}$. This caveat also applies to using means to assess goodness of match (using core $\delta^{18}\text{O}$ data; Sections 6.4 to 6.6) for PD and causes an important complication for LGM – PD and LGM. It must also be considered in assessing with $\delta^{18}\text{O}$ map comparison figures and $\delta^{18}\text{O}$ model/data plots for these eras. Out of this caveat/complication though comes the opportunity to address a major question of the LGM.

To understand the caveat first note, as discussed in Sections 2.1.3 and 3.3.4, that the mean ocean $\delta^{18}\text{O}_w$, i.e., $\delta^{18}\text{O}_w$ averaged over *all* OGCM grid boxes, $\bar{\delta}_w$, was just set in the CGCM as was thought appropriate for each era:

$$^P\bar{\delta}_w^M = 0.00\text{‰} \quad (6.5)$$

$$^L\bar{\delta}_w^M = 1.25\text{‰} \quad (6.6)$$

The ocean water $\delta^{18}\text{O}$, δ_w , which is averaged over some limited-observations subset of OGCM grid boxes, is just this all-grid-box mean ocean $\delta^{18}\text{O}_w$ plus some anomaly, δ'_w , averaged over the same subset of OGCM grid boxes⁷:

$$\delta_w = \bar{\delta}_w + \delta'_w \quad (6.7)$$

The ocean water $\delta^{18}\text{O}$ bias⁸ is thus:

$$^P\delta_w^M - ^P\delta_w^R = (^P\bar{\delta}_w^M - ^P\bar{\delta}_w^R) + (^P\delta'_w^M - ^P\delta'_w^R) \quad (6.8)$$

Further, precipitation $\delta^{18}\text{O}$ (e.g., for snow, $\delta^{18}\text{O}_i$) depends on ocean water $\delta^{18}\text{O}$ and some function, f , of other variables (primarily temperature):

$$\delta_i = \delta_w + f_i \quad (6.9)$$

Or, expanding with Equation 6.7:

$$\delta_i = \bar{\delta}_w + \delta'_w + f_i \quad (6.10)$$

⁷This anomaly averaged over *all* OGCM grid boxes should be zero so that $\delta_w = \bar{\delta}_w$.

⁸Similarly for in situ temperature, T.

The precipitation $\delta^{18}\text{O}$ bias is thus:

$${}^P\delta_i^M - {}^P\delta_i^R = ({}^P\bar{\delta}_w^M - {}^P\bar{\delta}_w^R) + ({}^P\delta_w^M - {}^P\delta_w^R) + ({}^Pf_i^M - {}^Pf_i^R) \quad (6.11)$$

Since ${}^P\bar{\delta}_w^M$ was arbitrarily set, $({}^P\bar{\delta}_w^M - {}^P\bar{\delta}_w^R)$ is not an inherent CGCM bias. If $({}^P\bar{\delta}_w^M - {}^P\bar{\delta}_w^R)$ is large in magnitude compared to the other RHS (right-hand side) terms in Equations 6.8 and 6.11, which are inherent CGCM biases, then using observations to calculate the LHS (left-hand side) of the equations to get an idea of the inherent CGCM biases is not useful. If it is large, $({}^P\bar{\delta}_w^M - {}^P\bar{\delta}_w^R)$ will also show up in the $\delta^{18}\text{O}$ map comparison figures and $\delta^{18}\text{O}$ model/data plots. However, $({}^P\bar{\delta}_w^M - {}^P\bar{\delta}_w^R)$ is believed with high confidence to be small, less than a tenth of a permil (i.e., ≈ 0), so ocean water $\delta^{18}\text{O}$ and precipitation $\delta^{18}\text{O}$ biases are assessed using means (Section 6.3).

To see how this arbitrary $\bar{\delta}_w^M$ setting affects assessing goodness of match by doing the mean ultimate comparisons 6.1 to 6.4 with the core $\delta^{18}\text{O}$ data, note first that, like precipitation $\delta^{18}\text{O}$, foraminifera $\delta^{18}\text{O}_c$ depends on ocean water $\delta^{18}\text{O}$ and some function, f , of other variables (primarily in situ temperature). Or, letting subscript “x” represent either subscript “c” or “i” so as to include both foraminifera $\delta^{18}\text{O}_c$ and snow/ice $\delta^{18}\text{O}_i$, respectively:

$$\delta_x = \delta_w + f_x \quad (6.12)$$

Again expanding with Equation 6.7 gives:

$$\delta_x = \bar{\delta}_w + \delta_w^M + f_x \quad (6.13)$$

The mean ultimate comparisons 6.1 to 6.4 are thus:

$$\delta_x^M - \delta_x^R = (\bar{\delta}_w^M - \bar{\delta}_w^R) + (\delta_w^M - \delta_w^R) + (f_x^M - f_x^R) \quad (6.14)$$

$$\begin{aligned} ({}^L\delta_x^M - {}^L\delta_x^R) - ({}^P\delta_x^M - {}^P\delta_x^R) &= [({}^L\bar{\delta}_w^M - {}^L\bar{\delta}_w^R) - ({}^P\bar{\delta}_w^M - {}^P\bar{\delta}_w^R)] \\ &+ [({}^L\delta_w^M - {}^L\delta_w^R) - ({}^P\delta_w^M - {}^P\delta_w^R)] \\ &+ [({}^Lf_x^M - {}^Lf_x^R) - ({}^Pf_x^M - {}^Pf_x^R)] \end{aligned} \quad (6.15)$$

In Equation 6.14, for LGM or PD, for foraminifera $\delta^{18}\text{O}_c$ or snow/ice $\delta^{18}\text{O}_i$, if the $(\bar{\delta}_w^M - \bar{\delta}_w^R)$ term is not small in magnitude compared to the $(\delta_w^M - \delta_w^R)$ and $(f_x^M - f_x^R)$ terms then doing the $\delta_x^M - \delta_x^R$ calculation with the core $\delta^{18}\text{O}$ data to see how large in

magnitude the RHS of the equation is is not a useful test of goodness of match. This is because $\bar{\delta}_w^M$ was arbitrarily set in the CGCM for both PD and LGM and if it differs from the real world $\bar{\delta}_w^R$ it does so independently at PD and LGM, i.e., $(\bar{\delta}_w^M - \bar{\delta}_w^R)$ is not an era-independent inherent bias in the CGCM, as $(\delta_w^M - \delta_w^R)$ and $(f_x^M - f_x^R)$ are, to be subtracted away by LGM – PD differencing. While as discussed for PD, $(\bar{\delta}_w^M - \bar{\delta}_w^R)$ is almost certainly insignificantly small, for the LGM, $(\bar{\delta}_w^M - \bar{\delta}_w^R)$ could be significantly large, a few tenths of a permil. For snow/ice $\delta^{18}\text{O}_i$, the $(f_x^M - f_x^R)$ term in Equation 6.14 is typically significantly larger than the $(\bar{\delta}_w^M - \bar{\delta}_w^R)$ term, for both PD and LGM, as well as LGM – PD. For foraminifera $\delta^{18}\text{O}_c$ though, the $(\bar{\delta}_w^M - \bar{\delta}_w^R)$ term is only small for PD. Thus, the $\delta_x^M - \delta_x^R$ calculation with the core $\delta^{18}\text{O}$ data can be done immediately as a test of goodness of match for foraminifera $\delta^{18}\text{O}_c$ and snow/ice $\delta^{18}\text{O}_i$ at PD (Section 6.4) but $(\bar{\delta}_w^M - \bar{\delta}_w^R)$ must be known to subtract off, at least for foraminifera $\delta^{18}\text{O}_c$, to do this at the LGM (Section 6.6). Further, $(\bar{\delta}_w^M - \bar{\delta}_w^R)$ is insignificant in all the related $\delta^{18}\text{O}$ map comparison figures and $\delta^{18}\text{O}$ model/data plots, except those for LGM foraminifera $\delta^{18}\text{O}_c$.

For LGM – PD, each of the $(\delta_w^M - \delta_w^R)$ and $(f_x^M - f_x^R)$ terms in Equation 6.14 is assumed to be the same at both PD and LGM, since they are assumed-era-independent inherent biases in the CGCM, so that the $[(^L\delta_w^M - ^L\delta_w^R) - (^P\delta_w^M - ^P\delta_w^R)]$ and $[(^Lf_x^M - ^Lf_x^R) - (^Pf_x^M - ^Pf_x^R)]$ terms in Equation 6.15 disappear. Using $(^P\bar{\delta}_w^M - ^P\bar{\delta}_w^R) \approx 0$ in the $[(^L\bar{\delta}_w^M - ^L\bar{\delta}_w^R) - (^P\bar{\delta}_w^M - ^P\bar{\delta}_w^R)]$ term in Equation 6.15, the equation thus usefully reduces to:

$$(^L\delta_x^M - ^L\delta_x^R) - (^P\delta_x^M - ^P\delta_x^R) = ^L\bar{\delta}_w^M - ^L\bar{\delta}_w^R \quad (6.16)$$

Given Equation 6.6, doing the $(^L\delta_x^M - ^L\delta_x^R) - (^P\delta_x^M - ^P\delta_x^R)$ calculation with the core $\delta^{18}\text{O}$ data is thus not a test of goodness of match but a method to calculate the real LGM mean ocean $\delta^{18}\text{O}_w$:

$$^L\bar{\delta}_w^R = 1.25\text{‰} - [(^L\delta_x^M - ^L\delta_x^R) - (^P\delta_x^M - ^P\delta_x^R)] \quad (6.17)$$

This value is a major question of the LGM,⁹ as discussed in Section 7.1 in the next chapter, and is calculated in Section 6.5 with $\delta^{18}\text{O}_c$ for each foraminifera species and with snow/ice $\delta^{18}\text{O}_i$. Note for the latter though, that the $(^Lf_x^M - ^Lf_x^R)$ and

⁹Actually, $^L\bar{\delta}_w^R - ^P\bar{\delta}_w^R$ is the value of interest but as indicated it is confidently assumed that $^P\bar{\delta}_w^R = 0$.

$(^P f_x^M - ^P f_x^R)$ terms in Equation 6.15 are typically much larger than the $(^L \bar{\delta}_x^M - ^L \bar{\delta}_x^R)$ term, so if the assumption that each of the former two terms is the same at both PD and LGM is a little incorrect, the error could swamp the $(^L \bar{\delta}_x^M - ^L \bar{\delta}_x^R)$ signal, i.e., using precipitation $\delta^{18}\text{O}_i$ to calculate $^L \bar{\delta}_w^R$ could be more inaccurate than using foraminifera $\delta^{18}\text{O}_c$. Finally, note that $(^L \bar{\delta}_w^M - ^L \bar{\delta}_w^R)$ is significant in the LGM – PD $\delta^{18}\text{O}_c$ map comparison figures and $\delta^{18}\text{O}_c$ model/data plots of Section 6.5.

Finally for the means, there is the issue of weighting when doing the averages over the OGCM grid boxes. When averaging ocean water $\delta^{18}\text{O}$ and temperature from the OGCM it makes sense to weight the value from each grid box by the mass of the water in that grid box because this mass varies so much from bottom to surface and equator to pole in the OGCM. This is thus also true for $\delta^{18}\text{O}_c$ from the foraminifera model, since it takes ocean water $\delta^{18}\text{O}$, temperature, and salinity from the OGCM. However, while the ocean sediment core foraminifera $\delta^{18}\text{O}_c$ data was gridded to the OGCM (see Chapter 5) they are actually point measurements, with no information about how much ocean water they are representative of. Still, it is at least consistent to weight these by the mass of the water in their assigned OGCM grid box. Note though, that near-bottom OGCM grid boxes have much more water mass than near-surface ones (see the OGCM level depths in Section 3.2.1) and near-equator OGCM grid boxes have more water mass than near-pole ones so the former in each case will have the largest effect in the means. Also note that while this is generally true, the water mass in each OGCM grid box is actually variable over time. The situation, and the decision, is similar for precipitation $\delta^{18}\text{O}$, except that the weighting is by precipitation rate (i.e., for a given period, mass) in each AGCM surface grid box and there are observations of this.

6.3 Present Day (PD) Simulation Compared to Observations

6.3.1 Maps

Comparing the PD simulation to observations using map comparison figures of certain variables in order to spatially assess important biases, all as outlined in Section 6.2.2,

it is perhaps fitting to proceed from the bottom¹⁰ ocean up through the atmosphere, following a path of the hydrological cycle. More general biases are readily apparent in the figures, but for predicting what effect biases will have on PD OGCM/foraminifera model simulated foraminifera $\delta^{18}\text{O}_c$ and PD AGCM simulated precipitation $\delta^{18}\text{O}$, areas where there are cores are concentrated on. For the former, it is useful to remember that higher ocean water $\delta^{18}\text{O}$ and colder ocean water in situ temperature both mean higher foraminifera $\delta^{18}\text{O}_c$ (see Section 2.2.1).

Starting with ocean $\delta^{18}\text{O}_w$ it should first be noted where its observations came from. All ocean $\delta^{18}\text{O}_w$ observations in this work are from Schmidt et al. 1999 gridded to the CGCM by equal-weights averaging the $\delta^{18}\text{O}_w$ measurements of all samples located in each three-dimensional OGCM grid box. The samples of Schmidt et al. 1999 were taken irregularly from 1949 to 2000 and at irregular times of the year; for some samples this information was unknown. To ameliorate the temporal and spatial sparsity of the observations, the 1949–2000 “annual” average here is actually the equal-weights average of whatever “monthly” means (usually from single instances during a month) were available in each grid box; this can be from only a single month. Those samples whose sampling month was unknown were considered as from a separate month from any other in the annual average, which is likely given the few months usually represented in the annual average. For the slow-changing deep ocean this annual average is probably fairly accurate but it becomes significantly less so towards the seasonally-changing surface.

Figure 6.5 is the map comparison figure for PD bottom ocean $\delta^{18}\text{O}_w$. Most of the benthic foraminifera ocean sediment cores are from the tropical Atlantic (see Figure 6.21b for core locations) so that region is concentrated on. Unfortunately, as Figure 6.5b shows, there aren’t that many PD bottom ocean $\delta^{18}\text{O}_w$ observations from the tropical Atlantic. However, Figure 6.5c implies that over most of the bottom OGCM Atlantic, $\delta^{18}\text{O}_w$ seems to be somewhat low compared to observations. This bias should tend to similarly lower the benthic foraminifera $\delta^{18}\text{O}_c$ output from the OGCM/foraminifera model there.

Turning to ocean in situ temperature, the source of its observations should be noted, which is that for salinity as well. All ocean in situ temperature and salinity

¹⁰Again, “bottom” as defined for benthic foraminifera in Section 6.1.

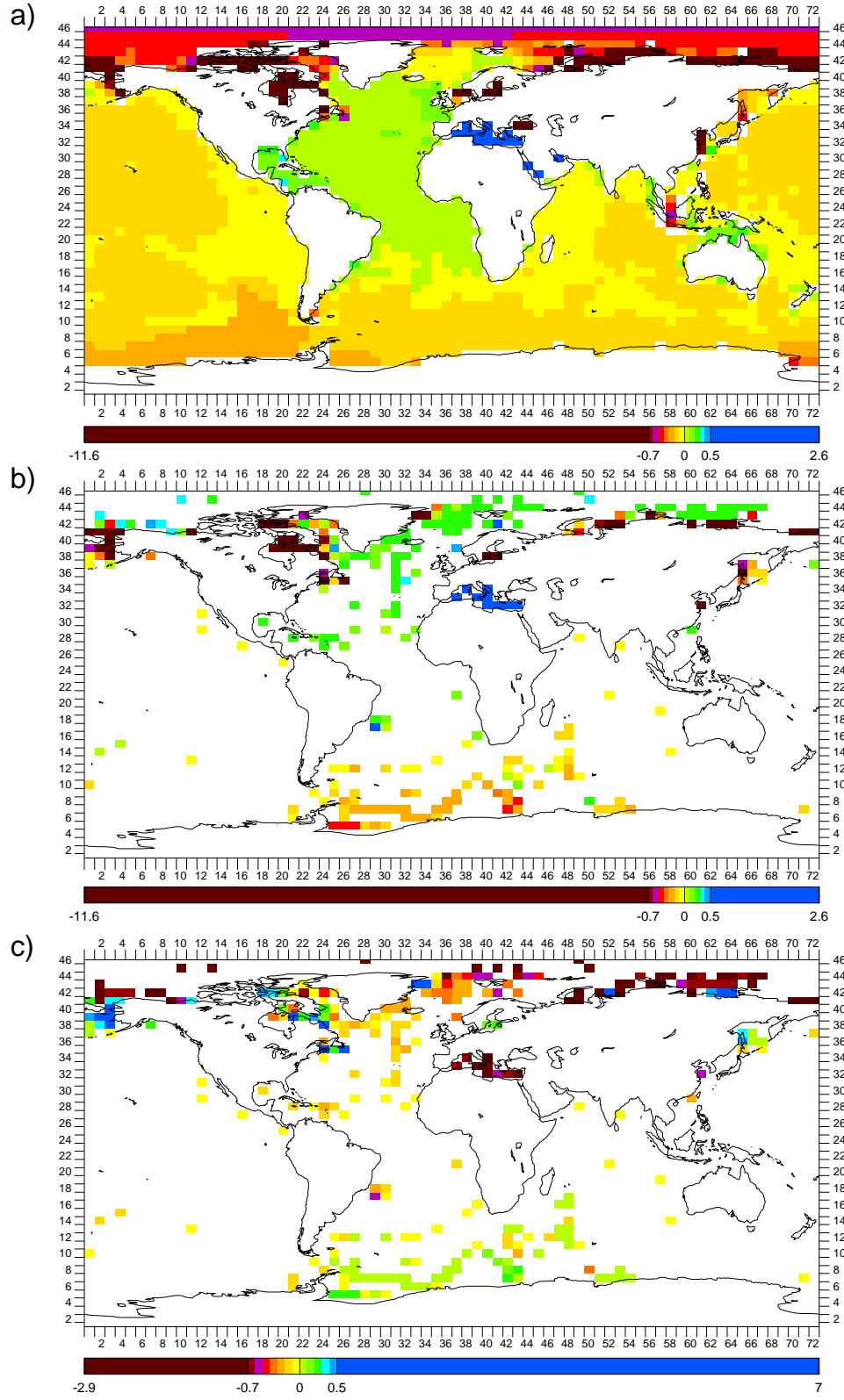


Figure 6.5: CGCM grid box maps of PD annual bottom ocean $\delta^{18}\text{O}_w$ (‰ SMOW) for: a) OGCM; b) observations; and c) OGCM minus observations

observations in this work are from Levitus 1998¹¹, but regridded in the horizontal from its 1° x 1° resolution to the OGCM's 5° x 4° resolution using an area-average-preserving algorithm and then regridded in the vertical from its various levels to those of the OGCM's using a level-proportional mixing algorithm. Levitus 1998 is for the period 1900–1997 and the annual average used here was calculated by them.

Figure 6.6 is the map comparison figure for PD bottom ocean in situ temperature. As Figure 6.6c shows, the tropical bottom OGCM North Atlantic seems to be too warm compared to observations and the tropical bottom South Atlantic somewhat too cold, except for its shores and Mid-Atlantic Ridge where it is also too warm. Note that the intersection of all this is where most of the benthic foraminifera ocean sediment cores are. The OGCM warm bias in the tropical bottom North Atlantic should tend to cause the benthic foraminifera $\delta^{18}\text{O}_c$ output from the OGCM/foraminifera model there to be low compared to core data, further reinforcing the low there from the bottom OGCM $\delta^{18}\text{O}_w$ bias. This would be true too of the shores and Mid-Atlantic Ridge of the tropical South Atlantic. In the rest of the tropical bottom South Atlantic though, the OGCM cold bias would tend to cause the benthic foraminifera $\delta^{18}\text{O}_c$ output from the OGCM/foraminifera model to be high there compared to core data, countering the low there from the bottom OGCM $\delta^{18}\text{O}_w$ bias.

Moving up through the ocean¹² in the Atlantic, where most of the ocean sediment cores are and which is of particular interest in this work, Figure 6.7 is the map comparison figure for PD ocean $\delta^{18}\text{O}_w$ along a section at OGCM lon# 30 (30–35°W). Although Schmidt et al. 1999 is sparse, Figure 6.7c does show that in the lower-latitude Atlantic, in the near-surface layers where planktonic foraminifera live, the OGCM $\delta^{18}\text{O}_w$ is low compared to observations, which should tend to cause the planktonic foraminifera $\delta^{18}\text{O}_c$ output from the OGCM/foraminifera model to be low there

¹¹Note that there are ocean temperature and salinity observations accompanying the ocean $\delta^{18}\text{O}_w$ observations of Schmidt et al. 1999 but the ocean temperature and salinity observations of Levitus 1998 have been used in this work since they are more comprehensive, i.e., cover the whole ocean. Reassuringly, the unshown ocean temperature and salinity observations from Schmidt et al. 1999 generally match well those from Levitus 1998.

¹²Salinity has a very small (if any) effect on the non-depth-varying benthic foraminifera, so bottom salinity was not shown.

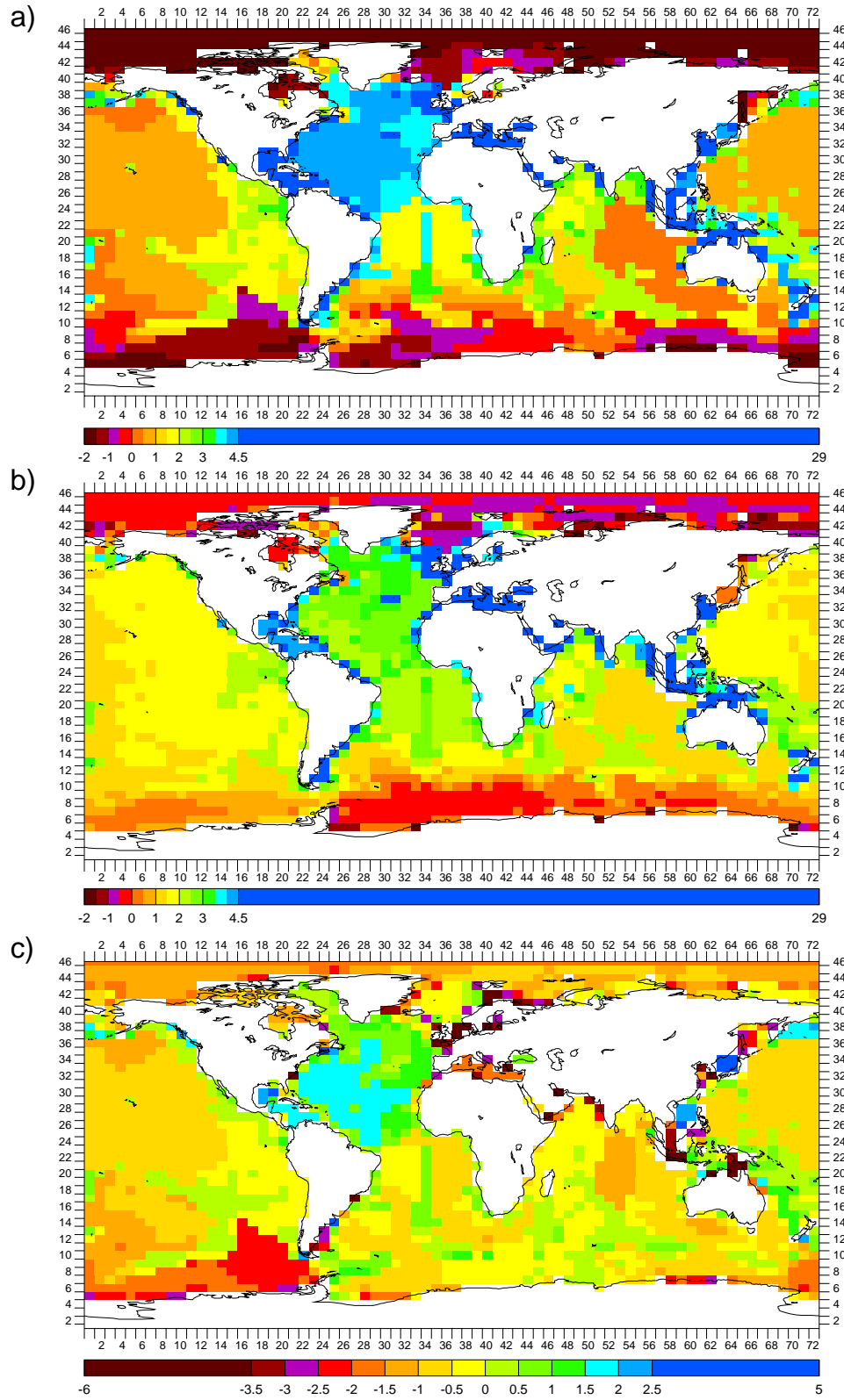


Figure 6.6: CGCM grid box maps of PD annual bottom ocean in situ temperature (C) for: a) OGCM; b) observations; and c) OGCM minus observations

compared to core data. Less obviously, in the near-surface layers of the high-latitude South Atlantic (i.e., the Southern Ocean), the OGCM $\delta^{18}\text{O}_w$ is somewhat high compared to observations, which should tend to cause the planktonic foraminifera $\delta^{18}\text{O}_c$ output from the OGCM/foraminifera model to be high compared to core data.

Figures 6.8 and 6.9 are the map comparison figures for PD ocean in situ temperature and salinity, respectively, along the same Atlantic section as Figure 6.7. Mirroring Figure 6.7c, Figures 6.8c and 6.9c show that in the lower-latitude Atlantic, in the near-surface layers where planktonic foraminifera live, the OGCM is too cold and too fresh, respectively, compared to the observations and in the near-surface layers of the high-latitude South Atlantic the OGCM is somewhat too warm and too salty, respectively. The cold bias in the lower-latitude Atlantic should tend to cause the planktonic foraminifera $\delta^{18}\text{O}_c$ output from the OGCM/foraminifera model to be high compared to core data, countering the OGCM low $\delta^{18}\text{O}_w$ bias there. The warm bias in the high-latitude South Atlantic should tend to cause the planktonic foraminifera $\delta^{18}\text{O}_c$ output from the OGCM/foraminifera model to be low there compared to core data, countering the OGCM high $\delta^{18}\text{O}_w$ bias there. All these sections suggest that the surface OGCM level (1), should be roughly representative of the near-surface levels where planktonic foraminifera also live. They also all suggest that the OGCM has too much deep convection in the Arctic and Antarctic. Antarctic deep convection is related to nearby upwelling of North Atlantic Deep Water and biases in these could affect AGCM Antarctic precipitation $\delta^{18}\text{O}$ and thus comparisons to Antarctic ice cores (see ahead).¹³ Finally, Figure 6.8a implies that the thermocline depth in the OGCM is realistic.

Moving to the surface ocean, Figure 6.10 is the comparison figure for PD surface ocean $\delta^{18}\text{O}_w$. The caveat about Schmidt et al. 1999 not being a true annual average is most applicable here. Most of the planktonic foraminifera ocean sediment cores are from (see Figures 6.22b to 6.27b for core locations) the Atlantic (into the Arctic Ocean), Indian, and Southern Ocean south of the Atlantic and Indian; there are also some cores from the south tropical Pacific and Mediterranean Sea. These regions are thus concentrated on. Figure 6.10c shows that in the surface lower-latitude Atlantic, Indian, south tropical Pacific, and Mediterranean Sea, the OGCM $\delta^{18}\text{O}_w$ is low com-

¹³Note that it is believed from proxy data that there was less NADW upwelling at the LGM.

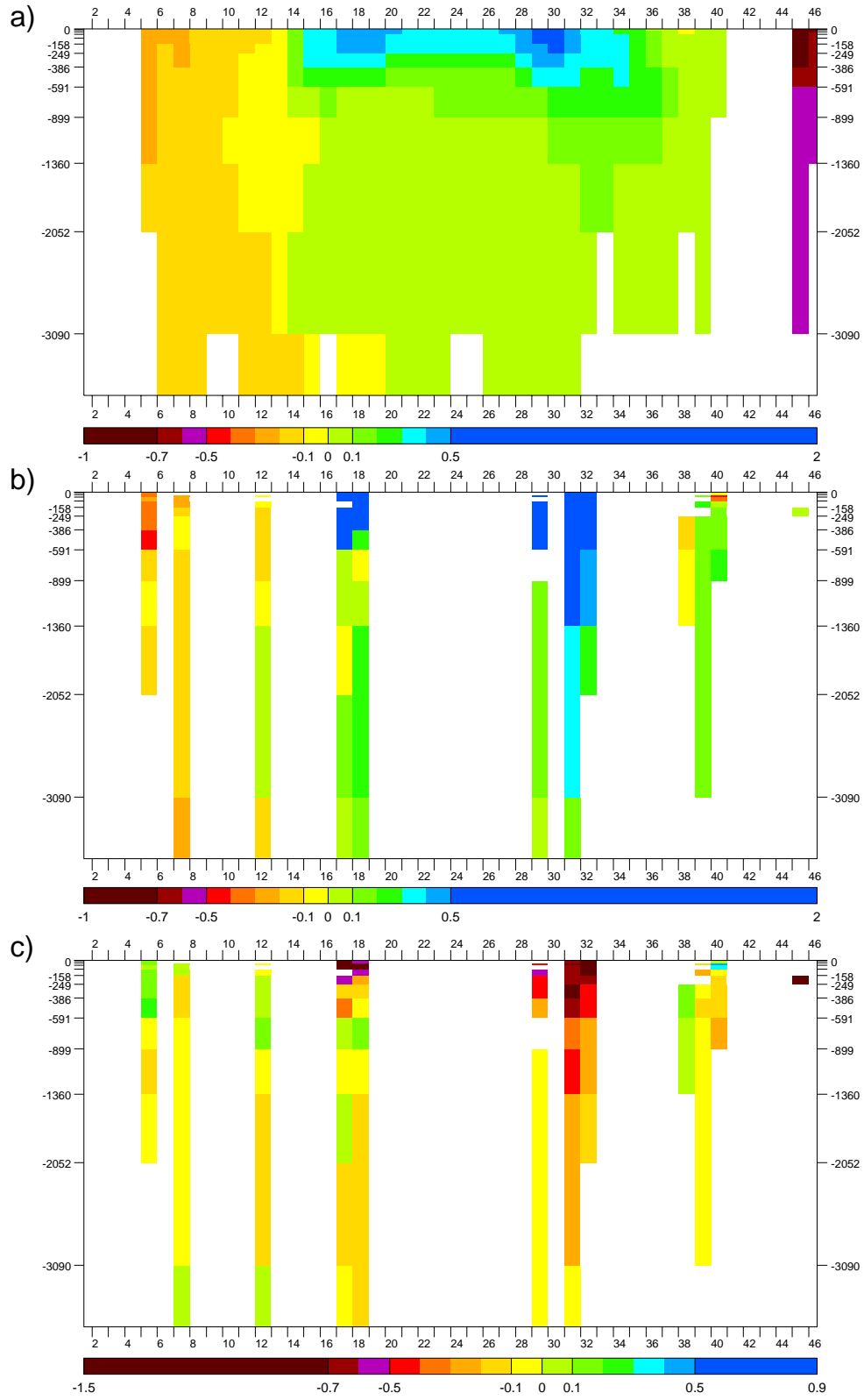


Figure 6.7: CGCM grid box lon# 30 (30–35°W) sections of PD annual ocean $\delta^{18}\text{O}_w$ (‰ SMOW) for: a) OGCM; b) observations; and c) OGCM minus observations

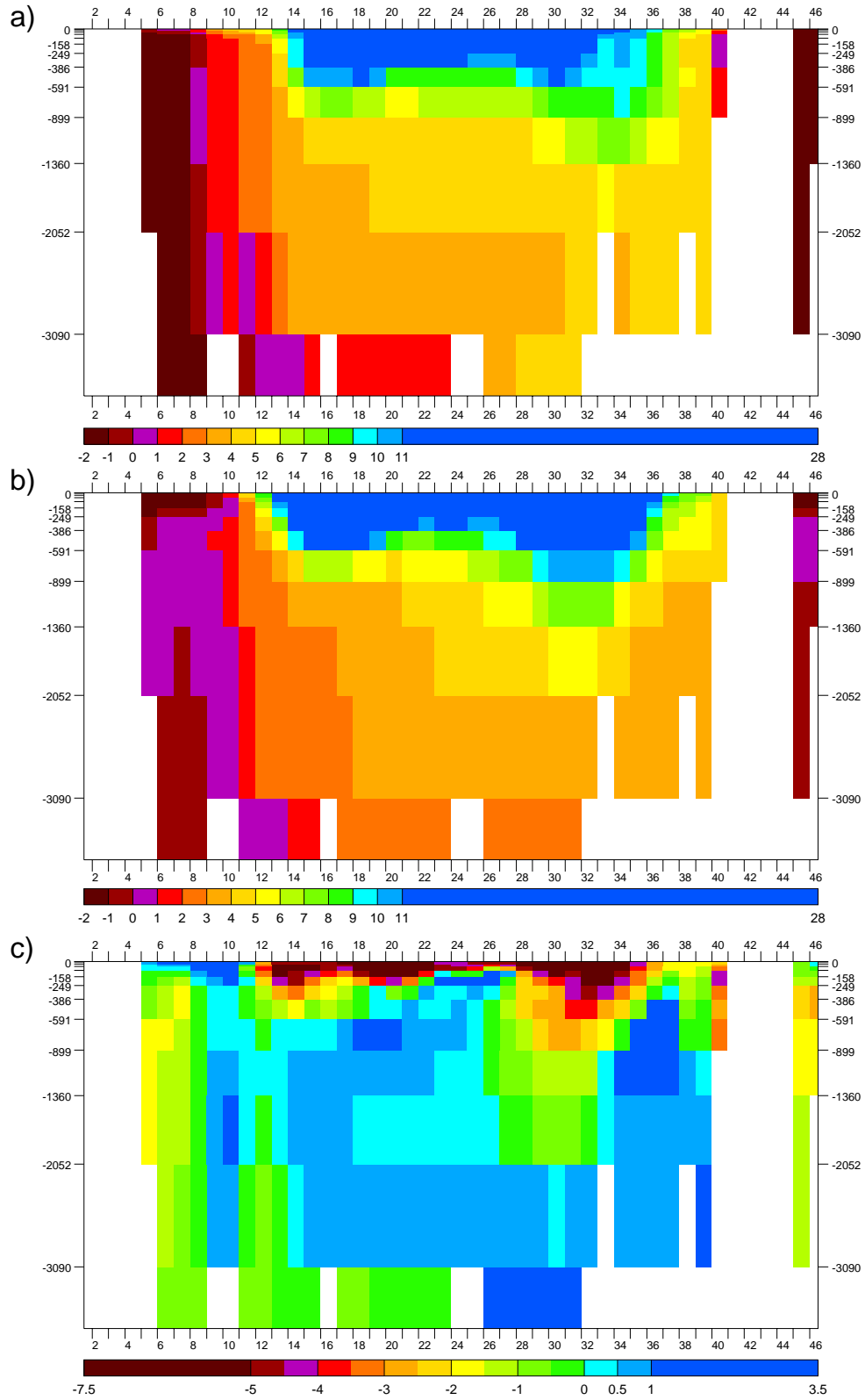


Figure 6.8: CGCM grid box lon# 30 (30–35°W) sections of PD annual ocean in situ temperature (C) for: a) OGCM; b) observations; and c) OGCM minus observations

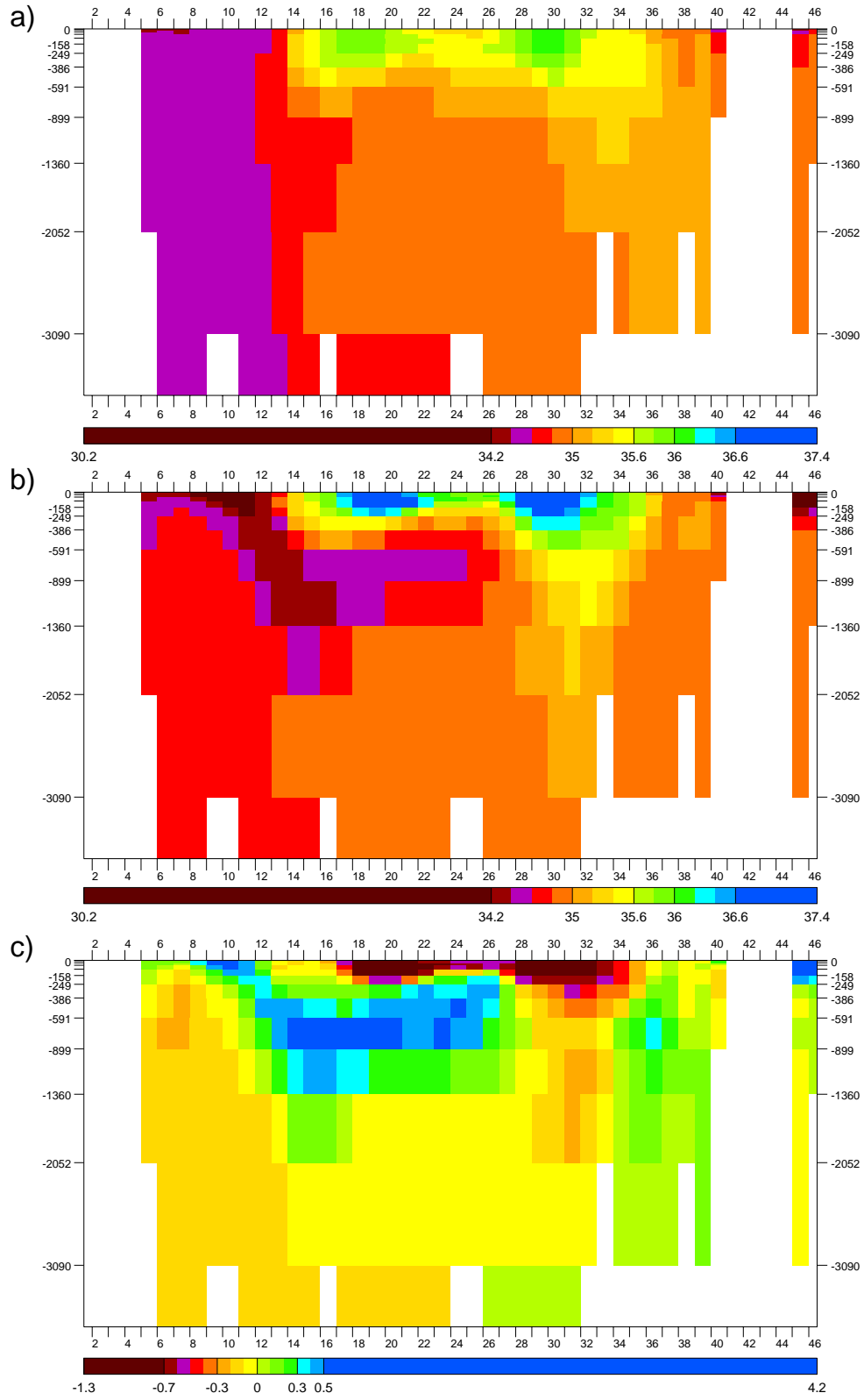


Figure 6.9: Grid box lon# 30 (30–35°W) sections of PD annual salinity (g/kg) for: a) OGCM; b) observations; and c) OGCM minus observations

pared to the observations and that in the surface Southern Ocean south of the Atlantic and Indian the OGCM $\delta^{18}\text{O}_w$ is somewhat high compared to the observations. Note also the large OGCM high $\delta^{18}\text{O}_w$ bias in the surface ocean off of northeast Greenland. All these biases should similarly affect the planktonic foraminifera $\delta^{18}\text{O}_c$ output from the OGCM/foraminifera model in those areas.

Surface ocean $\delta^{18}\text{O}_w$ (and salinity) is strongly affected by the difference between precipitation and evaporation. Precipitation, generally having a lower $\delta^{18}\text{O}$ than surface ocean water, tends to decrease that of surface ocean water and evaporation tends to increase it. However, there is no global dataset of truly observational $P - E$ to compare to the CGCM to check for $P - E$ biases causing the surface ocean $\delta^{18}\text{O}_w$ biases. This is because evaporation is notoriously difficult to reliably measure. A global dataset of observed evaporation is thus not available and estimates are the norm. Since this is the case it is not unreasonable to use evaporation data (actually latent heat flux) from Kanamitsu et al. 2002, which is a recent “reanalysis” project. Reanalysis essentially uses an AGCM constrained by assimilation of limited amounts/types of observed data to produce a consistent global set of climate fields. Those fields most directly influenced by the assimilated observed data tend to be the most reliable. Those fields least directly influenced by the assimilated observed data are more influenced by the AGCM itself and thus tend to be the least reliable. Since no observed evaporation data is assimilated, the reanalysis evaporation field is technically in the latter class. However, evaporation is most strongly influenced by wind and humidity and those two fields are strongly and moderately influenced, respectively, by the assimilated observed data. So, for the observational $P - E$, evaporation data from Kanamitsu et al. 2002 was used, by first regridding (preserving area averages) the original latent heat flux data from its $1.875^\circ \times 1.9^\circ$ resolution to that of the CGCM, then calculating an annual average for the 1979–1998 data, and finally converting the latent heat flux in W/m^2 to evaporation in mm/day using the latent heat of evaporation and other constants.

In contrast to evaporation, reanalysis precipitation is very GCM-dependent so rather unreliable. Thus, while it might seem more consistent to also use the precipitation rate data from Kanamitsu et al. 2002 in the observational $P - E$, a global dataset of observed (combined satellite and gauge data) precipitation rate was used

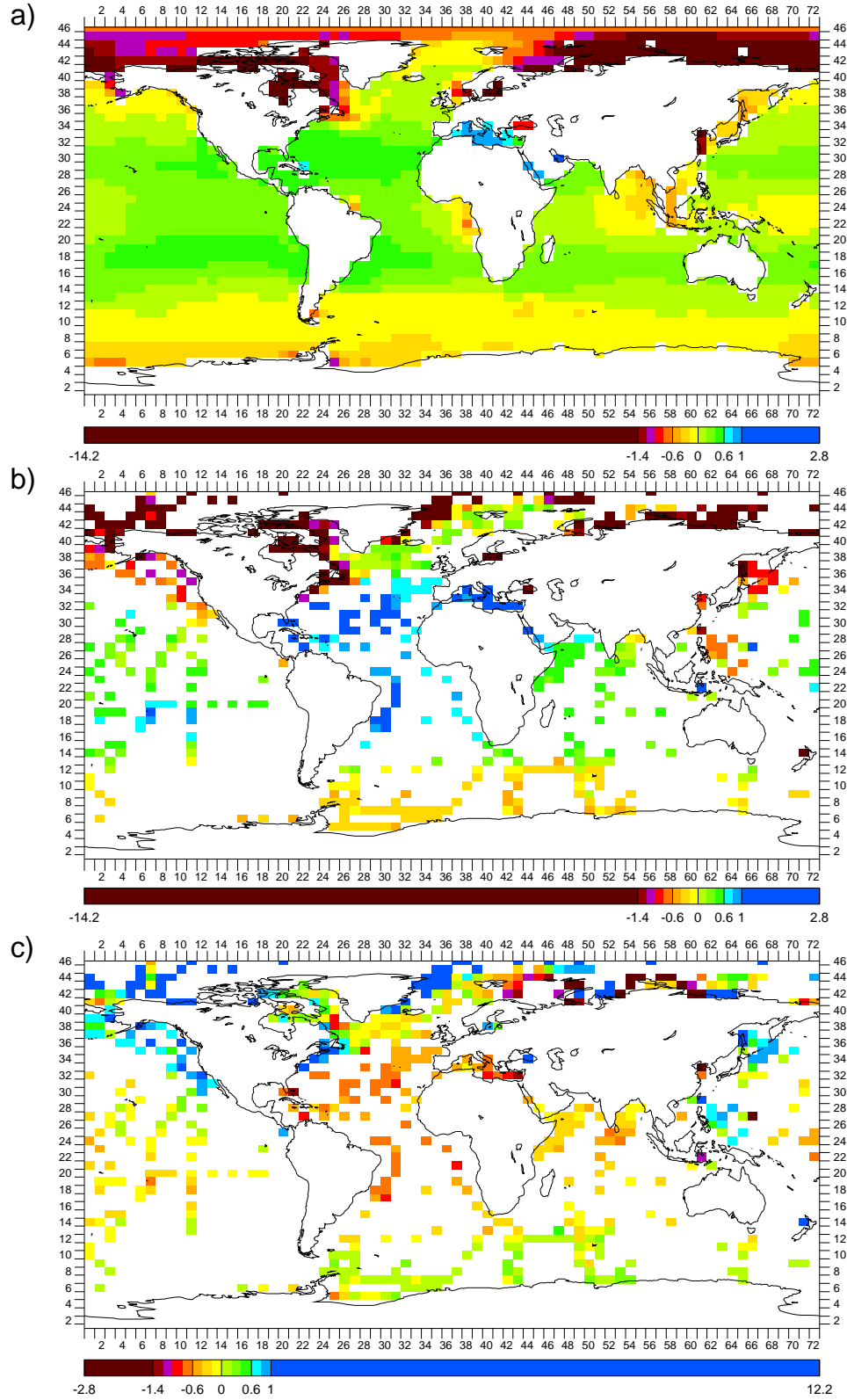


Figure 6.10: CGCM grid box maps of PD annual surface ocean $\delta^{18}\text{O}_w$ (‰ SMOW) for: a) OGCM; b) observations; and c) OGCM minus observations

instead. These and all precipitation rate observations in this work were taken from Huffman and Bolvin 2003 by calculating an average of the annual data for the years 1979–2001 and regridding (preserving area averages) from its $2.5^\circ \times 2.5^\circ$ resolution to that of the OGCM.

Figure 6.11 then, is the map comparison figure for PD $P - E$, with Figure 6.11b the resulting observational $P - E$. Figure 6.11c shows that in most of the lower-latitude Atlantic, Indian, south tropical Pacific, and Mediterranean Sea, all where there is an OGCM surface ocean $\delta^{18}O_w$ low bias, AGCM $P - E$ is too positive. That is, there is an excess of AGCM precipitation over evaporation there and as explained, this would indeed tend to cause the OGCM surface ocean $\delta^{18}O_w$ to be low compared to observations. Conversely, Figure 6.11c shows that in the Southern Ocean south of the Atlantic and Indian, where there is an OGCM surface ocean $\delta^{18}O_w$ high bias, AGCM $P - E$ is, correctly, too low compared to observations. Note that the AGCM $P - E$ bias off of northeast Greenland is small (possibly zero) throughout but, in much of the area, in the right direction (low) to explain the OGCM surface ocean $\delta^{18}O_w$ low biases there.

Sea ice can also affect the surface ocean $\delta^{18}O_w$ because as it forms it preferentially takes up ^{18}O and thus lowers surface ocean $\delta^{18}O_w$. It can also work in that direction by preventing surface ocean $\delta^{18}O_w$ increase through blocking surface ocean evaporation. Figure 6.12 is the map comparison figure for PD sea ice concentration, with Figure 6.12b satellite-derived observations taken from Armstrong and Knowles 2003 by calculating an annual 1986–1995 average and regridding (preserving area averages) from its $1^\circ \times 1^\circ$ resolution to that of the OGCM. As Figure 6.12c shows, in the Southern Ocean south of the Atlantic and Indian, the OGCM has too little sea ice compared to the observations. This would indeed tend to allow too much evaporation there compared to observations, as Figure 6.11c implies, and lead to a surface ocean $\delta^{18}O_w$ there that is high compared to observations, as Figure 6.10c indicates. That the CGCM has too much evaporation there is confirmed by looking at just the CGCM evaporation (not shown) compared to observations; looking at just the CGCM precipitation compared to observations (Figure 6.16c) though shows that generally the CGCM also has too little precipitation there. In the ocean off of northeast Greenland the OGCM has too much sea ice compared to observations.

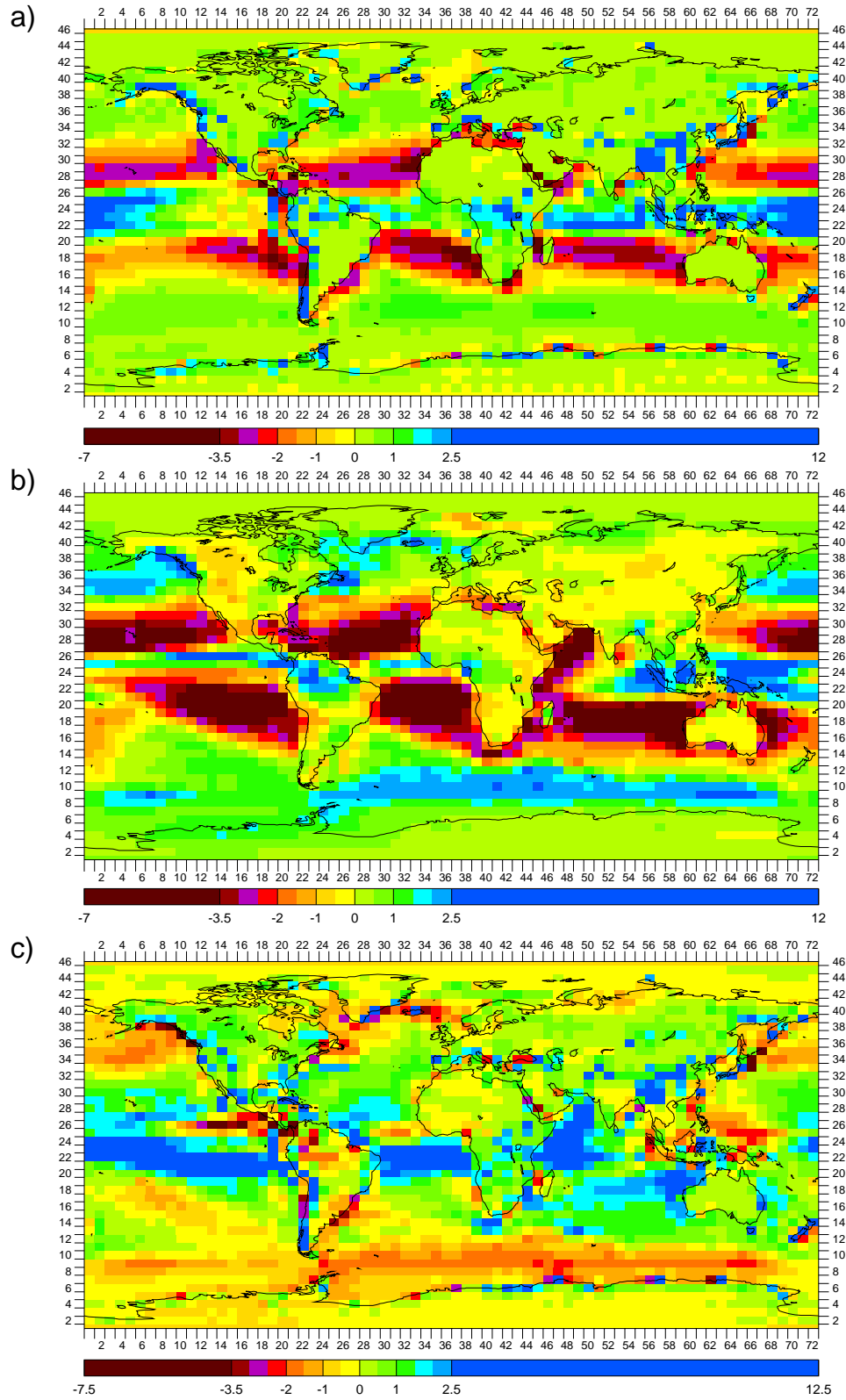


Figure 6.11: CGCM grid box maps of PD annual P - E (mm/day) for: a) AGCM; b) observations; and c) AGCM minus observations

However, there is incongruously somewhat too much CGCM evaporation (not shown) compared to observations; this though fits in with the OGCM surface ocean $\delta^{18}\text{O}_w$ being high there compared to observations (Figure 6.10c).

Finally for sea ice, it might be noted in Figure 6.12c that the OGCM sea ice concentration in the North Pole box is low compared to the observations. The sea ice concentration in the North Pole box of Figure 6.12b is actually not an “observation”: because the satellites did not cover the North Pole area the sea ice concentration there was just set by the dataset authors to a likely value of 100%. However, even if it was not 100% the OGCM value still seems anomalously low. While the exact cause is unknown, it seems to be a long-term effect in that it did not appear until after the PD simulation had run for many model decades. In any case, the expected effects from it are seen in the evaporation (not shown) and $P - E$ fields.

Figure 6.13 is the map comparison figure for PD surface salinity. As Figure 6.13c shows, in the surface lower-latitude Atlantic, Indian, south tropical Pacific (except far east), and Mediterranean Sea, the OGCM is too fresh compared to observations, correlating with ocean $\delta^{18}\text{O}_w$ being low there compared to observations (Figure 6.10c). Conversely, in the surface Southern Ocean south of the Atlantic and Indian the OGCM is too salty compared to observations, correlating with ocean $\delta^{18}\text{O}_w$ being high there compared to observations; similarly for the surface ocean off of northeast Greenland.

Figure 6.14 is the map comparison figure for PD surface ocean in situ temperature. As Figure 6.14c shows, in the surface Atlantic, Indian, south tropical Pacific, and the Mediterranean Sea, the OGCM is too cold compared to observations and in the surface Southern Ocean south of the Atlantic and Indian the OGCM is too warm compared to observations. Note the pronounced increase in the cold bias in going from east to west in the lower-latitude Atlantic. In any case, the cold bias should, as discussed, tend to cause the planktonic foraminifera $\delta^{18}\text{O}_c$ output from the OGCM/foraminifera model to be high compared to core data and vice versa for the warm bias. Comparing to Figure 6.10, this means that in most of the Atlantic, Indian, south tropical Pacific, Mediterranean Sea, and Southern Ocean south of the Atlantic and Indian, the surface OGCM in situ temperature biases should tend to counter the surface OGCM $\delta^{18}\text{O}_w$ biases in their effect on the planktonic foraminifera $\delta^{18}\text{O}_c$ output from the OGCM/foraminifera model. The most notable exception (in

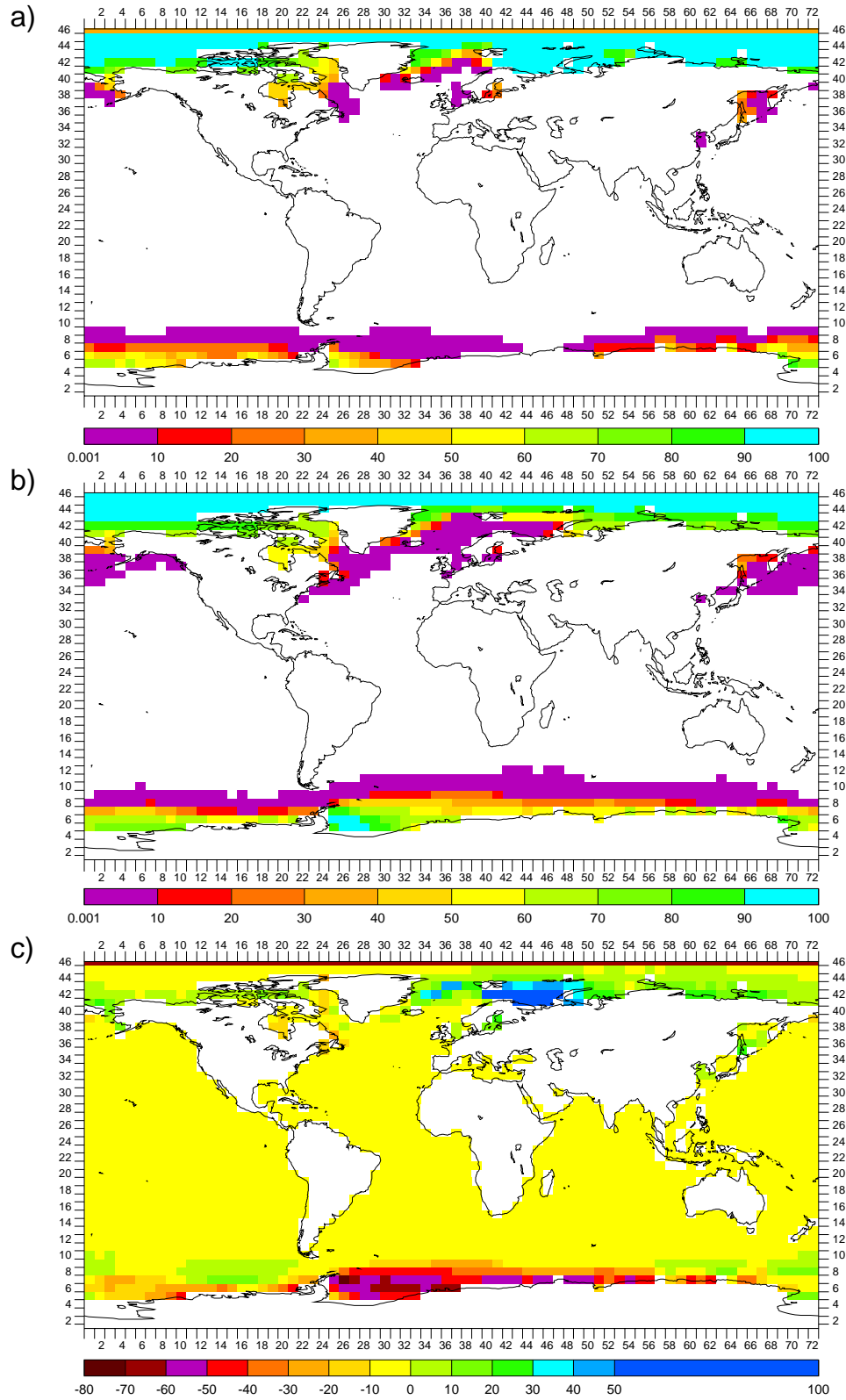


Figure 6.12: CGCM grid box maps of PD annual sea ice concentration (%) for: a) OGCM; b) observations; and c) OGCM minus observations

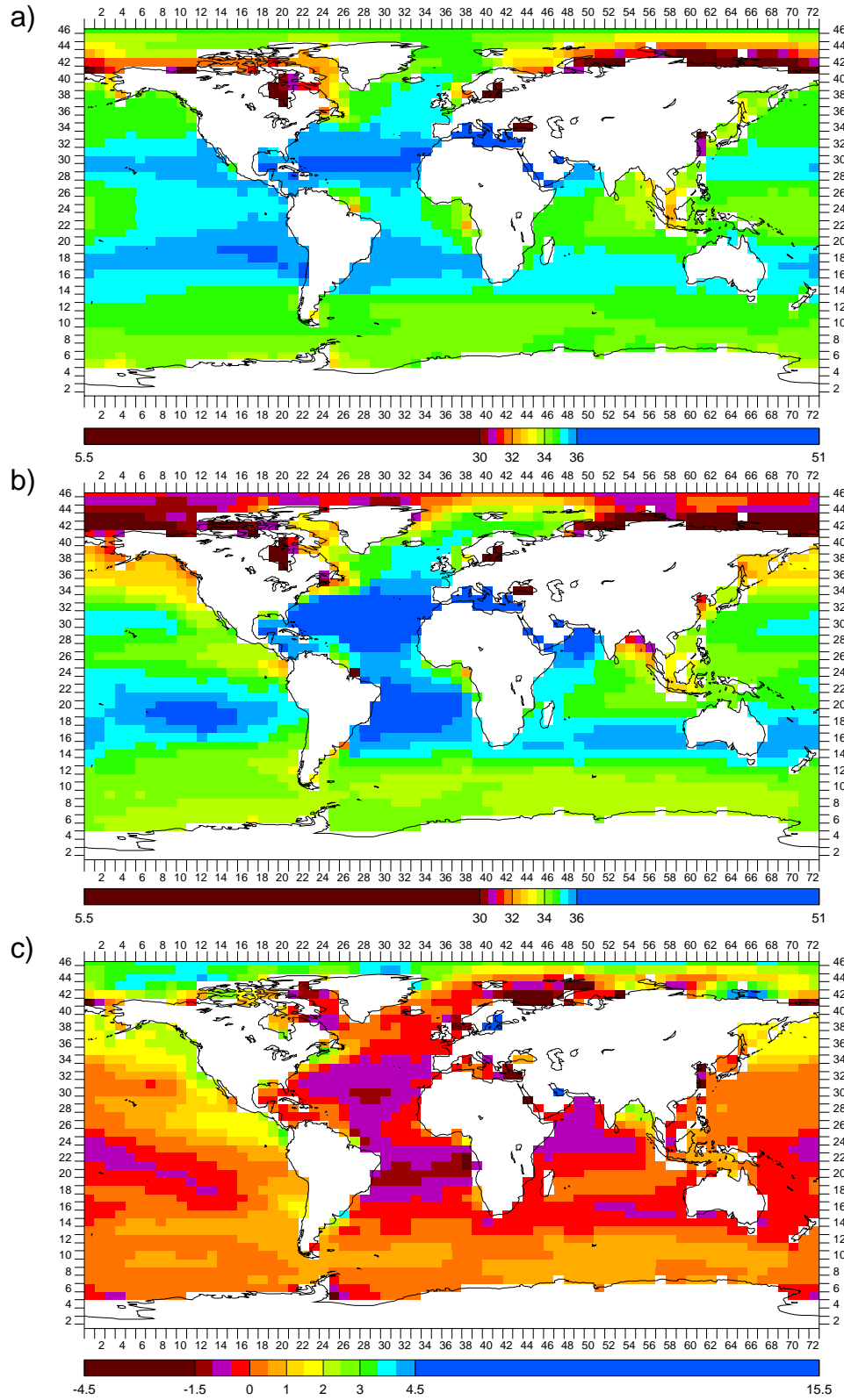


Figure 6.13: CGCM grid box maps of PD annual surface salinity (g/kg) for: a) OGCM; b) observations; and c) OGCM minus observations

areas where ocean sediment cores are) is off of northeast Greenland, where OGCM surface ocean $\delta^{18}\text{O}_w$ is high and surface ocean in situ temperature too cold compared to observations. More generally, the strong OGCM cold bias around the subtropical gyres must be noted. It is just such inherent CGCM biases that it is hoped the LGM – PD differencing will remove. Further, note also that Figure 6.14 suggests that the North Atlantic Drift does not penetrate far enough into the Arctic Ocean, which can also be seen in the sea ice of Figure 6.12 and the salinity of Figure 6.13.

Moving into the atmospheric part of the hydrological cycle, Figure 6.15 is the map comparison figure for PD precipitation $\delta^{18}\text{O}$. The precipitation $\delta^{18}\text{O}$ observations in it, like all in this work, are from IAEA 2001 gridded to the CGCM by equal-weights averaging the 1961–1999 annual (calculated by IAEA 2001) precipitation $\delta^{18}\text{O}$ of all stations in each CGCM grid box. Unfortunately, with one small exception there are no observations where there are ice cores (see Figure 6.28b) so nearby observations must be used to guess what the biases that will manifest in the ice core H_2O $\delta^{18}\text{O}$ predicted by the AGCM (i.e., in its precipitation $\delta^{18}\text{O}$) will be. To make matters worse, these “nearby” observations are often along steep topographic gradients to the ice cores, areas where the AGCM historically does not do well. With that warning, Figure 6.15c shows that near inland Antarctica and northeast Greenland the AGCM precipitation $\delta^{18}\text{O}$ is high compared to observations and near central Greenland it is low. In Bolivia, where there is an observation box matching one of the ice core boxes, AGCM precipitation $\delta^{18}\text{O}$ is somewhat low.

Figure 6.16 is the map comparison figure for PD precipitation rate (observations are from the described Huffman and Bolvin 2003). In Antarctica and Greenland where the ice cores are the AGCM precipitation rate biases are small enough not to expect resulting biases in AGCM precipitation $\delta^{18}\text{O}$. However, in Bolivia the AGCM has significantly too much precipitation compared to observations. This would tend to cause the AGCM precipitation $\delta^{18}\text{O}$ to be low compared to observations there (see Section 2.1.3) and this is just what was seen in the Bolivia box of Figure 6.15c (albeit a small bias).

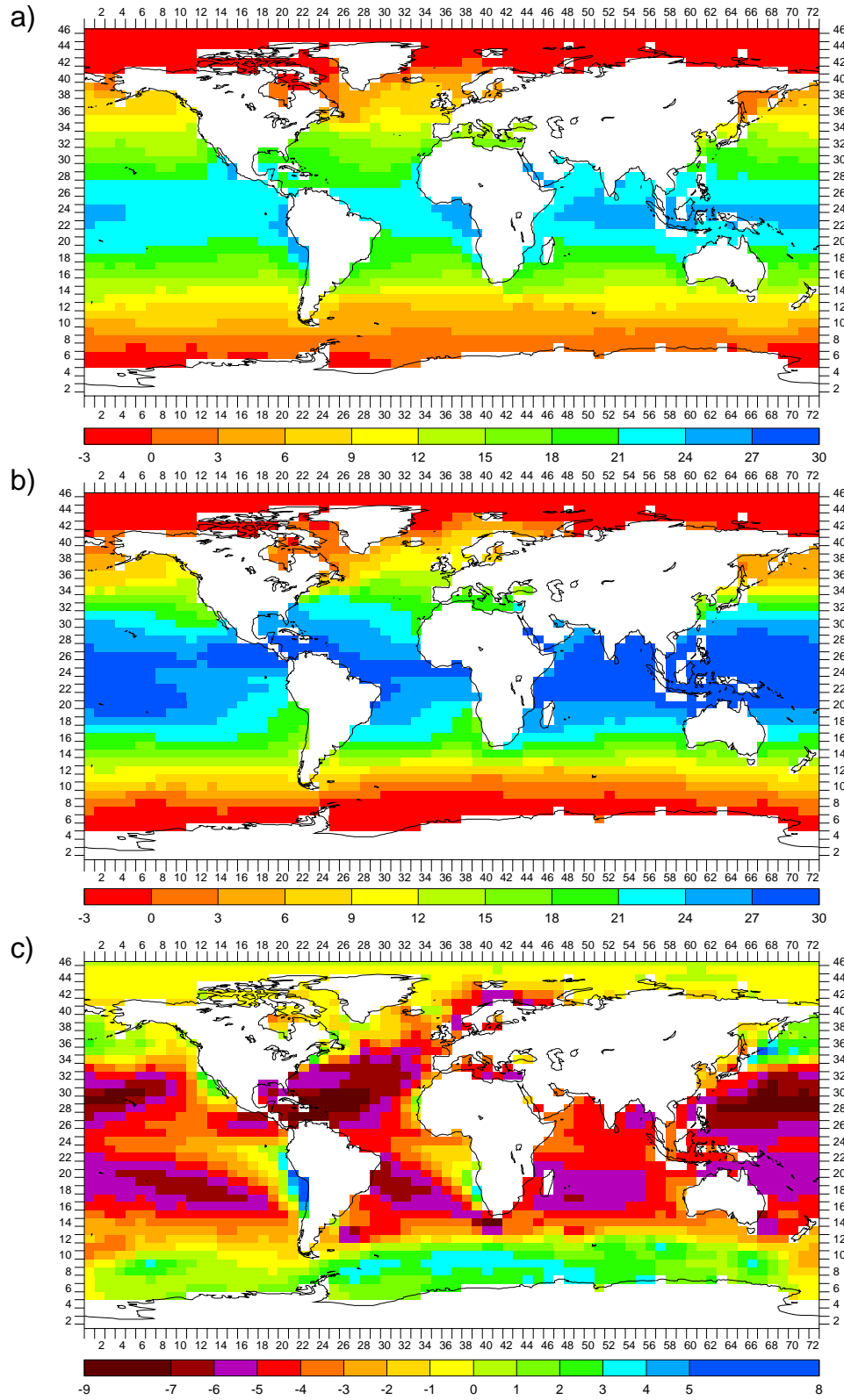


Figure 6.14: CGCM grid box maps of PD annual surface ocean in situ temperature (C) for: a) OGCM; b) observations; and c) OGCM minus observations

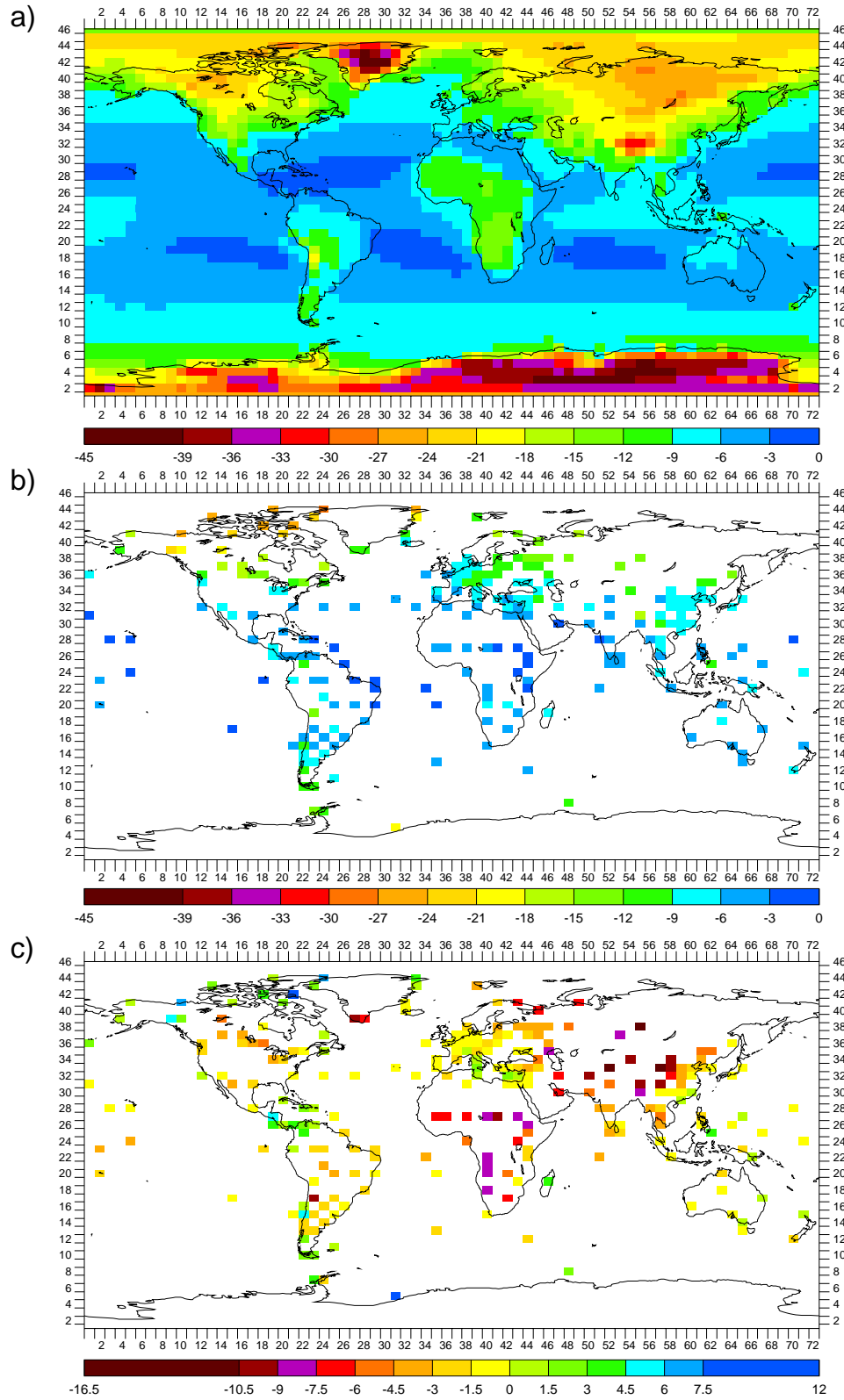


Figure 6.15: CGCM grid box maps of PD annual precipitation $\delta^{18}\text{O}$ (‰ SMOW) for: a) AGCM; b) observations; and c) AGCM minus observations

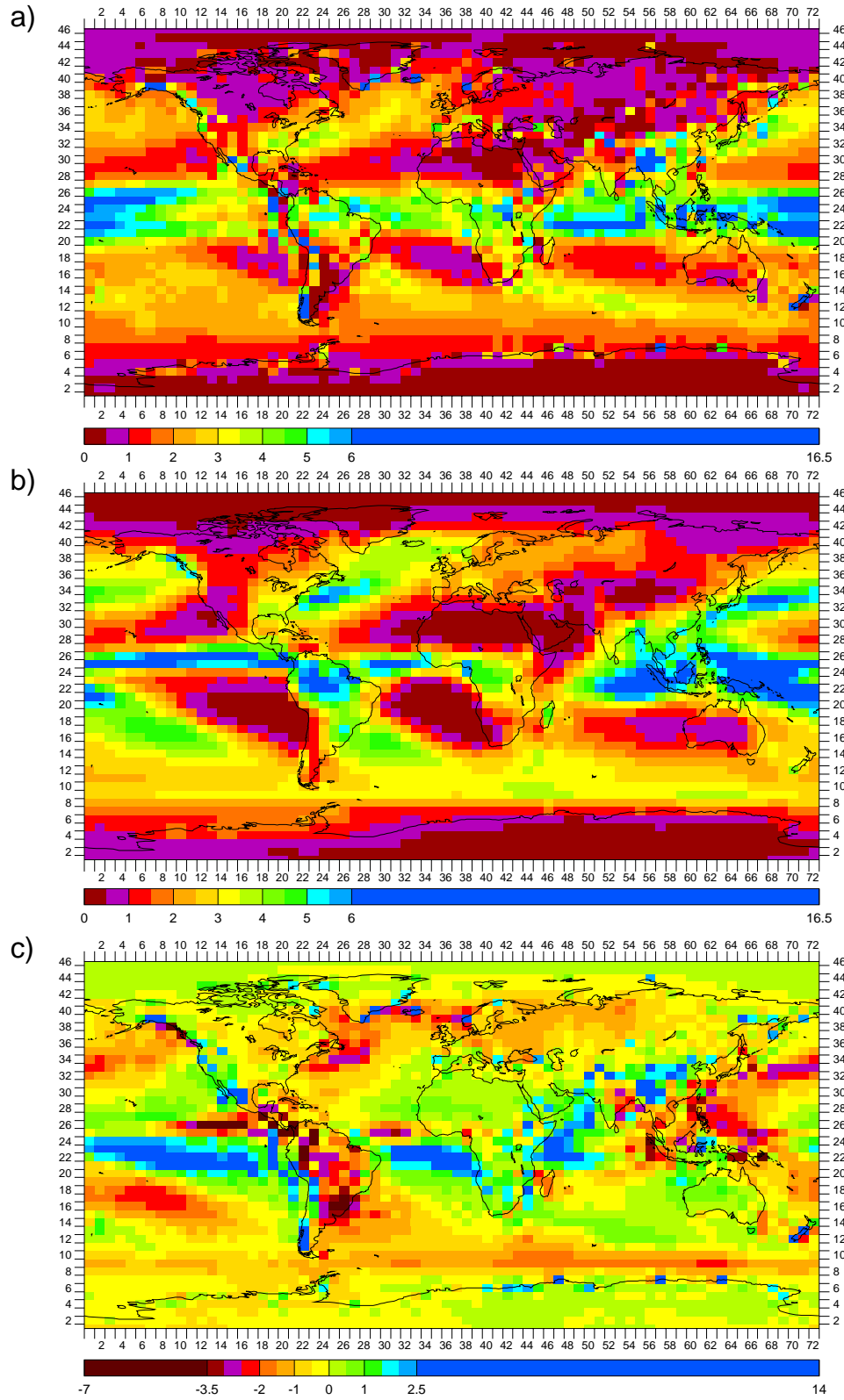


Figure 6.16: CGCM grid box maps of PD annual precipitation rate (mm/day) for: a) AGCM; b) observations; and c) AGCM minus observations

6.3.2 Plots

Comparing the PD simulation to observations with model/data plots of certain variables in order to assess their $\delta^{18}\text{O}$ -critical biases, all as outlined in Section 6.2.2, Figure 6.17 is the plot (top) of PD surface OGCM $\delta^{18}\text{O}_w$ versus observed surface ocean $\delta^{18}\text{O}_w$ in the corresponding grid boxes and the plot (bottom) of PD bottom OGCM $\delta^{18}\text{O}_w$ versus observed bottom $\delta^{18}\text{O}_w$ in the corresponding grid boxes. The top of Figure 6.18 is the plot of PD OGCM (all levels) $\delta^{18}\text{O}_w$ versus observed ocean $\delta^{18}\text{O}_w$ in the corresponding grid boxes. Overall, the biases in these three plots are fairly small. Figure 6.19 is the plot (top) of PD surface OGCM in situ temperature versus observed surface ocean in situ temperature in the corresponding grid boxes and the plot (bottom) of PD bottom OGCM in situ temperature versus observed bottom ocean in situ temperature in the corresponding grid boxes. The strong OGCM cold bias around all subtropical gyres (see Section 6.3.1) is apparent in the former but the latter does not seem to have any major biases. This is also seen in the all-level plot of Figure 6.18 (bottom). Figure 6.20 is a plot of PD AGCM precipitation $\delta^{18}\text{O}$ versus observed precipitation $\delta^{18}\text{O}$ in the corresponding grid boxes. The AGCM seems to have a low precipitation $\delta^{18}\text{O}$ bias.

6.3.3 Means

Comparing the PD simulation to observations using means of the variables in the model/data plots in order to bottom-line assess the biases, all as outlined in Section 6.2.2, Table 6.1 is the calculation for mean ocean $\delta^{18}\text{O}_w$ (over the entire ocean rather than just for the bottom or surface, which will be considered next). The magnitude of the resulting mean ocean $\delta^{18}\text{O}_w$ bias of the OGCM compared to observations is small enough (although near the tenth permil limit of what is considered small) to provide confidence in the CGCM to predict ocean water $\delta^{18}\text{O}$, as well as to not have been obvious in the corresponding map comparison figures and model/data plots.

Calculating the PD mean OGCM $\delta^{18}\text{O}_w$ by mass-weighted averaging *all* grid boxes provides an opportunity to estimate both the “locational bias” from the limited observations and the numerical error involved in the means. Table 6.2 shows these estimates. The magnitude of the locational bias is remarkably small, as is that of the

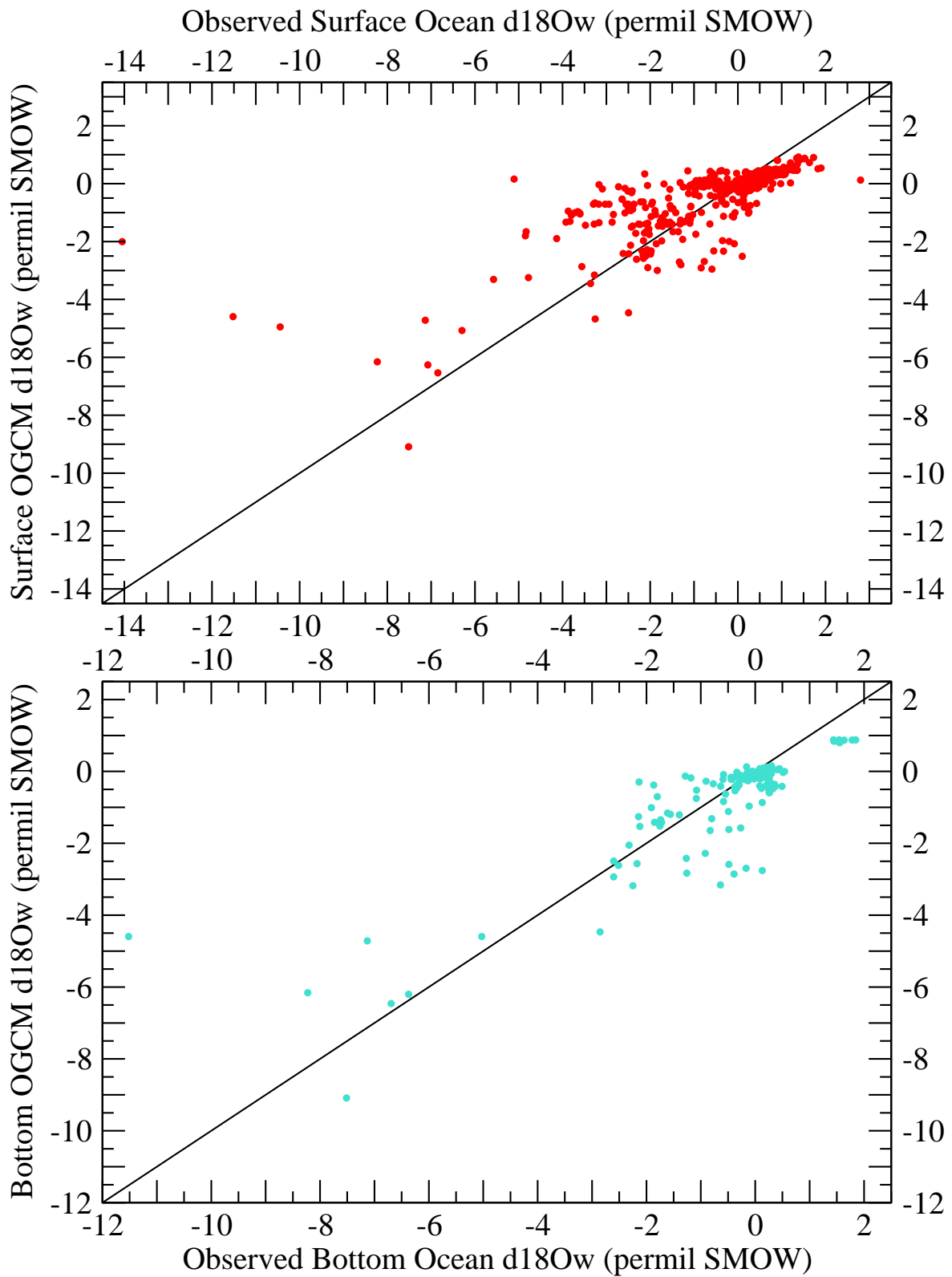


Figure 6.17: top) PD annual surface OGCM $\delta^{18}\text{O}_w$ versus observed surface ocean $\delta^{18}\text{O}_w$ (‰ SMOW); and bottom) PD annual bottom OGCM $\delta^{18}\text{O}_w$ versus observed bottom ocean $\delta^{18}\text{O}_w$ (‰ SMOW).

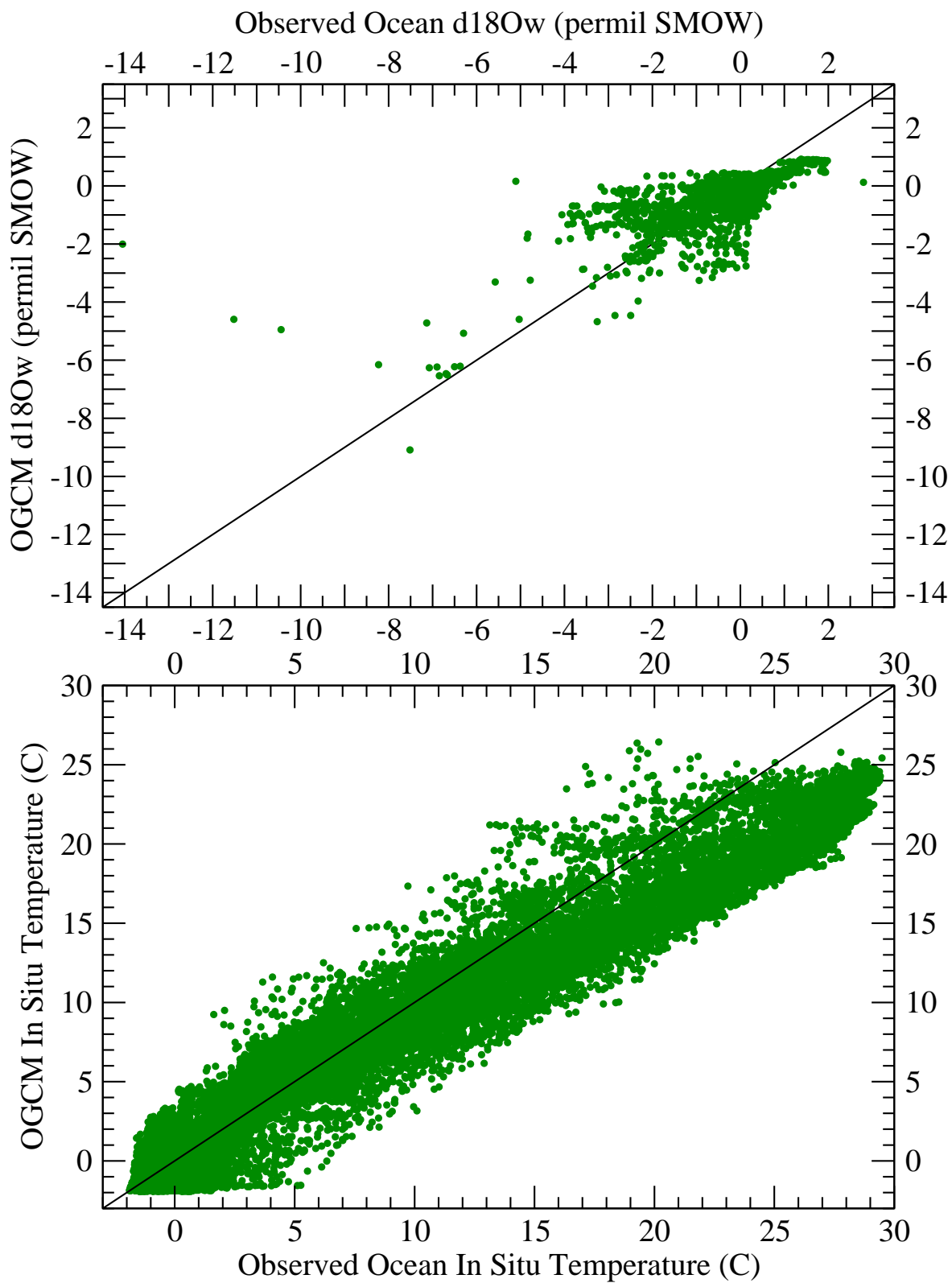


Figure 6.18: top) PD annual OGCM $\delta^{18}\text{O}_w$ versus observed ocean $\delta^{18}\text{O}_w$ (‰ SMOW); and bottom) PD annual OGCM in situ temperature versus observed ocean in situ temperature (C).

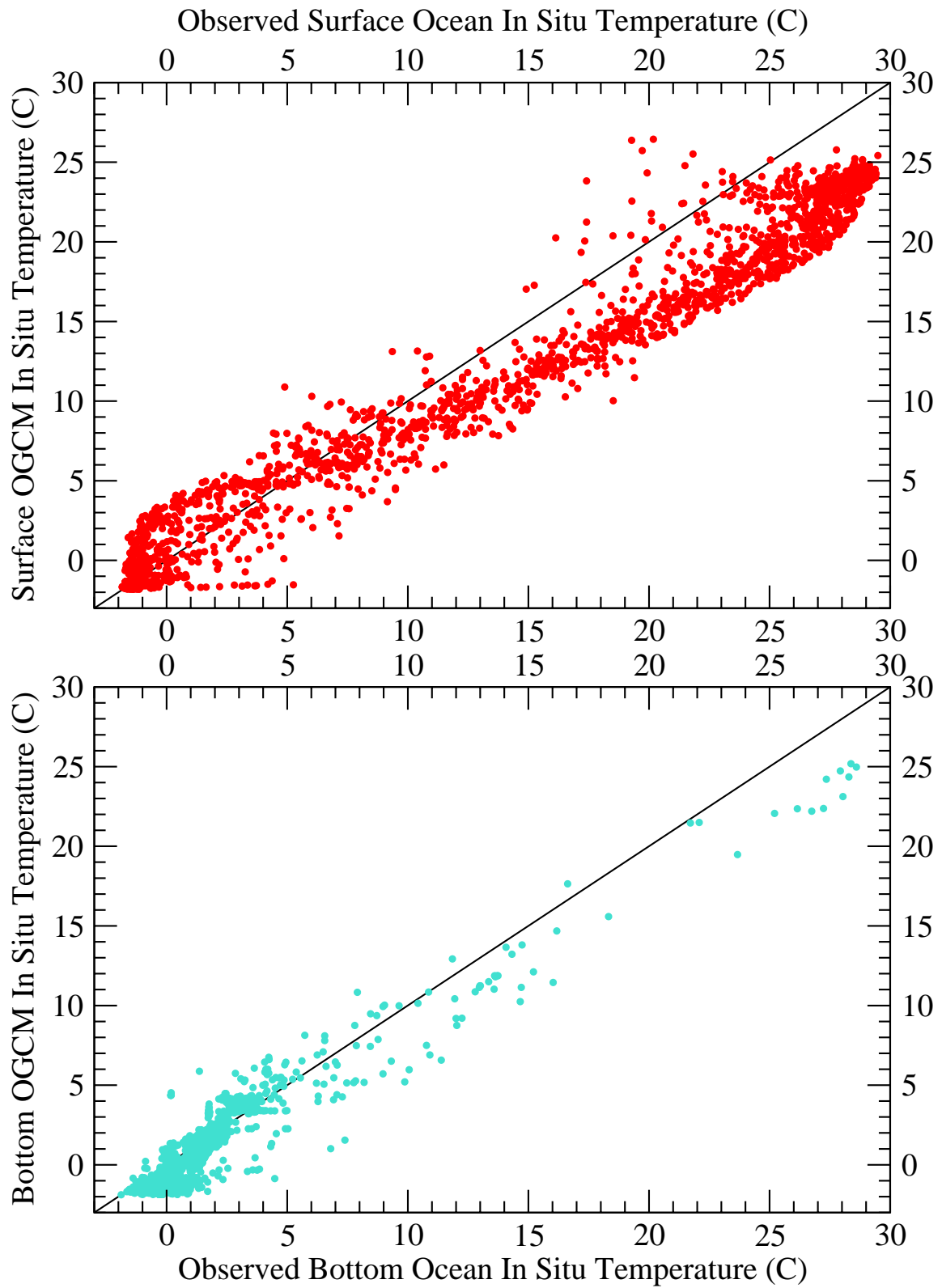


Figure 6.19: top) PD annual surface OGCM in situ temperature versus observed surface ocean in situ temperature (C); and bottom) PD annual bottom OGCM in situ temperature versus observed bottom ocean in situ temperature (C).

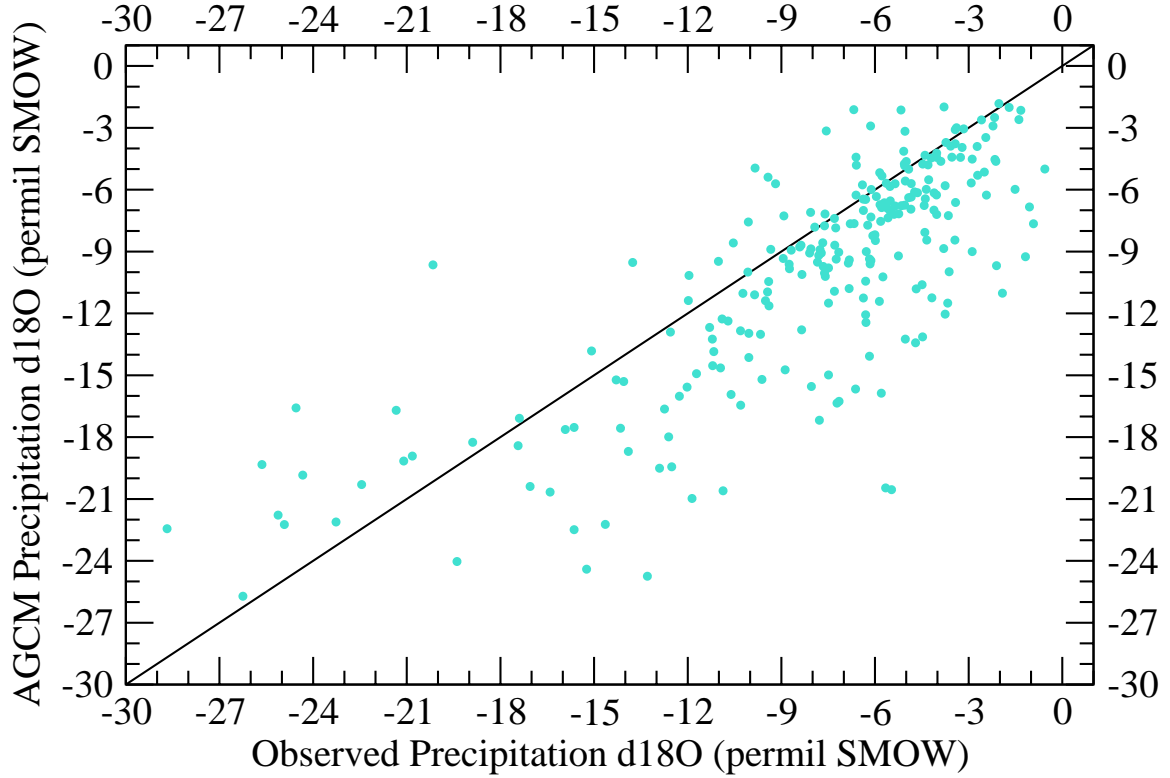


Figure 6.20: PD annual AGCM precipitation $\delta^{18}\text{O}$ versus observed precipitation $\delta^{18}\text{O}$ (‰ SMOW).

numerical error, especially considering the long duration of the run and the mass-weighted averaging.

For the purpose of planktonic and benthic foraminifera $\delta^{18}\text{O}_c$, Tables 6.3 and 6.4 are tables similar to Table 6.1 but for surface and bottom ocean water $\delta^{18}\text{O}$, respectively. In Table 6.3, the magnitude of the PD mean surface ocean $\delta^{18}\text{O}_w$ bias of the OGCM compared to observations is quite small. In Table 6.4, that for the bottom is just a tenth permil so still not of much concern. Thus there can be confidence in the ability of the CGCM to predict ocean water $\delta^{18}\text{O}$ at these levels individually. Note too that these biases are small enough to not have been obvious in the corresponding map comparison figures and model/data plots. Finally, to estimate at surface and bottom the described locational bias, in the respective tables (top line) are the means from averaging all grid boxes at these levels. These are quite close to the respective means from averaging grid boxes where there are observations (differences not explicitly shown).

$$\begin{aligned} &\text{PD annual mean OGCM } \delta^{18}\text{O}_w \text{ from mass-weighted} \\ &\text{averaging grid boxes where observations, } {}^P\delta_w^M = -0.025 \end{aligned}$$

$$\begin{aligned} &\text{PD mean ocean } \delta^{18}\text{O}_w \text{ from mass-weighted} \\ &\text{averaging observations (by grid box), } {}^P\delta_w^R = 0.072 \end{aligned}$$

$$\begin{aligned} &\Rightarrow \text{PD mass-weighted mean ocean } \delta^{18}\text{O}_w \text{ bias} \\ &\text{of OGCM compared to observations, } {}^P\delta_w^M - {}^P\delta_w^R = -0.097 \end{aligned}$$

Table 6.1: Calculation of PD mass-weighted mean ocean $\delta^{18}\text{O}_w$ bias (‰ SMOW) of OGCM compared to observations.

$$\begin{aligned} &\text{PD annual mean OGCM } \delta^{18}\text{O}_w \text{ from mass-weighted} \\ &\text{averaging all grid boxes, } ({}^P\bar{\delta}_w^M)_{\text{final}} = -0.020 \end{aligned}$$

$$\begin{aligned} &\text{PD mean OGCM } \delta^{18}\text{O}_w \text{ from mass-weighted} \\ &\text{averaging grid boxes where observations, } {}^P\delta_w^M = -0.025 \\ &\Rightarrow \text{Locational bias, } ({}^P\bar{\delta}_w^M)_{\text{final}} - {}^P\delta_w^M = 0.005 \end{aligned}$$

$$\begin{aligned} &\text{Initially set PD mass-weighted mean OGCM } \delta^{18}\text{O}_w, {}^P\bar{\delta}_w^M = 0.000 \\ &\Rightarrow \text{Numerical error, } ({}^P\bar{\delta}_w^M)_{\text{final}} - {}^P\bar{\delta}_w^M = -0.020 \end{aligned}$$

Table 6.2: Estimate of locational bias and numerical error using PD mean OGCM $\delta^{18}\text{O}_w$ from mass-weighted averaging all grid boxes.

$$\begin{aligned} &\text{PD annual mean surface OGCM } \delta^{18}\text{O}_w \text{ from mass-weighted} \\ &\text{averaging all surface grid boxes} = 0.069 \end{aligned}$$

$$\begin{aligned} &\text{PD mean surface OGCM } \delta^{18}\text{O}_w \text{ from mass-weighted} \\ &\text{averaging surface grid boxes where observations, } {}^P\delta_w^M = -0.056 \end{aligned}$$

$$\begin{aligned} &\text{PD mean surface ocean } \delta^{18}\text{O}_w \text{ from mass-weighted} \\ &\text{averaging surface observations (by grid box), } {}^P\delta_w^R = -0.028 \end{aligned}$$

$$\begin{aligned} &\Rightarrow \text{PD mass-weighted mean surface ocean } \delta^{18}\text{O}_w \text{ bias} \\ &\text{of OGCM compared to observations, } {}^P\delta_w^M - {}^P\delta_w^R = -0.028 \end{aligned}$$

Table 6.3: Calculation of PD mass-weighted mean surface ocean $\delta^{18}\text{O}_w$ bias (‰ SMOW) of OGCM compared to observations.

$$\begin{array}{l} \text{PD annual mean bottom OGCM } \delta^{18}\text{O}_w \text{ from mass-weighted} \\ \text{averaging all bottom grid boxes} \end{array} = -0.087$$

$$\begin{array}{l} \text{PD mean bottom OGCM } \delta^{18}\text{O}_w \text{ from mass-weighted} \\ \text{averaging bottom grid boxes where observations, } {}^P\delta_w^M \end{array} = -0.059$$

$$\begin{array}{l} \text{PD mean bottom ocean } \delta^{18}\text{O}_w \text{ from mass-weighted} \\ \text{averaging bottom observations (by grid box), } {}^P\delta_w^R \end{array} = 0.044$$

$$\begin{array}{l} \Rightarrow \text{PD mass-weighted mean bottom ocean } \delta^{18}\text{O}_w \text{ bias} \\ \text{of OGCM compared to observations, } {}^P\delta_w^M - {}^P\delta_w^R \end{array} = -0.103$$

Table 6.4: Calculation of PD mass-weighted mean bottom ocean $\delta^{18}\text{O}_w$ bias (‰ SMOW) of OGCM compared to observations.

Again for the purpose of planktonic and benthic foraminifera $\delta^{18}\text{O}_c$, Tables 6.5 and 6.6 are the similar tables for surface and bottom ocean in situ temperature, respectively. In Table 6.5, the magnitude of the PD mean surface ocean in situ temperature bias of the OGCM compared to observations is quite large. This surface OGCM low temperature bias was obvious in the corresponding model/data plot and map comparison figure, where it was noted to be from around the subtropical gyres. It would cause OGCM/foraminifera model $\delta^{18}\text{O}_c$ of planktonic foraminifera there to be significantly too high (several tenths of a permil), depending on the surface OGCM $\delta^{18}\text{O}_w$ bias in the corresponding grid boxes. It is hoped that the LGM – PD differencing will remove this inherent bias. In Table 6.6, the magnitude of the PD mean bottom ocean in situ temperature bias of the OGCM compared to observations is approaching a level of concern — it would cause just over a 0.1‰ error in the OGCM/foraminifera model $\delta^{18}\text{O}_c$ of benthic foraminifera (see Section 2.2.1), depending on the bottom OGCM $\delta^{18}\text{O}_w$ bias in the corresponding grid boxes. This bottom OGCM low temperature bias was still small enough not to be obvious in the corresponding map comparison figure and model/data plot. In Table 6.7 the magnitude of the PD mean ocean in situ temperature bias of the OGCM over all levels compared to observations is small. Finally, to estimate at surface, bottom and entire ocean the described locational bias, in the respective tables (top line) are the means from averaging all grid boxes at these levels. At the indicated precision, these are identical to the respective means from averaging grid boxes where there are observations, due to the completeness of Levitus

$$\begin{array}{l} \text{PD annual mean surface OGCM in situ temperature from} \\ \text{mass-weighted averaging all surface grid boxes} \end{array} = 14.98$$

$$\begin{array}{l} \text{PD annual mean surface OGCM in situ temperature from} \\ \text{mass-weighted averaging surface grid boxes where observations, } {}^PT_w^M \end{array} = 14.98$$

$$\begin{array}{l} \text{PD mean surface ocean in situ temperature from mass-weighted} \\ \text{averaging surface observations (by grid box), } {}^PT_w^R \end{array} = 18.16$$

$$\Rightarrow \text{PD mass-weighted mean surface ocean in situ temperature bias} \\ \text{of OGCM compared to observations, } {}^PT_w^M - {}^PT_w^R = -3.18$$

Table 6.5: Calculation of PD mass-weighted mean surface ocean in situ temperature bias (C) of OGCM compared to observations.

$$\begin{array}{l} \text{PD annual mean bottom OGCM in situ temperature from} \\ \text{mass-weighted averaging all bottom grid boxes} \end{array} = 1.35$$

$$\begin{array}{l} \text{PD annual mean bottom OGCM in situ temperature from} \\ \text{mass-weighted averaging bottom grid boxes where observations, } {}^PT_w^M \end{array} = 1.35$$

$$\begin{array}{l} \text{PD mean bottom ocean in situ temperature from mass-weighted} \\ \text{averaging bottom observations (by grid box), } {}^PT_w^R \end{array} = 1.75$$

$$\Rightarrow \text{PD mass-weighted mean bottom ocean in situ temperature bias} \\ \text{of OGCM compared to observations, } {}^PT_w^M - {}^PT_w^R = -0.40$$

Table 6.6: Calculation of PD mass-weighted mean bottom ocean in situ temperature bias (C) of OGCM compared to observations.

1998.

Finally for the means, Table 6.8 is the similar table for precipitation $\delta^{18}\text{O}$. The magnitude of the mean precipitation $\delta^{18}\text{O}$ bias of the AGCM compared to observations is significant. This AGCM low $\delta^{18}\text{O}$ bias was noted in the corresponding map comparison figures and model/data plots. It is hoped that the LGM – PD differencing will remove this inherent bias. Note that the mass-weighted averaging for the precipitation $\delta^{18}\text{O}$ observations was done with the described precipitation rate observations of Huffman and Bolvin 2003 and not with the AGCM precipitation rates, as for the AGCM precipitation $\delta^{18}\text{O}$ and as might be expected from how mass-weighted averaging was done for ocean water $\delta^{18}\text{O}$. The difference in the means using observed

$$\begin{array}{l} \text{PD annual mean OGCM in situ temperature from} \\ \text{mass-weighted averaging all grid boxes, } {}^P\bar{T}_w^M = 3.99 \end{array}$$

$$\begin{array}{l} \text{PD annual mean OGCM in situ temperature from} \\ \text{mass-weighted averaging grid boxes where observations, } {}^P T_w^M = 3.99 \end{array}$$

$$\begin{array}{l} \text{PD mean ocean in situ temperature from mass-weighted} \\ \text{averaging observations (by grid box), } {}^P T_w^R = 4.07 \end{array}$$

$$\begin{array}{l} \Rightarrow \text{PD mass-weighted mean ocean in situ temperature bias} \\ \text{of OGCM compared to observations, } {}^P T_w^M - {}^P T_w^R = -0.08 \end{array}$$

Table 6.7: Calculation of PD mass-weighted mean ocean in situ temperature bias (C) of OGCM compared to observations.

$$\begin{array}{l} \text{PD annual mean AGCM precipitation } \delta^{18}\text{O from mass-weighted} \\ \text{averaging all surface AGCM grid boxes} = -8.45 \end{array}$$

$$\begin{array}{l} \text{PD annual mean AGCM precipitation } \delta^{18}\text{O from mass-weighted} \\ \text{averaging surface AGCM grid boxes where observations, } {}^P \delta_i^M = -9.31 \end{array}$$

$$\begin{array}{l} \text{PD mean precipitation } \delta^{18}\text{O from mass-weighted} \\ \text{averaging observations (by grid box), } {}^P \delta_i^R = -6.90 \end{array}$$

$$\begin{array}{l} \Rightarrow \text{PD mass-weighted mean precipitation } \delta^{18}\text{O bias} \\ \text{of AGCM compared to observations, } {}^P \delta_i^M - {}^P \delta_i^R = -2.41 \end{array}$$

Table 6.8: PD mass-weighted mean precipitation $\delta^{18}\text{O}$ bias (‰ SMOW) of AGCM compared to observations.

versus AGCM precipitation rates is very small though (0.04‰). Finally, to estimate the described locational bias, in the table (top line) is the mean from averaging all grid boxes. This is quite close to the mean from averaging grid boxes where there are observations (difference not explicitly shown).

6.4 PD Simulation Compared to Ocean Sediment and Ice Coretop $\delta^{18}\text{O}$ Data

6.4.1 Maps

The PD simulation (CGCM and foraminifera model) is compared to coretop $\delta^{18}\text{O}$ data using map comparison figures of foraminifera $\delta^{18}\text{O}_c$ and precipitation $\delta^{18}\text{O}_i$ in order to spatially assess goodness of match, all as outlined in Section 6.2.2. Where there are cores, the biases noted in Section 6.3.1 are used to try to roughly, but quantitatively, explain any mismatch. To do this even roughly quantitatively, equations are necessary. For the one benthic foraminifera, *Cibicidoides wuellerstorfi*, at the sub-4°C in situ temperature most prevalent at the ocean bottom (which is stable year round), the equation relating $\delta^{18}\text{O}_c$ (‰ PDB) to ocean water $\delta^{18}\text{O}$ (‰ SMOW) and in situ temperature (C) is, from reducing that in Section 2.2.1:

$$\delta^{18}\text{O}_c = 3.315 - 0.280 * T_w + \delta^{18}\text{O}_w \quad (6.18)$$

As discussed in Section 2.2.1, planktonic foraminifera, unlike benthic foraminifera, form their CaCO_3 shells at changing near-surface depths, where ocean water $\delta^{18}\text{O}$ and temperatures vary with time (e.g., seasonally) and with depth. The foraminifera model accounts for this but the need for the model at all is because it can be quite complicated. However, because the surface OGCM level (1) is roughly representative of the near-surface levels (see Section 6.3.1), the effect of OGCM biases can still be roughly estimated using OGCM level 1 and the equation for planktonic foraminifera $\delta^{18}\text{O}_c$ in the foraminifera model, which is from reducing “KO97” in Schmidt and Mulitza 2002:

$$\delta^{18}\text{O}_c = 25.508 - 3.333 * \sqrt{43.704 + T_w} + \delta^{18}\text{O}_w \quad (6.19)$$

Both equations show the stated relationships that higher ocean water $\delta^{18}\text{O}$ and colder ocean water in situ temperature both imply higher foraminifera $\delta^{18}\text{O}_c$.

As to where the cores are, note that while often impossible, not having to make single CGCM grid box comparisons is desirable because given all the random real-world factors affecting $\delta^{18}\text{O}$ values from cores there are bound to occasionally be some that are erroneous, skewing a grid box’s $\delta^{18}\text{O}$ value even if averaged with those from

(usually few if any) other cores in the grid box (see Chapter 5). If a grid box is surrounded by several similarly-valued grid boxes from which it differs significantly, it can be more confidently ignored. Sparse cores are a problem and to lessen this for ocean sediment cores the $\delta^{18}\text{O}_c$ values of grid boxes that are considered land in the CGCM have not been masked out in the “b” CGCM grid box maps of the map comparison figures in this section, although they inherently end up masked out in the “c” maps. This masking was done however, for the ocean observations in the “b” CGCM grid box maps of the map comparison figures of Section 6.3.1 since the observations were not as sparse.

Figure 6.21 is the map comparison figure for PD $\delta^{18}\text{O}_c$ of benthic foraminifera *Cibicidoides wuellerstorfi*. Unfortunately, as Figure 6.21b shows, there are not many grid boxes with *C. wuellerstorfi* ocean sediment cores, making it difficult to see broad patterns and ignore incongruous grid boxes. Still, over most of the tropical bottom Atlantic where the cores are the OGCM has a $\delta^{18}\text{O}_w$ bias that is fairly constantly small and negative (see Figure 6.5c), whereas its temperature bias there varies from about -1 to $+2^\circ\text{C}$ (see Figure 6.6c). The pattern of the OGCM temperature bias is thus what should be seen in Figure 6.21c and, ignoring the occasional assumed-erroneous grid box, this does seem to be the case. Note in particular the good quantitative relationship (see Equation 6.18) between OGCM/foraminifera model $\delta^{18}\text{O}_c$ mismatch compared to core data and the bottom OGCM temperature and $\delta^{18}\text{O}_w$ biases at the north end of the South Mid-Atlantic Ridge and off of West Africa. On the Ridge and off of West Africa the temperature bias is about 1°C , with a $\delta^{18}\text{O}_w$ bias of about -0.1‰ , implying a $\delta^{18}\text{O}_c$ mismatch of about -0.4‰ , which is about what is seen. Around the top of the Ridge, the temperature bias is about -1°C , with a $\delta^{18}\text{O}_w$ bias of about -0.1‰ , implying a $\delta^{18}\text{O}_c$ mismatch of about 0.2‰ , which is about what is seen. Overall, for the benthic foraminifera *C. wuellerstorfi* it looks like the OGCM biases roughly explain much of the mismatch between the foraminifera model and the coretop $\delta^{18}\text{O}_c$ data, providing confidence in them.

Moving up to the planktonic foraminifera and looking first for broad patterns, note again that in the surface lower-latitude Atlantic the OGCM has a $\delta^{18}\text{O}_w$ bias that is fairly constantly small and negative (see Figure 6.10c), whereas there is a temperature bias there with a pronounced westward increase (see Figure 6.14c).

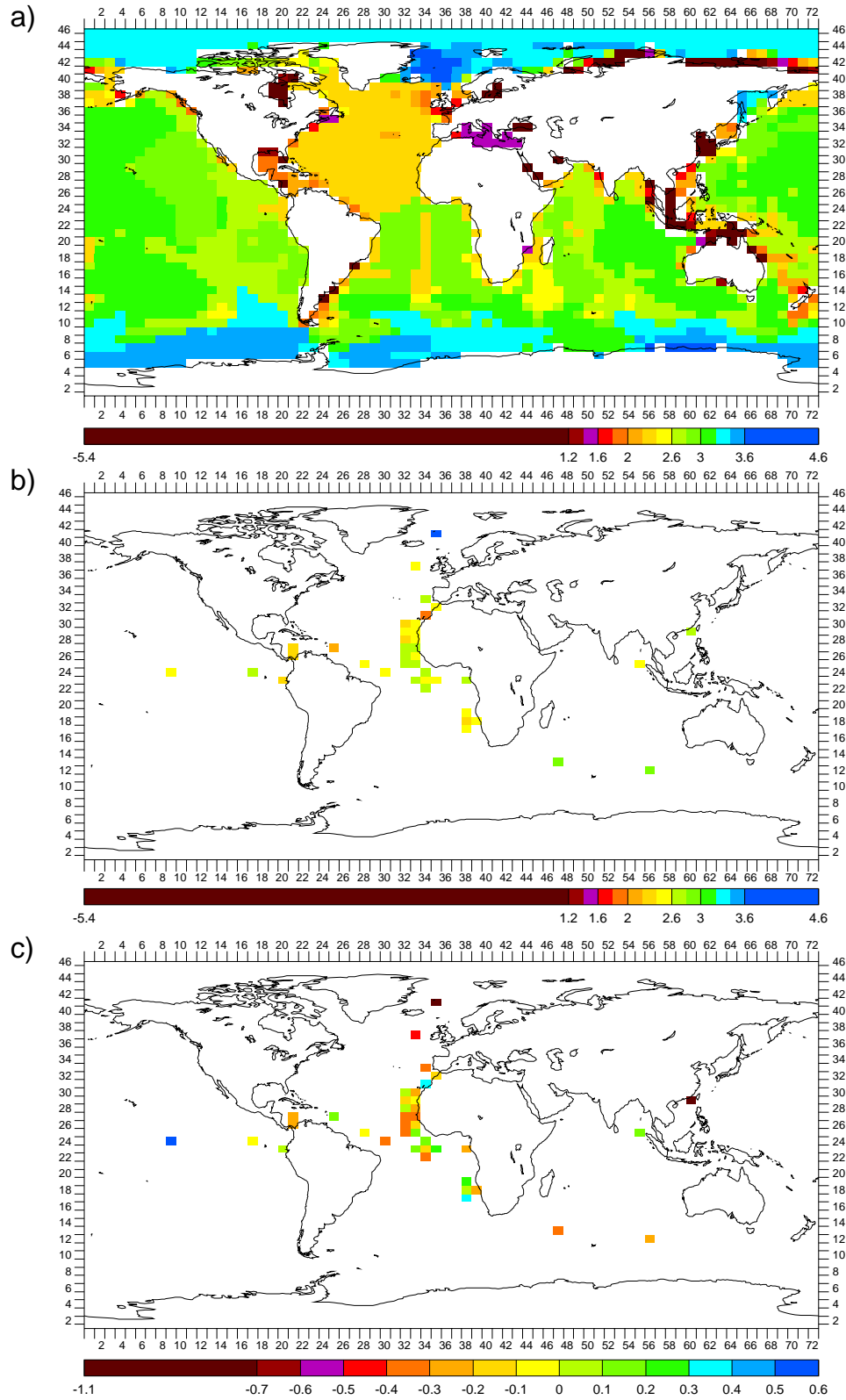


Figure 6.21: CGCM grid box maps of PD annual $\delta^{18}\text{O}_e$ (‰ PDB) of benthic foraminifera *C. wuellerstorfi* in: a) OGCM/foraminifera model; b) coretops; and c) OGCM/foraminifera model minus coretops

A westward increase in planktonic foraminifera $\delta^{18}\text{O}_c$ mismatch compared to core data should thus be seen there. For those planktonic foraminifera that occur in the lower-latitude Atlantic — *Globigerinoides sacculifer*, *Globigerinoides ruber* (white) and *Globigerinoides ruber* (pink) — and ignoring the occasional assumed-erroneous grid box, this pattern is indeed seen in Figures 6.22c, 6.23c and 6.24c, respectively. Note though, that for all three of the species there are ocean sediment cores with them poleward of where the OGCM/foraminifera model indicates the species would live. Differences in the spatial range of habitat of each foraminifera species as indicated by the OGCM/foraminifera model and as indicated by the ocean sediment cores is a simple but important comparison.

More quantitatively (see Equation 6.19), but still ignoring the occasional assumed-erroneous grid box, note in the surface Caribbean Sea, western equatorial Atlantic and eastern tropical South Atlantic, that the OGCM $\delta^{18}\text{O}_w$ biases are about -0.6, -0.7, and -0.8‰, respectively, and the OGCM temperature biases are about -8, -5, and -1°C, respectively. This implies OGCM/foraminifera model $\delta^{18}\text{O}_c$ mismatches compared to core data of about 1, 0.3, and -0.6‰, respectively, and looking at Figures 6.22c, 6.23c and 6.24c for *G. sacculifer*, *G. ruber* (white) and *G. ruber* (pink), respectively, this seems roughly to be the case. For *G. sacculifer* in the surface southern tropical Atlantic, the OGCM $\delta^{18}\text{O}_w$ and temperature biases are about -0.2‰ and 5°C, respectively, which implies an OGCM/foraminifera model $\delta^{18}\text{O}_c$ mismatch of about 0.8‰. Comparing to Figure 6.22c this seems to be significantly too high. For *G. sacculifer* and *G. ruber* (white) in the surface Indian, the OGCM $\delta^{18}\text{O}_w$ and temperature biases are about -0.4‰ and 4°C, respectively, which implies an OGCM/foraminifera model $\delta^{18}\text{O}_c$ mismatch of about 0.4‰. Comparing to Figures 6.22c and 6.23c this seems to be about right. For *G. ruber* (white) in the surface Mediterranean Sea, the OGCM $\delta^{18}\text{O}_w$ and temperature biases are about -0.6‰ and 2°C, respectively, which implies an OGCM/foraminifera model $\delta^{18}\text{O}_c$ mismatch of about -0.2‰. Comparing to Figure 6.23c this also seems to be about right.

Moving to the more-poleward planktonic foraminifera species, note first that in the foraminifera model *Globigerina bulloides* is treated as two species, a North Atlantic and a Southern Ocean species. The OGCM/foraminifera model results for these have been combined in Figure 6.25a, with the Southern Ocean species results south of grid

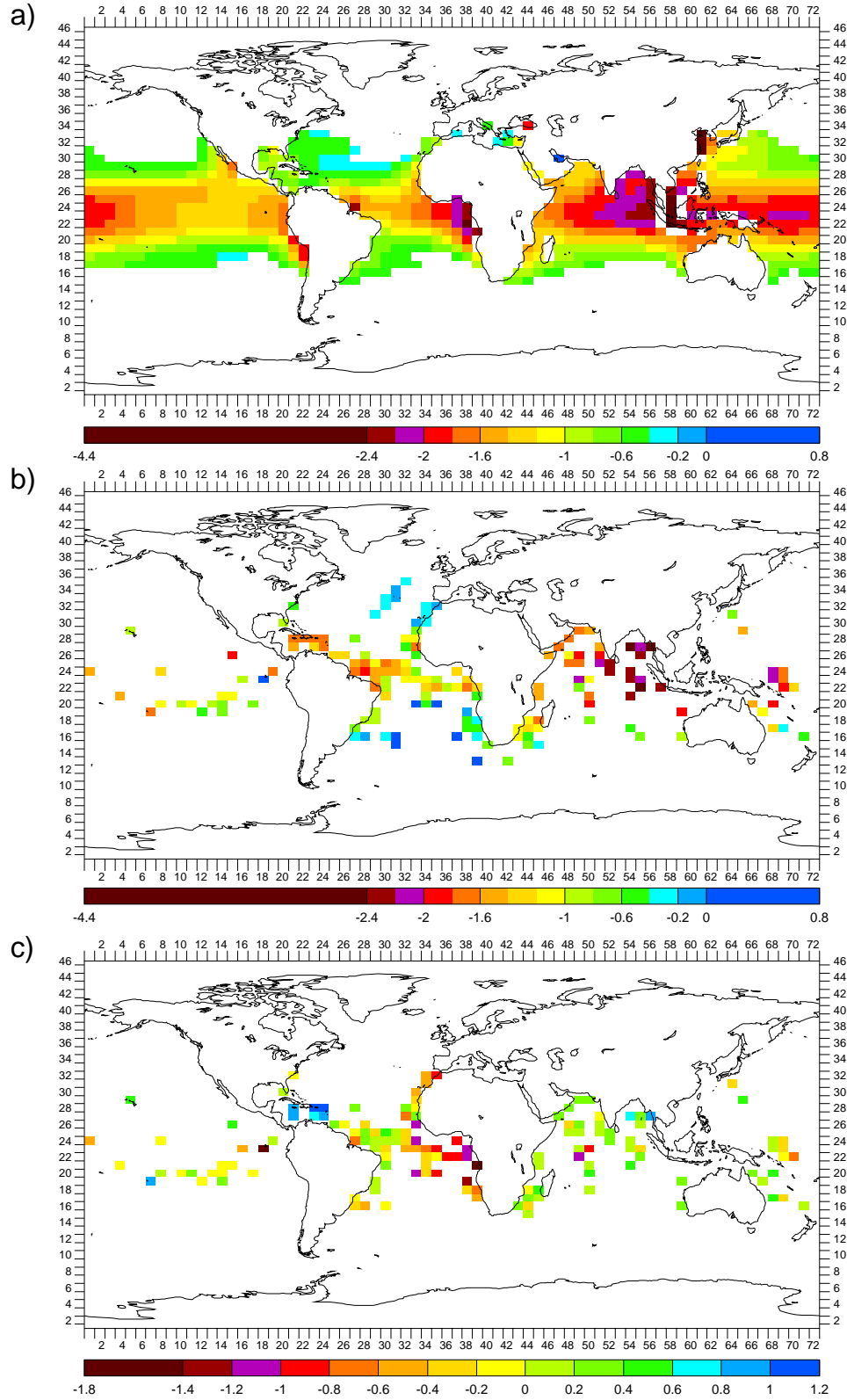


Figure 6.22: CGCM grid box maps of PD annual $\delta^{18}\text{O}_c$ (‰ PDB) of planktonic foraminifera *G. sacculifer* in: a) OGCM/foraminifera model; b) coretops; and c) OGCM/foraminifera model minus coretops

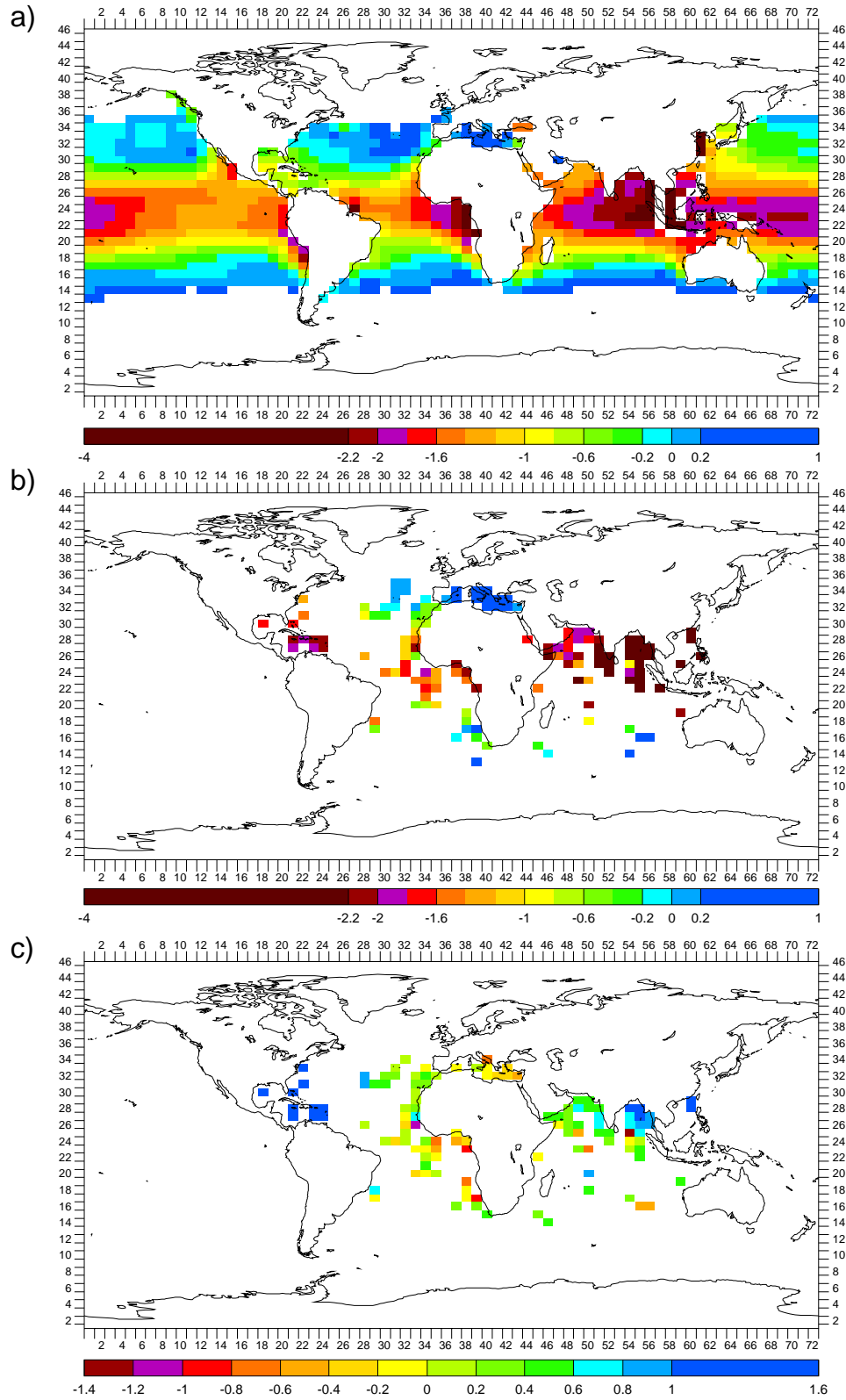


Figure 6.23: CGCM grid box maps of PD annual $\delta^{18}\text{O}_c$ (‰ PDB) of planktonic foraminifera *G. ruber* (white) in: a) OGCM/foraminifera model; b) coretops; and c) OGCM/foraminifera model minus coretops

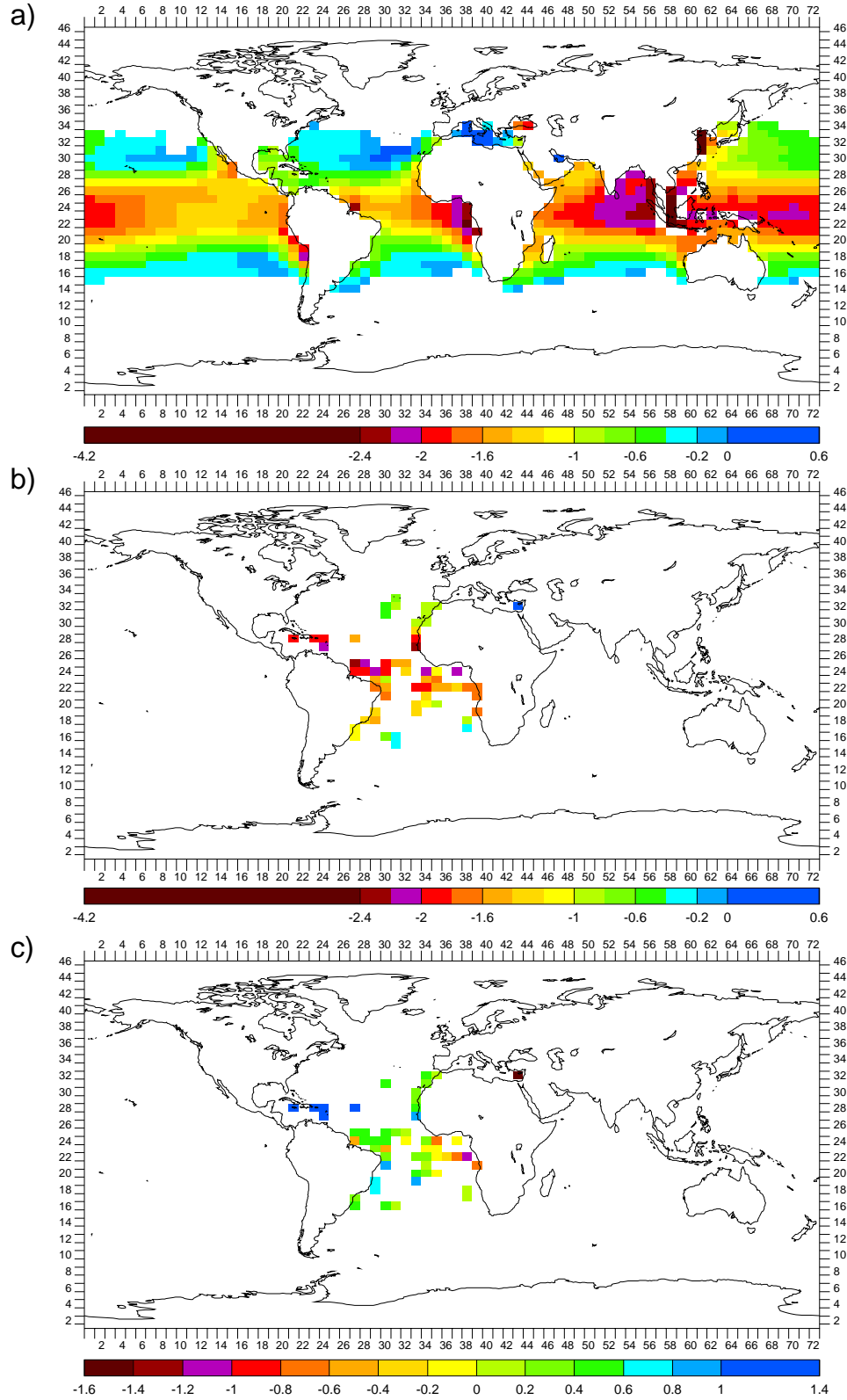


Figure 6.24: CGCM grid box maps of PD annual $\delta^{18}\text{O}_c$ (‰ PDB) of planktonic foraminifera *G. ruber* (pink) in: a) OGCM/foraminifera model; b) coretops; and c) OGCM/foraminifera model minus coretops

box lat# 23 (0–4°S) inclusive and the North Atlantic species results north of grid box lat# 23. Given the OGCM surface temperatures and the upper temperature limits of both species of *G. bulloides*, no habitat range truncation is required for either at the equator. For *G. bulloides*, *Neogloboquadrina pachyderma* (sinistral), and *Neogloboquadrina pachyderma* (dextral) then, in the surface Southern Ocean south of the Atlantic and Indian, the OGCM $\delta^{18}\text{O}_w$ and temperature biases are about 0.1‰ and 3°C, respectively, which implies an OGCM/foraminifera model $\delta^{18}\text{O}_c$ mismatch compared to core data of about -0.6‰. Comparing to Figures 6.25c, 6.26c, and 6.27c for *G. bulloides*, *N. pachyderma* (sinistral), and *N. pachyderma* (dextral), respectively, this seems to be about right. For *G. bulloides* in the surface north North Atlantic and Mediterranean Sea, the OGCM $\delta^{18}\text{O}_w$ biases are about -0.3 and -0.7‰ respectively, and the OGCM temperature biases are about -3 and -5°C, respectively, which imply OGCM/foraminifera model $\delta^{18}\text{O}_c$ mismatches of about 0.4 and 0.3‰. Comparing to Figure 6.25c this also seems to be about right. For *N. pachyderma* (sinistral) off of northeastern Greenland, the OGCM $\delta^{18}\text{O}_w$ and temperature biases are about 1‰ and 0°C, respectively, which implies an OGCM/foraminifera model $\delta^{18}\text{O}_c$ mismatch of about 1‰. Comparing to Figure 6.26c this seems to be about right as well. Note though, for all three of these more-poleward planktonic foraminifera species that there are ocean sediment cores with them equatorward of where the OGCM/foraminifera model indicates the species should occur.

Overall, for the planktonic foraminifera species it looks like the OGCM biases roughly explain many of the mismatches between the foraminifera model and the coretop $\delta^{18}\text{O}_c$ data, providing some confidence in them. The most notable exception is for *G. sacculifer* in the surface southern tropical Atlantic but the number and density of cores there is borderline for drawing conclusions anyway.

Figure 6.28 is the map comparison figure for PD $\delta^{18}\text{O}$ of precipitation H_2O . Unlike for foraminifera there is no model or equation for $\delta^{18}\text{O}_i$ of ice core H_2O — the $\delta^{18}\text{O}_i$ of ice core H_2O is assumed to be the same as that of the precipitation (i.e., snow) that formed the ice (Figure 6.28a is thus the same as Figure 6.15a). The described AGCM precipitation $\delta^{18}\text{O}$ biases of Figure 6.15c can thus be used directly to try to explain the differences between AGCM snow $\delta^{18}\text{O}_i$ and ice coretop H_2O $\delta^{18}\text{O}_i$ shown in Figure 6.28c, keeping in mind the warnings mentioned in describing the

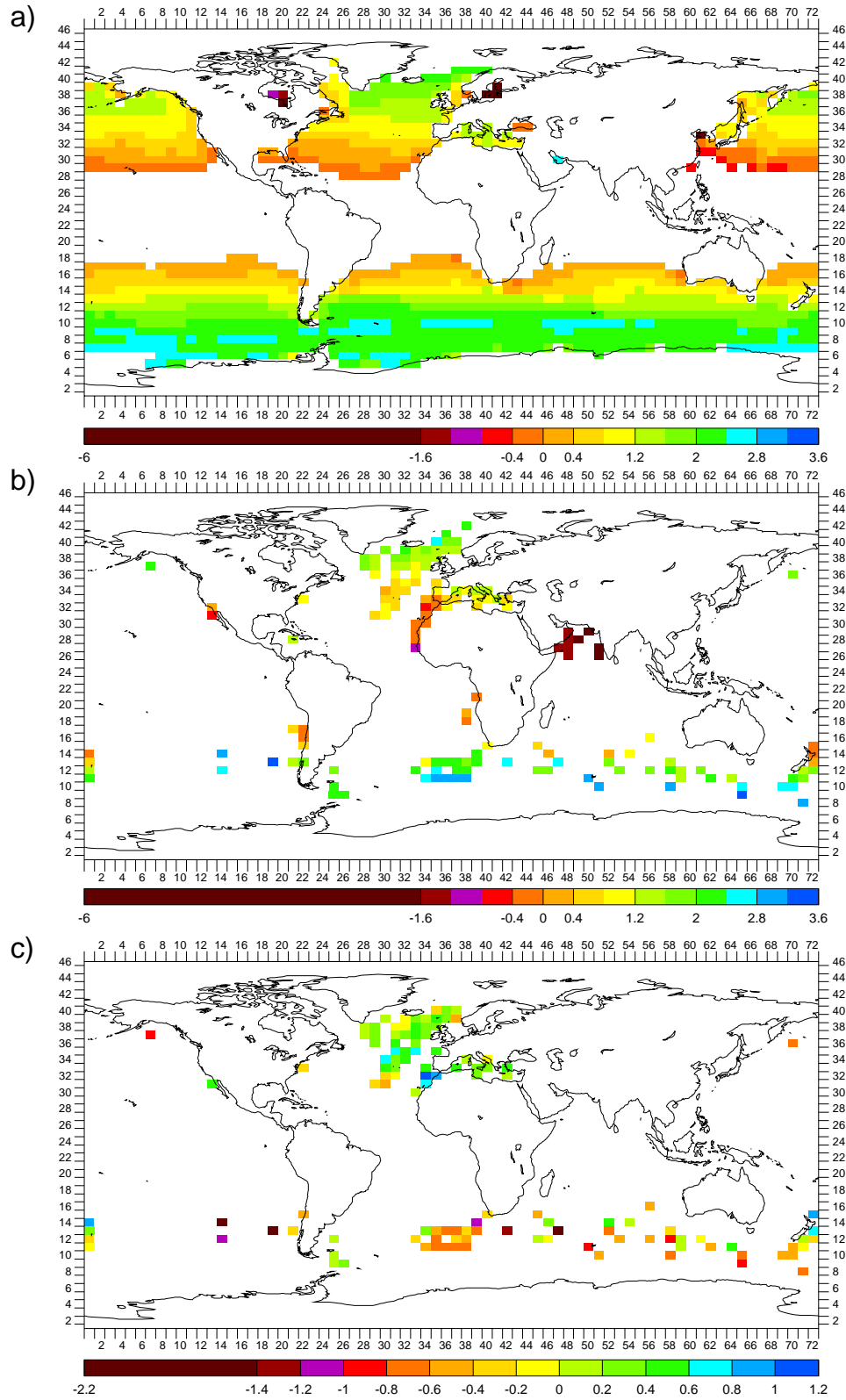


Figure 6.25: CGCM grid box maps of PD annual $\delta^{18}\text{O}_c$ (‰ PDB) of planktonic foraminifera *G. bulloides* in: a) OGCM/foraminifera model; b) coretops; and c) OGCM/foraminifera model minus coretops

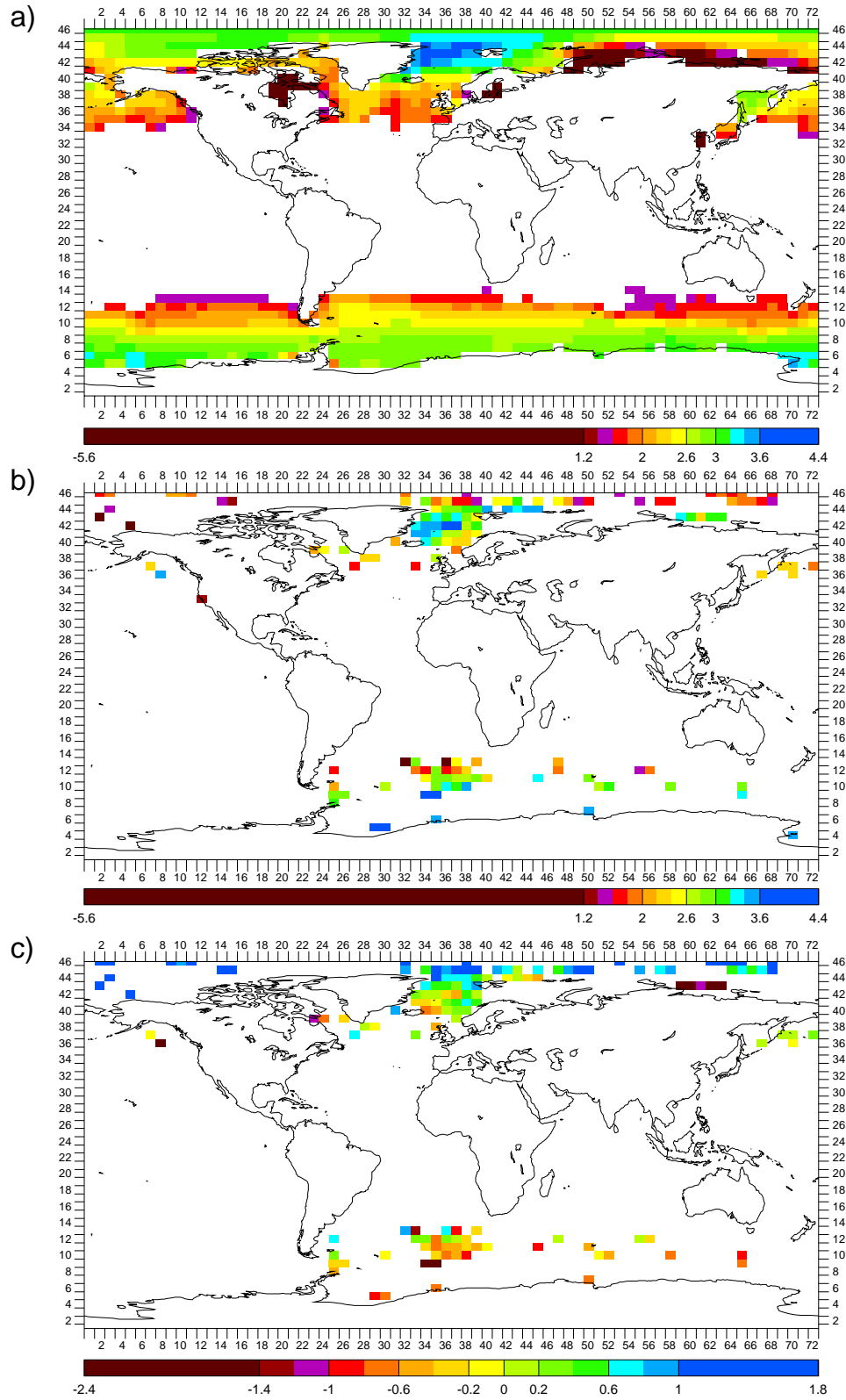


Figure 6.26: CGCM grid box maps of PD annual $\delta^{18}\text{O}_c$ (‰ PDB) of planktonic foraminifera *N. pachyderma* (sinistral) in: a) OGCM/foraminifera model; b) coretops; and c) OGCM/foraminifera model minus coretops

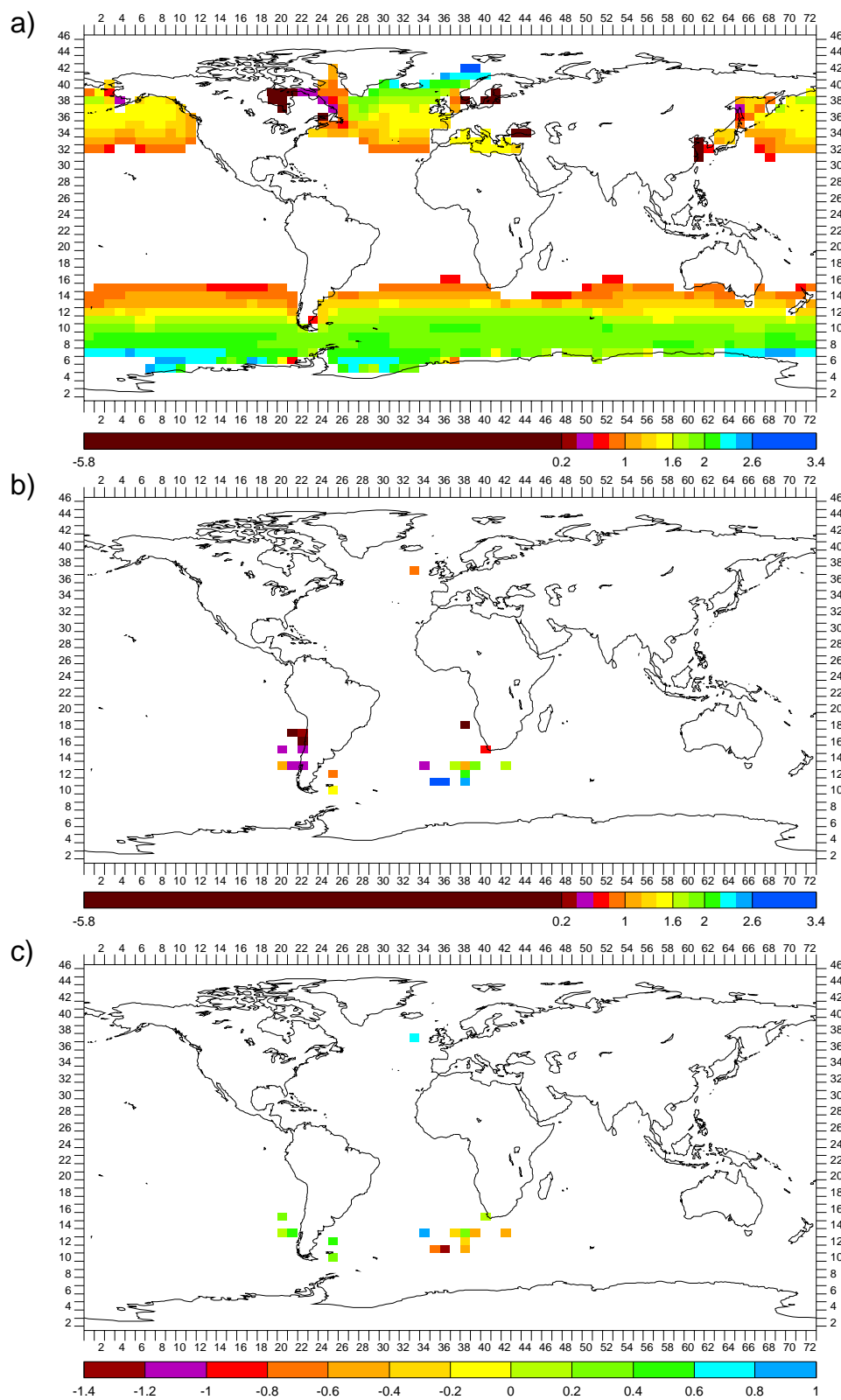


Figure 6.27: CGCM grid box maps of PD annual $\delta^{18}\text{O}_c$ (‰ PDB) of planktonic foraminifera *N. pachyderma* (dextral) in: a) OGCM/foraminifera model; b) coretops; and c) OGCM/foraminifera model minus coretops

AGCM precipitation $\delta^{18}\text{O}$ biases of Figure 6.15c (see Section 6.3.1). In Antarctica and northwest Greenland then, Figure 6.28c indicates that the AGCM snow $\delta^{18}\text{O}_i$ is too high by several permil compared to the ice coretop H_2O $\delta^{18}\text{O}_i$ and Figure 6.15c seems to imply a bias of AGCM precipitation $\delta^{18}\text{O}$ compared to observations that can account for this. In central Greenland, Figure 6.28c indicates that the AGCM snow $\delta^{18}\text{O}_i$ is too low by several permil compared to the ice coretop H_2O $\delta^{18}\text{O}_i$ and Figure 6.15c also seems to imply a bias of AGCM precipitation $\delta^{18}\text{O}$ compared to observations that can account for this. In Bolivia, Figure 6.28c indicates that the AGCM snow $\delta^{18}\text{O}_i$ is somewhat too high compared to the ice coretop H_2O $\delta^{18}\text{O}_i$ but Figure 6.15c seems to imply an AGCM bias of precipitation $\delta^{18}\text{O}$ somewhat low compared to observations. Overall though, it looks like the AGCM biases roughly explain most of the mismatch between AGCM snow $\delta^{18}\text{O}_i$ and ice coretop $\delta^{18}\text{O}_i$, providing some confidence in them.

6.4.2 Plots

Comparing the PD simulation (CGCM and foraminifera model) to coretop $\delta^{18}\text{O}$ data using model/data plots of foraminifera $\delta^{18}\text{O}_c$ and snow/ice $\delta^{18}\text{O}_i$ in order to assess goodness of match, all as outlined in Section 6.2.2, Figure 6.29 has plots of PD OGCM/foraminifera model $\delta^{18}\text{O}_c$ versus ocean sediment coretop foraminifera $\delta^{18}\text{O}_c$ and PD AGCM snow $\delta^{18}\text{O}_i$ versus ice coretop H_2O $\delta^{18}\text{O}_i$. While color-coded by species, the foraminifera $\delta^{18}\text{O}_c$ data is on one plot while the ice H_2O $\delta^{18}\text{O}_i$ data is on another (inset) because the foraminifera $\delta^{18}\text{O}_c$ data is of one nature and scale and the ice H_2O $\delta^{18}\text{O}_i$ data is of another. At the scales shown, the overall match seems good for the foraminifera but an AGCM high $\delta^{18}\text{O}_i$ bias is apparent for snow.

6.4.3 Means

The PD simulation (CGCM and foraminifera model) is compared to coretop $\delta^{18}\text{O}$ data using means of foraminifera $\delta^{18}\text{O}_c$ and snow/ice $\delta^{18}\text{O}_i$ in order to bottom-line assess goodness of match, all as outlined in Section 6.2.2. Table 6.9 is the calculation for the one benthic foraminifera species, *C. wuellerstorfi*. The magnitude of the mismatch is small and probably not misleading given the small bottom ocean $\delta^{18}\text{O}_w$ and in situ

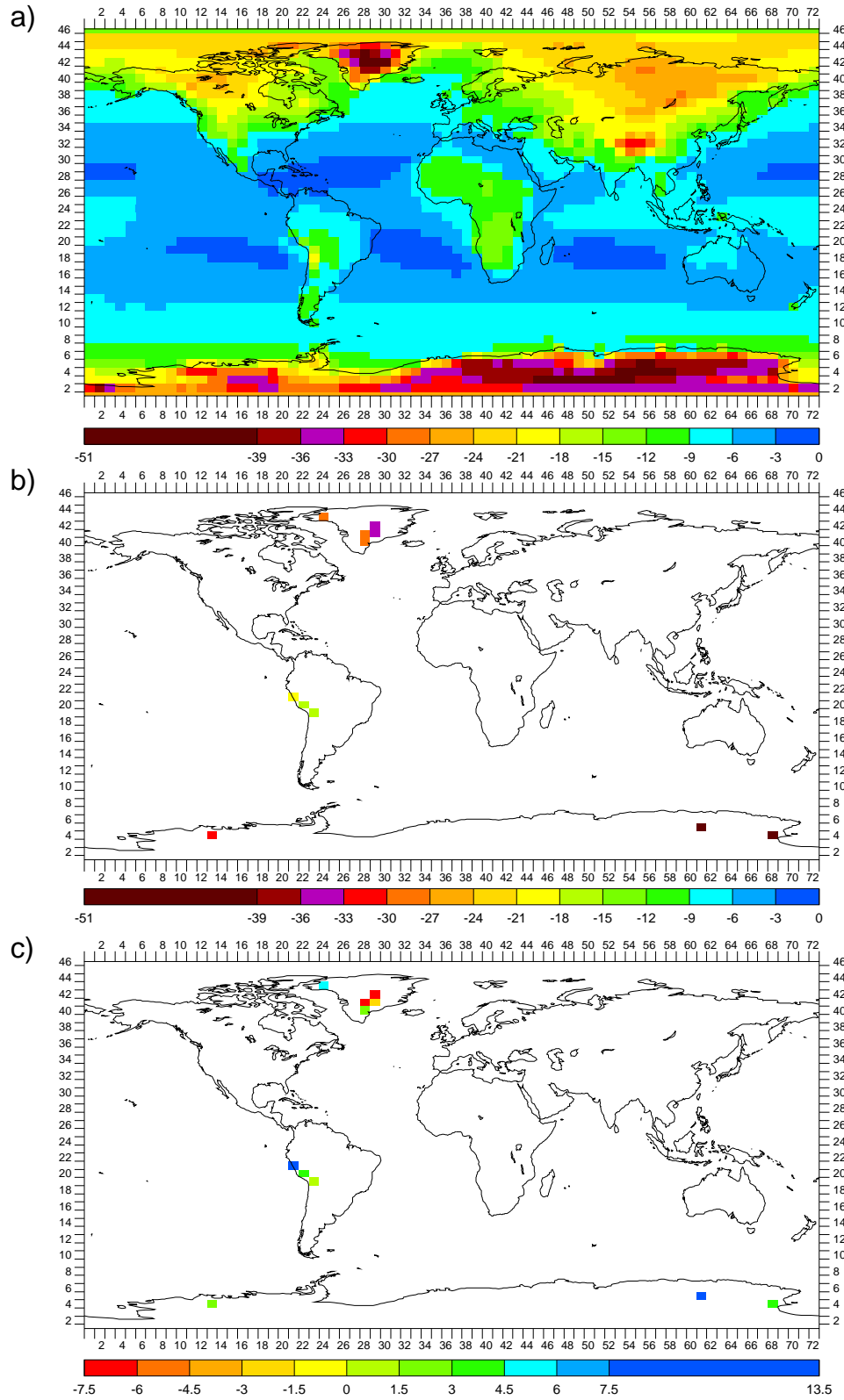


Figure 6.28: CGCM grid box maps of PD annual $\delta^{18}\text{O}$ (‰ SMOW) of: a) AGCM precipitation; b) ice core top H_2O ; and c) AGCM precipitation minus ice core top H_2O

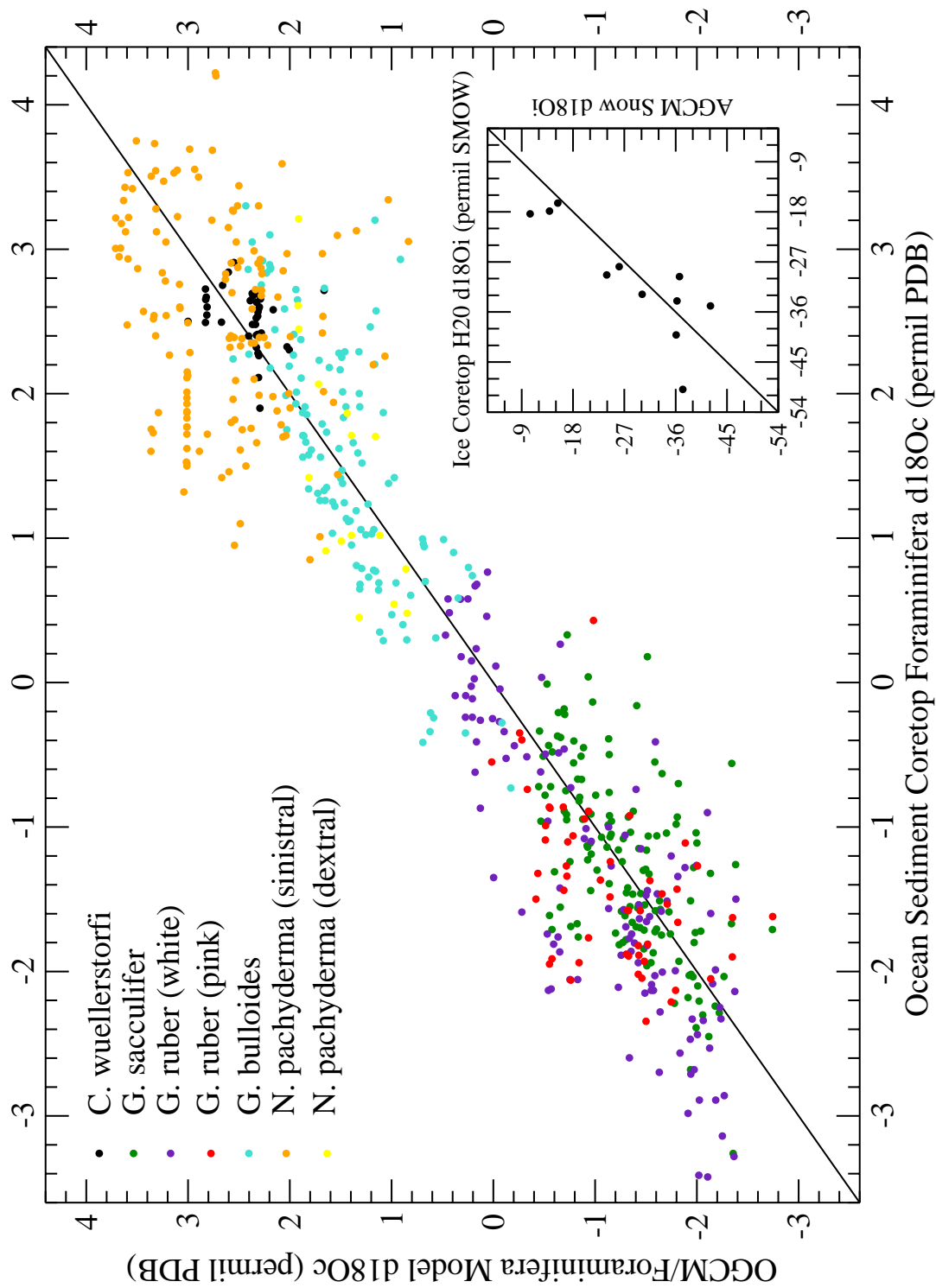


Figure 6.29: PD OGCM/foraminifera model annual $\delta^{18}\text{O}_c$ (‰ PDB) versus ocean sediment coretop foraminifera $\delta^{18}\text{O}_c$ (‰ PDB); and inset) PD AGCM annual snow $\delta^{18}\text{O}_i$ (‰ SMOW) versus ice coretop H_2O $\delta^{18}\text{O}_i$ (‰ SMOW).

$$\begin{array}{l} \text{PD annual mean OGCM/foraminifera model } C. \textit{ wuell. } \delta^{18}\text{O}_c \text{ from} \\ \text{mass-weighted averaging grid boxes where coretops, } {}^P\delta_c^M = 2.477 \end{array}$$

$$\begin{array}{l} \text{PD mean } C. \textit{ wuell. } \delta^{18}\text{O}_c \text{ from} \\ \text{mass-weighted averaging coretops (by grid box), } {}^P\delta_c^R = 2.544 \end{array}$$

$$\begin{array}{l} \Rightarrow \text{PD mass-weighted mean } C. \textit{ wuell. } \delta^{18}\text{O}_c \text{ mismatch} \\ \text{of OGCM/foraminifera model compared to coretops, } {}^P\delta_c^M - {}^P\delta_c^R = -0.067 \end{array}$$

Table 6.9: Calculation of PD mass-weighted mean *C. wuellerstorfi* $\delta^{18}\text{O}_c$ mismatch (‰ PDB) of OGCM/foraminifera model compared to ocean sediment coretops.

temperature biases.

Tables 6.10 to 6.15 are the calculations of mean $\delta^{18}\text{O}_c$ mismatch of the OGCM/foraminifera model compared to coretops for the six planktonic foraminifera species. First, to get an idea of the effect of the foraminifera model beyond Equation 6.19, henceforth referred to as “KO97” (see Schmidt and Mulitza 2002), the first line of each of these tables is the mean $\delta^{18}\text{O}_c$ using just KO97 with the surface OGCM $\delta^{18}\text{O}_w$ and T_w of OGCM grid boxes where there are coretops and where the OGCM/foraminifera model indicates that species would live. This is compared to the next line which is that of the full OGCM/foraminifera model. For all planktonic species except *N. pachyderma* (sinistral) the difference (not explicitly shown) is small (less than a tenth permil) and it’s not that large even for *N. pachyderma* (sinistral). This indicates that KO97 using the surface OGCM $\delta^{18}\text{O}_w$ and T_w is a good approximation of the foraminifera model.

The last lines in the tables are the mean $\delta^{18}\text{O}_c$ mismatch of the OGCM/foraminifera model compared to coretops. The magnitude of the mismatch is small for *G. sacculifer*, *G. bulloides* and *N. pachyderma* (dextral), borderline for *N. pachyderma* (sinistral), and significant for the two *G. ruber* species (although not to the point of being obvious in Figure 6.29). However, in Section 6.3.3 a large mean surface OGCM low temperature bias was noted, so this goodness of match is perhaps surprising for at least the first 3–4 listed planktonic species (even though different sets of grid boxes are involved and there may be a countering mean surface OGCM low $\delta^{18}\text{O}_w$ bias). In fact, it implies that there are biases in the foraminifera model that are lessening the mismatches, i.e., the model is “right for the wrong reason”.

PD annual mean OGCM/KO97 <i>G. sacc.</i> $\delta^{18}\text{O}_c$ from mass-weighted averaging grid boxes where coretops	=	-1.284
PD annual mean OGCM/foraminifera model <i>G. sacc.</i> $\delta^{18}\text{O}_c$ from mass-weighted averaging grid boxes where coretops, ${}^P\delta_c^M$	=	-1.340
PD mean <i>G. sacc.</i> $\delta^{18}\text{O}_c$ from mass-weighted averaging coretops (by grid box), ${}^P\delta_c^R$	=	-1.261
\Rightarrow PD mass-weighted mean <i>G. sacc.</i> $\delta^{18}\text{O}_c$ mismatch of OGCM/foraminifera model compared to coretops, ${}^P\delta_c^M - {}^P\delta_c^R$	=	-0.079

Table 6.10: Calculation of PD mass-weighted mean *G. sacculifer* $\delta^{18}\text{O}_c$ mismatch (‰ PDB) of OGCM/foraminifera model compared to ocean sediment coretops.

PD annual mean OGCM/KO97 <i>G. ruber</i> (w) $\delta^{18}\text{O}_c$ from mass-weighted averaging grid boxes where coretops	=	-1.012
PD annual mean OGCM/foraminifera model <i>G. ruber</i> (w) $\delta^{18}\text{O}_c$ from mass-weighted averaging grid boxes where coretops, ${}^P\delta_c^M$	=	-1.081
PD mean <i>G. ruber</i> (w) $\delta^{18}\text{O}_c$ from mass-weighted averaging coretops (by grid box), ${}^P\delta_c^R$	=	-1.361
\Rightarrow PD mass-weighted mean <i>G. ruber</i> (w) $\delta^{18}\text{O}_c$ mismatch of OGCM/foraminifera model compared to coretops, ${}^P\delta_c^M - {}^P\delta_c^R$	=	0.280

Table 6.11: Calculation of PD mass-weighted mean *G. ruber* (white) $\delta^{18}\text{O}_c$ mismatch (‰ PDB) of OGCM/foraminifera model compared to ocean sediment coretops.

PD annual mean OGCM/KO97 *G. ruber* (p) $\delta^{18}\text{O}_c$ from
mass-weighted averaging grid boxes where coretops = -1.099

PD annual mean OGCM/foraminifera model *G. ruber* (p) $\delta^{18}\text{O}_c$ from
mass-weighted averaging grid boxes where coretops, ${}^P\delta_c^M$ = -1.190

PD mean *G. ruber* (p) $\delta^{18}\text{O}_c$ from
mass-weighted averaging coretops (by grid box), ${}^P\delta_c^R$ = -1.446

\Rightarrow PD mass-weighted mean *G. ruber* (p) $\delta^{18}\text{O}_c$ mismatch
of OGCM/foraminifera model compared to coretops, ${}^P\delta_c^M - {}^P\delta_c^R$ = 0.256

Table 6.12: Calculation of PD mass-weighted mean *G. ruber* (pink) $\delta^{18}\text{O}_c$ mismatch (‰ PDB) of OGCM/foraminifera model compared to ocean sediment coretops.

PD annual mean OGCM/KO97 *G. bull.* $\delta^{18}\text{O}_c$ from
mass-weighted averaging grid boxes where coretops = 1.263

PD annual mean OGCM/foraminifera model *G. bull.* $\delta^{18}\text{O}_c$ from
mass-weighted averaging grid boxes where coretops, ${}^P\delta_c^M$ = 1.355

PD mean *G. bull.* $\delta^{18}\text{O}_c$ from
mass-weighted averaging coretops (by grid box), ${}^P\delta_c^R$ = 1.449

\Rightarrow PD mass-weighted mean *G. bull.* $\delta^{18}\text{O}_c$ mismatch
of OGCM/foraminifera model compared to coretops, ${}^P\delta_c^M - {}^P\delta_c^R$ = -0.094

Table 6.13: Calculation of PD mass-weighted mean *G. bulloides* $\delta^{18}\text{O}_c$ mismatch (‰ PDB) of OGCM/foraminifera model compared to ocean sediment coretops.

$$\begin{array}{l} \text{PD annual mean OGCM/KO97 } N. \text{ pachy. (s) } \delta^{18}\text{O}_c \text{ from} \\ \text{mass-weighted averaging grid boxes where coretops} \end{array} = 2.236$$

$$\begin{array}{l} \text{PD annual mean OGCM/foraminifera model } N. \text{ pachy. (s) } \delta^{18}\text{O}_c \text{ from} \\ \text{mass-weighted averaging grid boxes where coretops, } {}^P\delta_c^M \end{array} = 2.422$$

$$\begin{array}{l} \text{PD mean } N. \text{ pachy. (s) } \delta^{18}\text{O}_c \text{ from} \\ \text{mass-weighted averaging coretops (by grid box), } {}^P\delta_c^R \end{array} = 2.589$$

$$\begin{array}{l} \Rightarrow \text{PD mass-weighted mean } N. \text{ pachy. (s) } \delta^{18}\text{O}_c \text{ mismatch} \\ \text{of OGCM/foraminifera model compared to coretops, } {}^P\delta_c^M - {}^P\delta_c^R \end{array} = -0.167$$

Table 6.14: Calculation of PD mass-weighted mean *N. pachyderma* (sinistral) $\delta^{18}\text{O}_c$ mismatch (‰ PDB) of OGCM/foraminifera model compared to ocean sediment coretops.

$$\begin{array}{l} \text{PD annual mean OGCM/KO97 } N. \text{ pachy. (d) } \delta^{18}\text{O}_c \text{ from} \\ \text{mass-weighted averaging grid boxes where coretops} \end{array} = 1.420$$

$$\begin{array}{l} \text{PD annual mean OGCM/foraminifera model } N. \text{ pachy. (d) } \delta^{18}\text{O}_c \text{ from} \\ \text{mass-weighted averaging grid boxes where coretops, } {}^P\delta_c^M \end{array} = 1.400$$

$$\begin{array}{l} \text{PD mean } N. \text{ pachy. (d) } \delta^{18}\text{O}_c \text{ from} \\ \text{mass-weighted averaging coretops (by grid box), } {}^P\delta_c^R \end{array} = 1.412$$

$$\begin{array}{l} \Rightarrow \text{PD mass-weighted mean } N. \text{ pachy. (d) } \delta^{18}\text{O}_c \text{ mismatch} \\ \text{of OGCM/foraminifera model compared to coretops, } {}^P\delta_c^M - {}^P\delta_c^R \end{array} = -0.012$$

Table 6.15: Calculation of PD mass-weighted mean *N. pachyderma* (dextral) $\delta^{18}\text{O}_c$ mismatch (‰ PDB) of OGCM/foraminifera model compared to ocean sediment coretops.

For each of the six planktonic foraminifera species, Tables 6.16 to 6.21 analyze possible reduced mismatch due to foraminifera model bias. All calculations are with the set of OGCM grid boxes where there are surface ocean $\delta^{18}\text{O}_w$ observations and surface ocean in situ temperature observations and coretops for the species. For each species this will be a significantly smaller set (subset) than in the respective table of Tables 6.10 to 6.15. For reference, the OGCM and observed mean surface ocean $\delta^{18}\text{O}_w$ and in situ temperatures are given first in Tables 6.16 to 6.21, along with the resulting biases. Then using these in KO97 the resulting mean $\delta^{18}\text{O}_c$ from the OGCM and from observations are given, along with the resulting bias. Finally, the mean $\delta^{18}\text{O}_c$ from the full OGCM/foraminifera model and from the coretops are given, along with the resulting mismatch (note that due to the smaller set of OGCM grid boxes, these mismatches are different from the respective ones in Tables 6.10 to 6.15). For all but the two *G. ruber* species, the magnitude of the mean KO97 $\delta^{18}\text{O}_c$ bias of the OGCM compared to observations is significantly larger than that of the mean $\delta^{18}\text{O}_c$ mismatch of the OGCM/foraminifera model compared to coretops. As can be seen, this is largely due to the mean KO97 $\delta^{18}\text{O}_c$ from observations being so different from the mean $\delta^{18}\text{O}_c$ from coretops, since the mean KO97 $\delta^{18}\text{O}_c$ from the OGCM is so similar to the mean $\delta^{18}\text{O}_c$ from the full OGCM/foraminifera model. This is thus a shortcoming of the foraminifera model in using KO97 but it is hoped that the LGM – PD differencing will remove the resulting inherent biases.

Table 6.22 is the calculation of mean snow/ice $\delta^{18}\text{O}_i$ mismatch of the AGCM compared to coretops. The magnitude of the mismatch is significant (it's apparent in Figure 6.29) but is in the opposite sense from the significant mean precipitation $\delta^{18}\text{O}$ bias noted in Section 6.3.3. It is not definitely known what the problem is but is probably related to the significant surface OGCM low temperature bias. Note that for consistency with the means of the LGM (for which no observations are available) and LGM – PD the mass-weighted averaging was done with the PD AGCM precipitation rates and not with the precipitation rate observations of Huffman and Bolvin 2003 as in Section 6.3.3. However, this does not explain the mismatch since doing the averaging with the observations makes the mismatch worse.

$$\begin{aligned}
&\text{PD mass-weighted mean surface ocean } \delta^{18}\text{O}_w \text{ bias (}\text{‰}\text{ SMOW)} \\
&\quad \text{of OGCM compared to observations, } {}^P\delta_w^M - {}^P\delta_w^R \\
&\quad = 0.291 - 0.664 = -0.373
\end{aligned}$$

$$\begin{aligned}
&\text{PD mass-weighted mean surface ocean in situ temperature bias (C)} \\
&\quad \text{of OGCM compared to observations, } {}^PT_w^M - {}^PT_w^R \\
&\quad = 21.99 - 26.31 = -4.32
\end{aligned}$$

$$\begin{aligned}
&\text{PD mass-weighted mean KO97 } G. \text{ sacc. } \delta^{18}\text{O}_c \text{ bias} \\
&\quad \text{of OGCM compared to observations,} \\
&\quad -1.213 - -1.711 = 0.498
\end{aligned}$$

$$\begin{aligned}
&\text{PD mass-weighted mean } G. \text{ sacc. } \delta^{18}\text{O}_c \text{ mismatch} \\
&\quad \text{of OGCM/foraminifera model compared to coretops, } {}^P\delta_c^M - {}^P\delta_c^R \\
&\quad = -1.252 - -1.386 = 0.134
\end{aligned}$$

Table 6.16: Analysis of possible reduced model/data PD mass-weighted mean *G. sacculifer* $\delta^{18}\text{O}_c$ mismatch (‰ PDB) due to foraminifera model bias.

$$\begin{aligned}
&\text{PD mass-weighted mean surface ocean } \delta^{18}\text{O}_w \text{ bias (}\text{‰}\text{ SMOW)} \\
&\quad \text{of OGCM compared to observations, } {}^P\delta_w^M - {}^P\delta_w^R \\
&\quad = 0.318 - 0.747 = -0.429
\end{aligned}$$

$$\begin{aligned}
&\text{PD mass-weighted mean surface ocean in situ temperature bias (C)} \\
&\quad \text{of OGCM compared to observations, } {}^PT_w^M - {}^PT_w^R \\
&\quad = 19.96 - 24.49 = -4.53
\end{aligned}$$

$$\begin{aligned}
&\text{PD mass-weighted mean KO97 } G. \text{ ruber (w) } \delta^{18}\text{O}_c \text{ bias} \\
&\quad \text{of OGCM compared to observations,} \\
&\quad -0.755 - -1.258 = 0.503
\end{aligned}$$

$$\begin{aligned}
&\text{PD mass-weighted mean } G. \text{ ruber (w) } \delta^{18}\text{O}_c \text{ mismatch} \\
&\quad \text{of OGCM/foraminifera model compared to coretops, } {}^P\delta_c^M - {}^P\delta_c^R \\
&\quad = -0.877 - -1.278 = 0.401
\end{aligned}$$

Table 6.17: Analysis of possible reduced model/data PD mass-weighted mean *G. ruber* (white) $\delta^{18}\text{O}_c$ mismatch (‰ PDB) due to foraminifera model bias.

$$\begin{aligned}
&\text{PD mass-weighted mean surface ocean } \delta^{18}\text{O}_w \text{ bias (‰ SMOW)} \\
&\quad \text{of OGCM compared to observations, } {}^P\delta_w^M - {}^P\delta_w^R \\
&\quad \quad \quad = 0.395 - 0.972 = -0.577
\end{aligned}$$

$$\begin{aligned}
&\text{PD mass-weighted mean surface ocean in situ temperature bias (C)} \\
&\quad \text{of OGCM compared to observations, } {}^PT_w^M - {}^PT_w^R \\
&\quad \quad \quad = 20.22 - 24.75 = -4.53
\end{aligned}$$

$$\begin{aligned}
&\text{PD mass-weighted mean KO97 } G. \text{ ruber (p) } \delta^{18}\text{O}_c \text{ bias} \\
&\quad \text{of OGCM compared to observations,} \\
&\quad \quad \quad -0.741 - -1.088 = 0.347
\end{aligned}$$

$$\begin{aligned}
&\text{PD mass-weighted mean } G. \text{ ruber (p) } \delta^{18}\text{O}_c \text{ mismatch} \\
&\quad \text{of OGCM/foraminifera model compared to coretops, } {}^P\delta_c^M - {}^P\delta_c^R \\
&\quad \quad \quad = -0.912 - -1.472 = 0.560
\end{aligned}$$

Table 6.18: Analysis of possible reduced model/data PD mass-weighted mean *G. ruber* (pink) $\delta^{18}\text{O}_c$ mismatch (‰ PDB) due to foraminifera model bias.

$$\begin{aligned}
&\text{PD mass-weighted mean surface ocean } \delta^{18}\text{O}_w \text{ bias (‰ SMOW)} \\
&\quad \text{of OGCM compared to observations, } {}^P\delta_w^M - {}^P\delta_w^R \\
&\quad \quad \quad = 0.225 - 0.470 = -0.245
\end{aligned}$$

$$\begin{aligned}
&\text{PD mass-weighted mean surface ocean in situ temperature bias (C)} \\
&\quad \text{of OGCM compared to observations, } {}^PT_w^M - {}^PT_w^R \\
&\quad \quad \quad = 10.51 - 13.48 = -2.97
\end{aligned}$$

$$\begin{aligned}
&\text{PD mass-weighted mean KO97 } G. \text{ bull. } \delta^{18}\text{O}_c \text{ bias} \\
&\quad \text{of OGCM compared to observations,} \\
&\quad \quad \quad 1.211 - 0.807 = 0.404
\end{aligned}$$

$$\begin{aligned}
&\text{PD mass-weighted mean } G. \text{ bull. } \delta^{18}\text{O}_c \text{ mismatch} \\
&\quad \text{of OGCM/foraminifera model compared to coretops, } {}^P\delta_c^M - {}^P\delta_c^R \\
&\quad \quad \quad = 1.319 - 1.252 = 0.067
\end{aligned}$$

Table 6.19: Analysis of possible reduced model/data PD mass-weighted mean *G. bulloides* $\delta^{18}\text{O}_c$ mismatch (‰ PDB) due to foraminifera model bias.

$$\begin{aligned}
&\text{PD mass-weighted mean surface ocean } \delta^{18}\text{O}_w \text{ bias (‰ SMOW)} \\
&\text{of OGCM compared to observations, } {}^P\delta_w^M - {}^P\delta_w^R \\
&= -0.350 - -0.569 = 0.219
\end{aligned}$$

$$\begin{aligned}
&\text{PD mass-weighted mean surface ocean in situ temperature bias (C)} \\
&\text{of OGCM compared to observations, } {}^PT_w^M - {}^PT_w^R \\
&= 2.49 - 2.66 = -0.17
\end{aligned}$$

$$\begin{aligned}
&\text{PD mass-weighted mean KO97 } N. \text{ pachy. (s) } \delta^{18}\text{O}_c \text{ bias} \\
&\text{of OGCM compared to observations,} \\
&2.518 - 2.258 = 0.260
\end{aligned}$$

$$\begin{aligned}
&\text{PD mass-weighted mean } N. \text{ pachy. (s) } \delta^{18}\text{O}_c \text{ mismatch} \\
&\text{of OGCM/foraminifera model compared to coretops, } {}^P\delta_c^M - {}^P\delta_c^R \\
&= 2.613 - 2.678 = -0.065
\end{aligned}$$

Table 6.20: Analysis of possible reduced model/data PD mass-weighted mean *N. pachyderma* (sinistral) $\delta^{18}\text{O}_c$ mismatch (‰ PDB) due to foraminifera model bias.

$$\begin{aligned}
&\text{PD mass-weighted mean surface ocean } \delta^{18}\text{O}_w \text{ bias (‰ SMOW)} \\
&\text{of OGCM compared to observations, } {}^P\delta_w^M - {}^P\delta_w^R \\
&= 0.062 - 0.273 = -0.211
\end{aligned}$$

$$\begin{aligned}
&\text{PD mass-weighted mean surface ocean in situ temperature bias (C)} \\
&\text{of OGCM compared to observations, } {}^PT_w^M - {}^PT_w^R \\
&= 9.36 - 12.52 = -3.16
\end{aligned}$$

$$\begin{aligned}
&\text{PD mass-weighted mean KO97 } N. \text{ pachy. (d) } \delta^{18}\text{O}_c \text{ bias} \\
&\text{of OGCM compared to observations,} \\
&1.302 - 0.814 = 0.488
\end{aligned}$$

$$\begin{aligned}
&\text{PD mass-weighted mean } N. \text{ pachy. (d) } \delta^{18}\text{O}_c \text{ mismatch} \\
&\text{of OGCM/foraminifera model compared to coretops, } {}^P\delta_c^M - {}^P\delta_c^R \\
&= 1.369 - 1.008 = 0.361
\end{aligned}$$

Table 6.21: Analysis of possible reduced model/data PD mass-weighted mean *N. pachyderma* (dextral) $\delta^{18}\text{O}_c$ mismatch (‰ PDB) due to foraminifera model bias.

$$\begin{array}{l} \text{PD annual mean AGCM snow/ice } \delta^{18}\text{O}_i \text{ from} \\ \text{mass-weighted averaging grid boxes where coretops, } {}^P\delta_i^M = -16.07 \end{array}$$

$$\begin{array}{l} \text{PD mean snow/ice } \delta^{18}\text{O}_i \text{ from} \\ \text{mass-weighted averaging coretops (by grid box), } {}^P\delta_i^R = -20.17 \end{array}$$

$$\begin{array}{l} \Rightarrow \text{PD mass-weighted mean snow/ice } \delta^{18}\text{O}_i \text{ mismatch} \\ \text{of AGCM compared to coretops, } {}^P\delta_i^M - {}^P\delta_i^R = 4.10 \end{array}$$

Table 6.22: Calculation of PD mass-weighted mean snow/ice $\delta^{18}\text{O}_i$ (‰ SMOW) mismatch of AGCM compared to ice coretops.

6.5 LGM – PD of Simulations Compared to Ocean Sediment and Ice Core $\delta^{18}\text{O}$ Data

6.5.1 Means

The LGM – PD of simulations (CGCM and foraminifera model) is compared to core $\delta^{18}\text{O}$ data using means of foraminifera $\delta^{18}\text{O}_c$ and snow/ice $\delta^{18}\text{O}_i$ in order to calculate the real LGM mean ocean $\delta^{18}\text{O}_w$ and its difference from the LGM mean ocean $\delta^{18}\text{O}_w$ initially set in the OGCM, all as outlined in Section 6.2.2. The difference is necessary ahead to assess goodness of match using the $\delta^{18}\text{O}$ map comparison figures and $\delta^{18}\text{O}$ model/data plots for the LGM – PD and LGM, as well as using means for the LGM. The real LGM mean ocean $\delta^{18}\text{O}_w$ addresses a major question of the LGM.

Tables 6.23 to 6.29 do this calculation for the benthic foraminifera species, each of the planktonic foraminifera species, and snow/ice. Note that in each case the set of grid boxes for which this is done is smaller than that in the respective table for PD in Section 6.4.3. Each grid box had to have cores with the species at both the LGM and PD and there are fewer such grid boxes for the LGM. For the foraminifera, this requirement is in addition to having to have the OGCM/foraminifera model indicate that the species would live in the grid box. In fact, for *N. pachyderma* (dextral) there are no OGCM grid boxes that meet the requirements so that planktonic species is not done. The number of grid boxes used for each species will be apparent in the $\delta^{18}\text{O}$ map comparison figures and $\delta^{18}\text{O}$ model/data plots ahead, as it was in the previous sections, but for now this number is just listed first in each table. Note also that

$$\begin{array}{l} \text{Number of OGCM grid box values used (grid boxes having} \\ \text{cores with and inhabited by } C. \text{ wuell. at both LGM and PD)} \end{array} = 34$$

$$\begin{array}{l} \text{LGM mass-weighted mean } C. \text{ wuell. } \delta^{18}\text{O}_c \text{ mismatch} \\ \text{of OGCM/foraminifera model compared to cores, } {}^L\delta_c^M - {}^L\delta_c^R \\ = 4.256 - 4.085 \end{array} = 0.171$$

$$\begin{array}{l} \text{PD mass-weighted mean } C. \text{ wuell. } \delta^{18}\text{O}_c \text{ mismatch} \\ \text{of OGCM/foraminifera model compared to cores, } {}^P\delta_c^M - {}^P\delta_c^R \\ = 2.482 - 2.547 \end{array} = -0.065$$

$$\begin{array}{l} \Rightarrow \text{Real LGM mass-weighted mean ocean } \delta^{18}\text{O}_w \\ \text{from } C. \text{ wuell. } \delta^{18}\text{O}_c, {}^L\bar{\delta}_w^R \\ = {}^L\bar{\delta}_w^M - [({}^L\delta_c^M - {}^L\delta_c^R) - ({}^P\delta_c^M - {}^P\delta_c^R)] \\ = 1.25 - 0.236 \end{array} = 1.014$$

Table 6.23: Calculation of real LGM mass-weighted mean ocean $\delta^{18}\text{O}_w$ (‰ SMOW) from *C. wuellerstorfi* $\delta^{18}\text{O}_c$ (‰ PDB).

the mass weighting for the means was done with era-specific OGCM grid box water masses for foraminifera $\delta^{18}\text{O}_c$ and era-specific AGCM precipitation rates for snow/ice $\delta^{18}\text{O}_i$.

There are several reasonable ways to come up with a single value for the real LGM mean ocean $\delta^{18}\text{O}_w$ from the seven given in the tables. That from benthic foraminifera, particularly *C. wuellerstorfi*, has historically been given the most credibility due to benthic foraminifera being subject to fewer vagaries than planktonic foraminifera. In addition here, that from *C. wuellerstorfi* has by far the most grid box values going into it. To a tenth permil precision then, the real LGM mean ocean $\delta^{18}\text{O}_w$ is 1.0‰ SMOW. If the estimates from the planktonic foraminifera species are included, weighting each by the number of grid box values going into it or even weighting each equally, then to a tenth permil precision the real LGM mean ocean $\delta^{18}\text{O}_w$ is again 1.0‰ SMOW. Thus 1.0‰ SMOW is the best estimate for real LGM mean ocean $\delta^{18}\text{O}_w$ and the LGM mean ocean $\delta^{18}\text{O}_w$ initially set in the OGCM was 0.25‰ too high. Note that the real LGM mean ocean $\delta^{18}\text{O}_w$ estimate from snow/ice is wildly different from those from foraminifera and that the reason for this was warned about in Section 6.2.2. It is thus not used.

Number of OGCM grid box values used (grid boxes having
cores with and inhabited by *G. sacc.* at both LGM and PD) = 10

LGM mass-weighted mean *G. sacc.* $\delta^{18}\text{O}_c$ mismatch
of OGCM/foraminifera model compared to cores, ${}^L\delta_c^M - {}^L\delta_c^R$
= $0.406 - 0.265$ = 0.141

PD mass-weighted mean *G. sacc.* $\delta^{18}\text{O}_c$ mismatch
of OGCM/foraminifera model compared to cores, ${}^P\delta_c^M - {}^P\delta_c^R$
= $-1.536 - -1.431$ = -0.105

\Rightarrow Real LGM mass-weighted mean ocean $\delta^{18}\text{O}_w$
from *G. sacc.* $\delta^{18}\text{O}_c$, ${}^L\bar{\delta}_w^R$
= ${}^L\bar{\delta}_w^M - [({}^L\delta_c^M - {}^L\delta_c^R) - ({}^P\delta_c^M - {}^P\delta_c^R)]$
= $1.25 - 0.246$ = 1.004

Table 6.24: Calculation of real LGM mass-weighted mean ocean $\delta^{18}\text{O}_w$ (‰ SMOW) from *G. sacculifer* $\delta^{18}\text{O}_c$ (‰ PDB).

Number of OGCM grid box values used (grid boxes having
cores with and inhabited by *G. ruber* (w) at both LGM and PD) = 17

LGM mass-weighted mean *G. ruber* (w) $\delta^{18}\text{O}_c$ mismatch
of OGCM/foraminifera model compared to cores, ${}^L\delta_c^M - {}^L\delta_c^R$
= $0.555 - -0.059$ = 0.614

PD mass-weighted mean *G. ruber* (w) $\delta^{18}\text{O}_c$ mismatch
of OGCM/foraminifera model compared to cores, ${}^P\delta_c^M - {}^P\delta_c^R$
= $-1.401 - -1.571$ = 0.170

\Rightarrow Real LGM mass-weighted mean ocean $\delta^{18}\text{O}_w$
from *G. ruber* (w) $\delta^{18}\text{O}_c$, ${}^L\bar{\delta}_w^R$
= ${}^L\bar{\delta}_w^M - [({}^L\delta_c^M - {}^L\delta_c^R) - ({}^P\delta_c^M - {}^P\delta_c^R)]$
= $1.25 - 0.444$ = 0.806

Table 6.25: Calculation of real LGM mass-weighted mean ocean $\delta^{18}\text{O}_w$ (‰ SMOW) from *G. ruber* (white) $\delta^{18}\text{O}_c$ (‰ PDB).

Number of OGCM grid box values used (grid boxes having
cores with and inhabited by *G. ruber*. (p) at both LGM and PD) = 9

LGM mass-weighted mean *G. ruber* (p) $\delta^{18}\text{O}_c$ mismatch
of OGCM/foraminifera model compared to cores, ${}^L\delta_c^M - {}^L\delta_c^R$
= $0.529 - 0.179$ = 0.350

PD mass-weighted mean *G. ruber* (p) $\delta^{18}\text{O}_c$ mismatch
of OGCM/foraminifera model compared to cores, ${}^P\delta_c^M - {}^P\delta_c^R$
= $-1.339 - -1.403$ = 0.064

\Rightarrow Real LGM mass-weighted mean ocean $\delta^{18}\text{O}_w$
from *G. ruber* (p) $\delta^{18}\text{O}_c$, ${}^L\bar{\delta}_w^R$
= ${}^L\bar{\delta}_w^M - [({}^L\delta_c^M - {}^L\delta_c^R) - ({}^P\delta_c^M - {}^P\delta_c^R)]$
= $1.25 - 0.286$ = 0.964

Table 6.26: Calculation of real LGM mass-weighted mean ocean $\delta^{18}\text{O}_w$ (‰ SMOW) from *G. ruber* (pink) $\delta^{18}\text{O}_c$ (‰ PDB).

Number of OGCM grid box values used (grid boxes having
cores with and inhabited by *G. bull.* at both LGM and PD) = 9

LGM mass-weighted mean *G. bull.* $\delta^{18}\text{O}_c$ mismatch
of OGCM/foraminifera model compared to cores, ${}^L\delta_c^M - {}^L\delta_c^R$
= $2.850 - 2.927$ = -0.077

PD mass-weighted mean *G. bull.* $\delta^{18}\text{O}_c$ mismatch
of OGCM/foraminifera model compared to cores, ${}^P\delta_c^M - {}^P\delta_c^R$
= $1.144 - 1.046$ = 0.098

\Rightarrow Real LGM mass-weighted mean ocean $\delta^{18}\text{O}_w$
from *G. bull.* $\delta^{18}\text{O}_c$, ${}^L\bar{\delta}_w^R$
= ${}^L\bar{\delta}_w^M - [({}^L\delta_c^M - {}^L\delta_c^R) - ({}^P\delta_c^M - {}^P\delta_c^R)]$
= $1.25 - -0.175$ = 1.425

Table 6.27: Calculation of real LGM mass-weighted mean ocean $\delta^{18}\text{O}_w$ (‰ SMOW) from *G. bulloides* $\delta^{18}\text{O}_c$ (‰ PDB).

$$\begin{array}{l} \text{Number of OGCM grid box values used (grid boxes having} \\ \text{cores with and inhabited by } N. \text{ pachy. (s) at both LGM and PD)} \end{array} = 12$$

$$\begin{array}{l} \text{LGM mass-weighted mean } N. \text{ pachy. (s) } \delta^{18}\text{O}_c \text{ mismatch} \\ \text{of OGCM/foraminifera model compared to cores, } {}^L\delta_c^M - {}^L\delta_c^R \\ \hspace{15em} = 4.081 - 3.535 \end{array} = 0.546$$

$$\begin{array}{l} \text{PD mass-weighted mean } N. \text{ pachy. (s) } \delta^{18}\text{O}_c \text{ mismatch} \\ \text{of OGCM/foraminifera model compared to cores, } {}^P\delta_c^M - {}^P\delta_c^R \\ \hspace{15em} = 2.364 - 2.422 \end{array} = -0.058$$

$$\begin{array}{l} \Rightarrow \text{Real LGM mass-weighted mean ocean } \delta^{18}\text{O}_w \\ \hspace{10em} \text{from } N. \text{ pachy. (s) } \delta^{18}\text{O}_c, {}^L\bar{\delta}_w^R \\ = {}^L\bar{\delta}_w^M - [({}^L\delta_c^M - {}^L\delta_c^R) - ({}^P\delta_c^M - {}^P\delta_c^R)] \\ \hspace{15em} = 1.25 - 0.604 \end{array} = 0.646$$

Table 6.28: Calculation of real LGM mass-weighted mean ocean $\delta^{18}\text{O}_w$ (‰ SMOW) from *N. pachyderma* (sinistral) $\delta^{18}\text{O}_c$ (‰ PDB).

$$\begin{array}{l} \text{Number of AGCM grid box values used} \\ \text{(grid boxes having cores at both LGM and PD)} \end{array} = 5$$

$$\begin{array}{l} \text{LGM mass-weighted mean snow/ice } \delta^{18}\text{O}_i \text{ mismatch} \\ \text{of AGCM compared to cores, } {}^L\delta_i^M - {}^L\delta_i^R \\ \hspace{15em} = -17.69 - -25.19 \end{array} = 7.50$$

$$\begin{array}{l} \text{PD mass-weighted mean snow/ice } \delta^{18}\text{O}_i \text{ mismatch} \\ \text{of AGCM compared to cores, } {}^P\delta_i^M - {}^P\delta_i^R \\ \hspace{15em} = -19.59 - -21.16 \end{array} = 1.57$$

$$\begin{array}{l} \Rightarrow \text{Real LGM mass-weighted mean ocean } \delta^{18}\text{O}_w \\ \hspace{10em} \text{from snow/ice } \delta^{18}\text{O}_i, {}^L\bar{\delta}_w^R \\ = {}^L\bar{\delta}_w^M - [({}^L\delta_i^M - {}^L\delta_i^R) - ({}^P\delta_i^M - {}^P\delta_i^R)] \\ \hspace{15em} = 1.25 - 5.93 \end{array} = -4.68$$

Table 6.29: Calculation of real LGM mass-weighted mean ocean $\delta^{18}\text{O}_w$ (‰ SMOW) from snow/ice $\delta^{18}\text{O}_i$ (‰ SMOW).

6.5.2 Maps

Figures 6.30 to 6.37 are the map comparison figures of foraminifera $\delta^{18}\text{O}_c$ and precipitation $\delta^{18}\text{O}_i$ for comparing the LGM – PD of simulations (CGCM and foraminifera model) to core $\delta^{18}\text{O}$ data in order to spatially assess goodness of match, all as outlined in Section 6.2.2. The discussed 0.25‰ that the LGM mean ocean $\delta^{18}\text{O}_w$ initially set in the OGCM was too high by can be subtracted from the “c” map of each of these figures to on average correct for this non-inherent bias. As discussed in Section 6.2.2, it is confidently assumed that no such correction is necessary for the PD part. If this LGM correction is done then to varying degrees the matches seem fairly good, as far as can be determined from the sparse core $\delta^{18}\text{O}$ data and at this scale. This provides some confidence in the PD and LGM simulations, the CGCM, the foraminifera model, and the PD and LGM ocean sediment and ice core $\delta^{18}\text{O}$ data. Note in the “c” map for *N. pachyderma* (dextral) that as discussed in the previous section there are no grid boxes meeting the requirements for inclusion. Note too that, while in the right direction, subtracting 0.25‰ does little to help the match of precipitation $\delta^{18}\text{O}_i$, given the magnitudes involved. Finally, note for the planktonic foraminifera species that as a combined effect of the PD and LGM cases there are ocean sediment cores with them outside of the habitat ranges indicated for them by the OGCM/foraminifera model.

6.5.3 Plots

Comparing the LGM – PD simulation (CGCM and foraminifera model) to core $\delta^{18}\text{O}$ data using model/data plots of foraminifera $\delta^{18}\text{O}_c$ and snow/ice $\delta^{18}\text{O}_i$ in order to assess goodness of match, all as outlined in Section 6.2.2, Figure 6.38 has plots of LGM – PD OGCM/foraminifera model $\delta^{18}\text{O}_c$ versus ocean sediment core foraminifera $\delta^{18}\text{O}_c$ and LGM – PD AGCM snow $\delta^{18}\text{O}_i$ versus ice core H_2O $\delta^{18}\text{O}_i$. As with the map comparison figures, if the OGCM/foraminifera model values are shifted down by the discussed 0.25‰ that the LGM mean ocean $\delta^{18}\text{O}_w$ initially set in the OGCM was too high by then overall the matches seem fairly good. And again, while in the right direction, shifting the AGCM snow $\delta^{18}\text{O}_i$ values down by 0.25‰ does little to help the match, given the magnitudes involved.

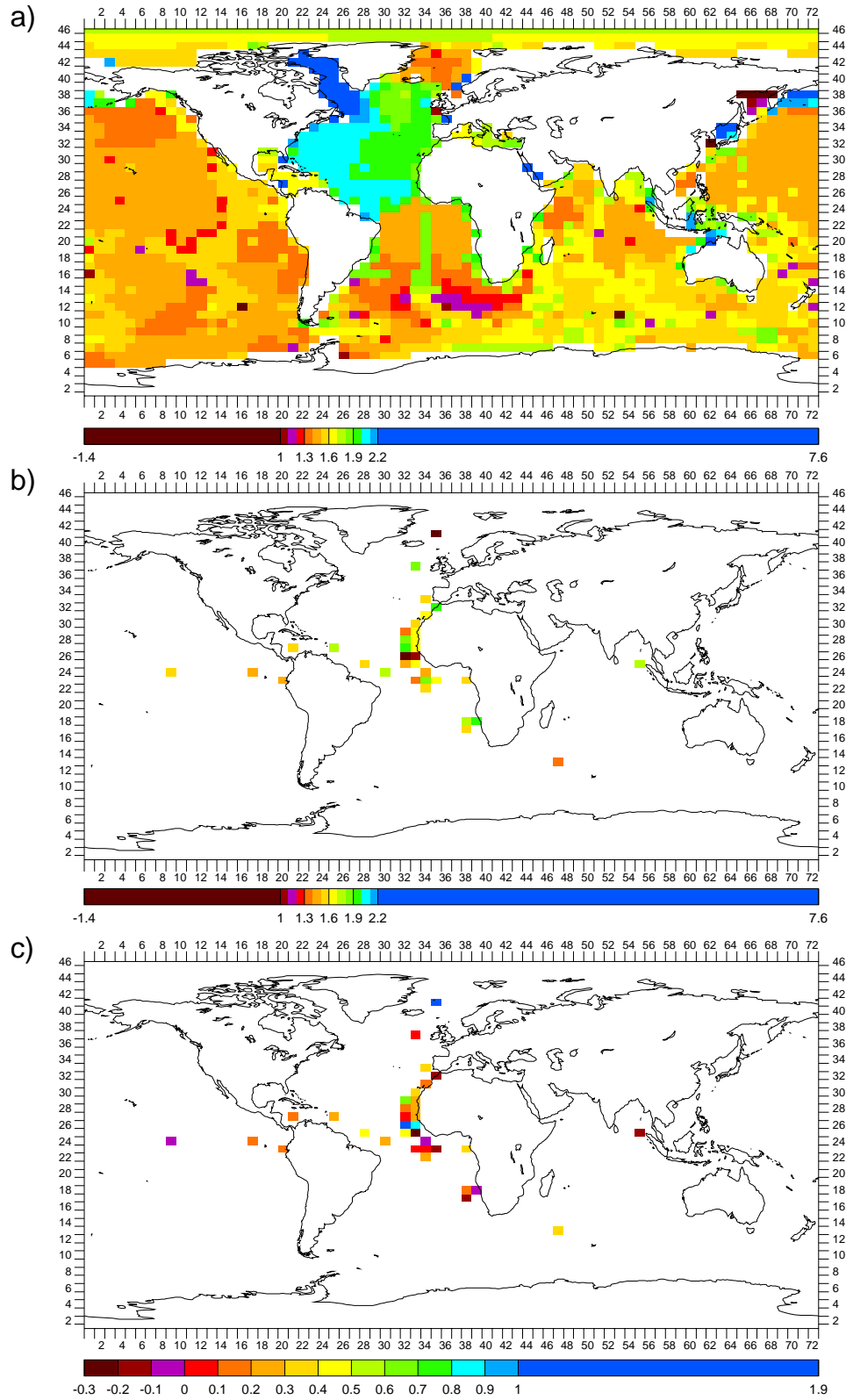


Figure 6.30: CGCM grid box maps of LGM – PD annual $\delta^{18}\text{O}_c$ (‰ PDB) of benthic foraminifera *C. wuellerstorfi* in: a) OGCM/foraminifera model; b) cores; and c) OGCM/foraminifera model minus cores

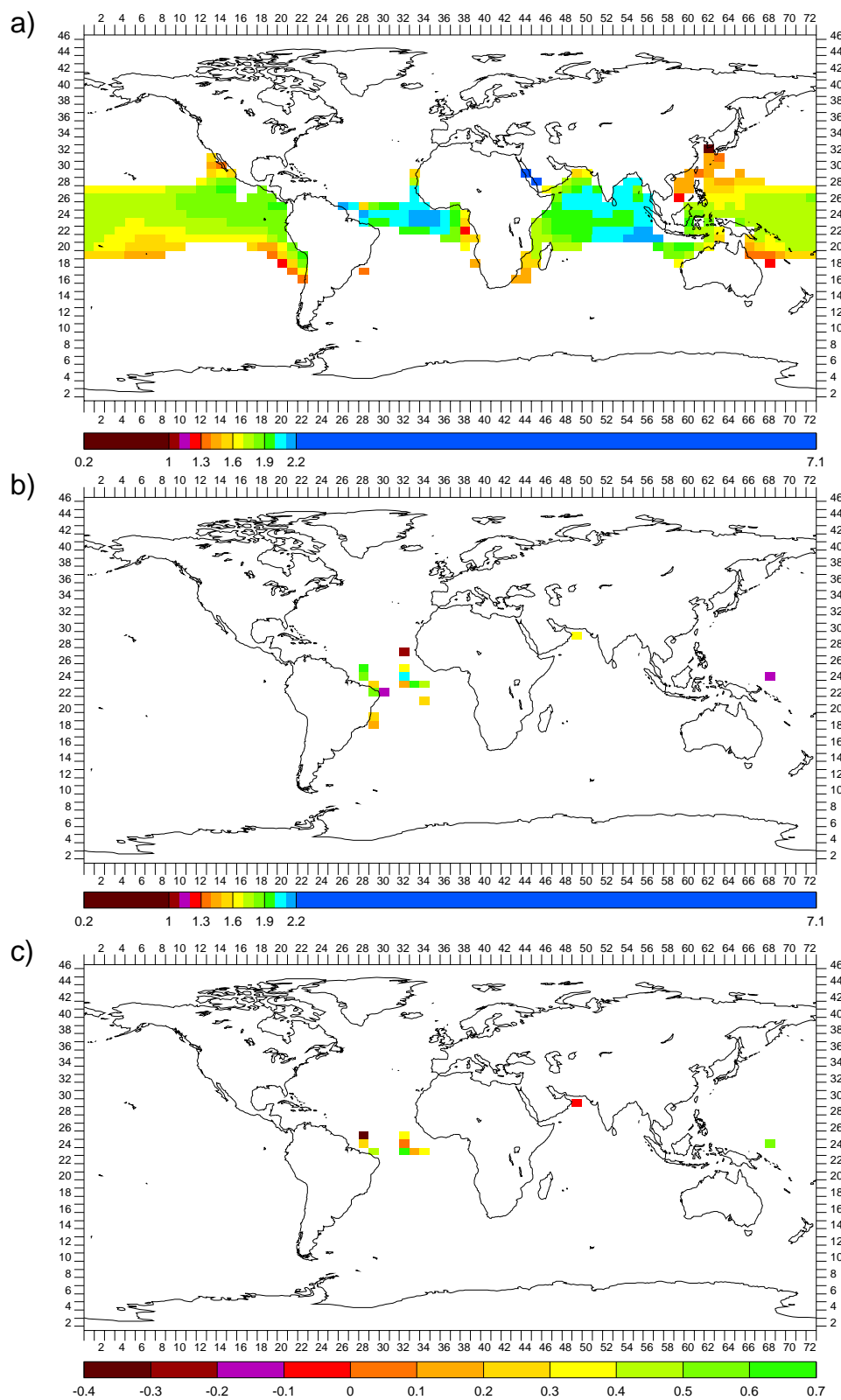


Figure 6.31: CGCM grid box maps of LGM – PD annual $\delta^{18}O_c$ (‰ PDB) of planktonic foraminifera *G. sacculifer* in: a) OGCM/foraminifera model; b) cores; and c) OGCM/foraminifera model minus cores

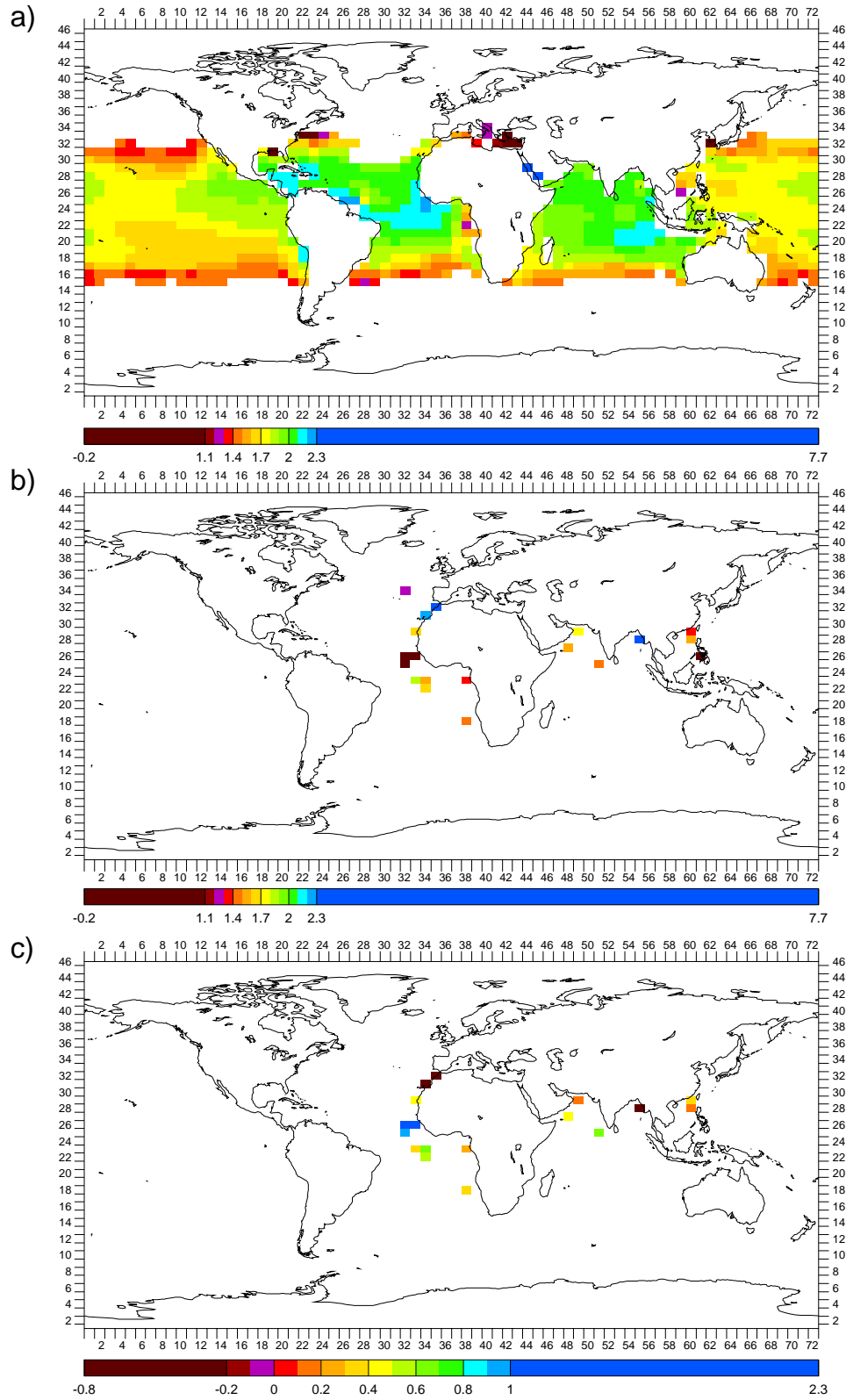


Figure 6.32: CGCM grid box maps of LGM – PD annual $\delta^{18}O_c$ (‰ PDB) of planktonic foraminifera *G. ruber* (white) in: a) OGCM/foraminifera model; b) cores; and c) OGCM/foraminifera model minus cores

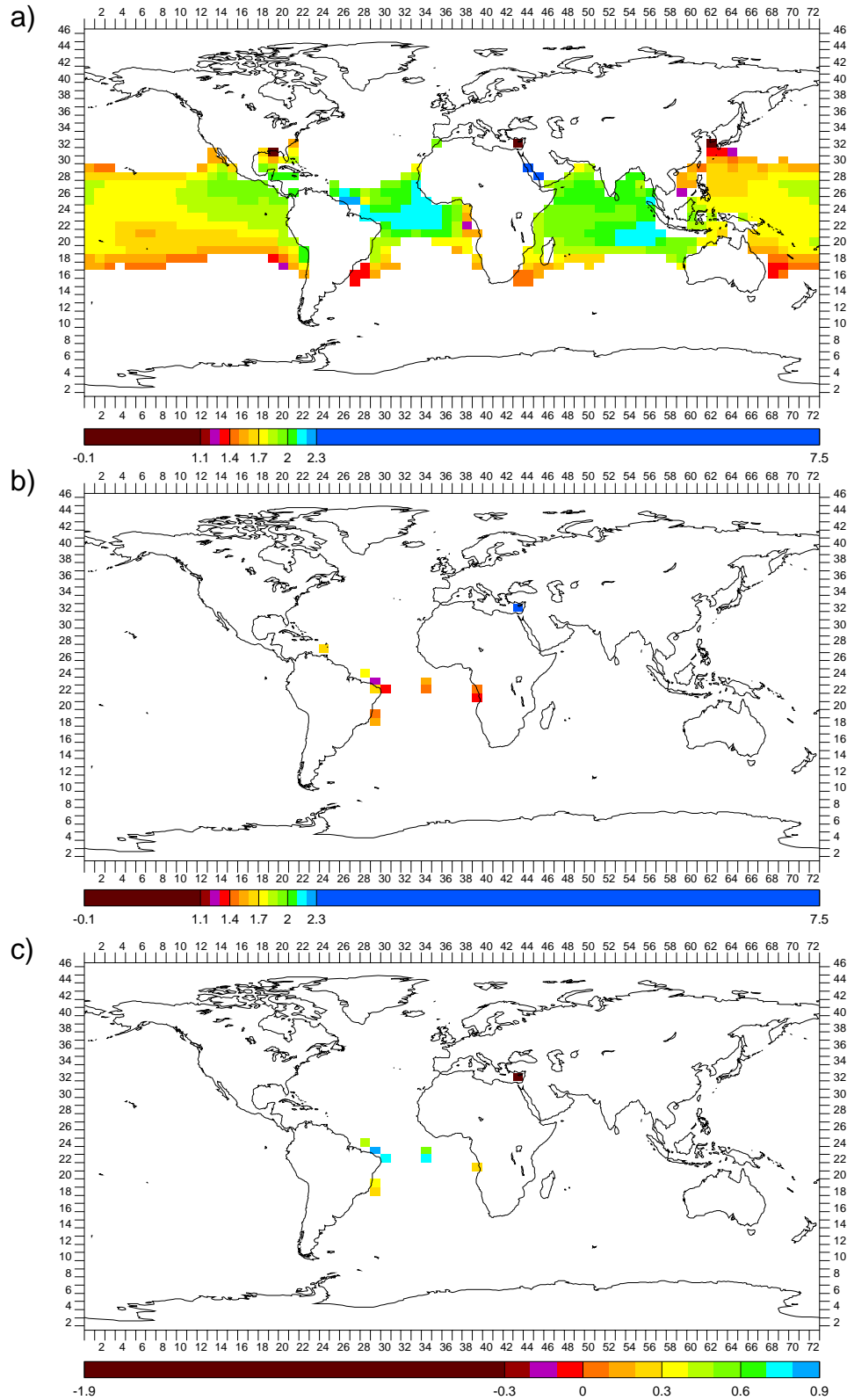


Figure 6.33: CGCM grid box maps of LGM – PD annual $\delta^{18}\text{O}_c$ (‰ PDB) of planktonic foraminifera *G. ruber* (pink) in: a) OGCM/foraminifera model; b) cores; and c) OGCM/foraminifera model minus cores

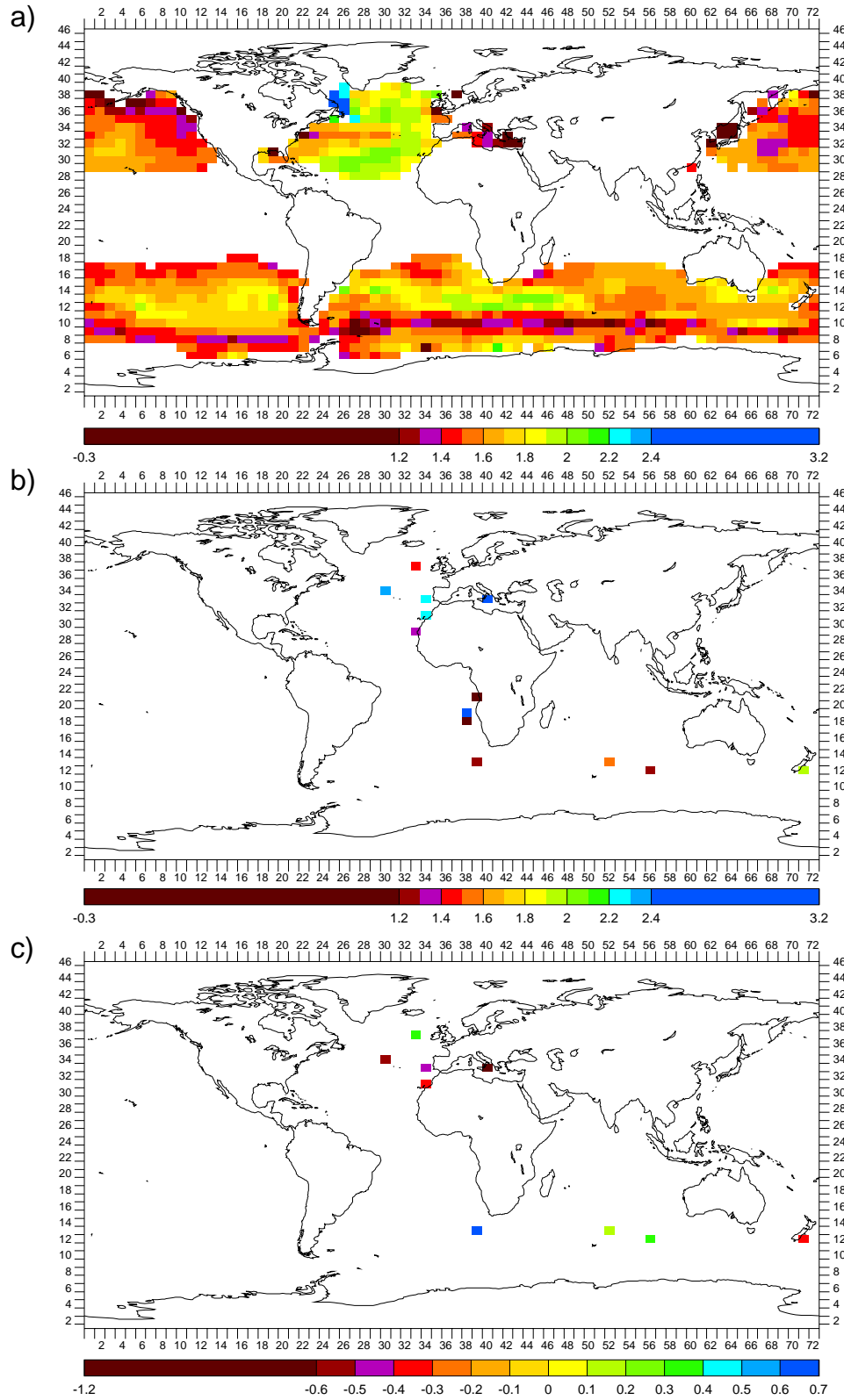


Figure 6.34: CGCM grid box maps of LGM – PD annual $\delta^{18}O_c$ (‰ PDB) of planktonic foraminifera *G. bulloides* in: a) OGCM/foraminifera model; b) cores; and c) OGCM/foraminifera model minus cores

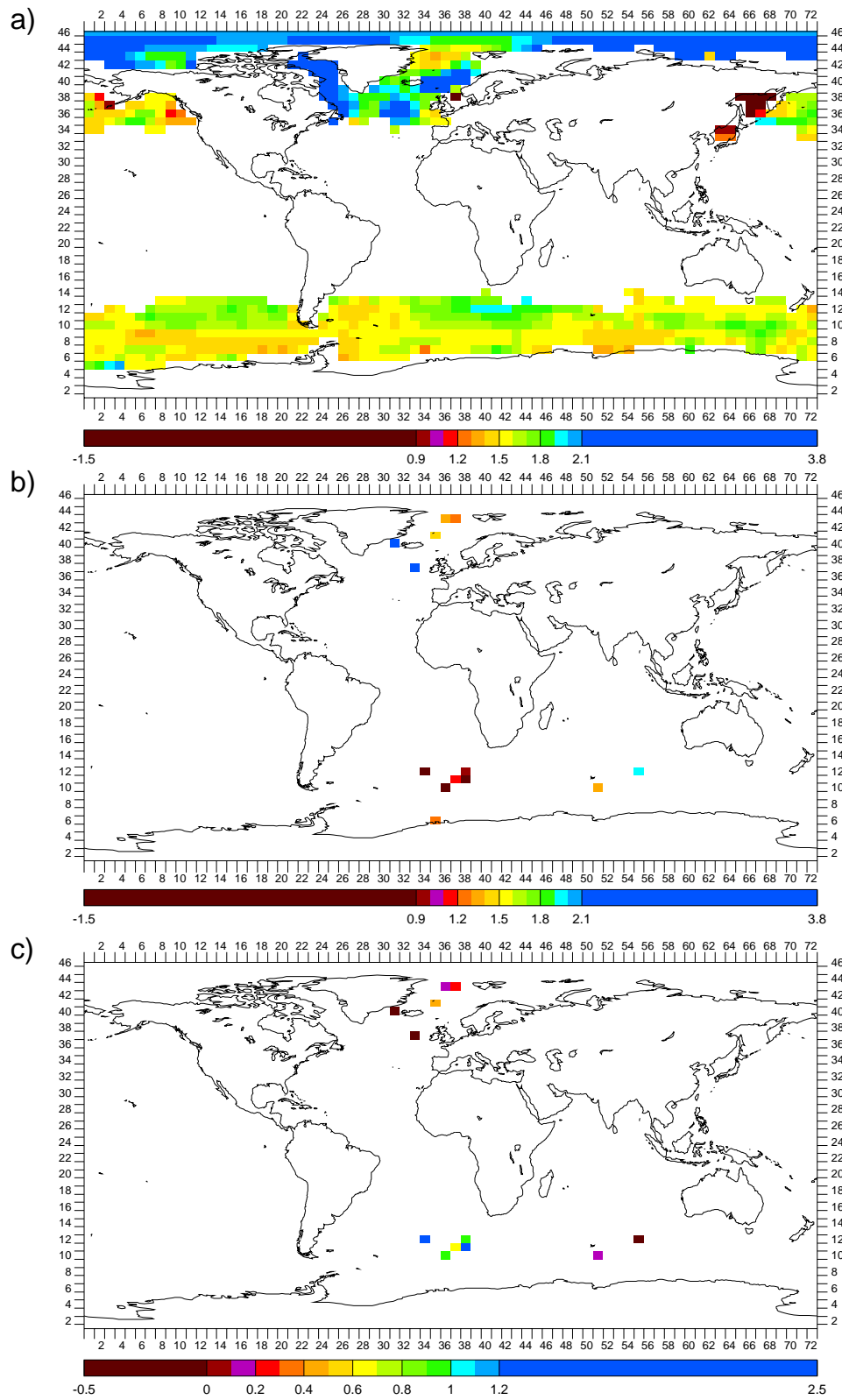


Figure 6.35: CGCM grid box maps of LGM – PD annual $\delta^{18}\text{O}_c$ (‰ PDB) of planktonic foraminifera *N. pachyderma* (sinistral) in: a) OGCM/foraminifera model; b) cores; and c) OGCM/foraminifera model minus cores

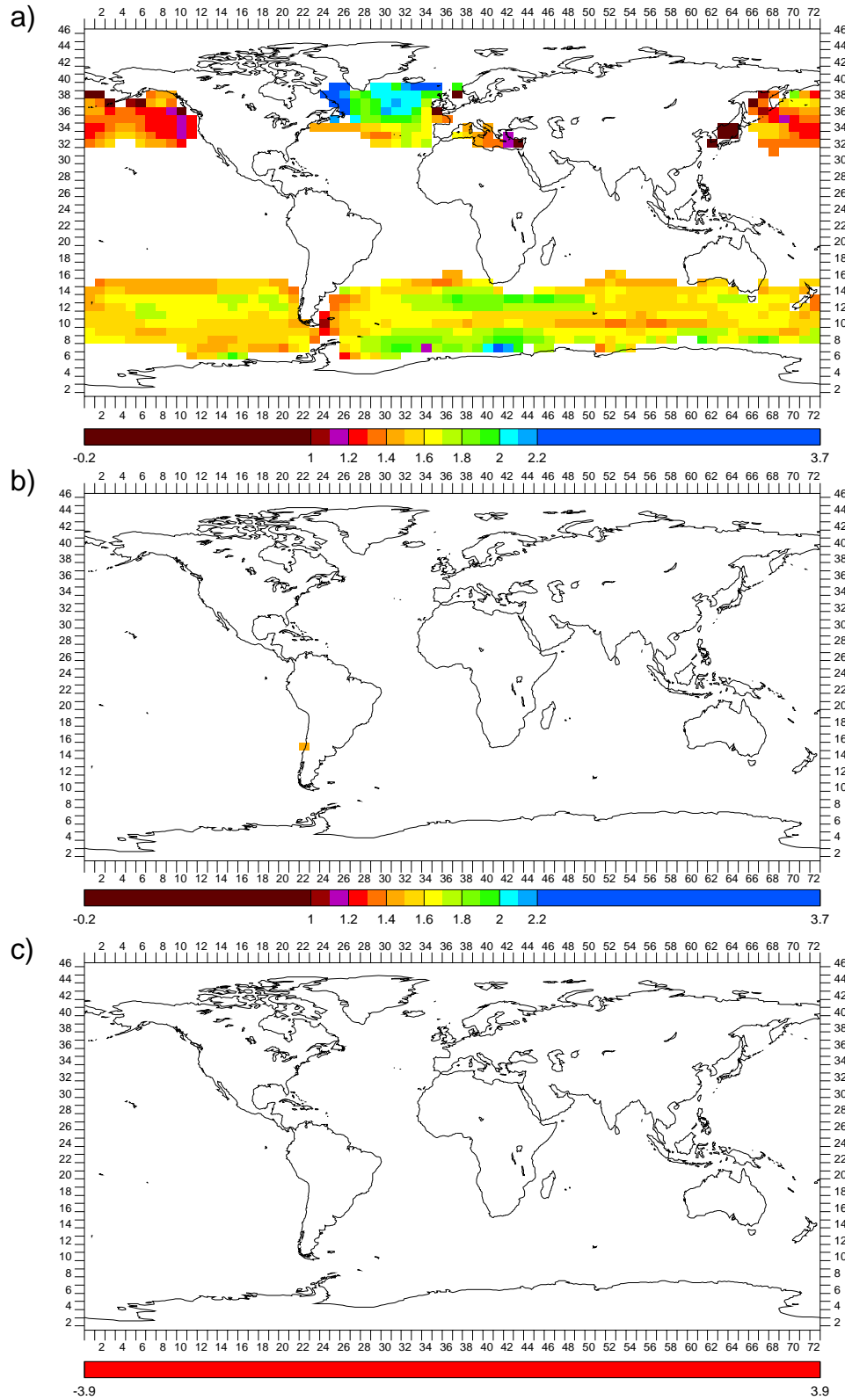


Figure 6.36: CGCM grid box maps of LGM – PD annual $\delta^{18}\text{O}_c$ (‰ PDB) of planktonic foraminifera *N. pachyderma* (dextral) in: a) OGCM/foraminifera model; b) cores; and c) OGCM/foraminifera model minus cores

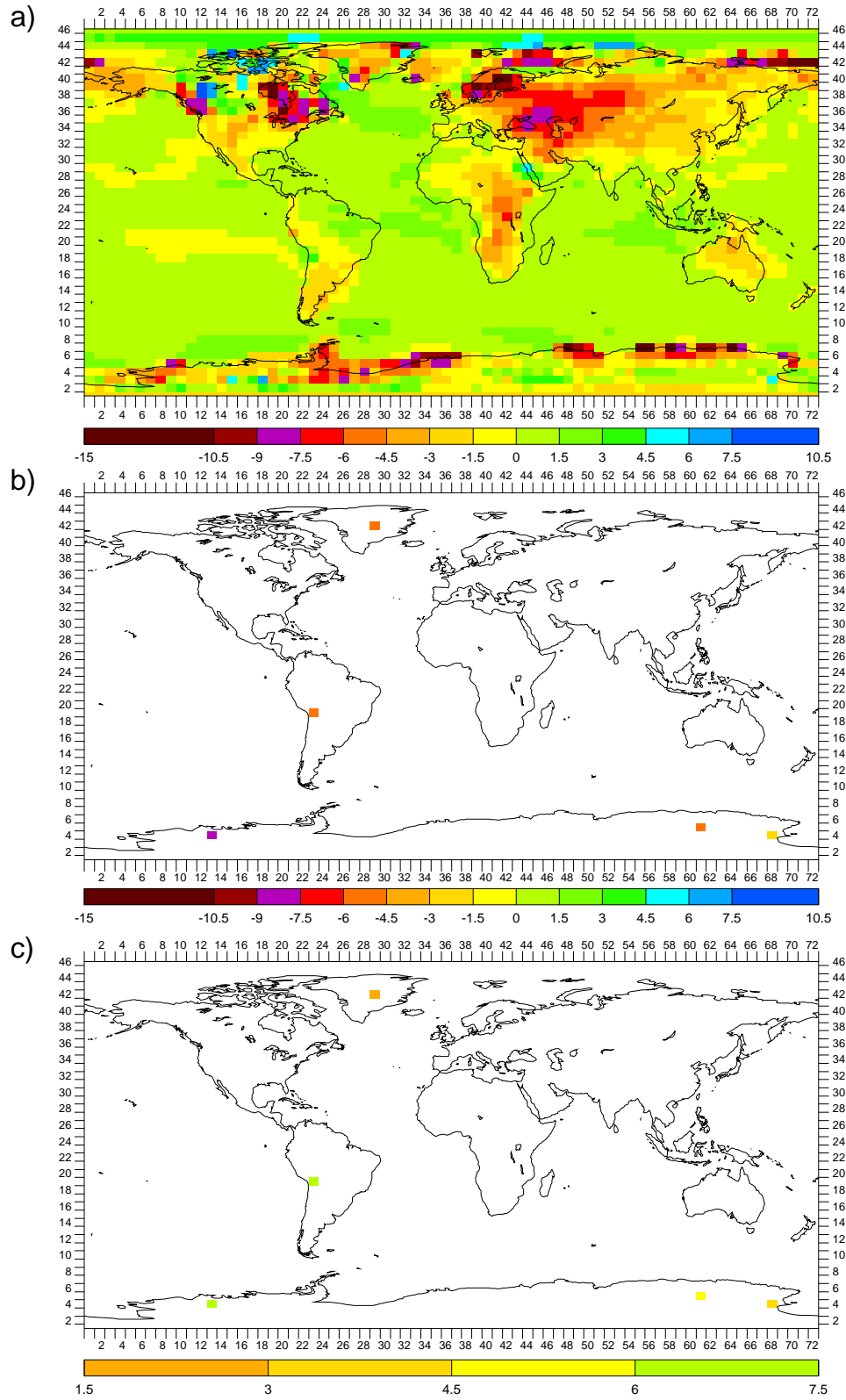


Figure 6.37: CGCM grid box maps of LGM – PD annual $\delta^{18}\text{O}$ (‰ SMOW) of: a) AGCM precipitation; b) ice core H_2O ; and c) AGCM precipitation minus ice core H_2O

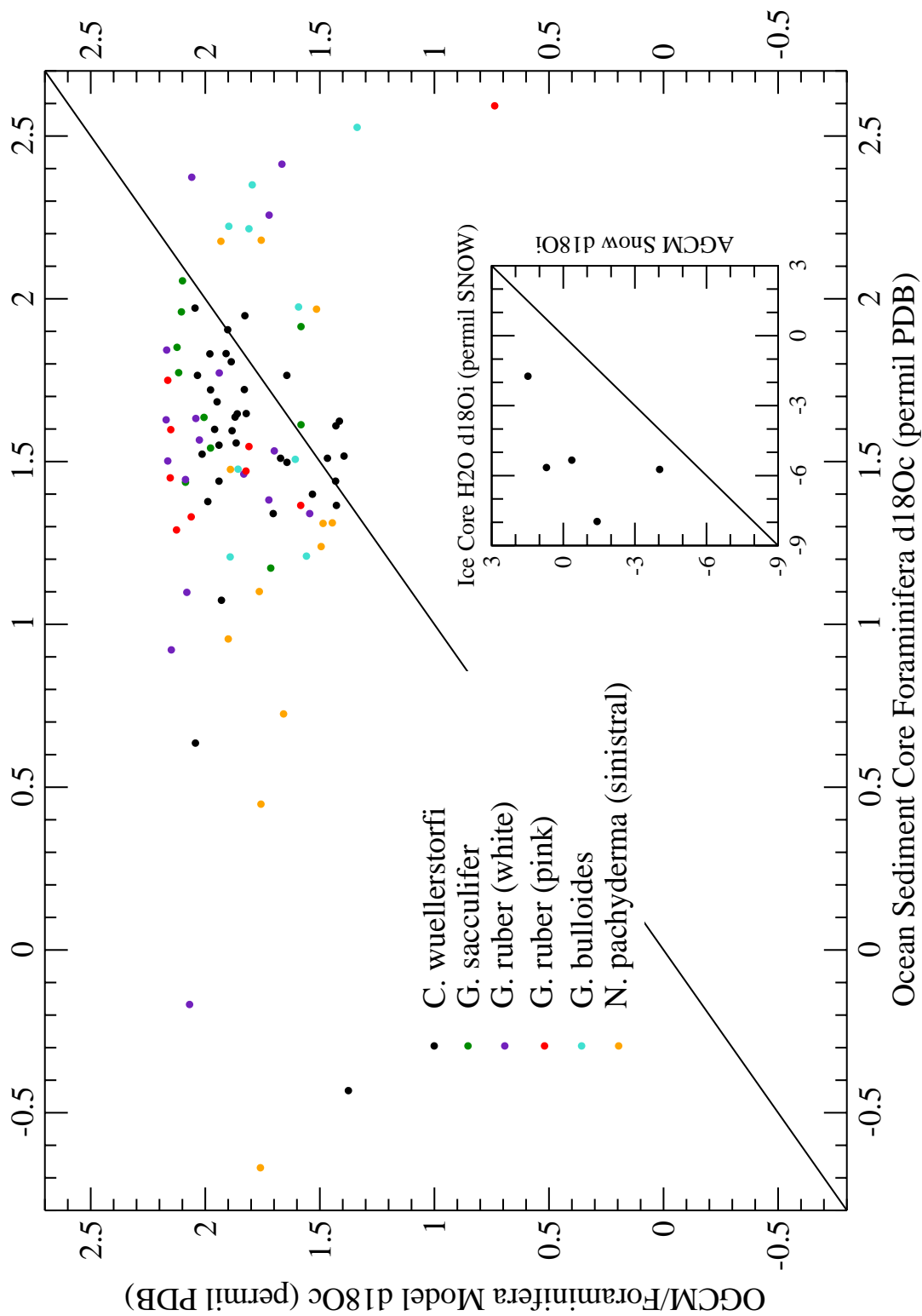


Figure 6.38: LGM – PD OGCM/foraminifera model annual $\delta^{18}\text{O}_c$ (‰ PDB) versus ocean sediment core foraminifera $\delta^{18}\text{O}_c$ (‰ PDB); and inset) LGM – PD AGCM annual snow $\delta^{18}\text{O}_i$ (‰ SMOW) versus ice core H_2O $\delta^{18}\text{O}_i$ (‰ SMOW).

6.6 LGM Simulation Compared to Ocean Sediment and Ice Core $\delta^{18}\text{O}$ Data

6.6.1 Maps

Figures 6.39 to 6.46 are the map comparison figures of foraminifera $\delta^{18}\text{O}_c$ and precipitation $\delta^{18}\text{O}_i$ for comparing the LGM simulations (CGCM and foraminifera model) to core $\delta^{18}\text{O}$ data in order to spatially assess goodness of match, all as outlined in Section 6.2.2. If the discussed 0.25‰ that the LGM mean ocean $\delta^{18}\text{O}_w$ initially set in the OGCM was too high by is subtracted from the “c” map of each of these figures, as in Section 6.5.2, then to varying degrees the matches seem fairly good, as far can be determined from the sparse core $\delta^{18}\text{O}$ data and at this scale. Note too that, while in the right direction, subtracting 0.25‰ does little to help the match of precipitation $\delta^{18}\text{O}_i$, given the magnitudes involved.

Realistically, the core $\delta^{18}\text{O}$ data is too sparse to see clearly even the broad patterns of the described CGCM biases, never mind checking for these more quantitatively as in Section 6.4.1. However, hints of varying degree for different foraminifera species of the described effects of the OGCM in situ temperature biases can be seen in the “c” maps: using Figure 6.6c’s bottom OGCM in situ temperature biases for the benthic Figure 6.39c and using Figure 6.14c’s surface OGCM in situ temperature biases for the remaining, planktonic, map comparison figures. To even a lesser extent, since they are generally small biases, this is also true for the described effects of the OGCM $\delta^{18}\text{O}_w$ biases: using Figure 6.5c’s bottom OGCM $\delta^{18}\text{O}_w$ biases for benthic Figure 6.39c and using Figure 6.10c’s surface OGCM $\delta^{18}\text{O}_w$ biases for the remaining, planktonic, map comparison figures. Finally, this is also similarly true for the AGCM precipitation $\delta^{18}\text{O}$ biases, using Figure 6.15c for map comparison Figure 6.46c. Thus, taking LGM – PD differences may have helped to remove the CGCM biases as hoped but it’s not clear.

Regarding the sparsity of the core $\delta^{18}\text{O}$ data, comparison to the corresponding “b” maps of the PD Figures 6.21 to 6.28 shows how much less ocean sediment and ice core $\delta^{18}\text{O}$ data there is for the LGM than for PD (see Chapter 5). Note also in the map comparison figures for the planktonic foraminifera that there are ocean sediment

cores with them outside of the habitat ranges indicated by the OGCM/foraminifera model. In Figure 6.43a note further that the combining of the results for the North Atlantic and Southern Ocean *G. bulloides* resulted in a truncation of the habitat ranges at the equator (see Section 6.4.1).

6.6.2 Plots

Comparing the LGM simulation (CGCM and foraminifera model) to core $\delta^{18}\text{O}$ data using model/data plots of foraminifera $\delta^{18}\text{O}_c$ and snow/ice $\delta^{18}\text{O}_i$ in order to assess goodness of match, all as outlined in Section 6.2.2, Figure 6.47 has plots of LGM OGCM/foraminifera model $\delta^{18}\text{O}_c$ versus ocean sediment core foraminifera $\delta^{18}\text{O}_c$ and LGM AGCM snow $\delta^{18}\text{O}_i$ versus ice core H_2O $\delta^{18}\text{O}_i$. As with the map comparison figures, if the OGCM/foraminifera model values are shifted down by the discussed 0.25‰ that the LGM mean ocean $\delta^{18}\text{O}_w$ initially set in the OGCM was too high by then overall the matches seem fairly good. And again, while in the right direction, shifting the AGCM snow $\delta^{18}\text{O}_i$ values down by 0.25‰ does little to help the match, given the magnitudes involved. Further, by comparing with the PD and LGM – PD AGCM snow $\delta^{18}\text{O}_i$ versus ice core H_2O $\delta^{18}\text{O}_i$ model/data plots of Figures 6.4.2 and 6.5.3, respectively, it is seems that the LGM is largely responsible for the mismatch in the latter.

Comparison to the corresponding PD Figure 6.29 shows again how much less ocean sediment and ice core $\delta^{18}\text{O}$ data there is for the LGM than for PD. Note that while the LGM was the limiting factor in the amount of core data used for LGM – PD (Section 6.5), there are grid boxes with core data used for the LGM that weren't used for LGM – PD.

6.6.3 Means

The LGM simulation (CGCM and foraminifera model) is compared to core $\delta^{18}\text{O}$ data using means of foraminifera $\delta^{18}\text{O}_c$ and snow/ice $\delta^{18}\text{O}_i$ in order to bottom-line assess goodness of match, all as outlined in Section 6.2.2. First though, as in Section 6.3.3 for PD, calculating the LGM mean OGCM $\delta^{18}\text{O}_w$ by mass-weighted averaging all grid boxes provides an opportunity to estimate the numerical error involved in the

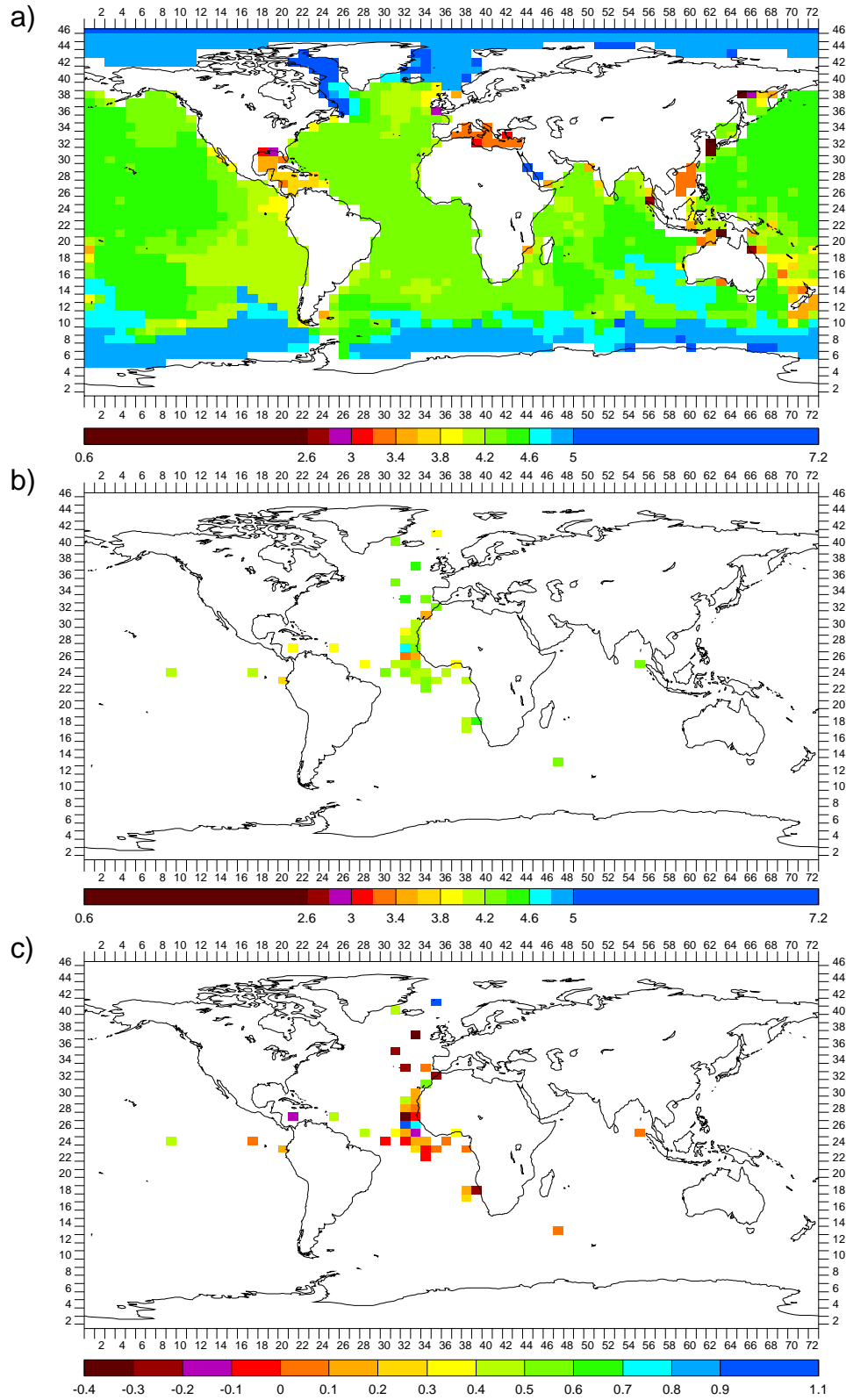


Figure 6.39: CGCM grid box maps of LGM annual $\delta^{18}\text{O}_c$ (‰ PDB) of benthic foraminifera *C. wuellerstorfi* in: a) OGCM/foraminifera model; b) cores; and c) OGCM/foraminifera model minus cores

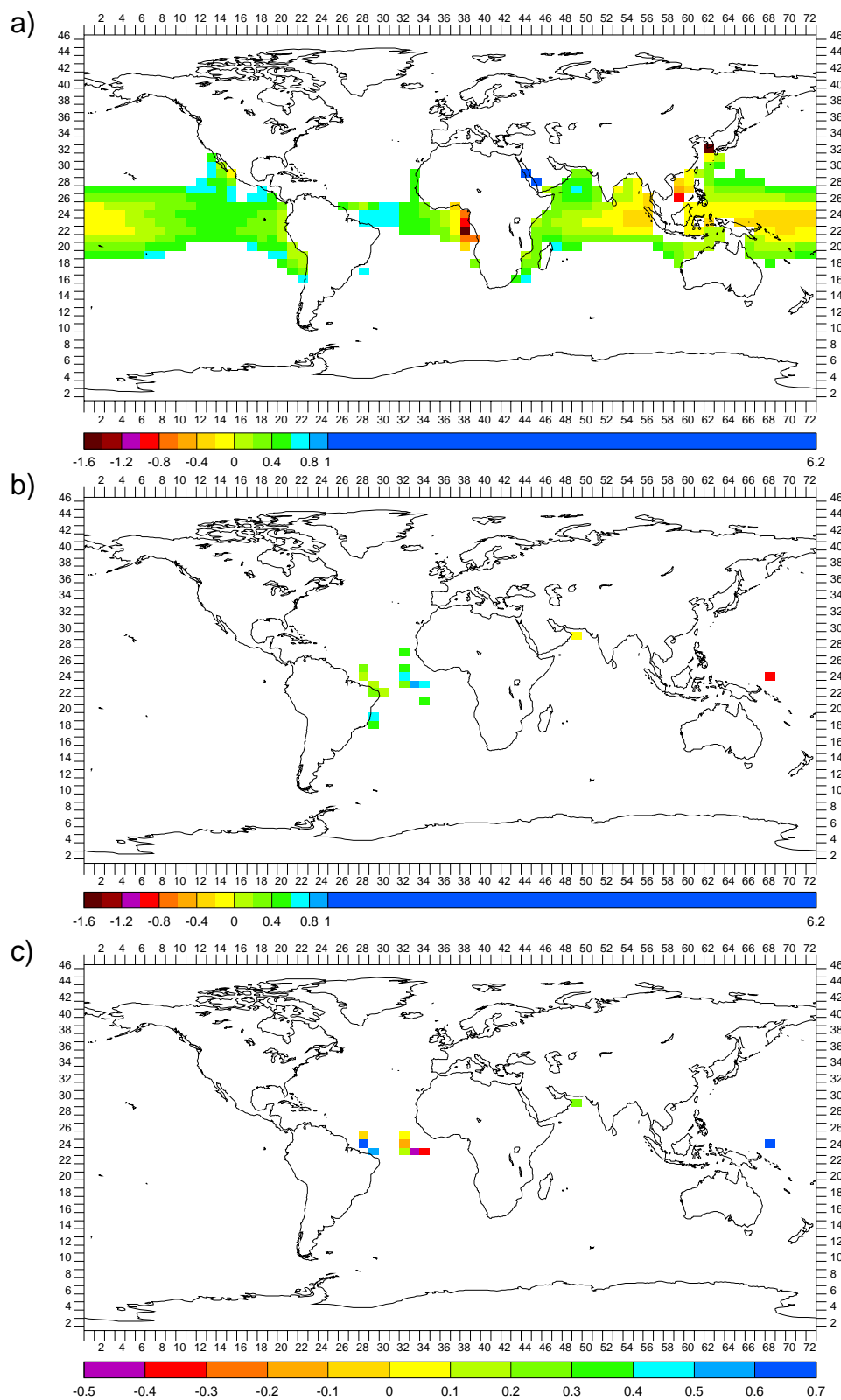


Figure 6.40: CGCM grid box maps of LGM annual $\delta^{18}\text{O}_c$ (‰ PDB) of planktonic foraminifera *G. sacculifer* in: a) OGCM/foraminifera model; b) cores; and c) OGCM/foraminifera model minus cores

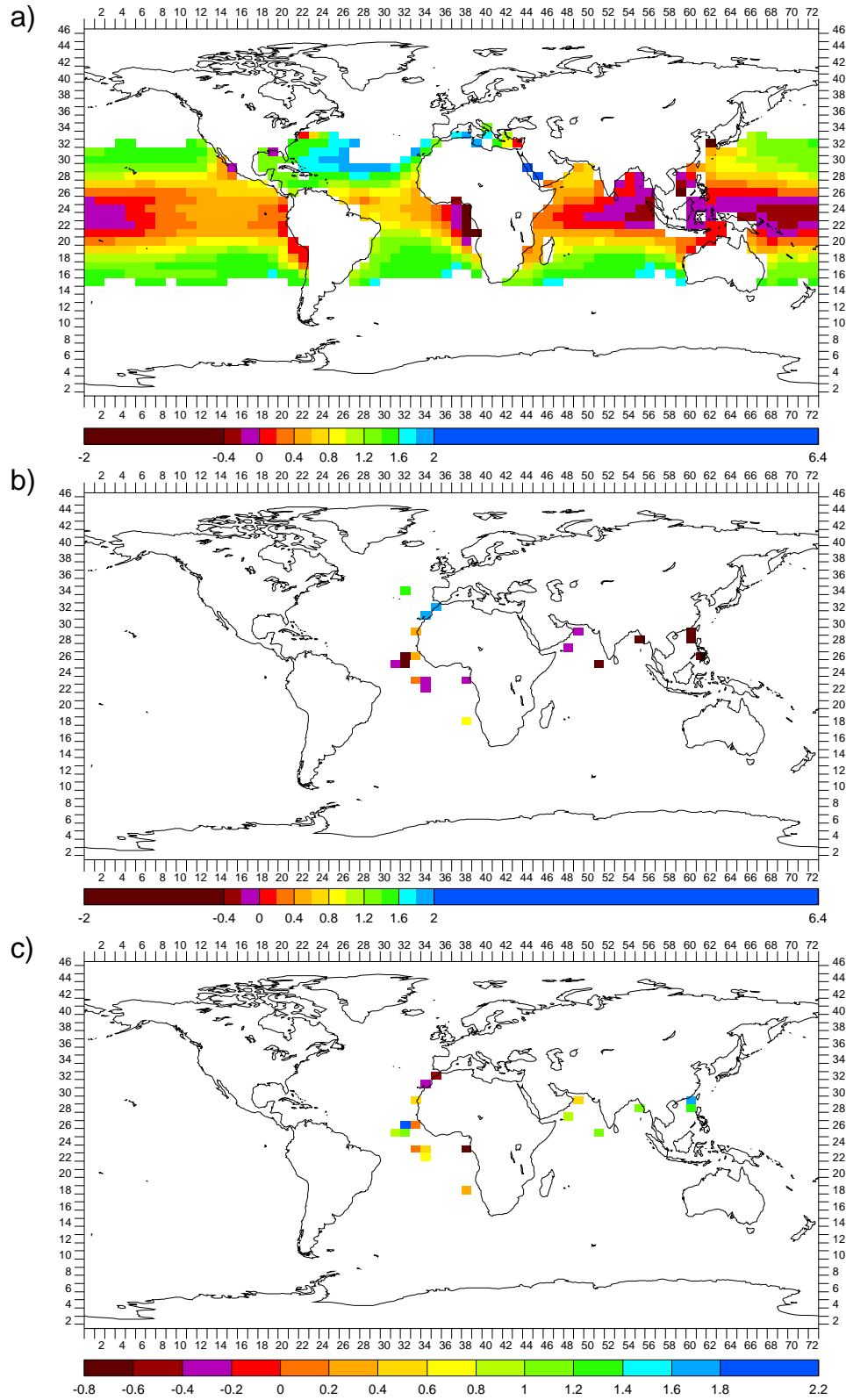


Figure 6.41: CGCM grid box maps of LGM annual $\delta^{18}\text{O}_c$ (‰ PDB) of planktonic foraminifera *G. ruber* (white) in: a) OGCM/foraminifera model; b) cores; and c) OGCM/foraminifera model minus cores

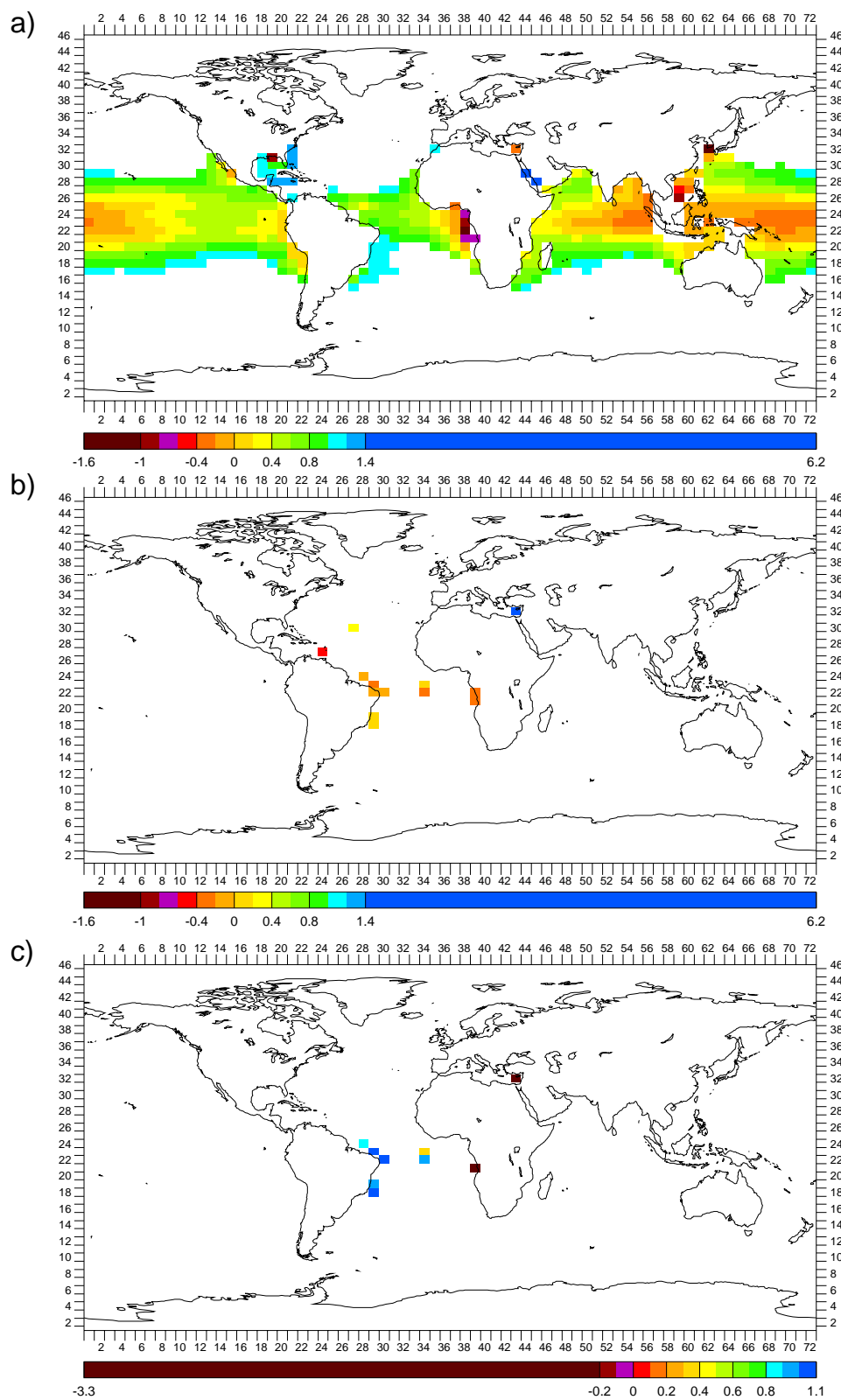


Figure 6.42: CGCM grid box maps of LGM annual $\delta^{18}\text{O}_c$ (‰ PDB) of planktonic foraminifera *G. ruber* (pink) in: a) OGCM/foraminifera model; b) cores; and c) OGCM/foraminifera model minus cores

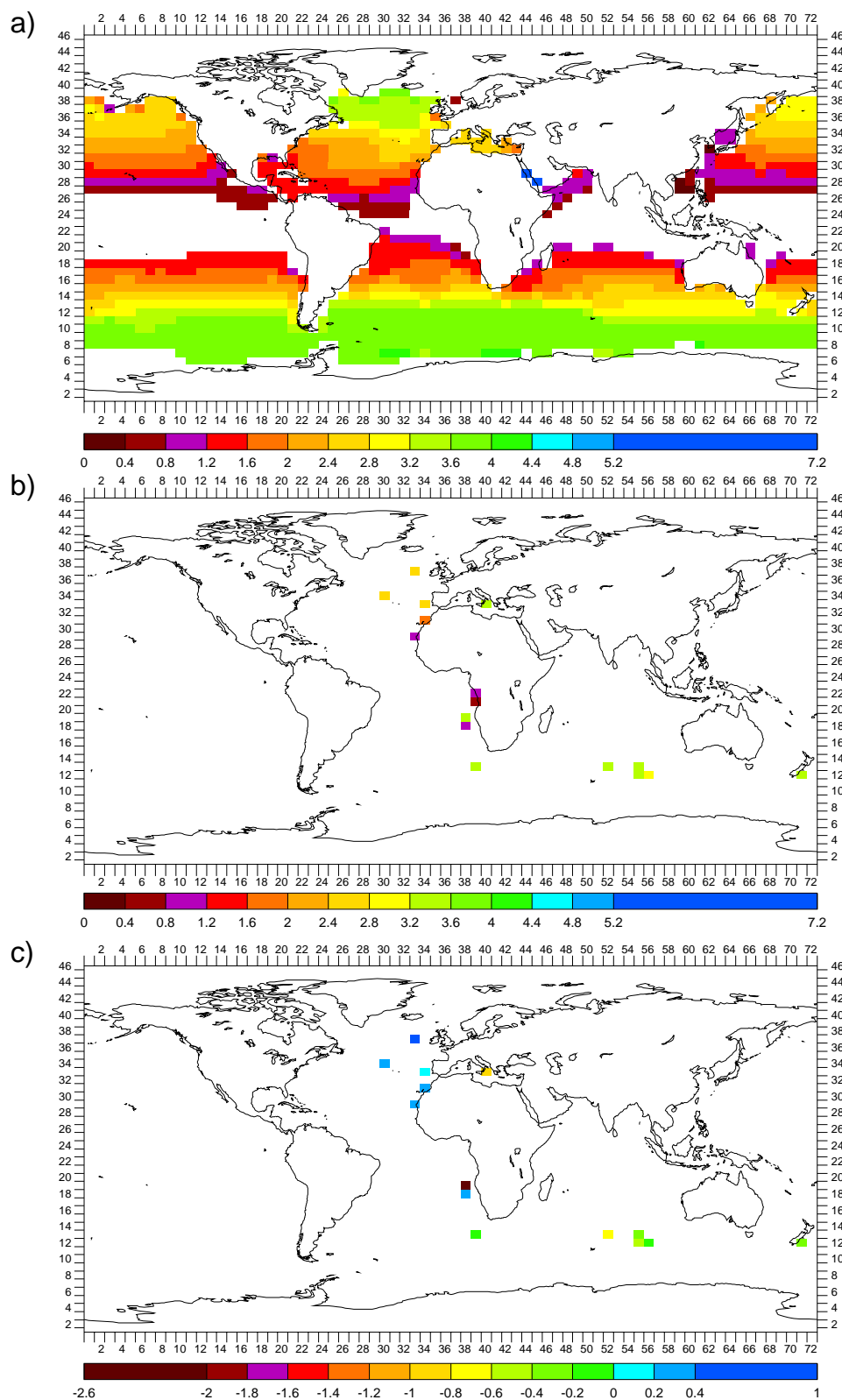


Figure 6.43: CGCM grid box maps of LGM annual $\delta^{18}O_c$ (‰ PDB) of planktonic foraminifera *G. bulloides* in: a) OGCM/foraminifera model; b) cores; and c) OGCM/foraminifera model minus cores

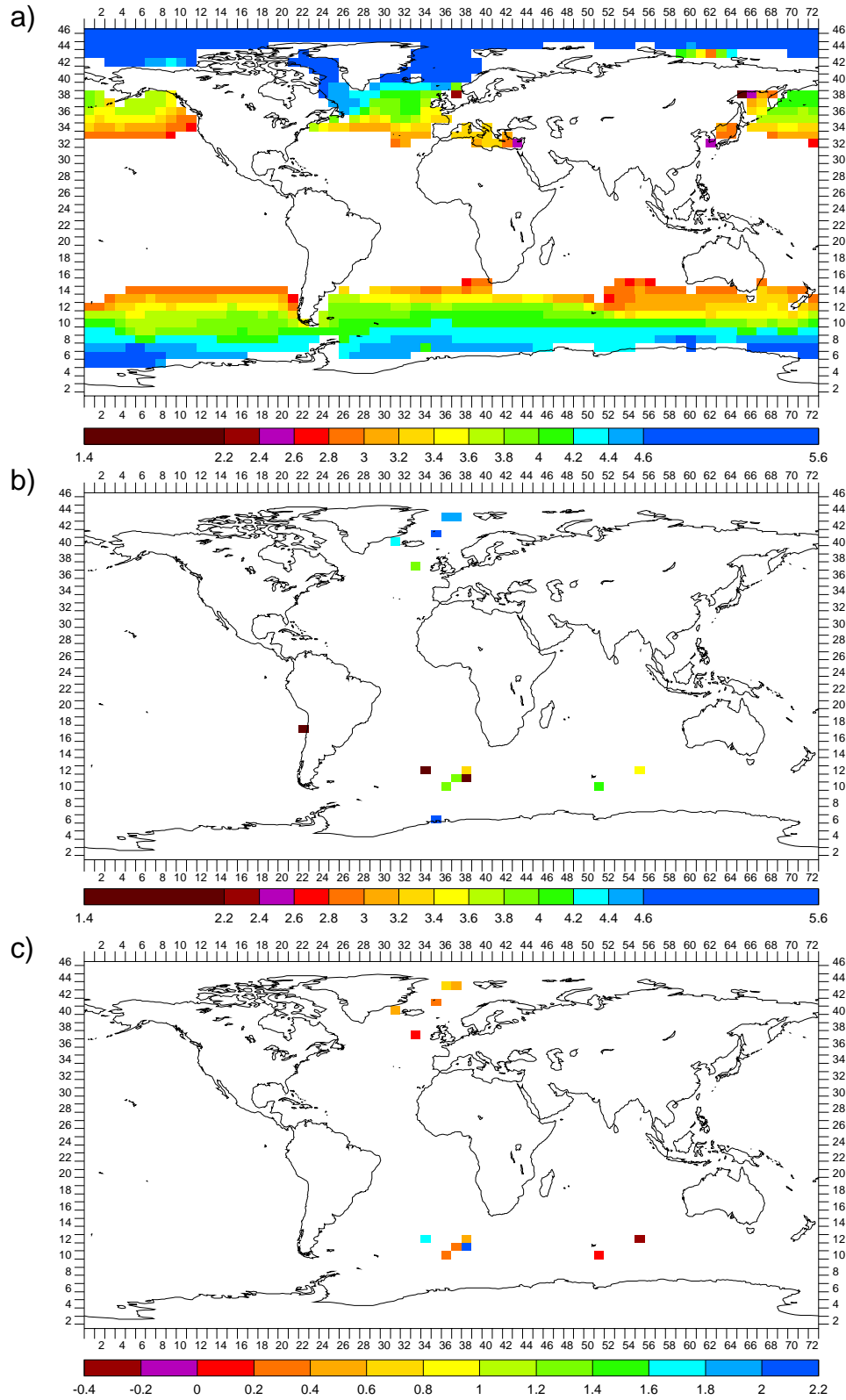


Figure 6.44: CGCM grid box maps of LGM annual $\delta^{18}\text{O}_c$ (‰ PDB) of planktonic foraminifera *N. pachyderma* (sinistral) in: a) OGCM/foraminifera model; b) cores; and c) OGCM/foraminifera model minus cores

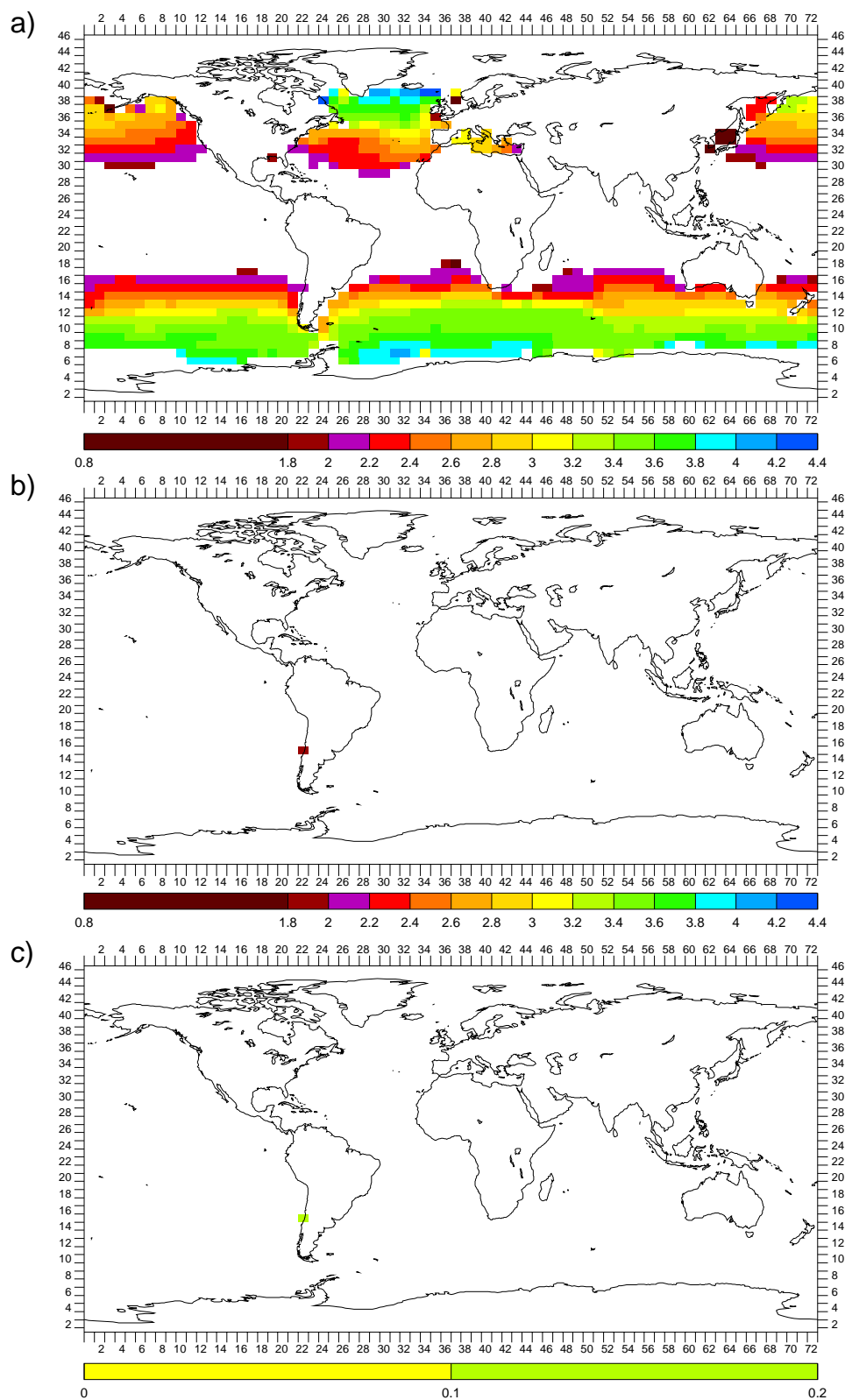


Figure 6.45: CGCM grid box maps of LGM annual $\delta^{18}\text{O}_c$ (‰ PDB) of planktonic foraminifera *N. pachyderma* (dextral) in: a) OGCM/foraminifera model; b) cores; and c) OGCM/foraminifera model minus cores

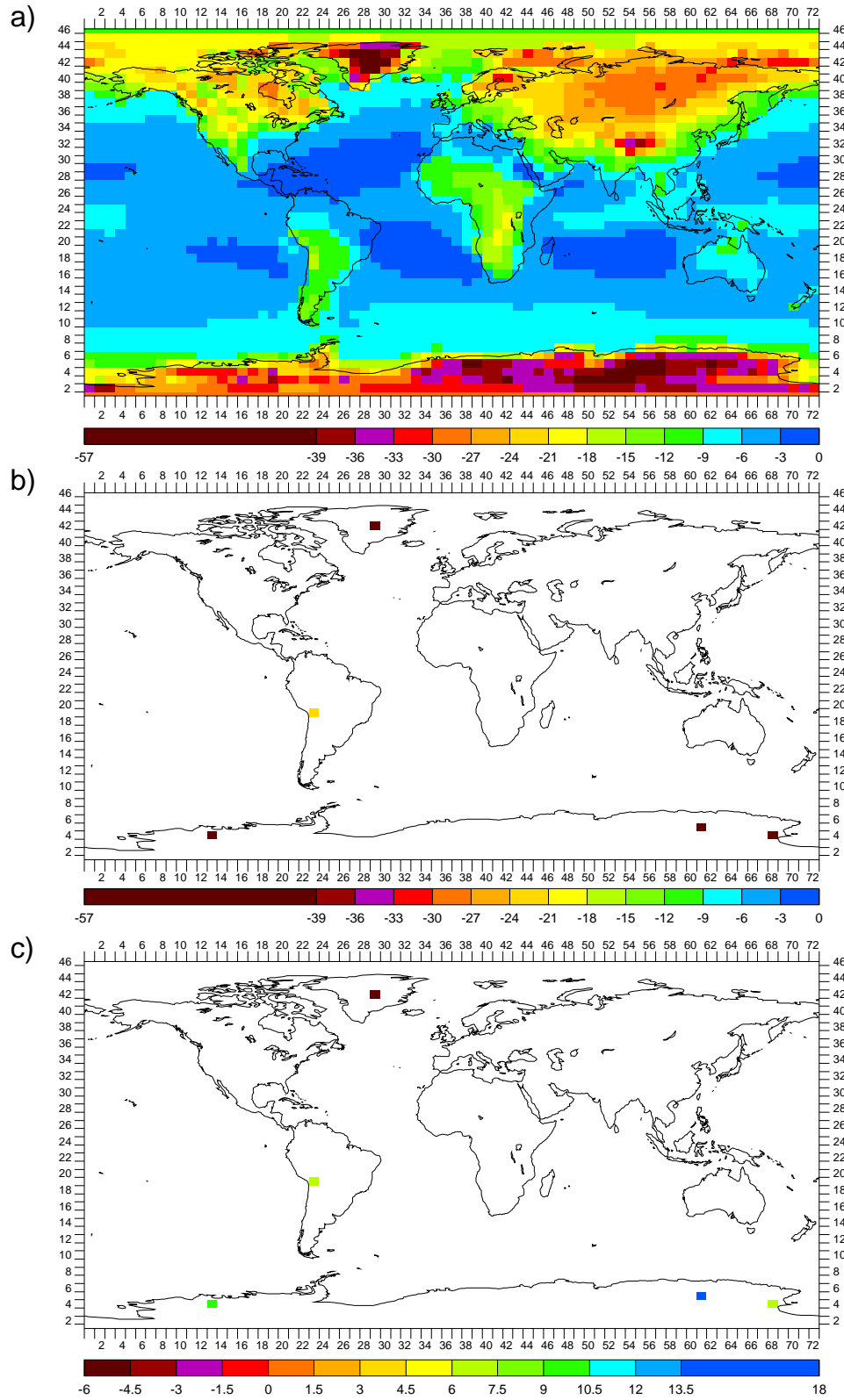


Figure 6.46: CGCM grid box maps of LGM annual $\delta^{18}\text{O}$ (‰ SMOW) of: a) AGCM precipitation; b) ice core H_2O ; and c) AGCM precipitation minus ice core H_2O

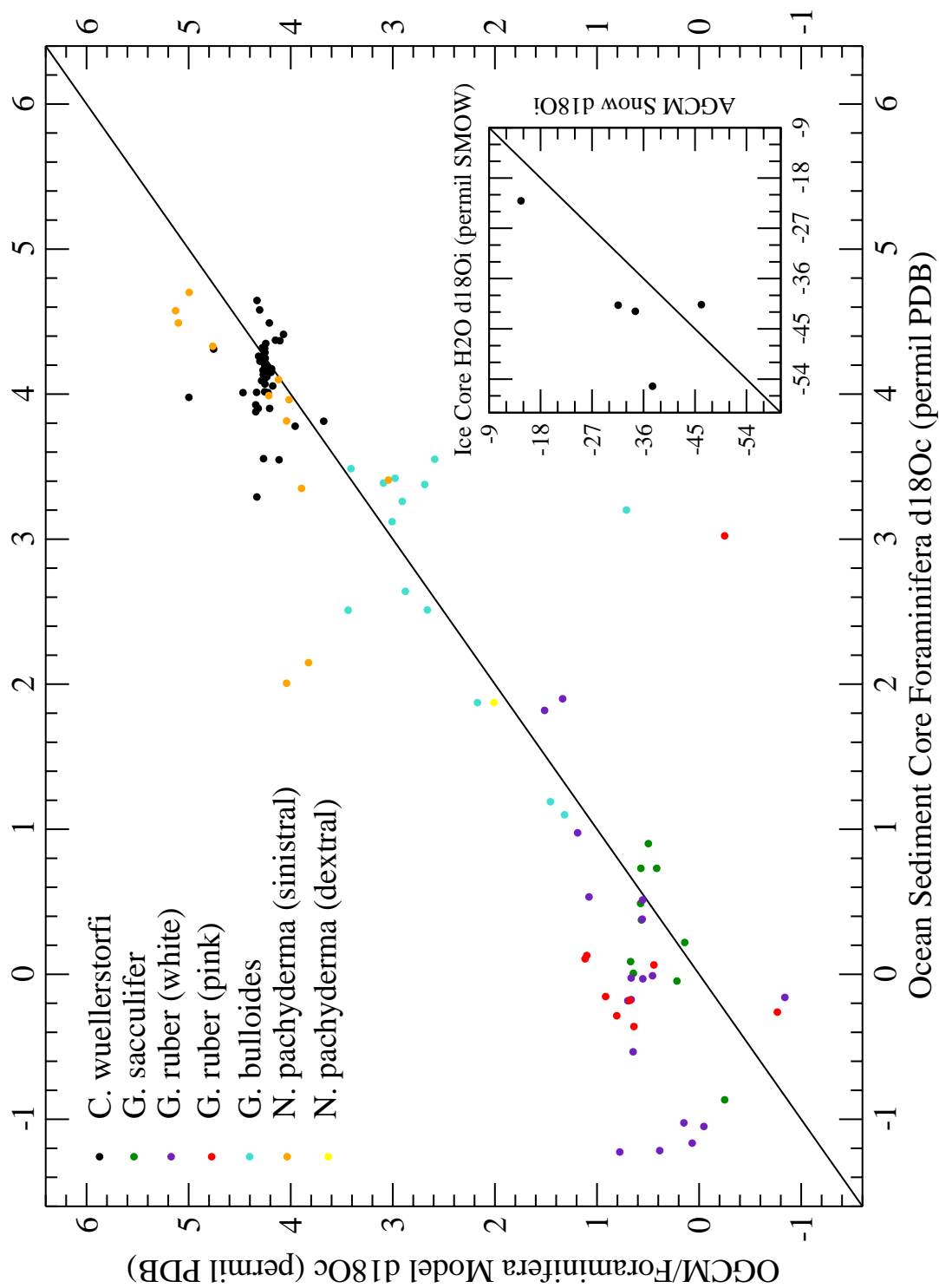


Figure 6.47: LGM OGCM/foraminifera model annual $\delta^{18}\text{O}_c$ (‰ PDB) versus ocean sediment core foraminifera $\delta^{18}\text{O}_c$ (‰ PDB); and inset) LGM AGCM annual snow $\delta^{18}\text{O}_i$ (‰ SMOW) versus ice core H₂O $\delta^{18}\text{O}$ (‰ SMOW).

$$\begin{aligned}
&\text{LGM annual mean OGCM } \delta^{18}\text{O}_w \text{ from mass-weighted} \\
&\quad \text{averaging all grid boxes, } ({}^L\bar{\delta}_w^M)_{\text{final}} = 1.242 \\
&\text{Initially set LGM mass-weighted mean OGCM } \delta^{18}\text{O}_w, {}^L\bar{\delta}_w^M = 1.250 \\
&\quad \Rightarrow \text{Numerical error, } ({}^L\bar{\delta}_w^M)_{\text{final}} - {}^L\bar{\delta}_w^M = -0.008
\end{aligned}$$

Table 6.30: Estimate of numerical error using LGM mean OGCM $\delta^{18}\text{O}_w$ from mass-weighted averaging all grid boxes.

$$\begin{aligned}
&\text{LGM annual mean OGCM/foraminifera model } C. \textit{wuellerstorfi} \delta^{18}\text{O}_c \text{ from} \\
&\quad \text{mass-weighted averaging grid boxes where cores, } {}^L\delta_c^M = 4.258 \\
&\quad \text{LGM mean } C. \textit{wuellerstorfi} \delta^{18}\text{O}_c \text{ from} \\
&\quad \text{mass-weighted averaging cores (by grid box), } {}^L\delta_c^R = 4.110 \\
&\quad \Rightarrow \text{LGM mass-weighted mean } C. \textit{wuellerstorfi} \delta^{18}\text{O}_c \text{ mismatch of} \\
&\quad \text{OGCM/foraminifera model compared to cores, } ({}^L\delta_c^M - {}^L\delta_c^R) - ({}^L\bar{\delta}_w^M - {}^L\bar{\delta}_w^R) \\
&\quad \quad \quad = 0.148 - 0.250 = -0.102
\end{aligned}$$

Table 6.31: Calculation of LGM mass-weighted mean *C. wuellerstorfi* $\delta^{18}\text{O}_c$ mismatch (‰ PDB) of OGCM/foraminifera model compared to ocean sediment cores.

means. Table 6.30 does this estimate. The magnitude of the numerical error is again remarkably small, especially considering the long duration of the run and the mass-weighted averaging.

Tables 6.31 to 6.37 are the calculations of mean $\delta^{18}\text{O}_c$ mismatch of the OGCM/foraminifera model compared to cores for each of the seven foraminifera species. Table 6.38 is the calculation of mean $\delta^{18}\text{O}_i$ mismatch of the AGCM compared to cores. In all, the discussed 0.25‰ that the LGM mean ocean $\delta^{18}\text{O}_w$ initially set in the OGCM was too high by is subtracted off to correct for this non-inherent bias. When this is done, the magnitude of the mismatch is borderline (i.e., $\approx 0.1\%$) for *C. wuellerstorfi*, *G. sacculifer*, *G. ruber* (pink), and *N. pachyderma* (dextral) but significant for *G. ruber* (white), *G. bulloides*, *N. pachyderma* (sinistral), and snow/ice. For the planktonic foraminifera species though, the foraminifera model biases discussed in Section 6.4.3 for PD by itself call these results into question for the LGM by itself as well (but not for LGM – PD).

$$\begin{array}{l} \text{LGM annual mean OGCM/foraminifera model } G. \text{ sacc. } \delta^{18}\text{O}_c \text{ from} \\ \text{mass-weighted averaging grid boxes where cores, } {}^L\delta_c^M = 0.406 \end{array}$$

$$\begin{array}{l} \text{LGM mean } G. \text{ sacc. } \delta^{18}\text{O}_c \text{ from} \\ \text{mass-weighted averaging cores (by grid box), } {}^L\delta_c^R = 0.265 \end{array}$$

$$\begin{array}{l} \Rightarrow \text{LGM mass-weighted mean } G. \text{ sacc. } \delta^{18}\text{O}_c \text{ mismatch of} \\ \text{OGCM/foraminifera model compared to cores, } ({}^L\delta_c^M - {}^L\delta_c^R) - ({}^L\bar{\delta}_w^M - {}^L\bar{\delta}_w^R) \\ = 0.141 - 0.250 = -0.101 \end{array}$$

Table 6.32: Calculation of LGM mass-weighted mean *G. sacculifer* $\delta^{18}\text{O}_c$ mismatch (% PDB) of OGCM/foraminifera model compared to ocean sediment cores.

$$\begin{array}{l} \text{LGM annual mean OGCM/foraminifera model } G. \text{ ruber (w) } \delta^{18}\text{O}_c \text{ from} \\ \text{mass-weighted averaging grid boxes where cores, } {}^L\delta_c^M = 0.563 \end{array}$$

$$\begin{array}{l} \text{LGM mean } G. \text{ ruber (w) } \delta^{18}\text{O}_c \text{ from} \\ \text{mass-weighted averaging cores (by grid box), } {}^L\delta_c^R = -0.066 \end{array}$$

$$\begin{array}{l} \Rightarrow \text{LGM mass-weighted mean } G. \text{ ruber (w) } \delta^{18}\text{O}_c \text{ mismatch of} \\ \text{OGCM/foraminifera model compared to cores, } ({}^L\delta_c^M - {}^L\delta_c^R) - ({}^L\bar{\delta}_w^M - {}^L\bar{\delta}_w^R) \\ = 0.629 - 0.250 = 0.379 \end{array}$$

Table 6.33: Calculation of LGM mass-weighted mean *G. ruber* (white) $\delta^{18}\text{O}_c$ mismatch (% PDB) of OGCM/foraminifera model compared to ocean sediment cores.

$$\begin{array}{l} \text{LGM annual mean OGCM/foraminifera model } G. \text{ ruber (p) } \delta^{18}\text{O}_c \text{ from} \\ \text{mass-weighted averaging grid boxes where cores, } {}^L\delta_c^M = 0.529 \end{array}$$

$$\begin{array}{l} \text{LGM mean } G. \text{ ruber (p) } \delta^{18}\text{O}_c \text{ from} \\ \text{mass-weighted averaging cores (by grid box), } {}^L\delta_c^R = 0.179 \end{array}$$

$$\begin{array}{l} \Rightarrow \text{LGM mass-weighted mean } G. \text{ ruber (p) } \delta^{18}\text{O}_c \text{ mismatch of} \\ \text{OGCM/foraminifera model compared to cores, } ({}^L\delta_c^M - {}^L\delta_c^R) - ({}^L\bar{\delta}_w^M - {}^L\bar{\delta}_w^R) \\ = 0.350 - 0.250 = 0.100 \end{array}$$

Table 6.34: Calculation of LGM mass-weighted mean *G. ruber* (pink) $\delta^{18}\text{O}_c$ mismatch (% PDB) of OGCM/foraminifera model compared to ocean sediment cores.

$$\begin{array}{l} \text{LGM annual mean OGCM/foraminifera model } G. \text{ bull. } \delta^{18}\text{O}_c \text{ from} \\ \text{mass-weighted averaging grid boxes where cores, } {}^L\delta_c^M = 2.426 \end{array}$$

$$\begin{array}{l} \text{LGM mean } G. \text{ bull. } \delta^{18}\text{O}_c \text{ from} \\ \text{mass-weighted averaging cores (by grid box), } {}^L\delta_c^R = 2.702 \end{array}$$

$$\begin{array}{l} \Rightarrow \text{LGM mass-weighted mean } G. \text{ bull. } \delta^{18}\text{O}_c \text{ mismatch of} \\ \text{OGCM/foraminifera model compared to cores, } ({}^L\delta_c^M - {}^L\delta_c^R) - ({}^L\bar{\delta}_w^M - {}^L\bar{\delta}_w^R) \\ = -0.276 - 0.250 = -0.526 \end{array}$$

Table 6.35: Calculation of LGM mass-weighted mean *G. bulloides* $\delta^{18}\text{O}_c$ mismatch (‰ PDB) of OGCM/foraminifera model compared to ocean sediment cores.

$$\begin{array}{l} \text{LGM annual mean OGCM/foraminifera model } N. \text{ pachy. (s) } \delta^{18}\text{O}_c \text{ from} \\ \text{mass-weighted averaging grid boxes where cores, } {}^L\delta_c^M = 4.081 \end{array}$$

$$\begin{array}{l} \text{LGM mean } N. \text{ pachy. (s) } \delta^{18}\text{O}_c \text{ from} \\ \text{mass-weighted averaging cores (by grid box), } {}^L\delta_c^R = 3.535 \end{array}$$

$$\begin{array}{l} \Rightarrow \text{LGM mass-weighted mean } N. \text{ pachy. (s) } \delta^{18}\text{O}_c \text{ mismatch of} \\ \text{OGCM/foraminifera model compared to cores, } ({}^L\delta_c^M - {}^L\delta_c^R) - ({}^L\bar{\delta}_w^M - {}^L\bar{\delta}_w^R) \\ = 0.546 - 0.250 = 0.296 \end{array}$$

Table 6.36: Calculation of LGM mass-weighted mean *N. pachyderma* (sinistral) $\delta^{18}\text{O}_c$ mismatch (‰ PDB) of OGCM/foraminifera model compared to ocean sediment cores.

$$\begin{array}{l} \text{LGM annual mean OGCM/foraminifera model } N. \text{ pachy. (d) } \delta^{18}\text{O}_c \text{ from} \\ \text{mass-weighted averaging grid boxes where cores, } {}^L\delta_c^M = 2.007 \end{array}$$

$$\begin{array}{l} \text{LGM mean } N. \text{ pachy. (d) } \delta^{18}\text{O}_c \text{ from} \\ \text{mass-weighted averaging cores (by grid box), } {}^L\delta_c^R = 1.873 \end{array}$$

$$\begin{array}{l} \Rightarrow \text{LGM mass-weighted mean } N. \text{ pachy. (d) } \delta^{18}\text{O}_c \text{ mismatch of} \\ \text{OGCM/foraminifera model compared to cores, } ({}^L\delta_c^M - {}^L\delta_c^R) - ({}^L\bar{\delta}_w^M - {}^L\bar{\delta}_w^R) \\ = 0.134 - 0.250 = -0.116 \end{array}$$

Table 6.37: Calculation of LGM mass-weighted mean *N. pachyderma* (dextral) $\delta^{18}\text{O}_c$ mismatch (‰ PDB) of OGCM/foraminifera model compared to ocean sediment cores.

$$\begin{array}{l} \text{LGM annual mean AGCM snow/ice } \delta^{18}\text{O}_i \text{ from} \\ \text{mass-weighted averaging grid boxes where cores, } {}^L\delta_i^M = -17.69 \end{array}$$

$$\begin{array}{l} \text{LGM mean snow/ice } \delta^{18}\text{O}_i \text{ from} \\ \text{mass-weighted averaging cores (by grid box), } {}^L\delta_i^R = -25.19 \end{array}$$

$$\begin{array}{l} \Rightarrow \text{LGM mass-weighted mean snow/ice } \delta^{18}\text{O}_i \text{ mismatch of} \\ \text{AGCM compared to cores, } ({}^L\delta_i^M - {}^L\delta_i^R) - ({}^L\bar{\delta}_w^M - {}^L\bar{\delta}_w^R) \\ \qquad \qquad \qquad = 7.50 - 0.25 = 7.25 \end{array}$$

Table 6.38: Calculation of LGM mass-weighted mean snow/ice $\delta^{18}\text{O}_i$ (‰ SMOW) mismatch of AGCM compared to ice cores.

6.7 LGM – PD of Simulations

The preceding sections of this chapter indicate that some confidence in the variables of the LGM – PD of simulations is warranted. Since they affect foraminifera $\delta^{18}\text{O}_c$ and precipitation $\delta^{18}\text{O}_i$, as outlined in Section 6.2.2, and since they are a start at addressing the next chapter’s questions of the LGM, Figures 6.48 to 6.55 are the map comparison figures of bottom ocean $\delta^{18}\text{O}_w$, bottom ocean in situ temperature, surface ocean $\delta^{18}\text{O}_w$, surface ocean in situ temperature, surface ocean salinity, sea ice concentration, precipitation $\delta^{18}\text{O}$, and precipitation rate.

Figure 6.48 is the map comparison figure for LGM – PD bottom OGCM $\delta^{18}\text{O}_w$. Note the shift of scales between the LGM (“a”) and PD (“b”) CGCM grid box maps by the $\approx 1.2\text{‰}$ difference between the LGM and PD initially set mean OGCM $\delta^{18}\text{O}_w$. This is apparent in the LGM – PD (“c”) CGCM grid box map as well. Further note that to correctly interpret them, the LGM and LGM – PD maps should have the discussed 0.25‰ that the LGM mean ocean $\delta^{18}\text{O}_w$ initially set in the OGCM was too high by subtracted from them. In any case, the LGM lack of low $\delta^{18}\text{O}_w$ water in the Arctic Ocean and in shallow enclosed basins due to blocking of rivers and removal of basins by continental glaciers and lowered sea level is apparent. There is also an indication of North Atlantic Deep Water (NADW) reaching farther south at the LGM.

Figure 6.49 is the map comparison figure for bottom OGCM in situ temperature. That the LGM bottom ocean was generally colder than PD is apparent, with NADW

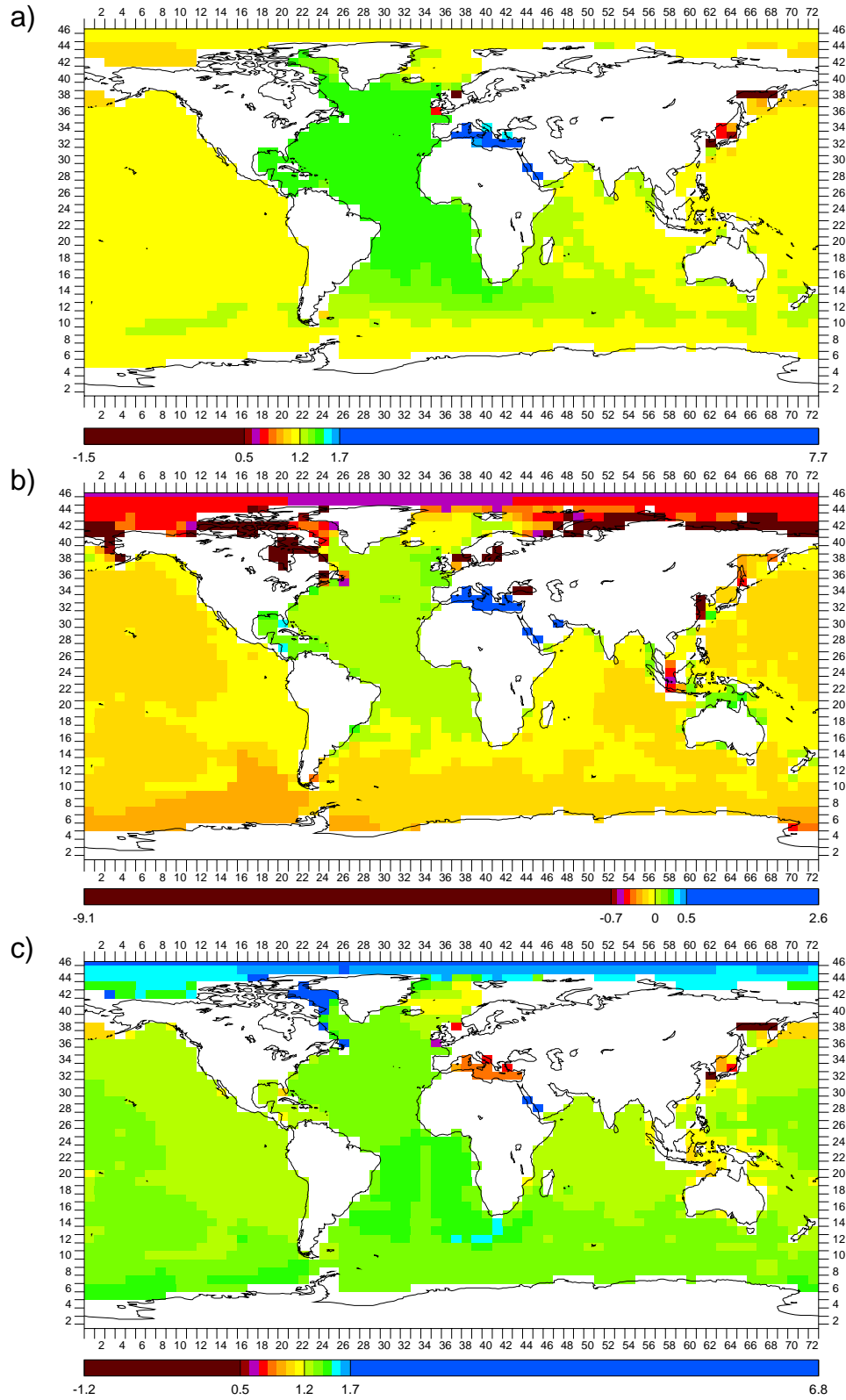


Figure 6.48: CGCM grid box maps of annual bottom OGCM $\delta^{18}\text{O}_w$ (‰ SMOW) for: a) LGM; b) PD; and c) LGM – PD. Note shift of scale of 1.2‰ between a) and b) and the effect in c).

particularly colder. There is again also an indication of NADW reaching farther south at the LGM (noting that NADW then is still warmer than Antarctic Bottom Water).

Figure 6.50 is the map comparison figure for surface OGCM $\delta^{18}\text{O}_w$. As in the case of bottom OGCM $\delta^{18}\text{O}_w$, note the shift of scale of 1.2‰ between the LGM and PD maps, the effect in the LGM – PD map, and that for correct interpretation 0.25‰ should be subtracted from the LGM and LGM – PD maps. The LGM lack of low $\delta^{18}\text{O}_w$ water in the Arctic Ocean and in shallow enclosed basins due to blocking of rivers and removal of basins by continental glaciers and lowered sea level is again apparent. Otherwise, the LGM global pattern is very similar to PD.

Figure 6.51 is the map comparison figure for surface OGCM in situ temperature. That the LGM surface ocean was generally colder than PD is apparent. This is particularly pronounced in the tropical Atlantic, followed by the northern North Atlantic, the north Pacific, and then the tropical Indian and the tropical Pacific.

Figure 6.52 is the map comparison figure for surface OGCM salinity. Note the shift of scales between the LGM and PD maps by the ≈ 1 g/kg difference between the LGM and PD initially set mean OGCM salinity (see Section 3.3.4). This is apparent in the LGM – PD map as well. Similarly to surface OGCM $\delta^{18}\text{O}_w$, the LGM lack of fresher water in the Arctic Ocean and in shallow enclosed basins due to blocking of rivers and removal of basins by continental glaciers and lowered sea level is apparent, but otherwise the LGM global pattern is very similar to PD. Further, for both PD and LGM the pattern closely correlates to that for surface OGCM $\delta^{18}\text{O}_w$ (Figure 6.50).

Figure 6.53 is the map comparison figure for OGCM sea ice concentration. The LGM equatorward general increase in sea ice in both hemispheres is apparent. Note the indication of the LGM retreat of the North Atlantic Drift.

Figure 6.54 is the map comparison figure for AGCM precipitation $\delta^{18}\text{O}$. The most significant changes at the LGM are decreases over the east Laurentide and Fennoscandian continental glaciers and over east Europe/west Asia. Note that at the LGM there are decreases over the interior of Greenland but there are increases over much of the interior of Antarctica; vice versa for the coasts.

Figure 6.55 is the map comparison figure for AGCM precipitation rate. At the LGM there seems to be decreased precipitation over the Laurentide and Fennoscandian continental glaciers but little change over the interiors of Greenland and Antarc-

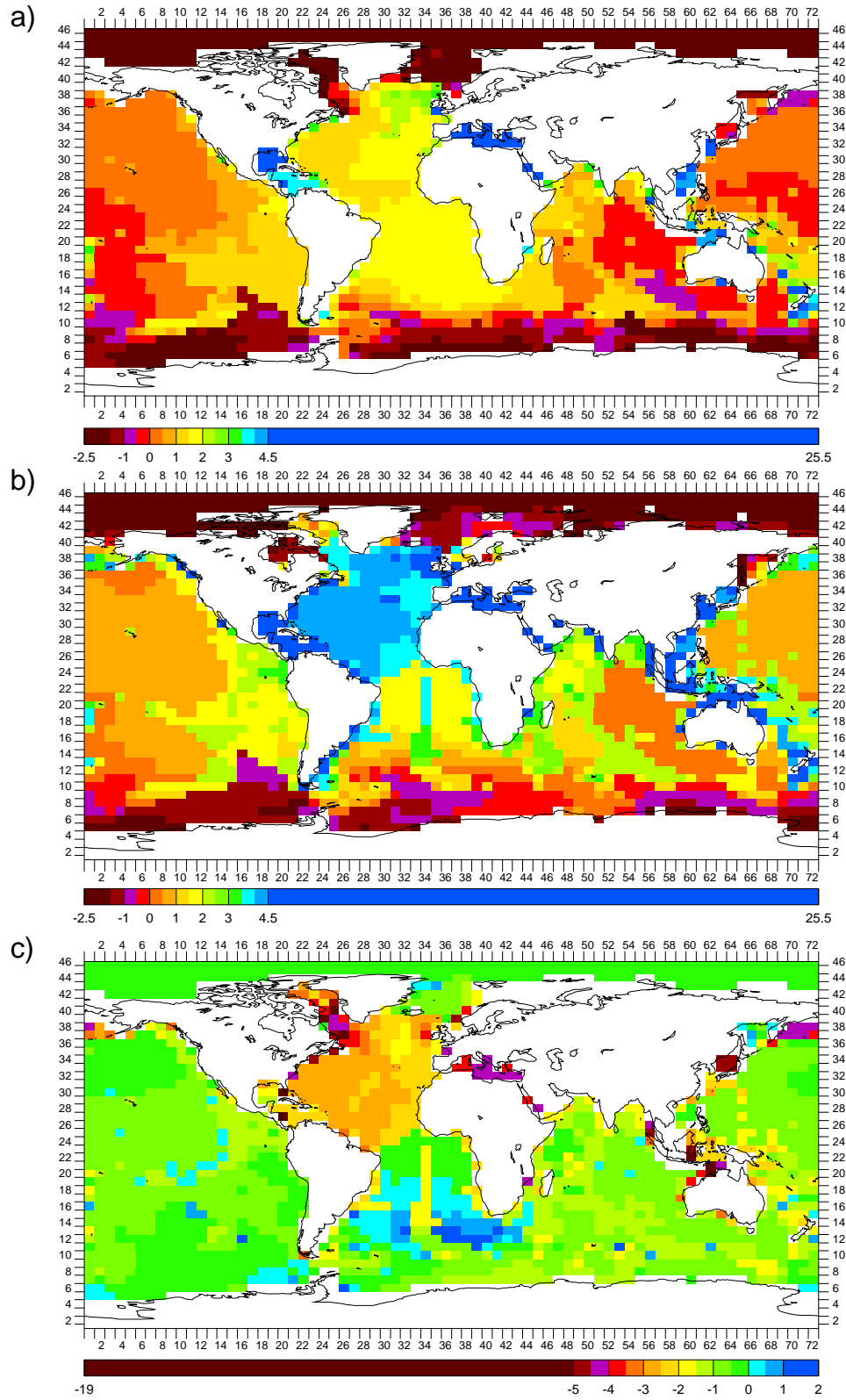


Figure 6.49: CGCM grid box maps of annual bottom OGCM in situ temperature (C) for: a) LGM; b) PD; and c) LGM – PD

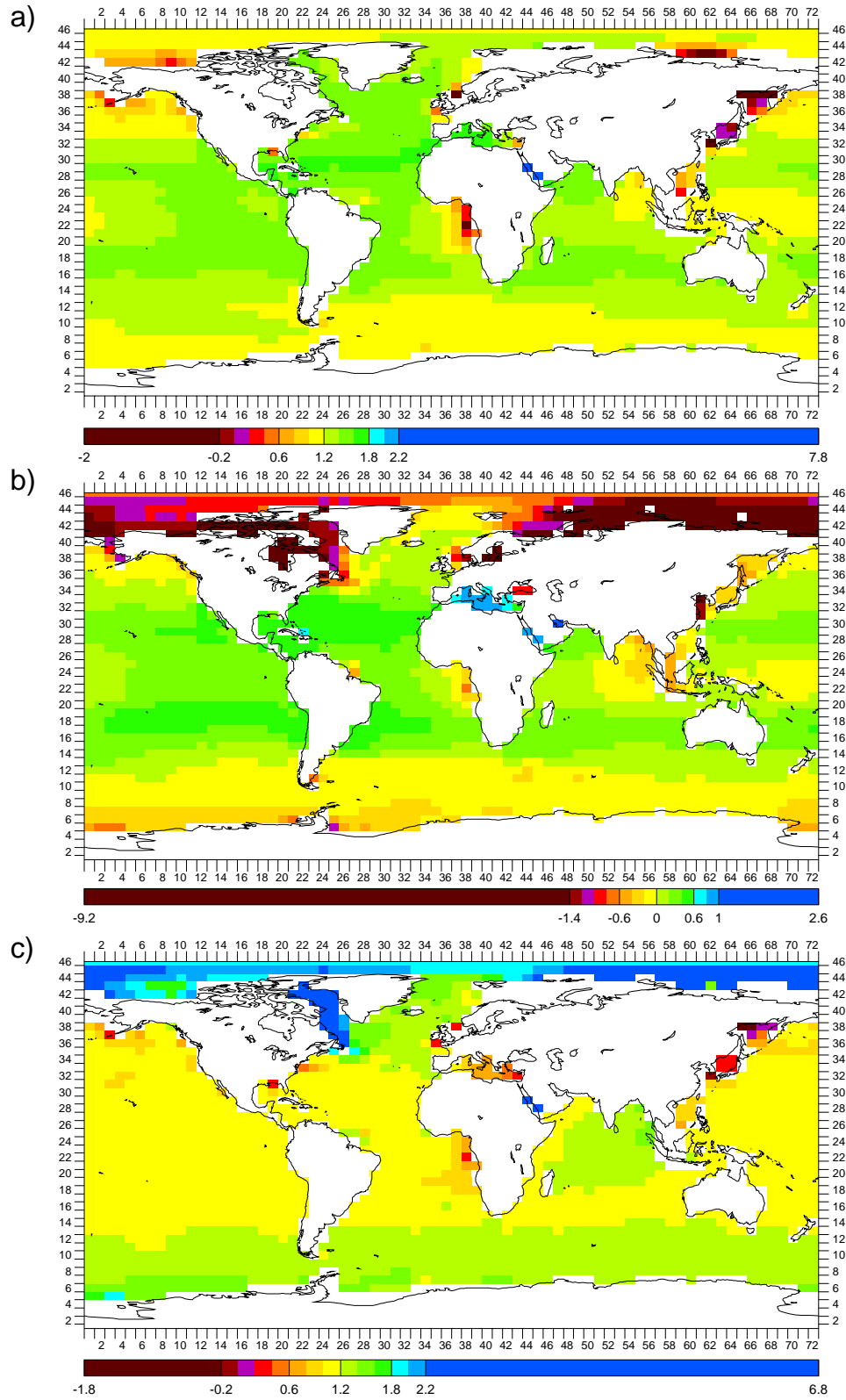


Figure 6.50: CGCM grid box maps of annual surface OGCM $\delta^{18}\text{O}_w$ (‰ SMOW) for: a) LGM; b) PD; and c) LGM – PD. Note shift of scale of 1.2‰ between a) and b) and the effect in c).

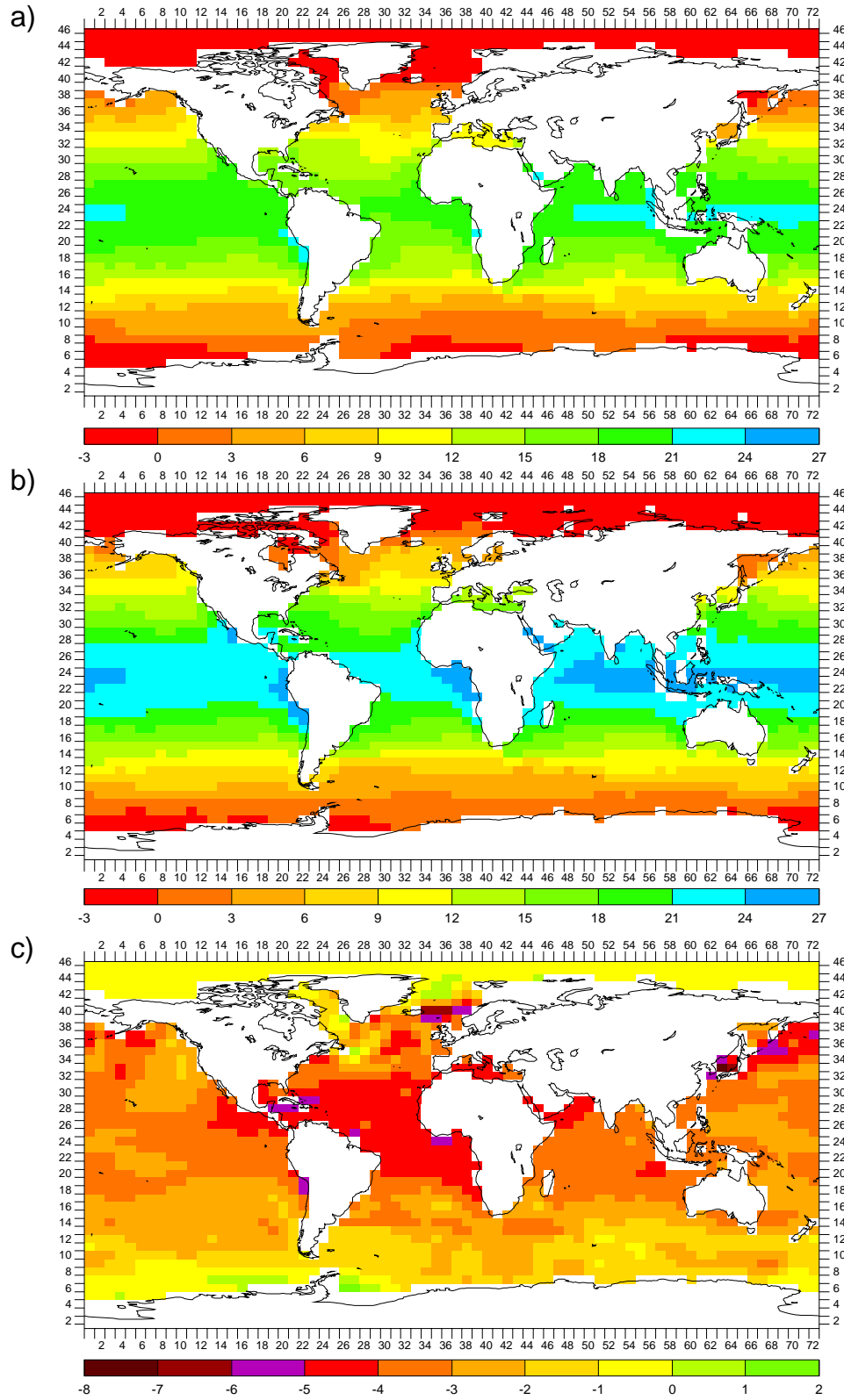


Figure 6.51: CGCM grid box maps of annual surface OGCM in situ temperature (C) for: a) LGM; b) PD; and c) LGM – PD

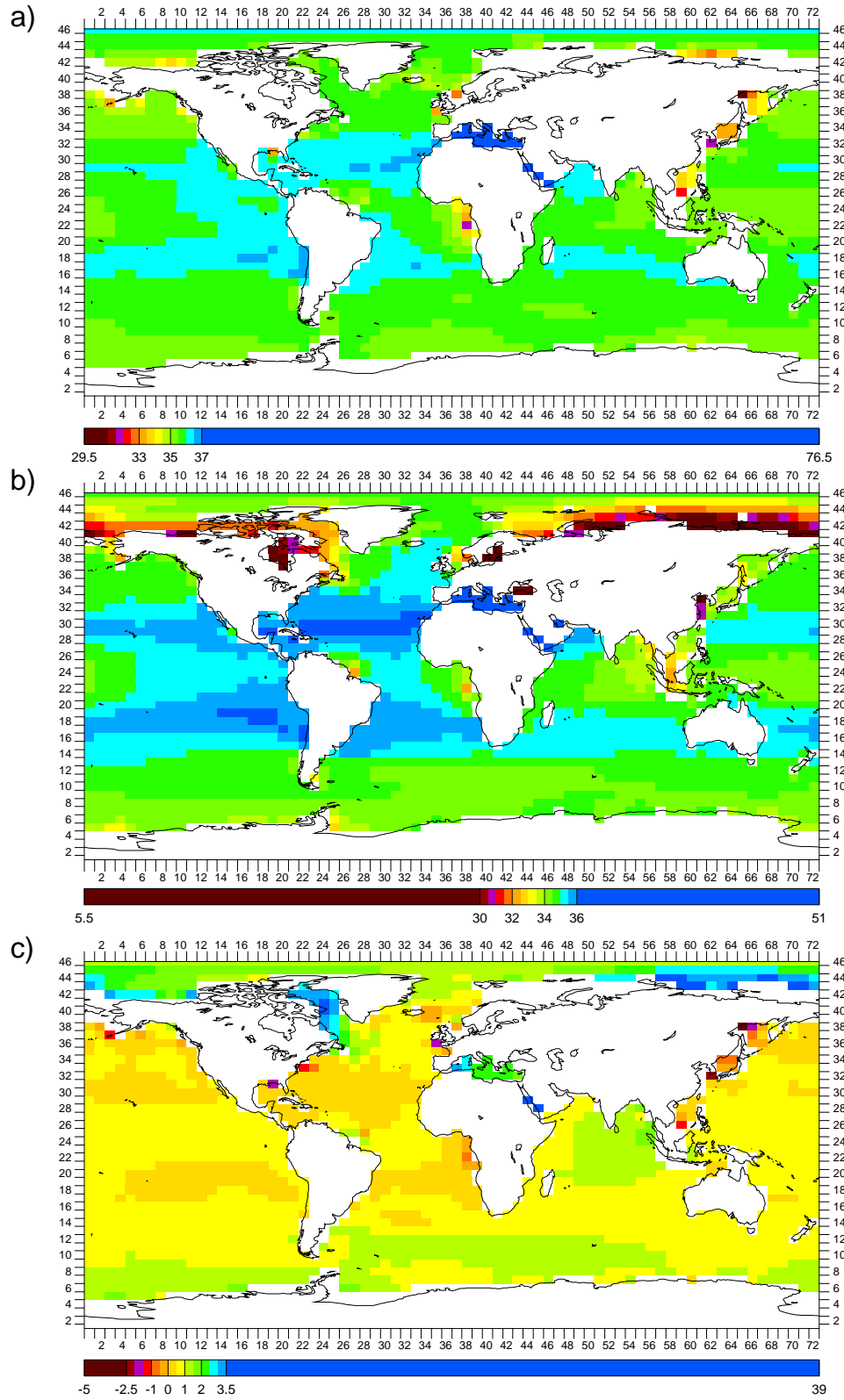


Figure 6.52: CGCM grid box maps of annual surface OGCM salinity (g/kg) for: a) LGM; b) PD; and c) LGM – PD. Note shift of scale of 1 g/kg between a) and b) and the effect in c).

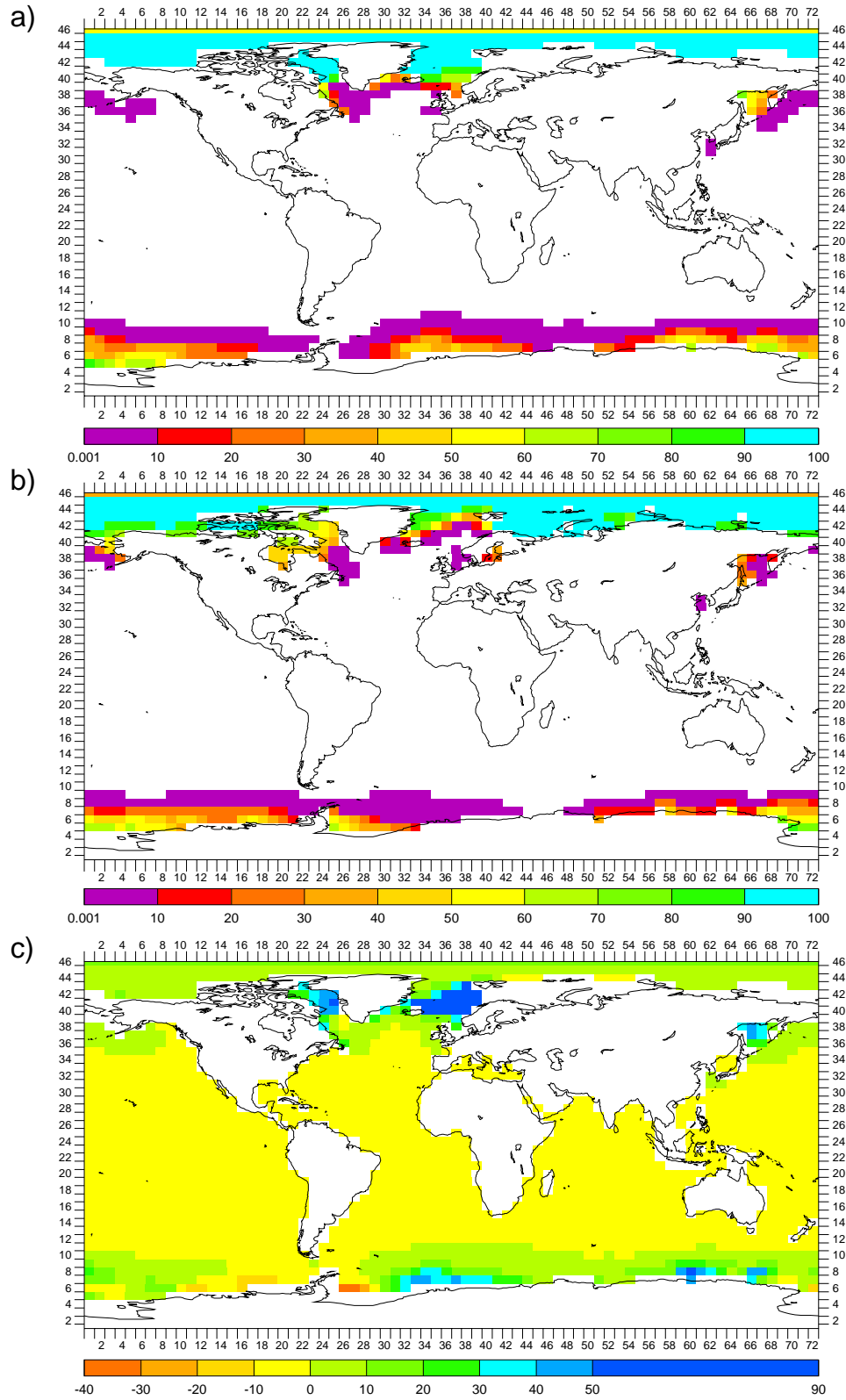


Figure 6.53: CGCM grid box maps of annual OGCM sea ice concentration (%) for: a) LGM; b) PD; and c) LGM – PD

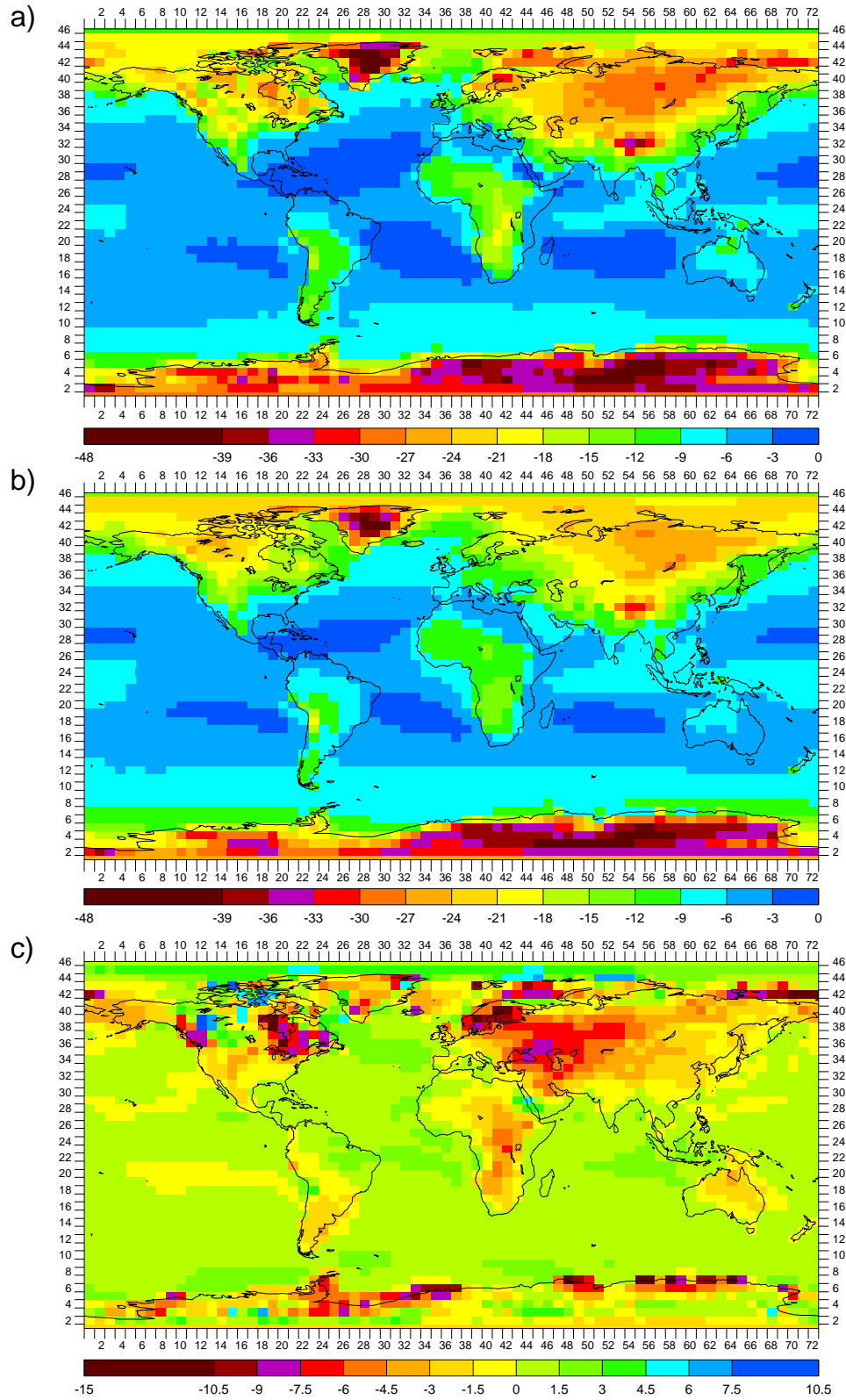


Figure 6.54: CGCM grid box maps of annual AGCM precipitation $\delta^{18}\text{O}$ (‰ SMOW) for: a) LGM; b) PD; and c) LGM – PD

tica.

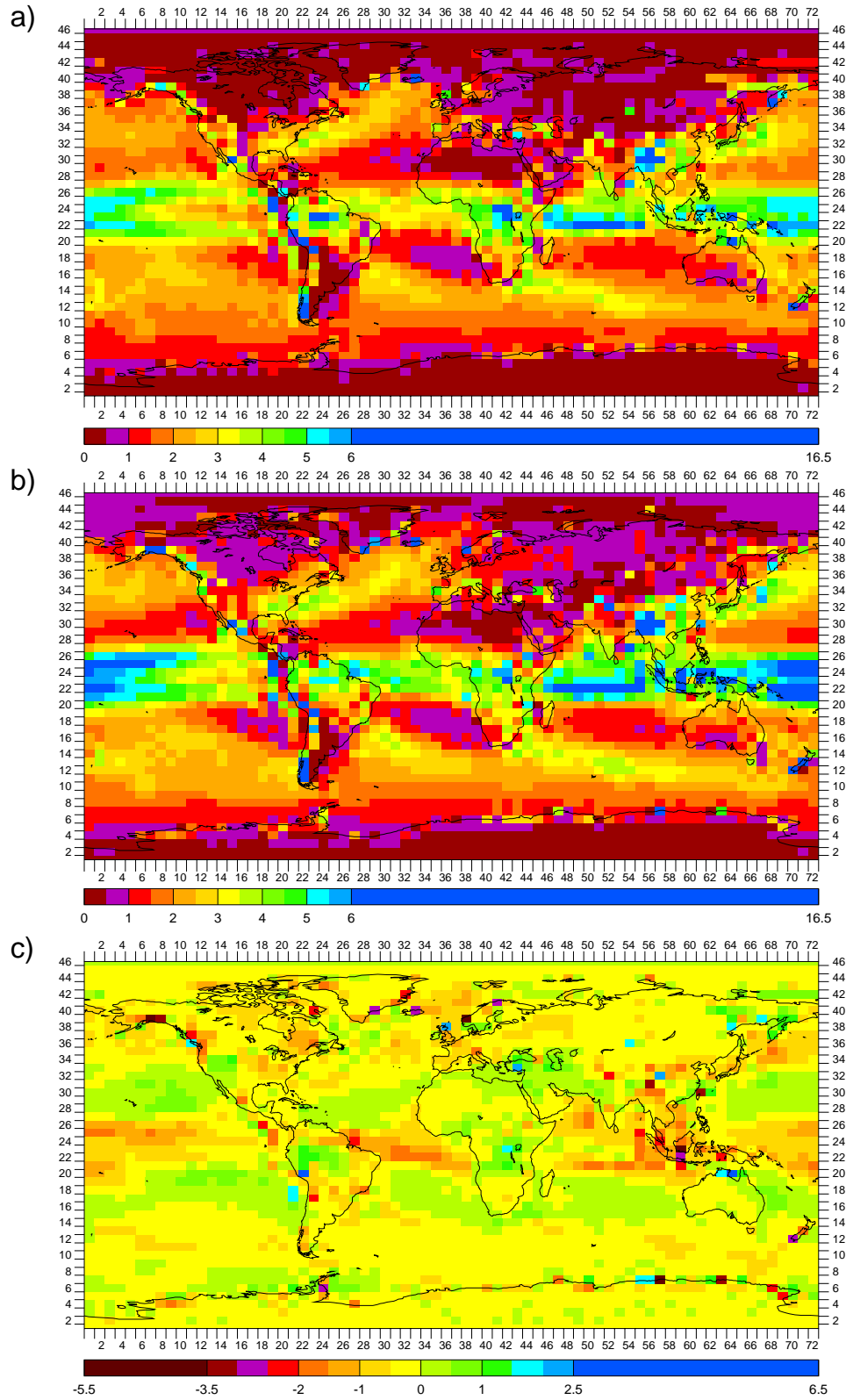


Figure 6.55: CGCM grid box maps of annual AGCM precipitation rate (mm/day) for: a) LGM; b) PD; and c) LGM – PD

Chapter 7

Addressing Questions of the LGM

7.1 Mean Ocean $\delta^{18}\text{O}_w$

The LGM – PD change in mean ocean $\delta^{18}\text{O}_w$ is an important quantity to know well. As discussed, it is positive, with the mean ocean $\delta^{18}\text{O}_w$ greater at the LGM¹ due to the extra ≈ 120 m of water from the ocean that was locked up in the increased continental glaciers then — having gotten there as precipitation, this water was depleted in ^{18}O , making the remaining ocean water enriched in ^{18}O . First then, knowing the LGM – PD mean ocean $\delta^{18}\text{O}_w$ well provides information about the LGM – PD change in continental glaciers. Second, and as described in this work, determining the LGM – PD change in ocean temperatures from ocean sediment core foraminifera $\delta^{18}\text{O}_c$ requires subtracting off the LGM – PD mean ocean $\delta^{18}\text{O}_w$. While a useful first-order calculation, this does not account for the $\delta^{18}\text{O}_w$ variation about this mean at the core location. A CGCM can account for local variation and give ocean temperatures directly but as discussed it too needs the LGM – PD mean ocean $\delta^{18}\text{O}_w$ for its initial settings. As a final example, the Dole effect is defined as the difference between the $\delta^{18}\text{O}$ of atmospheric² O_2 and the contemporaneous mean ocean $\delta^{18}\text{O}_w$. Changes in the Dole effect with time, such as LGM – PD, reflect changes in interesting global

¹As discussed in Section 6.2.2 the PD mean ocean $\delta^{18}\text{O}_w$ is confidently assumed to be 0‰ so the LGM – PD mean ocean $\delta^{18}\text{O}_w$ is numerically just the LGM mean ocean $\delta^{18}\text{O}_w$.

²Atmospheric O_2 is well mixed and as mentioned in Section 2.2.3 paleosamples of it typically come from ice cores.

botanic (as well as hydrologic) processes (e.g., Bender et al. 1994). Thus, determining the LGM – PD mean ocean $\delta^{18}\text{O}_w$, as was done in this work (Section 6.5.1), is an important question of the LGM to address.

A widely-cited estimate of LGM – PD mean ocean $\delta^{18}\text{O}_w$ — and the one used in this work to initially set the mean ocean $\delta^{18}\text{O}_w$ in the OGCM — is the 1.25‰ (SMOW) stated in Guilderson et al. 1994. This was calculated using: 1) a factor (.011‰/m) from Fairbanks and Matthews 1978 relating the change in mean ocean $\delta^{18}\text{O}_w$ to the change in sea level (thus glacier ice volume); and 2) an LGM – PD sea level estimate from Fairbanks 1989. Both of these were from work with coral terraces in Barbados. 1.25‰ was indicated to be a maximum value and was from globally extrapolating from a single surface location — where there are probably significant but unknown local $\delta^{18}\text{O}_w$ changes about the LGM – PD mean ocean $\delta^{18}\text{O}_w$. These and its other shortcomings are reviewed in Schrag et al. 2002.

A more recent estimate of LGM – PD mean ocean $\delta^{18}\text{O}_w$ is the 1.0‰ (SMOW) arrived at in Schrag et al. 1996, Adkins and Schrag 2001, and Schrag et al. 2002. In a technique analogous to borehole thermometry, these used the $\delta^{18}\text{O}$ of pore water samples down ocean sediment cores and fit this $\delta^{18}\text{O}$ profile using a diffusion model. This model had as its top boundary condition the temporal variation of bottom ocean $\delta^{18}\text{O}_w$, which was from a composite benthic foraminiferal $\delta^{18}\text{O}$ curve spliced at around 20 ka with the later coral-derived record of sea level change. Given the value of the diffusion constant all that can be seen in a $\delta^{18}\text{O}$ profile are a peak, assumed to be from the LGM, and the shift to the PD value. After repeated trials with different values of the LGM – PD $\delta^{18}\text{O}_w$ change in the model top boundary condition, the one that resulted in the best fit of the profile was taken as the LGM – PD change in the bottom ocean $\delta^{18}\text{O}_w$ at that location. The uncertainty given for this was just a visually acceptable range of “best fit”. The estimate of the LGM – PD mean ocean $\delta^{18}\text{O}_w$ of 1.0 ± 0.1 ‰ was from globally extrapolating from single bottom ocean locations, using various methods and making certain assumptions (see Adkins and Schrag 2001 and Schrag et al. 1996).

While the LGM – PD mean ocean $\delta^{18}\text{O}_w$ value determined by Schrag et al. from ocean sediment core pore water is strikingly the same as that calculated in this work and it is tempting to declare them in support of each other, they could be just

coincidentally the same. Since the Schrag et al. work used six spatially-separated cores, albeit all in the Atlantic (four in the North Atlantic), a good test is to see how the LGM – PD bottom ocean $\delta^{18}\text{O}_w$ determined from the pore water of each core compares to the LGM – PD bottom OGCM $\delta^{18}\text{O}_w$ at the same locations. Figure 7.1 then, is the CGCM grid box maps of LGM – PD bottom ocean $\delta^{18}\text{O}_w$ from the OGCM, pore water, and OGCM minus pore water. Additionally, Figure 7.2 is the corresponding model/data plot³. The figures show that the bottom OGCM $\delta^{18}\text{O}_w$ is too high compared to that from pore water at all core locations. However, this is without correcting for the 0.25‰ that the LGM mean ocean $\delta^{18}\text{O}_w$ initially set in the OGCM was too high by, as discussed in Section 6.2.2 and calculated in Section 6.5.1. Still, when this is subtracted off the northernmost four OGCM values are about 0.25‰ too high and the next northernmost is about 0.5‰ too high. Only the southernmost then matches reasonably well at only about 0.1‰ too low. The LGM – PD mass-weighted⁴ mean bottom OGCM $\delta^{18}\text{O}_w$ at the core locations is 1.38‰ and that from the pore water is 0.82‰, a mismatch of 0.56‰.

There are a couple of less-serious possibilities for the significant mismatches. One is that they are due to the LGM – PD bottom OGCM $\delta^{18}\text{O}_w$ not having reached equilibrium at the core locations. However, at all core locations the LGM – PD bottom OGCM $\delta^{18}\text{O}_w$ was leveling off by the averaging period of the runs (see Section 6.1) or was actually increasing, i.e., it seems the mismatches are not going to diminish. Another possibility is the difference in the depth of the bottom between the real ocean and the OGCM at these locations. The OGCM bottom is the result of binning into one of thirteen unequally-thick levels (see Section 3.2.1) the mean depth of 5° x 4° boxes of the real ocean (worse, a digitized approximation of it). The depth range of a bottom OGCM grid box where a core is located may thus not even encompass the real depth of the core. In fact, this is true at five of the six core locations: in two, the bottom OGCM grid box is one level deeper, in two it is one level shallower, and in one it is two levels shallower (no change between LGM and PD). However, in the locations where the bottom OGCM grid box is deeper, the LGM – PD $\delta^{18}\text{O}_w$ of the OGCM grid box above it, which corresponds to the core

³A “model/data plot” as described in Section 6.2.2.

⁴See Section 6.2.2.

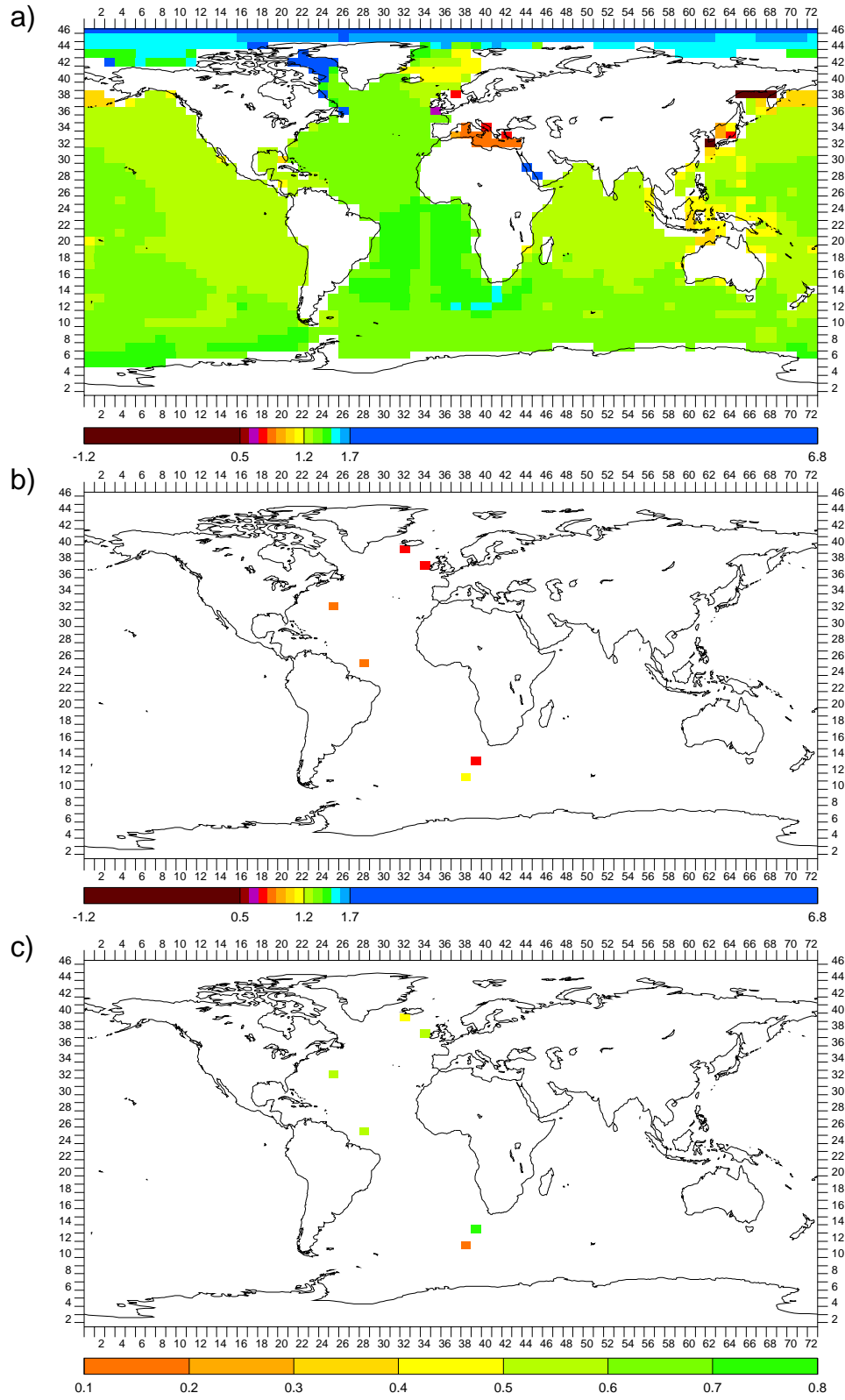


Figure 7.1: CGCM grid box maps of LGM – PD annual bottom ocean $\delta^{18}\text{O}_w$ (‰ SMOW) for: a) OGCM; b) pore water; and c) OGCM minus pore water.

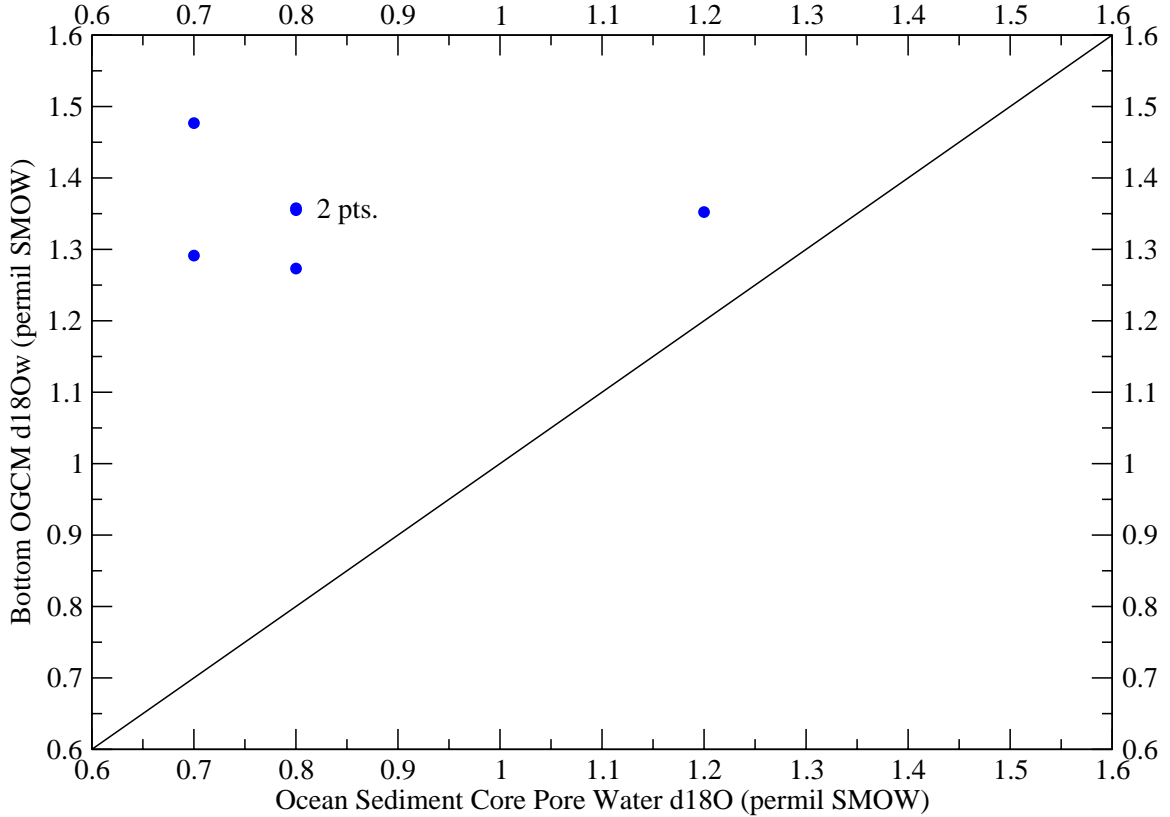


Figure 7.2: LGM – PD annual bottom OGCM $\delta^{18}\text{O}_w$ versus ocean sediment core pore water $\delta^{18}\text{O}$ (‰ SMOW).

depth, is no more than 0.1‰ lower (where the bottom OGCM grid box is shallower there is no core-depth-corresponding OGCM grid box available).

The two more-serious possibilities for the significant mismatches are that the bottom ocean $\delta^{18}\text{O}_w$ values from the ocean sediment core pore water technique are wrong or those from the OGCM are. The former is not out of the question, given the indirectness and assumptions of the technique. Again for example, it (like the technique using Barbados corals) suffers from globally extrapolating from a single location using simplistic gross calculations and assumptions (in this work, the LGM – PD mean ocean $\delta^{18}\text{O}_w$ was determined using ocean sediment cores from numerous locations and globally extrapolating in a physically-consistent way by using the OGCM). Further, the pore water results have not otherwise been directly well-verified. The bottom ocean $\delta^{18}\text{O}_w$ values from the CGCM may also be wrong. In fact, as shown in Section 7.3 ahead, the CGCM has a North Atlantic meridional overturning circulation

at the LGM that is significantly increased compared to PD, which is inconsistent with several proxies. This may be bringing too much higher $\delta^{18}\text{O}$ water from the surface North Atlantic (see Figure 6.50) down to the bottom there at the LGM and causing the discussed mismatches. In any case, the LGM – PD mean ocean $\delta^{18}\text{O}_w$ determined by Schrag et al. from ocean sediment core pore water and that calculated in this work may quite possibly be just coincidentally the same.

7.2 CLIMAP Tropical SSTs

CLIMAP (CLIMAP 1976) — “Climate Long-range Investigation, Mapping And Prediction” — was a multi-institutional consortium of scientists formed in 1971 as part of the National Science Foundation’s International Decade of Ocean Exploration. Its purpose was to study the history of global climate over the past million years, particularly using proxy data from ocean sediment cores. One of its goals was to reconstruct for specific times the climate-relevant aspects of the Earth’s surface for use as boundary conditions for atmospheric GCMs. Its first time slice was the LGM, thought at the time from radiocarbon dating to be 18 kyBP. The climate-relevant aspects of the Earth’s surface were essentially those discussed in Chapter 4, “CGCM Boundary Conditions”, except that since atmosphere-only GCMs were to be used, sea surface temperatures (SSTs) were also necessary. To determine these, CLIMAP compiled relative abundances of plankton species in a suite of globally-distributed (albeit sparse in many regions) cores. Species assemblages were then defined in the coretop (i.e., PD) samples by factor analysis, which gives numerical values that indicate the relative importance of each species in each assemblage and of each assemblage in each sample. These were checked to see that their distribution pattern in the ocean could be related to PD surface water masses. A regression equation relating PD SSTs over the cores to the numerical values of the assemblages was then developed. This resulting transfer function was tested for accuracy and reproducibility on an independent set of data. It was assumed to be valid through the past, in the downcore samples such as those from the LGM. These were located using paleontological, geochemical, and paleomagnetic chronostratigraphic techniques and the same abundances/assemblages/transfer function procedure was applied to them to get LGM SSTs. Finally, these LGM SSTs

were plotted and contoured to yield paleoisotherm maps.

The most striking and perpetually controversial CLIMAP result was that LGM tropical SSTs were on average no more than about 1°C colder than PD, essentially the same as PD given the measurement uncertainty. This result was actually from CLIMAP 1981, which was a reassessment of the original CLIMAP 1976 SST reconstruction and is what is usually meant when referring to “CLIMAP” results. CLIMAP 1976 showed somewhat greater mean cooling (about 2°C) and was only for LGM August. An LGM February was done for the reassessment and it gave a result similar to August’s. Figures 7.3b and 7.4b are the CGCM grid box maps of CLIMAP 1981 LGM – PD August and February SSTs, respectively. The LGM – PD August area-weighted⁵ mean tropical SST is -1.18°C . Tropical is defined here as CGCM grid box lat# 18 to lat# 29 inclusive, which is 24°S to 24°N . The LGM – PD February area-weighted mean tropical SST is -0.50°C .

7.2.1 Comparison to CGCM Results

The CLIMAP LGM – PD tropical SST result was striking because it was counterintuitive but it has remained controversial because the later evidence regarding it has been equivocal. CGCM results are an important part of this evidence and, as will be seen from the shortcomings of other CGCM simulations, which will be described, the CGCM LGM simulation of this work is one of the best to date. Figures 7.3a and 7.4a then, are the CGCM grid box maps of OGCM LGM – PD August and February SSTs, respectively. (All GCM fields in this chapter are again 100-year averages as described in Section 6.1.) It is clear that OGCM LGM tropical SSTs were everywhere several degrees more than 1°C colder than PD. This point is further made in Figures 7.3c and 7.4c, which are the corresponding CGCM grid box maps of the OGCM minus CLIMAP differences and show that the OGCM gives several degrees more LGM tropical SST cooling than did CLIMAP. The OGCM LGM – PD August and February area-weighted mean tropical SSTs are -3.55°C and -3.59°C , respectively.

Early LGM simulations were with atmosphere-only GCMs, which had to use prescribed SSTs (CLIMAP’s usually) and thus could only be used to indicate if the

⁵Similar to the mass weighting of Section 6.2.2; for SSTs the third dimension is unnecessary.

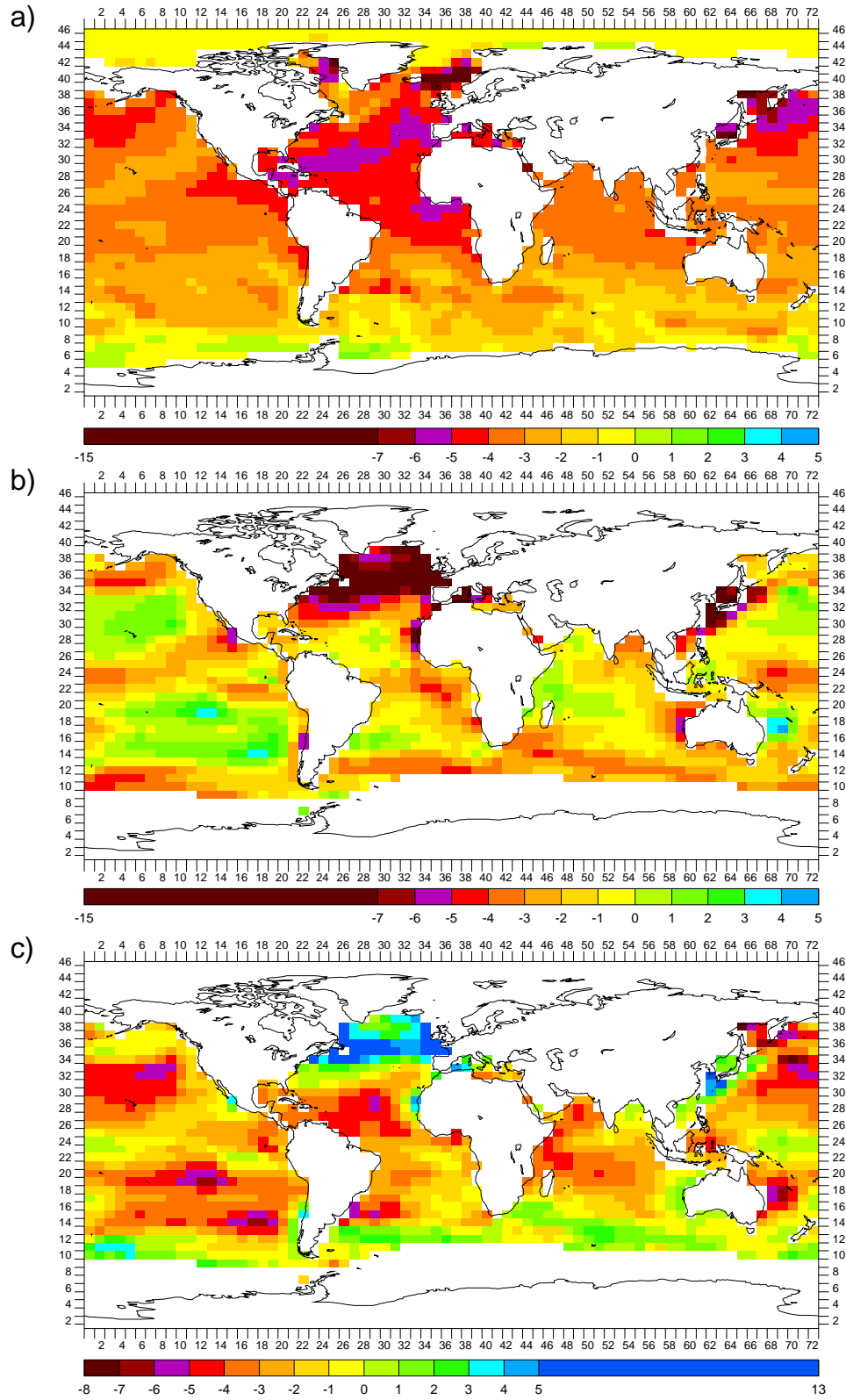


Figure 7.3: CGCM grid box maps of LGM – PD August SSTs (C) for: a) OGCM; b) CLIMAP; and c) OGCM minus CLIMAP

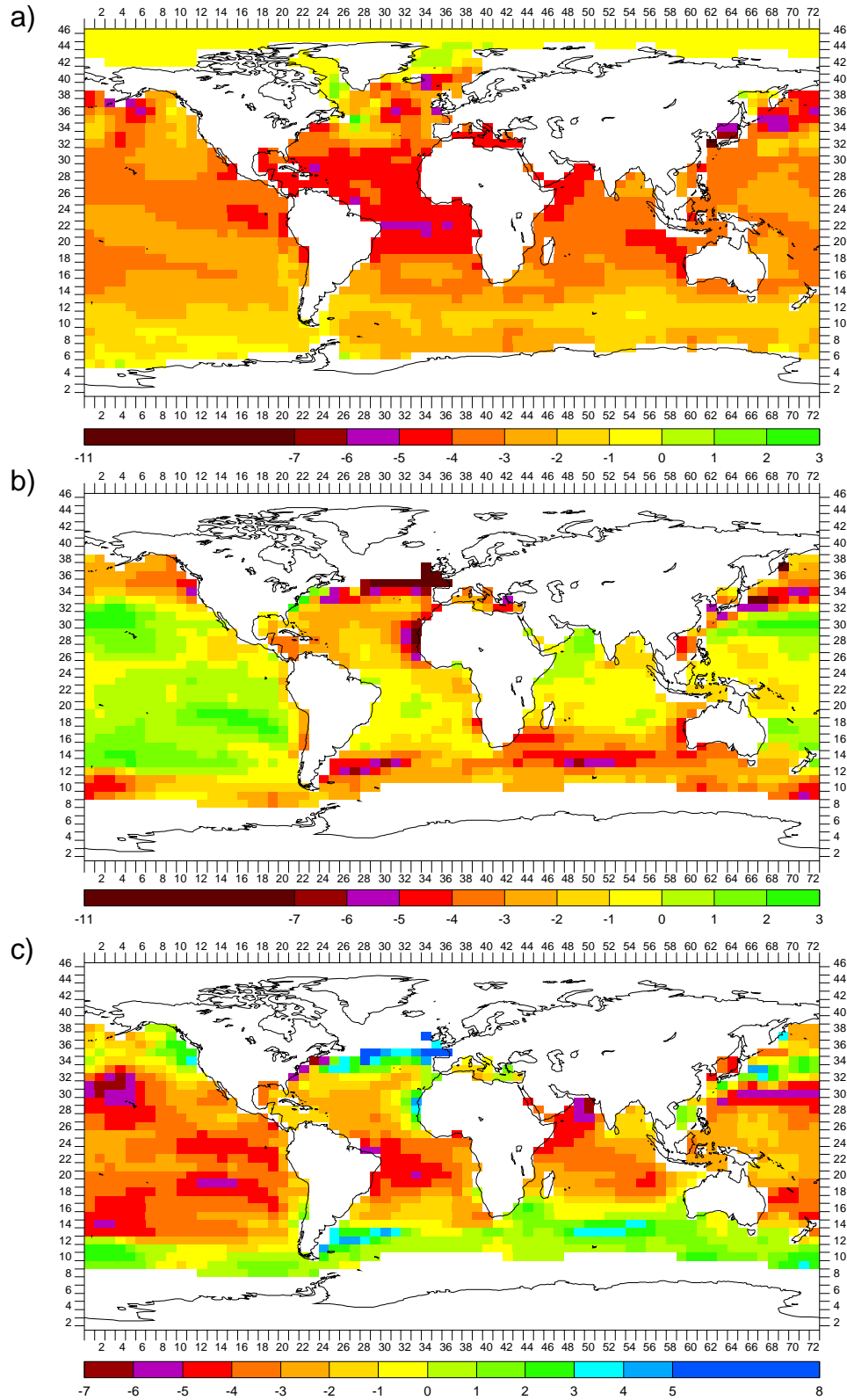


Figure 7.4: CGCM grid box maps of LGM – PD February SSTs (C) for: a) OGCM; b) CLIMAP; and c) OGCM minus CLIMAP

resulting atmospheric conditions were consistent with terrestrial proxy data. Later, mixed layer (a.k.a. “slab”) ocean models were added to these AGCMs. However, SSTs are also a function of ocean heat transport, which itself had to be prescribed in these slab ocean models. Ocean GCMs were also used but LGM atmospheric boundary conditions for them are even more uncertain than LGM SSTs so some reduced complexity atmospheric model was typically coupled to them.

Only recently has computer speed increased to the point of making feasible LGM simulations with full coupled GCMs, which are the most physically-consistent means for reconstructing LGM SSTs. Only a few of these simulations have been done and most suffer from shortcomings that could have affected their tropical SST results and/or have reported their tropical SST results in such a way as to make comparisons to CLIMAP difficult. As an example of the former, in all the following cited work the erred topography of Peltier 1994 was used (see Section 4.4). Bush and Philander 1998 and the more-detailed Bush and Philander 1999 used a somewhat higher resolution CGCM (a 14-level $3.75^\circ \times 2.25^\circ$ AGCM and a 15-level $3.62^\circ \times 2^\circ$ OGCM) than in this work but only did a 40-year PD run and a 15-year LGM run. Only annual (not August or February) tropical SSTs were reported, with no overall mean value, but contour maps show roughly similar LGM – PD tropical SSTs to that found in this work and a range of $4\text{--}6^\circ\text{C}$ for LGM tropical SST cooling was given (the OGCM LGM – PD annual area-weighted mean tropical SST in this work is -3.60°C). Similarly, Hewitt et al. 2001 and the later Hewitt et al. 2003 used a higher resolution CGCM (a 19-level $3.75^\circ \times 2.5^\circ$ AGCM and a 20-level $1.25^\circ \times 1.25^\circ$ OGCM). They did a 1000-year LGM simulation but early on used an acceleration technique that could potentially change the equilibrium (as implied in this work; see Section 3.2.4) and did not fully account for the increased LGM mean ocean salinity. Further, their “PD” simulation used a pre-industrial (Holocene) atmospheric CO_2 concentration of 280 ppmv instead of the ≈ 330 ppmv more appropriate for PD. Regardless, they did not report LGM tropical SSTs in any form. Kitoh et al. 2001 and the more-detailed Kitoh and Murakami 2002 also used a higher resolution CGCM (a 15-level $5^\circ \times 4^\circ$ AGCM and a 21-level $2.5^\circ \times 0.5\text{--}2^\circ$ OGCM) but ignored the land-sea distribution change from LGM to PD. The CGCM used flux adjustments for heat and fresh water and the LGM simulation only ran for about 270 years, with the early part of that

employing a potentially equilibrium-changing acceleration technique and “freshwater preconditioning”. Still, they reported the LGM SSTs in the tropics (20°S to 20°N) being 1.7°C cooler than the PD simulation. Shin et al. 2003 used a higher resolution CGCM (an 18-level $\approx 3.75^\circ \times \approx 3.75^\circ$ AGCM and a 25-level $3.6^\circ \times 0.8\text{--}1.85^\circ$ OGCM) but the simulations with the CGCM were only for 110 years; the AGCM and OGCM were spun up separately, with the OGCM using a potentially equilibrium-changing acceleration technique, and then they were recoupled. Shin et al. 2003 reports only a zonal annual LGM tropical SST cooling, which was 2°C. Finally, Kim et al. 2003 and its background Kim et al. 2002 also used a higher resolution CGCM (a 10-level $3.75^\circ \times 3.75^\circ$ AGCM and a 29-level $1.875^\circ \times 1.875^\circ$ OGCM) but did not account for the different LGM insolation. The CGCM used flux adjustments for heat and fresh water and while the simulations ran for 900 years this consisted of cycles of short periods of the CGCM then longer periods of the OGCM only, as part of a potentially equilibrium-changing acceleration technique. Still, Kim et al. 2003 gives contour maps of LGM – PD August SSTs that show several degrees more LGM tropical SST cooling than CLIMAP (even more than in this work), with a mean cooling of 6.5°C reported.

In summary, CGCM results seem to generally show greater LGM tropical SST cooling than CLIMAP but the range of this cooling is relatively large and may be due to shortcomings in the CGCMs used and/or how the tropical SSTs are reported. The CGCM LGM simulation in this work has perhaps the fewest shortcomings and shows an area-weighted mean tropical SST cooling at the LGM of about 3.6°C.

7.2.2 Comparison to $U_{37}^{K'}$ SST Results

Alkenones, specifically long chain C₃₇ methyl alkenones, are organic compounds produced by *Prymnesiophyceae* phytoplankton, most notably the predominant coccolith species *Emiliana huxleyi*. *Prymnesiophyceae* phytoplankton are restricted to the photic zone and in much of the ocean this is entirely in the well-mixed layer, whose temperature is close to that of SST. The Ketone Unsaturation index, $U_{37}^{K'}$, is the ratio of diunsaturated C₃₇ alkenones to the total of diunsaturated and triunsaturated C₃₇ alkenones (it is a simplified version of an earlier index and was thus “primed”). $U_{37}^{K'}$ has been empirically shown to be linearly related to local water temperature,

both in water samples and in samples from the underlying ocean sediment, where these alkenones are resistant to change. Thus, by measuring $U_{37}^{K'}$ in samples down through ocean sediment cores and applying an empirical $T(U_{37}^{K'})$ calibration, a record of paleo-SST can be derived.

Early, and several later, $U_{37}^{K'}$ SST records from the tropics indicated LGM – PD tropical SSTs of about -2°C and this was interpreted as substantiation of CLIMAP’s LGM – PD mean tropical SST of about -1°C , especially since terrestrial proxy data indirectly indicated LGM – PD tropical SSTs of about -5°C (see Section 7.2.4 ahead). As indicated, it can be very misleading to extrapolate from single locations so all available $U_{37}^{K'}$ SST data was compiled for this work. This was largely from the same major public databases (e.g., PANGAEA, NGDC) discussed in Chapter 5 for ocean sediment core $\delta^{18}\text{O}$ data. Moreover, the same difficulties (e.g., sparsity), age model requirements (e.g., calendar ages via SPECMAP or calibrated ^{14}C) and averaging (e.g., within downcore time interval, for multiple measurements, within grid box) described for the $\delta^{18}\text{O}$ data in Chapter 5 apply to the $U_{37}^{K'}$ SST data in this work. Similarly, Appendix C is a compilation of the information about the ocean sediment cores from which $U_{37}^{K'}$ SST time series were gathered and Appendix D contains the plots of the $U_{37}^{K'}$ SST time series, although since there is no species-specificity for $U_{37}^{K'}$ SST data, the subappendices are divided into southern extra-tropics, tropics, and northern extra-tropics plots for convenience with this section.

The resulting $U_{37}^{K'}$ LGM – PD area-weighted mean tropical SST is -2.38°C . To begin a more detailed analysis though, Figure 7.5a is the CGCM grid box map of $U_{37}^{K'}$ LGM – PD SSTs. For comparison to CLIMAP, Figure 7.5b and c are the CGCM grid box maps of CLIMAP minus $U_{37}^{K'}$ LGM – PD August and February SSTs, respectively (see Figures 7.3b and 7.4b for CLIMAP LGM – PD August and February SSTs, respectively).⁶ Additionally, the top of Figure 7.6 contains the corresponding CLIMAP/ $U_{37}^{K'}$ plot⁷. Both August and February are included in the figures because there is some question as to what season $U_{37}^{K'}$ SSTs really reflects; there are no CLIMAP SSTs available for an annual comparison. Based on the figures and the

⁶Note in such $U_{37}^{K'}$ grid box maps that some $U_{37}^{K'}$ grid boxes are “lost” due to being outside the imposed CGCM ocean mask.

⁷A “model/data plot” as described in Section 6.2.2.

means of the values in them, August provides just a slightly better match.

To see what month of the OGCM SST results better matches the $U_{37}^{K'}$ SST data and whether the CLIMAP or the OGCM SST results better match the $U_{37}^{K'}$ SST data, Figure 7.7a, b, and c are the CGCM grid box maps of OGCM minus $U_{37}^{K'}$ LGM – PD annual, August and February SSTs, respectively (see Figure 6.51c for OGCM LGM – PD annual SSTs). Additionally, the bottom of Figure 7.6 contains the corresponding OGCM/ $U_{37}^{K'}$ plot. Based on the figures and the means of the values in them, February provides just a slightly better match.

For both the CLIMAP and OGCM comparisons, the month does not really make much of a difference. Regardless of month, the CLIMAP SST results better match the $U_{37}^{K'}$ SST data than do the OGCM SST results. However, this should not be taken as evidence of the accuracy of CLIMAP SST results or inaccuracy of the OGCM SST results (although they may very well be inaccurate). The same factors that make the CLIMAP SST results questionable make the $U_{37}^{K'}$ SST data questionable — they are both strongly dependent on the complicated not-well-known ecology of plankton. How accurate a paleothermometer $U_{37}^{K'}$ is is still a matter of some controversy. Furthermore, the $U_{37}^{K'}$ SST data is sparse, which can strongly skew results, and it is dominated by coastal African cores.

7.2.3 Comparison to Mg/Ca SST Results

Magnesium (Mg) can substitute for some calcium (Ca) in the calcite (CaCO_3) of foraminifera shells (as well as of corals and of the shells of other marine organisms like ostracods). The ratio of magnesium to calcium (Mg/Ca) in the calcite is thought to be related primarily to the temperature of the water in which the foraminifera precipitated its shell. Since the ocean Mg/Ca ratio is stable on a much longer time scale than that of glacials, foraminifera Mg/Ca does not have a confusing continental glacier ice volume component like $\delta^{18}\text{O}$. Further, it can be measured concurrently with $\delta^{18}\text{O}_c$ in the same foraminifera sample and used to separate out the temperature component of the $\delta^{18}\text{O}$, without the cross-dating ambiguity of other external paleothermometers. Just as for $\delta^{18}\text{O}_c$, the T(Mg/Ca) calibration is species-specific. By choosing an appropriate planktonic foraminifera species, SST can be calculated and by measuring Mg/Ca in samples down through ocean sediment cores, a record

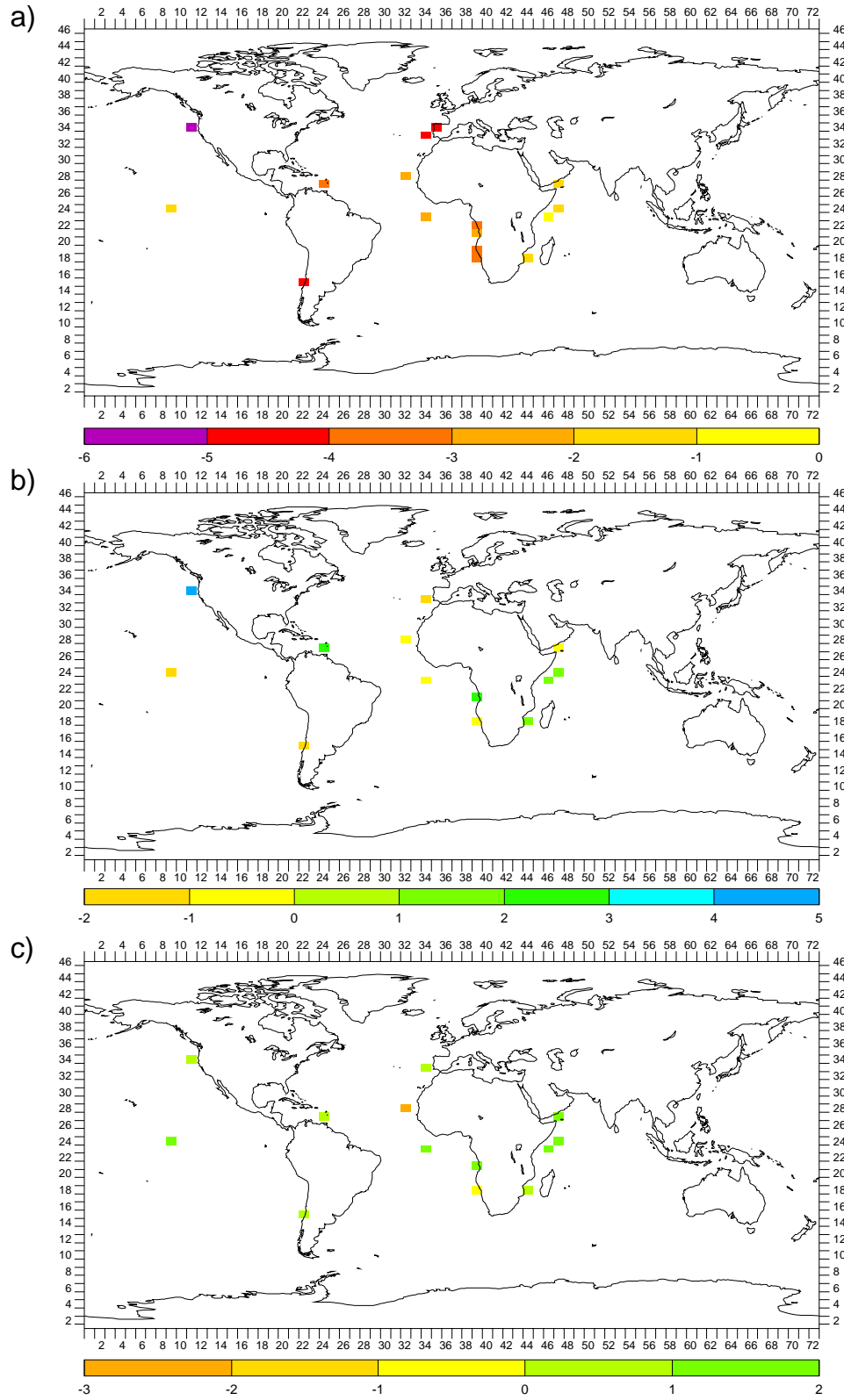


Figure 7.5: CGCM grid box maps of: a) $U_{37}^{K'}$ LGM - PD SSTs (C); and CLIMAP minus $U_{37}^{K'}$ LGM - PD SSTs (C) for b) August; and c) February

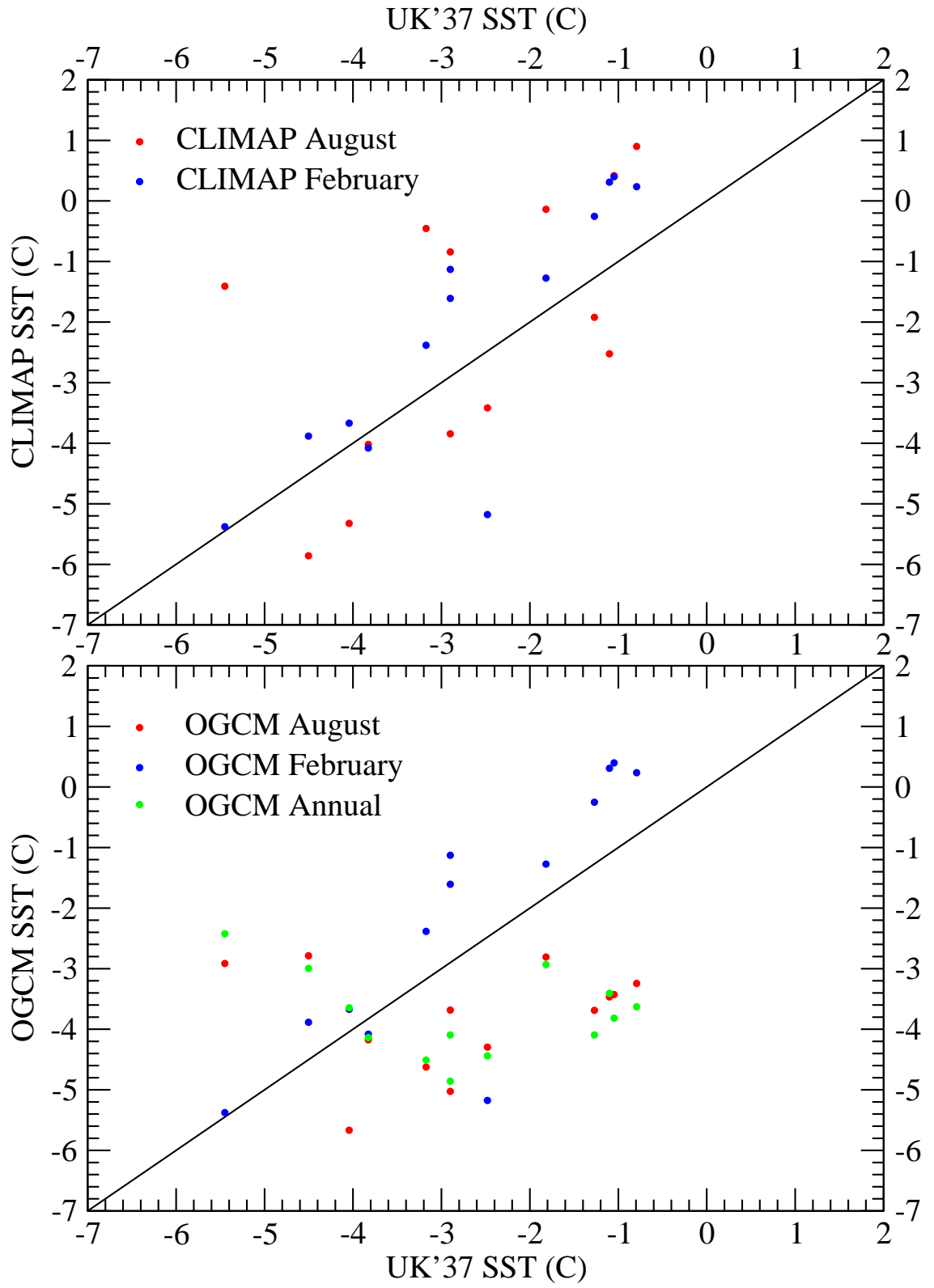


Figure 7.6: top) LGM – PD CLIMAP SSTs versus $U_{37}^{K'}$ SSTs (C); and bottom) LGM – PD OGCM SSTs versus $U_{37}^{K'}$ SSTs (C).

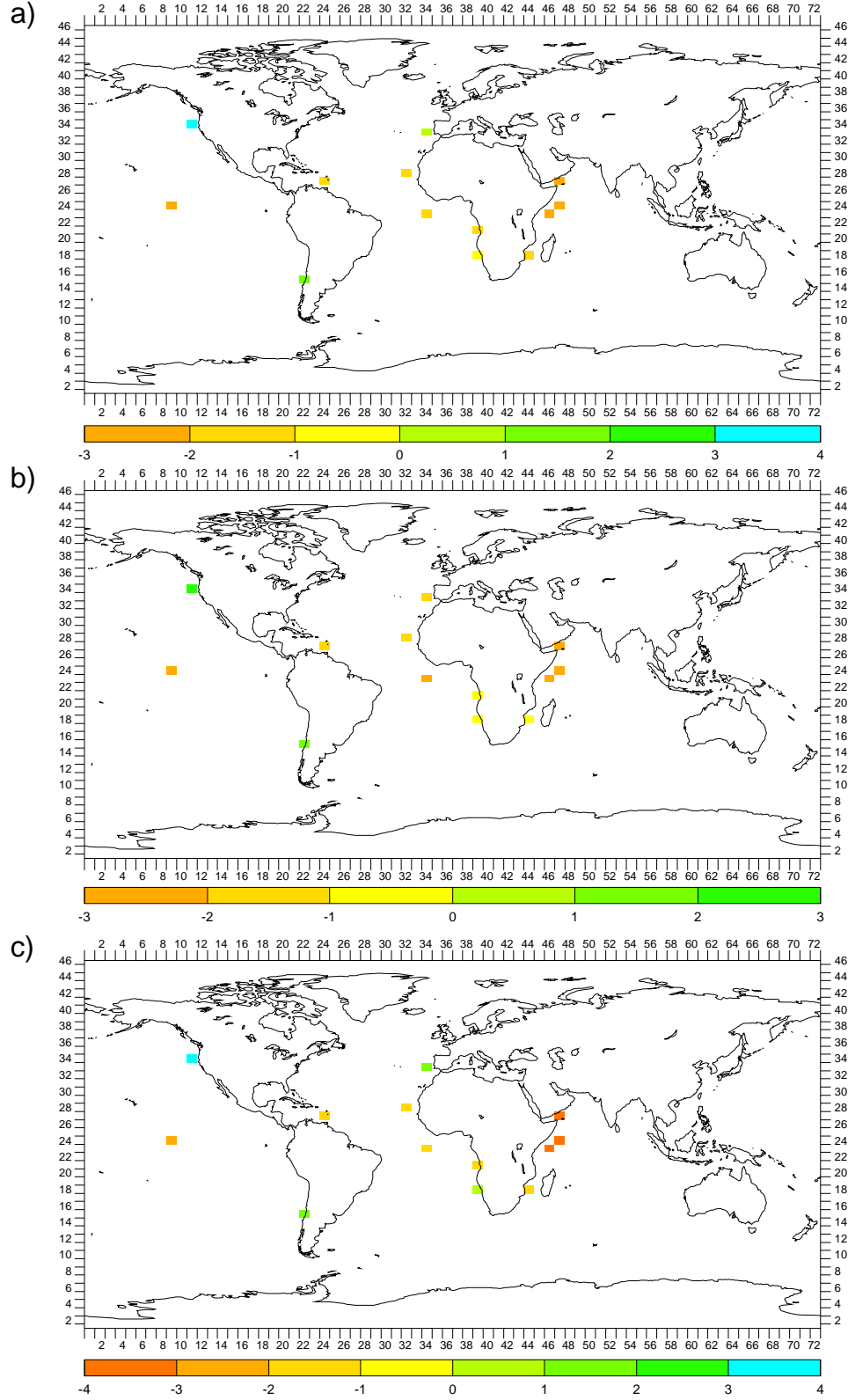


Figure 7.7: CGCM grid box maps of OGCM minus $U_{37}^{K'}$ LGM – PD SSTs for: a) annual; b) August; and c) February

of paleo-SST can be derived.

Only within the past few years has the Mg/Ca ratio in foraminifera shells started to be considered a reliable paleothermometer and there is thus even less Mg/Ca SST data than the already-sparse $U_{37}^{K'}$ SST data. Again, it can be very misleading to extrapolate from single locations so all available Mg/Ca SST data was compiled here. This was largely from the discussed NGDC database or from the published references themselves. The same difficulties (e.g., sparsity), age model requirements (e.g., calendar ages via SPECMAP or calibrated ^{14}C) and averaging (e.g., within downcore time interval, for multiple measurements, within grid box) described for the $\delta^{18}\text{O}$ data in Chapter 5 and the $U_{37}^{K'}$ SST data of the previous section apply to the Mg/Ca SST data in this work. Similarly, Appendix E is a compilation of the information about the ocean sediment cores from which Mg/Ca SST time series were gathered and Appendix F contains the plots of the Mg/Ca SST time series, with subappendices by foraminifera species.

The resulting Mg/Ca LGM – PD area-weighted mean tropical SST is -2.10°C . To begin a more detailed analysis though, Figure 7.8a is the CGCM grid box map of Mg/Ca LGM – PD SSTs using the ocean sediment cores of all planktonic foraminifera species. For comparison to CLIMAP, Figure 7.8b and c are the CGCM grid box maps of CLIMAP minus Mg/Ca LGM – PD August and February SSTs, respectively (see Figures 7.3b and 7.4b for CLIMAP LGM – PD August and February SSTs, respectively).⁸ Additionally, the top of Figure 7.9 contains the corresponding CLIMAP/Mg/Ca plot. Both August and February are included in the figures because there is some question as to what season Mg/Ca SSTs really reflects; there are no CLIMAP SSTs available for an annual comparison. Based on the figures and the means of the values in them, February provides just a slightly better match.

To see what month of the OGCM SST results better matches the Mg/Ca SST data and whether the CLIMAP or the OGCM SST results better match the Mg/Ca SST data, Figure 7.10a, b, and c are the CGCM grid box maps of OGCM minus Mg/Ca LGM – PD annual, August and February SSTs, respectively (see Figure 6.51c for OGCM LGM – PD annual SSTs). Additionally, the bottom of Figure 7.9 contains

⁸Note in such Mg/Ca grid box maps that one Mg/Ca grid box is “lost” due to being outside the imposed CGCM ocean mask.

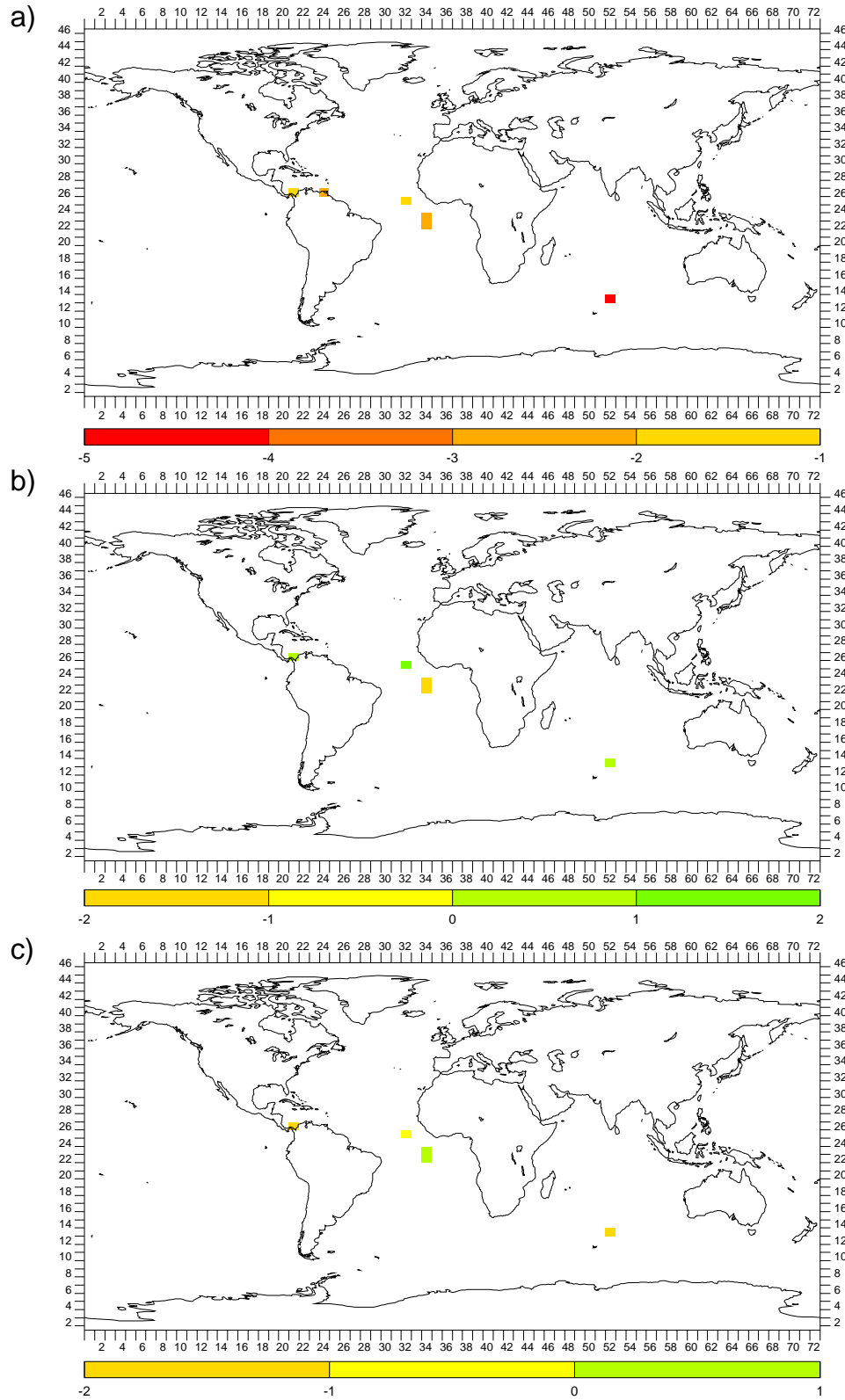


Figure 7.8: CGCM grid box maps of: a) Mg/Ca LGM - PD SSTs (C); and CLIMAP minus Mg/Ca LGM - PD SSTs (C) for b) August; and c) February

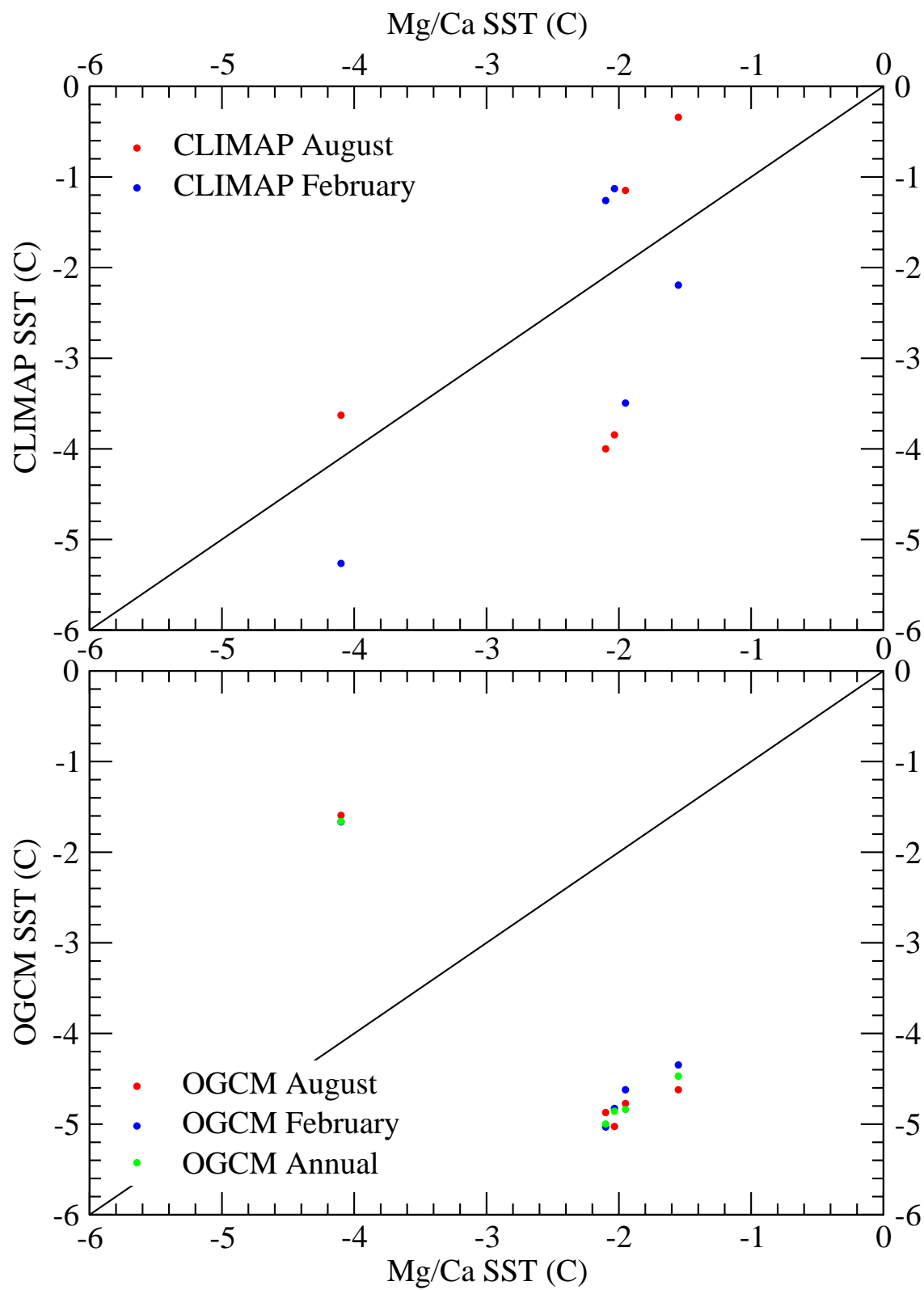


Figure 7.9: top) LGM – PD CLIMAP SSTs versus Mg/Ca SSTs (C); and bottom) LGM – PD OGCM SSTs versus Mg/Ca SSTs (C).

the corresponding OGCM/Mg/Ca plot. Based on the figures and the means of the values in them, February provides just a slightly better match.

For both the CLIMAP and OGCM comparisons, the month does not really make much of a difference. Regardless of month, the CLIMAP SST results better match the Mg/Ca SST data than do the OGCM SST results. Again however, as for the $U_{37}^{K'}$ SST data, this should not be taken as evidence of the accuracy of CLIMAP SST results or inaccuracy of the OGCM SST results (although they may very well be inaccurate). The same factors that make the CLIMAP SST results questionable and required a foraminifera model in this work make the Mg/Ca SST data questionable — they are strongly dependent on the complicated not-well-known ecology of planktonic foraminifera. How accurate a paleothermometer Mg/Ca is is a matter of some controversy (e.g., Nürnberg et al. 2000). Furthermore, the Mg/Ca SST data is very sparse and this can strongly skew results.

7.2.4 From Terrestrial Temperature Proxy Data

Terrestrial temperature proxy data has also been applied to the question of CLIMAP tropical SSTs. The most geographically widespread, and thus probably the most robust, is the tropical snow line and vegetation zone altitude data. Rind and Peteet 1985 and Broecker and Denton 1989 are oft-cited summaries of these and found on average an ≈ 1 km lowering of tropical snow lines and vegetation zones at the LGM compared to PD. For a typical PD atmospheric lapse rate that is constant from LGM to PD within the ≈ 1 km transition zones, Rind and Peteet 1985 proposed a 5–6°C LGM to PD annual temperature increase in the zones; Broecker and Denton 1989 proposed a 4.2–6.5°C increase. As has been done in several papers, applying this LGM – PD temperature to tropical SSTs contradicts CLIMAP but requires assuming that the atmospheric lapse rate from the transition zones right down to the sea surface over a large area has remained the same from LGM to PD.

Also from the tropical mountains, but a more isolated terrestrial temperature proxy, is the Bolivian (Sajama) ice core of Thompson et al. 1998. They argued that the ice core indirectly indicates LGM tropical Atlantic SST was $\approx 5^\circ\text{C}$ colder than PD, contradicting CLIMAP. Further, the $\delta^{18}\text{O}_i$ record was shown to be similar to that of the nearby Peruvian (Huascarán) ice core of Thompson et al. 1995. Thompson

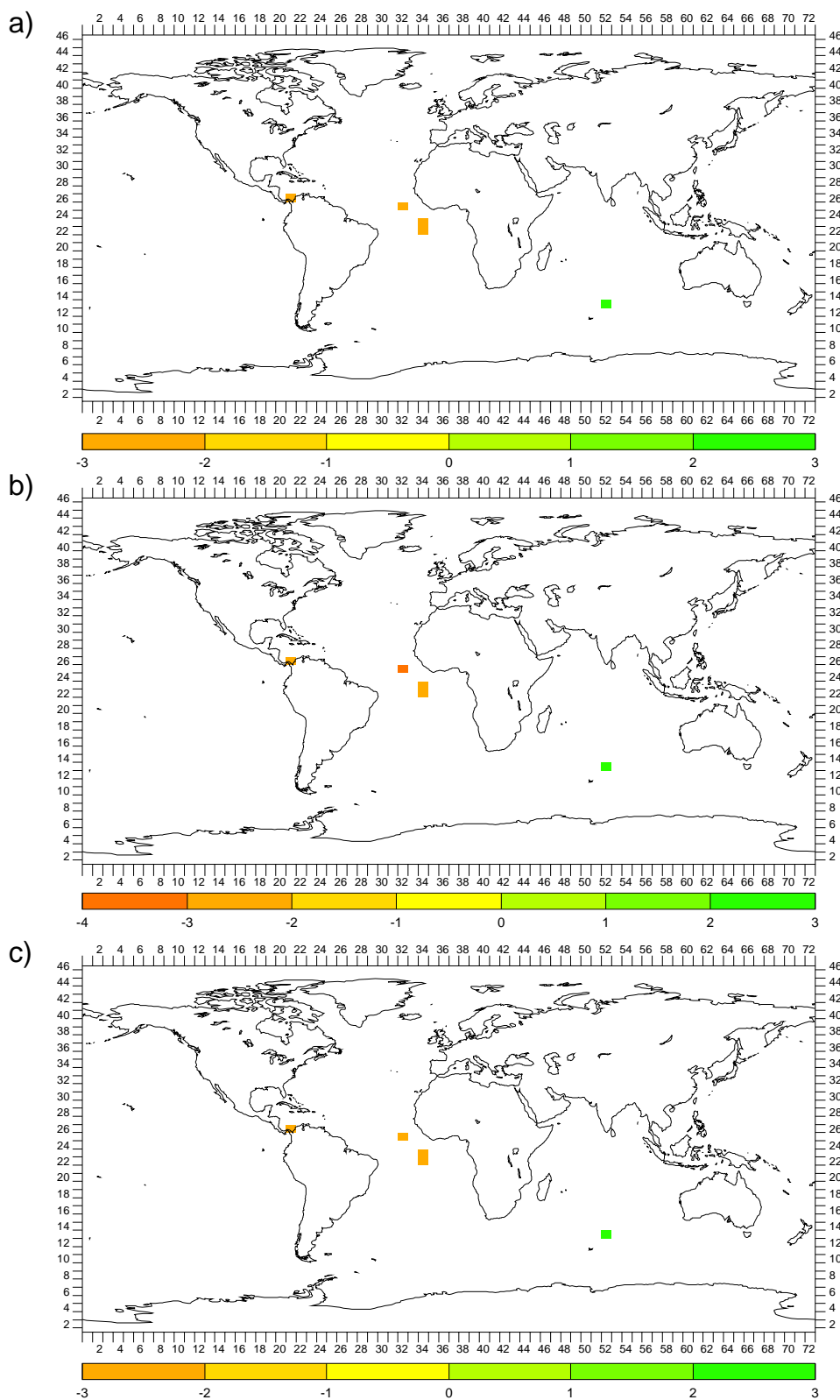


Figure 7.10: CGCM grid box maps of OGCM minus Mg/Ca LGM - PD SSTs for:
a) annual; b) August; and c) February

et al. 1995 used a simple $\delta^{18}\text{O}$ -temperature relation⁹, presumably assumed a constant atmospheric lapse rate and extrapolated back to the LGM to state that the Peruvian ice core $\delta^{18}\text{O}_i$ record is at odds with CLIMAP.

A lower elevation but also isolated terrestrial temperature proxy that has been applied to the question of CLIMAP tropical SSTs is noble gas concentrations in groundwater. The oft-cited work is Stute et al. 1995 and also contradicts CLIMAP. It has been considered convincing on that question because it is from a tropical Brazilian site (7°S, 41.5°W) that is only about 400 m above sea level, i.e., the atmospheric lapse rate was considered unimportant. The method of determining paleotemperatures from noble gas concentrations in groundwater is somewhat complicated and explained in Stute et al. 1995 but their result was that it was $5.4 \pm 0.6^\circ\text{C}$ cooler there during the LGM compared to PD. Note that this is consistent with the higher-elevation data and thus with a constant atmospheric lapse rate from the LGM to PD.

While the atmospheric lapse rate per se can be checked in the LGM and PD simulations of this work, of more direct relevance is the LGM – PD average temperature of the variously-elevated tropical surface AGCM grid boxes (i.e., land) compared to the LGM – PD average temperature of the tropical surface OGCM grid boxes (i.e., SST). Further, by exemplifying the situation using a Cordilleran transect of the Americas up through the tropics, Broecker and Denton 1989 suggest a good region to look at. So, the LGM – PD average temperature of the tropical (lat# 18 to lat# 29 inclusive, i.e., 24°S to 24°N) American surface AGCM grid boxes was calculated in 200 m bins of elevation above 200 m for the August, February and annual cases. Then an LGM – PD average temperature was calculated for the surrounding tropical Pacific and Atlantic surface OGCM grid boxes from lon# 7 to lon# 37 inclusive, which is 150°W to 5°E. This is somewhat arbitrary but is intended to roughly include sea surface that might be most directly climatologically connected to the indicated land. No area averaging was done but since it is the tropics this should have a negligible effect in this rough calculation. The results, along with those for CLIMAP SSTs and with standard deviations, are given in Table 7.1.

First note that, as expected from Section 7.2.1, this region's LGM – PD average SST from the OGCM is significantly larger in magnitude than that from CLIMAP.

⁹As will be shown in Section 7.4, such a relation may be significantly in error.

Elevation (m)	Aug. LGM – PD T_S (C)	Aug. Std. Dev.	Feb. LGM – PD T_S (C)	Feb. Std. Dev.	Ann. LGM – PD T_S (C)	Ann. Std. Dev.
3200–3400	-8.9	2.8	-9.0	0.4	-9.4	1.6
3000–3200	-4.4	N/A	-6.0	N/A	-5.2	N/A
2200–2400	-4.9	N/A	-4.9	N/A	-4.9	N/A
1800–2000	-5.7	N/A	-6.8	N/A	-6.1	N/A
1200–1400	-6.0	1.9	-5.9	0.7	-6.1	0.2
1000–1200	-5.8	1.2	-4.5	0.5	-5.0	0.5
800–1000	-5.2	1.8	-4.0	1.2	-4.5	1.3
600–800	-5.7	1.8	-5.1	0.8	-5.4	0.7
400–600	-5.7	1.3	-5.5	1.2	-5.6	0.8
200–400	-5.5	1.1	-5.8	1.3	-5.7	0.5
SS	-3.9	0.8	-3.8	0.7	-3.9	0.7
CLIMAP SS	-1.2	1.7	-0.6	1.6	N/A	N/A

Table 7.1: August, February and annual LGM – PD average temperatures/standard deviations (C): of tropical (lat# 18 to lat# 29 inclusive) American surface AGCM grid boxes at available elevations; of surrounding (lon# 7 to lon# 37) tropical Pacific/Atlantic surface OGCM grid boxes; and of CLIMAP surrounding sea surface. An “N/A” Std. Dev. indicates there isn’t one available because $N = 1$; annual CLIMAP SSTs are also not available.

Then, except for the highest elevation bin during all periods and a couple of other elevation bins during February, the LGM – PD average temperature of the tropical American surface AGCM grid boxes is quite consistent with the estimates of Rind and Peteet 1985 and Broecker and Denton 1989, which is good confirmation. Furthermore, the temperatures from the highest elevation bin are consistent with the temperatures calculated from the high-altitude Peruvian ice core by Thompson et al. 1995.

Regarding the ice core terrestrial temperature proxies, the $\delta^{18}\text{O}_i$ record of the Bolivian ice core is included in this work. The $\delta^{18}\text{O}_i$ record of the Peruvian ice core is also included in this work but does not quite go far enough back in time (≈ 500 years short) to reach the LGM as defined in this work (21 ± 1.5 kyBP). As Figure 6.37 shows, the corresponding LGM – PD annual $\delta^{18}\text{O}_i$ from the AGCM is significantly larger than that from the Bolivian ice core, i.e., the AGCM does not confirm the ice core. The biases affecting AGCM precipitation $\delta^{18}\text{O}$ in this area are discussed in Sections 6.3.1 and 6.4.1 but the reason for the discrepancy is still not clear.

Finally though, in the AGCM grid box ([28,22]) corresponding to the Brazilian

groundwater site, the LGM – PD annual surface AGCM temperature was -5.1°C (-5.5 for August, -3.7 for February), which is a good match to what Stute et al. 1995 found.

7.3 North Atlantic Meridional Overturning Circulation

The North Atlantic meridional overturning circulation (NAMOC) was introduced in Section 3.3.2. Put simply, it is commonly believed that during the LGM the NAMOC was weaker, shallower and farther south than PD. This belief stems from the interpretation of most proxies and some model results. Additionally, there is the idea that the NAMOC brings a significant amount of heat to Western Europe, making it warmer than it otherwise would be at its latitudes, and thus that a clearly colder Western Europe during the LGM (as indicated by more direct proxies) implies a reduced NAMOC then.

The CLIMAP results can also be applied to NAMOC, i.e., act as an indirect proxy. From CLIMAP 1976 regarding cryospheric conditions at the LGM: “This extensive ice cover in the North Atlantic and southern oceans may have reduced the loss of heat from the oceans to the atmosphere in high latitudes, where today most of the world ocean’s bottom and intermediate waters are formed. Permanent sea-ice cover in the Norwegian, Greenland, and Labrador seas must have precluded the formation of North Atlantic deep water.” CLIMAP sea ice results consist only of extent, not concentration, and are simply shown by ocean areas where there are no SSTs given (hence, conversely, no high-latitude CLIMAP SSTs are available). They are thus somewhat ambiguous. Figure 7.11 a and b and Figure 7.12 a and b are the CGCM grid box maps of CLIMAP LGM and PD August SSTs and CLIMAP LGM and PD February SSTs, respectively. Comparing LGM and PD, the reason for the preceding CLIMAP remarks is clear. Figure 7.13 a and b and Figure 7.14 a and b are the CGCM grid box maps of OGCM LGM and PD August sea ice concentration and OGCM LGM and PD February sea ice concentration, respectively. Compared to CLIMAP at PD, the OGCM seems to overestimate equatorward sea ice extent,

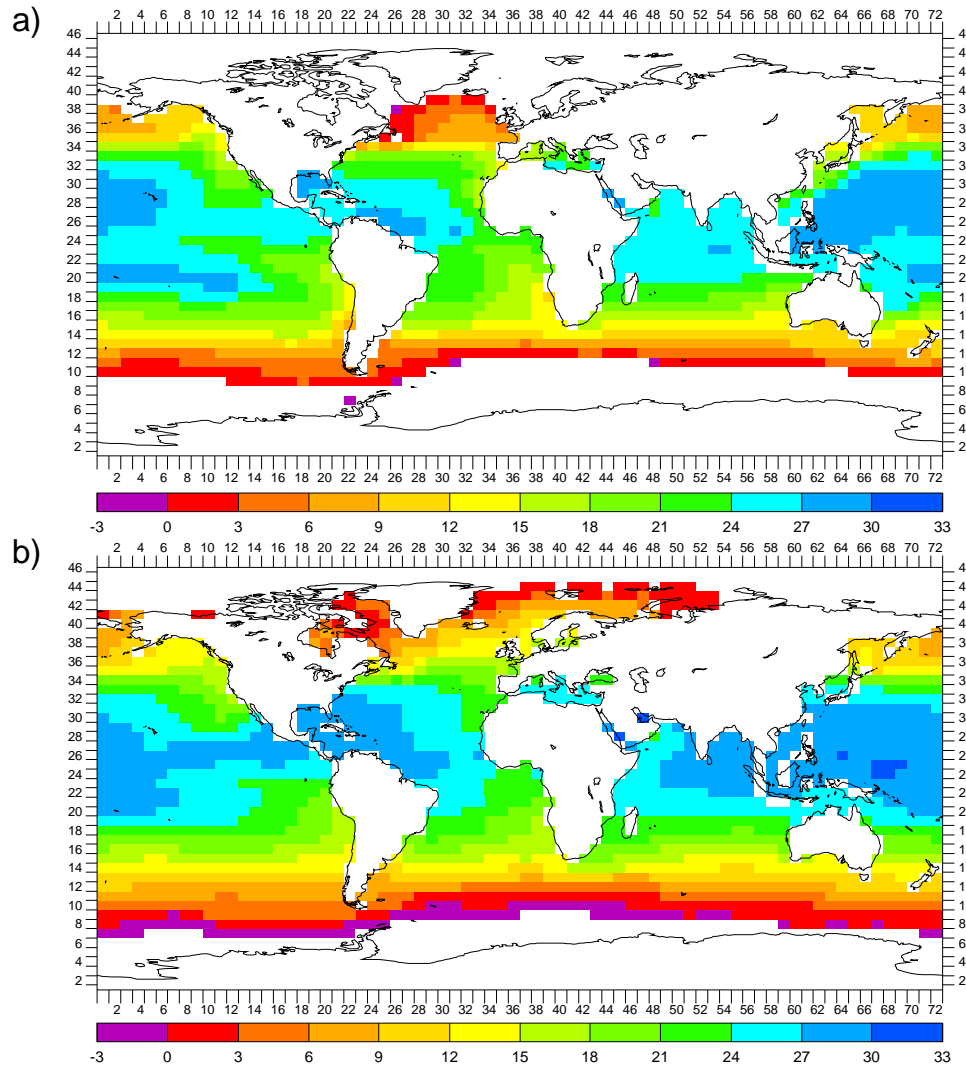


Figure 7.11: CGCM grid box maps of CLIMAP August SSTs (C) for: a) LGM; and b) PD. CLIMAP sea ice extent is indicated by ocean areas where no SSTs are given.

particularly in the North Atlantic, but with the ambiguity of converting OGCM sea ice concentration to CLIMAP sea ice extent. Compared to CLIMAP at the LGM, the OGCM seems to underestimate equatorward sea ice extent, particularly in the North Atlantic, but again with the same ambiguity. This would tend to allow more deep convection in the OGCM, and thus an increased NAMOC, at the LGM compared to that indicated by CLIMAP.

As the newest and most direct NAMOC strength proxy, Lynch-Stieglitz et al. 1999b used $\delta^{18}\text{O}_c$ of benthic foraminifera from ocean sediment cores up both sides of the Florida Straits to reconstruct the water density profile across it, and thus the

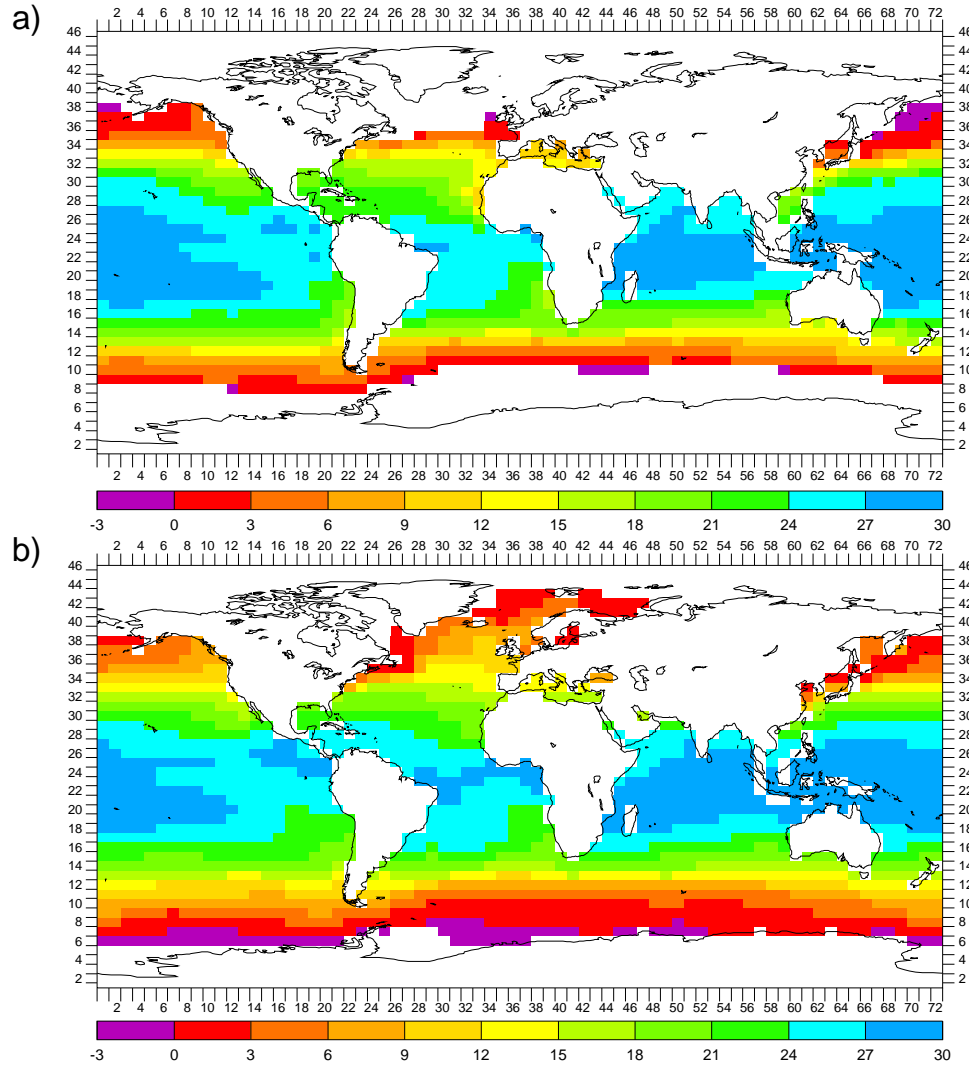


Figure 7.12: CGCM grid box maps of CLIMAP February SSTs (C) for: a) LGM; and b) PD. CLIMAP sea ice extent is indicated by ocean areas where no SSTs are given.

geostrophic flow through it (see Lynch-Stieglitz et al. 1999a for a more complete method description). They estimated this flow there at the LGM was about two-thirds that of PD. Significant assumptions are necessary to extrapolate from the Florida Straits to the whole NAMOC though.

A more prevalent proxy is $\delta^{13}\text{C}$. Photosynthesis in surface ocean water preferentially extracts ^{12}C , enriching the water in ^{13}C and thus increasing its¹⁰ $\delta^{13}\text{C}$. Where deep convection occurs, $\delta^{13}\text{C}$ in both planktonic and benthic foraminifera will be

¹⁰Defined similarly to $\delta^{18}\text{O}$ (^{16}O , ^{18}O).

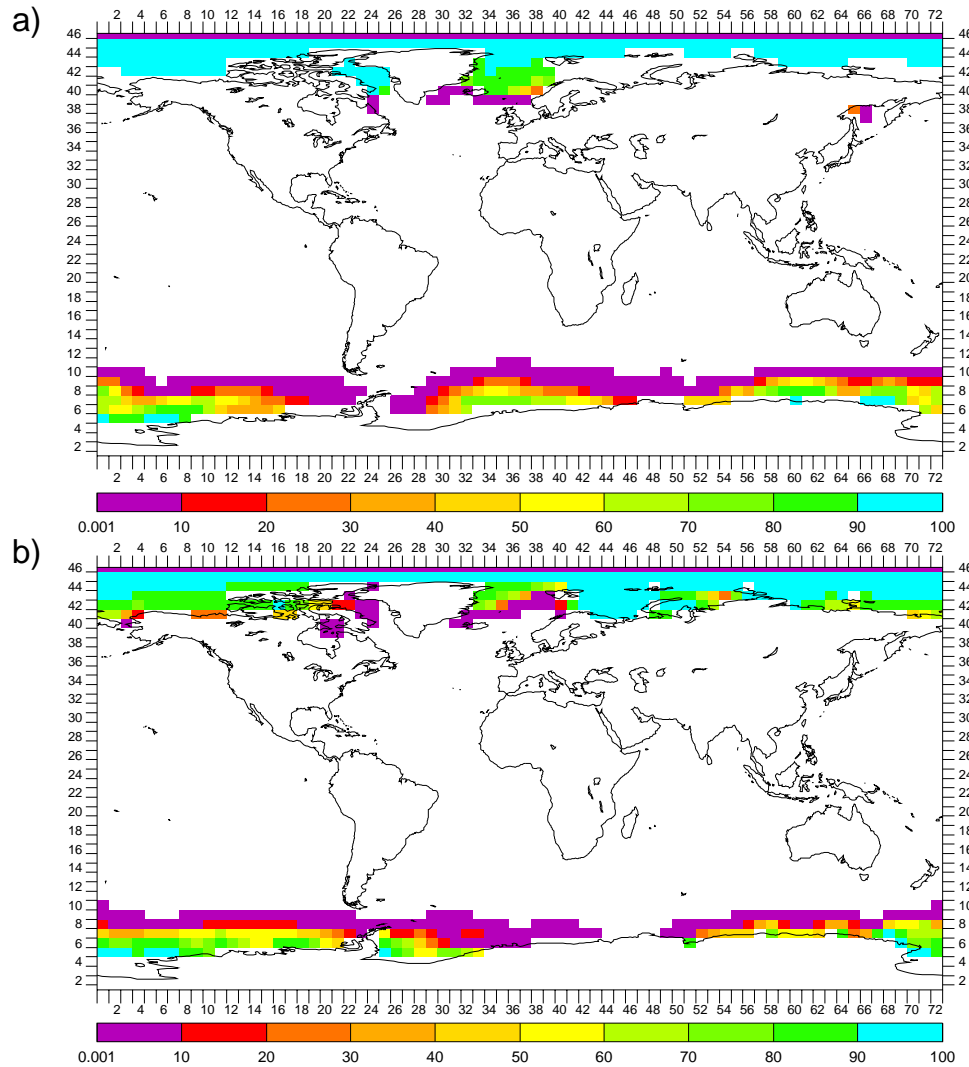


Figure 7.13: CGCM grid box maps of OGCM August sea ice concentration (%) for: a) LGM; and b) PD.

similarly large (e.g., Duplessy et al. 1988) and the formed deepwater can be traced with this $\delta^{13}\text{C}$ of benthic foraminifera (e.g., Curry et al. 1988). Using this proxy, Duplessy et al. 1988, Sarnthein et al. 1994 and other less direct¹¹ work seemed to find greatly reduced North Atlantic Deep Water formation at the LGM, replaced to some degree by the formation of shallower, Glacial North Atlantic Intermediate Water. This rather indirect proxy though, can be complicated and contradictory and

¹¹Less centered on the North Atlantic and inferred more from the South Atlantic and Southern Ocean.

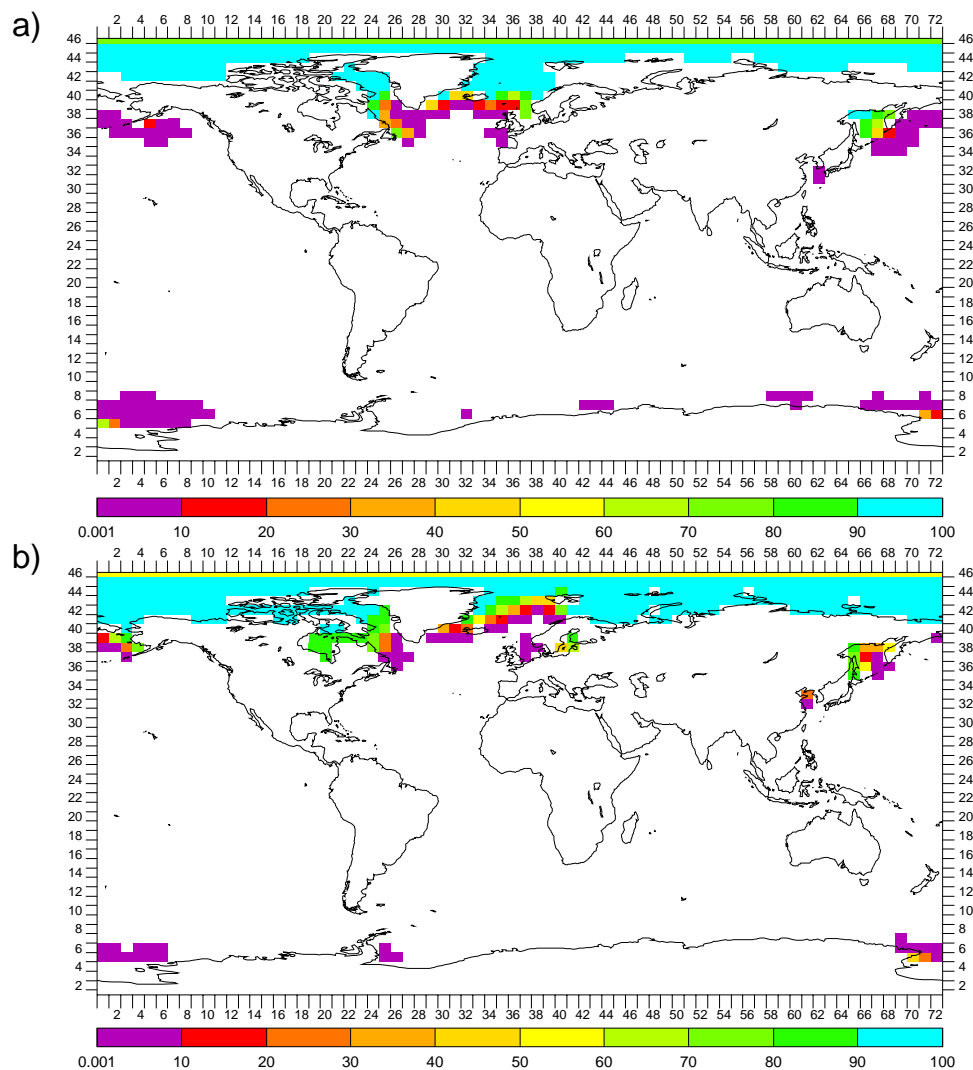


Figure 7.14: CGCM grid box maps of OGCM February sea ice concentration (%) for: a) LGM; and b) PD.

thus difficult to interpret.

The oceanic distribution of cadmium closely resembles that of phosphorus (e.g., Boyle 1988), which is a nutrient. As photosynthesis tends to deplete surface ocean water of nutrients, it does the same to cadmium. This is mirror opposite to ^{13}C , with which it is often used in conjunction and, in the Cd/Ca ratio of foraminifera shells, used in the same fashion, with similar caveats. In an example most directly related to NAMOC, Boyle and Keigwin 1982 used these and also seemed to find reduced (halved) North Atlantic Deep Water at the LGM.

^{231}Pa (protactinium) and ^{230}Th (thorium) are uniformly produced in the ocean via

α -decay from uranium, which is essentially conservative in the ocean. ^{230}Th is more particle-reactive than ^{231}Pa so is more quickly scavenged to sediment as they both are advected through the ocean, particularly from the Atlantic to the Southern Ocean. The ocean sediment $^{231}\text{Pa}/^{230}\text{Th}$ ratio can thus be used to make inferences about this advection in the past. Yu et al. 1996 did this and found similar or slightly more advection of North Atlantic Deep/Intermediate Water south at the LGM compared to PD. However, the method is relatively new and has numerous complications.

Turning to just CGCM NAMOC results, starting with this work, Figure 7.15 contains depth-latitude sections of annual Atlantic OGCM meridional overturning circulation streamfunction (Sv) for LGM and PD. Clearly, NAMOC is stronger and goes deeper at the LGM than at PD. Before examining why this might be, note that the value for grid box lat# 35 (44–48°N) at OGCM level 10 (899–1360 m depth) was used for Figure 6.4, the time series of the single-value measure of annual North Atlantic OGCM meridional overturning circulation streamfunction. While, as seen, this grid box is not positioned at the maximum at either the LGM or PD, it does reflect the change in the maximum between the LGM and PD.

For both the LGM and PD the largest and deepest vertical mass flux (not shown), and thus that primarily seen in Figure 7.15, occurs along grid box lon# 28 (40–45°E) in a few grid boxes south of Greenland, in/near the Labrador Sea. One immediate shortcoming of the PD simulation then, is that there is not more such convection in the GIN Seas region. To start tracing the causes of the increase in this deep convection south of Greenland at the LGM though, Figure 7.16 contains the CGCM grid box maps of annual AGCM precipitation minus evaporation ($P - E$) for LGM, PD and LGM – PD. In the indicated south of Greenland grid boxes, $P - E$ is decreased at the LGM compared to PD, which would tend to cause increased convection through increased salinity (as well as cooling). However, this does not definitely mean an increase in convection. This conclusion would be strengthened if at the LGM the surface ocean water in these grid boxes was coming from grid boxes where there was also decreased $P - E$ compared to PD, including from the original grid boxes (i.e., it was recirculated), or from where the water was not fresher. Figure 7.17 contains the CGCM grid box maps of annual surface OGCM current speeds¹² and vectors for

¹²Note that the size of the OGCM grid boxes does not change between the LGM and PD and

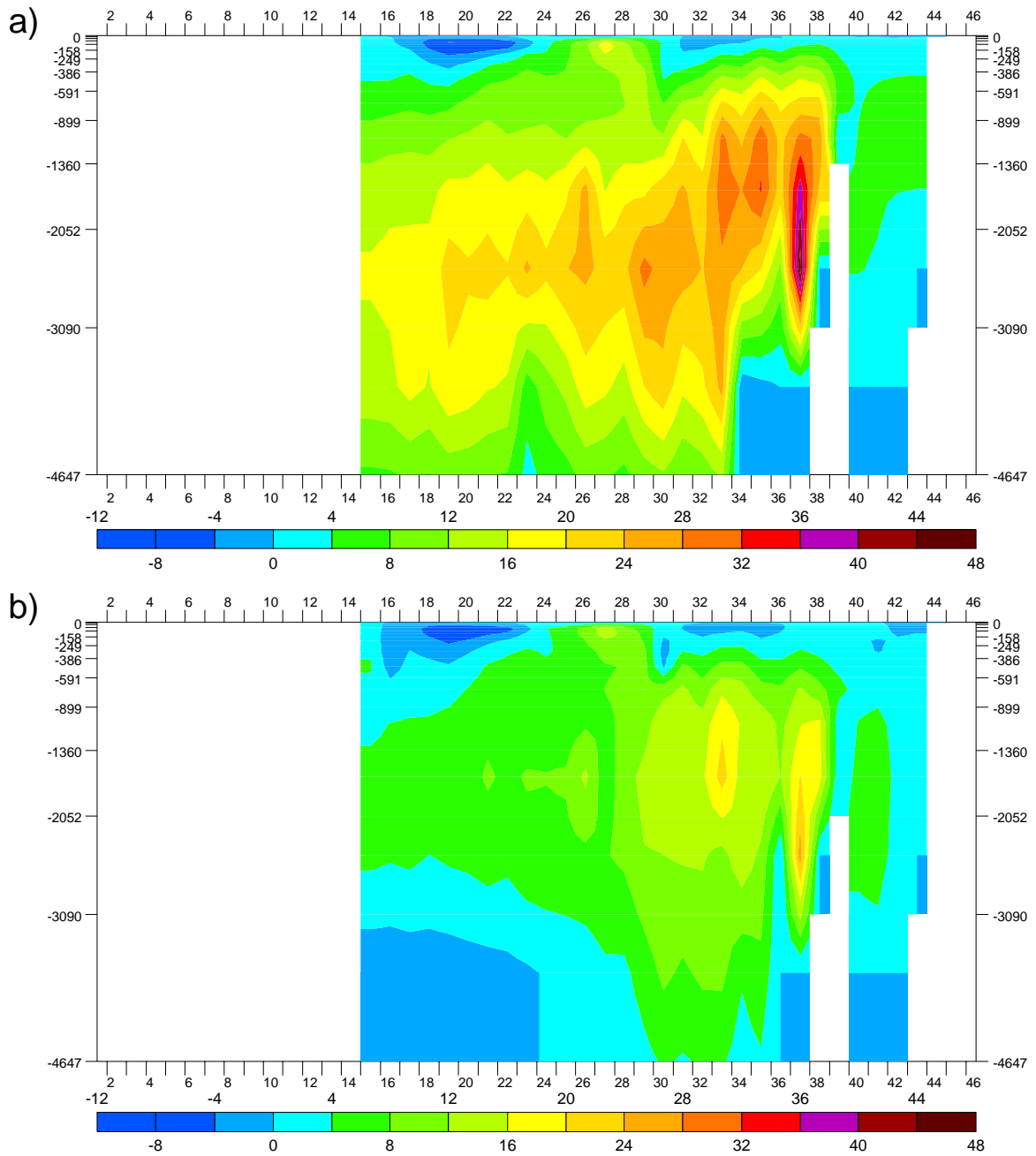


Figure 7.15: Depth-latitude (m-lat#) sections of annual Atlantic OGCM meridional overturning circulation streamfunction (Sv) for: a) LGM; and b) PD.

LGM, PD and LGM – PD. At the LGM, Baffin Bay/Labrador Sea has become a single-opening distilling inland sea due to the closing off by glaciers of its various PD sources of fresher water, i.e., river/runoff (not shown), including via Hudson Bay/Strait and the Arctic Ocean. Surface ocean water just flows in and then out south of Greenland, going through areas of decreased $P - E$ along the way. Further, as the earlier Figure 6.52 shows, while at PD the surface water flowing out of the Labrador Sea is fresher than that going in, at the LGM the water is at least as salty. The recirculation and decreased $P - E$ in the Labrador Sea at the LGM is aided by the different winds there then. Figure 7.18 contains CGCM grid box maps of annual surface AGCM wind speeds and vectors for LGM, PD and LGM – PD. At the LGM the pattern of the winds over the Labrador Sea is well-suited for causing the recirculation there and the wind speed is significantly increased over PD. The wind pattern may be being imposed by the high glaciers surrounding the Labrador Sea at the LGM. Note that the overall situation with the Labrador Sea at the LGM may have made the NAMOC more sensitive to melting of the glaciers (as will be shown though, this may not have been that climatically important).

It is difficult to compare the strength of the NAMOC between different CGCMs, especially using the streamfunction value from a single grid box, which may be a different box between different CGCMs. However, they should be roughly comparable in regards to increases versus decreases from the LGM to PD. The few existing CGCM LGM and PD simulations looked at in Section 7.2.1 for tropical SST comparison were also looked at for NAMOC comparison. Table 7.2 lists the single-value NAMOC streamfunctions of these CGCM simulations. All the shortcomings of these CGCM simulations discussed in Section 7.2.1 as possibly affecting tropical SSTs should also be considered here as affecting NAMOC. Still, that NAMOC was stronger during the LGM than PD is not a result peculiar to the CGCM simulations in this work. Furthermore, for Hewitt et al. 2001/Hewitt et al. 2003 their reasons for the increase are discussed in them and are quite similar to those just discussed here.

In general, the NAMOC from proxies do not seem to match that from the CGCMs in this and some other works. However, the NAMOC is not part of a rigid “conveyor

thus that a change in (the more intuitive) current speed is directly reflective of a change in mass transport.

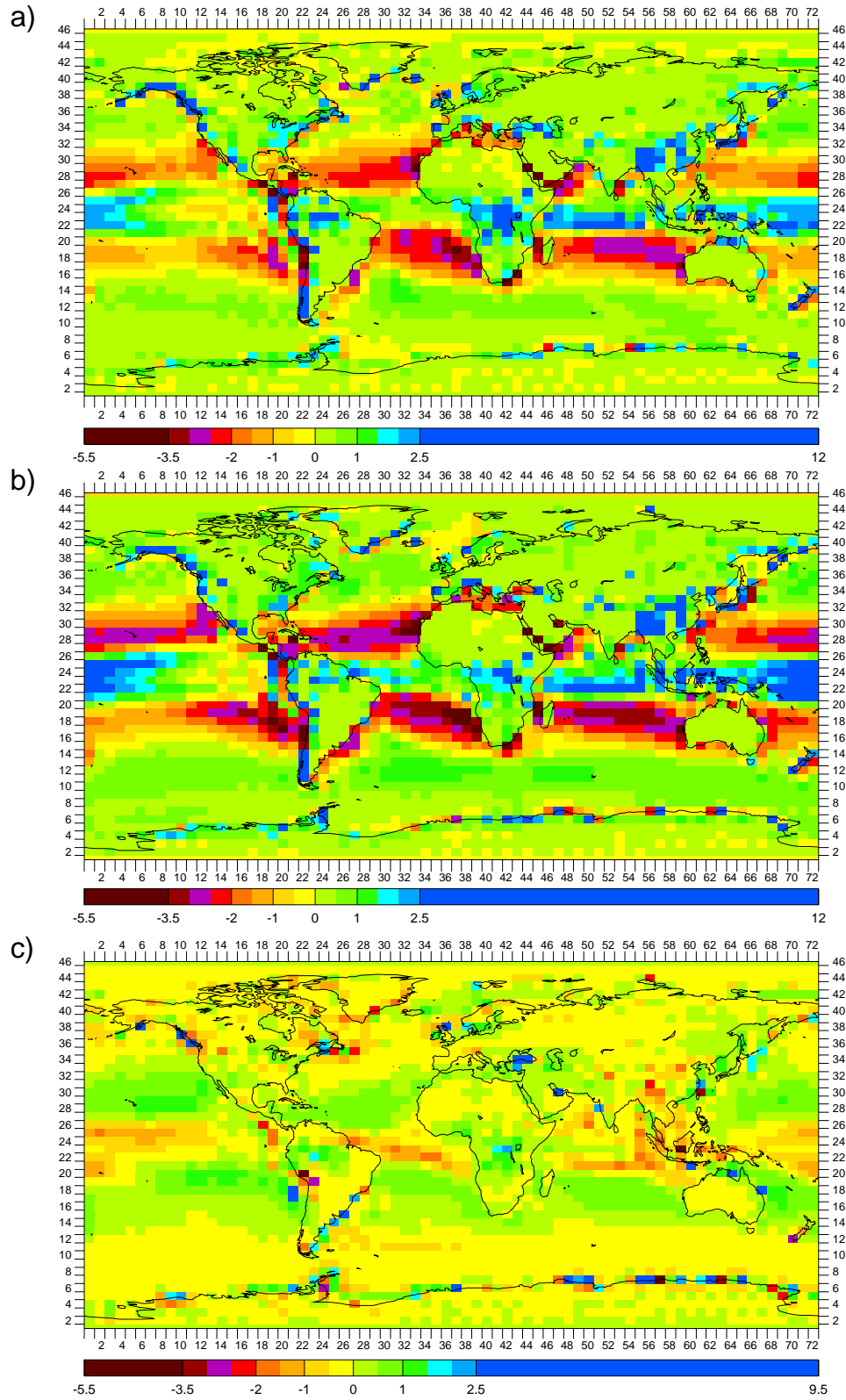


Figure 7.16: CGCM grid box maps of annual AGCM precipitation minus evaporation (mm/day) for: a) LGM; b) PD; and c) LGM – PD

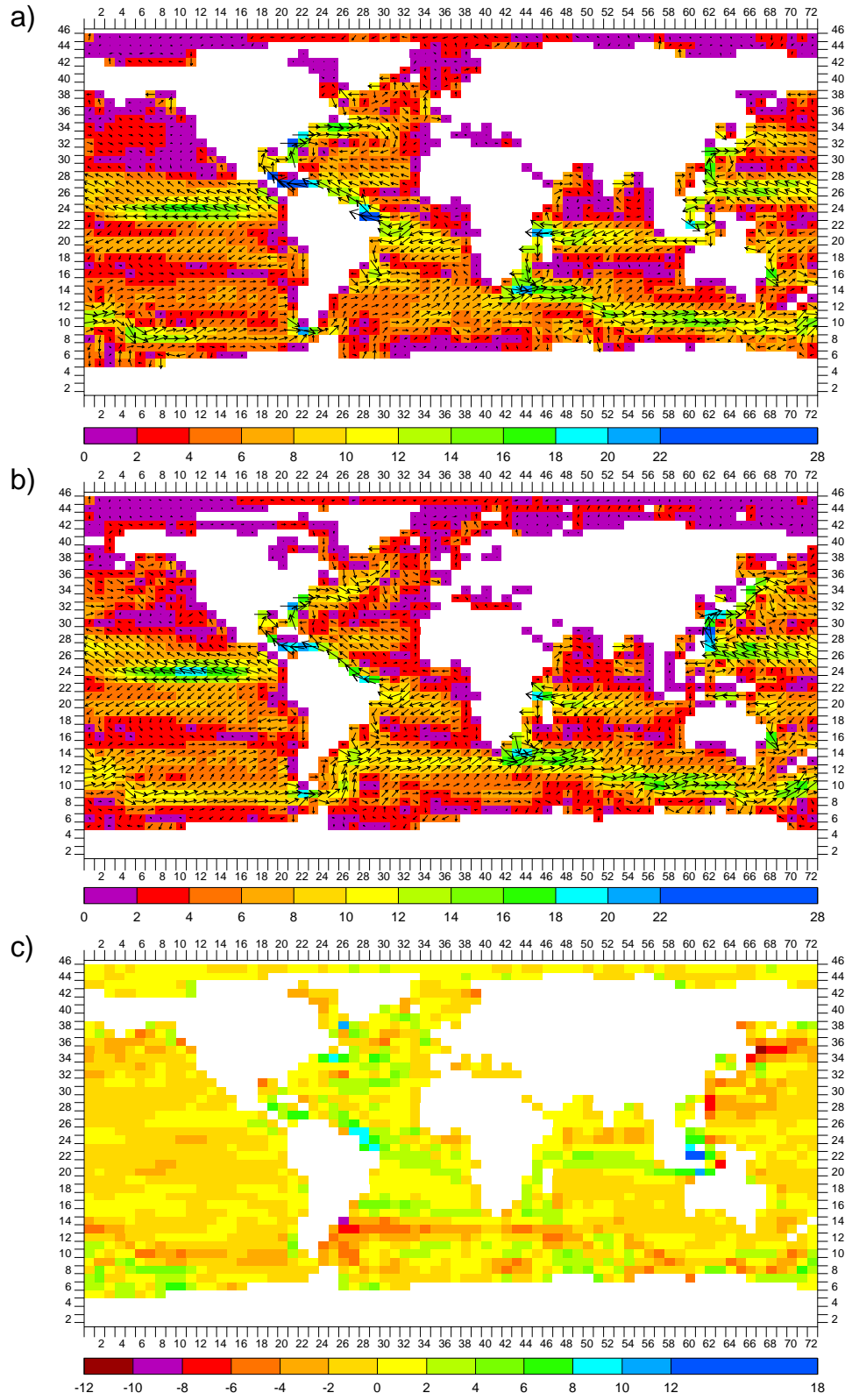


Figure 7.17: CGCM grid box maps of annual surface OGCM current speeds (cm/s) and vectors (overlain) for: a) LGM; b) PD; and c) LGM – PD (no vectors)

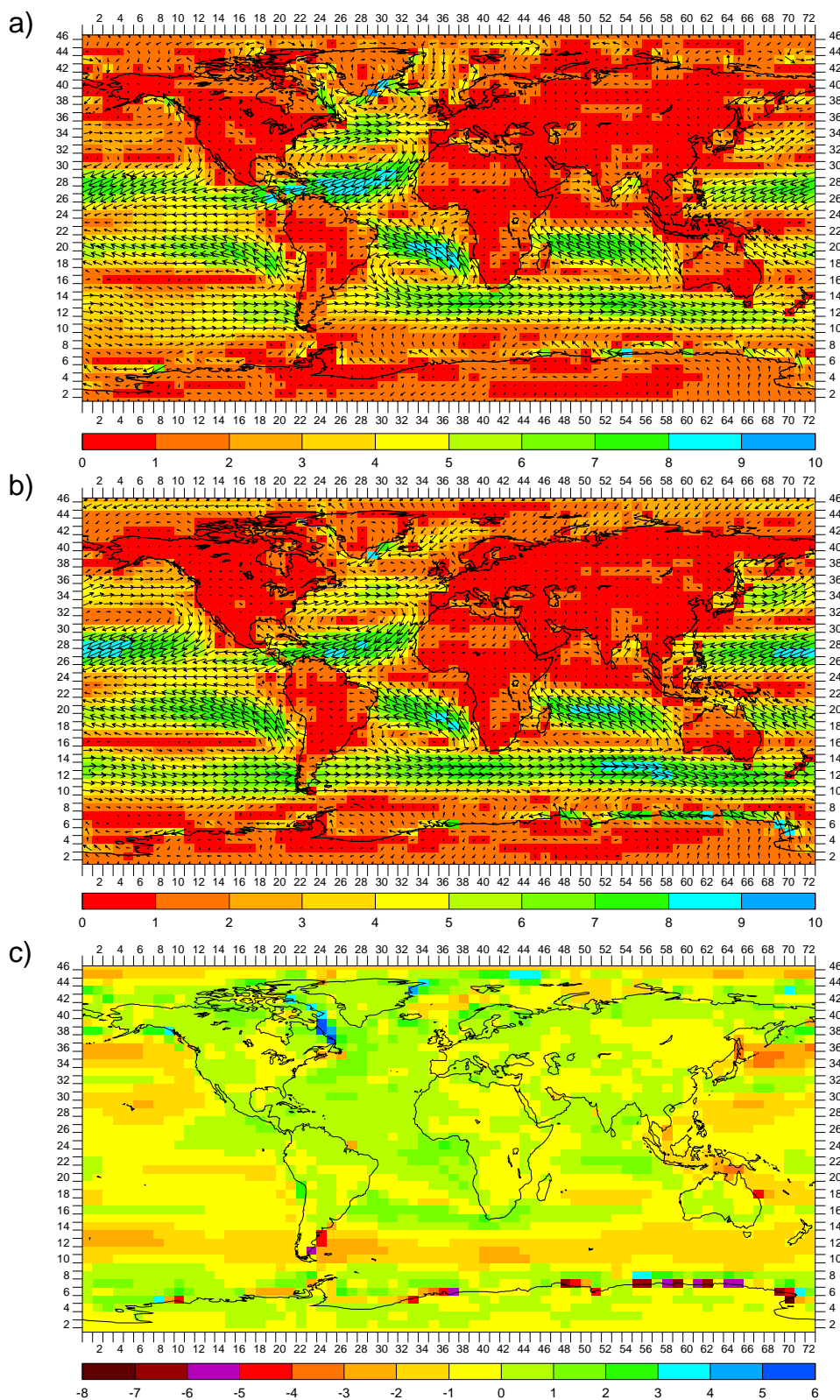


Figure 7.18: CGCM grid box maps of annual surface AGCM wind speeds (m/s) and vectors (overlain) for: a) LGM; b) PD; and c) LGM – PD (no vectors)

Reference	LGM	PD
This work (see Figure 6.4)	31	15
Bush and Philander 1998, Bush and Philander 1999	Not reported	
Hewitt et al. 2001, Hewitt et al. 2003	23	19
Kitoh et al. 2001, Kitoh and Murakami 2002	30	24
Shin et al. 2003	24	30
Kim et al. 2002, Kim et al. 2003	4	10

Table 7.2: Single-value North Atlantic meridional overturning streamfunction (Sv) for existing CGCM simulations of LGM and PD.

belt”. As seen, changes in it can have significant 3-D spatial variation — it can get stronger in one location and weaker in another, increasing, decreasing or staying the same overall. This spatial variation may explain many of the discrepancies with the proxies but good detailed model/data comparisons to determine this would be very involved and are beyond the scope of this work. In fact, for just such comparisons, the forward modelling of $\delta^{13}\text{C}$, just as for $\delta^{18}\text{O}$ in this work, has been proposed as future work (see Section 8.2).

Figure 7.19 contains CGCM grid box maps of annual surface AGCM temperature for LGM, PD and LGM – PD. Western Europe is significantly colder at the LGM than at PD. And yet as discussed above, at least one part of the CGCM NAMOC, the northernmost subsurface part, is significantly increased at the LGM. However, the Gulf Stream is the part of the NAMOC most often mentioned in conjunction with the “latitudinally-incorrect” warmth of Western Europe and Figure 7.17 shows that, at least southeast of Canada, the Gulf Stream is significantly increased at the LGM; in many other places it is the same as PD. Figure 7.20 contains CGCM grid box maps of annual surface OGCM heat flux for LGM, PD and LGM – PD and seems to indicate that the Gulf Stream there is indeed transporting more heat at the LGM (if it was stronger but carrying colder water, as it would be at the LGM, it might not be transporting more heat). In any case, it shows that it is possible to have a stronger NAMOC, with increased heat transport, and still have a colder Western Europe. As Seager et al. 2002 shows, while contrary to common belief this is not that outrageous. Further, it should not be that surprising because continental glaciers like that sitting on northern Europe at the LGM have an overwhelming impact on regional terrestrial

climate but less on more distant ocean climate.

Finally, note that a reduced NAMOC at the LGM is at odds with the concurrent belief that there was increased windiness then, as indicated by proxies, because the thermohaline circulation of which NAMOC is a part is actually thought to be primarily wind-driven (e.g., Wunsch 2002). Note that, at least over most of the Atlantic, Figure 7.18c also indicates increased AGCM windiness at the LGM compared to PD.

7.4 Temporal and Spatial Relationships of Surface Air Temperature Versus Precipitation $\delta^{18}\text{O}$

Ice core H_2O $\delta^{18}\text{O}_i$ has been used to determine past surface air temperatures. The relationship between surface air temperature and precipitation $\delta^{18}\text{O}$ though is not simply derived from the basic physics. Rather, it is an empirical relationship. An oft-cited one is

$$\delta^{18}\text{O} = .69 * T_S - 13.6 \Rightarrow T_S = 1.45 * \delta^{18}\text{O} + 19.71$$

from Dansgaard 1964, who formulated it by plotting PD annual surface air temperatures (C) versus precipitation $\delta^{18}\text{O}$ (‰ SMOW) from various temperate to polar sites, including Greenland, and fitting a line to it. It is thus a PD spatial relationship and there is no obvious physical reason why it should be applicable temporally, in order to determine past surface air temperatures from ice core $\delta^{18}\text{O}_i$. However, it has been used for this because there has been little alternative, such as a tested temporal relationship, and no definitive disproof. Recently though, the method of borehole paleothermometry has been applied to ice core boreholes in glaciers and GCMs carrying ^{18}O as a water tracer have been developed.

Borehole paleothermometry has been applied to the GRIP (Johnsen et al. 1995) and GISP2 (Cuffey et al. 1995, Cuffey and Clow 1997) ice core boreholes in Greenland. For a concise description of the technique see Jouzel et al. 1997 but it should be noted that it is essentially a method to calibrate the ice core $\delta^{18}\text{O}_i$ time series curve and is thus not strictly a $\delta^{18}\text{O}$ -independent estimate of paleotemperature. The GRIP (37.62°W, 72.57°N, 3230 m elevation) and GISP2 sites (38.48°W, 72.58°N, 3208 m elevation) are in the same AGCM grid box and are thus averaged together here

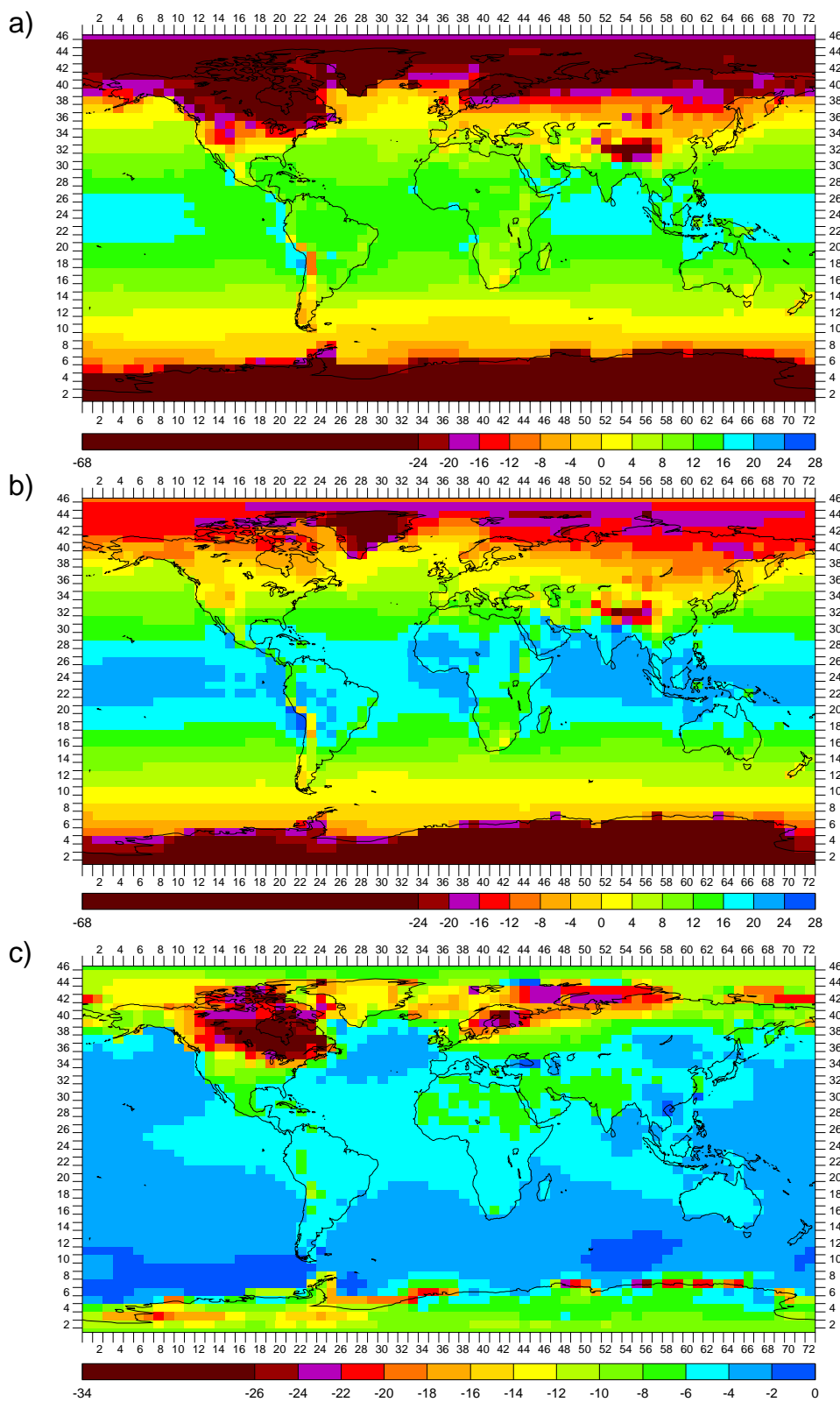


Figure 7.19: CGCM grid box maps of annual surface AGCM temperature (C) for: a) LGM; b) PD; and c) LGM – PD

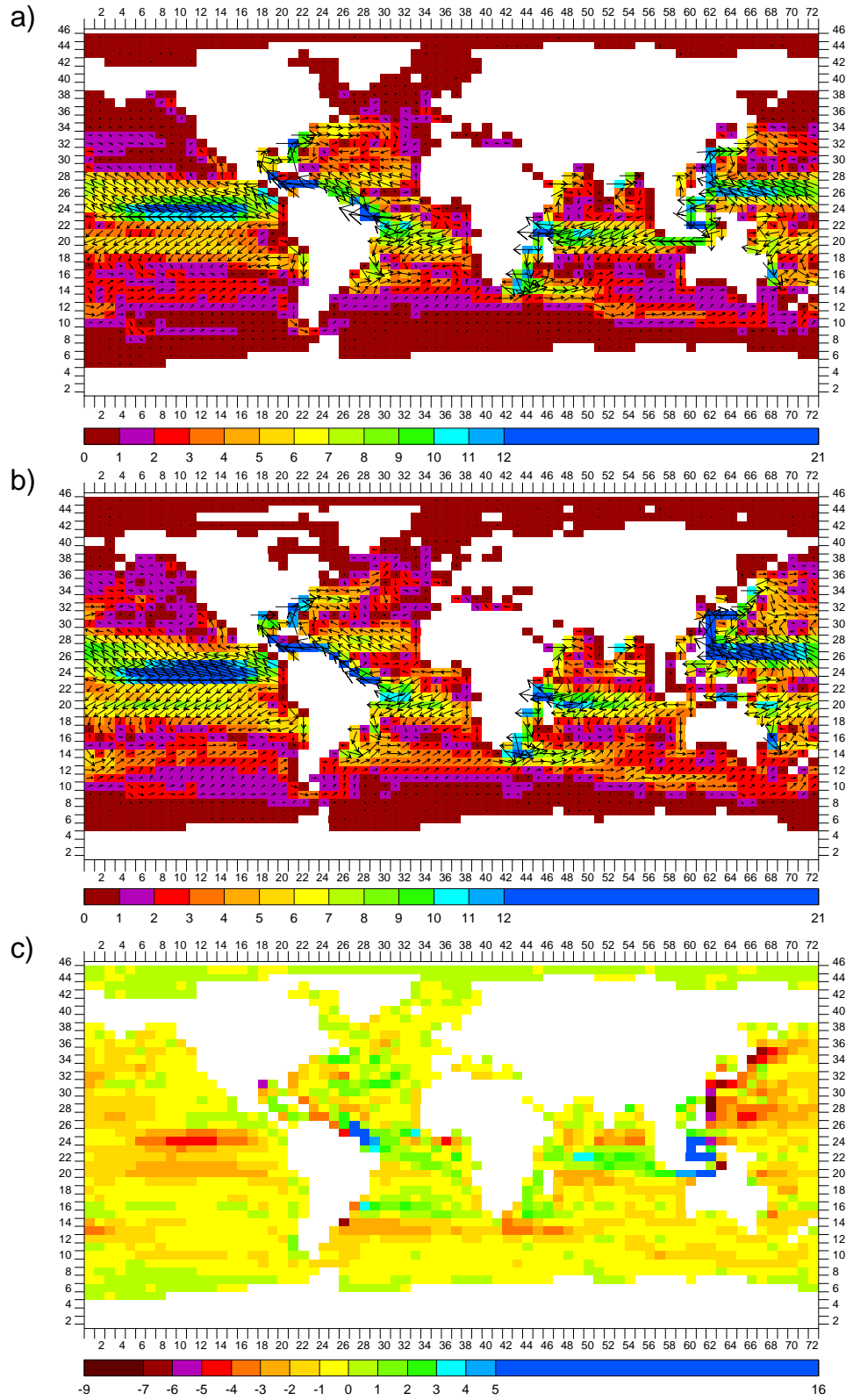


Figure 7.20: CGCM grid box maps of annual surface OGCM heat flux (MW/m²) for: a) LGM; b) PD; and c) LGM – PD

(3219 m average elevation to start). The PD annual surface air temperatures of the GRIP (Johnsen et al. 1992) and GISP2 (Grootes et al. 1993) sites are -32°C and -31°C , respectively, for an average of -31.5°C . The PD (1978 A.D.) ice core $\delta^{18}\text{O}_i$ for the GRIP and GISP2 ice cores (from the $\delta^{18}\text{O}$ database compiled for this research and the references therein; see Chapter 5) are -35‰ and -34.4‰ , respectively, for an average of -34.7‰ . The Dansgaard 1964 spatial $T_S(\delta^{18}\text{O})$ relationship has been slightly modified specifically for Greenland by Johnsen et al. 1995 to give

$$\delta^{18}\text{O}_i = .67 * T_S - 13.5 \Rightarrow T_S = 1.50 * \delta^{18}\text{O}_i + 20.3$$

and when this is applied to the PD ice core $\delta^{18}\text{O}_i$ it implies PD annual surface air temperatures of -32.2°C and -31.3°C for the GRIP and GISP2 sites, respectively, for an average of -31.75°C . These are very close to the stated observed values, which is as it should be since the relationship was derived from observations.

The LGM (21 ± 1.5 kyBP) ice core $\delta^{18}\text{O}_i$ for the GRIP and GISP2 ice cores (from the $\delta^{18}\text{O}$ database compiled for this research and the references therein) are -41.1‰ and -40.3‰ , respectively, for an average of -40.7‰ . When the Johnsen et al. 1995 spatial $T_S(\delta^{18}\text{O}_i)$ relationship is applied to these, they imply LGM annual surface air temperatures for the GRIP and GISP2 sites of -41.35°C and -40.15°C , respectively, for an average of -40.75°C . However, when borehole paleothermometry is applied to the GRIP (Johnsen et al. 1995) and GISP2 (Cuffey and Clow 1997) ice core boreholes it gives LGM temperatures of -52°C and -48°C , respectively, for an average of -50°C . These significant discrepancies (10.65°C , 7.85°C , and 9.25°C for GRIP, GISP2, and average, respectively) are good evidence that the PD spatial $T_S(\delta^{18}\text{O})$ relationship doesn't work temporally (i.e., doesn't work to find temperatures at one site in the past — the PD spatial $T_S(\delta^{18}\text{O})$ relationship may or may not hold spatially in the past).

Note that since the isotopic and observed PD surface air temperatures, which are the baselines for the isotopic and borehole LGM – PD temperatures, respectively, are essentially the same, comparing the isotopic (-9.15°C , -8.85°C , and -9°C for GRIP, GISP2 and average, respectively) and borehole (-20°C , -17°C , and -18.5°C for GRIP, GISP2 and average, respectively) LGM – PD temperatures does not significantly lessen the discrepancies. Looking at it another way, when the LGM – PD ice core

$\delta^{18}\text{O}_i$ (-6.1‰, -5.9‰, and -6‰ for GRIP, GISP2, and average, respectively) is divided by these borehole LGM – PD temperatures, a slope of a linear temporal $\delta^{18}\text{O}_i(T_S)$ relationship is arrived at. This temporal slope is 0.31‰/°C and 0.35‰/°C for GRIP and GISP2, respectively, for an average of 0.33‰/°C, and this is significantly different from the 0.67‰/°C slope of the stated PD linear spatial $\delta^{18}\text{O}_i(T_S)$ relationship.

A more widely applicable (spatial $T_S(\delta^{18}\text{O})$ relationships in the past can even be determined) and truly independent technique for determining a temporally-valid $T_S(\delta^{18}\text{O})$ relationship is through the use of GCMs carrying ^{18}O as a water tracer. Werner et al. 2000 used just an AGCM (3.75° x 3.75° resolution) carrying ^{18}O as a water tracer to do 10-model-year LGM and PD simulations. CLIMAP boundary conditions were used except for the Greenland topography, which was a lowered version of the erred Peltier 1994. Further, their LGM $\delta^{18}\text{O}$ values were manually corrected by 1.5‰ to account for the higher mean ocean $\delta^{18}\text{O}_w$ then (as indicated, probably 0.5‰ too high but negligible compared to the range of precipitation $\delta^{18}\text{O}$). From plotting 10-year mean annual AGCM precipitation $\delta^{18}\text{O}_i$ versus 10-year mean annual surface AGCM temperatures in an unreported subset of Greenland grid boxes and doing a linear regression, Werner et al. 2000 reported a PD spatial $\delta^{18}\text{O}_i(T_S)$ slope of 0.58‰/°C and an LGM spatial $\delta^{18}\text{O}_i(T_S)$ slope of 0.38‰/°C; compare to the 0.67‰/°C slope of the stated PD observed linear spatial $\delta^{18}\text{O}_i(T_S)$ relationship. From plotting AGCM precipitation $\delta^{18}\text{O}_i$ versus surface AGCM temperature in the GRIP/GISP2 grid box from all years of their PD and LGM simulations and doing a linear regression, Werner et al. 2000 reported a temporal $\delta^{18}\text{O}_i(T_S)$ slope of 0.23‰/°C; compare to the stated 0.33‰/°C temporal $\delta^{18}\text{O}_i(T_S)$ slope from borehole paleothermometry. Werner et al. 2000 would thus seem to indicate that the PD observed linear spatial $T_S(\delta^{18}\text{O})$ relationship doesn't work temporally and suggests instead using a temporal $T_S(\delta^{18}\text{O})$ relationship similar to that from borehole paleothermometry.

A similar procedure can be applied to the LGM and PD simulations of this work. Here however, a full CGCM is used, as described, with 100 sampled years each and the changed LGM mean ocean $\delta^{18}\text{O}_w$ set in the CGCM itself (probably 0.25‰ too high, as discussed, but again negligible compared to the range of precipitation $\delta^{18}\text{O}$). Figure 7.21 then, plots 100-year mean annual AGCM precipitation $\delta^{18}\text{O}_i$ versus 100-year mean annual surface AGCM temperature in all 38 Greenland grid boxes for

both the LGM and PD simulations, with linear regressions through each era's set of points. Further, annual AGCM precipitation $\delta^{18}\text{O}_i$ is plotted versus annual surface AGCM temperature in the GRIP/GISP2 grid box ([29,42]) for each of the 100 sampled years of the PD and LGM simulations, with a linear regression through all 200 points. The resulting 1.11‰/°C slope of the PD linear spatial $\delta^{18}\text{O}_i(T_S)$ relationship is significantly larger than the 0.67‰/°C PD observed one but it is not known what effect there is from the differing AGCM Greenland topography (due to discretization; for example, the PD AGCM grid box [29,42] elevation is only 2981 m) and the greater number of AGCM years and sites sampled. Interestingly, the resulting 1.28‰/°C slope of the LGM linear spatial $\delta^{18}\text{O}_i(T_S)$ relationship is similar to that of the PD one. More importantly, the resulting 0.32‰/°C slope of the linear temporal $\delta^{18}\text{O}_i(T_S)$ relationship is significantly smaller than either the PD or LGM spatial slope and is about the same as the stated 0.33‰/°C temporal slope from borehole paleothermometry. Thus, the PD observed linear spatial $T_S(\delta^{18}\text{O})$ relationship doesn't work temporally and a temporal $T_S(\delta^{18}\text{O})$ relationship like that from borehole paleothermometry should be used.

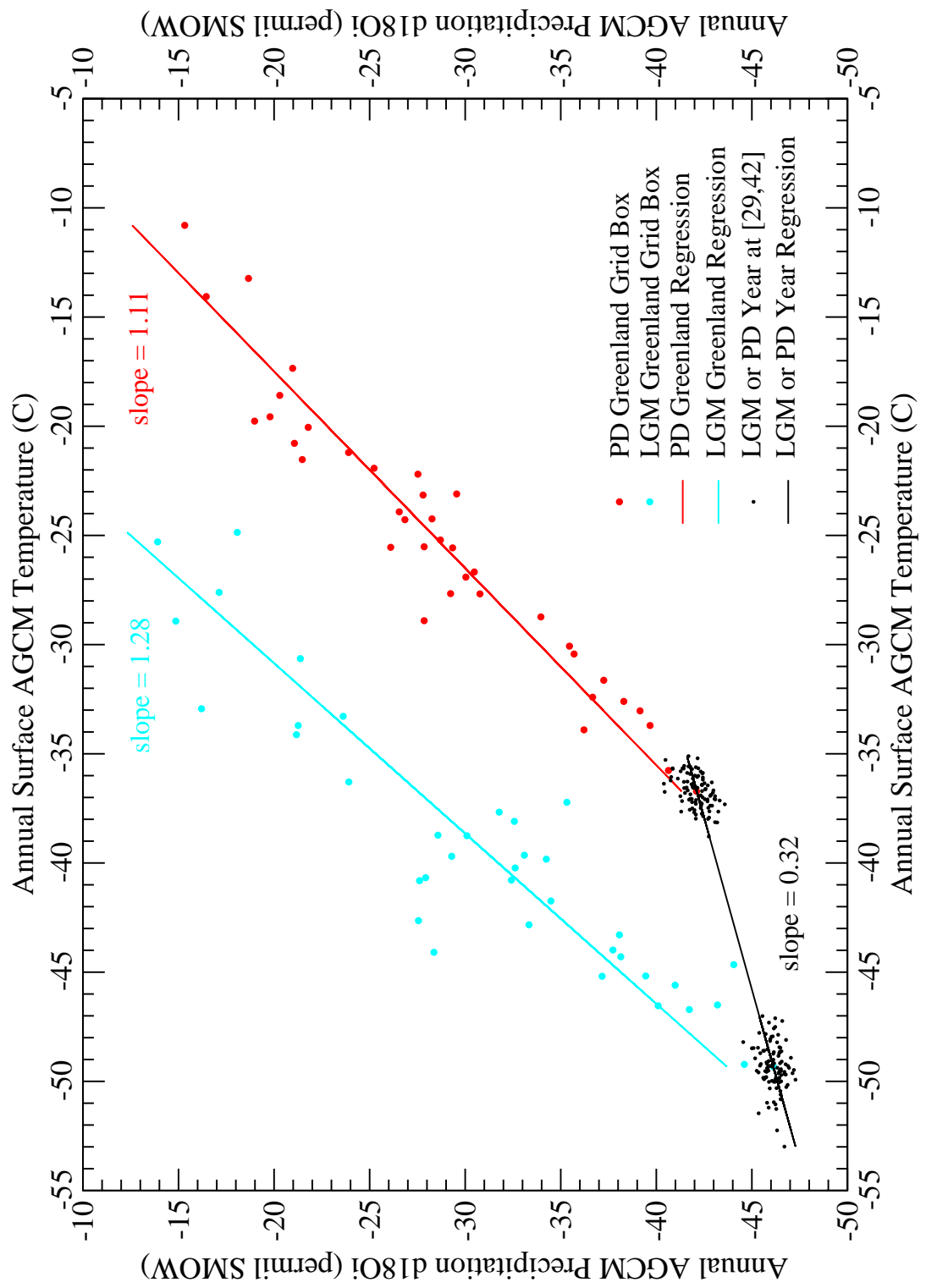


Figure 7.21: Plot, with linear regressions, of 100-year mean annual AGCM precipitation $\delta^{18}\text{O}_i$ (‰ SMOW) versus 100-year mean annual surface AGCM temperature (C) in PD and LGM Greenland grid boxes and of annual AGCM precipitation $\delta^{18}\text{O}_i$ (‰ SMOW) versus annual surface AGCM temperature (C) in grid box [29,42] for each of the 100 sampled years of the LGM and PD simulations.

Chapter 8

Conclusions and Future Work

8.1 Conclusions

From the research of Sections 3.2.3 and 3.2.4 it was concluded that using the Reduced Gravity and the Distorted Physics OGCM acceleration schemes, respectively, can result in equilibriums different from that of the unaccelerated OGCM (as well as from each other's). This may have important wider implications because these or similar OGCM acceleration schemes, particularly those involving changing timesteps, may be being used in the GCM simulations of other researchers and their equilibriums, and thus climate inferences, may be being affected. It was not concluded from the research of Section 3.2.5 and 3.2.2 whether the acceleration schemes of program parallelization and starting from another equilibrium, respectively, affect the equilibriums reached but program parallelization seemed least likely to affect equilibrium and starting from another equilibrium was the easiest to implement so it was concluded that they should both be used.

From the research of Section 3.3.2, as well as from the long-term results of the LGM and PD simulations with the CGCM as described in Section 6.1, it was concluded that a steady realistically strong North Atlantic meridional overturning circulation (NAMOC), as measured by its streamfunction, requires running to near-equilibrium. It was further concluded that a realistically strong NAMOC streamfunction requires a CGCM rather than just an OGCM. Also, seemingly-minor topography changes seemed to help and this conclusion was further backed, as found in the research of

Section 7.3, by the very strong NAMOC streamfunction in the LGM simulation, with its different non-PD topography (from the research of Section 4.4).

From the research of Sections 4.1, 4.3, and 4.2, respectively, it was concluded that LGM greenhouse gas concentrations and insolation can be known very accurately for use as boundary conditions in a CGCM but that aerosols currently cannot. Further, it was concluded from the research of Sections 4.4 and 4.5, respectively, that LGM topography, with its extensive continental glaciers, lower sea level and closed straits, can be known fairly well for use as CGCM boundary conditions but that LGM land surface characteristics currently cannot.

From the research of Chapter 5 it was concluded that there was currently publically available a useful amount of published ocean sediment and ice core $\delta^{18}\text{O}$ data but that this could be significantly increased and to great benefit.

From the research of Chapter 6 it was concluded that the forward modelling technique — inputting CGCM simulation results into a climate proxy model and then comparing the proxy model results directly to the proxy data — is useful and promising for $\delta^{18}\text{O}$. Future work is thus based on this technique. However, from Section 6.4.3 it was concluded that the foraminifera model needed improvement in predicting the $\delta^{18}\text{O}_c$ of planktonic foraminifera. Finally from Chapter 6, it was concluded that some confidence in conclusions drawn from the LGM – PD of simulations is warranted.

As calculated in Section 6.5.1 and discussed in Section 7.1, it was concluded that the LGM – PD mean ocean $\delta^{18}\text{O}_w$ was 1.0‰ SMOW. From the research of Section 7.1 it was further concluded that while this CGCM estimate matches that from ocean sediment core pore water research, in detail they do not support each other. From the research of Section 7.2 it was concluded that the LGM – PD mean tropical SST was -3.6°C , at least a 2°C greater change than that determined by CLIMAP. Further, this was at least a 1°C greater change than that indicated by alkenones or foraminifera Mg/Ca and there was little indication about which month the SSTs from these represented. Also, it was concluded that terrestrial temperature proxies, which dispute CLIMAP, were consistent with the CGCM. From the research of Section 7.3 it was concluded that, contrary to its proxies, the North Atlantic meridional overturning circulation was stronger at the LGM than at PD, even though the LGM was colder. Further, this was because the Labrador Sea was isolated from its PD fresher

water sources by surrounding continental glaciers at the LGM and wind/current patterns/strengths were changed such as to further increase water density, and thus deep convection, south of Greenland at the LGM. Finally, from the research of Section 7.4 it was concluded that, consistent with ice core borehole paleothermometry, the spatial relationship of surface air temperature versus precipitation $\delta^{18}\text{O}$ is significantly different from the temporal one at a location, i.e., the former shouldn't be used to determine paleotemperatures from ice cores.

8.2 Future Work

While the forward modelling technique has been shown in this work to be useful for $\delta^{18}\text{O}$, the model/data comparisons could be refined and the foraminifera model improved with the addition of more and more geographically diverse ocean sediment and ice cores. Since it has been more than two years since the ocean sediment and ice core $\delta^{18}\text{O}$ data was compiled (see Section 5.1) and in the meantime new data has become available, a renewed gathering of $\delta^{18}\text{O}$ data would aid these two goals. Additionally, ocean sediment cores that were previously excluded because they had age models based only on unconverted ^{14}C ages could be added by converting these ages to calendar ages.

The simulations continued to run even after the model years sampled for this work (see Section 6.1) so the model/data comparisons could also be refined by using the latest model years. Figures 8.1 to 8.4 are the latest versions of Figures 6.1 to 6.4, respectively. It is clear that the runs are closer to equilibrium and this may have an effect on the model/data comparisons.

The model/data comparisons with precipitation $\delta^{18}\text{O}$ could be done more extensively, particularly with regards to the seasonality factor (see Section 2.2.3) and the deuterium excess (see Section 2.1.3).

Improving the foraminifera model might additionally be done by not necessarily using an existing empirical equation for foraminifera $\delta^{18}\text{O}_c$ from ocean in situ temperature and $\delta^{18}\text{O}_w$ but instead developing a model that just most accurately predicts ocean sediment core foraminifera $\delta^{18}\text{O}_c$ from ocean variables. One possibility to do this is a neural net trained with observed ocean variables and coretop foraminifera

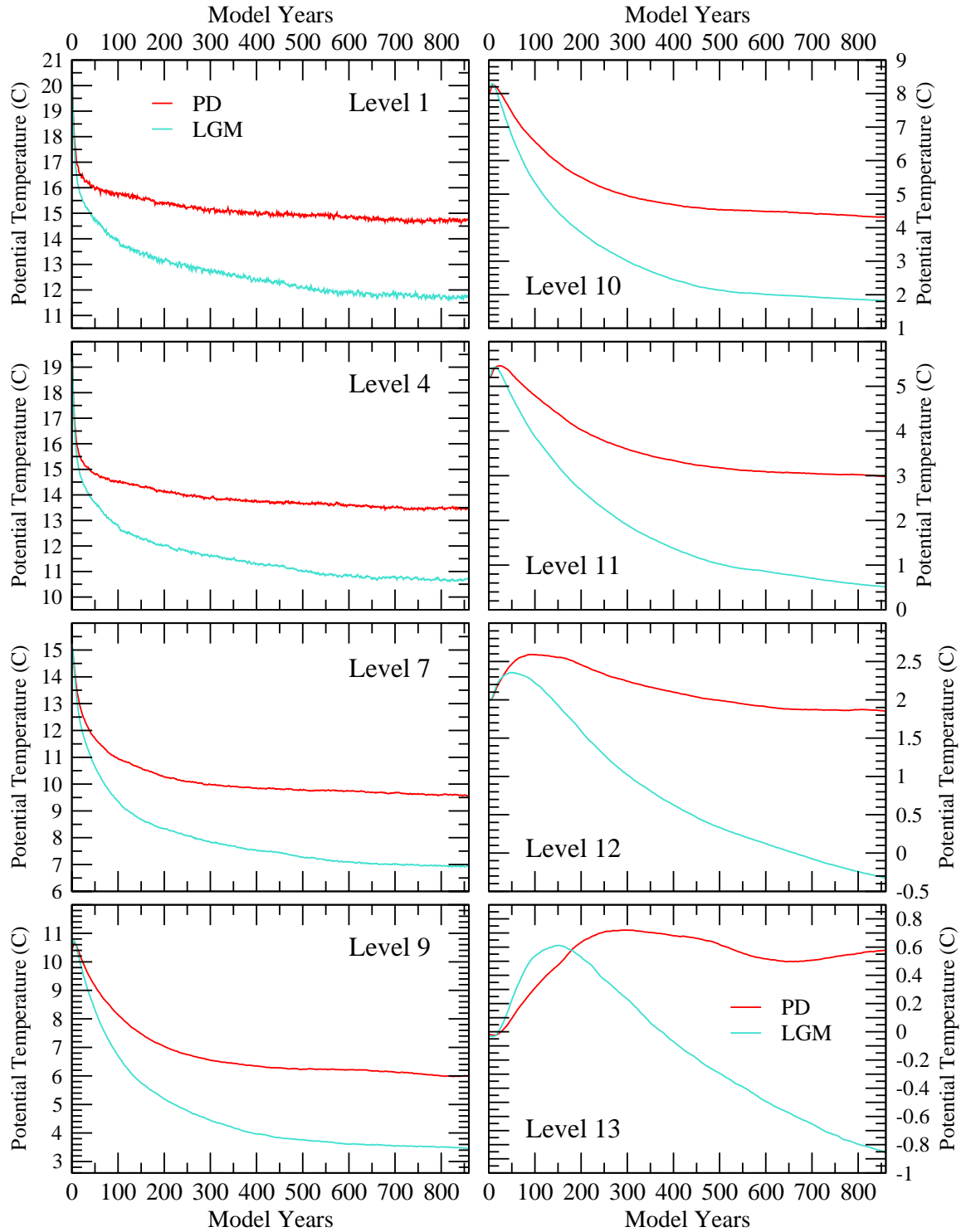


Figure 8.1: Latest mean global/annual OGCM potential temperature (C) versus model years at selected OGCM levels for PD and LGM runs.

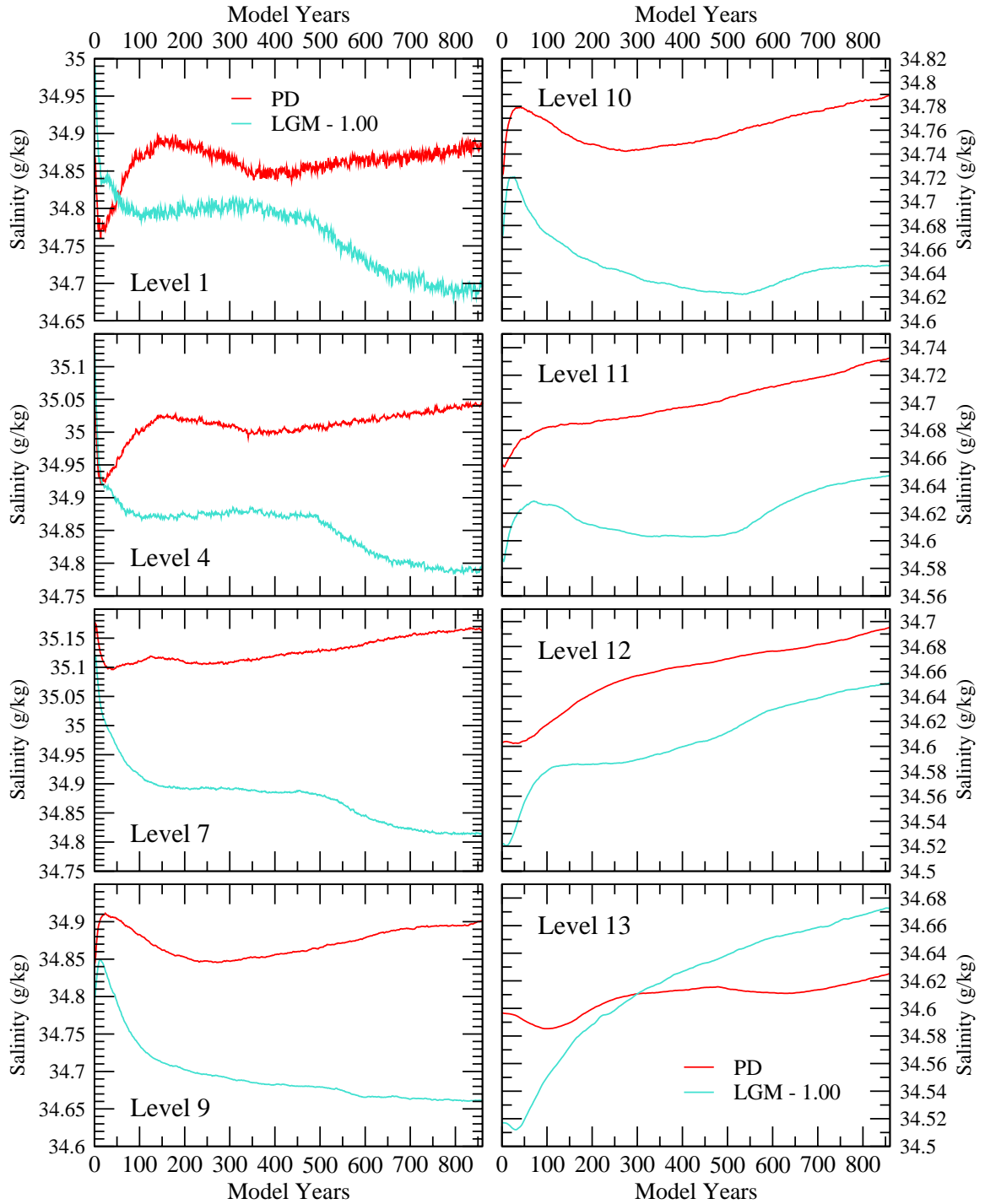


Figure 8.2: Latest mean global/annual salinity (g/kg; minus 1.00 for LGM) versus model years at selected OGCM levels for PD and LGM runs.

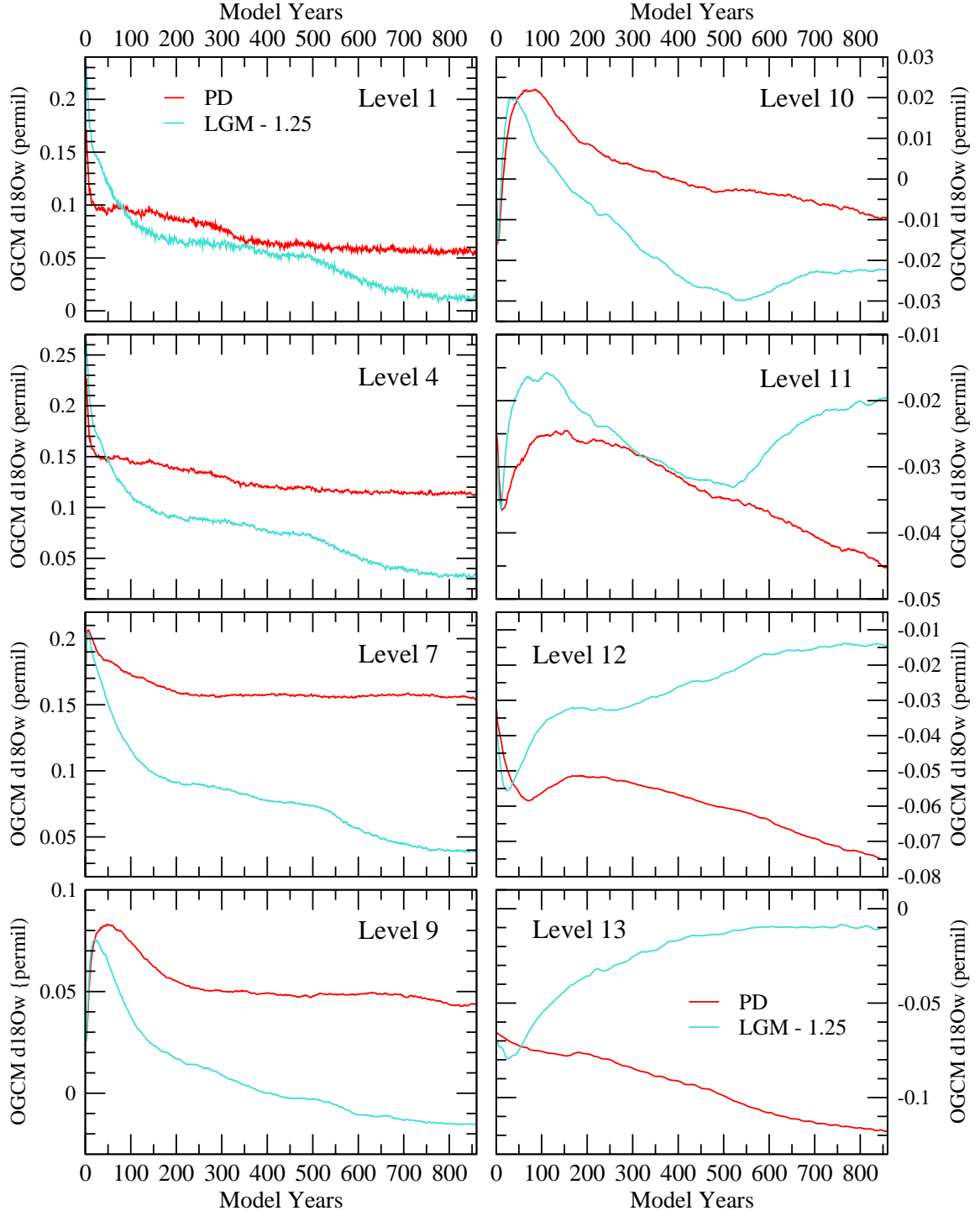


Figure 8.3: Latest mean global/annual OGCM $\delta^{18}\text{O}_w$ (‰ SMOW; minus 1.25 for LGM) versus model years at selected OGCM levels for PD and LGM runs.

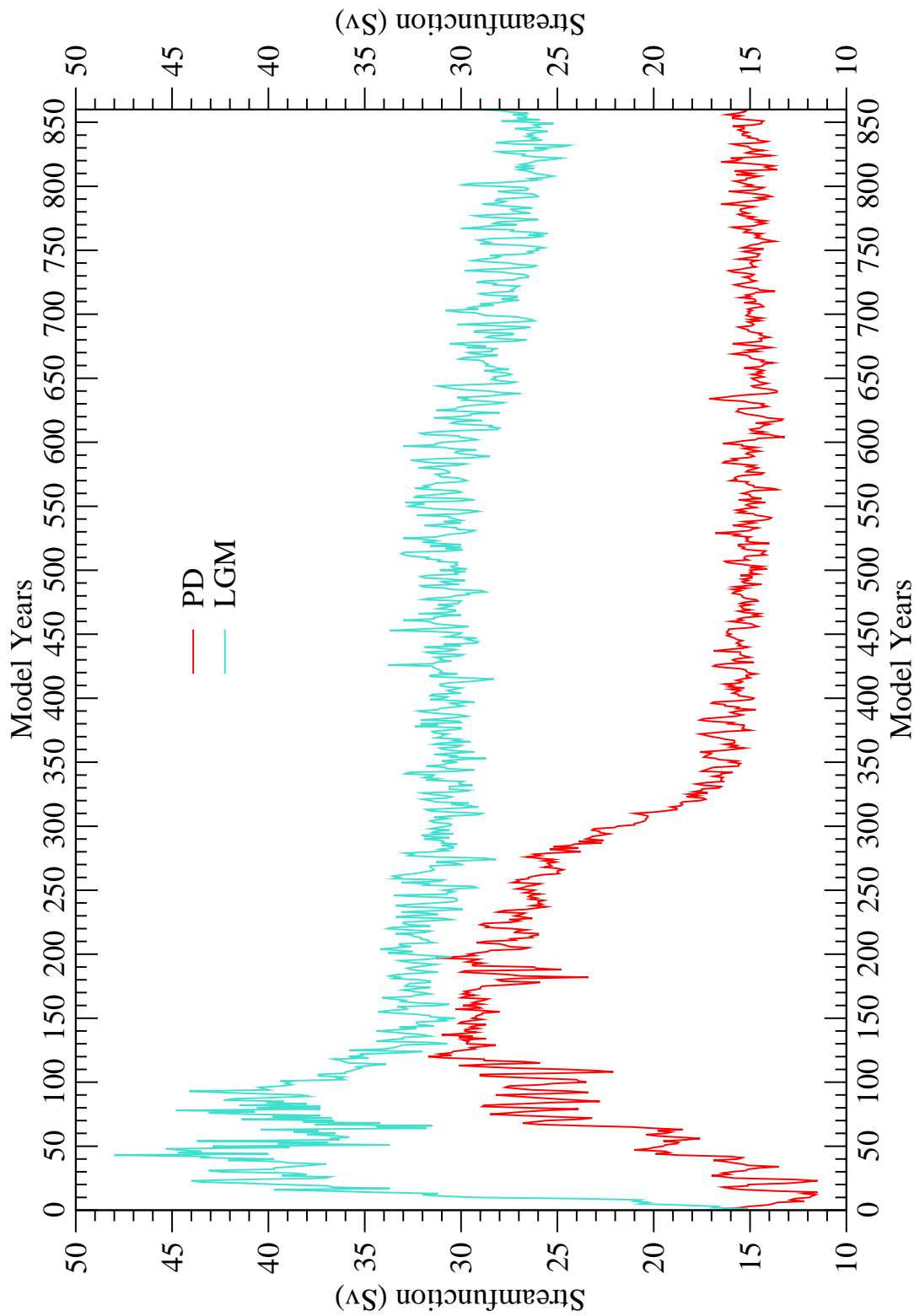


Figure 8.4: Latest annual NAMOC streamfunction value (Sv) at OGCM grid box lat# 35 (44–48°N), level 10 (899–1360 m depth) versus model years for PD and LGM runs.

$\delta^{18}\text{O}_c$.

The foraminifera model could also be improved by making it account for the important effect of the ocean carbonate/alkalinity/pH system on foraminifera $\delta^{18}\text{O}_c$. The first step towards this would be adding surface ocean CO_2 gas exchange to the CGCM. This would be straightforward because CFCs were added to the OGCM as tracers as part of Thresher 1999 and the surface gas exchange added to the OGCM for them is readily adapted for CO_2 .

As an expansion of forward modelling of foraminifera proxies, the carbon isotopes ^{14}C and ^{13}C could, as part of a carbon cycle, be added as tracers in the CGCM and to the foraminifera model. Adding ^{14}C is important because the dating of the ocean sediment cores is. This dating is often based on $\Delta^{14}\text{C}$, which has significant uncertainties. For example, even for coretop samples representing PD it is uncertain what $\Delta^{14}\text{C}$ reservoir correction to use at a core location. This information at downcore paleosamples, when the circulation (especially upwelling) may have been different, is even more uncertain. The first step in adding ^{14}C would be adding the simpler abiotic part of the carbon cycle, of which the mentioned surface OGCM gas exchange is a major part. Addition of era-dependent production of ^{14}C in the AGCM would be straightforward and from current research in that area. Ocean sediment core $\Delta^{14}\text{C}$ data would have to be compiled for comparison but from the research of Chapter 5 there appears to be quite a bit available.

Adding ^{13}C is important because foraminifera $\delta^{13}\text{C}$ is a prevalent but complicated ocean proxy, as discussed in Section 7.3, and its forward modelling would be very useful for doing enlightening comparisons. This would require adding the more complicated biotic part of the carbon cycle. Possibly, existing offline biotic carbon cycle models could be used with the existing LGM and PD simulation results. Ocean sediment core $\delta^{13}\text{C}$ data would have to be compiled for comparison but again there appears to be quite a bit available. $\delta^{18}\text{O}$, $\Delta^{14}\text{C}$, and $\delta^{13}\text{C}$ are important proxies in ocean sediment cores and the forward modelling of all three together would make for a very powerful paleoclimate tool.

As an expansion of forward modelling to other climate proxies, it would be worth modelling corals, speleothems, and tree cellulose and gathering $\delta^{18}\text{O}$ records for them, as described in Sections 2.2.2 and 2.2.4.

Different eras could also be simulated. As mentioned in Chapter 1, the LGM and PD were chosen as the stable end states of the most recent large climate change. Thus, the Deglaciation transition in between could now be studied. Section 4.1 outlines a series of times slices useful for this and Section 4.3 provides orbital parameters for them. Of particular interest would be the Younger Dryas and for it and the other time slices glacial meltwater experiments could be done to see if that improves the simulations compared to available proxy data.

Finally, as discussed in Section 4.2, more realistic aerosols could be added to the CGCM for the paleosimulations. This would be a large task but is of considerable interest and importance and has already been proposed for an LGM simulation with this CGCM (Ron Miller, personal communication).

References

- Adkins, J. and D. Schrag, 2001: Pore fluid constraints on deep ocean temperature and salinity during the last glacial maximum *Geophysical Research Letters*, **28**, 771–774.
- Aksu, A., R. Hiscott, M. Kaminski, P. Mudie, H. Gillespie, T. Abrajano, and D. Yaşar, 2002: Last glacial-Holocene paleoceanography of the Black Sea and Marmara Sea: stable isotopic, foraminiferal and coccolith evidence *Marine Geology*, **190**, 119–149.
- Anderson, D. M. and W. L. Prell, 1993: A 300 KYR RECORD OF UPWELLING OFF OMAN DURING THE LATE QUATERNARY: EVIDENCE OF THE ASIAN SOUTHWEST MONSOON *Paleoceanography*, **8**, 193–208.
- Armstrong, R. L. and K. Knowles, 2003: The International Satellite Land Surface Climatology Project (ISLSCP) Initiative II Data Collection: Global Monthly Sea Ice Concentration Technical report, National Snow and Ice Data Center (NSIDC), University of Colorado, Boulder, Colorado, Documentation is at http://islscp2.sesda.com/ISLSCP2_1/data/snow_sea-ice_oceans/sea_ice_extent_xdeg/sea_ice_extent_xdeg_doc.pdf and data is at http://islscp2.sesda.com/ISLSCP2_1/data/snow_sea-ice_oceans/sea_ice_extent_xdeg.
- Arz, H., J. Pätzold, and G. Wefer, 1999a: Climatic changes during the last deglaciation recorded in sediment cores from the northeastern Brazilian Continental Margin *Geo-Marine Letters*, **19**, 209–218.
- Arz, H. W., S. Gerhardt, J. Pätzold, and U. Röhl, 2001: Millennial-scale changes of surface- and deep-water flow in the western tropical Atlantic linked to Northern Hemisphere high-latitude climate during the Holocene *Geology*, **29**, 239–242.
- Arz, H. W., J. Pätzold, and G. Wefer, 1998: Correlated Millennial-Scale Changes in Surface Hydrography and Terrigenous Sediment Yield Inferred from Last-Glacial Marine Deposits off Northeastern Brazil *Quaternary Research*, **50**, 157–166.
- Arz, H. W., J. Pätzold, and G. Wefer, 1999b: The deglacial history of the western tropical Atlantic as inferred from high resolution stable isotope records off northeastern Brazil *Earth and Planetary Science Letters*, **167**, 105–117.
- Bard, E., G. Raisbeck, F. Yiou, and J. Jouzel, 2000: Solar irradiance during the last 1200 years based on cosmogenic nuclides *Tellus*, **52B**, 985–992.

- Bard, E., F. Rostek, and C. Sonzogni, 1997: Interhemispheric synchrony of the last deglaciation inferred from alkenone palaeothermometry *Nature*, **385**, 707–710.
- Bard, E., F. Rostek, J.-L. Turon, and S. Gendreau, 2000: Hydrological Impact of Heinrich Events in the Subtropical Northeast Atlantic *Science*, **289**, 1321–1324.
- Bareille, G., F. E. Grousset, M. Labracherie, L. Labeyrie, and J.-R. Petit, 1994: Origin of detrital fluxes in the southeast Indian Ocean during the last climatic cycles *Paleoceanography*, **9**, 799–819.
- Bassinot, F. C., L. D. Labeyrie, E. Vincent, X. Quidelleur, N. J. Shackleton, and Y. Lancelot, 1994: The astronomical theory of climate and the age of the Brunhes-Matuyama magnetic reversal *Earth and Planetary Science Letters*, **126**, 91–108.
- Bauch, H. A., H. Erlenkeuser, R. F. Spielhagen, U. Struck, J. Matthiessen, J. Thiede, and J. Heinemeier, 2001: A multiproxy reconstruction of the evolution of deep and surface waters in the subarctic Nordic seas over the last 30,000 yr *Quaternary Science Reviews*, **20**, 659–678.
- Bemis, B. E., H. J. Spero, J. Bijma, and D. W. Lea, 1998: Reevaluation of the oxygen isotopic composition of planktonic foraminifera: Experimental results and revised paleotemperature equations *Paleoceanography*, **13**, 150–160.
- Bender, M., T. Sowers, and L. Labeyrie, 1994: The Dole effect and its variations during the last 130,000 years as measure in the Vostok ice core *Global Biogeochemical Cycles*, **8**, 363–376.
- Berger, A., J. Imbrie, J. Hays, G. Kukla, and B. Saltzman (Eds.), 1984: *Milankovitch and Climate : Understanding the Response to Astronomical Forcing*, Volume 126 of *NATO ASI Series C: Mathematical and Physical Sciences* Boston: D. Reidel Publishing Company.
- Berger, A., M.-F. Loutre, and C. Tricot, 1993: Insolation and Earth's Orbital Periods *Journal of Geophysical Research*, **98**, 10,341–10,362.
- Berger, A. L., 1978a: Long-Term Variations of Daily Insolation and Quaternary Climatic Changes *Journal of the Atmospheric Sciences*, **35**, 2362–2367.
- Berger, A. L., 1978b: A SIMPLE ALGORITHM TO COMPUTE LONG-TERM VARIATIONS OF DAILY OR MONTHLY INSOLATION Contribution No. 18, L'Institut d'Astronomie et de Géophysique, Université Catholique de Louvain, Louvain-la-Neuve, Belgium, .
- Berger, W., T. Bickert, M. Yasuda, and G. Wefer, 1996: Reconstruction of atmospheric CO₂ from ice-core data and the deep-sea record of Ontong Java plateau: the Milankovitch chron *Geol Rundsch (International Journal of Earth Sciences)*, **85**, 466–495.
- Beveridge, N., H. Elderfield, and N. Shackleton, 1995: Deep thermohaline circulation in the low-latitude Atlantic during the last glacial *Paleoceanography*, **10**, 643–660.

- Bickert, T. and G. Wefer, 1996: Late Quaternary Deep Water Circulation in the South Atlantic: Reconstruction from Carbonate Dissolution and Benthic Stable Isotopes *The South Atlantic: Present and Past Circulation*, G. Wefer, W. H. Berger, G. Siedler, and D. J. Webb, Eds., 599–620. Springer-Verlag.
- Biscaye, P., F. Grousset, M. Revel, S. V. der Gaast, G. Zielinski, A. Vaars, and G. Kukla, 1997: Asian provenance of glacial dust (stage 2) in the Greenland Ice Sheet Project 2 Ice Core, Summit, Greenland *Journal of Geophysical Research*, **102**, 26,765–26,781.
- Blunier, T., J. Chappellaz, J. Schwander, A. Dällenbach, B. Stauffer, T. Stocker, D. Raynaud, J. Jouzel, H. Clausen, C. Hammer, and S. Johnsen, 1998: Asynchrony of Antarctic and Greenland climate change during the last glacial period *Nature*, **394**, 739–743.
- Bond, G., W. Showers, M. Cheseby, R. Lotti, P. Almasi, P. deMenocal, P. Priore, H. Cullen, I. Hajdas, and G. Bonani, 1997: A Pervasive Millennial-Scale Cycle in North Atlantic Holocene and Glacial Climates *Science*, **278**, 1257–1266.
- Boyle, E. A., 1988: CADMIUM: CHEMICAL TRACER OF DEEPWATER PALEOCEANOGRAPHY *Paleoceanography*, **3**, 471–489.
- Boyle, E. A. and L. D. Keigwin, 1982: Deep Circulation of the North Atlantic over the Last 200,000 Years: Geochemical Evidence *Science*, **218**, 784–787.
- Bradley, R., 1985: *Quaternary Paleoclimatology: Methods of Paleoclimatic Reconstruction* London, England, U.K.: Chapman & Hall.
- Broecker, W. S. and G. H. Denton, 1989: The role of ocean-atmosphere reorganizations in glacial cycles *Geochimica et Cosmochimica Acta*, **53**, 2465–2501.
- Bryan, K., 1984: Accelerating the Convergence to Equilibrium of Ocean-Climate Models *Journal of Physical Oceanography*, **14**, 666–673.
- Budziak, D., R. R. Schneider, F. Rostek, P. J. Müller, E. Bard, and G. Wefer, 2000: Late Quaternary insolation forcing on total organic carbon and C₃₇ alkenone variations in the Arabian Sea *Paleoceanography*, **15**, 307–321.
- Bush, A. B. and S. G. H. Philander, 1998: The Role of Ocean-Atmosphere Interactions in Tropical Cooling During the Last Glacial Maximum *Science*, **279**, 1341–1344.
- Bush, A. B. and S. G. H. Philander, 1999: The climate of the Last Glacial Maximum: Results from a coupled atmosphere-ocean general circulation model *Journal of Geophysical Research*, **104**, 24,509–24,525.
- Cayre, O., Y. Lancelot, E. Vincent, and M. A. Hall, 1999: Paleoceanographic reconstructions from planktonic foraminifera off the Iberian Margin: Temperature, salinity and Heinrich events *Paleoceanography*, **14**, 384–396.
- Chapman, M., N. Shackleton, M. Zhao, and G. Eglinton, 1996: Faunal and alkenone reconstructions of subtropical North Atlantic surface hydrography and paleotemperature over the last 28 kyr *Paleoceanography*, **11**, 343–357.

- Charles, C., D. Rind, R. Healy, and R. Webb, 2001: Tropical cooling and the isotopic composition of precipitation in general circulation model simulations of the ice age climate *Climate Dynamics*, **17**, 489–502.
- Charles, C., D. Rind, J. Jouzel, R. Koster, and R. Fairbanks, 1994: Glacial-Interglacial Changes in Moisture Sources for Greenland: Influences on the Ice Core Record of Climate *Science*, **263**, 508–511.
- Charles, C. D., P. N. Froelich, M. A. Zibello, R. A. Mortlock, and J. J. Morley, 1991: BIOGENIC OPAL IN SOUTHERN OCEAN SEDIMENTS OVER THE LAST 450,000 YEARS: IMPLICATIONS FOR SURFACE WATER CHEMISTRY AND CIRCULATION *Paleoceanography*, **6**, 697–728.
- Chen, J., J. W. Farrell, D. W. Murray, and W. L. Prell, 1995: Timescale and paleoceanographic implications of a 3.6 m.y. oxygen isotope record from the northeast Indian Ocean (Ocean Drilling Program site 758) *Paleoceanography*, **10**, 21–47.
- Chivas, A. R., A. García, S. van der Kaars, M. J. Couapel, S. Holt, J. M. Reeves, D. J. Wheeler, A. D. Switzer, C. V. Murray-Wallace, D. Banerjee, D. M. Price, S. X. Wang, G. Pearson, N. T. Edgar, L. Beaufort, P. D. Deckker, E. Lawson, and C. B. Cecil, 2001: Sea-level and environmental changes since the last interglacial in the Gulf of Carpentaria, Australia: an overview *Quaternary International*, **83–85**, 19–46.
- Clausen, H., N. Gundestrup, S. Johnsen, R. Bindshadler, and J. Zwally, 1988: GLACIOLOGICAL INVESTIGATIONS IN THE CRÊTE AREA, CENTRAL GREENLAND: A SEARCH FOR A NEW DEEP-DRILLING SITE *Annals of Glaciology*, **10**, 10–15.
- CLIMAP, P. M., 1976: The Surface of the Ice-Age Earth *Science*, **191**, 1131–1137.
- CLIMAP, P. M., 1981: *Seasonal Reconstructions of the Earth's Surface at the Last Glacial Maximum*, Volume MC-36 of *Map and Chart Series* Boulder, CO: Geological Society of America.
- Cole, J. E., D. Rind, and R. G. Fairbanks, 1993: ISOTOPIC RESPONSES TO INTERANNUAL CLIMATE VARIABILITY SIMULATED BY AN ATMOSPHERIC GENERAL CIRCULATION MODEL *Quaternary Science Reviews*, **12**, 387–406.
- Cole, J. E., D. Rind, R. S. Webb, J. Jouzel, and R. Healy, 1999: Climatic controls on interannual variability of precipitation $\delta^{18}\text{O}$: Simulated influence of temperature, precipitation amount, and vapor source region *Journal of Geophysical Research*, **104**, 14,223–14,235.
- Collina-Girard, J., 2001: Atlantis off the Gibraltar Strait? Myth and geology *Earth and Planetary Sciences*, **333**, 233–240.
- Crusius, J., T. F. Pedersen, S. E. Calvert, G. L. Cowie, and T. Oba, 1999: A 36 kyr geochemical record from the Sea of Japan of organic matter flux variations and changes in intermediate water oxygen concentrations *Paleoceanography*.

- Cuffey, K. M. and G. D. Clow, 1997: Temperature, accumulation, and ice sheet elevation in central Greenland through the last deglacial transition *Journal of Geophysical Research*, **102**, 26,383–26,396.
- Cuffey, K. M., G. D. Clow, R. B. Alley, M. Stuiver, E. D. Waddington, and R. W. Saltus, 1995: Large Arctic Temperature Change at the Wisconsin-Holocene Glacial Transition *Science*, **270**, 455–458.
- Curry, W., 1996: Late Quaternary Deep Circulation in the Western Equatorial Atlantic *The South Atlantic: Present and Past Circulation*, G. Wefer, W. H. Berger, G. Siedler, and D. J. Webb, Eds., 577–598. Springer-Verlag.
- Curry, W., J. Duplessy, L. Labeyrie, and N. Shackleton, 1988: CHANGES IN THE DISTRIBUTION OF $\delta^{13}\text{C}$ OF DEEP WATER ΣCO_2 BETWEEN THE LAST GLACIATION AND THE HOLOCENE *Paleoceanography*, **3**, 317–341.
- Curry, W., T. Marchitto, J. McManus, D. Oppo, and K. Laarkamp, 1999: Millennial-scale Changes in Ventilation of the Thermocline, Intermediate, and Deep Waters of the Glacial North Atlantic *Mechanisms of Global Climate Change at Millennial Time Scales*, P. U. Clark, R. S. Webb, and L. D. Keigwin, Eds., Volume 112 of *Geophysical Monograph*, 59–76. American Geophysical Union.
- Curry, W. and D. Oppo, 1997: Synchronous, high-frequency oscillations in tropical sea surface temperatures and North Atlantic Deep Water production during the last glacial cycle *Paleoceanography*, **12**, 1–14.
- Curry, W. B. and T. J. Crowley, 1987: THE $\delta^{13}\text{C}$ OF EQUATORIAL ATLANTIC SURFACE WATERS: IMPLICATIONS FOR ICE AGE pCO_2 LEVELS *Paleoceanography*, **2**, 489–517.
- Dansgaard, W., 1964: Stable isotopes in precipitation *Tellus*, **16**, 436–468.
- Dansgaard, W., H. Clausen, N. Gundestrup, S. Johnsen, and C. Rygner, 1985: DATING AND CLIMATIC INTERPRETATION OF TWO DEEP GREENLAND ICE CORES *Greenland Ice Core : Geophysics, Geochemistry, and the Environment*, C. Langway, H. Oeschger, and W. Dansgaard, Eds., Volume 33 of *Geophysical Monograph*, 71–76. American Geophysical Union.
- Dansgaard, W., S. Johnsen, H. Clausen, D. Dahl-Jensen, N. Gundestrup, C. Hammer, C. Hvidberg, J. Steffensen, A. Sveinbjörnsdottir, J. Jouzel, and G. Bond, 1993: Evidence for general instability of past climate from a 250-kyr ice-core record *Nature*, **364**, 218–220.
- Dansgaard, W., S. Johnsen, N. Reeh, N. Gundestrup, H. Clausen, and C. Hammer, 1975: Climatic changes, Norsemen and modern man *Nature*, **255**, 24–28.
- Deckker, P. D., N. Tapper, and S. van der Kaars, 2002: The status of the Indo-Pacific Warm Pool and adjacent land at the Last Glacial Maximum *Global and Planetary Change*, **35**, 25–35.

- Delaygue, G., J. Jouzel, and J.-C. Dutay, 2000: Oxygen 18-salinity relationship simulated by an oceanic general circulation model *Earth and Planetary Science Letters*, **178**, 113–123.
- deMenocal, P. B., D. W. Oppo, R. G. Fairbanks, and W. L. Prell, 1992: PLEISTOCENE $\delta^{13}\text{C}$ VARIABILITY OF NORTH ATLANTIC INTERMEDIATE WATER *Paleoceanography*, **7**, 229–250.
- deMenocal, P. B., W. F. Ruddiman, and E. M. Pokras, 1993: INFLUENCES OF HIGH- AND LOW-LATITUDE PROCESSES ON AFRICAN TERRESTRIAL CLIMATE: PLEISTOCENE EOLIAN RECORDS FROM EQUATORIAL ATLANTIC OCEAN DRILLING PROGRAM SITE 663 *Paleoceanography*, **8**, 209–242.
- Duplessy, J., N. Shackleton, R. Fairbanks, L. Labeyrie, D. Oppo, and N. Kallel, 1988: DEEPWATER SOURCE VARIATIONS DURING THE LAST CLIMATIC CYCLE AND THEIR IMPACT ON THE GLOBAL DEEPWATER CIRCULATION *Paleoceanography*, **3**, 343–360.
- Duplessy, J.-C., L. Labeyrie, and C. Waelbroeck, 2002: Constraints on the ocean oxygen isotopic enrichment between the Last Glacial Maximum and the Holocene: Paleoceanographic implications *Quaternary Science Reviews*, **21**, 315–330.
- Elkins, J., T. Thompson, J. Butler, R. Myers, A. Clarke, T. Swanson, D. Endres, A. Yoshinaga, R. Schnell, M. Winey, B. Mendonca, M. Losleben, N. Trivett, D. Worthy, V. Hudec, V. Chorney, P. Fraser, and L. Porter., 1994: Global and hemispheric means of CFC-11 and CFC-12 from the NOAA/CMDL flask sampling program *Trends: A Compendium of Data on Global Change. ORNL/CDIAC-65*. Oak Ridge, Tenn., U.S.A. Description at http://cdiac.esd.ornl.gov/trends/trace/meth_cfc.htm and data at <http://cdiac.esd.ornl.gov/ftp/trends93/trace/global12.427> and <http://cdiac.esd.ornl.gov/ftp/trends93/trace/global11.426>.
- England, J., 1999: Coalescent Greenland and Inuitian ice during the Last Glacial Maximum: revising the Quaternary of the Canadian High Arctic *Quaternary Science Reviews*, **18**, 421–456.
- Fairbanks, R. G., 1989: A 17,000-year glacio-eustatic sea level record: influence of glacial melting rates on the Younger Dryas event and deep-ocean circulation *Nature*, **342**, 637–642.
- Fairbanks, R. G. and R. Matthews, 1978: The Marine Oxygen Isotope Record in Pleistocene Coral, Barbados, West Indies *Quaternary Research*, **10**, 181–196.
- Flückiger, J., A. Dällenbach, T. Blunier, B. Stauffer, T. Stocker, D. Raynaud, and J.-M. Barnola, 1999: Variations in Atmospheric N_2O Concentration During Abrupt Climatic Changes *Science*, **285**, 227–230 (Data available at ftp://ftp.ngdc.noaa.gov/paleo/icecore/greenland/summit/grip/gases/grip_n2o_tr_99.txt).

- Fontugne, M. and S. Calvert, 1992: LATE PLEISTOCENE VARIABILITY OF THE CARBON ISOTOPIC COMPOSITION OF ORGANIC MATTER IN THE EASTERN MEDITERRANEAN: MONITOR OF CHANGES IN CARBON SOURCES AND ATMOSPHERIC CO₂ CONCENTRATIONS *Paleoceanography*, **7**, 1–20.
- Fröhlich, C., 2002: TOTAL SOLAR IRRADIANCE VARIATIONS SINCE 1978 *Advances in Space Research*, **29**, 1409–1416.
- Gat, J., 1996: OXYGEN AND HYDROGEN ISOTOPES IN THE HYDROLOGIC CYCLE *Annual Review of Earth and Planetary Sciences*, **24**, 225–262.
- Gent, P. R. and J. C. McWilliams, 1990: Isopycnal Mixing in Ocean Circulation Models *Journal of Physical Oceanography*, **20**, 150–155.
- Gent, P. R., J. Willebrand, T. J. McDougall, and J. C. McWilliams, 1995: Parameterizing Eddy-Induced Tracer Transports in Ocean Circulation Models *Journal of Physical Oceanography*, **25**, 463–474.
- Grobe, H. and A. Mackensen, 1992: LATE QUATERNARY CLIMATIC CYCLES AS RECORDED IN SEDIMENTS FROM THE ANTARCTIC CONTINENTAL MARGIN *The Antarctic Paleoenvironment: A Perspective On Global Change*, J. P. Kennett and D. A. Warnke, Eds., Volume 56 of *Antarctic Research Series*, 349–376.
- Grootes, P. and M. Stuiver, 1997: Oxygen 18/16 variability in Greenland snow and ice with 10⁻³- to 10⁵-year time resolution *Journal of Geophysical Research*, **102**, 26,455–26,470.
- Grootes, P., M. Stuiver, J. White, S. Johnsen, and J. Jouzel, 1993: Comparison of oxygen isotope records from the GISP2 and GRIP Greenland ice cores *Nature*, **366**, 552–554.
- Grousset, F., L. Labeyrie, J. Sinko, M. Cremer, G. Bond, J. Duprat, E. Cortijo, and S. Huon, 1993: PATTERNS OF ICE-RAFTED DETRITUS IN THE GLACIAL NORTH ATLANTIC (40–55°N) *Paleoceanography*, **8**, 175–192.
- Guilderson, T. P., R. G. Fairbanks, and J. L. Rubenstone, 1994: Tropical Temperature Variations Since 20,000 Years Ago: Modulating Interhemispheric Climate Change *Science*, **263**, 663–665.
- Hammer, C., H. Clausen, and C. Langway, 1994: Electrical conductivity method (ECM) stratigraphic dating of the Byrd Station ice core, Antarctica *Annals of Glaciology*, **20**, 115–120.
- Hansen, J., M. Sato, L. Nazarenko, R. Ruedy, A. Lacis, D. Koch, I. Tegen, T. Hall, D. Shindell, B. Santer, P. Stone, T. Novakov, L. Thomason, R. Wang, Y. Wang, D. Jacob, S. Hollandsworth, L. Bishop, J. Logan, A. Thompson, R. Stolarski, J. Lean, R. Willson, S. Levitus, J. Antonov, N. Rayner, D. Parker, and J. Christy, 2002: Climate forcings in Goddard Institute for Space Studies SI2000 simulations *Journal of Geophysical Research*, **107**, 2–1 – 2–37 (4347, doi:10.1029/2001JD001143).

- Harrison, S. P., K. E. Kohfeld, C. Roelandt, and T. Claquin, 2001: The role of dust in climate changes today, at the last glacial maximum and in the future *Earth-Science Reviews*, **54**, 43–80.
- Hastings, D. W., A. D. Russell, and S. R. Emerson, 1998: Foraminiferal magnesium in *Globigerinoides sacculifer* as a paleotemperature proxy *Paleoceanography*, **13**, 161–169.
- Hebbeln, D. and G. Wefer, 1997: Late Quaternary paleoceanography in the Fram Strait *Paleoceanography*, **12**, 65–78.
- Hermelin, J. O. R. and G. B. Shimmield, 1995: Impact of productivity events on the benthic foraminiferal fauna in the Arabian Sea over the last 150,000 years *Paleoceanography*, **10**, 85–116.
- Hewitt, C., R. Stouffer, A. Broccoli, J. Mitchell, and P. J. Valdes, 2003: The effect of ocean dynamics in a coupled GCM simulation of the Last Glacial Maximum *Climate Dynamics*, **20**, 203–218 (DOI 10.1007/s00382-002-0272-6).
- Hewitt, C. D., A. J. Broccoli, J. F. Mitchell, and R. J. Stouffer, 2001: A coupled model study of the last glacial maximum: Was part of the North Atlantic relatively warm? *Geophysical Research Letters*, **28**, 1571–1574.
- Hodell, D. A., 1993: LATE PLEISTOCENE PALEOCEANOGRAPHY OF THE SOUTH ATLANTIC SECTOR OF THE SOUTHERN OCEAN: OCEAN DRILLING PROGRAM HOLE 704A *Paleoceanography*, **8**, 47–67.
- Hoffmann, G. and M. Heimann, 1997: WATER ISOTOPE MODELING IN THE ASIAN MONSOON REGION *Quaternary International*, **37**, 115–128.
- Hoffmann, G., M. Werner, and M. Heimann, 1998: Water isotope module of the ECHAM atmospheric general circulation model: A study on timescales from days to several years *Journal of Geophysical Research*, **103**, 16,871–16,896.
- Howard, W. R. and W. L. Prell, 1992: LATE QUATERNARY SURFACE CIRCULATION OF THE SOUTHERN INDIAN OCEAN AND ITS RELATIONSHIP TO ORBITAL VARIATIONS *Paleoceanography*, **7**, 79–117.
- Huffman, G. J. and D. T. Bolvin, 2003: GPCP VERSION 2 COMBINED PRECIPITATION DATA SET DOCUMENTATION Technical report, SSAI and Laboratory for Atmospheres, NASA Goddard Space Flight Center, Greenbelt, Maryland, Documentation is at ftp://precip.gsfc.nasa.gov/pub/gpcp-v2/doc/V2_doc and data is at <ftp://precip.gsfc.nasa.gov/pub/gpcp-v2/psg>.
- Hut, G., 1987: Consultants group meeting on stable isotope reference samples for geochemical and hydrological investigations Report to the director general, International Atomic Energy Agency, Vienna, 42 pages.
- IAEA, 2001: GNIP Maps and Animations, International Atomic Energy Agency, Vienna. Accessible at <http://isohis.iaea.org>. Specifically, the data is at <http://isohis.iaea.org/userupdate/waterloo/gnipcl.xls>.

- Imbrie, J., J. Hays, D. Martinson, A. McIntyre, A. Mix, J. Morley, N. Pisias, W. Prell, and N. Shackleton, 1984: THE ORBITAL THEORY OF PLEISTOCENE CLIMATE: SUPPORT FROM A REVISED CHRONOLOGY OF THE MARINE $\delta^{18}\text{O}$ RECORD *Milankovitch and Climate: Understanding the Response to Astronomical Forcing, Part 1*, A. Berger, J. Imbrie, J. Hays, G. Kukla, and B. Saltzman, Eds., Volume 126 of *NATO ASI Series C: Mathematical and Physical Sciences*, 269–305. Boston: D. Reidel Publishing Company.
- Ishiwatari, R., M. Houtatsu, and H. Okada, 2001: Alkenone-sea surface temperatures in the Japan Sea over the past 36 kyr: warm temperatures at the last glacial maximum *Organic Geochemistry*, **32**, 57–67.
- Jasper, J. P., J. Hayes, A. Mix, and F. Prahl, 1994: Photosynthetic fractionation of ^{13}C and concentrations of dissolved CO_2 in the central equatorial Pacific during the last 255,000 years *Paleoceanography*, **9**, 781–798.
- Johnsen, S., H. Clausen, W. Dansgaard, K. Fuhrer, N. Gundestrup, C. Hammer, P. Iverson, J. Jouzel, B. Stauffer, and J. Steffensen, 1992: Irregular glacial interstadials recorded in a new Greenland ice core *Nature*, **359**, 311–313.
- Johnsen, S., W. Dansgaard, H. Clausen, and C. Langway, 1970: Climate Oscillations 1200–2000 AD *Nature*, **227**, 482–483.
- Johnsen, S., W. Dansgaard, H. Clausen, and C. Langway, 1972: Oxygen Isotope Profiles through the Antarctic and Greenland Ice Sheets *Nature*, **235**, 429–434.
- Johnsen, S. J., H. B. Clausen, W. Dansgaard, N. S. Gundestrup, C. U. Hammer, U. Andersen, K. K. Andersen, C. S. Hvidberg, , D. Dahl-Jensen, J. P. Steffensen, H. Shoji, Árný E. Sveinbjörnsdóttir, J. White, J. Jouzel, and D. Fisher, 1997: The $\delta^{18}\text{O}$ record along the Greenland Ice Core Project deep ice core and the problem of possible Eemian climatic instability *Journal of Geophysical Research*, **102**, 26,397–26,410.
- Johnsen, S. J., D. Dahl-Jensen, W. Dansgaard, and N. Gundestrup, 1995: Greenland palaeotemperatures derived from GRIP bore hole temperature and ice core isotope profiles *Tellus*, **47B**, 624–629.
- Joussaume, S. and J. Jouzel, 1993: Paleoclimatic Tracers: An Investigation Using an Atmospheric General Circulation Model Under Ice Age Conditions 2. Water Isotopes *Journal of Geophysical Research*, **98**, 2807–2830.
- Joussaume, S., R. Sadourny, and J. Jouzel, 1984: A general circulation model of water isotope cycles in the atmosphere *Nature*, **311**, 24–29.
- Joussaume, S. and K. Taylor, 1993: Paleoclimate Modeling Intercomparison Project Newsletter N. 1, e-mail newsletter. Available at <ftp.ngdc.noaa.gov> in the /paleo/pmip/newsletters_etc directory.
- Joussaume, S. and K. Taylor, 1994: Paleoclimate Modeling Intercomparison Project Newsletter N. 3, e-mail newsletter. Available at <ftp.ngdc.noaa.gov> in the /paleo/pmip/newsletters_etc directory.

- Jouzel, J., R. Alley, K. Cuffey, W. Dansgaard, P. Grootes, G. Hoffmann, S. Johnsen, R. Koster, D. Peel, C. Shuman, M. Stievenard, M. Stuiver, and J. White, 1997: Validity of the temperature reconstruction from water isotopes in ice cores *Journal of Geophysical Research*, **102**, 26,471–26,487.
- Jouzel, J., G. Hoffmann, R. Koster, and V. Masson, 2000: Water isotopes in precipitation: data/model comparison for present-day and past climates *Quaternary Science Reviews*, **19**, 363–379.
- Jouzel, J., R. Koster, R. Suozzo, G. Russell, J. White, and W. Broecker, 1991: SIMULATIONS OF THE HDO AND H₂¹⁸O ATMOSPHERIC CYCLES USING THE NASA GISS GENERAL CIRCULATION MODEL: SENSITIVITY EXPERIMENTS FOR PRESENT-DAY CONDITIONS *Journal of Geophysical Research*, **96**, 7495–7507.
- Jouzel, J., R. D. Koster, R. J. Suozzo, and G. L. Russell, 1994: Stable water isotope behavior during the last glacial maximum: A general circulation model analysis *Journal of Geophysical Research*, **99**, 25,791–25,801.
- Jouzel, J., G. Russell, R. Suozzo, R. Koster, J. White, and W. Broecker, 1987: Simulations of the HDO and H₂¹⁸O Atmospheric Cycles Using the NASA GISS General Circulation Model: The Seasonal Cycle for Present-Day Conditions *Journal of Geophysical Research*, **92**, 14,739–14,760.
- Kanamitsu, M., W. Ebisuzaki, J. Woollen, S.-K. Yang, J. Hnilo, M. Fiorino, and G. Potter, 2002: NCEP-DOE AMIP-II REANALYSIS (R-2) *Bulletin of the American Meteorological Society*, **83**, 1631–1643 (Data is available by ftping to wesley.wwb.noaa.gov and going to the pub/data2/reanalysis/reanalysis2-C/month/flx directory).
- Keeling, C. and T. Whorf, 2001: Atmospheric CO₂ records from sites in the SIO air sampling network *Trends: A Compendium of Data on Global Change*. Oak Ridge, Tenn., U.S.A. Description at <http://cdiac.esd.ornl.gov/trends/co2/sio-mlo.htm> and data at <http://cdiac.esd.ornl.gov/ftp/maunaloa-co2/maunaloa.co2>.
- Keigwin, L. and S. Gorbarenko, 1992: Sea Level, Surface Salinity of the Japan Sea, and the Younger Dryas Event in the Northwest Pacific Ocean *Quaternary Research*, **37**, 346–360.
- Kellogg, T. B., J. C. Duplessy, and N. J. Shackleton, 1978: Planktonic foraminiferal and oxygen isotopic stratigraphy and paleoclimatology of Norwegian Sea deep-sea cores *Boreas*, **7**, 61–73.
- Khalil, M. and R. Rasmussen, 1994: GLOBAL EMISSIONS OF METHANE DURING THE LAST SEVERAL CENTURIES *Chemosphere*, **29**, 833–842.
- Khalil, M., R. Rasmussen, and M. Shearer, 2002: Atmospheric nitrous oxide: patterns of global change during recent decades and centuries *Chemosphere (in press)*.

- Kim, J.-H., R. R. Schneider, D. Hebbeln, P. J. Müller, and G. Wefer, 2002: Last deglacial sea-surface temperature evolution in the Southeast Pacific compared to climate changes on the South American continent *Quaternary Science Reviews*, **21**, 2085–2097.
- Kim, J.-H., R. R. Schneider, P. J. Müller, and G. Wefer, 2002a: Erratum to: ‘Interhemispheric comparison of deglacial sea-surface temperature patterns in Atlantic eastern boundary currents’ [Earth Planet. Sci. Lett. 194 (2002) 383–393] *Earth and Planetary Science Letters*, **203**, 779–780.
- Kim, J.-H., R. R. Schneider, P. J. Müller, and G. Wefer, 2002b: Interhemispheric comparison of deglacial sea-surface temperature patterns in Atlantic eastern boundary currents *Earth and Planetary Science Letters*, **194**, 383–393.
- Kim, S.-J., G. Flato, and G. Boer, 2003: A coupled climate model simulation of the Last Glacial Maximum, Part 2: approach to equilibrium *Climate Dynamics*, **20**, 635–661.
- Kim, S.-J., G. Flato, G. Boer, and N. McFarlane, 2002: A coupled climate model simulation of the Last Glacial Maximum, Part 1: transient multi-decadal response *Climate Dynamics*, **19**, 515–537.
- Kirst, G. J., R. R. Schneider, P. J. Müller, I. von Storch, and G. Wefer, 1999: Late Quaternary Temperature Variability in the Benguela Current System Derived from Alkenones *Quaternary Research*, **52**, 92–103.
- Kitoh, A. and S. Murakami, 2002: Tropical Pacific climate at the mid-Holocene and the Last Glacial Maximum simulated by a coupled ocean-atmosphere general circulation model *Paleoceanography*, **17**, 19–1 – 19–13 (1047, doi:10.1029/2001PA000724).
- Kitoh, A., S. Murakami, and H. Koide, 2001: A simulation of the Last Glacial Maximum with a coupled atmosphere-ocean GCM *Geophysical Research Letters*, **28**, 2221–2224.
- Kudrass, H., A. Hofmann, H. Dose, K. Emeis, and H. Erlenkeuser, 2001: Modulation and amplification of climatic changes in the Northern Hemisphere by the Indian summer monsoon during the past 80 k.y. *Geology*, **29**, 63–66.
- Labeyrie, L., M. Labracherie, N. Gorfti, J. J. Pichon, M. Vautravers, M. Arnold, J.-C. Duplessy, M. Paterne, E. Michel, J. Duprat, M. Caralp, and J.-L. Turon, 1996: Hydrographic changes of the Southern Ocean (southeast Indian sector) over the last 230 kyr *Paleoceanography*, **11**, 57–76.
- Labracherie, M., L. D. Labeyrie, J. Duprat, E. Bard, M. Arnold, J.-J. Pichon, and J.-C. Duplessy, 1989: THE LAST DEGLACIATION IN THE SOUTHERN OCEAN *Paleoceanography*, **4**, 629–638.
- Lacis, A. A. and V. Oinas, 1991: A Description of the Correlated k Distribution Method for Modeling Nongray Gaseous Absorption, Thermal Emission, and Multiple Scattering in Vertically Inhomogeneous Atmospheres *Journal of Geophysical Research*, **96**, 9027–9063.

- Lambeck, K., 1997: Sea-level change along the French Atlantic and Channel coasts since the time of the Last Glacial Maximum *Palaeogeography, Palaeoclimatology, Palaeoecology*, **129**, 1–22.
- Lamy, F., D. Hebbeln, and G. Wefer, 1998: Late Quaternary precessional cycles of terrigenous sediment input off the Norte Chico, Chile (27.5°S) and paleoclimatic implications, *Palaeogeography, Palaeoclimatology, Palaeoecology*, **141**, 233–251.
- Lamy, F., D. Hebbeln, and G. Wefer, 1999: High-Resolution Marine Record of Climatic Change in Mid-latitude Chile during the Last 28,000 Years Based on Terrigenous Sediment Parameters *Quaternary Research*, **51**, 83–93.
- Lamy, F., J. Klump, D. Hebbeln, and G. Wefer, 2000: Late Quaternary rapid climate change in northern Chile *Terra Nova*, **12**, 8–13.
- Langway, C., K. Osada, H. Clausen, C. Hammer, H. Shoji, and A. Mitani, 1994: New chemical stratigraphy over the last millennium for Byrd Station, Antarctica *Tellus*, **46B**, 40–51.
- Large, W., J. McWilliams, and S. Doney, 1994: OCEANIC VERTICAL MIXING: A REVIEW AND A MODEL WITH A NONLOCAL BOUNDARY LAYER PARAMETERIZATION *Reviews of Geophysics*, **32**, 363–403.
- Le, J. and N. Shackleton, 1992: CARBONATE DISSOLUTION FLUCTUATIONS IN THE WESTERN EQUATORIAL PACIFIC DURING THE LATE QUATERNARY *Paleoceanography*, **7**, 21–42.
- Lea, D. W., D. K. Pak, L. C. Peterson, and K. A. Hughen, 2003: Synchronicity of Tropical and High-Latitude Atlantic Temperatures over the Last Glacial Termination *Science*, **301**, 1361–1364.
- Lebreiro, S., J. Moreno, F. Abrantes, and U. Pflaumann, 1997: Productivity and paleoceanographic implications on the Tore Seamount (Iberian Margin) during the last 225 kyr: Foraminiferal evidence *Paleoceanography*, **12**, 718–727.
- Lebreiro, S., J. Moreno, I. McCave, and P. Weaver, 1996: Evidence for Heinrich layers off Portugal (Tore Seamount: 39°N, 12°W) *Marine Geology*, **131**, 47–56.
- Leuenberger, M. and U. Siegenthaler, 1992: Ice-age atmospheric concentration of nitrous oxide from an Antarctic ice core *Nature*, **360**, 449–451.
- Levitus, 1998: *NODC (Levitus) World Ocean Atlas 1998* Boulder, Colorado, USA and <http://www.cdc.noaa.gov/>: NOAA-CIRES Climate Diagnostics Center Specifically, the data is at <http://www.cdc.noaa.gov/cdc/data.nodc.woa98.html>.
- Levitus, S., R. Burgett, T. P. Boyer, and Ocean Climate Laboratory of the National Oceanographic Data Center, 1994: *World Ocean Atlas 1994* NOAA Atlas NESDIS. Washington D.C.: U.S. Department of Commerce, National Oceanic and Atmospheric Administration, National Environmental Satellite, Data and Information Service.

- Linsley, B. K. and R. B. Dunbar, 1994: The late Pleistocene history of surface water $\delta^{13}\text{C}$ in the Sulu Sea: Possible relationship to Pacific deepwater $\delta^{13}\text{C}$ changes *Paleoceanography*, **9**, 317–340.
- Lorius, C., L. Merlivat, J. Jouzel, and M. Pourchet, 1979: A 30,000-yr isotope climatic record from Antarctic ice *Nature*, **280**, 644–648.
- Luz, B., E. Barkan, M. Bender, M. H. Thiemens, and K. A. Boering, 1999: Triple-isotope composition of atmospheric oxygen as a tracer of biosphere productivity *Nature*, **400**, 547–550.
- Lyle, M., R. Zahn, F. Prahl, J. Dymond, R. Collier, N. Pisias, and E. Suess, 1992: PALEOPRODUCTIVITY AND CARBON BURIAL ACROSS THE CALIFORNIA CURRENT: THE MULTITRACERS TRANSECT, 42°N *Paleoceanography*, **7**, 251–272.
- Lynch-Stieglitz, J., W. B. Curry, and N. Slowey, 1999a: A geostrophic transport estimate for the Florida Current from the oxygen isotope composition of benthic foraminifera *Paleoceanography*, **14**, 360–373.
- Lynch-Stieglitz, J., W. B. Curry, and N. Slowey, 1999b: Weaker Gulf Stream in the Florida Straits during the Last Glacial Maximum *Nature*, **402**, 644–648.
- Mackensen, A., H. Grobe, H.-W. Hubberten, and G. Kuhn, 1994: BENTHIC FORAMINIFERAL ASSEMBLAGES AND THE $\delta^{13}\text{C}$ -SIGNAL IN THE ATLANTIC SECTOR OF THE SOUTHERN OCEAN: GLACIAL-TO-INTERGLACIAL CONTRASTS *Carbon Cycling in the Glacial Ocean: Constraints on the Ocean's Role in Global Change*, R. Zahn, T. F. Pederson, M. A. Kaminiski, and L. Labeyrie, Eds., Volume 17 of *NATO ASI Series I*, 105–144. Springer-Verlag.
- Mackensen, A., H. Grobe, H.-W. Hubberten, V. Spiess, and D. Fütterer, 1989: Stable Isotope Stratigraphy from the Antarctic Continental Margin During the Last One Million Years *Marine Geology*, **87**, 315–321.
- Mamedov, A., 1997: THE LATE PLEISTOCENE-HOLOCENE HISTORY OF THE CASPIAN SEA *Quaternary International*, **41/42**, 161–166.
- Martinson, D. G., N. G. Pisias, J. D. Hays, J. Imbrie, T. C. Moore, and N. J. Shackleton, 1987: Age Dating and the Orbital Theory of the Ice Ages: Development of a High-Resolution 0 to 300,000-Year Chronostratigraphy *Quaternary Research*, **27**, 1–29.
- Mashiotta, T. A., D. W. Lea, and H. J. Spero, 1999: Glacial-interglacial changes in Subantarctic sea surface temperature and $\delta^{18}\text{O}$ -water using foraminiferal Mg *Earth and Planetary Science Letters*, **170**, 417–432.
- Mathieu, R., D. Pollard, J. E. Cole, J. W. White, R. S. Webb, and S. L. Thompson, 2002: Simulation of stable water isotope variations by the GENESIS GCM for modern conditions *Journal of Geophysical Research*, **107**, 2–1 – 2–18 (10.1029/2001JD900255).

- McIntyre, A., W. F. Ruddiman, K. Karlin, and A. C. Mix, 1989: SURFACE WATER RESPONSE OF THE EQUATORIAL ATLANTIC OCEAN TO ORBITAL FORCING *Paleoceanography*, **4**, 19–55.
- Mix, A., N. Pisias, R. Zahn, W. Rugh, C. Lopez, and K. Nelson, 1991: CARBON 13 IN PACIFIC DEEP AND INTERMEDIATE WATERS, 0-370 KA: IMPLICATIONS FOR OCEAN CIRCULATION AND PLEISTOCENE CO₂ *Paleoceanography*, **6**, 205–226.
- Monnin, E., A. Indermühle, A. Dällenbach, J. Flückiger, B. Stauffer, T. F. Stocker, D. Raynaud, and J.-M. Barnola, 2001: Atmospheric CO₂ Concentrations over the Last Glacial Termination *Science*, **291**, 112–114 (Data available at ftp://ftp.ngdc.noaa.gov/paleo/icecore/antarctica/domec/domec_co2.txt and ftp://ftp.ngdc.noaa.gov/paleo/icecore/antarctica/domec/domec_ch4.txt).
- Mulitza, S., 2001: A global compilation of planktonic foraminiferal $\delta^{18}\text{O}$ from core tops <http://www.pangaea.de/home/smultipa> Specifically, the dataset is at <http://www.pangaea.de/ddi?datasetid=60896&login=0&format=text>.
- Mulitza, S., C. Rühlemann, T. Bickert, W. Hale, J. Pätzold, and G. Wefer, 1998: Late Quaternary $\delta^{13}\text{C}$ gradients and carbonate accumulation in the western equatorial Atlantic *Earth and Planetary Science Letters*, **155**, 237–249.
- Müller, P. J., G. Kirst, G. Ruhland, I. von Storch, and A. Rosell-Melé, 1998: Calibration of the alkenone paleotemperature index $U_{37}^{K'}$ based on core-tops from the eastern South Atlantic and the global ocean (60°N–60°S) *Geochimica et Cosmochimica Acta*, **62**, 1757–1772.
- Nelson, C. S., P. J. Cooke, C. H. Hendy, and A. M. Cuthbertson, 1993: OCEANOGRAPHIC AND CLIMATIC CHANGES OVER THE PAST 160,000 YEARS AT DEEP SEA DRILLING PROJECT SITE 594 OFF SOUTHEASTERN NEW ZEALAND, SOUTHWEST PACIFIC OCEAN *Paleoceanography*, **8**, 435–458.
- Ninnemann, U. S. and C. D. Charles, 1997: Regional differences in Quaternary Subantarctic nutrient cycling: Link to intermediate and deep water ventilation *Paleoceanography*, **12**, 560–567.
- Noone, D. and I. Simmonds, 2002: Associations between $\delta^{18}\text{O}$ of Water and Climate Parameters in a Simulation of Atmospheric Circulation for 1979–95 *Journal of Climate*, **15**, 3150–3169.
- Nürnberg, D., A. Müller, and R. R. Schneider, 2000: Paleo-sea surface temperature calculations in the equatorial east Atlantic from Mg/Ca ratios in planktic foraminifera: A comparison to sea surface temperature estimates from $U_{37}^{K'}$, oxygen isotopes, and foraminiferal transfer function *Paleoceanography*, **15**, 124–134.
- Oppo, D. and R. Fairbanks, 1990: ATLANTIC OCEAN THERMOHALINE CIRCULATION OF THE LAST 150,000 YEARS: RELATIONSHIP TO CLIMATE AND ATMOSPHERIC CO₂ *Paleoceanography*, **5**, 277–288.

- Overpeck, J., D. Rind, A. Lacis, and R. Healy, 1996: Possible role of dust-induced regional warming in abrupt climate change during the last glacial period *Nature*, **384**, 447–449.
- Pailler, D. and E. Bard, 2002: High frequency palaeoceanographic changes during the past 140 000 yr recorded by the organic matter in sediments of the Iberian Margin *Palaeogeography, Palaeoclimatology, Palaeoecology*, **181**, 431–452.
- Paul, A., S. Mulitza, J. Pätzold, and T. Wolff, 1999: Simulation of Oxygen Isotopes in a Global Ocean Model *Use of Proxies in Paleoceanography: Examples from the South Atlantic*, G. Fischer and G. Wefer, Eds., 655–686. Springer-Verlag.
- Peltier, W. and L. Solheim, 2001: Ice in the Climate System: Paleoclimatological Perspectives *Present and Future of Modeling Global Environmental Change: Toward Integrated Modeling*, T. Matsuno and H. Kida, Eds., 221–241. TER-RAPUB.
- Peltier, W. R., 1994: Ice Age Paleotopography *Science*, **265**, 195–201.
- Peltier, W. R., 1998: “Implicit ice” in the global theory of glacial isostatic adjustment *Geophysical Research Letters*, **25**, 3955–3958.
- Petit, J., J. Jouzel, D. Raynaud, N. Barkov, J.-M. Barnola, I. Basile, M. Bender, J. Chappellaz, M. Davis, G. Delaygue, M. Delmotte, V. Kotlyakov, M. Legrand, V. Lipenkov, C. Lorius, L. Peépin, C. Ritz, E. Saltzman, and M. Stievenard, 1999: Climate and atmospheric history of the past 420,000 years from the Vostok ice core, Antarctica *Nature*, **399**, 429–436.
- Pisias, N. G., A. C. Mix, and R. Zahn, 1990: NONLINEAR RESPONSE IN THE GLOBAL CLIMATE SYSTEM: EVIDENCE FROM BENTHIC OXYGEN ISOTOPIC RECORD IN CORE RC13-110, *Paleoceanography*, **5**, 147–160.
- Prahl, F., L. Muehlhausen, and M. Lyle, 1989: AN ORGANIC GEOCHEMICAL ASSESSMENT OF OCEANOGRAPHIC CONDITIONS AT MANOP SITE C OVER THE PAST 26,000 YEARS *Paleoceanography*, **4**, 495–510.
- Prahl, F. G., N. Pisias, M. A. Sparrow, and A. Sabin, 1995: Assessment of sea-surface temperature at 42°N in the California Current over the last 30,000 years *Paleoceanography*, **10**, 763–773.
- Rasmussen, R. and M. Khalil, 1986: Atmospheric Trace Gases: Trends and Distributions Over the Last Decade *Science*, **232**, 1623–1624.
- Rind, D., P. deMenocal, G. Russell, S. Sheth, D. Collins, G. Schmidt, and J. Teller, 2001: Effects of glacial meltwater in the GISS coupled atmosphere-ocean model 1. North Atlantic Deep Water response *Journal of Geophysical Research*, **106**, 27,335–27,353.
- Rind, D. and D. Peteet, 1985: Terrestrial Conditions at the Last Glacial Maximum and CLIMAP Sea-Surface Temperature Estimates: Are They Consistent? *Quaternary Research*, **24**, 1–22.

- Rind, D., G. Russell, G. Schmidt, S. Sheth, D. Collins, P. deMenocal, and J. Teller, 2001: Effects of glacial meltwater in the GISS coupled atmosphere-ocean model 2. A bipolar seesaw in Atlantic Deep Water production *Journal of Geophysical Research*, **106**, 27,355–27,365.
- Robertson, I., J. Waterhouse, A. Barker, A. Carter, and V. Switsur, 2001: Oxygen isotope ratios of oak in east England: implications for reconstructing the isotopic composition of precipitation *Earth and Planetary Science Letters*, **191**, 21–31.
- Rohling, E. and W. Zachariasse, 1996: RED SEA OUTFLOW DURING THE LAST GLACIAL MAXIMUM *Quaternary International*, **31**, 77–83.
- Rosenthal, Y., E. Boyle, L. Labeyrie, and D. Oppo, 1995: Glacial enrichments of authigenic Cd and U in Subantarctic sediments: A climatic control on the elements' oceanic budget? *Paleoceanography*, **10**, 395–413.
- Rostek, F., E. Bard, L. Beaufort, C. Sonzogni, and G. Ganssen, 1997: Sea surface temperature and productivity records for the past 240 kyr in the Arabian Sea *Deep-Sea Research II*, **44**, 1461–1480.
- Rostek, F., G. Ruhland, F. C. Bassinot, P. J. Müller, L. D. Labeyrie, Y. Lancelot, and E. Bard, 1993: Reconstructing sea surface temperature and salinity using $\delta^{18}\text{O}$ and alkenone records *Nature*, **364**, 319–321.
- Rühlemann, C., M. Frank, W. Hale, A. Mangini, S. Mulitza, P. Müller, and G. Wefer, 1996: Late Quaternary productivity changes in the western equatorial Atlantic: Evidence from ^{230}Th -normalized carbonate and organic carbon accumulation rates *Marine Geology*, **135**, 127–152.
- Rühlmann, C., S. Mulitza, P. J. Müller, G. Wefer, and R. Zahn, 1999: Warming of the tropical Atlantic Ocean and slowdown of thermohaline circulation during the last deglaciation *Nature*, **402**, 511–514.
- Russell, G., 1999: Sea Ice in GISS Models.
- Russell, G. L., J. R. Miller, and D. Rind, 1995: A Coupled Atmosphere-Ocean Model for Transient Climate Change Studies *Atmosphere-Ocean*, **33**, 683–730.
- Sarnthein, M., K. Winn, S. J. Jung, J.-C. Duplessy, L. Labeyrie, H. Erlenkeuser, and G. Ganssen, 1994: Changes in east Atlantic deepwater circulation over the last 30,000 years: Eight time slice reconstructions *Paleoceanography*, **9**, 209–267.
- Schlünz, B., R. Schneider, P. Müller, and G. Wefer, 2000: Late Quaternary organic carbon accumulation south of Barbados: influence of the Orinoco and Amazon rivers? *Deep-Sea Research I*, **47**, 1101–1124.
- Schmidt, G., 1997: Reduced Gravity mode for Ocean-only runs.
- Schmidt, G., G. Bigg, and E. Rohling, 1999: Global Seawater Oxygen-18 Database <http://www.giss.nasa.gov/data/o18data/>.

- Schmidt, G. A., 1998: Oxygen-18 variations in a global ocean model *Geophysical Research Letters*, **25**, 1201–1204.
- Schmidt, G. A., 1999: Forward modeling of carbonate proxy data from planktonic foraminifera using oxygen isotope tracers in a global ocean model *Paleoceanography*, **14**, 482–497.
- Schmidt, G. A. and S. Mulitza, 2002: Global calibration of ecological models for planktic foraminifera from core-top carbonate oxygen-18 *Marine Micropaleontology*, **44**, 125–140.
- Schmiedl, G., C. Hemleben, J. Keller, and M. Segl, 1998: Impact of climatic changes on the benthic foraminiferal fauna in the Ionian Sea during the last 330,000 years *Paleoceanography*, **13**, 447–458.
- Schmiedl, G. and A. Mackensen, 1997: Late Quaternary paleoproductivity and deep water circulation in the eastern South Atlantic Ocean: Evidence from benthic foraminifera *Palaeogeography, Palaeoclimatology, Palaeoecology*, **130**, 43–80.
- Schneider, R., P. Müller, G. Ruhland, G. Meinecke, H. Schmidt, and G. Wefer, 1996: Late Quaternary Surface Temperatures and Productivity in the East-Equatorial South Atlantic: Response to Changes in Trade/Monsoon Wind Forcing and Surface Water Advection *The South Atlantic: Present and Past Circulation*, G. Wefer, W. H. Berger, G. Siedler, and D. J. Webb, Eds., 527–551. Springer-Verlag.
- Schneider, R. R., P. J. Müller, and G. Ruhland, 1995: Late Quaternary surface circulation in the east equatorial South Atlantic: Evidence from alkenone sea surface temperatures *Paleoceanography*, **10**, 197–219.
- Schneider, R. R., P. J. Müller, and G. Wefer, 1994: Late Quaternary paleoproductivity changes off the Congo deduced from stable carbon isotopes of planktonic foraminifera *Palaeogeography, Palaeoclimatology, Palaeoecology*, **110**, 255–274.
- Schrag, D. P., J. F. Adkins, K. McIntyre, J. L. Alexander, D. A. Hodell, C. D. Charles, and J. F. McManus, 2002: The oxygen isotopic composition of seawater during the Last Glacial Maximum *Quaternary Science Reviews*, **21**, 331–342.
- Schrag, D. P., G. Hampt, and D. W. Murray, 1996: Pore Fluid Constraints on the Temperature and Oxygen Isotopic Composition of the Glacial Ocean *Science*, **272**, 1930–1932.
- Schulz, H., U. von Rad, and H. Erlenkeuser, 1998: Correlation between Arabian Sea and Greenland climate oscillations of the past 110,000 years *Nature*, **393**, 54–57.
- Seager, R., D. Battisti, J. Yin, N. Gordon, N. Naik, A. Clement, and M. Cane, 2002: Is the Gulf Stream responsible for Europe's mild winters? *Quarterly Journal of the Royal Meteorological Society*, **128**, 2563–2586 (doi: 10.1256/qj.01.128).
- Shackleton, N. J., M. A. Hall, and E. Vincent, 2000: Phase relationships between millennial-scale events 64,000–24,000 years ago *Paleoceanography*, **15**, 565–569.

- Shin, S.-I., Z. Liu, B. Otto-Bliesner, E. Brady, J. Kutzbach, and S. Harrison, 2003: A Simulation of the Last Glacial Maximum climate using the NCAR-CCSM *Climate Dynamics*, **20**, 127–151.
- Sirocko, F., M. Sarnthein, H. Erlenkeusers, H. L. M. Arnold, and J. Duplessy, 1993: Century-Scale events in monsoonal climate over the past 24,000 years *Nature*, **364**, 322–324.
- Sonzogni, C., E. Bard, and F. Rostek, 1998: TROPICAL SEA-SURFACE TEMPERATURES DURING THE LAST GLACIAL PERIOD: A VIEW BASED ON ALKENONES IN INDIAN OCEAN SEDIMENTS *Quaternary Science Reviews*, **17**, 1185–1201.
- Steig, E. J., D. L. Morse, E. D. Waddington, M. Stuiver, P. M. Grootes, P. Mayewski, M. S. Twickler, and S. I. Whitlow, 2000: WISCONSINAN AND HOLOCENE CLIMATE HISTORY FROM AN ICE CORE AT TAYLOR DOME, WESTERN ROSS EMBAYMENT, ANTARCTICA *Geografiska Annaler*, **82A**, 213–235.
- Stuiver, M., P. M. Grootes, and T. F. Brazunias, 1995: The GISP2 $\delta^{18}\text{O}$ Climate Record of the Past 16,500 Years and the Role of the Sun, Ocean, and Volcanoes *Quaternary Research*, **44**, 341–354.
- Stuiver, M. and P. J. Reimer, 1993: EXTENDED ^{14}C DATA BASE AND REVISED CALIB 3.0 ^{14}C AGE CALIBRATION PROGRAM *Radiocarbon*, **35**, 215–230.
- Stuiver, M., P. J. Reimer, E. Bard, J. W. Beck, G. Burr, K. A. Hughen, B. Kromer, G. McCormac, J. V. der Plicht, and M. Spurk, 1998: INTCAL98 RADIOCARBON AGE CALIBRATION, 24,000–0 cal BP *Radiocarbon*, **40**, 1041–1083.
- Stute, M., M. Forster, H. Frischkorn, A. Serejo, J. Clark, P. Schlosser, W. Broecker, and G. Bonani, 1995: Cooling of Tropical Brazil (5°C) During the Last Glacial Maximum *Science*, **269**, 379–383.
- Teller, J., K. Glennie, N. Lancaster, and A. Singhavi, 2000: Calcareous dunes of the United Arab Emirates and Noah's Flood: the postglacial reflooding of the Persian (Arabian) Gulf *Quaternary International*, **68–71**, 297–308.
- Thompson, L., M. Davis, E. Mosley-Thompson, T. Sowers, K. Henderson, V. Zagorodnov, P.-N. Lin, V. Mikhalenko, R. Campen, J. Bolzan, J. Cole-Dai, and B. Francou, 1998: A 25,000-Year Tropical Climate History from Bolivian Ice Cores *Science*, **282**, 1858–1864.
- Thompson, L., E. Mosley-Thompson, J. Bolzan, and B. Koci, 1985: A 1500-Year Record of Tropical Precipitation in Ice Cores from the Quelccaya Ice Cap, Peru *Science*, **229**, 971–973.
- Thompson, L., E. Mosley-Thompson, M. Davis, P.-N. Lin, K. Henderson, J. Cole-Dai, J. Bolzan, and K. b. Liu, 1995: Late Glacial Stage and Holocene Tropical Ice Core Records from Huascarán, Peru *Science*, **269**, 46–50.

- Thompson, L. G., 2000: Ice core evidence for climate change in the Tropics: implications for our future *Quaternary Science Reviews*, **19**, 19–35.
- Thresher, D., 1999: OGCM Development Through the Addition of CFCs as Tracers Orals Research Project Report.
- Tiedemann, R., M. Sarnthein, and N. J. Shackleton, 1994: Astronomic timescale for the Pliocene Atlantic $\delta^{18}\text{O}$ and dust flux records of Ocean Drilling Program site 659 *Paleoceanography*, **9**, 619–638.
- Tomczak, M. and J. S. Godfrey, 1994: *Regional Oceanography: An Introduction* Oxford, England, U.K.: Pergamon (Elsevier Science Ltd).
- Tsimplis, M. and H. Bryden, 2000: Estimation of the transports through the Strait of Gibraltar *Deep Sea Research I*, **47**, 2219–2242.
- Wadley, M. R., G. R. Bigg, E. J. Rohling, and A. J. Payne, 2002: On modelling present-day and last glacial maximum oceanic $\delta^{18}\text{O}$ distributions *Global and Planetary Change*, **32**, 89–109.
- Wang, L., M. Sarnthein, H. Erlenkeuser, J. Grimalt, P. Grootes, S. Heilig, E. Ivanova, M. Kienast, C. Pelejero, and U. Pflaumann, 1999: East Asian monsoon climate during the Late Pleistocene: high-resolution sediment records from the South China Sea *Marine Geology*, **156**, 245–284.
- Wefer, G., W. Berger, T. Bickert, B. Donner, G. Fischer, S. K. von Mücke, G. Meincke, P. Müller, S. Mulitza, H.-S. Niebler, J. Pätzold, H. Schmidt, R. Schneider, and M. Segl, 1996: Late Quaternary Surface Circulation of the South Atlantic: The Stable Isotope Record and Implications for Heat Transport and Productivity *The South Atlantic: Present and Past Circulation*, G. Wefer, W. H. Berger, G. Siedler, and D. J. Webb, Eds., 461–502. Springer-Verlag.
- Werner, M., U. Mikolajewicz, M. Heimann, and G. Hoffmann, 2000: Borehole versus isotope temperatures on Greenland: Seasonality does matter *Geophysical Research Letters*, **27**, 723–726.
- Winograd, I. J., B. J. Szabo, T. B. Coplen, and A. C. Riggs, 1988: A 250,000-Year Climatic Record from Great Basin Vein Calcite Implications for Milankovitch Theory *Science*, **242**, 1275–1280.
- Wollenburg, J. E., W. Kuhnt, and A. Mackensen, 2001: Changes in Arctic Ocean paleoproductivity and hydrography during the last 145 kyr: The benthic foraminiferal record *Paleoceanography*, **16**, 65–77.
- Wood, R., 1995: ‘Distorted physics’, timestep sensitivity and the spinup of ocean GCMs Ocean Applications Technical Note 6, Meteorological Office, London Road, Bracknell, Berkshire, RG12 2SZ, UK, .
- Wood, R. A., 1998: Time Step Sensitivity and Accelerated Spinup of an Ocean GCM with a Complex Mixing Scheme *Journal of Atmospheric and Oceanic Technology*, **15**, 482–495.
- Wunsch, C., 2002: What Is the Thermohaline Circulation? *Science*, **298**, 1179–1181.

- Yu, E.-F., R. Francois, and M. P. Bacon, 1996: Similar rates of modern and last-glacial ocean thermohaline circulation inferred from radiochemical data *Nature*, **379**, 689–694.

Appendix A

Downcore $\delta^{18}\text{O}$ Time Series Core Information

Cores are listed numerically and alphabetically by core name.

Core: 12328-5 **Lat:** 21° 9' **Lon:** -18° 34.2' **Depth:** 2778 m **$\delta^{18}\text{O}$ Sources:** *Globigerinoides ruber (white)*, *Uvigerina peregrina*, *Cibicidoides wuellerstorfi* **References:** Sarnthein et al. 1994 **Age Model:** Using other cores from the reference, an event stratigraphy was defined for the last 30,000 years based on the $\delta^{18}\text{O}$ records of *C. wuellerstorfi*; in six of these records the event stratigraphy was dated directly by AMS ^{14}C ages; based on the average ages of six ^{14}C dated events a framework of age control points was defined, comprising 9.1 ka for the end and 10.4 ka for the beginning of Termination Ib, 13.6 ka for the end and 14.8 ka for the beginning of Termination Ia, 20 ka for a $\delta^{18}\text{O}$ minimum in the middle of $\delta^{18}\text{O}$ Stage 2 and 26 ka for $\delta^{18}\text{O}$ event 3.1; “AMS ^{14}C analog ages” then estimated for all other $\delta^{18}\text{O}$ records not directly dated by ^{14}C ages; to allow for linear interpolations between age control points (since ^{14}C age scale nonlinear), ^{14}C age control points converted into calendar ages using the tree ring conversion scheme of Stuiver et al. 1991 for the Holocene and the conversion into U/Th years between 10 ka and 30 ka as published by Bard et al. 1990; resulting calendar age control points are 9.8 ka (9.1 ^{14}C ka), 11.6 ka (10 ^{14}C ka), 12.4 ka (10.4 ^{14}C ka), 15 ka (13 ^{14}C ka), 17.1 ka (13.6 ^{14}C ka), and 29.5 ka (26 ^{14}C ka). No reservoir corrections to ^{14}C ages. **Notes:** Core name above is specific form of that from reference, which mentions cores 12328-4 and 12328-5 as just 12328; known as GIK12328-5 in dataset. Lat minutes and Lon minutes are from reference; given as 8.7 and 34.4 in dataset. **Dataset Sources:** <http://www.pangaea.de/ddi?datasetid=52049&login=0&format=text>

Core: 12329-4 **Lat:** 19° 22.2' **Lon:** -19° 55.8' **Depth:** 3314 m **$\delta^{18}\text{O}$ Sources:**

Cibicidoides wuellerstorfi **References:** Sarnthein et al. 1994 **Age Model:** See Core 12328-5. **Notes:** Core name above is from reference; known as GIK12329-4 in dataset. Ocean depth above is from reference; that given in dataset is 3315 m. Similarly, Lat minutes is from reference; given as 22.0 in dataset. **Dataset Sources:** <http://www.pangaea.de/ddi?datasetid=54362&login=0&format=text>

Core: 12329-6 **Lat:** 19° 22.2' **Lon:** -19° 55.8' **Depth:** 3320 m $\delta^{18}\text{O}$ **Sources:** *Cibicidoides wuellerstorfi*, *Pyrgo* spp. **References:** Sarnthein et al. 1994 **Age Model:** See Core 12328-5. For ages older than 29.5 ka, $\delta^{18}\text{O}$ record events were given ages after Martinson et al. 1987. **Notes:** Core name above is from reference; known as GIK12329-6 in dataset. Lat minutes is from reference; given as 22.0 in dataset. **Dataset Sources:** <http://www.pangaea.de/ddi?datasetid=54362&login=0&format=text>

Core: 12337-4 **Lat:** 15° 57' **Lon:** -18° 7.8' **Depth:** 3088 m $\delta^{18}\text{O}$ **Sources:** *Globigerinoides ruber (white)*, *Cibicidoides wuellerstorfi* **References:** Sarnthein et al. 1994 **Age Model:** See Core 12328-5. **Notes:** Core name above is specific form of that from reference, which mentions cores 12337-4 and 12337-5 as just 12337; known as GIK12337-4 in dataset. Ocean depth above is from reference for 12337; that given in dataset is 3094 m. Lat minutes and Lon minutes are from reference; given as 57.2 and 7.98 in dataset. **Dataset Sources:** <http://www.pangaea.de/ddi?datasetid=54363&login=0&format=text>

Core: 12337-5 **Lat:** 15° 57' **Lon:** -18° 7.8' **Depth:** 3088 m $\delta^{18}\text{O}$ **Sources:** *Globigerinoides ruber (white)*, *Cibicidoides wuellerstorfi* **References:** Sarnthein et al. 1994 **Age Model:** See Core 12328-5. **Notes:** Core name above is specific form of that from reference, which mentions cores 12337-4 and 12337-5 as just 12337; known as GIK12337-5 in dataset. Ocean depth above is from reference for 12337; that given in dataset is 3082 m. Lat minutes and Lon minutes are from reference; given as 57.2 and 7.98 in dataset. **Dataset Sources:** <http://www.pangaea.de/ddi?datasetid=54363&login=0&format=text>

Core: 12347-2 **Lat:** 15° 49.8' **Lon:** -17° 51.6' **Depth:** 2576 m $\delta^{18}\text{O}$ **Sources:** *Uvigerina peregrina*, *Cibicidoides wuellerstorfi* **References:** Sarnthein et al. 1994 **Age Model:** See Core 12328-5. **Notes:** Core name above is specific form of that from reference, which mentions cores 12347-1 and 12347-2 as just 12347; known as GIK12347-2 in dataset. Lat minutes and Lon minutes are from reference; given as 49.5 and 51.7 in dataset. **Dataset Sources:** <http://www.pangaea.de/ddi?datasetid=54364&login=0&format=text>

Core: 12379-3 **Lat:** 23° 8.4' **Lon:** -17° 45' **Depth:** 2136 m $\delta^{18}\text{O}$ **Sources:** *Uvigerina hollicki*, *Uvigerina peregrina*, *Cibicidoides wuellerstorfi* **References:** Sarnthein et al. 1994 **Age Model:** See Core 12328-5. For ages older than 29.5 ka, $\delta^{18}\text{O}$ record events were given ages after Martinson et al. 1987. **Notes:** Core name above is specific form of that from reference, which mentions cores 12379-1 and 12379-3 as

just 12379; known as GIK12379-3 in dataset. Lat minutes and Lon minutes are from reference; given as 8.1 and 44.7 in dataset. **Dataset Sources:** <http://www.pangaea.de/ddi?datasetid=54365&login=0&format=text>

Core: 12392 **Lat:** 25° 10.2' **Lon:** -16° 51' **Depth:** 2575 m $\delta^{18}\text{O}$ **Sources:** *Uvigerina hollicki*, *Cibicidoides wuellerstorfi* **References:** Sarnthein et al. 1994 **Age Model:** See Core 12328-5. For ages older than 29.5 ka, $\delta^{18}\text{O}$ record events were given ages after Martinson et al. 1987. **Notes:** Core name above is from reference; known as GIK12392-1 in dataset. Lat minutes and Lon minutes above are from reference; given as 10.3 and 50.7 in dataset. *C. wuellerstorfi* $\delta^{18}\text{O}$ data seems also to be in second dataset but with a different age model; not used here since from an older reference. A more recent age model available in third dataset; not published so not used here. **Dataset Sources:** <http://www.pangaea.de/ddi?datasetid=54366&login=0&format=text>, <http://www.pangaea.de/ddi?datasetid=52281&login=0&format=text>, <http://www.pangaea.de/ddi?datasetid=59653&login=0&format=text>

Core: 13289-2 **Lat:** 18° 4.2' **Lon:** -18° .6' **Depth:** 2490 m $\delta^{18}\text{O}$ **Sources:** *Uvigerina peregrina*, *Cibicidoides wuellerstorfi* **References:** Sarnthein et al. 1994 **Age Model:** See Core 12328-5. **Notes:** Core name above is specific form of that from reference, which mentions cores 13289-1 and 13289-2 as just 13289; known as GIK13289-2 in dataset. Ocean depth above is from reference for 13289; that given in dataset is 2485 m. Lat minutes and Lon minutes are from reference; given as 4.39 and .55 in dataset. **Dataset Sources:** <http://www.pangaea.de/ddi?datasetid=54367&login=0&format=text>

Core: 13519 **Lat:** 5° 39.6' **Lon:** -19° 51' **Depth:** 2862 m $\delta^{18}\text{O}$ **Sources:** *Cibicidoides wuellerstorfi*, *Uvigerina hollicki* **References:** Sarnthein et al. 1994 **Age Model:** See Core 12328-5. For ages older than 29.5 ka, $\delta^{18}\text{O}$ record events were given ages after Martinson et al. 1987 or, for ages 303 ka or older, after Imbrie et al. 1984. One age (78240 yr) is out of sequence. **Notes:** Core name above is from reference; known as GIK13519-1 in datasets. Lat minutes and Lon minutes are from reference; given as 40.2 and 51.1 in datasets. A SPECMAP-based age model is available in second dataset; less recent so not used here. A more recent age model is available in third dataset; unpublished so not used here. **Dataset Sources:** <http://www.pangaea.de/ddi?datasetid=54360&login=0&format=text>, <http://www.pangaea.de/ddi?datasetid=59895&login=0&format=text>, <http://www.pangaea.de/ddi?datasetid=59657&login=0&format=text>

Core: 13521 **Lat:** 3° 1.2' **Lon:** -22° 1.8' **Depth:** 4504 m $\delta^{18}\text{O}$ **Sources:** *Globigerinoides sacculifer*, *Cibicidoides wuellerstorfi* **References:** Sarnthein et al. 1994 **Age Model:** See Core 12328-5. For ages older than 29.5 ka, $\delta^{18}\text{O}$ record events were given ages after Martinson et al. 1987. **Notes:** Core name above is from reference; known as GIK13521-1 in dataset. Lon minutes is from reference; given as 1.9 in dataset. **Dataset Sources:** <http://www.pangaea.de/ddi?datasetid=54368&login=0&format=text>

Core: 15612 **Lat:** 44° 41.4' **Lon:** -26° 32.4' **Depth:** 3050 m $\delta^{18}\text{O}$ **Sources:** *Cibicidoides wuellerstorfi*, *Uvigerina* spp. **References:** Sarnthein et al. 1994 **Age Model:** See Core 12328-5. For ages older than 29.5 ka, $\delta^{18}\text{O}$ record events were given ages after Martinson et al. 1987. **Notes:** Core name above is from reference; known as GIK15612-2 in dataset. Lat minutes and Lon minutes are from reference; given as 21.6 and 32.6 in dataset. **Dataset Sources:** <http://www.pangaea.de/ddi?datasetid=54369&login=0&format=text>

Core: 15627 **Lat:** 29° 10.2' **Lon:** -12° 5.4' **Depth:** 1024 m $\delta^{18}\text{O}$ **Sources:** *Cibicidoides wuellerstorfi*, *Globorotalia inflata* **References:** Sarnthein et al. 1994 **Age Model:** See Core 12328-5. For ages older than 29.5 ka, $\delta^{18}\text{O}$ record events were given ages after Martinson et al. 1987. **Notes:** Core name above is from reference; known as GIK15627-3 in dataset. Lat minutes and Lon minutes are from reference; given as 10 and 5.2 in dataset. **Dataset Sources:** <http://www.pangaea.de/ddi?datasetid=54360&login=0&format=text>

Core: 15637 **Lat:** 27° .6' **Lon:** -18° 59.4' **Depth:** 3849 m $\delta^{18}\text{O}$ **Sources:** *Cibicidoides wuellerstorfi*, *Uvigerina hollicki* **References:** Sarnthein et al. 1994 **Age Model:** See Core 12328-5. For ages older than 29.5 ka, $\delta^{18}\text{O}$ record events were given ages after Martinson et al. 1987 or, for ages 303 ka or older, after Imbrie et al. 1984. **Notes:** Core name above is from reference; known as GIK15637-1 in dataset. Lat minutes and Lon minutes are from reference; given as .3 and 59.2 in dataset. **Dataset Sources:** <http://www.pangaea.de/ddi?datasetid=54360&login=0&format=text>

Core: 15666 **Lat:** 34° 57.6' **Lon:** -7° 7.2' **Depth:** 803 m $\delta^{18}\text{O}$ **Sources:** *Uvigerina mediterranea*, *Planulina ariminensis* **References:** Sarnthein et al. 1994 **Age Model:** See Core 12328-5. For ages older than 29.5 ka, $\delta^{18}\text{O}$ record events were given ages after Martinson et al. 1987. **Notes:** Core name above is from reference; known as GIK15666-6 in dataset. Lon minutes is from reference; given as 7.1 in dataset. **Dataset Sources:** <http://www.pangaea.de/ddi?datasetid=54381&login=0&format=text>

Core: 15669-1 **Lat:** 34° 53.4' **Lon:** -7° 49.2' **Depth:** 2022 m $\delta^{18}\text{O}$ **Sources:** *Cibicidoides wuellerstorfi* **References:** Sarnthein et al. 1994 **Age Model:** See Core 12328-5. For ages older than 29.5 ka, $\delta^{18}\text{O}$ record events were given ages after Martinson et al. 1987. **Notes:** Core name above is from reference; known as GIK15669-1 in dataset. Lat minutes and Lon minutes are from reference; given as 53.5 and 48.9 in dataset. **Dataset Sources:** <http://www.pangaea.de/ddi?datasetid=54360&login=0&format=text>

Core: 15670 **Lat:** 34° 54.6' **Lon:** -7° 34.8' **Depth:** 1482 m $\delta^{18}\text{O}$ **Sources:** *Cibicidoides kullenbergi* **References:** Sarnthein et al. 1994 **Age Model:** See Core 12328-5. **Notes:** Core name above is from reference; known as GIK15670-5 in

dataset. Lat minutes and Lon minutes are from reference; given as 54.5 and 34.6 in dataset. **Dataset Sources:** <http://www.pangaea.de/ddi?datasetid=54382&login=0&format=text>

Core: 15672-1 **Lat:** 34° 51.6' **Lon:** -8° 7.2' **Depth:** 2455 m **$\delta^{18}\text{O}$ Sources:** *Globigerinoides ruber (white)*, *Cibicidoides wuellerstorfi* **References:** Sarnthein et al. 1994 **Age Model:** See Core 12328-5. For ages older than 29.5 ka, $\delta^{18}\text{O}$ record events were given ages after Martinson et al. 1987. **Notes:** Core name above is from reference; known as GIK15672-1 in dataset. Lon minutes is from reference; given as 7.6 in dataset. **Dataset Sources:** <http://www.pangaea.de/ddi?datasetid=54370&login=0&format=text>

Core: 15672-2 **Lat:** 34° 51.6' **Lon:** -8° 7.8' **Depth:** 2435 m **$\delta^{18}\text{O}$ Sources:** *Globigerinoides ruber (white)*, *Cibicidoides wuellerstorfi* **References:** Sarnthein et al. 1994 **Age Model:** See Core 12328-5. **Notes:** Core name above is from reference; known as GIK15672-2 in dataset. Lon minutes is from reference; given as 7.6 in dataset. **Dataset Sources:** <http://www.pangaea.de/ddi?datasetid=54370&login=0&format=text>

Core: 16004 **Lat:** 29° 58.8' **Lon:** -10° 39' **Depth:** 1512 m **$\delta^{18}\text{O}$ Sources:** *Globorotalia inflata*, *Globigerina bulloides*, *Globigerinoides ruber (white)*, *Cibicidoides wuellerstorfi*, *Pyrgo murrhina* **References:** Sarnthein et al. 1994 **Age Model:** See Core 12328-5. For ages older than 29.5 ka, $\delta^{18}\text{O}$ record events were given ages after Martinson et al. 1987. **Notes:** Core name above is from reference; known as GIK16004-1 in dataset. Lat minutes and Lon minutes are from reference; given as 58.7 and 38.8 in dataset. **Dataset Sources:** <http://www.pangaea.de/ddi?datasetid=54371&login=0&format=text>

Core: 16006 **Lat:** 29° 16.2' **Lon:** -11° 30' **Depth:** 796 m **$\delta^{18}\text{O}$ Sources:** *Planulina ariminensis*, *Cibicidoides wuellerstorfi* **References:** Sarnthein et al. 1994 **Age Model:** See Core 12328-5. For ages older than 29.5 ka, $\delta^{18}\text{O}$ record events were given ages after Martinson et al. 1987. **Notes:** Core name above is from reference; known as GIK16006-1 in dataset. Lat minutes and Lon minutes are from reference; given as 14.8 and 29.8 in dataset. **Dataset Sources:** <http://www.pangaea.de/ddi?datasetid=54372&login=0&format=text>

Core: 16017 **Lat:** 21° 15' **Lon:** -17° 48' **Depth:** 812 m **$\delta^{18}\text{O}$ Sources:** *Globigerinoides ruber (white)*, *Cibicidoides wuellerstorfi* **References:** Sarnthein et al. 1994 **Age Model:** See Core 12328-5. **Notes:** Core name above is from reference; known as GIK16017-2 in dataset. Lat minutes and Lon minutes are from reference; given as 14.7 and 48.2 in dataset. **Dataset Sources:** <http://www.pangaea.de/ddi?datasetid=54373&login=0&format=text>

Core: 16030 **Lat:** 21° 14.4' **Lon:** -18° 3.6' **Depth:** 1500 m **$\delta^{18}\text{O}$ Sources:** *Globorotalia inflata*, *Globigerina bulloides*, *Globigerinoides ruber (white)*, *Globigeri-*

noides ruber (pink), *Cibicidoides wuellerstorfi*, *Uvigerina peregrina* **References:** Sarnthein et al. 1994 **Age Model:** See Core 12328-5. For ages older than 29.5 ka, $\delta^{18}\text{O}$ record events were given ages after Martinson et al. 1987. **Notes:** Core name above is from reference; known as GIK16030-1 in dataset. Ocean depth above is from reference; that given in dataset is 1516 m. Similarly, Lat minutes and Lon minutes are from reference; given as 14.1 and 3.3 in dataset. **Dataset Sources:** <http://www.pangaea.de/ddi?datasetid=54374&login=0&format=text>

Core: 16402-1 **Lat:** 14° 25.2' **Lon:** -20° 34.2' **Depth:** 4203 m $\delta^{18}\text{O}$ **Sources:** *Globigerinoides sacculifer*, *Cibicidoides wuellerstorfi* **References:** Sarnthein et al. 1994 **Age Model:** See Core 12328-5. **Notes:** Core name above is specific form of that from reference, which mentions cores 16402-1 and 16402-2 as just 16402; known as GIK16402-1 in dataset. Lat minutes and Lon minutes are from reference; given as 25.0 and 34.0 in dataset. **Dataset Sources:** <http://www.pangaea.de/ddi?datasetid=54375&login=0&format=text>

Core: 16402-2 **Lat:** 14° 25.2' **Lon:** -20° 34.2' **Depth:** 4203 m $\delta^{18}\text{O}$ **Sources:** *Globigerinoides sacculifer*, *Cibicidoides wuellerstorfi*, *Uvigerina hollicki* **References:** Sarnthein et al. 1994 **Age Model:** See Core 12328-5. For ages older than 29.5 ka, $\delta^{18}\text{O}$ record events were given ages after Martinson et al. 1987. **Notes:** Core name above is specific form of that from reference, which mentions cores 16402-1 and 16402-2 as just 16402; known as GIK16402-2 in dataset. Ocean depth above is from reference for 16402; given as 4234 m in dataset. Similarly, Lat minutes and Lon minutes are from reference for 16402; given as 27.5 and 32.5 in dataset. **Dataset Sources:** <http://www.pangaea.de/ddi?datasetid=54375&login=0&format=text>

Core: 16408-2 **Lat:** 9° .6' **Lon:** -21° 30' **Depth:** 4336 m $\delta^{18}\text{O}$ **Sources:** *Globigerinoides ruber (white)*, *Cibicidoides wuellerstorfi* **References:** Sarnthein et al. 1994 **Age Model:** See Core 12328-5. **Notes:** Core name above is specific form of that from reference, which mentions cores 16408-2 and 16408-5 as just 16408; known as GIK16408-2 in dataset. Ocean depth above is from reference for 16408; given as 4239 in dataset. Similarly, Lat minutes and Lon minutes are from reference; given as .8 and 27.4 in dataset. **Dataset Sources:** <http://www.pangaea.de/ddi?datasetid=54376&login=0&format=text>

Core: 16408-5 **Lat:** 9° .6' **Lon:** -21° 30' **Depth:** 4336 m $\delta^{18}\text{O}$ **Sources:** *Cibicidoides wuellerstorfi* **References:** Sarnthein et al. 1994 **Age Model:** See Core 12328-5. **Notes:** Core name above is specific form of that from reference, which mentions cores 16408-2 and 16408-5 as just 16408; known as GIK16408-5 in dataset. Lat minutes and Lon minutes are from reference; given as .3 and 29.9 in dataset. **Dataset Sources:** <http://www.pangaea.de/ddi?datasetid=54376&login=0&format=text>

Core: 16415-1 **Lat:** 9° 34.2' **Lon:** -19° 6.6' **Depth:** 3841 m $\delta^{18}\text{O}$ **Sources:** *Globigerinoides ruber (white)*, *Cibicidoides wuellerstorfi* **References:** Sarnthein et al.

1994 **Age Model:** See Core 12328-5. **Notes:** Core name above is specific form of that from reference, which mentions cores 16415-1 and 16415-2 as just 16415; known as GIK16415-1 in dataset. Lat minutes and Lon minutes are from reference; given as 34.0 and 6.4 in dataset. **Dataset Sources:** <http://www.pangaea.de/ddi?datasetid=54377&login=0&format=text>

Core: 16415-2 **Lat:** 9° 34.2' **Lon:** -19° 6.6' **Depth:** 3841 m $\delta^{18}\text{O}$ **Sources:** *Cibicidoides wuellerstorfi* **References:** Sarnthein et al. 1994 **Age Model:** See Core 12328-5. **Notes:** Core name above is specific form of that from reference, which mentions cores 16415-1 and 16415-2 as just 16415; known as GIK16415-2 in dataset. Ocean depth above is from reference; that given in dataset is 3851 m. Similarly, Lat minutes and Lon minutes are from reference; given as 34.0 and 5.7 in dataset. **Dataset Sources:** <http://www.pangaea.de/ddi?datasetid=54377&login=0&format=text>

Core: 16453 **Lat:** 4° 43.8' **Lon:** -20° 57' **Depth:** 2675 m $\delta^{18}\text{O}$ **Sources:** *Globigerinoides ruber (white)*, *Globigerinoides sacculifer*, *Cibicidoides wuellerstorfi* **References:** Sarnthein et al. 1994 **Age Model:** See Core 12328-5. Linear interpolation calculated here for a few missing ages. **Notes:** Core name above is from reference; known as GIK16453-2 in dataset. Lat minutes and Lon minutes are from reference; given as 44.0 and 56.5 in dataset. **Dataset Sources:** <http://www.pangaea.de/ddi?datasetid=54378&login=0&format=text>

Core: 16455 **Lat:** 5° 16.2' **Lon:** -22° 52.2' **Depth:** 4160 m $\delta^{18}\text{O}$ **Sources:** *Globigerinoides sacculifer*, *Cibicidoides wuellerstorfi* **References:** Sarnthein et al. 1994 **Age Model:** See Core 12328-5. **Notes:** Core name above is from reference; known as GIK16455-1 in dataset. Lon minutes is from reference; given as 51.9 in dataset. **Dataset Sources:** <http://www.pangaea.de/ddi?datasetid=54379&login=0&format=text>

Core: 16457 **Lat:** 5° 23.4' **Lon:** -21° 43.2' **Depth:** 3291 m $\delta^{18}\text{O}$ **Sources:** *Cibicidoides wuellerstorfi*, *Globigerinoides sacculifer* **References:** Sarnthein et al. 1994 **Age Model:** See Core 12328-5. **Notes:** Core name above is from reference; known as GIK16457-1 in dataset. Lat minutes is from reference; given as 23.5 in dataset. **Dataset Sources:** <http://www.pangaea.de/ddi?datasetid=54360&login=0&format=text>

Core: 16458-1 **Lat:** 5° 20.4' **Lon:** -22° 3.6' **Depth:** 3518 m $\delta^{18}\text{O}$ **Sources:** *Globigerinoides sacculifer* **References:** Sarnthein et al. 1994 **Age Model:** See Core 12328-5. For ages older than 29.5 ka, $\delta^{18}\text{O}$ record events were given ages after Martinson et al. 1987. **Notes:** Core name above is specific form of that from reference, which mentions cores 16458-1 and 16458-2 as just 16458; known as GIK16458-1 in dataset. Lat minutes and Lon minutes are from reference; given as 20.1 and 3.2 in dataset. **Dataset Sources:** <http://www.pangaea.de/ddi?datasetid=54389&login=0&format=text>

Core: 16458-2 **Lat:** 5° 20.4' **Lon:** -22° 3.6' **Depth:** 3518 m $\delta^{18}\text{O}$ **Sources:** *Globigerinoides ruber (white)*, *Globigerinoides sacculifer* **References:** Sarnthein et al. 1994 **Age Model:** See Core 12328-5. **Notes:** Core name above is specific form of that from reference, which mentions cores 16458-1 and 16458-2 as just 16458; known as GIK16458-2 in dataset. Lat minutes and Lon minutes are from reference; given as 20.1 and 3.3 in dataset. **Dataset Sources:** <http://www.pangaea.de/ddi?datasetid=54389&login=0&format=text>

Core: 16459 **Lat:** 7° 16.8' **Lon:** -26° 11.4' **Depth:** 4835 m $\delta^{18}\text{O}$ **Sources:** *Cibicidoides wuellerstorfi*, *Globigerinoides ruber (white)* **References:** Sarnthein et al. 1994 **Age Model:** See Core 12328-5. **Notes:** Core name above is from reference; known as GIK16459-1 in dataset. Lat minutes and Lon minutes are from reference; given as 16.6 and 11.2 in dataset. **Dataset Sources:** <http://www.pangaea.de/ddi?datasetid=54360&login=0&format=text>

Core: 16771-2 **Lat:** -0° 49.2' **Lon:** -15° 30.6' **Depth:** 2764 m $\delta^{18}\text{O}$ **Sources:** *Cibicidoides wuellerstorfi*, *Globigerinoides sacculifer*, *Globigerinoides ruber (white)* **References:** Sarnthein et al. 1994 **Age Model:** See Core 12328-5. For ages older than 29.5 ka, $\delta^{18}\text{O}$ record events were given ages after Martinson et al. 1987. **Notes:** Core name above is specific form of that from reference, which mentions cores 16771-1 and 16771-2 as just 16771; known as GIK16771-2 in dataset. Lat minutes is from reference; given as 49.0 in dataset. Dataset incorrectly gives Lat degrees as positive/North. **Dataset Sources:** <http://www.pangaea.de/ddi?datasetid=54360&login=0&format=text>

Core: 16772-1 **Lat:** -1° 12.6' **Lon:** -11° 57.6' **Depth:** 3912 m $\delta^{18}\text{O}$ **Sources:** *Cibicidoides wuellerstorfi*, *Globigerinoides sacculifer* **References:** Sarnthein et al. 1994 **Age Model:** See Core 12328-5. **Notes:** Core name above is specific form of that from reference, which mentions cores 16772-1 and 16772-2 as just 16772; known as GIK16772-1 in dataset. Ocean depth above is from reference for 16772; given in dataset as 3911 m. Lat minutes and Lon minutes are from reference; given as 20.4 and 58.4 in dataset. **Dataset Sources:** <http://www.pangaea.de/ddi?datasetid=54360&login=0&format=text>

Core: 16772-2 **Lat:** -1° 12.6' **Lon:** -11° 57.6' **Depth:** 3912 m $\delta^{18}\text{O}$ **Sources:** *Cibicidoides wuellerstorfi*, *Globigerinoides sacculifer* **References:** Sarnthein et al. 1994 **Age Model:** See Core 12328-5. For ages older than 29.5 ka, $\delta^{18}\text{O}$ record events were given ages after Martinson et al. 1987 or, for ages 303 ka or older, after Imbrie et al. 1984. One age (201100 yr) is out of sequence. **Notes:** Core name above is specific form of that from reference, which mentions cores 16772-1 and 16772-2 as just 16772; known as GIK16772-2 in dataset. Lat minutes and Lon minutes are from reference; given as 21.0 and 57.7 in dataset. **Dataset Sources:** <http://www.pangaea.de/ddi?datasetid=54360&login=0&format=text>

Core: 16773 **Lat:** -0° 58.2' **Lon:** -9° 26.4' **Depth:** 4662 m **$\delta^{18}\text{O}$ Sources:** *Globigerinoides ruber (white)*, *Cibicidoides wuellerstorfi* **References:** Sarnthein et al. 1994 **Age Model:** See Core 12328-5. **Notes:** Core name above is from reference; known as GIK16773-1 in dataset. Lat minutes and Lon minutes are from reference; given as 58.3 and 26.6 in dataset. **Dataset Sources:** <http://www.pangaea.de/ddi?datasetid=54390&login=0&format=text>

Core: 16867-1 **Lat:** -2° 12' **Lon:** 5° 6' **Depth:** 3891 m **$\delta^{18}\text{O}$ Sources:** *Globigerinoides ruber (white)*, *Cibicidoides wuellerstorfi* **References:** Sarnthein et al. 1994 **Age Model:** See Core 12328-5. **Notes:** Core name above is specific form of that from reference, which mentions cores 16867-1, 16867-2 and 16867-3 as just 16867; known as GIK16867-1 in second dataset. Lat minutes and Lon minutes are from reference; given as 12.2 and 6.01 in second dataset. First dataset is a “preprint” of the corrected version of the second dataset, which had erroneous data when this was written. **Dataset Sources:** File GIK16867_reimport from Mara Weinelt (mw@gpi.uni-kiel.de), <http://www.pangaea.de/ddi?datasetid=54392&login=0&format=text>

Core: 16867-2 **Lat:** -2° 12' **Lon:** 5° 6' **Depth:** 3891 m **$\delta^{18}\text{O}$ Sources:** *Globigerinoides ruber (white)*, *Cibicidoides wuellerstorfi* **References:** Sarnthein et al. 1994 **Age Model:** See Core 12328-5. For ages older than 29.5 ka, $\delta^{18}\text{O}$ record events were given ages after Martinson et al. 1987. **Notes:** Core name above is specific form of that from reference, which mentions cores 16867-1, 16867-2 and 16867-3 as just 16867; known as GIK16867-2 in second dataset. Lat minutes and Lon minutes are from reference; given as 12.1 and 6.1 in second dataset. First dataset is a “preprint” of the corrected version of the second dataset, which had erroneous data when this was written. **Dataset Sources:** File GIK16867_reimport from Mara Weinelt (mw@gpi.uni-kiel.de), <http://www.pangaea.de/ddi?datasetid=54392&login=0&format=text>

Core: 16867-3 **Lat:** -2° 12' **Lon:** 5° 6' **Depth:** 3891 m **$\delta^{18}\text{O}$ Sources:** *Globigerinoides ruber (white)*, *Cibicidoides wuellerstorfi* **References:** Sarnthein et al. 1994 **Age Model:** $\delta^{18}\text{O}$ record events were given ages after Martinson et al. 1987. Linear interpolation assumed between age control points and calculated here, with no extrapolation beyond last age control point. **Notes:** Core name above is specific form of that from reference, which mentions cores 16867-1, 16867-2 and 16867-3 as just 16867; known as GIK16867-3 in second dataset. Ocean depth above is from reference; given in second dataset as 3894 m. Lat minutes and Lon minutes are from reference; given as 12 and 6 in second dataset. First dataset is a “preprint” of the corrected version of the second dataset, which had erroneous data when this was written. **Dataset Sources:** File GIK16867_reimport from Mara Weinelt (mw@gpi.uni-kiel.de), <http://www.pangaea.de/ddi?datasetid=54392&login=0&format=text>

Core: 17045-2 **Lat:** 52° 25.8' **Lon:** -16° 39.6' **Depth:** 3663 m **$\delta^{18}\text{O}$ Sources:** *Neogloboquadrina pachyderma (dextral)*, *Globigerina bulloides*, *Globorotalia inflata*, *Cibicidoides wuellerstorfi* **References:** Sarnthein et al. 1994 **Age Model:** See Core 12328-5. **Notes:** Core name above is specific form of that from reference,

which mentions cores 17045-2 and 17045-3 as just 17045; known as GIK17045-2 in dataset. Ocean depth above is from reference for 17045; given in dataset as 3653 m. Similarly, Lat minutes and Lon minutes are from reference; given as 26.9 and 39.4 in dataset. **Dataset Sources:** <http://www.pangaea.de/ddi?datasetid=54393&login=0&format=text>

Core: 17045-3 **Lat:** 52° 25.8' **Lon:** -16° 39.6' **Depth:** 3663 m $\delta^{18}\text{O}$ **Sources:** *Neogloboquadrina pachyderma (dextral)*, *Globigerina bulloides*, *Globorotalia inflata*, *Cibicidoides wuellerstorfi*, *Neogloboquadrina pachyderma (sinistral)* **References:** Sarnthein et al. 1994 **Age Model:** See Core 12328-5. **Notes:** Core name above is specific form of that from reference, which mentions cores 17045-2 and 17045-3 as just 17045; known as GIK17045-3 in dataset. Lat minutes and Lon minutes are from reference; given as 25.5 and 39.9 in dataset. **Dataset Sources:** <http://www.pangaea.de/ddi?datasetid=54393&login=0&format=text>

Core: 17048-3 **Lat:** 54° 18.6' **Lon:** -18° 10.8' **Depth:** 1859 m $\delta^{18}\text{O}$ **Sources:** *Neogloboquadrina pachyderma (dextral)*, *Globigerina bulloides*, *Globorotalia inflata*, *Cibicidoides wuellerstorfi*, *Neogloboquadrina pachyderma (sinistral)* **References:** Sarnthein et al. 1994 **Age Model:** See Core 12328-5. **Notes:** Core name above is specific form of that from reference, which mentions cores 17048-3 and 17048-4 as just 17048; known as GIK17048-3 in dataset. Lat minutes and Lon minutes are from reference; given as 18.4 and 10.6 in dataset. **Dataset Sources:** <http://www.pangaea.de/ddi?datasetid=54394&login=0&format=text>

Core: 17048-4 **Lat:** 54° 18.6' **Lon:** -18° 10.8' **Depth:** 1859 m $\delta^{18}\text{O}$ **Sources:** *Neogloboquadrina pachyderma (dextral)*, *Globigerina bulloides*, *Globorotalia inflata*, *Cibicidoides wuellerstorfi* **References:** Sarnthein et al. 1994 **Age Model:** See Core 12328-5. **Notes:** Core name above is specific form of that from reference, which mentions cores 17048-3 and 17048-4 as just 17048; known as GIK17048-4 in dataset. Ocean depth above is from reference for 17048; given in dataset as 1848 m. Similarly, Lat minutes and Lon minutes are from reference; given as 18.5 and 10.6 in dataset. **Dataset Sources:** <http://www.pangaea.de/ddi?datasetid=54394&login=0&format=text>

Core: 17939-2 **Lat:** 19° 58.2' **Lon:** 117° 27.3' **Depth:** 2474 m $\delta^{18}\text{O}$ **Sources:** *Globigerinoides ruber (white)* **References:** Wang et al. 1999 **Age Model:** Reservoir-corrected AMS ^{14}C ages converted to calendar ages under various schemes at various ages; see reference Table 3 notes. Some resulting ages out of sequence. The calendar ages of reference Table 3, which are all based on ^{14}C ages with a 400-yr reservoir correction, are used instead of the corrections discussed in the reference text (Sec. 3.2). Linear interpolation between calendar ages assumed and calculated here; no extrapolation before first, or after last, age control point. **Notes:** Core name above is from reference; known as GIK17939-2 in datasets. Core's depth/age data from second dataset applied to its foram $\delta^{18}\text{O}$ data from first dataset. Second dataset data printed in reference. **Dataset Sources:** <http://www.pangaea.de/ddi?datasetid=54712&log>

in=0&format=text, <http://www.pangaea.de/ddi?datasetid=55578&login=0&format=text>

Core: 17940-2 **Lat:** 20° 7' **Lon:** 117° 23' **Depth:** 1727 m $\delta^{18}\text{O}$ **Sources:** *Cibicidoides wuellerstorfi*, *Cibicidoides kullenbergi*, *Cibicidoides spp.*, *Globigerinoides ruber (white)* **References:** Wang et al. 1999 **Age Model:** See Core 17939-2. **Notes:** Core name above is from reference; known as GIK17940-2 in datasets. Core's depth/age data from third dataset applied to its foram $\delta^{18}\text{O}$ data from first and second datasets. Third dataset data printed in reference. **Dataset Sources:** <http://www.pangaea.de/ddi?datasetid=55575&login=0&format=text>, <http://www.pangaea.de/ddi?datasetid=55901&login=0&format=text>, <http://www.pangaea.de/ddi?datasetid=55578&login=0&format=text>

Core: 17961-2 **Lat:** 8° 30.4' **Lon:** 112° 19.9' **Depth:** 1968 m $\delta^{18}\text{O}$ **Sources:** *Globigerinoides ruber (white)*, *Cibicidoides wuellerstorfi* **References:** Wang et al. 1999 **Age Model:** See Core 17939-2. **Notes:** Core name above is from reference; known as GIK17961-2 in datasets. Core's depth/age data from third dataset applied to its foram $\delta^{18}\text{O}$ data from first and second datasets. Third dataset data printed in reference. **Dataset Sources:** <http://www.pangaea.de/ddi?datasetid=54712&login=0&format=text>, <http://www.pangaea.de/ddi?datasetid=54714&login=0&format=text>, <http://www.pangaea.de/ddi?datasetid=55578&login=0&format=text>

Core: 17964-2 **Lat:** 6° 9.5' **Lon:** 112° 12.8' **Depth:** 1556 m $\delta^{18}\text{O}$ **Sources:** *Globigerinoides ruber (white)* **References:** Wang et al. 1999 **Age Model:** See Core 17939-2. **Notes:** Core name above is from reference; known as GIK17964-2 in datasets. Core's depth/age data from third dataset applied to its foram $\delta^{18}\text{O}$ data from first and second datasets. Third dataset data printed in reference. **Dataset Sources:** <http://www.pangaea.de/ddi?datasetid=55612&login=0&format=text>, <http://www.pangaea.de/ddi?datasetid=55611&login=0&format=text>, <http://www.pangaea.de/ddi?datasetid=55578&login=0&format=text>

Core: 502B **Lat:** 11° 0' **Lon:** -80° 0' **Depth:** 3051 m $\delta^{18}\text{O}$ **Sources:** *Cibicidoides wuellerstorfi* **References:** deMenocal et al. 1992 **Age Model:** Initially constrained by Kent and Spariosu 1982 paleomagnetic data; further refined by $\delta^{18}\text{O}$ correlation with the TP607 time scale of Ruddiman et al. 1989, which is based on the orbitally tuned, high resolution $\delta^{18}\text{O}$ record from core 607. **Notes:** Core name above is from reference; known as 68-502B in datasets. Lat minutes, Lon degrees, and Lon minutes are from reference; given as 29.51, -79, and 22.69 in datasets. A SPECMAP-based age model is available in second dataset; less recent so not used here. **Dataset Sources:** <http://www.pangaea.de/ddi?datasetid=55456&login=0&format=text>, <http://www.pangaea.de/ddi?datasetid=59900&login=0&format=text>

Core: 594 **Lat:** -45° 31.41' **Lon:** 174° 56.88' **Depth:** 1204 m $\delta^{18}\text{O}$ **Sources:** *Globigerina bulloides*, *Uvigerina spp.* **References:** Nelson et al. 1993 **Age Model:** From a calibration curve based on the depth of the isotopic stage boundaries and

their Martinson et al. 1987 ages; one AMS date. **Notes:** Core name above is from reference; known as 90-594 in dataset. Dataset data printed in Table 1 of reference. **Dataset Sources:** <http://www.pangaea.de/ddi?datasetid=52601&login=0&format=text>

Core: 659 **Lat:** 18° 5' **Lon:** -21° 2' **Depth:** 3070 m **$\delta^{18}\text{O}$ Sources:** *Cibicidoides wuellerstorfi* **References:** Tiedemann et al. 1994 **Age Model:** Back to 2.85 Ma, visual correlation of the C. wuellerstorfi oxygen isotope stages to the benthic isotope records of Ruddiman et al. 1989 (site 607) and Shackleton et al. 1990 (site 677); ages then assigned following isotopic timescale of Shackleton et al. 1990. From 2.85 Ma to 5 Ma, orbital frequency tuning of the C. wuellerstorfi oxygen isotope record, after initial age interpolation from four dated paleomagnetic and biostratigraphic events. **Notes:** Depth/age model control points and depth/ $\delta^{18}\text{O}$ datasets available from Pangaea; ages between control points can be linearly interpolated (using composite depth) and applied to $\delta^{18}\text{O}$ data; datasource used has all this together. **Dataset Sources:** File ISOTOPE.659 from rtiedemann@geomar.de

Core: 663 **Lat:** -1° 11.9' **Lon:** -11° 52.7' **Depth:** 3708 m **$\delta^{18}\text{O}$ Sources:** *Globigerinoides ruber (white)* **References:** deMenocal et al. 1993 **Age Model:** Correlation of Globigerinoides ruber(white) oxygen isotope record with SPECMAP stack timescale from 0 to 580 ka and with Shackleton et al. 1990 ODP site 677 timescale from 580 to 918 ka (that timescale is equivalent to SPECMAP from 0 to 620 ka). **Notes:** Core name above is from reference; known as 108-663A and 108-663B in dataset (presented as a composite in reference and here). Ocean depth above is from reference; given as 3697.6 and 3697.4 m in dataset. **Dataset Sources:** <http://www.pangaea.de/ddi?datasetid=55506&login=0&format=text>

Core: 704A **Lat:** -46° 52.8' **Lon:** 7° 25.3' **Depth:** 2532 m **$\delta^{18}\text{O}$ Sources:** *Neogloboquadrina pachyderma (sinistral)*, *Cibicidoides spp.*, *Gyroidinoides spp.* **References:** Hodell 1993 **Age Model:** Correlation of the oxygen isotopic record with the SPECMAP stacked record; linear interpolation between these dated stage and substage (although many unidentifiable due to low resolution) boundaries; isotopic event ages from Imbrie et al. 1984, modified by Ruddiman et al. 1989 for stages beyond 16; constrained by five biostratigraphic events. **Notes:** Core name above is from reference; known as 114-704A in dataset. **Dataset Sources:** <http://www.pangaea.de/ddi?datasetid=52609&login=0&format=text>

Core: 723A **Lat:** 18° 3' **Lon:** 57° 36' **Depth:** 800 m **$\delta^{18}\text{O}$ Sources:** *Pulleniatina obliquiloculata*, *Uvigerina excellens* **References:** Anderson and Prell 1993 **Age Model:** Oxygen isotope event correlation to the Imbrie et al. 1984 SPECMAP planktonic isotope composite record and the Martinson et al. 1982 benthic isotope composite record; linear interpolation between events; no extrapolation done beyond last age control point. **Notes:** Core name above is from reference; known as 117-723A in dataset. Ocean depth above is from reference; that in dataset is 805.7 m. Similarly, Lat minutes and Lon minutes are from reference; those given in dataset

are 3.11 and 36.54. Core's depth/age data from second dataset applied to its foram $\delta^{18}\text{O}$ data from first dataset. **Dataset Sources:** <http://www.pangaea.de/ddi?datasetid=51922&login=0&format=text>, <http://www.pangaea.de/ddi?datasetid=52590&login=0&format=text>

Core: 74KL **Lat:** 14° 19.26' **Lon:** 57° 20.82' **Depth:** 3212 m $\delta^{18}\text{O}$ **Sources:** *Globigerinoides ruber (white)* **References:** Sirocko et al. 1993 **Age Model:** AMS ^{14}C dates on *Globigerinoides ruber*(white) calibrated to calendar years and including a 400-year seawater age correction (although reference says 800 years would have been closer to direct measurements of seawater age there); data file implies ages are ^{14}C but reference indicates they are calendar **Dataset Sources:** ftp://ftp.ngdc.noaa.gov/paleo/paleocean/sediment_files/isotope/74kl.isotope.tab

Core: 758 **Lat:** 5° 23' **Lon:** 90° 21' **Depth:** 2925 m $\delta^{18}\text{O}$ **Sources:** *Cibicidoides wuellerstorfi* **References:** Chen et al. 1995 **Age Model:** Matching, correlating and tuning of the *Cibicidoides wuellerstorfi* oxygen isotope record to the Imbrie and Imbrie 1980 model simulation of ice volume. **Notes:** Core name above is from reference; known as 121-758A and 121-758B in datasets (presented as a composite in reference and here). Lon minutes and ocean depth above are from reference; given as 21.7 and 2923.6/2925.6 m in dataset. Depth/multisamples of first dataset were averaged and matched with depth/age of second dataset. **Dataset Sources:** <http://www.pangaea.de/ddi?datasetid=52683&login=0&format=text>, <http://www.pangaea.de/ddi?datasetid=52684&login=0&format=text>

Core: 769A **Lat:** 8° 47.136' **Lon:** 121° 17.652' **Depth:** 3656 m $\delta^{18}\text{O}$ **Sources:** *Globigerinoides ruber (white)*, **References:** Linsley and Dunbar 1994 **Age Model:** Peak to peak matching of the oxygen isotope record with the Imbrie et al. 1984 SPECMAP stacked oxygen isotope record; position of the Brunhes/Matuyama paleomagnetic reversal (780 kyBP). **Notes:** Ocean depth above is from Site/Hole Summary on ODP web site (since not given in reference!); that given in dataset is 3644.8 m. Some deeper samples had an insufficient number of *Globigerinoides ruber*(white) so oxygen isotopes in *Neogloboquadrina dutertrei* were analyzed instead and corrected to G. sac. based on comparative enrichment measurements in samples with both species; these deeper samples were omitted here. Dataset data printed in reference. **Dataset Sources:** <http://www.pangaea.de/ddi?datasetid=55527&login=0&format=text>

Core: BOFS26K **Lat:** 25° 0' **Lon:** -20° 0' **Depth:** 3680 m $\delta^{18}\text{O}$ **Sources:** *Cibicidoides wuellerstorfi* **References:** Beveridge et al. 1995 **Age Model:** Detailed correlation between events in the benthic oxygen isotope records (event 3.1, start of Termination 1A and end of Termination 1B) with similar events in other cores from the eastern Atlantic which have been dated by a series of AMS ^{14}C ages, as listed by Winn et al. 1991; ^{14}C ages calibrated to calendar years using the marine calibration set of Stuiver and Braziunas 1993 and Bard et al. 1993 with the program Calib 3.0 of Stuiver and Reimer 1993; intermediate ages calculated by linear interpolation.

Notes: Core name above is from reference; known as BOFS26/6K in dataset. Lat degrees, Lat minutes, and Lon degrees, Lon minutes above are from reference; given as 24, 27.02 and 19, 50.20 in dataset. No depth given in dataset. Age data missing from dataset so manually added from reference's Table 3f. **Dataset Sources:** <http://www.pangaea.de/ddi?datasetid=52682&login=0&format=text>

Core: BOFS28K **Lat:** 24° 0' **Lon:** -22° 0' **Depth:** 4900 m $\delta^{18}\text{O}$ **Sources:** *Cibicidoides wuellerstorfi* **References:** Beveridge et al. 1995 **Age Model:** See Core BOFS26K. **Notes:** Core name above is from reference; known as BOFS28/3M in dataset. Lat minutes and Lon minutes above are from reference and probably due to omission; given as 36.9 and 45.72 in dataset. No depth given in dataset. Age data missing from dataset so manually added from reference's Table 3d. **Dataset Sources:** <http://www.pangaea.de/ddi?datasetid=52682&login=0&format=text>

Core: BOFS29K **Lat:** 20° 0' **Lon:** -21° 0' **Depth:** 4000 m $\delta^{18}\text{O}$ **Sources:** *Cibicidoides wuellerstorfi* **References:** Beveridge et al. 1995 **Age Model:** See Core BOFS26K. **Notes:** Core name above is from reference; known as BOFS29/1K in dataset. Lat minutes and Lon minutes above are from reference and probably due to omission; given as 31.01 and 7.01 in dataset. No depth given in dataset. Age data missing from dataset so manually added from reference's Table 3c. **Dataset Sources:** <http://www.pangaea.de/ddi?datasetid=52682&login=0&format=text>

Core: BOFS30K **Lat:** 19° 0' **Lon:** -20° 0' **Depth:** 3580 m $\delta^{18}\text{O}$ **Sources:** *Cibicidoides wuellerstorfi* **References:** Beveridge et al. 1995 **Age Model:** See Core BOFS26K. **Notes:** Core name above is from reference; known as BOFS30/3K in dataset. Lat minutes and Lon minutes above are from reference and probably due to omission; given as 44.81 and 43.46 in dataset. No depth given in dataset (and note typo in reference's Table 3e). Age data missing from dataset so manually added from reference's Table 3e. **Dataset Sources:** <http://www.pangaea.de/ddi?datasetid=52682&login=0&format=text>

Core: BOFS31K **Lat:** 19° 0' **Lon:** -20° 0' **Depth:** 3300 m $\delta^{18}\text{O}$ **Sources:** *Cibicidoides wuellerstorfi* **References:** Beveridge et al. 1995 **Age Model:** See Core BOFS26K. **Notes:** Core name above is from reference; known as BOFS31/1K in dataset. Lat minutes and Lon minutes above are from reference and probably due to roundoff; given as 59.87 (with Lat degrees then 18) and 9.73 in dataset. No depth given in dataset (and note typo in reference's Table 2). Age data missing from dataset so manually added from reference's Table 3b. **Dataset Sources:** <http://www.pangaea.de/ddi?datasetid=52681&login=0&format=text>

Core: BT4 **Lat:** -4° 0' **Lon:** 10° 0' **Depth:** 1000 m $\delta^{18}\text{O}$ **Sources:** *Cibicidoides spp.* **References:** Curry et al. 1988, Sarnthein et al. 1994 **Age Model:** Using other cores from second reference, an event stratigraphy was defined for the last 30,000 years based on the $\delta^{18}\text{O}$ records of *C. wuellerstorfi*; in six of these records the event stratigraphy was dated directly by AMS ^{14}C ages; based on the average ages

of six ^{14}C dated events a framework of age control points was defined, comprising 9.1 ka for the end and 10.4 ka for the beginning of Termination Ib, 13.6 ka for the end and 14.8 ka for the beginning of Termination Ia, 20 ka for a $\delta^{18}\text{O}$ minimum in the middle of $\delta^{18}\text{O}$ Stage 2 and 26 ka for $\delta^{18}\text{O}$ event 3.1; “AMS ^{14}C analog ages” then estimated for all other $\delta^{18}\text{O}$ records not directly dated by ^{14}C ages; to allow for linear interpolations between age control points (since ^{14}C age scale nonlinear), ^{14}C age control points converted into calendar ages using the tree ring conversion scheme of Stuiver et al. 1991 for the Holocene and the conversion into U/Th years between 10 ka and 30 ka as published by Bard et al. 1990; resulting calendar age control points are 9.8 ka (9.1 ^{14}C ka), 11.6 ka (10 ^{14}C ka), 12.4 ka (10.4 ^{14}C ka), 15 ka (13 ^{14}C ka), 17.1 ka (13.6 ^{14}C ka), and 29.5 ka (26 ^{14}C ka). No reservoir corrections to ^{14}C ages. **Notes:** Lat minutes and Lon minutes are from first reference and datasets; given as 19.8 and 25.8 in second reference. First dataset, used here, is based on the more recent age model of the second reference/dataset rather than the age model of first reference/third dataset. Depth/age/ $\delta^{18}\text{O}$ data of third dataset printed in first reference’s APPENDIX 1. First reference/third dataset indicates the $\delta^{18}\text{O}$ source is actually *Cibicidoides* spp. rather than just *Cibicidoides wuellerstorfi* as indicated by first dataset. **Dataset Sources:** <http://www.pangaea.de/ddi?datasetid=54402&login=0&format=text>, <http://www.pangaea.de/ddi?datasetid=54401&login=0&format=text>, <http://www.pangaea.de/ddi?datasetid=52328&login=0&format=text>

Core: Byrd **Lat:** -80° 0' **Lon:** -120° 0' **Depth:** -1530 m **$\delta^{18}\text{O}$ Sources:** *glacier ice H₂O* **References:** Johnsen et al. 1972, Blunier et al. 1998, Hammer et al. 1994 **Age Model:** Comparison of the ice core’s CH₄ record to that of the GRIP ice core, whose timescale (ss08) was obtained by counting annual layers downward from the surface back to 14.5 kyrBP and beyond this using a modified steady-state flow model, with two nonobservable parameters chosen to assign well-established ages to two characteristic features in the GRIP $\delta^{18}\text{O}$ record: (1) 11.5 kyrBP for the end of the Younger Dryas event; and (2) 110 kyrBP for marine isotope stage 5d. For the ice core in the Holocene some support was obtained from the third reference’s chronology, although this needed corrections due to lack of data in the core’s brittle zone (300-880m). **Notes:** Ocean depth above is from third reference. lat/lon info is from second and third reference. The top almost 88m of the ice core was recovered in unsatisfactory physical condition which precluded using it for detailed laboratory analyses. Dataset seems to give ages as kyr before 1989; these are converted here to yrBP (1950). **Dataset Sources:** byrd-blunier.txt from sigfus@gfy.ku.dk

Core: CD17-30 **Lat:** 20° 5.0' **Lon:** 61° 41.1' **Depth:** 3580 m **$\delta^{18}\text{O}$ Sources:** *Globigerinoides sacculifer*, *Uvigerina peregrina* **References:** Hermelin and Shimmiel 1995 **Age Model:** Correlation of oxygen isotopic stage boundaries to those of Imbrie et al. 1984 SPECMAP **Notes:** Lat degrees and Lat minutes actually given in reference are 19 and 65.0; the latter is greater than 60 so the Lat degrees and Lat minutes have been converted to 20 and 5.0, which are the values given in the dataset. Dataset data is printed in reference. **Dataset Sources:** <http://www.pangaea.de/ddi?datasetid=52686&login=0&format=text>

Core: CH72-02 **Lat:** 40° 0' **Lon:** -22° 0' **Depth:** 3485 m $\delta^{18}\text{O}$ **Sources:** *Globigerinoides ruber (white)*, *Cibicidoides spp.*, *Uvigerina peregrina* **References:** Curry et al. 1988, Sarnthein et al. 1994 **Age Model:** See Core BT4. For ages older than 29.5 ka, $\delta^{18}\text{O}$ record events were given ages after Martinson et al. 1987. No extrapolation beyond last age control point. **Notes:** Lat minutes, Lon degrees, and Lon minutes are from first reference and datasets; given in second reference as 36.0, 21, and 42.0. First dataset, used here, is based on the more recent age model of the second reference/dataset rather than the age model of first reference/third dataset. Depth/age/ $\delta^{18}\text{O}$ data of third dataset printed in first reference's APPENDIX 1. First reference/third dataset indicates the $\delta^{18}\text{O}$ source is actually *Cibicidoides spp.* rather than just *Cibicidoides wuellerstorfi* as indicated by first dataset. **Dataset Sources:** <http://www.pangaea.de/ddi?datasetid=54403&login=0&format=text>, <http://www.pangaea.de/ddi?datasetid=54401&login=0&format=text>, <http://www.pangaea.de/ddi?datasetid=52325&login=0&format=text>

Core: CH73-139 **Lat:** 55° 0' **Lon:** -16° 0' **Depth:** 2209 m $\delta^{18}\text{O}$ **Sources:** *Cibicidoides wuellerstorfi* **References:** Curry et al. 1988 **Age Model:** Correlated to Pacific Ocean core V19-30 (Shackleton et al. 1983a,b), whose $\delta^{18}\text{O}$ record is correlated with the chronology of Imbrie et al. 1984. **Notes:** Lat degrees, Lat minutes, and Lon minutes are from reference; given as 54, 38.0, and 21.0 in dataset. Depth/age/ $\delta^{18}\text{O}$ data of dataset printed in reference APPENDIX 1. **Dataset Sources:** <http://www.pangaea.de/ddi?datasetid=52277&login=0&format=text>

Core: CH74-227 **Lat:** 35° 0' **Lon:** -29° 0' **Depth:** 3225 m $\delta^{18}\text{O}$ **Sources:** *Cibicidoides spp.*, *Uvigerina pygmaea*, *Uvigerina peregrina*, *Nonion barleanum*, *Oridorsalis umbonatus* **References:** Curry et al. 1988, Sarnthein et al. 1994 **Age Model:** See Core BT4. **Notes:** Lat minutes and Lon minutes are from first reference; given as 16.0 and 15.0 in datasets. First dataset, used here, is based on the more recent age model of the second reference/dataset rather than the age model of first reference/third dataset. Core is not explicitly mentioned in second reference but does seem to have been part of that work (age model, forams used). Depth/age/ $\delta^{18}\text{O}$ data of third dataset printed in first reference's APPENDIX 1. First reference/third dataset indicates the $\delta^{18}\text{O}$ source is actually *Cibicidoides spp.* rather than just *Cibicidoides wuellerstorfi* as indicated by first dataset. **Dataset Sources:** <http://www.pangaea.de/ddi?datasetid=54404&login=0&format=text>, <http://www.pangaea.de/ddi?datasetid=54401&login=0&format=text>, <http://www.pangaea.de/ddi?datasetid=52279&login=0&format=text>

Core: CH75-03 **Lat:** 10° 0' **Lon:** -57° 0' **Depth:** 3410 m $\delta^{18}\text{O}$ **Sources:** *Cibicidoides spp.* **References:** Curry et al. 1988 **Age Model:** See Core CH73-139. **Notes:** Depth/age/ $\delta^{18}\text{O}$ data of dataset printed in reference APPENDIX 1. **Dataset Sources:** <http://www.pangaea.de/ddi?datasetid=52326&login=0&format=text>

Core: CH75-04 **Lat:** 10° 0' **Lon:** -56° 0' **Depth:** 3820 m $\delta^{18}\text{O}$ **Sources:** *Cibi-*

cidoides spp. **References:** Curry et al. 1988 **Age Model:** See Core CH73-139. **Notes:** Depth/age/ $\delta^{18}\text{O}$ data of dataset printed in reference APPENDIX 1. **Dataset Sources:** <http://www.pangaea.de/ddi?datasetid=52324&login=0&format=text>

Core: CHN82-24 **Lat:** 43° 0' **Lon:** -30° 0' **Depth:** 3070 m $\delta^{18}\text{O}$ **Sources:** *Cibicidoides* spp. (*C. wuellerstorfi*, *C. kullenbergi*) **References:** Curry et al. 1988, Oppo and Fairbanks 1990 **Age Model:** Oxygen isotope record correlated to the benthic isotope stratigraphy of Martinson et al. 1987. **Notes:** Ocean depth above is from first reference and datasets; given in second reference as 3427 m. Similarly, Lon degrees is from first reference and datasets; that given in second reference is -33. Second dataset/reference contains a more-recent age model than first dataset/reference so is used here: second dataset's depth/age data (printed in second reference's TABLE 2) is applied to first dataset's foram depth/ $\delta^{18}\text{O}$ data (printed in first reference's APPENDIX 1.) **Dataset Sources:** <http://www.pangaea.de/ddi?datasetid=52327&login=0&format=text>, <http://www.pangaea.de/ddi?datasetid=52403&login=0&format=text>

Core: CampCentury **Lat:** 77° 10' **Lon:** -61° 8' **Depth:** ? m $\delta^{18}\text{O}$ **Sources:** *glacier ice H₂O* **References:** Johnsen et al. 1970 **Age Model:** Ages calculated by considering a simple ice flow model that uses an average accumulation rate and assumes a uniform strain rate above a set distance from the core bottom. **Notes:** lat/lon info is from second dataset. First dataset gives ages as year AD; these are converted here to yrBP (1950). There is a less-recent age model than the one used. **Dataset Sources:** <ftp://ftp.ngdc.noaa.gov/paleo/icecore/greenland/gisp/campcentury/cc-1ynew.txt>, <http://www.ngdc.noaa.gov/paleo/icecore/greenland/gisp/campcentury/campc.html>

Core: Crete **Lat:** 71° 7.22' **Lon:** -37° 18.98' **Depth:** -3172 m $\delta^{18}\text{O}$ **Sources:** *glacier ice H₂O* **References:** Clausen et al. 1988, Dansgaard et al. 1975 **Age Model:** Comparison of the seasonally varying $\delta^{18}\text{O}$ and acidity profiles provides an absolute chronology, checked with dated distinct stratigraphic volcanic markers and a melt feature. **Notes:** Lat minutes and Lon minutes are from first reference; given as 7 and 19 in second reference. First dataset is upper section of ice core and second dataset is lower section; there is a 5-point overlap between them. Datasets give ages as year AD; these are converted here to yrBP (1950). **Dataset Sources:** <ftp://ftp.ngdc.noaa.gov/paleo/icecore/greenland/gisp/crete/ct74-12.txt>, <ftp://ftp.ngdc.noaa.gov/paleo/icecore/greenland/gisp/crete/ct74-12b.txt>

Core: D11957P **Lat:** 39° 3' **Lon:** -12° 35' **Depth:** 3585 m $\delta^{18}\text{O}$ **Sources:** *Globigerinoides ruber* (white), *Globigerina bulloides* **References:** Lebreiro et al. 1997, Lebreiro et al. 1996 **Age Model:** Interpolation (linear) between the boundaries of oxygen isotope stages placed in the $\delta^{18}\text{O}$ record, using the values given in Martinson et al. 1987. Interpolation calculated here and, based on Fig. 3 of second reference, extrapolation done beyond the last age using the slope of the last two actual depth/ages. **Notes:** Lon minutes is from first reference and datasets; that

given in second reference is 36. Core's depth/age data from second dataset applied to its foram $\delta^{18}\text{O}$ data from first dataset. Second dataset data printed in reference. **Dataset Sources:** <http://www.pangaea.de/ddi?datasetid=53371&login=0&format=text>, <http://www.pangaea.de/ddi?datasetid=53372&login=0&format=text>

Core: DomeC **Lat:** $-74^{\circ} 39'$ **Lon:** $124^{\circ} 10'$ **Depth:** -3240 m **$\delta^{18}\text{O}$ Sources:** *glacier ice H_2O* **References:** Lorius et al. 1979 **Age Model:** A simple ice flow model (Nye 1957) that assumes a uniform vertical strain rate and a constant value of snow accumulation; in going back through the LGM there is large uncertainty from the assumption of steady-state conditions. **Notes:** Lat minutes and Lon degrees are from reference; given as 30.0 and 123 in first dataset. Second dataset is just an alternate source. **Dataset Sources:** <http://www.pangaea.de/ddi?datasetid=57629&login=0&format=text>, <ftp://ftp.ngdc.noaa.gov/paleo/icecore/antarctica/domec/domec1.txt>

Core: Dye3 **Lat:** $65^{\circ} 12'$ **Lon:** $-43^{\circ} 48'$ **Depth:** ? m **$\delta^{18}\text{O}$ Sources:** *glacier ice H_2O* **References:** Dansgaard et al. 1985 **Age Model:** Counting of summer $\delta^{18}\text{O}$ peaks downward from the surface, cross-checked with profiles of other seasonally varying parameters. **Notes:** Dataset gives ages as year AD; these are converted here to yrBP (1950). **Dataset Sources:** <ftp://ftp.ngdc.noaa.gov/paleo/icecore/greenland/gisp/dye3/dye3-1yr.txt>

Core: E45-29 **Lat:** $-44^{\circ} 53'$ **Lon:** $106^{\circ} 31'$ **Depth:** 3863 m **$\delta^{18}\text{O}$ Sources:** *Globigerina bulloides* **References:** Howard and Prell 1992 **Age Model:** Oxygen isotope event classification for the Pleistocene of Prell et al. 1986 and age assignments of these following Imbrie et al. 1984 (SPECMAP time scale); linear interpolation between events; interpolation calculated here but with no extrapolation beyond last isotopic event age. **Notes:** Core name above is from reference; known as ELT45.029-PC in dataset. Ocean depth above is from reference; that in dataset is 3867 m. Similarly, Lat minutes and Lon minutes are from reference; those given in dataset are 52.62 and 31.08. Core's depth/age data from second dataset applied to its foram $\delta^{18}\text{O}$ data from first dataset. First dataset data printed in reference. **Dataset Sources:** <http://www.pangaea.de/ddi?datasetid=51613&login=0&format=text>, <http://www.pangaea.de/ddi?datasetid=51622&login=0&format=text>

Core: E49-17 **Lat:** $-48^{\circ} 17'$ **Lon:** $90^{\circ} 15'$ **Depth:** 3542 m **$\delta^{18}\text{O}$ Sources:** *Globigerina bulloides* **References:** Howard and Prell 1992 **Age Model:** Oxygen isotope event classification for the Pleistocene of Prell et al. 1986 and age assignments of these following Imbrie et al. 1984 (SPECMAP time scale); linear interpolation between events; interpolation calculated here but with no extrapolation beyond last isotopic event age. **Notes:** Core name above is from reference; known as ELT49.017-PC in dataset. Ocean depth above is from reference; that in dataset is 3546 m. Similarly, Lat minutes and Lon minutes are from reference; those given in dataset are 16.8 and 14.82. Core's depth/age data from second dataset applied to its foram $\delta^{18}\text{O}$ data from first dataset. First dataset data printed in reference. **Dataset Sources:** <http://www.pangaea.de/ddi?datasetid=51613&login=0&format=text>

w.pangaea.de/ddi?datasetid=51614&login=0&format=text, <http://www.pangaea.de/ddi?datasetid=51622&login=0&format=text>

Core: E49-18 **Lat:** -46° 3' **Lon:** 90° 10' **Depth:** 3291 m $\delta^{18}\text{O}$ **Sources:** *Globigerina bulloides* **References:** Howard and Prell 1992 **Age Model:** Oxygen isotope event classification for the Pleistocene of Prell et al. 1986 and age assignments of these following Imbrie et al. 1984 (SPECMAP time scale); linear interpolation between events; interpolation calculated here. **Notes:** Core name above is from reference; known as ELT49.018-PC in dataset. Ocean depth above is from reference; that in dataset is 3282 m. Similarly, Lon minutes is from reference; that given in dataset is 9.3. Core's depth/age data from second dataset applied to its foram $\delta^{18}\text{O}$ data from first dataset. First dataset data printed in reference. **Dataset Sources:** <http://www.pangaea.de/ddi?datasetid=51615&login=0&format=text>, <http://www.pangaea.de/ddi?datasetid=51622&login=0&format=text>

Core: E49-19 **Lat:** -43° 53' **Lon:** 90° 6' **Depth:** 3069 m $\delta^{18}\text{O}$ **Sources:** *Cibicides spp.* **References:** Charles et al. 1991 **Age Model:** Following method of Imbrie et al. 1984, identification and age assignation of distinct oxygen isotope events in the core; ages from Martinson et al. 1987 and Imbrie et al. 1984, the SPECMAP chronology. Other control points include ^{14}C dates and biostratigraphic events (e.g. the universal extinction of the radiolarian *Stylatractus universus*). **Notes:** Ocean depth of core given above is from reference; that given in dataset is 3057 m. Core name in dataset is ELT49.019-PC **Dataset Sources:** <http://www.pangaea.de/ddi?datasetid=52436&login=0&format=text>

Core: E49-21 **Lat:** -42° 11' **Lon:** 94° 53' **Depth:** 3328 m $\delta^{18}\text{O}$ **Sources:** *Globigerina bulloides* **References:** Howard and Prell 1992 **Age Model:** See Core E49-17. **Notes:** Core name above is from reference; known as ELT49.021-PC in dataset. Ocean depth above is from reference; that in dataset is 3319 m. Similarly, Lat minutes and Lon minutes are from reference; those given in dataset are 11.1 and 53.1. Core's depth/age data from second dataset applied to its foram $\delta^{18}\text{O}$ data from first dataset. First dataset data printed in reference. **Dataset Sources:** <http://www.pangaea.de/ddi?datasetid=51616&login=0&format=text>, <http://www.pangaea.de/ddi?datasetid=51622&login=0&format=text>

Core: E49-23 **Lat:** -47° 7' **Lon:** 95° 5' **Depth:** 3206 m $\delta^{18}\text{O}$ **Sources:** *Globigerina bulloides* **References:** Howard and Prell 1992 **Age Model:** See Core E49-18. **Notes:** Core name above is from reference; known as ELT49.023-PC in dataset. Ocean depth above is from reference; that in dataset is 3285 m. Similarly, Lat minutes and Lon minutes are from reference; those given in dataset are 7.68 and 4.8. Core's depth/age data from second dataset applied to its foram $\delta^{18}\text{O}$ data from first dataset. First dataset data printed in reference. **Dataset Sources:** <http://www.pangaea.de/ddi?datasetid=51617&login=0&format=text>, <http://www.pangaea.de/ddi?datasetid=51622&login=0&format=text>

Core: EN066-10 **Lat:** 6° 39' **Lon:** -21° 54' **Depth:** 3527 m **$\delta^{18}\text{O}$ Sources:** *Cibicidoides wuellerstorfi* **References:** Curry et al. 1988, Sarnthein et al. 1994 **Age Model:** See Core BT4. **Notes:** Core name above is from references; known as EN06601-0010PG in datasets. Lat degrees and Lon degrees are from second reference and datasets; given as 7 and 22 in first reference. Lat minutes and Lon minutes are from second reference; given as 0 and 0 in first reference and 38.4 and 53.82 in datasets. Reference given in datasets is incorrect; should be first reference for first dataset and second reference for second dataset. Depth/ $\delta^{18}\text{O}$ data of first dataset printed in first reference's APPENDIX 1. First reference contains an age model based on Imbrie et al. 1984; less recent so not used here. **Dataset Sources:** <http://www.pangaea.de/ddi?datasetid=52295&login=0&format=text>, <http://www.pangaea.de/ddi?datasetid=54409&login=0&format=text>

Core: EN066-16 **Lat:** 5° 27.6' **Lon:** -21° 8.4' **Depth:** 3152 m **$\delta^{18}\text{O}$ Sources:** *Cibicidoides wuellerstorfi* **References:** Curry et al. 1988, Sarnthein et al. 1994 **Age Model:** See Core BT4. **Notes:** Core name above is from references; known as EN06601-0016PG in dataset. Ocean depth above is from references; given in dataset as 3160 m. Lat minutes and Lon minutes are from second reference; given as 0 and 0 in first reference and 27.18 and 8.58 in dataset. Reference given in dataset is incorrect; should be first and second references. Depth/ $\delta^{18}\text{O}$ data of dataset printed in first reference's APPENDIX 1. First reference contains an age model based on Imbrie et al. 1984; less recent so not used here. **Dataset Sources:** <http://www.pangaea.de/ddi?datasetid=54409&login=0&format=text>

Core: EN066-21 **Lat:** 4° 13.8' **Lon:** -21° 37.8' **Depth:** 3995 m **$\delta^{18}\text{O}$ Sources:** *Cibicidoides wuellerstorfi* **References:** Curry et al. 1988, Sarnthein et al. 1994 **Age Model:** See Core BT4. **Notes:** Core name above is from references; known as EN06601-0021PG in dataset. Ocean depth above is from references; given in dataset as 3792 m. Lon degrees is from references; given as -21 in dataset. Lat minutes and Lon minutes are from second reference; given as 0 and 0 in first reference and 13.98 and 37.5 in dataset. Reference given in dataset is incorrect; should be first and second references. Depth/ $\delta^{18}\text{O}$ data of dataset printed in first reference's APPENDIX 1. First reference contains an age model based on Imbrie et al. 1984; less recent so not used here. **Dataset Sources:** <http://www.pangaea.de/ddi?datasetid=54409&login=0&format=text>

Core: EN066-26 **Lat:** 3° 5.4' **Lon:** -20° 1.2' **Depth:** 4745 m **$\delta^{18}\text{O}$ Sources:** *Cibicidoides wuellerstorfi* **References:** Curry et al. 1988, Sarnthein et al. 1994 **Age Model:** See Core BT4. **Notes:** Core name above is from references; known as EN06601-0026PG in dataset. Lat minutes and Lon minutes are from second reference; given as 0 and 0 in first reference and 5.1 and .9 in dataset. Reference given in dataset is incorrect; should be first and second references. Depth/ $\delta^{18}\text{O}$ data of dataset printed in first reference's APPENDIX 1. First reference contains an age model based on Imbrie et al. 1984; less recent so not used here. **Dataset Sources:** <http://www.pangaea.de/ddi?datasetid=54409&login=0&format=text>

Core: EN066-29 **Lat:** 2° 27.6' **Lon:** -19° 45.6' **Depth:** 5104 m **$\delta^{18}\text{O}$ Sources:** *Cibicidoides wuellerstorfi* **References:** Curry et al. 1988, Sarnthein et al. 1994 **Age Model:** See Core BT4. **Notes:** Core name above is from references; known as EN06601-0029PG in dataset. Ocean depth above is from references; given in dataset as 5105 m. Lon degrees is from second reference and dataset; given as -20 in first reference. Lat minutes is from second reference and dataset; given as 0 in first reference. Lon minutes is from second reference; given as 0 in first reference and 45.72 in dataset. Reference given in dataset is incorrect; should be first and second references. Depth/ $\delta^{18}\text{O}$ data of dataset printed in first reference's APPENDIX 1. First reference contains an age model based on Imbrie et al. 1984; less recent so not used here. **Dataset Sources:** <http://www.pangaea.de/ddi?datasetid=54409&login=0&format=text>

Core: EN066-32 **Lat:** 2° 28.2' **Lon:** -19° 43.8' **Depth:** 5003 m **$\delta^{18}\text{O}$ Sources:** *Cibicidoides wuellerstorfi* **References:** Curry et al. 1988, Sarnthein et al. 1994 **Age Model:** See Core BT4. **Notes:** Core name above is from references; known as EN06601-0032PG in dataset. Ocean depth above is from references; given in dataset as 4998 m. Lon degrees is from second reference and dataset; given as -20 in first reference. Lat minutes and Lon minutes are from second reference; given as 0 and 0 in first reference and 28.32 and 43.98 in dataset. Reference given in dataset is incorrect; should be first and second references. Depth/ $\delta^{18}\text{O}$ data of dataset printed in first reference's APPENDIX 1. First reference contains an age model based on Imbrie et al. 1984; less recent so not used here. **Dataset Sources:** <http://www.pangaea.de/ddi?datasetid=54409&login=0&format=text>

Core: EN066-36 **Lat:** 4° 0' **Lon:** -20° 0' **Depth:** 4270 m **$\delta^{18}\text{O}$ Sources:** *Cibicidoides wuellerstorfi* **References:** Curry et al. 1988, Sarnthein et al. 1994 **Age Model:** See Core BT4. **Notes:** Core name above is from first reference; known as EN06601-0036PG in dataset. Core is not explicitly mentioned in second reference but does seem to have been part of that work (age model, forams used). Ocean depth above is from first reference; given in dataset as 4095 m. Lat minutes and Lon minutes are from first reference; given as 18.3 and 12.72 in dataset. Reference given in dataset is incorrect; should be first and second references. Depth/ $\delta^{18}\text{O}$ data of dataset printed in first reference's APPENDIX 1. First reference contains an age model based on Imbrie et al. 1984; less recent so not used here. **Dataset Sources:** <http://www.pangaea.de/ddi?datasetid=54409&login=0&format=text>

Core: EN066-38 **Lat:** 4° 55' **Lon:** -20° 30' **Depth:** 2931 m **$\delta^{18}\text{O}$ Sources:** *Globigerinoides sacculifer*, *Neogloboquadrina dutertrei*, *Cibicidoides wuellerstorfi* **References:** Curry and Crowley 1987, Curry et al. 1988, Sarnthein et al. 1994 **Age Model:** For first and second $\delta^{18}\text{O}$ source (first reference/dataset): levels in the $\delta^{18}\text{O}$ record correlating to the isotopic events defined by Prell et al. 1986 were identified and put on the time scale of Imbrie et al. 1984. For third $\delta^{18}\text{O}$ source (second reference/dataset): using other cores from third reference (age model of second dataset),

an event stratigraphy was defined for the last 30,000 years based on the $\delta^{18}\text{O}$ records of C. wuellerstorfi; in six of these records the event stratigraphy was dated directly by AMS ^{14}C ages; based on the average ages of six ^{14}C dated events a framework of age control points was defined, comprising 9.1 ka for the end and 10.4 ka for the beginning of Termination Ib, 13.6 ka for the end and 14.8 ka for the beginning of Termination Ia, 20 ka for a $\delta^{18}\text{O}$ minimum in the middle of $\delta^{18}\text{O}$ Stage 2 and 26 ka for $\delta^{18}\text{O}$ event 3.1; “AMS ^{14}C analog ages” then estimated for all other $\delta^{18}\text{O}$ records not directly dated by ^{14}C ages; to allow for linear interpolations between age control points (since ^{14}C age scale nonlinear), ^{14}C age control points converted into calendar ages using the tree ring conversion scheme of Stuiver et al. 1991 for the Holocene and the conversion into U/Th years between 10 ka and 30 ka as published by Bard et al. 1990; resulting calendar age control points are 9.8 ka (9.1 ^{14}C ka), 11.6 ka (10 ^{14}C ka), 12.4 ka (10.4 ^{14}C ka), 15 ka (13 ^{14}C ka), 17.1 ka (13.6 ^{14}C ka), and 29.5 ka (26 ^{14}C ka). No reservoir corrections to ^{14}C ages. The two age models differ by as much as 3.1 kyr at .49 m core depth but it’s not clear which is better so that associated with each $\delta^{18}\text{O}$ source is used. There is also an Imbrie et al. 1984-related age model in second reference; considered not to be as good as those used so not used here. **Notes:** Core name above is from second and third reference; known as EN066-38GGC in first reference and EN06601-0038PG in datasets. Ocean depth above is from references; given in datasets as 2937 m. Lat degrees is from first/third reference and datasets; given as 5 in second reference. Lat minutes is from first reference; given as 0 in second reference, 55.2 in third reference, and 55.08 in datasets. Lon minutes is from first reference; given as 0 in second reference and 29.88 in datasets. Reference given in second dataset is incorrect; should be second and third references. Depth/age/ $\delta^{18}\text{O}$ data of first/second $\delta^{18}\text{O}$ source and first dataset are printed in first reference’s TABLE 2a. Depth/ $\delta^{18}\text{O}$ data of third $\delta^{18}\text{O}$ source/dataset printed in second reference’s APPENDIX 1. **Dataset Sources:** <http://www.pangaea.de/ddi?datasetid=59888&login=0&format=text>, <http://www.pangaea.de/ddi?datasetid=54409&login=0&format=text>

Core: EN066-44 **Lat:** 5° 15.6' **Lon:** -21° 42.6' **Depth:** 3428 m **$\delta^{18}\text{O}$ Sources:** *Cibicidoides wuellerstorfi* **References:** Curry et al. 1988, Sarnthein et al. 1994 **Age Model:** See Core BT4. **Notes:** Core name above is from references; known as EN06601-0044PG in dataset. Ocean depth above is from references; given in dataset as 3423 m. Lon degrees is from second reference and dataset; given as -22 in first reference. Lat minutes and Lon minutes are from second reference; given as 0 and 0 in first reference and 15.78 and 42.72 in dataset. Reference given in dataset is incorrect; should be first and second references. Depth/ $\delta^{18}\text{O}$ data of dataset printed in first reference’s APPENDIX 1. First reference contains an age model based on Imbrie et al. 1984; less recent so not used here. **Dataset Sources:** <http://www.pangaea.de/ddi?datasetid=54409&login=0&format=text>

Core: ERDC-093P **Lat:** -2° 14.5' **Lon:** 157° .5' **Depth:** 1619 m **$\delta^{18}\text{O}$ Sources:** *Globigerinoides sacculifer* **References:** Le and Shackleton 1992 **Age Model:** Correlation of the $\delta^{18}\text{O}$ record with the SPECMAP stack of Imbrie et al. 1984; correlation

of fragmentation and $\delta^{13}\text{C}$ incorporated where $\delta^{18}\text{O}$ record detail lacking but given secondary priority. Linear interpolation between age control points assumed and calculated here; no extrapolation beyond last age control point. **Notes:** Ocean depth above is from reference; that given in datasets is 1604 m. Core's depth/age data from second dataset applied to its foram $\delta^{18}\text{O}$ data from first dataset. Dataset data printed in reference. **Dataset Sources:** <http://www.pangaea.de/ddi?datasetid=52476&login=0&format=text>, <http://www.pangaea.de/ddi?datasetid=52479&login=0&format=text>

Core: EW9209-1JPC **Lat:** 5° 54.4' **Lon:** -44° 11.7' **Depth:** 4056 m $\delta^{18}\text{O}$ **Sources:** *Globigerinoides sacculifer*, *Globigerinoides ruber*, *Cibicidoides wuellerstorfi*, *Cibicidoides spp.*, *Nuttallides umbonifera* **References:** Curry and Oppo 1997, Curry et al. 1999, Curry 1996 **Age Model:** AMS ^{14}C dates on *Globigerinoides sacculifer* based on a half-life of 5568 years; calendar ages then calculated using a 400-year reservoir correction and applying the Stuiver and Braziunas 1993 calibration curve for the younger ages and a Bard et al. 1992 U/Th calibration curve for the older ages; linear interpolation between; correlation with SPECMAP chronology of Martinson et al. 1987, especially beyond ^{14}C dates. 3 oldest AMS ^{14}C dates of Curry 1999 not included. Imbrie et al. 1993 SPECMAP chronology correlation of Curry 1996 not used here. **Notes:** Used revised (post-recalibration) not original published $\delta^{18}\text{O}$ data; see readme file at data source. The related datasets from Pangaea contain the unrevised data. **Dataset Sources:** ftp://www.ngdc.noaa.gov/paleo/contributions_by_author/curry1997/

Core: GIK13239-1 **Lat:** 13° 52.6' **Lon:** -18° 18.8' **Depth:** 3156 m $\delta^{18}\text{O}$ **Sources:** *Cibicidoides wuellerstorfi*, *Uvigerina hollicki* **References:** Sarnthein et al. 1994 **Age Model:** See Core 12328-5. **Notes:** Core is not explicitly mentioned in reference (given in dataset) but does seem to have been part of that work (age model, forams used). **Dataset Sources:** <http://www.pangaea.de/ddi?datasetid=54360&login=0&format=text>

Core: GIK16856-2 **Lat:** 4° 48.3' **Lon:** 3° 24.1' **Depth:** 2861 m $\delta^{18}\text{O}$ **Sources:** *Cibicidoides wuellerstorfi*, *Cibicidoides kullenbergi* **References:** Sarnthein et al. 1994 **Age Model:** See Core 12328-5. For ages older than 29.5 ka, $\delta^{18}\text{O}$ record events were given ages after Martinson et al. 1987. **Notes:** Core is not explicitly mentioned in reference (given in dataset) but does seem to have been part of that work (age model, forams used). **Dataset Sources:** <http://www.pangaea.de/ddi?datasetid=54391&login=0&format=text>

Core: GIK17748-2 **Lat:** -32° 45' **Lon:** -72° 2' **Depth:** 2545 m $\delta^{18}\text{O}$ **Sources:** *Neogloboquadrina pachyderma (dextral)* **References:** Lamy et al. 1999 **Age Model:** Based on six AMS ^{14}C dates that were corrected for C_{13} and for a reservoir age of 400 years and that were converted to calendar years after the method of Bard et al. 1993. Linear interpolation between these age control points was specified in reference but omitted in dataset so calculated here using a zero-age depth of -13 m (since core top

missing) and a core bottom age of 15.6 kyr, both as specified in reference. **Dataset Sources:** <http://www.pangaea.de/ddi?datasetid=58254&login=0&format=text>

Core: GISP2 **Lat:** 72° 34.8' **Lon:** -38° 28.8' **Depth:** -3208 m $\delta^{18}\text{O}$ **Sources:** *glacier ice H₂O* **References:** Grootes and Stuiver 1997, Stuiver et al. 1995, Grootes et al. 1993 **Age Model:** Annual layer counting down to about 2430 m/50,000 years (Meese et al. 1994); beyond that, derived by correlating the $\delta^{18}\text{O}$ of O₂ in the gas bubbles to that of the Vostok core, where the timescale is based on a combination of flow modeling and a match to the Imbrie et al. 1984 SPECMAP chronology by Sowers et al 1993. **Notes:** Ocean depth above is from third reference. Similarly, Lat minutes and Lon minutes are from third reference; given as 35.3 and 27.45 in second dataset. Second dataset is an alternate source with fewer references and less supplementary information given. **Dataset Sources:** <ftp://ftp.ngdc.noaa.gov/paleo/icecore/greenland/summit/gisp2/isotopes/gispd18o.txt>, <http://www.pangaea.de/ddi?datasetid=56094&login=0&format=text>

Core: GRIP **Lat:** 72° 34' **Lon:** -37° 37' **Depth:** -3232 m $\delta^{18}\text{O}$ **Sources:** *glacier ice H₂O* **References:** Johnsen et al. 1997, Dansgaard et al. 1993, Grootes et al. 1993 **Age Model:** GRIP timescale ss09. Based on a Dansgaard-Johnsen (1969) type flow model, with a 1500 m lower shear layer, 13.5 percent bottom sliding and accumulation rates which are a function of the $\delta^{18}\text{O}$ values: 23.0 cm of ice at -35.2 per mil with 8 percent and 18 percent change per per mil at -35.2 per mil and -40 per mil, respectively. **Notes:** Ocean depth above is from first reference; given as -3238 m in second reference. Similarly, Lat minutes and Lon minutes are from first reference; given as 34.8 and 38.4 in second reference and 35.23 and 38.53 in third dataset. Third dataset is an alternate source with fewer references given. Second dataset is description of timescale used, which is not that given in first and second references. **Dataset Sources:** <ftp://ftp.ngdc.noaa.gov/paleo/icecore/greenland/summit/grip/isotopes/gripd18o.txt>, <ftp://ftp.ngdc.noaa.gov/paleo/icecore/greenland/summit/grip/depthage/gripage.txt>, <http://www.pangaea.de/ddi?datasetid=55091&login=0&format=text>

Core: GeoB1008-3 **Lat:** -6° 34.9' **Lon:** 10° 19.1' **Depth:** 3124 m $\delta^{18}\text{O}$ **Sources:** *Globigerina bulloides*, *Globigerinoides ruber (pink)* **References:** Schneider et al. 1995, Schneider et al. 1994 **Age Model:** Comparison of the $\delta^{18}\text{O}$ records against the SPECMAP stacked record of Imbrie et al. 1984; dataset implies ages are ¹⁴C but references indicate they are calendar. **Notes:** Lat minutes and Lon minutes are from first reference; those in dataset are 34.54 and 19.06. **Dataset Sources:** ftp://ftp.ngdc.noaa.gov/paleo/paleocean/sediment_files/isotope/gb10083.isotope.tab

Core: GeoB1016-3 **Lat:** -11° 46.2' **Lon:** 11° 40.9' **Depth:** 3411 m $\delta^{18}\text{O}$ **Sources:** *Globigerina bulloides*, *Globigerinoides ruber (pink)* **References:** Schneider et al. 1995 **Age Model:** Comparison of the $\delta^{18}\text{O}$ records against the SPECMAP stacked record of Imbrie et al. 1984; dataset implies ages are ¹⁴C but reference indicates they are calendar. **Notes:** Lat minutes and Lon minutes are from reference; those in dataset are 46.02 and 40.54. **Dataset Sources:** <ftp://ftp.ngdc.noaa.gov/paleo/>

paleocean/sediment_files/isotope/gb10163.isotope.tab

Core: GeoB1028-5 **Lat:** -20° 6.2' **Lon:** 9° 11.1' **Depth:** 2209 m **$\delta^{18}\text{O}$ Sources:** *Globigerina bulloides*, *Globigerinoides ruber* (white), *Globorotalia inflata* **References:** Schneider et al. 1995, Wefer et al. 1996 **Age Model:** See Core GeoB1008-3. **Notes:** Lat minutes and Lon minutes above are from references; those in first dataset are 6.12 and 11.06. Second reference gives ocean depth as 2215 m. Data of first dataset printed in Table A3 of first reference. Core's depth/age data from first dataset applied to its *Globorotalia inflata* $\delta^{18}\text{O}$ data from second dataset. Second dataset has incorrect(?) *G. ruber*(white) $\delta^{18}\text{O}$ of 0.40 at 2.13 m core depth compared to .04 at that depth in first reference and dataset. **Dataset Sources:** ftp://ftp.ngdc.noaa.gov/paleo/paleocean/sediment_files/isotope/gb10285.isotope.tab, http://www.pangaea.de/ddi?datasetid=54653&login=0&format=text

Core: GeoB1032-2 **Lat:** -22° 54.9' **Lon:** 6° 2.2' **Depth:** 2505 m **$\delta^{18}\text{O}$ Sources:** *Cibicidoides wuellerstorfi*, *Globigerinoides ruber* (white), *Globorotalia inflata*, *Globorotalia truncatulinoides* (sinistral, small), *Globorotalia truncatulinoides* (sinistral, medium), *Globorotalia truncatulinoides* (sinistral, large) **References:** Bickert and Wefer 1996, Wefer et al. 1996 **Age Model:** Graphic correlation of the oxygen isotope record to the Imbrie et al. 1984 SPECMAP standard record. **Notes:** Ocean depth above is that given in references for GeoB1032-2/3; that in datasets for this core is 2490 m. Similarly, Lat minutes and Lon minutes are from references; those given in datasets are 54.8 and 1.6. For *Globorotalia truncatulinoides* (sinistral), small = 150-212um, medium = 212-355um, large = 425-500um. Core's depth/age data from first dataset applied to its non-*Cibicidoides wuellerstorfi* data from second dataset. **Dataset Sources:** http://www.pangaea.de/ddi?datasetid=58770&login=0&format=text, http://www.pangaea.de/ddi?datasetid=54655&login=0&format=text

Core: GeoB1032-3 **Lat:** -22° 54.9' **Lon:** 6° 2.2' **Depth:** 2505 m **$\delta^{18}\text{O}$ Sources:** *Cibicidoides wuellerstorfi*, *Globigerinoides ruber* (white), *Globorotalia inflata*, *Globorotalia truncatulinoides* (sinistral, small), *Globorotalia truncatulinoides* (sinistral, medium), *Globorotalia truncatulinoides* (sinistral, large) **References:** Bickert and Wefer 1996, Wefer et al. 1996 **Age Model:** See Core GeoB1032-2. **Notes:** Lat minutes and Lon minutes above are from references; those given in datasets are 54.8 and 1.6. For *Globorotalia truncatulinoides* (sinistral), small = 150-212um, medium = 212-355um, large = 425-500um. Core's depth/age data from first dataset applied to its non-*Cibicidoides wuellerstorfi* data from second dataset. **Dataset Sources:** http://www.pangaea.de/ddi?datasetid=58770&login=0&format=text, http://www.pangaea.de/ddi?datasetid=54655&login=0&format=text

Core: GeoB1034-1 **Lat:** -21° 44.1' **Lon:** 5° 25.3' **Depth:** 3772 m **$\delta^{18}\text{O}$ Sources:** *Cibicidoides wuellerstorfi* **References:** Bickert and Wefer 1996 **Age Model:** See Core GeoB1032-2. **Notes:** Ocean depth above is that given in reference for GeoB1034-1/3; that in dataset for this core is 3731 m. Similarly, Lat minutes and Lon minutes are from reference; those given in dataset are 43.3 and 25.8 **Dataset**

Sources: <http://www.pangaea.de/ddi?datasetid=58772&login=0&format=text>

Core: GeoB1034-3 **Lat:** -21° 44.1' **Lon:** 5° 25.3' **Depth:** 3772 m $\delta^{18}\text{O}$ **Sources:** *Cibicidoides wuellerstorfi* **References:** Bickert and Wefer 1996 **Age Model:** See Core GeoB1032-2. **Dataset Sources:** <http://www.pangaea.de/ddi?datasetid=58772&login=0&format=text>

Core: GeoB1035-3 **Lat:** -21° 35.2' **Lon:** 5° 1.7' **Depth:** 4453 m $\delta^{18}\text{O}$ **Sources:** *Cibicidoides wuellerstorfi* **References:** Bickert and Wefer 1996 **Age Model:** See Core GeoB1032-2. **Notes:** Ocean depth above is that given in reference for GeoB1035-3/4; that in dataset for this core is 4450 m. Similarly, Lat minutes and Lon minutes are from reference; those given in dataset are 36.1 and 1.9 **Dataset Sources:** <http://www.pangaea.de/ddi?datasetid=58766&login=0&format=text>

Core: GeoB1035-4 **Lat:** -21° 35.2' **Lon:** 5° 1.7' **Depth:** 4453 m $\delta^{18}\text{O}$ **Sources:** *Cibicidoides wuellerstorfi* **References:** Bickert and Wefer 1996 **Age Model:** See Core GeoB1032-2. **Dataset Sources:** <http://www.pangaea.de/ddi?datasetid=58766&login=0&format=text>

Core: GeoB1041-1 **Lat:** -3° 28.5' **Lon:** -7° 36.0' **Depth:** 4033 m $\delta^{18}\text{O}$ **Sources:** *Cibicidoides wuellerstorfi* **References:** Bickert and Wefer 1996 **Age Model:** See Core GeoB1032-2. **Notes:** Ocean depth above is that given in reference for GeoB1035-3/4; that in dataset for this core is 4035 m. Similarly, Lat minutes and Lon minutes are from reference; those in dataset are 28.8 and 35.5 **Dataset Sources:** <http://www.pangaea.de/ddi?datasetid=58771&login=0&format=text>

Core: GeoB1041-3 **Lat:** -3° 28.5' **Lon:** -7° 36.0' **Depth:** 4033 m $\delta^{18}\text{O}$ **Sources:** *Cibicidoides wuellerstorfi* **References:** Bickert and Wefer 1996 **Age Model:** See Core GeoB1032-2. **Dataset Sources:** <http://www.pangaea.de/ddi?datasetid=58771&login=0&format=text>

Core: GeoB1101-4 **Lat:** 1° 39.5' **Lon:** -10° 58.8' **Depth:** 4588 m $\delta^{18}\text{O}$ **Sources:** *Cibicidoides wuellerstorfi* **References:** Bickert and Wefer 1996 **Age Model:** See Core GeoB1032-2. **Notes:** Ocean depth above is that given in reference for GeoB1101-4/5; that in dataset for this core is 4567 m. Similarly, Lat minutes and Lon minutes are from reference; those in dataset are 39.8 and 58.6 **Dataset Sources:** <http://www.pangaea.de/ddi?datasetid=58784&login=0&format=text>

Core: GeoB1101-5 **Lat:** 1° 39.5' **Lon:** -10° 58.8' **Depth:** 4588 m $\delta^{18}\text{O}$ **Sources:** *Cibicidoides wuellerstorfi* **References:** Bickert and Wefer 1996 **Age Model:** See Core GeoB1032-2. **Dataset Sources:** <http://www.pangaea.de/ddi?datasetid=58784&login=0&format=text>

Core: GeoB1105-3 **Lat:** -1° 39.9' **Lon:** -12° 25.7' **Depth:** 3225 m $\delta^{18}\text{O}$ **Sources:** *Cibicidoides wuellerstorfi*, *Globigerinoides ruber* (pink), *Globorotalia inflata*, *Globoro-*

talia crassaformis **References:** Bickert and Wefer 1996, Wefer et al. 1996 **Age Model:** See Core GeoB1032-2. **Notes:** Ocean depth above is that given in references for GeoB1105-3/4; that in dataset for this core is 3231 m. Core's depth/age data from first dataset applied to its non-Cibicidoides wuellerstorfi data from second dataset. **Dataset Sources:** <http://www.pangaea.de/ddi?datasetid=58768&login=0&format=text>, <http://www.pangaea.de/ddi?datasetid=54656&login=0&format=text>

Core: GeoB1105-4 **Lat:** -1° 39.9' **Lon:** -12° 25.7' **Depth:** 3225 m $\delta^{18}\text{O}$ **Sources:** *Cibicidoides wuellerstorfi*, *Globigerinoides ruber (pink)*, *Globorotalia inflata*, *Globorotalia crassaformis* **References:** Bickert and Wefer 1996, Wefer et al. 1996 **Age Model:** See Core GeoB1032-2. **Notes:** Core's depth/age data from first dataset applied to its non-Cibicidoides wuellerstorfi data from second dataset. **Dataset Sources:** <http://www.pangaea.de/ddi?datasetid=58768&login=0&format=text>, <http://www.pangaea.de/ddi?datasetid=54656&login=0&format=text>

Core: GeoB1112-3 **Lat:** -5° 46.2' **Lon:** -10° 44.7' **Depth:** 3122 m $\delta^{18}\text{O}$ **Sources:** *Cibicidoides wuellerstorfi* **References:** Bickert and Wefer 1996 **Age Model:** See Core GeoB1032-2. **Notes:** Ocean depth above is that given in reference for GeoB1112-3/4; that in dataset for this core is 3128 m. Similarly, Lat minutes and Lon minutes are from reference (latitude mistakenly given as N there); those in dataset are 46.7 and 44.6 **Dataset Sources:** <http://www.pangaea.de/ddi?datasetid=58773&login=0&format=text>

Core: GeoB1112-4 **Lat:** -5° 46.2' **Lon:** -10° 44.7' **Depth:** 3122 m $\delta^{18}\text{O}$ **Sources:** *Cibicidoides wuellerstorfi*, *Globigerinoides ruber (pink)*, *Globorotalia crassaformis* **References:** Bickert and Wefer 1996 **Age Model:** See Core GeoB1032-2. **Notes:** Ocean depth above is that given in reference for GeoB1112-3/4; that in dataset for this core is 3125 m. Similarly, Lat minutes and Lon minutes are from reference (latitude mistakenly given as N there); those in dataset are 46.7 and 45.0. Core's depth/age data from first dataset applied to its non-Cibicidoides wuellerstorfi data from second dataset. **Dataset Sources:** <http://www.pangaea.de/ddi?datasetid=58773&login=0&format=text>, <http://www.pangaea.de/ddi?datasetid=54657&login=0&format=text>

Core: GeoB1113-4 **Lat:** -5° 45' **Lon:** -11° 2.4' **Depth:** 2374 m $\delta^{18}\text{O}$ **Sources:** *Globigerinoides ruber (white)*, *Cibicidoides wuellerstorfi* **References:** Sarnthein et al. 1994 **Age Model:** See Core 12328-5. For ages older than 29.5 ka, $\delta^{18}\text{O}$ record events were given ages after Martinson et al. 1987. **Notes:** Core name above is specific form of that from reference, which mentions cores GeoB1113-4 and GeoB1113-7 as just GeoB1113; known as GeoB1113-4 in dataset. Lat minutes and Lon minutes are from reference for GeoB1113; given as 44.7 and 2.2 in dataset. **Dataset Sources:** <http://www.pangaea.de/ddi?datasetid=54395&login=0&format=text>

Core: GeoB1113-7 **Lat:** -5° 45' **Lon:** -11° 2.4' **Depth:** 2374 m $\delta^{18}\text{O}$ **Sources:**

Globigerinoides ruber (white), *Cibicidoides wuellerstorfi* **References:** Sarnthein et al. 1994 **Age Model:** See Core 12328-5. **Notes:** Core name above is specific form of that from reference, which mentions cores GeoB1113-4 and GeoB1113-7 as just GeoB1113; known as GeoB1113-7 in dataset. Ocean depth above is from reference for GeoB1113; given in dataset as 2373 m. Similarly, Lat minutes and Lon minutes are from reference; given as 44.7 and 2.1 in dataset. **Dataset Sources:** <http://www.pangaea.de/ddi?datasetid=54395&login=0&format=text>

Core: GeoB1115-3 **Lat:** -3° 33.7' **Lon:** -12° 33.6' **Depth:** 2945 m $\delta^{18}\text{O}$ **Sources:** *Cibicidoides wuellerstorfi* **References:** Bickert and Wefer 1996 **Age Model:** See Core GeoB1032-2. **Dataset Sources:** <http://www.pangaea.de/ddi?datasetid=58779&login=0&format=text>

Core: GeoB1115-4 **Lat:** -3° 33.7' **Lon:** -12° 33.6' **Depth:** 2945 m $\delta^{18}\text{O}$ **Sources:** *Cibicidoides wuellerstorfi* **References:** Bickert and Wefer 1996 **Age Model:** See Core GeoB1032-2. **Notes:** Ocean depth above is that given in reference for GeoB1115-4/3; that in dataset for this core is 2921 m. Similarly, Lat minutes and Lon minutes are from reference; those in dataset are 33.5 and 34.8 **Dataset Sources:** <http://www.pangaea.de/ddi?datasetid=58779&login=0&format=text>

Core: GeoB1117-2 **Lat:** -3° 48.9' **Lon:** -14° 53.8' **Depth:** 3984 m $\delta^{18}\text{O}$ **Sources:** *Cibicidoides wuellerstorfi* **References:** Bickert and Wefer 1996 **Age Model:** See Core GeoB1032-2. **Dataset Sources:** <http://www.pangaea.de/ddi?datasetid=58780&login=0&format=text>

Core: GeoB1118-2 **Lat:** -3° 33.6' **Lon:** -16° 25.7' **Depth:** 4671 m $\delta^{18}\text{O}$ **Sources:** *Cibicidoides wuellerstorfi* **References:** Bickert and Wefer 1996 **Age Model:** See Core GeoB1032-2. **Notes:** Ocean depth above is that given in reference for GeoB1118-2/3; that in dataset for this core is 4675 m. Similarly, Lon minutes is from reference; that in dataset is 25.9 **Dataset Sources:** <http://www.pangaea.de/ddi?datasetid=58781&login=0&format=text>

Core: GeoB1118-3 **Lat:** -3° 33.6' **Lon:** -16° 25.7' **Depth:** 4671 m $\delta^{18}\text{O}$ **Sources:** *Cibicidoides wuellerstorfi* **References:** Bickert and Wefer 1996 **Age Model:** See Core GeoB1032-2. **Dataset Sources:** <http://www.pangaea.de/ddi?datasetid=58781&login=0&format=text>

Core: GeoB1211-1 **Lat:** -24° 28.5' **Lon:** 7° 32.0' **Depth:** 4084 m $\delta^{18}\text{O}$ **Sources:** *Cibicidoides wuellerstorfi* **References:** Bickert and Wefer 1996 **Age Model:** See Core GeoB1032-2. **Notes:** Ocean depth above is that given in reference for GeoB1211-1/3; that in dataset for this core is 4089 m. Similarly, Lat minutes and Lon minutes are from reference; those in dataset are 28.4 and 32.2 **Dataset Sources:** <http://www.pangaea.de/ddi?datasetid=58782&login=0&format=text>

Core: GeoB1211-3 **Lat:** -24° 28.5' **Lon:** 7° 32.0' **Depth:** 4084 m $\delta^{18}\text{O}$ **Sources:**

Cibicidoides wuellerstorfi **References:** Bickert and Wefer 1996 **Age Model:** See Core GeoB1032-2. **Dataset Sources:** <http://www.pangaea.de/ddi?datasetid=58782&login=0&format=text>

Core: GeoB1214-1 **Lat:** -24° 41.4' **Lon:** 7° 14.5' **Depth:** 3210 m $\delta^{18}\text{O}$ **Sources:** *Cibicidoides wuellerstorfi* **References:** Bickert and Wefer 1996 **Age Model:** See Core GeoB1032-2. **Notes:** Lon minutes above is that given in reference for GeoB1214-2/1; that in dataset for this core is 14.4 **Dataset Sources:** <http://www.pangaea.de/ddi?datasetid=58783&login=0&format=text>

Core: GeoB1214-2 **Lat:** -24° 41.4' **Lon:** 7° 14.5' **Depth:** 3210 m $\delta^{18}\text{O}$ **Sources:** *Cibicidoides wuellerstorfi* **References:** Bickert and Wefer 1996 **Age Model:** See Core GeoB1032-2. **Notes:** Ocean depth above is that given in reference for GeoB1214-2/1; that in dataset for this core is 3220 m. **Dataset Sources:** <http://www.pangaea.de/ddi?datasetid=58783&login=0&format=text>

Core: GeoB1523-1 **Lat:** 3° 49.9' **Lon:** -41° 37.3' **Depth:** 3292 m $\delta^{18}\text{O}$ **Sources:** *Globigerinoides ruber (pink)*, *Globigerinoides sacculifer*, *Globorotalia crassaformis*, *Globorotalia truncatulinoides (dextral)* **References:** Rühlemann et al. 1996, Mulitza et al. 1998 **Age Model:** Graphic correlation of characteristic isotopic events in the *Globigerinoides sacculifer* oxygen isotope record to the Imbrie et al. SPECMAP stacked record, following Prell et al. 1986 **Notes:** *Globigerinoides sacculifer* oxygen isotope and age data given in Appendix of Rühlemann 1996; from dataset, used age data of Rühlemann 1996. Additional references given in dataset. **Dataset Sources:** <http://www.pangaea.de/ddi?datasetid=56532&login=0&format=text>

Core: GeoB1710 **Lat:** -23° 26' **Lon:** 11° 42' **Depth:** 2987 m $\delta^{18}\text{O}$ **Sources:** *Cibicidoides wuellerstorfi* **References:** Schmiedl and Mackensen 1997 **Age Model:** Graphic correlation of the $\delta^{18}\text{O}$ record with the SPECMAP standard record of Imbrie et al. 1984. Linear interpolation between age control points assumed and calculated here; based on reference Fig. 3, a 0.0-depth/0.0-age point is assumed and included in interpolation. **Notes:** Core name above is from reference; known as GeoB1710-3 in datasets. Lat minutes and Lon minutes are from reference; those given in dataset are 25.9 and 42.9. Core's depth/age data from second dataset applied to its foram $\delta^{18}\text{O}$ data from first dataset. Second dataset data printed in reference's Table A1. **Dataset Sources:** <http://www.pangaea.de/ddi?datasetid=52771&login=0&format=text>, <http://www.pangaea.de/ddi?datasetid=52769&login=0&format=text>

Core: GeoB3005 **Lat:** 14° 58.3' **Lon:** 54° 22.2' **Depth:** 2316 m $\delta^{18}\text{O}$ **Sources:** *Neogloboquadrina dutertrei* **References:** Budziak et al. 2000 **Age Model:** Stable oxygen isotope record of *N. dutertrei* correlated to marine oxygen isotope stages of SPECMAP stack of Imbrie et al. 1984 using program AnalySeries 1.0a7 of Paillard et al. 1996. **Notes:** Dataset with depth, age model control points and $\delta^{18}\text{O}$ values available from Pangaea; ages between control points can be linearly interpolated; datasource used has all this together. (Core name above is from reference; known as

GeoB3005-1, GeoB3005-2 and GeoB3005-3 in Pangaea dataset; presented as a composite in reference and here. Ocean depth above is from reference for cores -1 and -3; 2309 m for -2; 2316 for -1 in Pangaea dataset but given as 2330 and 2314 for -2 and -3 there.) **Dataset Sources:** File from d.budziak@bgr.de

Core: GeoB3104-1 **Lat:** -3° 40.0' **Lon:** -37° 43.0' **Depth:** 767 m **$\delta^{18}\text{O}$ Sources:** *Globigerinoides sacculifer*, *Globigerinoides ruber* (pink), *Cibicides pseudoungerianus*, *Planulina ariminensis* **References:** Arz et al. 1999a, Arz et al. 1999b, Arz et al. 1998 **Age Model:** AMS ^{14}C dates on *Globigerinoides sacculifer* transformed to calendar years after Bard et al. 1993 and including a 400-year reservoir correction, U/Th-calibration and linear interpolation between. **Dataset Sources:** <http://www.pangaea.de/ddi/Isotopes.tab?datasetid=58293&login=0&format=text>

Core: GeoB3117-1 **Lat:** -4° 11.1' **Lon:** -37° 8.0' **Depth:** 930 m **$\delta^{18}\text{O}$ Sources:** *Globigerinoides sacculifer*, *Globigerinoides ruber* (pink) **References:** Arz et al. 1999a, Arz et al. 1999b **Age Model:** Stratigraphically linked via graphical correlation of isotope, color and XRF data to cores GeoB3129-1 and GeoB3911-3, which have AMS ^{14}C dates on *Globigerinoides sacculifer* transformed to calendar years after Bard et al. 1993 and include a 400-year reservoir correction, U/Th-calibration and linear interpolation between. **Dataset Sources:** <http://www.pangaea.de/ddi/Isotopes.tab?datasetid=58293&login=0&format=text>

Core: GeoB3129-1 **Lat:** -4° 36.8' **Lon:** -36° 38.2' **Depth:** 830 m **$\delta^{18}\text{O}$ Sources:** *Globigerinoides sacculifer*, *Globigerinoides ruber* (pink) **References:** Arz et al. 1999a, Arz et al. 1999b **Age Model:** See Core GeoB3104-1. **Dataset Sources:** <http://www.pangaea.de/ddi/Isotopes.tab?datasetid=58293&login=0&format=text>

Core: GeoB3176-1 **Lat:** -7° .7' **Lon:** -34° 26.5' **Depth:** 1385 m **$\delta^{18}\text{O}$ Sources:** *Globigerinoides sacculifer*, *Globigerinoides ruber* (pink) **References:** Arz et al. 1999a, Arz et al. 1999b **Age Model:** See Core GeoB3117-1. **Dataset Sources:** <http://www.pangaea.de/ddi/Isotopes.tab?datasetid=58293&login=0&format=text>

Core: GeoB3202-1 **Lat:** -21° 37.0' **Lon:** -39° 58.7' **Depth:** 1090 m **$\delta^{18}\text{O}$ Sources:** *Globigerinoides sacculifer*, *Globigerinoides ruber* (pink), *Uvigerina peregrina* **References:** Arz et al. 1999b **Age Model:** See Core GeoB3104-1. **Dataset Sources:** <http://www.pangaea.de/ddi/Isotopes.tab?datasetid=58293&login=0&format=text>

Core: GeoB3229-1 **Lat:** -19° 38.5' **Lon:** -38° 43.0' **Depth:** 775 m **$\delta^{18}\text{O}$ Sources:** *Globigerinoides sacculifer*, *Globigerinoides ruber* (pink) **References:** Arz et al. 1999b **Age Model:** Stratigraphically linked by correlation of sediment color, carbonate content and XRF data to cores GeoB3104-1, GeoB3129-1, GeoB3911-3 and GeoB3202-1, which have AMS ^{14}C dates on *Globigerinoides sacculifer* transformed to calendar years after Bard et al. 1993 and include a 400-year reservoir correction, U/Th-calibration and linear interpolation between. **Notes:** Not specifically described in reference; assumed related to core GeoB3229-2 **Dataset Sources:** <http://www.pangaea.de/ddi/Isotopes.tab?datasetid=58293&login=0&format=text>

pangaea.de/ddi/Isotopes.tab?datasetid=58293&login=0&format=text

Core: GeoB3229-2 **Lat:** -19° 38.5' **Lon:** -38° 43.0' **Depth:** 780 m **$\delta^{18}\text{O}$ Sources:** *Globigerinoides sacculifer*, *Globigerinoides ruber* (pink) **References:** Arz et al. 1999b **Age Model:** See Core GeoB3229-1. **Dataset Sources:** <http://www.pangaea.de/ddi/Isotopes.tab?datasetid=58293&login=0&format=text>

Core: GeoB3302-1 **Lat:** -33° 13' **Lon:** -72° 6' **Depth:** 1498 m **$\delta^{18}\text{O}$ Sources:** *Neogloboquadrina pachyderma* (dextral) **References:** Lamy et al. 1999 **Age Model:** Principally based on seven AMS ^{14}C dates that were corrected for C13 and for a reservoir age of 400 years and that were converted to calendar years after the method of Bard et al. 1993; linear interpolation applied between these control points; additionally, for the uppermost sample, the oxygen isotope record was correlated with that for core GIK17748-2. **Notes:** Lat minutes and Lon minutes above are from reference; given as 13.1 and 5.4 in dataset. **Dataset Sources:** <http://www.pangaea.de/ddi?datasetid=58255&login=0&format=text>

Core: GeoB3375-1 **Lat:** -27° 28' **Lon:** -71° 15' **Depth:** 1947 m **$\delta^{18}\text{O}$ Sources:** *Neogloboquadrina pachyderma* (sinistral) **References:** Lamy et al. 1998, Lamy et al. 2000 **Age Model:** In the upper half of the core, based on seven AMS ^{14}C dates that were corrected for C13 and for a reservoir age of 400 years and that were converted to calendar years using the Stuiver and Reimer 1993 Calib4.0 software (upper four dates) or following the methods of Bard 1998 (next 3 dates); in the middle of the core, a graphical correlation of the oxygen isotope record with Stage 4.2 of the Imbrie et al. 1984 SPECMAP stack; in the lower part of the core, correlation of grain-size minima of the median record to maxima of the precession index. Linear interpolation between these age control points was specified in references but omitted in dataset so calculated here; similarly for extrapolation beyond these points (Lamy, personal communication). **Notes:** Second dataset was used to update and add age control points to first dataset. **Dataset Sources:** <http://www.pangaea.de/ddi?datasetid=58250&login=0&format=text>, <http://www.pangaea.de/ddi?datasetid=58451&login=0&format=text>

Core: GeoB3910-2 **Lat:** -4° 14.7' **Lon:** -36° 20.7' **Depth:** 2362 m **$\delta^{18}\text{O}$ Sources:** *Globigerinoides sacculifer*, *Globorotalia tumida* **References:** Arz et al. 2001 **Age Model:** See Core GeoB3104-1. **Notes:** Assumed done similarly to core GeoB3104-1 **Dataset Sources:** <http://www.pangaea.de/ddi/Isotopes.tab?datasetid=58290&login=0&format=text>

Core: GeoB3911-1 **Lat:** -4° 36.8' **Lon:** -36° 38.1' **Depth:** 826 m **$\delta^{18}\text{O}$ Sources:** *Globigerinoides sacculifer*, *Globigerinoides ruber* (pink) **References:** Arz et al. 1999a, Arz et al. 1999b **Age Model:** See Core GeoB3104-1. **Notes:** Not specifically described in either reference; assumed related to core GeoB3911-3 **Dataset Sources:** <http://www.pangaea.de/ddi/Isotopes.tab?datasetid=58293&login=0&format=text>

Core: GeoB3911-3 **Lat:** -4° 36.8' **Lon:** -36° 38.2' **Depth:** 828 m $\delta^{18}\text{O}$ **Sources:** *Globigerinoides sacculifer*, *Globigerinoides ruber* (pink) **References:** Arz et al. 1999a, Arz et al. 1999b **Age Model:** See Core GeoB3104-1. **Dataset Sources:** <http://www.pangaea.de/ddi/Isotopes.tab?datasetid=58293&login=0&format=text>

Core: GeoB3912-1 **Lat:** -3° 40.0' **Lon:** -37° 43.0' **Depth:** 772 m $\delta^{18}\text{O}$ **Sources:** *Globigerinoides sacculifer*, *Globigerinoides ruber* (pink) **References:** Arz et al. 1999a, Arz et al. 1998 **Age Model:** See Core GeoB3104-1. **Notes:** Assumed done similarly to core GeoB3104-1 **Dataset Sources:** <http://www.pangaea.de/ddi/Isotopes.tab?datasetid=58292&login=0&format=text>

Core: GeoB3912-2 **Lat:** -3° 40.0' **Lon:** -37° 43.1' **Depth:** 772 m $\delta^{18}\text{O}$ **Sources:** *Globigerinoides sacculifer*, *Globigerinoides ruber* (pink) **References:** Arz et al. 1999a, Arz et al. 1998 **Age Model:** See Core GeoB3104-1. **Notes:** Not specifically described in either reference; assumed related to core GeoB3912-1 **Dataset Sources:** <http://www.pangaea.de/ddi/Isotopes.tab?datasetid=58292&login=0&format=text>

Core: GeoB3935-2 **Lat:** 12° 36.8' **Lon:** -59° 23.2' **Depth:** 1558 m $\delta^{18}\text{O}$ **Sources:** *Cibicides wuellerstorfi* **References:** Schlünz et al. 2000 **Age Model:** Best fit of the oxygen isotope record of *C. wuellerstorfi* to the reference record provided by Martinson et al. 1987. **Notes:** Lon degrees and Lon minutes above are from dataset; given in reference as -46 and 20.6, which the reference's Fig. 1 map indicates are erroneous. **Dataset Sources:** <http://www.pangaea.de/ddi?datasetid=54943&login=0&format=text>

Core: GeoB3938-1 **Lat:** 12° 15.5' **Lon:** -58° 19.8' **Depth:** 1972 m $\delta^{18}\text{O}$ **Sources:** *Cibicides wuellerstorfi* **References:** Schlünz et al. 2000 **Age Model:** See Core GeoB3935-2. **Notes:** Lat degrees and Lat minutes above are from dataset; given in reference as 5 and 54.4, which the reference's Fig. 1 map indicates are erroneous. **Dataset Sources:** <http://www.pangaea.de/ddi?datasetid=54944&login=0&format=text>

Core: Huascaran2 **Lat:** -9° 6.68' **Lon:** -77° 36.88' **Depth:** -6048 m $\delta^{18}\text{O}$ **Sources:** *glacier ice H₂O* **References:** Thompson et al. 1995, Thompson 2000 **Age Model:** For core depth 0-120m (0-.27ka): the annual layers of dust, NO₃-, and $\delta^{18}\text{O}$ were counted (since seasonally fluctuating, with all max during the May-Aug dry season). For core depth 120-163m (.27-9ka): matching of the $\delta^{18}\text{O}_{\text{atm}}$ record with that from other dated ice cores. For core depth 163-166m (9-19.1ka): cross-correlation of the $\delta^{18}\text{O}$ record to the *Globigerina bulloides* $\delta^{18}\text{O}$ record from marine core SU81-18 off Portugal, which had AMS ¹⁴C dates calibrated to calendar years using Stuiver and Reimer 1993. **Notes:** Lat minutes and Lon minutes are from first reference; given as 7 and 37 in second reference. Second dataset gives description of time scale, which, for the lower sections, were updated from first reference and whose results are shown in second reference. **Dataset Sources:** <ftp://ftp.ngdc.noaa.gov/paleo/icecore/trop/huascaran/hs2-100a.txt>, <ftp://ftp.ngdc.noaa.gov/paleo/icecore/trop/huascaran/age>

.txt

Core: KNR110-43PC **Lat:** 4° 43' **Lon:** -43° 39' **Depth:** 3436 m **$\delta^{18}\text{O}$ Sources:** *Globigerinoides sacculifer* **References:** Curry and Crowley 1987 **Age Model:** Levels in the $\delta^{18}\text{O}$ record correlating to the isotopic events defined by Prell et al. 1986 were identified and put on the time scale of Imbrie et al. 1984. **Notes:** Core name above is from reference; known as KN11002-0043PC in dataset. Lat minutes and Lon minutes are from reference; given as 43.32 and 39.12 in dataset. Depth/age/ $\delta^{18}\text{O}$ data of dataset printed in reference TABLE 2b. **Dataset Sources:** <http://www.pangaea.de/ddi?datasetid=59889&login=0&format=text>

Core: KNR110-50 **Lat:** 5° 0' **Lon:** -43° 0' **Depth:** 3995 m **$\delta^{18}\text{O}$ Sources:** *Cibicidoides wuellerstorfi* **References:** Curry et al. 1988 **Age Model:** See Core CH73-139. **Notes:** Core name above is from reference; known as KN11002-0050PG in dataset. Lat degrees, Lat minutes and Lon minutes are from reference; given as 4, 51.9 and 12.3 in dataset. Depth/age/ $\delta^{18}\text{O}$ data of dataset printed in reference APPENDIX 1. **Dataset Sources:** <http://www.pangaea.de/ddi?datasetid=52287&login=0&format=text>

Core: KNR110-55 **Lat:** 5° 0' **Lon:** -43° 0' **Depth:** 4556 m **$\delta^{18}\text{O}$ Sources:** *Cibicidoides wuellerstorfi* **References:** Curry et al. 1988 **Age Model:** See Core CH73-139. **Notes:** Core name above is from reference; known as KN11002-0055PG in dataset. Lat degrees, Lat minutes and Lon minutes are from reference; given as 4, 56.88 and 53.52 in dataset. Depth/age/ $\delta^{18}\text{O}$ data of dataset printed in reference APPENDIX 1. **Dataset Sources:** <http://www.pangaea.de/ddi?datasetid=52289&login=0&format=text>

Core: KNR110-58 **Lat:** 5° 0' **Lon:** -43° 0' **Depth:** 4341 m **$\delta^{18}\text{O}$ Sources:** *Cibicidoides wuellerstorfi* **References:** Curry et al. 1988 **Age Model:** See Core CH73-139. **Notes:** Core name above is from reference; known as KN11002-0058PG in dataset. Lat degrees, Lat minutes and Lon minutes are from reference; given as 4, 47.52 and 2.28 in dataset. Depth/age/ $\delta^{18}\text{O}$ data of dataset printed in reference APPENDIX 1. **Dataset Sources:** <http://www.pangaea.de/ddi?datasetid=52288&login=0&format=text>

Core: KNR110-66 **Lat:** 5° 0' **Lon:** -43° 0' **Depth:** 3547 m **$\delta^{18}\text{O}$ Sources:** *Cibicidoides wuellerstorfi* **References:** Curry et al. 1988 **Age Model:** See Core CH73-139. **Notes:** Core name above is from reference; known as KN11002-0066PG in dataset. Lat degrees, Lat minutes and Lon minutes are from reference; given as 4, 33.78 and 22.92 in dataset. Depth/age/ $\delta^{18}\text{O}$ data of dataset printed in reference APPENDIX 1. **Dataset Sources:** <http://www.pangaea.de/ddi?datasetid=52285&login=0&format=text>

Core: KNR110-71 **Lat:** 4° 0' **Lon:** -44° 0' **Depth:** 3164 m **$\delta^{18}\text{O}$ Sources:** *Cibicidoides wuellerstorfi* **References:** Curry et al. 1988 **Age Model:** See Core

CH73-139. **Notes:** Core name above is from reference; known as KN11002-0071PG in dataset. Lat minutes and Lon minutes are from reference; given as 21.78 and 41.82 in dataset. Depth/age/ $\delta^{18}\text{O}$ data of dataset printed in reference APPENDIX 1. **Dataset Sources:** <http://www.pangaea.de/ddi?datasetid=52284&login=0&format=text>

Core: KNR110-75 **Lat:** 4° 0' **Lon:** -43° 0' **Depth:** 3063 m **$\delta^{18}\text{O}$ Sources:** *Cibicidoides wuellerstorfi* **References:** Curry et al. 1988 **Age Model:** See Core CH73-139. **Notes:** Core name above is from reference; known as KN11002-0075PG in dataset. Lat minutes and Lon minutes are from reference; given as 20.52 and 24.48 in dataset. Depth/age/ $\delta^{18}\text{O}$ data of dataset printed in reference APPENDIX 1. **Dataset Sources:** <http://www.pangaea.de/ddi?datasetid=52283&login=0&format=text>

Core: KNR110-82 **Lat:** 4° 20' **Lon:** -43° 29' **Depth:** 2816 m **$\delta^{18}\text{O}$ Sources:** *Globigerinoides sacculifer*, *Cibicidoides wuellerstorfi* **References:** Curry and Crowley 1987, Curry et al. 1988 **Age Model:** For first reference/ $\delta^{18}\text{O}$ source/dataset: levels in the $\delta^{18}\text{O}$ record correlating to the isotopic events defined by Prell et al. 1986 were identified and put on the time scale of Imbrie et al. 1984. For second reference/ $\delta^{18}\text{O}$ source/dataset: correlated to Pacific Ocean core V19-30 (Shackleton et al. 1983a,b), whose $\delta^{18}\text{O}$ record is correlated with the chronology of Imbrie et al. 1984. The two age models differ by as much as 3 kyr at .8 m core depth but it's not clear which is better so that associated with each reference/ $\delta^{18}\text{O}$ source is used. **Notes:** Core name above is from second reference; known as KNR110-82GGC in first reference and KN11002-0082PG in datasets. Lat minutes and Lon minutes are from first reference; given as 0 and 0 in second reference and 20.22 and 29.22 in datasets. Depth/age/ $\delta^{18}\text{O}$ data of first dataset printed in first reference's TABLE 2c. Depth/age/ $\delta^{18}\text{O}$ data of second dataset printed in second reference's APPENDIX 1. **Dataset Sources:** <http://www.pangaea.de/ddi?datasetid=59890&login=0&format=text>, <http://www.pangaea.de/ddi?datasetid=52282&login=0&format=text>

Core: KNR110-91 **Lat:** 5° 0' **Lon:** -43° 0' **Depth:** 3810 m **$\delta^{18}\text{O}$ Sources:** *Cibicidoides wuellerstorfi* **References:** Curry et al. 1988 **Age Model:** See Core CH73-139. **Notes:** Core name above is from reference; known as KN11002-0091PG in dataset. Lat degrees, Lat minutes and Lon minutes are from reference; given as 4, 45.6 and 18.42 in dataset. Depth/age/ $\delta^{18}\text{O}$ data of dataset printed in reference APPENDIX 1. **Dataset Sources:** <http://www.pangaea.de/ddi?datasetid=52286&login=0&format=text>

Core: KNR73-4-3 **Lat:** -0° 0' **Lon:** -106° 0' **Depth:** 3606 m **$\delta^{18}\text{O}$ Sources:** *Cibicidoides* spp. (*C. wuellerstorfi*, *C. kullenbergi*) **References:** Curry et al. 1988 **Age Model:** See Core CH73-139. **Notes:** Core name above is from reference; known as KN07304-0003PG in dataset. Lat minutes and Lon minutes are from reference; given as 22.38 and 10.68 in dataset. Reference indicates the $\delta^{18}\text{O}$ source is actually *Cibicidoides* spp. rather than just *Cibicidoides wuellerstorfi* as indicated

by dataset. Depth/age/ $\delta^{18}\text{O}$ data of dataset printed in reference APPENDIX 1. **Dataset Sources:** <http://www.pangaea.de/ddi?datasetid=52308&login=0&format=text>

Core: M12328-5 **Lat:** 21° 0' **Lon:** -19° 0' **Depth:** 2778 m **$\delta^{18}\text{O}$ Sources:** *Uvigerina peregrina* **References:** Beveridge et al. 1995 **Age Model:** See Core BOFS26K. **Notes:** Core name above is from reference (note typo in Table 3a though); known as GIK12328-5 in dataset. Latmin and Lon minutes above are from reference (note Lat degrees typo in Table 1) and probably due to roundoff; given as 8.7 and 34.4 in dataset. *Uvigerina peregrina* oxygen isotope values from Zahn-Knoll 1986. Age data missing from dataset so manually added from reference's Table 3a. **Dataset Sources:** <http://www.pangaea.de/ddi?datasetid=52681&login=0&format=text>

Core: M25/4-KL13 **Lat:** 37° 33.2' **Lon:** 17° 49.2' **Depth:** 2533 m **$\delta^{18}\text{O}$ Sources:** *Globigerina bulloides* **References:** Schmiedl et al. 1998 **Age Model:** Graphic correlation of the *G. bulloides* oxygen isotope curve with the SPECMAP standard record of Imbrie et al. 1984 using the software package AnalySeries of Paillard et al. 1996. **Notes:** Lon minutes above is from dataset; given in reference as 49.44. Used Pangaea dataset; NGDC dataset is alternate source. **Dataset Sources:** <http://www.pangaea.de/ddi?datasetid=54941&login=0&format=text>, ftp://www.ngdc.noaa.gov/paleo/contributions_by_author/schmiedl1998/ionian2.txt

Core: M35003-4 **Lat:** 12° 5' **Lon:** -61° 15' **Depth:** 1299 m **$\delta^{18}\text{O}$ Sources:** *Globigerinoides ruber (pink)* **References:** Rühlmann et al. 1999 **Age Model:** Nine ^{14}C ages were determined on monospecific samples of *G. ruber* (white) and four ages on a mixture of *G. ruber* (white and pink), *Globigerinoides sacculifer* and *Orbulina universa*. The ^{14}C ages were corrected for a reservoir age of 400 years (Hughen 1998); they were then converted to calendar ages using the program CALIB 3.0.3c (Stuiver and Reimer 1993) for ages < 20,000 yr and using the equation given in the caption of Figure 3 of Bard et al. 1997 for ages > 20,000 yr. For the deglacial, conservatively estimated the calendar year chronology to be good within ± 500 yr. Before about 25 cal. kyr BP there are only a limited number of calibration points, thus the assumed correction has an uncertainty within at least $\pm 1,500$ yr. **Notes:** Dataset is from GeoB of Institute part of Pangaea; the associated dataset in the core data part (DataSet ID 55923) does not have the ages interpolated (linearly?) between the corrected/calibrated ^{14}C ages. **Dataset Sources:** http://www.pangaea.de/ddi?retr=/Institutes/GeoB/CRuehlemann/Nature_1999.retr&conf=/Projects/GeoB/CRuehlemann/Nature_1999_2.conf&format=textfile

Core: MD76-125 **Lat:** 8° 0' **Lon:** 75° 0' **Depth:** 1878 m **$\delta^{18}\text{O}$ Sources:** *Cibicidoides spp.* **References:** Curry et al. 1988 **Age Model:** See Core CH73-139. **Notes:** Ocean depth above is from reference; given in dataset as 1877 m. Lat minutes and Lon minutes are from reference; given as 21.0 and 12.0 in dataset. Depth/age/ $\delta^{18}\text{O}$ data of dataset printed in reference APPENDIX 1. **Dataset Sources:** <http://www.pangaea.de/ddi?datasetid=52306&login=0&format=text>

Core: MD76-135 **Lat:** 14° 0' **Lon:** 51° 0' **Depth:** 1895 m $\delta^{18}\text{O}$ **Sources:** *Cibicidoides spp.* **References:** Curry et al. 1988 **Age Model:** See Core CH73-139. **Notes:** Lat minutes, Lon degrees and Lon minutes are from reference; given as 16.2, 50, and 18.6 in dataset. Depth/age/ $\delta^{18}\text{O}$ data of dataset printed in reference APPENDIX 1. **Dataset Sources:** <http://www.pangaea.de/ddi?datasetid=52304&login=0&format=text>

Core: MD79-254 **Lat:** -18° 0' **Lon:** 39° 0' **Depth:** 1934 m $\delta^{18}\text{O}$ **Sources:** *Cibicidoides spp.* **References:** Curry et al. 1988 **Age Model:** See Core CH73-139. **Notes:** Lat degrees, Lat minutes, Lon degrees and Lon minutes are from reference; given as -17, 31.8, 38 and 24 in dataset. Depth/age/ $\delta^{18}\text{O}$ data of dataset printed in reference APPENDIX 1. **Dataset Sources:** <http://www.pangaea.de/ddi?datasetid=52305&login=0&format=text>

Core: MD84-527 **Lat:** -43° 49.3' **Lon:** 51° 19.1' **Depth:** 3269 m $\delta^{18}\text{O}$ **Sources:** *Cibicidoides wuellerstorfi*, *Neogloboquadrina pachyderma (sinistral)*, *Globigerina bulloides* **References:** Curry et al. 1988, Labracherie et al. 1989 **Age Model:** From first reference/dataset: correlated to Pacific Ocean core V19-30 (Shackleton et al. 1983a,b), whose $\delta^{18}\text{O}$ record is correlated with the chronology of Imbrie et al. 1984. For second and third $\delta^{18}\text{O}$ source: linear interpolation between age control points calculated here; no extrapolation before first age control point. **Notes:** Ocean depth above is from references; given in datasets as 3262 m. Lat degrees is from second reference and datasets; given as 44 in first reference. Lat minutes and Lon minutes are from second reference; given as 0 and 0 in first reference and 29.4 and 11.4 in datasets. Depth/age/ $\delta^{18}\text{O}$ (first $\delta^{18}\text{O}$ source) data of first dataset printed in first reference's APPENDIX 1. Depth/age/ $\delta^{18}\text{O}$ (all $\delta^{18}\text{O}$ source) data of second dataset printed in second reference's TABLE 3; in these the $\delta^{18}\text{O}$ values of the first $\delta^{18}\text{O}$ source have a specific fractionation correction of 0.64 permil added to them so the uncorrected values of the first reference/dataset are used instead. First reference/dataset indicates first $\delta^{18}\text{O}$ source is *Cibicidoides spp.* but the second reference/dataset and other closer references indicate it is just *Cibicidoides wuellerstorfi*. Second through fourth datasets contain age models indicating just ^{14}C years so not used here; fifth dataset contains an age model with calendar years but is unpublished so is not used here. **Dataset Sources:** <http://www.pangaea.de/ddi?datasetid=52302&login=0&format=text>, <http://www.pangaea.de/ddi?datasetid=52466&login=0&format=text>, <http://www.pangaea.de/ddi?datasetid=52610&login=0&format=text>, <http://www.pangaea.de/ddi?datasetid=52483&login=0&format=text>, <http://www.pangaea.de/ddi?datasetid=51966&login=0&format=text>

Core: MD84-551 **Lat:** -55° .5' **Lon:** 73° 16.9' **Depth:** 2230 m $\delta^{18}\text{O}$ **Sources:** *Neogloboquadrina pachyderma (sinistral)* **References:** Labracherie et al. 1989, Bareille et al. 1994 **Age Model:** All the stratigraphic parameters ($\delta^{18}\text{O}$ records, carbonate and opal content variations, and variations in the abundance of the radiolaria *Cycladophora davisiana*) were reported and calibrated to those of core RC11-

120, whose reference ages were derived from the $\delta^{18}\text{O}$ record by detailed correlation of stages with the SPECMAP-stacked, $\delta^{18}\text{O}$ signal of Imbrie et al. 1984 and Martinson et al. 1987. **Notes:** Lat minutes and Lon minutes are from first reference; given as 0 and 20 in second reference and .6 and 10.2 in datasets. Depth/ $\delta^{18}\text{O}$ data of first dataset printed in first reference's TABLE 3. Third dataset contains an age model giving just ^{14}C dates back through the LGM so not used here; fourth dataset contains an age model with calendar years but is unpublished so is not used here. **Dataset Sources:** <http://www.pangaea.de/ddi?datasetid=52466&login=0&format=text>, <http://www.pangaea.de/ddi?datasetid=51873&login=0&format=text>, <http://www.pangaea.de/ddi?datasetid=52484&login=0&format=text>, <http://www.pangaea.de/ddi?datasetid=51966&login=0&format=text>

Core: MD84641 **Lat:** 33° 2' **Lon:** 32° 38' **Depth:** 1375 m **$\delta^{18}\text{O}$ Sources:** *Globigerinoides ruber (pink)* **References:** Fontugne and Calvert 1992 **Age Model:** Stage boundary correlation of the oxygen isotope record with the Martinson et al. 1987 SPECMAP stack; ^{14}C dating in the upper 135 cm of the core; paleomagnetic reversal stratigraphy. **Notes:** Core name above is from reference; known as MD84-641 in dataset. Latmin and Lon minutes above are from reference; these numbers are given as the decimal parts of the lat and lon in the dataset! **Dataset Sources:** <http://www.pangaea.de/ddi?datasetid=52475&login=0&format=text>

Core: MD88-769 **Lat:** -46° 4' **Lon:** 90° 7' **Depth:** 3420 m **$\delta^{18}\text{O}$ Sources:** *Neogloboquadrina pachyderma (sinistral)* **References:** Rosenthal et al. 1995 **Age Model:** Correlation of globally recognizable events in the N. pachyderma(s) oxygen isotope record with the stacked planktonic foraminifera oxygen isotope record of Imbrie et al. 1984; additionally, the upper 2.8 m of the core was correlated with the nearby AMS ^{14}C -dated core MD88-770 using benthic foram oxygen isotope and other sediment properties; those radiocarbon dates were converted to calendar ages using the tree ring/coral calibration of Bard et al. 1990 and Edwards et al. 1993. Ages between these age control points were linearly interpolated (Rosenthal, personal communication) and are calculated here. **Notes:** Lat minutes and Lon minutes above are from reference; given in dataset as 4.16 and 6.67. $\delta^{18}\text{O}$ values and age control points printed in reference. A less recent age model based on $\delta^{18}\text{O}$ correlation to core RC11-120, which is part of Imbrie et al. 1984 SPECMAP and Martinson et al. 1987, is available in second dataset. **Dataset Sources:** <http://www.pangaea.de/ddi?datasetid=52699&login=0&format=text>, <http://www.pangaea.de/ddi?datasetid=51873&login=0&format=text>

Core: MD88-770 **Lat:** -46° 1' **Lon:** 96° 28' **Depth:** 3290 m **$\delta^{18}\text{O}$ Sources:** *Globigerina bulloides*, *Neogloboquadrina pachyderma (sinistral)*, *Cibicidoides wuellerstorfi*, *Epistominella exigua*, *Melonis barleeanum* **References:** Labeyrie et al. 1996, Bareille et al. 1994 **Age Model:** From second reference/dataset: all the stratigraphic parameters ($\delta^{18}\text{O}$ records, carbonate and opal content variations, and variations in the abundance of the radiolaria *Cycladophora davisiana*) were reported and calibrated to those of core RC11-120, whose reference ages were derived from the

$\delta^{18}\text{O}$ record by detailed correlation of stages with the SPECMAP-stacked, $\delta^{18}\text{O}$ signal of Imbrie et al. 1984 and Martinson et al. 1987. **Notes:** Lat minutes and Lon minutes are from references; given as 1.32 and 27.64 in datasets. Depth/ $\delta^{18}\text{O}$ data of first dataset printed in first reference's Table 1. First reference/third dataset contains an age model giving only uncalibrated (but reservoir corrected) AMS ^{14}C dates back through LGM so not used here. Fourth dataset contains a Martinson et al. 1987 SPECMAP age model; less recent so not used here. In first reference/dataset, $\delta^{18}\text{O}$ values of *C. wuellerstorfi*, *E. exigua* and *M. barleeanum* are given with specific fractionation corrections of +0.64, +0.22, and +0.40 per mil; these corrections are unwanted here so are subtracted. It is "Melonis barleeanum" in the first reference (and used here) but "Melonis barleanum" in first dataset; seems to be same confusion elsewhere as well. **Dataset Sources:** <http://www.pangaea.de/ddi?datasetid=52728&login=0&format=text>, <http://www.pangaea.de/ddi?datasetid=51873&login=0&format=text>, <http://www.pangaea.de/ddi?datasetid=52730&login=0&format=text>, <http://www.pangaea.de/ddi?datasetid=52606&login=0&format=text>

Core: MD900963 **Lat:** 5° 3.30' **Lon:** 73° 52.6' **Depth:** 2446 m **$\delta^{18}\text{O}$ Sources:** *Globigerinoides ruber (white)* **References:** Bassinot et al. 1994 **Age Model:** Tuning of the complete unfiltered $\delta^{18}\text{O}$ curve to orbital functions directly, the target curve being constructed from the ice model of Imbrie and Imbrie 1980 and the 65N July monthly insolation curve of Berger and Loutre 1991; further improvements performed by fine tuning the extracted precession components of the $\delta^{18}\text{O}$ record to the precession components of the ice volume model using the inverse approach for signal correlation of Martinson 1982. **Notes:** Core name above is from reference; known as MD90-963 in dataset. Lat minutes and Lon minutes are from reference; given as 2.4 and 31.8 in dataset. Depth/age/ $\delta^{18}\text{O}$ data of dataset printed in reference Table 2. **Dataset Sources:** <http://www.pangaea.de/ddi?datasetid=60026&login=0&format=text>

Core: MD95-2042 **Lat:** 37° 48' **Lon:** -10° 10' **Depth:** 3146 m **$\delta^{18}\text{O}$ Sources:** *Globigerina bulloides*, *Cibicidoides wuellerstorfi*, *Globobulimina affinis*, *Uvigerina peregriana* **References:** Shackleton et al. 2000, Cayre et al. 1999 **Age Model:** Correlation of the interstadial bases of the *Globigerina bulloides* oxygen isotope record with those of the dated GRIP ice core oxygen isotope record; linear interpolation between these control points. **Notes:** Known as MD 952042 in second reference. For *Globigerina bulloides*, depth/multisamples of first dataset were averaged and matched with depth/age of second dataset. For benthic species, depth/multisamples of third dataset were averaged and matched with depth/age of fourth dataset; the unadjusted $\delta^{18}\text{O}$ s for each species were used. **Dataset Sources:** <http://www.pangaea.de/ddi?datasetid=58195&login=0&format=text>, <http://www.pangaea.de/ddi?datasetid=58210&login=0&format=text>, <http://www.pangaea.de/ddi?datasetid=58220&login=0&format=text>, <http://www.pangaea.de/ddi?datasetid=58228&login=0&format=text>

Core: Milcent **Lat:** -80° 0' **Lon:** -120° 0' **Depth:** -1530 m **$\delta^{18}\text{O}$ Sources:** *glacier ice H₂O* **References:** Langway et al. 1994 **Age Model:** The ECM (Electrical

Conductivity Method of Hammer 1980, 1983) data series was cross-correlated with the ionic chemistry stratigraphy; three main prominently defined volcanic horizons at 1884 AD (Krakatoa, 1883 AD), 1816 AD (Tambora, 1815 AD) and 1259 AD (unidentified) were established as prime index layers using ECM peaks combined with a physical depth-age model; final dating of the entire core from the surface to bottom was established by multi-parameter time-series analysis. **Notes:** lat/lon info and ocean depth above are for nearby Byrd ice core. File Table2.tab contains the age control points (dates at center of depth intervals) between which ages were linearly interpolated and was typed in from reference but includes the addition of the top (assumed) and bottom (Clausen, email) dates and the correction (assumed) of a typo. Center of each depth interval in file Nb1d1mep.txt was assigned that interval's $\delta^{18}\text{O}$ value. **Dataset Sources:** File Nb1d1mep.txt and email from HBC@gf.ku.dk

Core: ODP806B **Lat:** $0^{\circ} 19.1'$ **Lon:** $159^{\circ} 21.7'$ **Depth:** 2520 m **$\delta^{18}\text{O}$ Sources:** *Globigerinoides sacculifer*, *Pulleniatina obliquiloculata*, *Planulina wuellerstorfi* **References:** Berger et al. 1996 **Age Model:** Derivation of a timescale template by numerical integration of an equation/model that tracks ice volume through time (involves sea level change, max ice buildup rate, 65 degree N July insolation, current ice mass, average ice mass over a period, and exponents set for best fit to sea-level and Brunhes-Matuyama paleomagnetic data, as well as Imbrie et al. SPECMAP oxygen isotope record) and correlation of the *Globigerinoides sacculifer* oxygen isotope record to this. **Notes:** Core name above is from reference; known as 130-806B in dataset. Lat minutes, Lon minutes and ocean depth are from reference; given as 19.2, 21.6 and 2519 m in dataset. Berger et al. 1995, whose data is also available, is earlier version of this with somewhat different resulting timescale. The *G. sacc.* $\delta^{18}\text{O}$ and *P. obliqu.* $\delta^{18}\text{O}$ values in dataset are all positive but should be all negative according to reference (see Table A5 column headings) and Berger et al. 1995 data. **Dataset Sources:** <http://www.pangaea.de/ddi?datasetid=52113&login=0&format=text>

Core: PS1230 **Lat:** $78^{\circ} 51.32'$ **Lon:** $-4^{\circ} 46.87'$ **Depth:** 1249 m **$\delta^{18}\text{O}$ Sources:** *Neogloboquadrina pachyderma (sinistral)* **References:** Bauch et al. 2001 **Age Model:** AMS ^{14}C dates measured on *Neogloboquadrina pachyderma (sinistral)* with a 400-year ocean inventory age correction subtracted; ages between these fixpoints obtained using calculated linear sedimentation rates; calendar year ages back to 18 ^{14}C ka given following Stuiver and Reimers 1993 and for older core section, following Bard et al. 1994 **Dataset Sources:** http://www.pangaea.de/ddi/PS1230-1_foram_records.tab?datasetid=58455&login=0&format=text

Core: PS1243 **Lat:** $69^{\circ} 22.31'$ **Lon:** $-6^{\circ} 33.18'$ **Depth:** 2711 m **$\delta^{18}\text{O}$ Sources:** *Neogloboquadrina pachyderma (sinistral)*, *Cibicidoides wuellerstorfi*, *Oridorsalis umbonatus* **References:** Bauch et al. 2001 **Age Model:** See Core PS1230. **Dataset Sources:** http://www.pangaea.de/ddi/PS1243-1_foram_records.tab?datasetid=58453&login=0&format=text

Core: PS1297-4 **Lat:** $78^{\circ} .8'$ **Lon:** $-1^{\circ} .8'$ **Depth:** 3051 m **$\delta^{18}\text{O}$ Sources:**

Neogloboquadrina pachyderma (sinistral) **References:** Hebbeln and Wefer 1997 **Age Model:** Back to 124 ka, determination of the best fit of the oxygen isotope record to the SPECMAP stack and occurrence of benthic foram *Pullenia bulloides*, which is indicative of oxygen isotope stage 5.1 in this region. **Notes:** Ocean depth above is from reference; that given in dataset is 3050 m. Similarly, the differing Lat minutes and Lon minutes given in the dataset are 59.7 (with Lat degrees = 77) and 3.2 **Dataset Sources:** <http://www.pangaea.de/ddi?datasetid=58360&login=0&format=text>

Core: PS1320-2 **Lat:** 77° 59.2' **Lon:** 0° 32.3' **Depth:** 3104 m $\delta^{18}\text{O}$ **Sources:** *Neogloboquadrina pachyderma (sinistral)* **References:** Hebbeln and Wefer 1997 **Age Model:** See Core PS1297-4. For older part of core, there is coccolith (occurrence of *Coccolithus pelagicus* = 250 ka) and high-resolution paleomagnetic data (4 events). **Notes:** Ocean depth above is from reference; that given in dataset is 3112 m. Similarly, the differing Lat minutes and Lon minutes given in the dataset are 59.6 and 33.5 **Dataset Sources:** <http://www.pangaea.de/ddi?datasetid=58340&login=0&format=text>

Core: PS1388-3 **Lat:** -69° 2' **Lon:** -5° 55' **Depth:** 2536 m $\delta^{18}\text{O}$ **Sources:** *Epistominella exigua*, *Neogloboquadrina pachyderma (sinistral)* **References:** Mackensen et al. 1989, Grobe and Mackensen 1992 **Age Model:** Stratigraphic fixed points were defined where specific lithologic changes (carbonate, silica, opal, clay, illite) could be correlated with distinct events of the isotope chronostratigraphy; fix points up to event 8.0 were derived from the compiled chronostratigraphy of Martinson et al. 1987 and further stratigraphic calculations were based on the SPECMAP data set of Imbrie et al. 1984 with stage boundaries as defined by Prell et al. 1986; sedimentation rate problems around event 7.1 were solved using insolation. Constant sedimentation between isotopic events was assumed so linear interpolation between age control points assumed and calculated here. **Notes:** Core name above is from first reference and datasets; known as PS1388 in second reference. Ocean depth above is from first reference; given in second reference as 2517 m and in datasets as 2526 m. Lat degrees and Lon degrees are from references; given as -68 and -6 in datasets. Lon minutes is from first reference and datasets; given as 53.0 in second reference. Core's depth/age data from second dataset applied to its foram $\delta^{18}\text{O}$ data from first dataset. Most of first dataset data printed in first reference's TABLE 1; most of second dataset data printed in second reference's TABLE 2. **Dataset Sources:** <http://www.pangaea.de/ddi?datasetid=57029&login=0&format=text>, <http://www.pangaea.de/ddi?datasetid=50556&login=0&format=text>

Core: PS1506 **Lat:** -68° 45' **Lon:** -5° 53' **Depth:** 2405 m $\delta^{18}\text{O}$ **Sources:** *Neogloboquadrina pachyderma (sinistral)*, *Epistominella exigua*, *Oridorsalis umbonatus*, *Cibicides spp.* **References:** Mackensen et al. 1994 **Age Model:** Graphical correlation of benthic and planktonic foraminiferal oxygen isotope records with the Imbrie et al. 1984 SPECMAP record, aided by the computer program of Paillard et al. 1992; oxygen isotope stratigraphy also correlated with several lithological param-

eters, the opal and Ba content, the benthic foraminiferal fauna and the C13 records of infaunal benthic foraminifera. Based on Figure 3 of reference, linear interpolation between age control points given in dataset is assumed and calculated here. **Notes:** Core name above is from reference; known as PS1506-1 in dataset. Ocean depth above is from reference; that in dataset is 2426 m. Similarly, Lat minutes and Lon minutes are from reference; those given in dataset are 44 and 51. **Dataset Sources:** <http://www.pangaea.de/ddi?datasetid=50031&login=0&format=text>

Core: PS2082 **Lat:** -43° 13' **Lon:** 11° 45' **Depth:** 4661 m $\delta^{18}\text{O}$ **Sources:** *Cibicides spp.*, *Globigerina bulloides*, *Neoglobobulimina pachyderma* (all) **References:** Mackensen et al. 1994 **Age Model:** Graphical correlation of benthic and planktonic foraminiferal oxygen isotope records with the Imbrie et al. 1984 SPECMAP record, aided by the computer program of Paillard et al. 1992; during short sequences, corroborated by a detailed *Cycladophora davisiana* record. Based on Figure 3 of reference, linear interpolation between age control points given in dataset is assumed and calculated here; no extrapolation done beyond last age control point. **Notes:** Core name above is from reference; known as PS2082-1 in dataset. Ocean depth above is from reference; that in dataset is 4610 m. Similarly, Lat minutes and Lon minutes are from reference; those given in dataset are 13.2 and 44.3. **Dataset Sources:** <http://www.pangaea.de/ddi?datasetid=50113&login=0&format=text>

Core: PS2138-1 **Lat:** 81° 32' **Lon:** 30° 36' **Depth:** 995 m $\delta^{18}\text{O}$ **Sources:** *Melonis zaandami*, *Cassidulina teretis* **References:** Wollenburg et al. 2001 **Age Model:** From oxygen isotope record of *Neoglobobulimina pachyderma* (sinistral) (see Knies and Stein 1998), definition of stages and conversion into absolute ages following timescale of Martinson et al. 1987; further modified by several AMS ^{14}C dates ($\delta^{13}\text{C}$ -normalized and with 440-year reservoir correction) and maxima of certain benthic forams that indicate certain stages. **Notes:** Ocean depth above is from reference; that given in dataset is 862 m. Similarly, the differing Lat minutes and Lon minutes given in the dataset are 32.1 and 35.6 **Dataset Sources:** <http://www.pangaea.de/ddi?datasetid=56206&login=0&format=text>

Core: PS2212-3 **Lat:** 82° 4' **Lon:** 15° 43' **Depth:** 2550 m $\delta^{18}\text{O}$ **Sources:** *Oridorsalis tener* **References:** Wollenburg et al. 2001 **Age Model:** Because of extended foram-barren zones, not directly dated; instead correlated to nearby well-dated core PS1533-3 using paleomagnetic data **Notes:** Ocean depth above is from reference; that given in dataset is 2531 m. Similarly, the differing Lat minutes and Lon minutes given in the dataset are 1.42 and 40.34 **Dataset Sources:** <http://www.pangaea.de/ddi?datasetid=56207&login=0&format=text>

Core: Quelccaya1 **Lat:** -13° 56' **Lon:** -70° 50' **Depth:** -5670 m $\delta^{18}\text{O}$ **Sources:** *glacier ice H₂O* **References:** Thompson et al. 1985 **Age Model:** Counting of visibly distinct annual dust layers. **Notes:** Other references available in dataset. Dataset gives ages as year AD; these are converted here to yrBP (1950). **Dataset Sources:** <ftp://ftp.ngdc.noaa.gov/paleo/icecore/trop/quelccaya/q83cor1.txt>

Core: QuelccayaSummit **Lat:** -13° 56' **Lon:** -70° 50' **Depth:** -5670 m $\delta^{18}\text{O}$ **Sources:** *glacier ice H₂O* **References:** Thompson et al. 1985 **Age Model:** See Core Quelccaya1. **Notes:** Other references available in dataset. Dataset gives ages as year AD; these are converted here to yrBP (1950). **Dataset Sources:** ftp://ftp.ngdc.noaa.gov/paleo/icecore/trop/quelccaya/q83summ.txt

Core: RC11-120 **Lat:** -43° 31' **Lon:** 79° 52' **Depth:** 3193 m $\delta^{18}\text{O}$ **Sources:** *Cibicidoides spp.*, *Globigerina bulloides* **References:** Curry et al. 1988, Imbrie et al. 1984, Martinson et al. 1987 **Age Model:** Core is that used in Martinson et al. 1987: use of stacked oxygen-isotope stratigraphy and four different orbital tuning approaches, each of which is based upon a different assumption concerning the response of the orbital signal recorded in the data. Linear interpolation between age control points calculated here. **Notes:** Lat degrees is from second reference and datasets; given as -44 in first reference. Lat minutes and Lon minutes are from second reference; given as 0 and 0 in first reference and 31.2 and 52.02 in datasets. Depth/age/ $\delta^{18}\text{O}$ data of first $\delta^{18}\text{O}$ source/dataset printed in first reference's APPENDIX 1. Age model of first reference/dataset considered not to be as good as that of third reference/dataset so not used here; later slight modifications of age model used are available in fourth through sixth datasets. Age model based on calibrated ^{14}C dates available in seventh dataset; not published so not used here. **Dataset Sources:** <http://www.pangaea.de/ddi?datasetid=52303&login=0&format=text>, <http://www.pangaea.de/ddi?datasetid=52126&login=0&format=text>, <http://www.pangaea.de/ddi?datasetid=56018&login=0&format=text>, <http://www.pangaea.de/ddi?datasetid=51921&login=0&format=text>, <http://www.pangaea.de/ddi?datasetid=51622&login=0&format=text>, <http://www.pangaea.de/ddi?datasetid=52463&login=0&format=text>, <http://www.pangaea.de/ddi?datasetid=51966&login=0&format=text>

Core: RC13-110 **Lat:** 0° 6' **Lon:** -95° 39' **Depth:** 3231 m $\delta^{18}\text{O}$ **Sources:** *Cibicidoides wuellerstorfi* **References:** Mix et al. 1991, Pisias et al. 1990 **Age Model:** Correlation to the Imbrie et al. 1984 SPECMAP time scale using the method of Martinson et al. 1982. **Notes:** Lat minutes above is from references; that in dataset is 5.82. Dataset data is printed in references. *Cibicidoides wuellerstorfi* = *Cibicides wuellerstorfi* = *Planulina wuellerstorfi* = *Fontbatia wuellerstorfi*. In dataset and references, $\delta^{18}\text{O}$ values for *C. wuellerstorfi* were corrected to *Uvigerina* by adding 0.64; this is undone here by subtracting 0.64. **Dataset Sources:** <http://www.pangaea.de/ddi?datasetid=51844&login=0&format=text>

Core: RC13-228 **Lat:** -22° 19.8' **Lon:** 11° 12' **Depth:** 3204 m $\delta^{18}\text{O}$ **Sources:** *Cibicidoides spp.* **References:** Curry et al. 1988, Sarnthein et al. 1994 **Age Model:** See Core BT4. **Notes:** Lat minutes is from second reference and datasets; given as 0 in first reference. Lon minutes is from second reference; given as 0 in first reference and 11.88 in datasets. First dataset, used here, is based on the more recent age model of the second reference/dataset rather than the age model of first

reference/third dataset. Different age models, but SPECMAP-related like first reference/third dataset, exist in fourth and fifth datasets but are less recent than the one used here. Depth/age/ $\delta^{18}\text{O}$ data of third dataset printed in first reference's APPENDIX 1. First reference/third dataset indicates the $\delta^{18}\text{O}$ source is actually *Cibicidoides* spp. rather than just *Cibicidoides wuellerstorfi* as indicated by first dataset. **Dataset Sources:** <http://www.pangaea.de/ddi?datasetid=54407&login=0&format=text>, <http://www.pangaea.de/ddi?datasetid=54401&login=0&format=text>, <http://www.pangaea.de/ddi?datasetid=52300&login=0&format=text>, <http://www.pangaea.de/ddi?datasetid=52131&login=0&format=text>, <http://www.pangaea.de/ddi?datasetid=51622&login=0&format=text>

Core: RC13-229 **Lat:** -25° 30' **Lon:** 11° 18' **Depth:** 4194 m **$\delta^{18}\text{O}$ Sources:** *Uvigerina* spp., *Cibicidoides* spp. (*C. wuellerstorfi*, *C. kullenbergi*) **References:** Curry et al. 1988, Sarnthein et al. 1994 **Age Model:** See Core BT4. **Notes:** Ocean depth above is from references; given in datasets as 4191 m. Lat minutes and Lon minutes are from second reference; given as 0 and 0 in first reference and 29.4 and 18.42 in datasets. First dataset, used here, is based on the more recent age model of the second reference/dataset rather than the age model of first reference/third dataset. Different age models, but SPECMAP-related like first reference/third dataset, exist in fourth through seventh datasets but are less recent or less universal than the one used here. Depth/age/ $\delta^{18}\text{O}$ (*Cibicidoides* spp.) data of third dataset printed in first reference's APPENDIX 1. First reference indicates the $\delta^{18}\text{O}$ source is actually *Cibicidoides* spp. rather than just *Cibicidoides wuellerstorfi* as indicated by first and third datasets. **Dataset Sources:** <http://www.pangaea.de/ddi?datasetid=54407&login=0&format=text>, <http://www.pangaea.de/ddi?datasetid=54401&login=0&format=text>, <http://www.pangaea.de/ddi?datasetid=52301&login=0&format=text>, <http://www.pangaea.de/ddi?datasetid=52699&login=0&format=text>, <http://www.pangaea.de/ddi?datasetid=52664&login=0&format=text>, <http://www.pangaea.de/ddi?datasetid=52655&login=0&format=text>, <http://www.pangaea.de/ddi?datasetid=51854&login=0&format=text>

Core: RC13-254 **Lat:** -48° 34' **Lon:** 5° 7' **Depth:** 3636 m **$\delta^{18}\text{O}$ Sources:** *Neogloboquadrina pachyderma (sinistral)* **References:** Charles et al. 1991 **Age Model:** See Core E49-19. **Dataset Sources:** <http://www.pangaea.de/ddi?datasetid=52430&login=0&format=text>

Core: RC13-259 **Lat:** -53° 53' **Lon:** -4° 56' **Depth:** 2677 m **$\delta^{18}\text{O}$ Sources:** *Neogloboquadrina pachyderma (sinistral)* **References:** Charles et al. 1991 **Age Model:** See Core E49-19. **Notes:** Ocean depth of core given above is from reference; that given in dataset is 1754 m. **Dataset Sources:** <http://www.pangaea.de/ddi?datasetid=52428&login=0&format=text>

Core: RC13-271 **Lat:** -51° 59' **Lon:** 4° 31' **Depth:** 3634 m **$\delta^{18}\text{O}$ Sources:** *Neogloboquadrina pachyderma (sinistral)* **References:** Charles et al. 1991 **Age Model:** See Core E49-19. **Dataset Sources:** <http://www.pangaea.de/ddi?datasetid=52428&login=0&format=text>

id=52429&login=0&format=text

Core: RC15-93 **Lat:** -46° 6' **Lon:** -13° 13' **Depth:** 2714 m $\delta^{18}\text{O}$ **Sources:** *Neogloboquadrina pachyderma (sinistral)*, *Cibicidoides spp.* **References:** Charles et al. 1991 **Age Model:** See Core E49-19. **Dataset Sources:** <http://www.pangaea.de/ddi?datasetid=52431&login=0&format=text>

Core: RC15-94 **Lat:** -42° 54' **Lon:** -20° 51' **Depth:** 3762 m $\delta^{18}\text{O}$ **Sources:** *Neogloboquadrina pachyderma (sinistral)*, *Cibicidoides spp.* **References:** Charles et al. 1991 **Age Model:** See Core E49-19. **Notes:** Reference incorrectly gives an E longitude in its Table A6 **Dataset Sources:** <http://www.pangaea.de/ddi?datasetid=52432&login=0&format=text>

Core: RC17-177 **Lat:** 1° 45' **Lon:** 159° 27' **Depth:** 2600 m $\delta^{18}\text{O}$ **Sources:** *Globigerinoides sacculifer* **References:** Le and Shackleton 1992 **Age Model:** Correlation of the $\delta^{18}\text{O}$ record with the SPECMAP stack of Imbrie et al. 1984; correlation of fragmentation and $\delta^{13}\text{C}$ incorporated where $\delta^{18}\text{O}$ record detail lacking but given secondary priority. Linear interpolation between age control points assumed and calculated here. **Notes:** Lat minutes is from reference; that given in dataset is 45.3. Core's depth/age data from second dataset applied to its foram $\delta^{18}\text{O}$ data from first dataset. Dataset data printed in reference. **Dataset Sources:** <http://www.pangaea.de/ddi?datasetid=52478&login=0&format=text>, <http://www.pangaea.de/ddi?datasetid=52479&login=0&format=text>

Core: RC24-16 **Lat:** -5° 2.3' **Lon:** -10° 11.5' **Depth:** 3559 m $\delta^{18}\text{O}$ **Sources:** *Neogloboquadrina dutertrei* **References:** McIntyre et al. 1989 **Age Model:** Identification, where possible, of the dated SPECMAP isotope events in the $\delta^{18}\text{O}$ record and then linear interpolation between the ages of these events. Interpolation calculated here; no extrapolation beyond last age control point. **Notes:** Ocean depth above is from reference; given in dataset as 3543 m. Similarly, Lon minutes is from reference; given as 11.4 in dataset. Core's depth/age data from second dataset applied to its foram $\delta^{18}\text{O}$ data from first dataset. **Dataset Sources:** <http://www.pangaea.de/ddi?datasetid=56373&login=0&format=text>, <http://www.pangaea.de/ddi?datasetid=55571&login=0&format=text>

Core: SO90-93KL **Lat:** 23° 35' **Lon:** 64° 13' **Depth:** 1802 m $\delta^{18}\text{O}$ **Sources:** *Globigerinoides ruber (white)* **References:** Schulz et al. 1998 **Age Model:** Martinson et al. 1987 used for the designation and presentation of the glacial/interglacial stage structure; higher-resolution ages achieved by fitting the core sound velocity data, which shows strong interstadial/stadial variability, and the oxygen isotope record to the GISP2 record (Schulz, personal communication). **Notes:** Lat minutes above is from reference; given in dataset as 35.3. **Dataset Sources:** <http://www.pangaea.de/ddi?datasetid=55230&login=0&format=text>

Core: SO93-126KL **Lat:** 19° 58.4' **Lon:** 90° 2.03' **Depth:** 1253 m $\delta^{18}\text{O}$ **Sources:**

Globigerinoides ruber (white) **References:** Kudrass et al. 2001 **Age Model:** Starting from the isochronous time mark of the Toba ash (70ka), the $\delta^{18}\text{O}$ values were correlated with the Dansgaard-Oeschger cycles in the $\delta^{18}\text{O}$ of the GISP2 ice core. **Notes:** Core is also variously referred to as KL126 and 126KL in reference. Ocean depth above is from reference; given in dataset as 1250 m. Lon minutes above is from reference; given as 2.00 in dataset. **Dataset Sources:** <http://www.pangaea.de/ddi?datasetid=58759&login=0&format=text>

Core: SU-9008 **Lat:** 43° 30' **Lon:** -30° 24' **Depth:** 3100 m $\delta^{18}\text{O}$ **Sources:** *Globigerina bulloides* **References:** Grousset et al. 1993 **Age Model:** Detailed correlation of stages of *Globigerina bulloides* oxygen isotope record with SPECMAP stacked oxygen isotope signal of Martinson et al. 1987; intermediate ages estimated by polynomial interpolations between SPECMAP ages; additional age control from identification of ash-zone I and II of Ruddiman and Glover 1972. **Notes:** Core name above is from reference; known as SU90-08 in dataset. Latmin, Lon minutes and ocean depth above are from reference; given as 21.2, 24.5 and 3080 m in dataset. **Dataset Sources:** <http://www.pangaea.de/ddi?datasetid=52593&login=0&format=text>

Core: SU92-21 **Lat:** 36° 34.2' **Lon:** -23° 44.4' **Depth:** 4170 m $\delta^{18}\text{O}$ **Sources:** *Cibicidoides wuellerstorfi* **References:** Sarnthein et al. 1994 **Age Model:** See Core 12328-5. **Notes:** Lat minutes and Lon minutes are from reference; given as 30.7 and 44.2 in dataset. **Dataset Sources:** <http://www.pangaea.de/ddi?datasetid=54412&login=0&format=text>

Core: Sajama1 **Lat:** -18° 6' **Lon:** -68° 53' **Depth:** -6542 m $\delta^{18}\text{O}$ **Sources:** *glacier ice H₂O* **References:** Thompson et al. 1998 **Age Model:** Seasonal variations in $\delta^{18}\text{O}$, dust, and NO₃- allowed layer counting in the upper 41.5m (100yr) of the ice core, calibrated by identification of the 1964 A.D. tritium peak. For the rest of the Holocene part of the core, age control points were provided by: identification at 64.8m of the 1600 A.D. Huaynaputina ash horizon; ¹⁴C dates at 78.3m and 92.1m converted (Stuiver and Reimer 1993) to calendar ages of 970 and 3390 yrBP; and correlation of $\delta^{18}\text{O}_{\text{atm}}$ at 101.2m and 103.8m to the layer-count-dated GISP2 $\delta^{18}\text{O}_{\text{atm}}$ record. For the bottom, glacial part of the ice core, age control points were provided by: matching at 14 points (104m to 123m; 11 kyrBP to 21 kyrBP) the $\delta^{18}\text{O}$ record to that of GISP2; and a ¹⁴C date at 130.8m converted to a calendar age of 24487 yrBP. **Dataset Sources:** <ftp://ftp.ngdc.noaa.gov/paleo/icecore/trop/sajama/sc1-100a.txt>

Core: TR163-31 **Lat:** -4° 0' **Lon:** -84° 0' **Depth:** 3210 m $\delta^{18}\text{O}$ **Sources:** *Cibicidoides spp.* **References:** Curry et al. 1988 **Age Model:** See Core CH73-139. **Notes:** Depth/age/ $\delta^{18}\text{O}$ data of dataset printed in reference APPENDIX 1. **Dataset Sources:** <http://www.pangaea.de/ddi?datasetid=52329&login=0&format=text>

Core: TaylorDome **Lat:** -77° 47.78' **Lon:** 158° 43.43' **Depth:** -2365 m $\delta^{18}\text{O}$

Sources: *glacier ice H₂O* **References:** Steig et al. 2000 **Age Model:** For core depth 0-140m (0-2.5ka): R.B. Hawley measured vertical strain in a borehole 50m from the ice core site and then, using surface measurements of accumulation rate as a boundary condition, he integrated the measured strain rates to obtain the modern vertical velocity distribution and determined the depth-age distribution associated with that flow pattern, assumed to be in steady state over the age of the firn column. For core depth 140-356m (2.5-11.7ka): interpolation guided by the finite-element ice flow model of Raymond 1983, which uses a Glen-type glacier flow law; assuming a steady-state dome geometry and accumulation rate, a determination was made of the shape function that when multiplied by the accumulation rate at the time of deposition gave the annual layer thickness at depth; the depth-age relationship was then given by an integral of layer thickness over ice equivalent depth, which was converted to true depth using firn density measurements; by adjusting the accumulation rate a timescale that matched the end point of the next core segment was obtained. For core depth 345-380m (11.7-20ka): identical to Steig et al. 1998b, which was developed by correlating CH₄ to $\delta^{18}\text{O}_{\text{atm}}$ between Taylor Dome and GISP2 and using dD-based estimates of temperature and 10Be-based estimates of accumulation rate to determine the gas-ice age difference. For core depth greater than 380m (20ka): approximated the depth-age relationship using a third-order spline that minimized the distance to control points from the Sucher 1997 and Brook et al. 1999 gas-age chronologies, where the gas-ice age difference was estimated as for the core segment above; independent validation provided by two 10Be anomalies at 37 ka and 64 ka. **Notes:** There is a less-recent age model than the one used; see reference and second dataset. **Dataset Sources:** ftp://ftp.ngdc.noaa.gov/paleo/icecore/antarctica/taylor/hi18o_td.txt, http://www.ngdc.noaa.gov/paleo/icecore/antarctica/taylor/taylor_data.html

Core: V19-27 **Lat:** -0° 28.2' **Lon:** -82° 4.2' **Depth:** 1373 m $\delta^{18}\text{O}$ **Sources:** *Cibicidoides wuellerstorfi* **References:** Mix et al. 1991 **Age Model:** See Core RC13-110. **Notes:** Latmin above is from reference; that in dataset is 28.02. Dataset data is printed in reference. *Cibicidoides wuellerstorfi* = *Cibicides wuellerstorfi* = *Planulina wuellerstorfi* = *Fontbatia wuellerstorfi*. In dataset and references, $\delta^{18}\text{O}$ values for *C. wuellerstorfi* were corrected to *Uvigerina* by adding 0.64; this is undone here by subtracting 0.64. **Dataset Sources:** <http://www.pangaea.de/ddi?datasetid=51844&login=0&format=text>

Core: V19-30 **Lat:** -3° 0' **Lon:** -83° 0' **Depth:** 3091 m $\delta^{18}\text{O}$ **Sources:** *Cibicidoides spp.* **References:** Curry et al. 1988, Bond et al. 1997 **Age Model:** AMS ¹⁴C ages corrected by -500 years for the age of the surface ocean reservoir and then calibrated to calendar years according to Bard et al. 1993. Core top is assumed here to be of zero age and linear interpolation between age control points is calculated here. **Notes:** Core name above is from first reference and datasets; known as VM 19-30 in second reference. Lat minutes and Lon minutes are from first reference; given as 22.98 and 31.2 in datasets. Depth/ $\delta^{18}\text{O}$ data of first dataset printed in first reference's APPENDIX 1 and depth/age data of second dataset printed in second reference's Table 1. First reference contains an age model based on Imbrie et al.

1984; similarly for third dataset, which also indicates 0.0 core depth is age 0.0; both less recent so not used here. **Dataset Sources:** <http://www.pangaea.de/ddi?datasetid=52309&login=0&format=text>, <http://www.pangaea.de/ddi?datasetid=53125&login=0&format=text>, <http://www.pangaea.de/ddi?datasetid=53275&login=0&format=text>

Core: V22-108 **Lat:** -43° 11' **Lon:** -3° 15' **Depth:** 4171 m **$\delta^{18}\text{O}$ Sources:** *Cibicidoides spp.* **References:** Charles et al. 1991 **Age Model:** See Core E49-19. **Notes:** Reference incorrectly gives an E longitude in its Table A7 **Dataset Sources:** <http://www.pangaea.de/ddi?datasetid=52433&login=0&format=text>

Core: V22-174 **Lat:** -10° 4' **Lon:** -12° 49' **Depth:** 2630 m **$\delta^{18}\text{O}$ Sources:** *Globigerinoides sacculifer* **References:** Imbrie et al. 1984 **Age Model:** Core is one used in SPECMAP (Imbrie et al. 1984): tuning of the $\delta^{18}\text{O}$ record to the orbital parameters (obliquity and precession index) curves starting with radiometric and paleomagnetic age control points; linear interpolation between resulting isotopic event ages. Interpolation calculated here. **Notes:** Lat minutes and Lon minutes are from reference; those given in dataset are 4.2 and 49.2. Core's depth/age data from second dataset applied to its foram $\delta^{18}\text{O}$ data from first dataset. **Dataset Sources:** <http://www.pangaea.de/ddi?datasetid=56359&login=0&format=text>, <http://www.pangaea.de/ddi?datasetid=56358&login=0&format=text>

Core: V22-197 **Lat:** 14° 0' **Lon:** -10° 0' **Depth:** 3167 m **$\delta^{18}\text{O}$ Sources:** *Cibicidoides spp.* **References:** Curry et al. 1988 **Age Model:** See Core CH73-139. **Notes:** Lat minutes, Lon degrees and Lon minutes are from reference; given as 10.02, -18, and 34.8 in dataset. Depth/age/ $\delta^{18}\text{O}$ data of dataset printed in reference APPENDIX 1. A more recent age model available in second dataset; not published so not used here. **Dataset Sources:** <http://www.pangaea.de/ddi?datasetid=52291&login=0&format=text>, <http://www.pangaea.de/ddi?datasetid=59746&login=0&format=text>

Core: V24-109 **Lat:** 0° 25.8' **Lon:** 158° 48' **Depth:** 2367 m **$\delta^{18}\text{O}$ Sources:** *Globigerinoides sacculifer* **References:** Le and Shackleton 1992 **Age Model:** See Core RC17-177. **Notes:** Lat minutes is from reference; that given in dataset is 25.98. Core's depth/age data from second dataset applied to its foram $\delta^{18}\text{O}$ data from first dataset. Dataset data printed in reference. **Dataset Sources:** <http://www.pangaea.de/ddi?datasetid=52477&login=0&format=text>, <http://www.pangaea.de/ddi?datasetid=52479&login=0&format=text>

Core: V25-21 **Lat:** 26° 24' **Lon:** -45° 27' **Depth:** 3693 m **$\delta^{18}\text{O}$ Sources:** *Globigerinoides ruber (pink)* **References:** Curry and Crowley 1987 **Age Model:** See Core KNR110-43PC. **Notes:** Depth/age/ $\delta^{18}\text{O}$ data of dataset printed in reference TABLE 2d. **Dataset Sources:** <http://www.pangaea.de/ddi?datasetid=59891&login=0&format=text>

Core: V25-59 **Lat:** 1° 22.4' **Lon:** -33° 28.9' **Depth:** 3824 m **$\delta^{18}\text{O}$ Sources:** *Cibicidoides wuellerstorfi* **References:** McIntyre et al. 1989 **Age Model:** See Core RC24-16. **Notes:** Lat minutes and Lon minutes are from reference; given as 22.0 and 28.8 in dataset. Core's depth/age data from second dataset applied to its foram $\delta^{18}\text{O}$ data from first dataset. A different shorter age model available in third dataset; from an older reference so not used here. A more recent age model available in fourth dataset; not published so not used here. **Dataset Sources:** <http://www.pangaea.de/ddi?datasetid=52122&login=0&format=text>, <http://www.pangaea.de/ddi?datasetid=52136&login=0&format=text>, <http://www.pangaea.de/ddi?datasetid=52290&login=0&format=text>, <http://www.pangaea.de/ddi?datasetid=59749&login=0&format=text>

Core: V26-176 **Lat:** 36° 0' **Lon:** -72° 0' **Depth:** 3942 m **$\delta^{18}\text{O}$ Sources:** *Cibicidoides* spp. (*C. wuellerstorfi*, *C. kullenbergi*) **References:** Curry et al. 1988 **Age Model:** See Core CH73-139. **Notes:** Lat minutes and Lon minutes are from reference; given as 3.0 and 22.8 in dataset. Depth/age/ $\delta^{18}\text{O}$ data of dataset printed in reference APPENDIX 1. **Dataset Sources:** <http://www.pangaea.de/ddi?datasetid=52278&login=0&format=text>

Core: V28-127 **Lat:** 12° 0' **Lon:** -80° 0' **Depth:** 3623 m **$\delta^{18}\text{O}$ Sources:** *Cibicidoides wuellerstorfi* **References:** Oppo and Fairbanks 1990 **Age Model:** See Core CHN82-24. Difficulty in assigning the core depth of the stage 4/3 transition because of highly variable $\delta^{18}\text{O}$ values there, probably due to a turbidite near 3.2 m core depth; also a turbidite near 5.5 m core depth, on the stage 6/5e transition, although no evident $\delta^{18}\text{O}$ disturbance there; much of the 5b/5a transition probably missing. Linear interpolation assumed between age control points and calculated here; no extrapolation beyond last age control point. **Notes:** Ocean depth above is from reference; given in dataset as 3237 m. Lat degrees, Lat minutes and Lon minutes are from reference; those given in dataset are 11, 39.0 and 7.8. Core's depth/age data from second dataset applied to its foram $\delta^{18}\text{O}$ data from first dataset. **Dataset Sources:** <http://www.pangaea.de/ddi?datasetid=52404&login=0&format=text>, <http://www.pangaea.de/ddi?datasetid=52403&login=0&format=text>

Core: V28-14 **Lat:** 64° 47' **Lon:** -29° 34' **Depth:** 1855 m **$\delta^{18}\text{O}$ Sources:** *Cibicidoides wuellerstorfi*, *Neogloboquadrina pachyderma (sinistral)* **References:** Curry et al. 1988, Kellogg et al. 1978 **Age Model:** See Core CH73-139. For second $\delta^{18}\text{O}$ source/dataset, no extrapolation before first or beyond last age control point (first dataset). **Notes:** Lat degrees and Lon degrees are from second reference and datasets; given as 65 and -30 in first reference. Lat minutes and Lon minutes are from second reference; given as 0 and 0 in first reference and 46.98 and 34.2 in datasets. Depth/age/ $\delta^{18}\text{O}$ data of first dataset printed in first reference's APPENDIX 1; depth/ $\delta^{18}\text{O}$ data of second dataset printed in second reference's Table 1. A more recent age model is available in third dataset; too short to be really useful here so not used. More recent age models also available in fourth and fifth datasets; not published so not used here (also too short). **Dataset Sources:** <http://www.pangaea.de>

/ddi?datasetid=52276&login=0&format=text, <http://www.pangaea.de/ddi?datasetid=51708&login=0&format=text>, <http://www.pangaea.de/ddi?datasetid=53125&login=0&format=text>, <http://www.pangaea.de/ddi?datasetid=59754&login=0&format=text>, <http://www.pangaea.de/ddi?datasetid=51966&login=0&format=text>

Core: V28-304 **Lat:** 29° 0' **Lon:** 134° 0' **Depth:** 2942 m **$\delta^{18}\text{O}$ Sources:** *Cibicidoides* spp. **References:** Curry et al. 1988 **Age Model:** See Core CH73-139. **Notes:** Lat degrees, Lat minutes and Lon minutes are from reference; given as 28, 31.8 and 7.8 in dataset. Depth/age/ $\delta^{18}\text{O}$ data of dataset printed in reference APPENDIX 1. **Dataset Sources:** <http://www.pangaea.de/ddi?datasetid=52307&login=0&format=text>

Core: V29-135 **Lat:** -19° 36' **Lon:** 8° 52.8' **Depth:** 2675 m **$\delta^{18}\text{O}$ Sources:** *Globigerina bulloides*, *Uvigerina peregrina*, *Cibicidoides wuellerstorfi* **References:** Sarnthein et al. 1994 **Age Model:** See Core 12328-5. For ages older than 29.5 ka, $\delta^{18}\text{O}$ record events were given ages after Martinson et al. 1987. No extrapolation here beyond last age control point. **Notes:** Lat minutes and Lon minutes are from reference; given as 42.0 and 53.0 in dataset. **Dataset Sources:** <http://www.pangaea.de/ddi?datasetid=54408&login=0&format=text>

Core: V30-40 **Lat:** -0° 12' **Lon:** -23° 9' **Depth:** 3706 m **$\delta^{18}\text{O}$ Sources:** *Globigerinoides sacculifer* **References:** Imbrie et al. 1984 **Age Model:** See Core V22-174. **Notes:** Core's depth/age data from second dataset applied to its foram $\delta^{18}\text{O}$ data from first dataset. **Dataset Sources:** <http://www.pangaea.de/ddi?datasetid=56361&login=0&format=text>, <http://www.pangaea.de/ddi?datasetid=56360&login=0&format=text>

Core: V30-49 **Lat:** 18° 0' **Lon:** -21° 0' **Depth:** 3093 m **$\delta^{18}\text{O}$ Sources:** *Cibicidoides wuellerstorfi* **References:** Curry et al. 1988 **Age Model:** See Core CH73-139. **Notes:** Lat minutes and Lon minutes are from reference; given as 26.0 and 4.8 in dataset. Depth/age/ $\delta^{18}\text{O}$ data of first dataset printed in reference APPENDIX 1. A more recent age model available in second dataset; not published so not used here. **Dataset Sources:** <http://www.pangaea.de/ddi?datasetid=52280&login=0&format=text>, <http://www.pangaea.de/ddi?datasetid=59758&login=0&format=text>

Core: V35-05 **Lat:** 7° 0' **Lon:** 112° 0' **Depth:** 1950 m **$\delta^{18}\text{O}$ Sources:** *Cibicidoides* spp. (*C. wuellerstorfi*, *C. kullenbergi*) **References:** Curry et al. 1988 **Age Model:** See Core CH73-139. **Notes:** Core name above is from reference; known as V35-5 in dataset. Ocean depth above is from reference; given in dataset as 1953 m. Lat minutes and Lon minutes are from reference; given as 11.7 and 4.8 in dataset. Reference indicates the $\delta^{18}\text{O}$ source is actually *Cibicidoides* spp. rather than just *Cibicidoides wuellerstorfi* as indicated by dataset. Depth/ $\delta^{18}\text{O}$ data of dataset printed in reference APPENDIX 1. **Dataset Sources:** <http://www.pangaea.de/ddi?datasetid=52310&login=0&format=text>

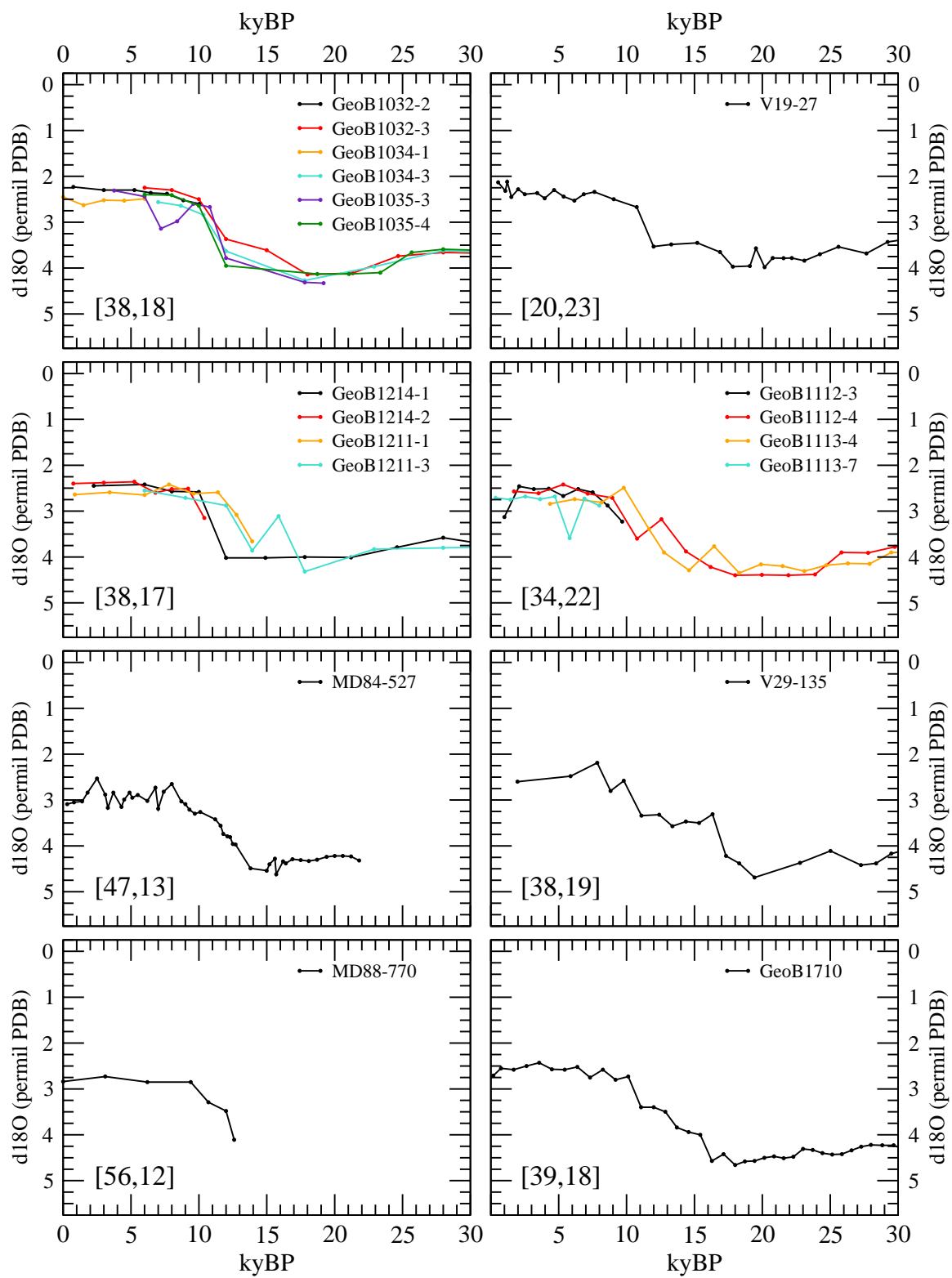
Core: W8402A-14GC **Lat:** 0° 57.2' **Lon:** -138° 57.3' **Depth:** 4287 m **References:** Jasper et al. 1994 $\delta^{18}\text{O}$ **Sources:** *Neogloboquadrina dutertrei*, *Cibicides wuellerstorfi* **Age Model:** Ages are based on visual correlation of the benthic foraminiferal oxygen isotope record with the SPECMAP stacked benthic foraminiferal $\delta^{18}\text{O}$ timescale of Martinson et al. 1987; oxygen isotope stage boundaries were determined by application of the SPECMAP chronological method of Imbrie et al. 1984 to the $\delta^{18}\text{O}$ -C. wuellerstorfi record. Linear interpolation between age control points calculated here; no extrapolation after last age control point. **Notes:** Core name above is from reference; known as W8402A-14 in datasets. Core's depth/age data from second dataset applied to its foram $\delta^{18}\text{O}$ data from first dataset. First dataset data is printed in reference's Table 1 but there appear to be numerous errors in Table 1 (some ages not consistent with Table 2's age control points). Second dataset data printed in reference's Table 2. **Dataset Sources:** <http://www.pangaea.de/ddi?datasetid=56368&login=0&format=text>, <http://www.pangaea.de/ddi?datasetid=52672&login=0&format=text>

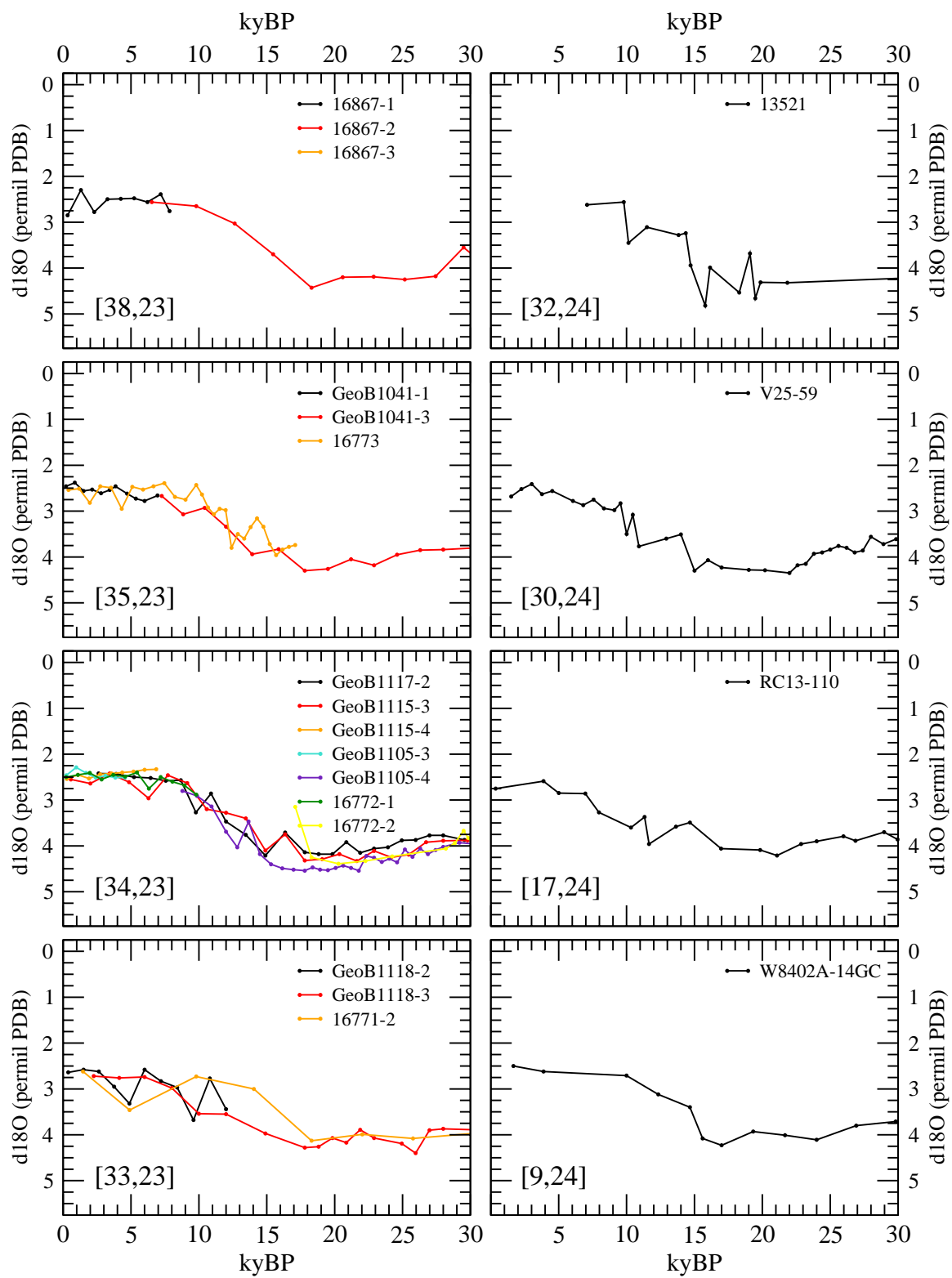
Appendix B

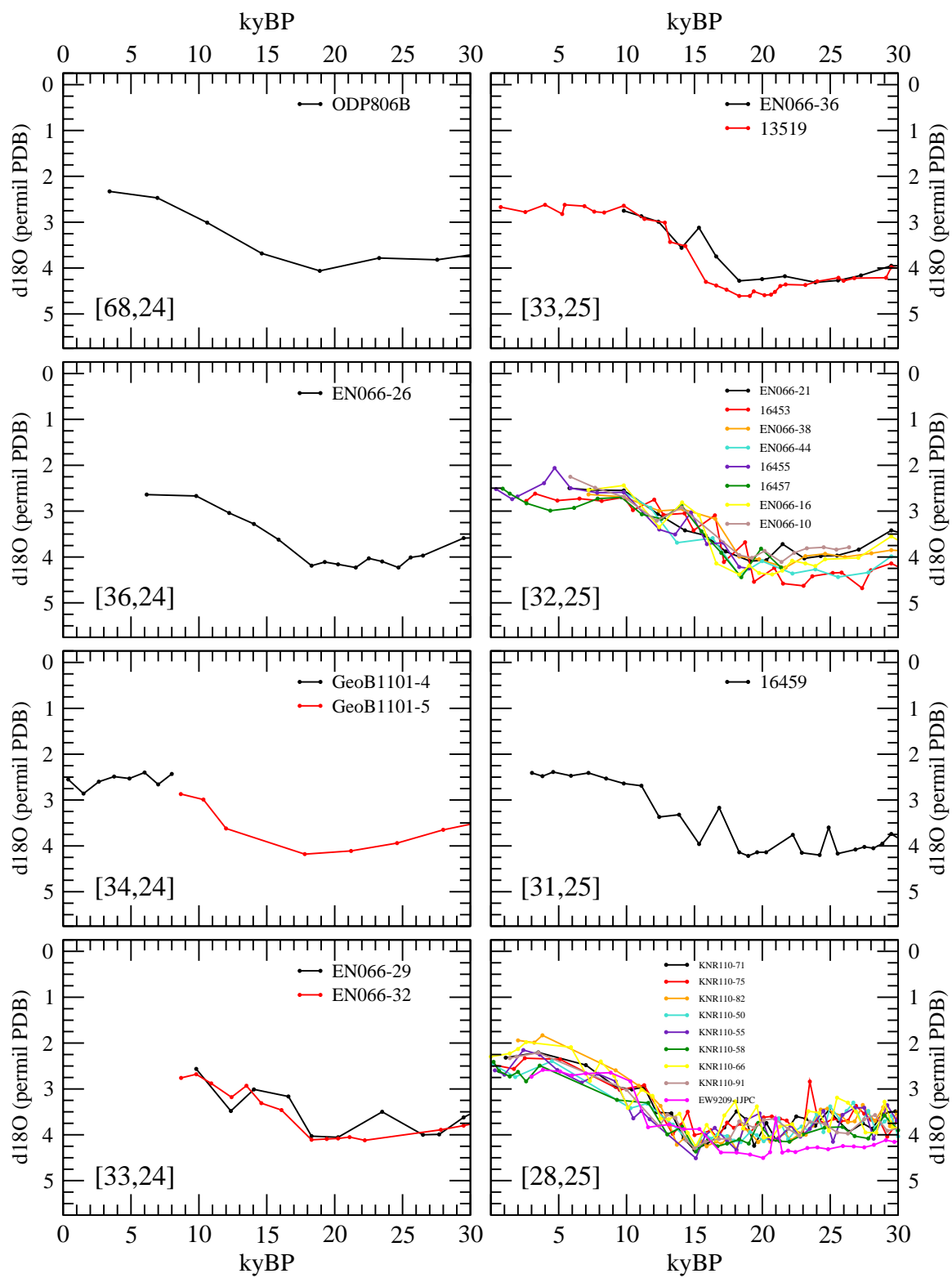
Downcore $\delta^{18}\text{O}$ Time Series Plots

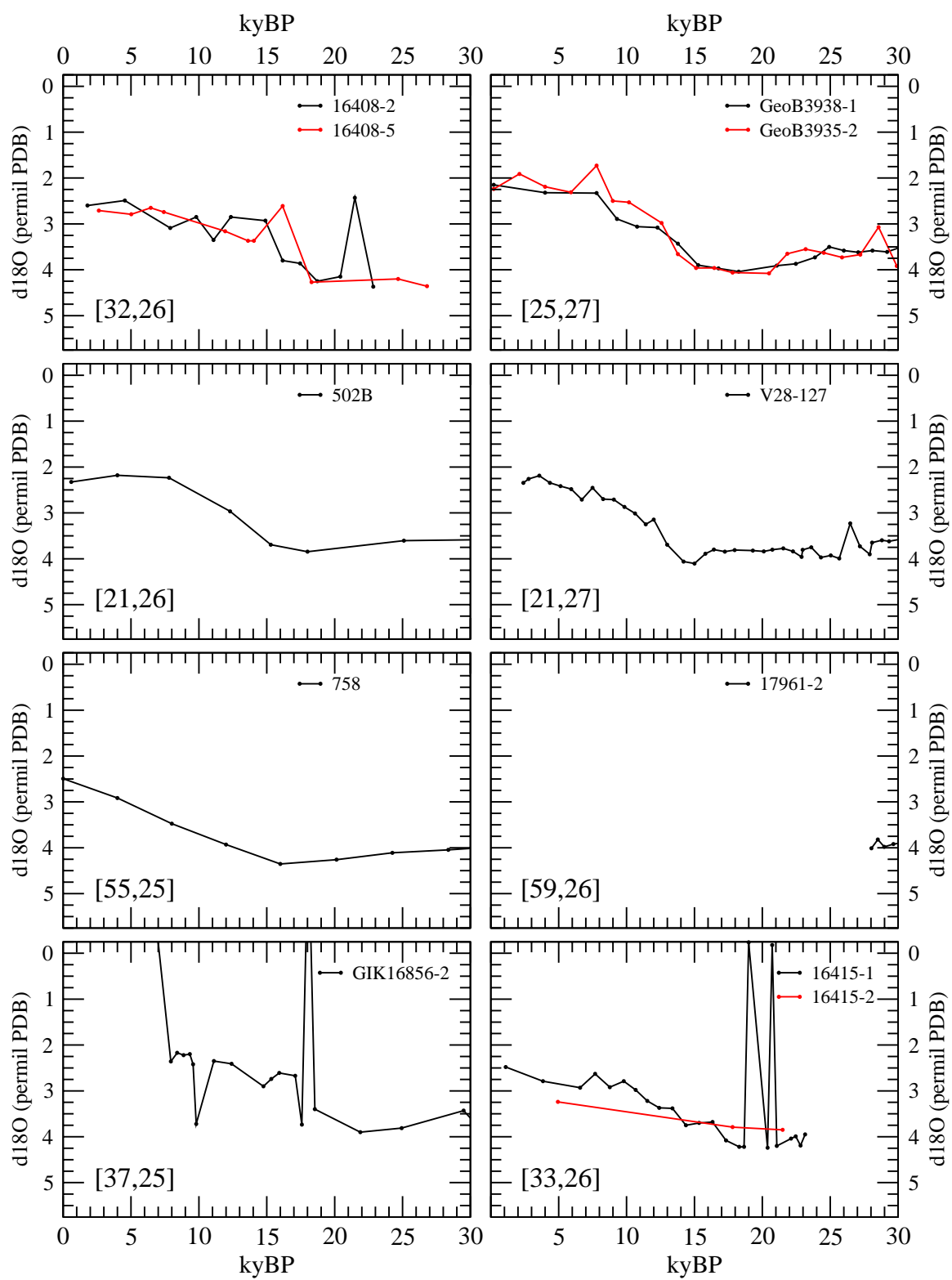
B.1 Downcore $\delta^{18}\text{O}$ Time Series Plots for *Cibicides wuellerstorfi*

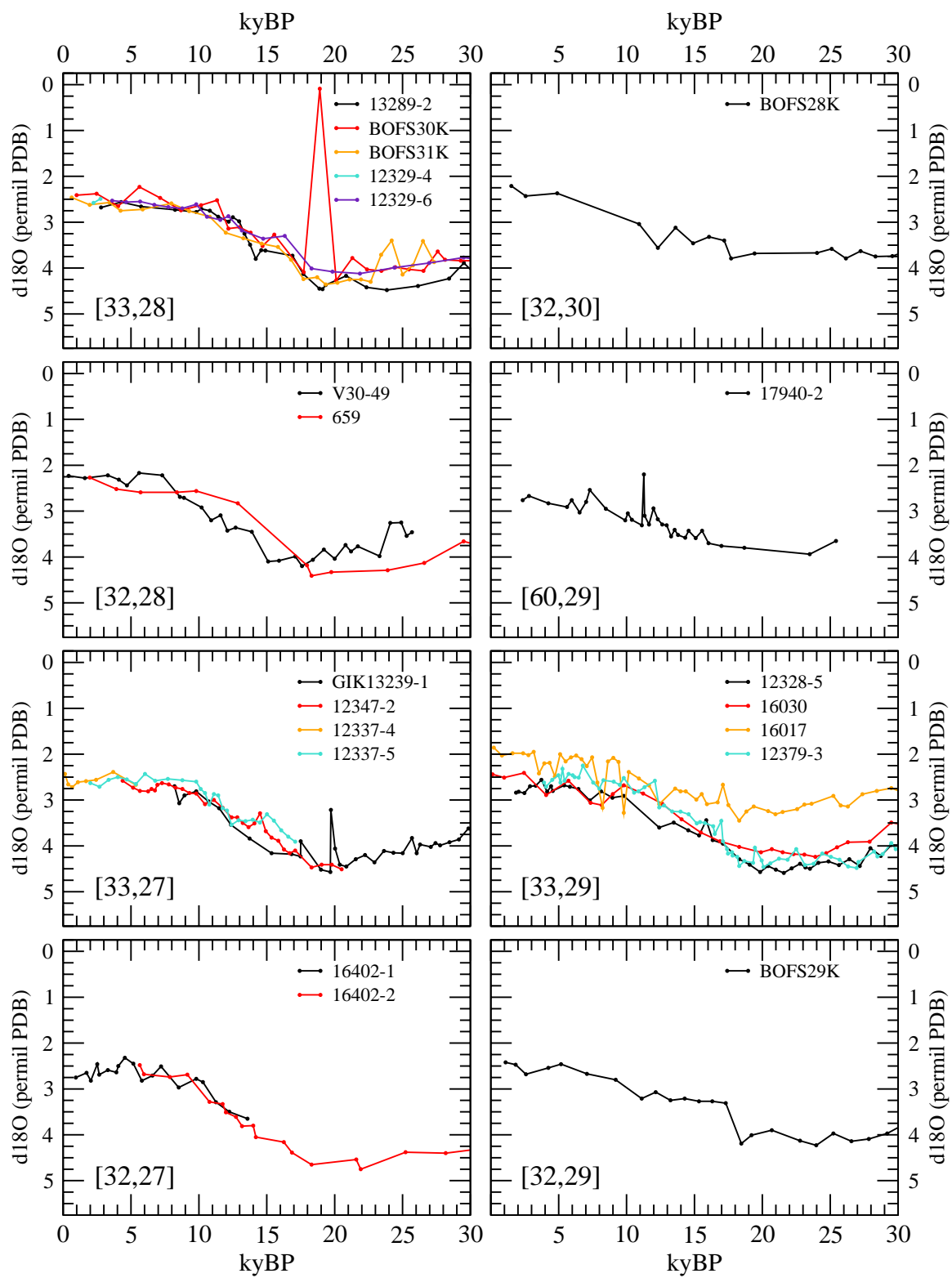
Each plot corresponds to a $5^\circ \times 4^\circ$ CGCM grid box and includes the downcore $\delta^{18}\text{O}$ time series of all the cores whose locations are encompassed by that grid box. The [lon#,lat#] of the CGCM grid box is in the lower left corner of each plot. See any of the CGCM grid box maps in this work to locate it on a world map. The plots are arranged in order of increasing latitude starting from lower left and proceeding in an “N” on each page. This may cause seemingly oddly placed stray plots. All x axes are time in kyBP and only go from 0 to 30 kyBP, spanning just the eras of interest in this work and even though data going further back may have been compiled. All y axes are $\delta^{18}\text{O}$ in permil PDB, span the maximum range resulting from including all cores in all grid boxes, and are inverted to be reminiscent of the global mean temperature increase from the LGM to PD. See Chapter 5 for a description of the data, its averaging, and caveats.

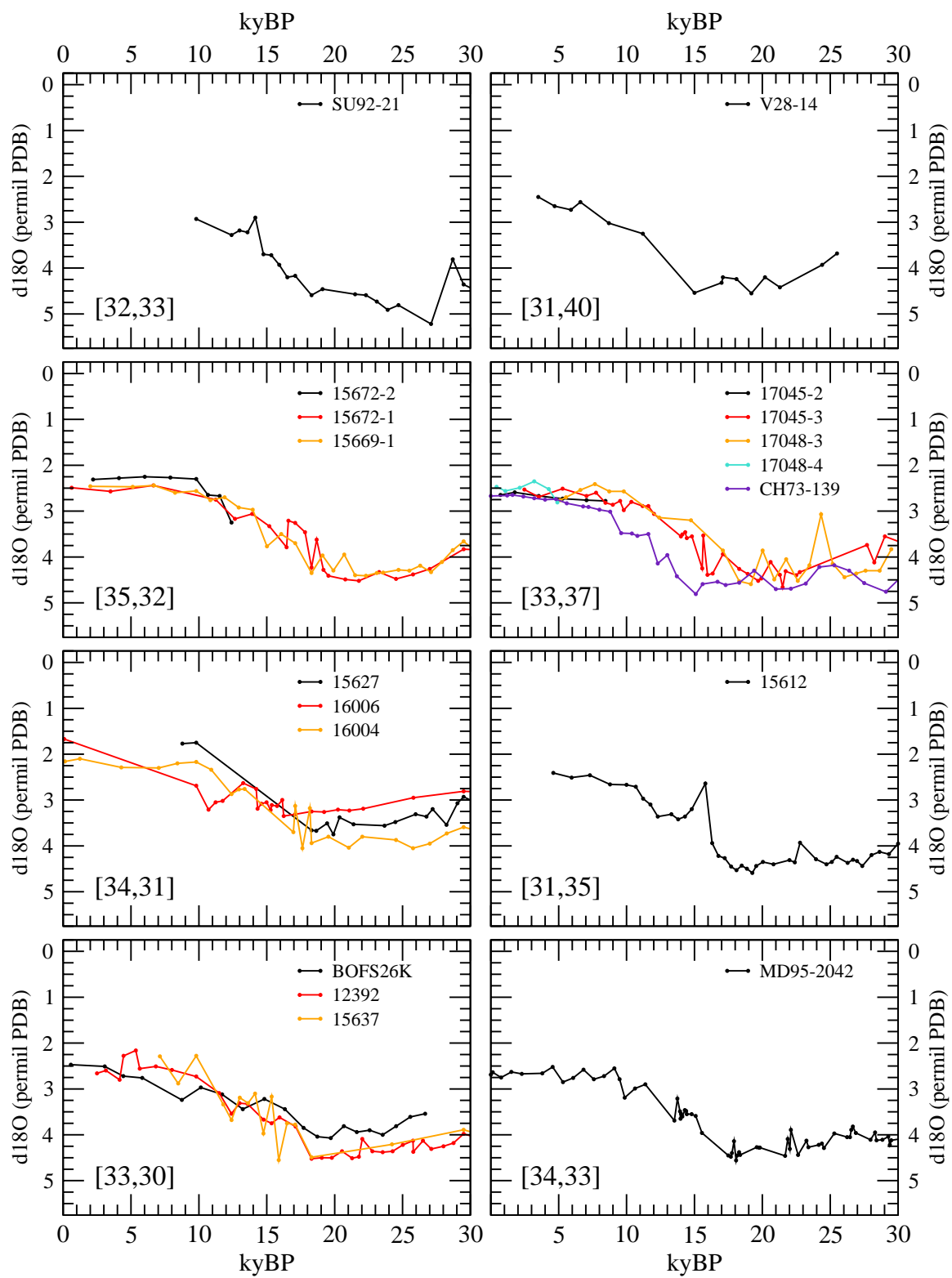


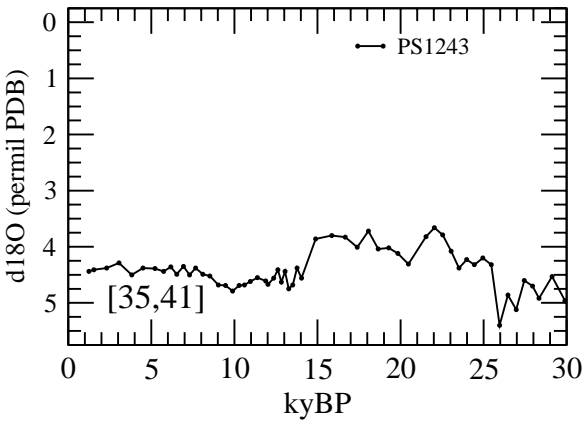






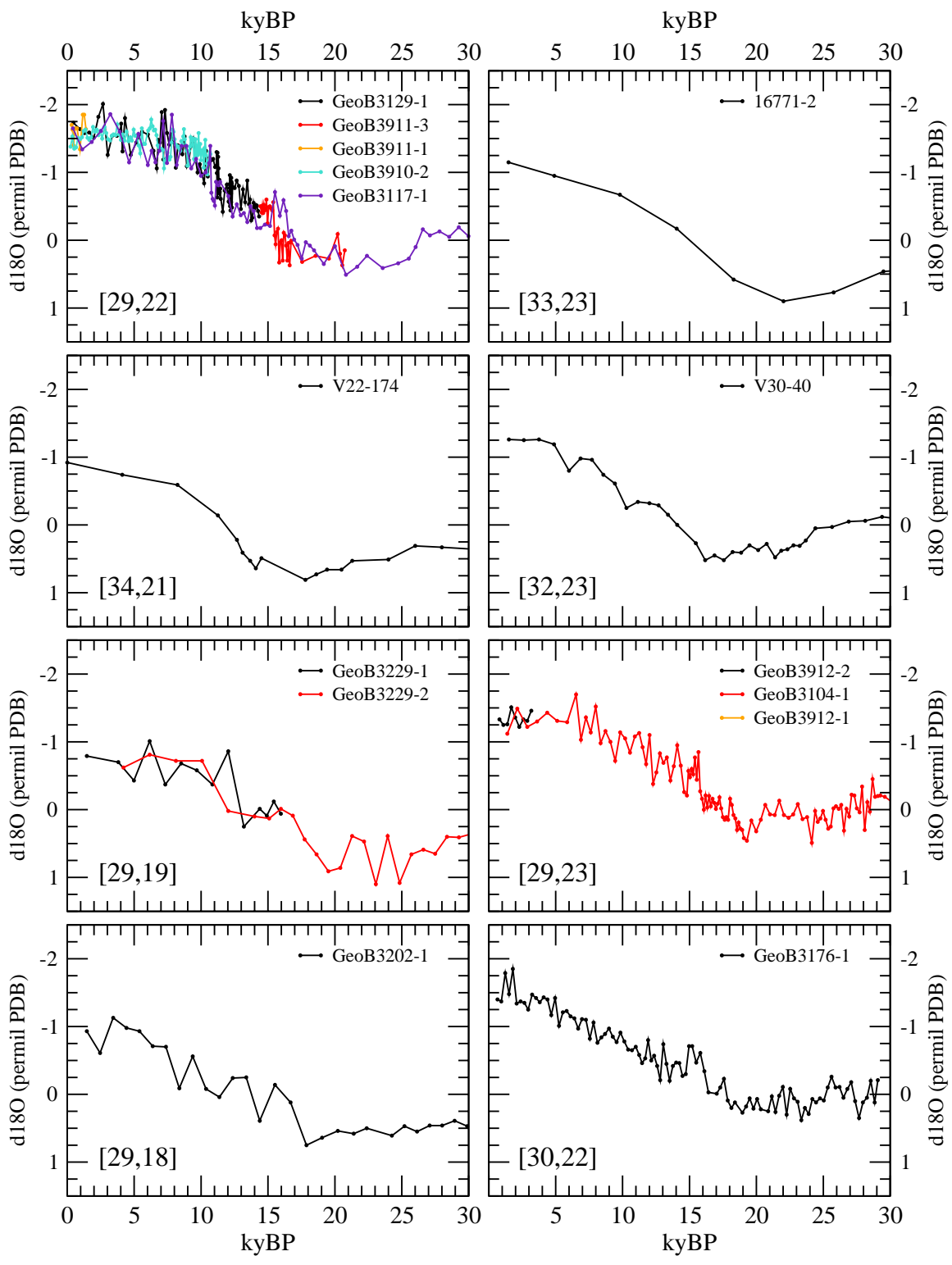


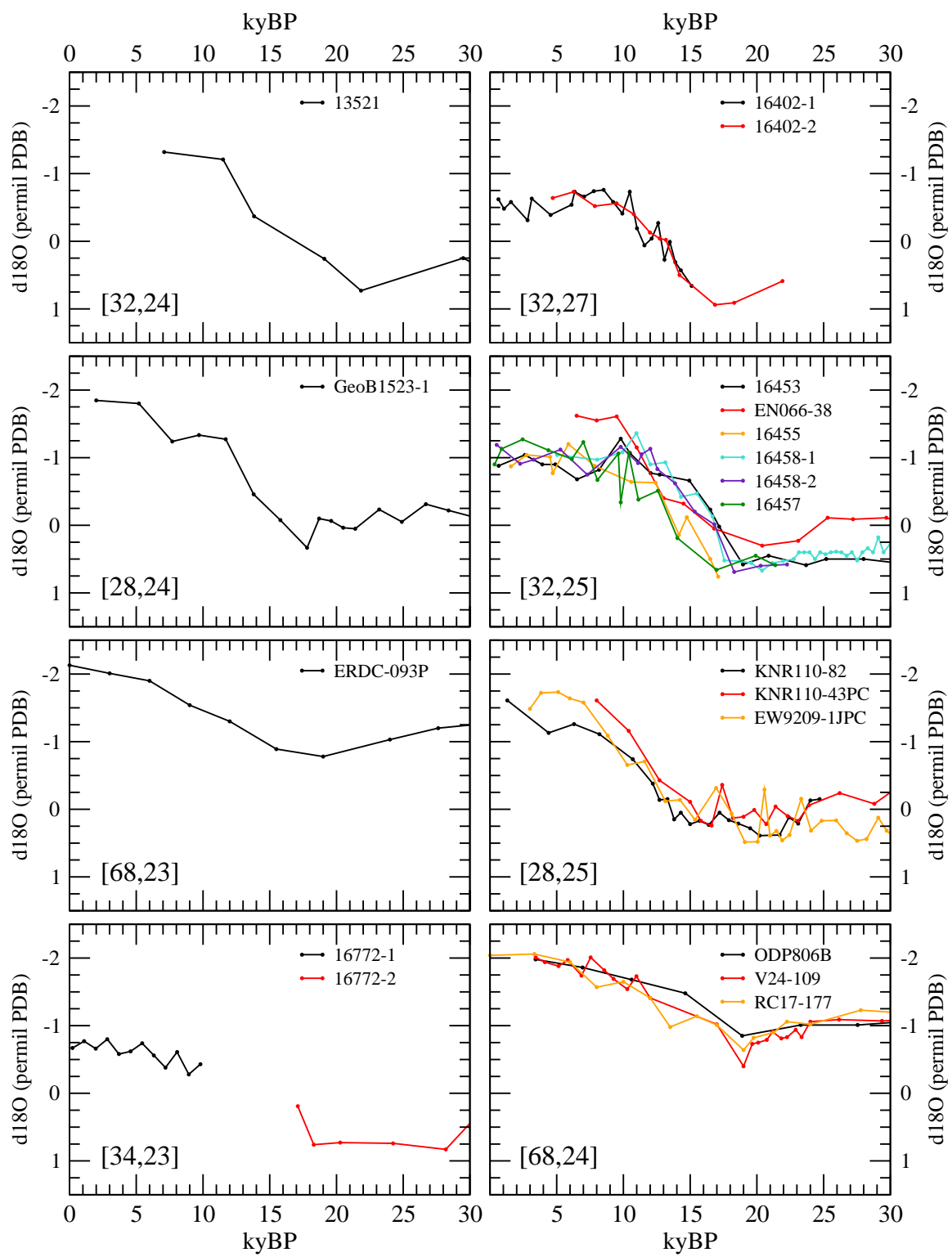


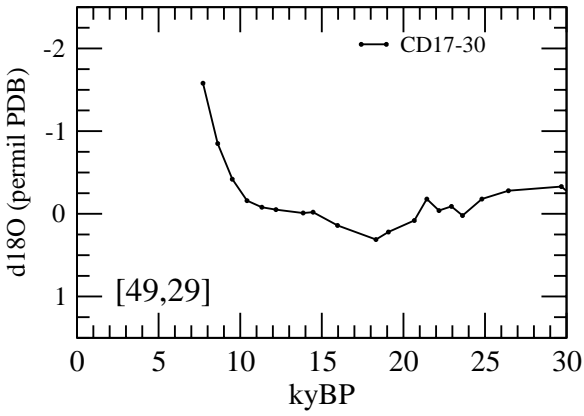


B.2 Downcore $\delta^{18}\text{O}$ Time Series Plots for *Globigerinoides sacculifer*

Each plot corresponds to a $5^\circ \times 4^\circ$ CGCM grid box and includes the downcore $\delta^{18}\text{O}$ time series of all the cores whose locations are encompassed by that grid box. The [lon#,lat#] of the CGCM grid box is in the lower left corner of each plot. See any of the CGCM grid box maps in this work to locate it on a world map. The plots are arranged in order of increasing latitude starting from lower left and proceeding in an “N” on each page. This may cause seemingly oddly placed stray plots. All x axes are time in kyBP and only go from 0 to 30 kyBP, spanning just the eras of interest in this work and even though data going further back may have been compiled. All y axes are $\delta^{18}\text{O}$ in permil PDB, span the maximum range resulting from including all cores in all grid boxes, and are inverted to be reminiscent of the global mean temperature increase from the LGM to PD. See Chapter 5 for a description of the data, its averaging, and caveats.

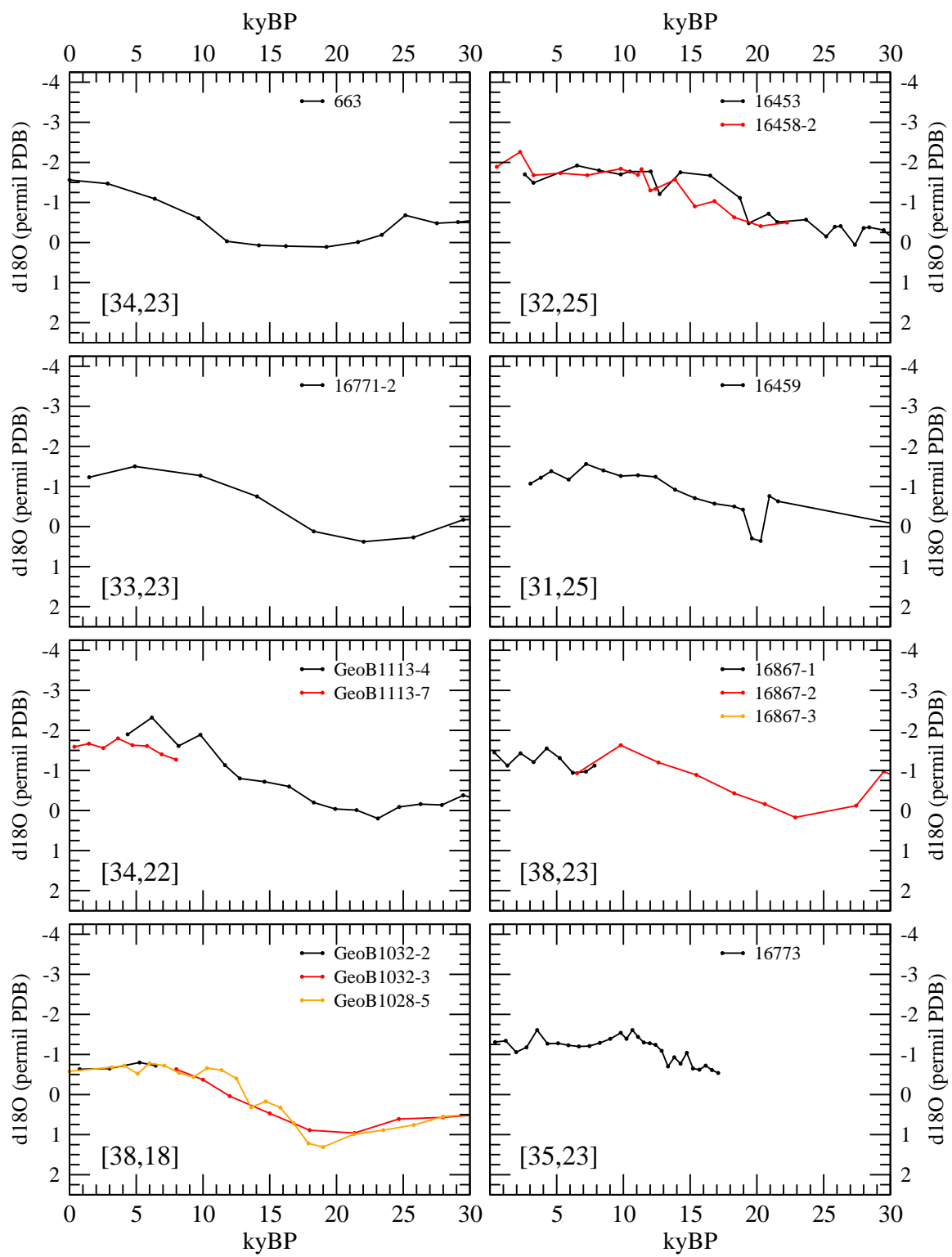


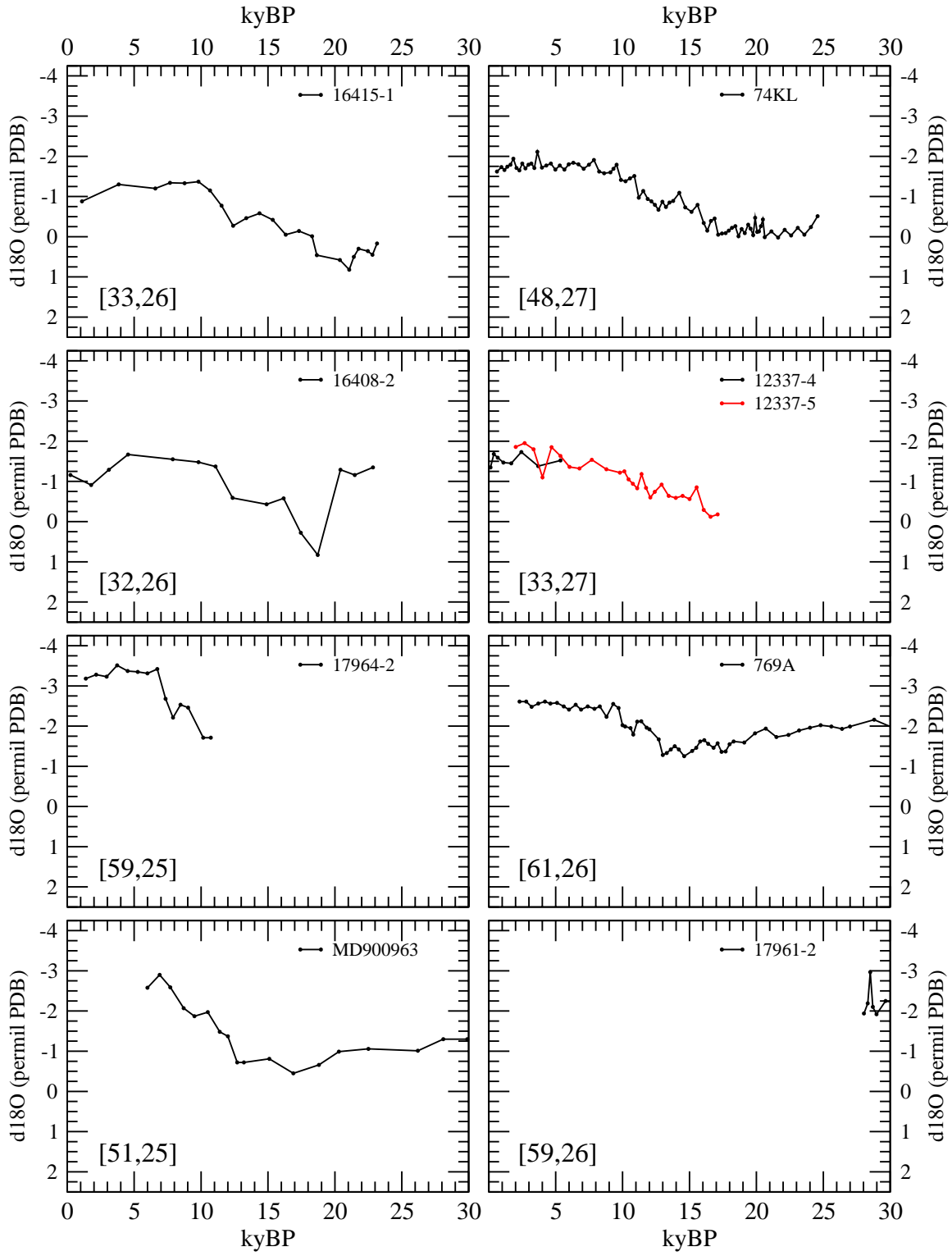


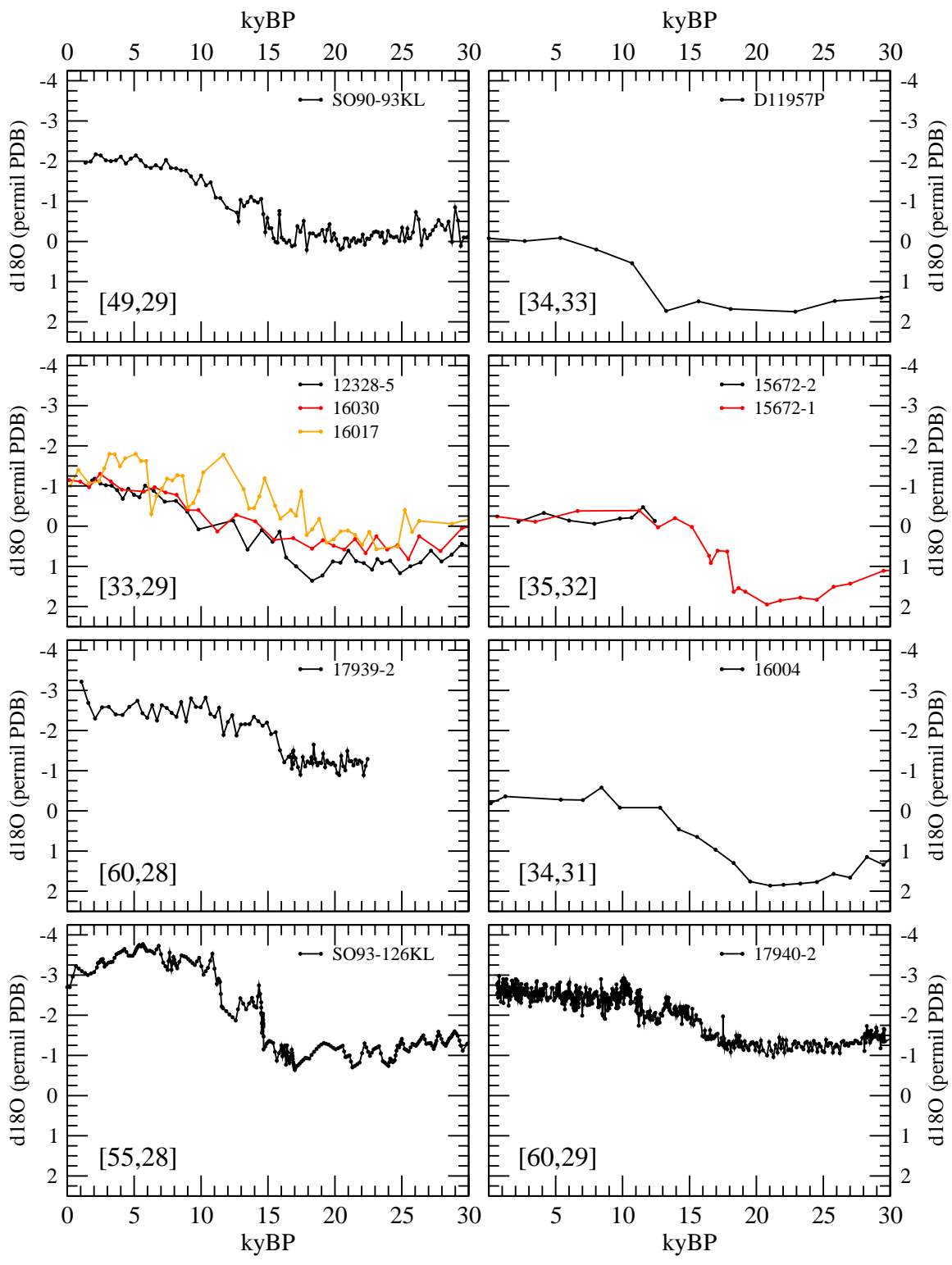


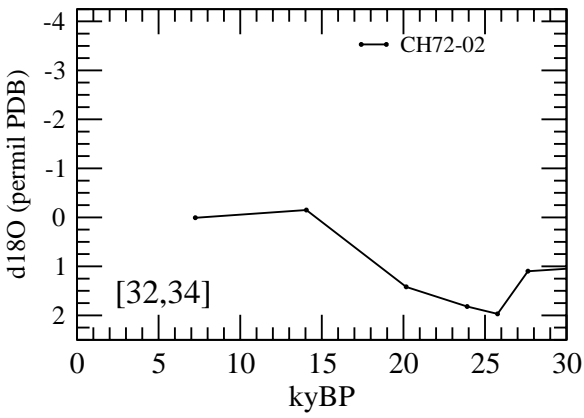
B.3 Downcore $\delta^{18}\text{O}$ Time Series Plots for *Globigerinoides ruber* (white)

Each plot corresponds to a $5^\circ \times 4^\circ$ CGCM grid box and includes the downcore $\delta^{18}\text{O}$ time series of all the cores whose locations are encompassed by that grid box. The [lon#,lat#] of the CGCM grid box is in the lower left corner of each plot. See any of the CGCM grid box maps in this work to locate it on a world map. The plots are arranged in order of increasing latitude starting from lower left and proceeding in an “N” on each page. This may cause seemingly oddly placed stray plots. All x axes are time in kyBP and only go from 0 to 30 kyBP, spanning just the eras of interest in this work and even though data going further back may have been compiled. All y axes are $\delta^{18}\text{O}$ in permil PDB, span the maximum range resulting from including all cores in all grid boxes, and are inverted to be reminiscent of the global mean temperature increase from the LGM to PD. See Chapter 5 for a description of the data, its averaging, and caveats.



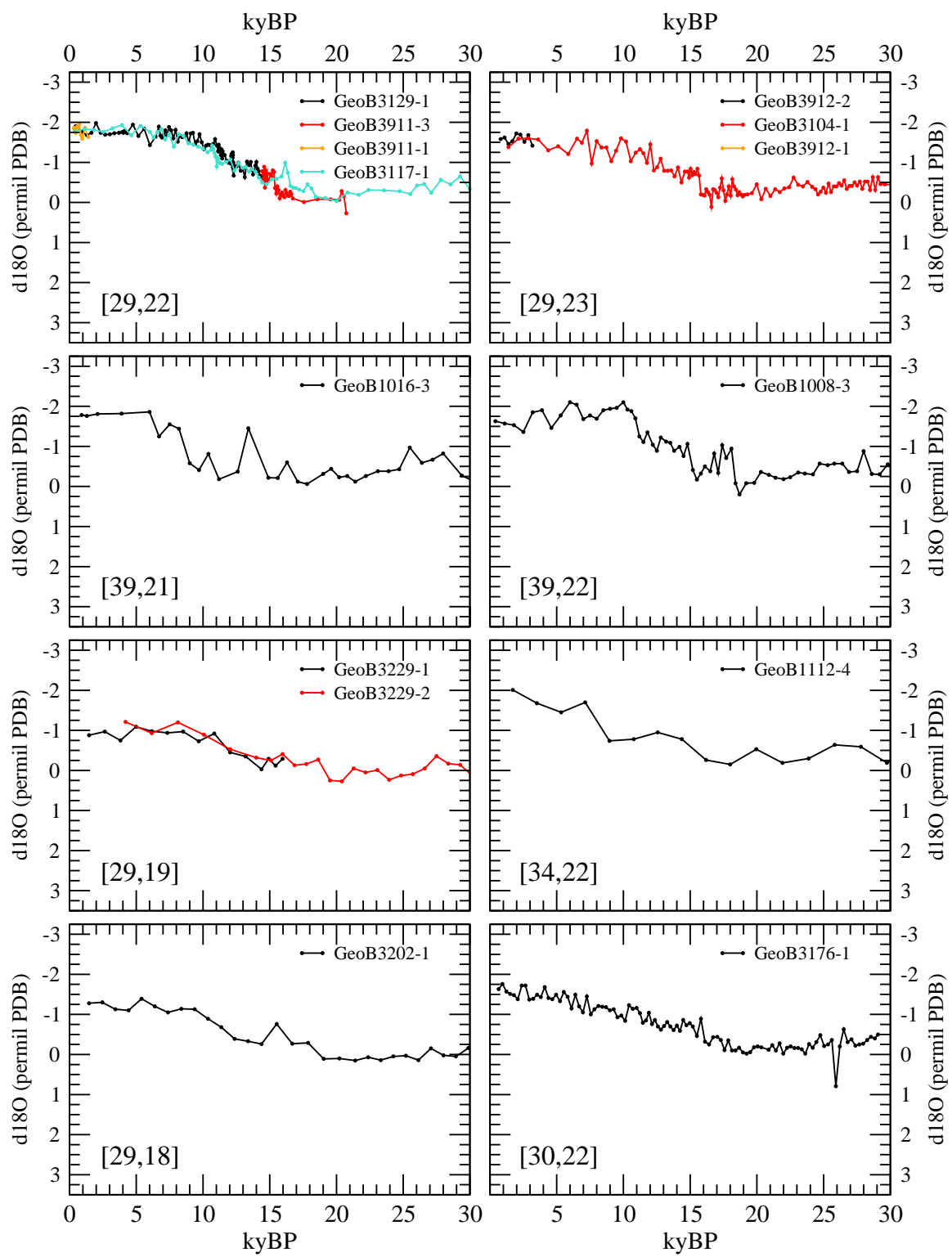


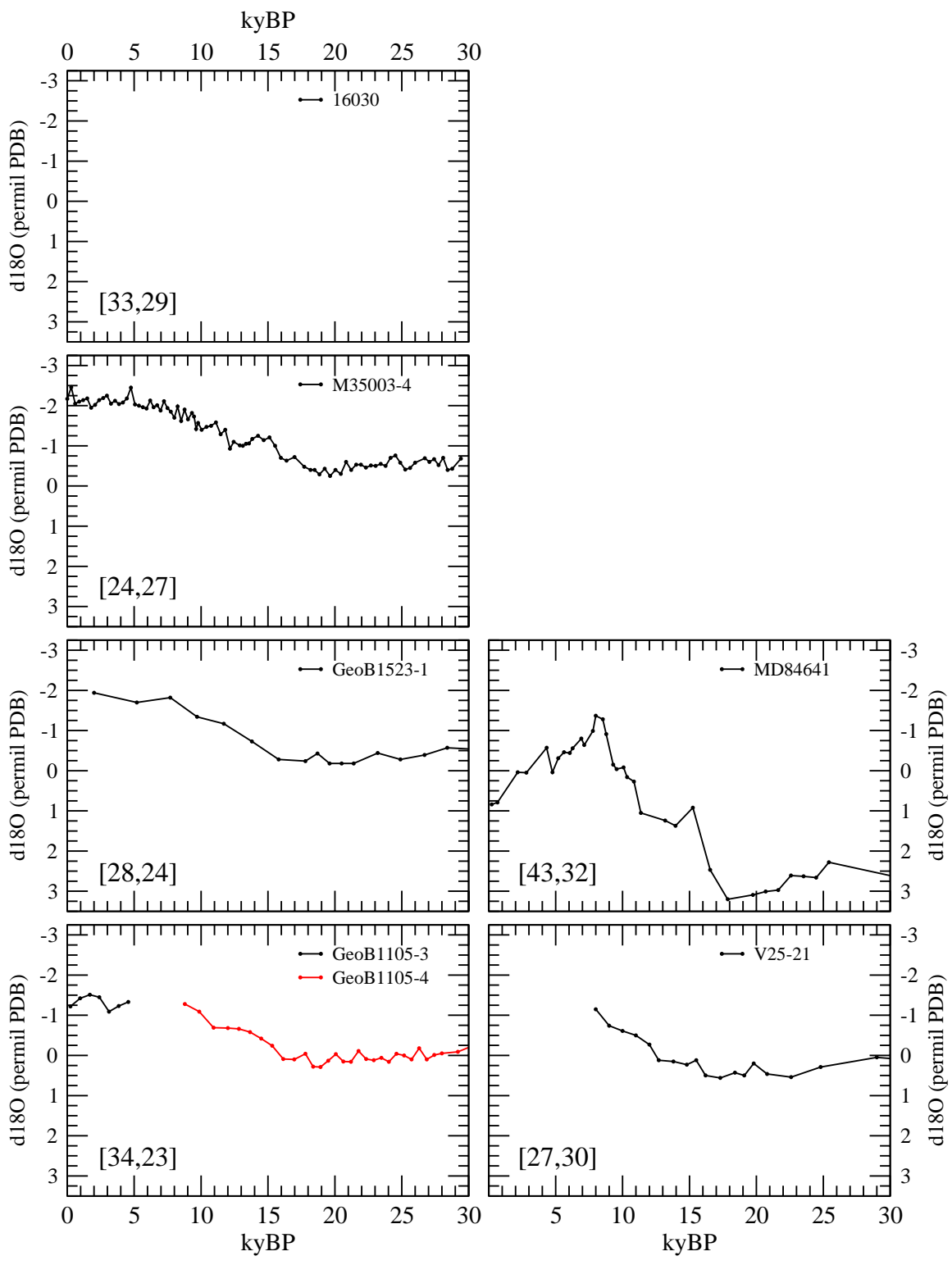




B.4 Downcore $\delta^{18}\text{O}$ Time Series Plots for *Globigerinoides ruber* (pink)

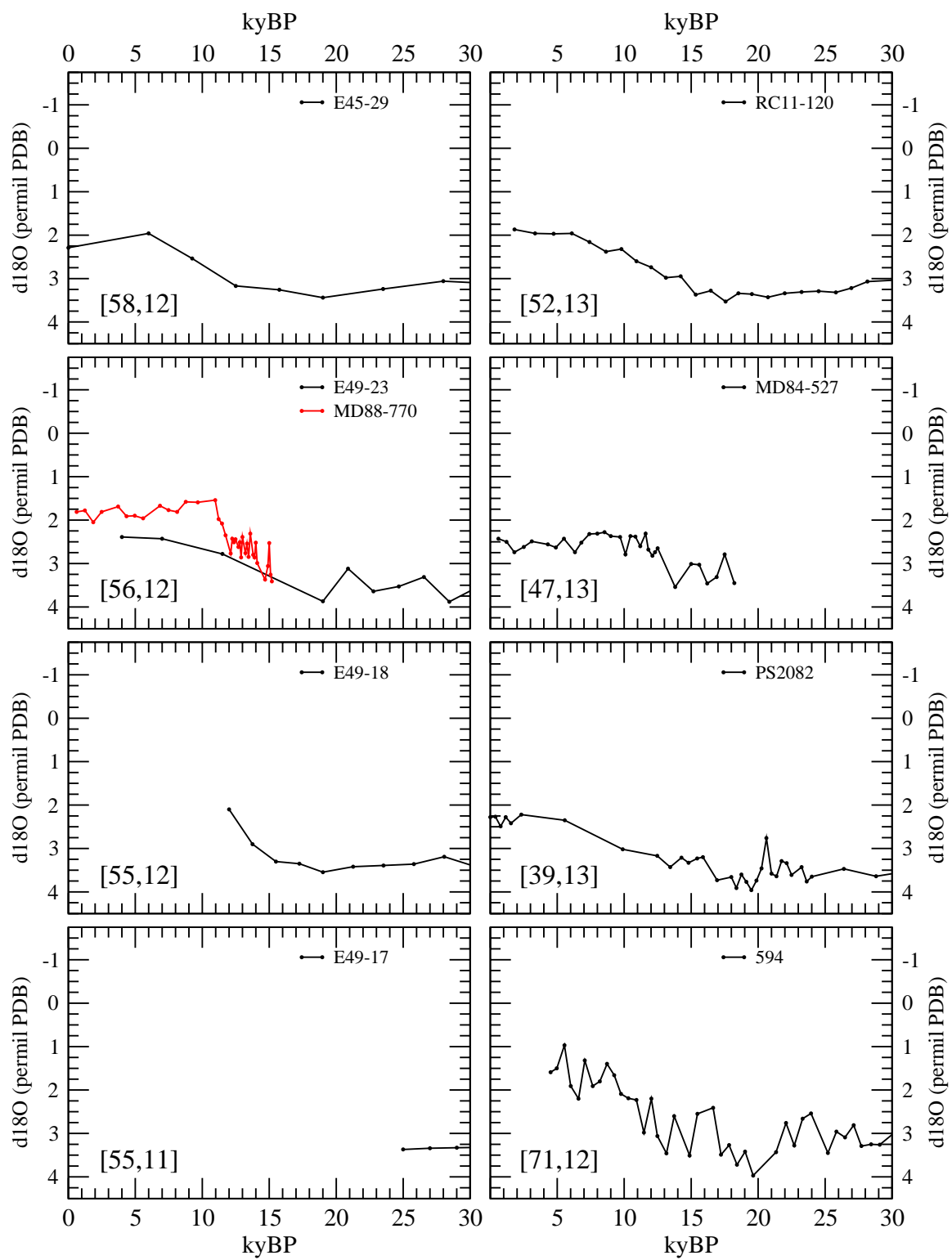
Each plot corresponds to a $5^\circ \times 4^\circ$ CGCM grid box and includes the downcore $\delta^{18}\text{O}$ time series of all the cores whose locations are encompassed by that grid box. The [lon#,lat#] of the CGCM grid box is in the lower left corner of each plot. See any of the CGCM grid box maps in this work to locate it on a world map. The plots are arranged in order of increasing latitude starting from lower left and proceeding in an “N” on each page. This may cause seemingly oddly placed stray plots. All x axes are time in kyBP and only go from 0 to 30 kyBP, spanning just the eras of interest in this work and even though data going further back may have been compiled. All y axes are $\delta^{18}\text{O}$ in permil PDB, span the maximum range resulting from including all cores in all grid boxes, and are inverted to be reminiscent of the global mean temperature increase from the LGM to PD. See Chapter 5 for a description of the data, its averaging, and caveats.

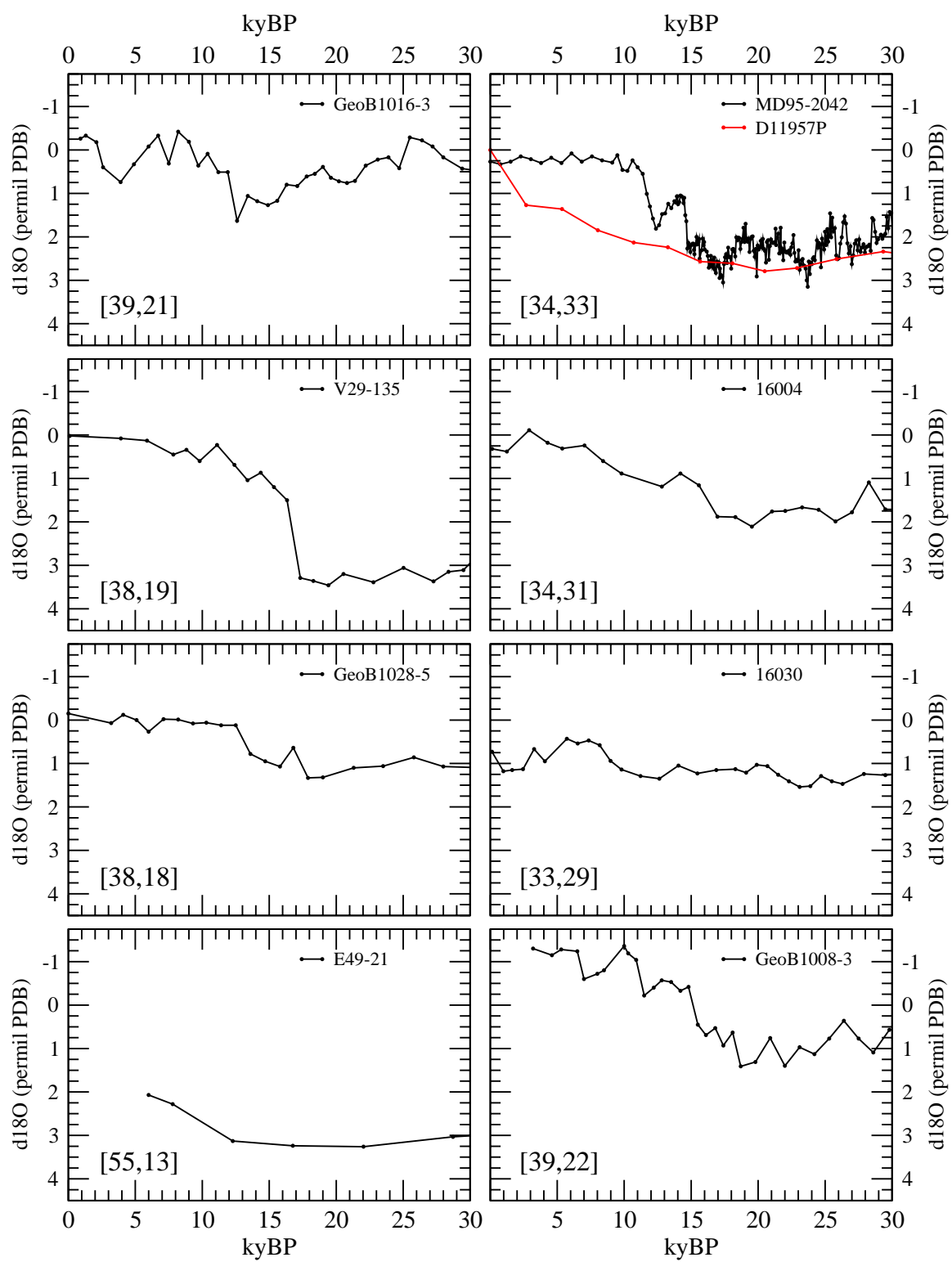


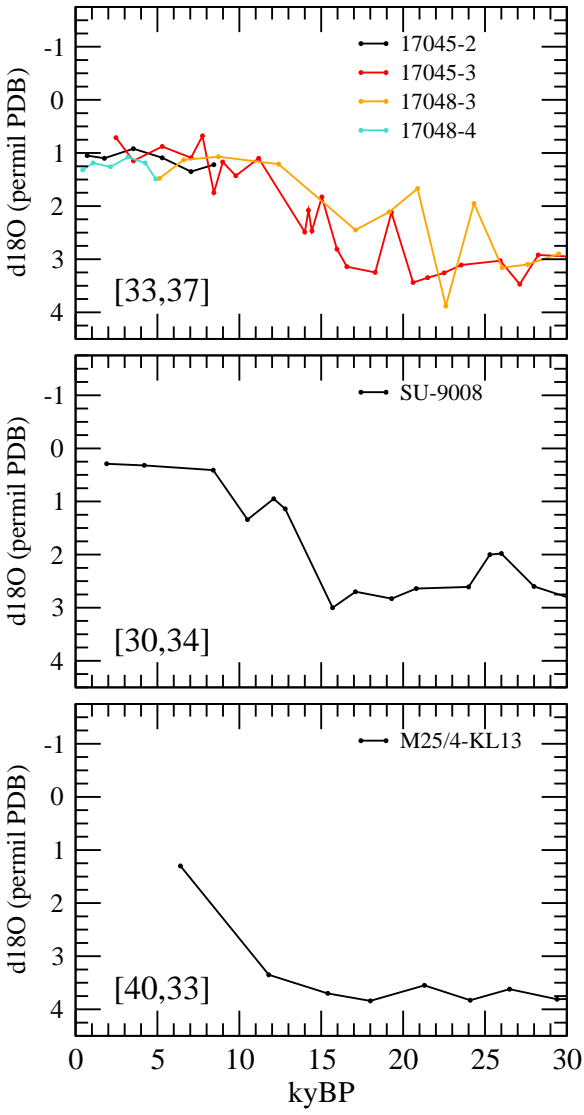


B.5 Downcore $\delta^{18}\text{O}$ Time Series Plots for *Globigerina bulloides*

Each plot corresponds to a $5^\circ \times 4^\circ$ CGCM grid box and includes the downcore $\delta^{18}\text{O}$ time series of all the cores whose locations are encompassed by that grid box. The [lon#,lat#] of the CGCM grid box is in the lower left corner of each plot. See any of the CGCM grid box maps in this work to locate it on a world map. The plots are arranged in order of increasing latitude starting from lower left and proceeding in an “N” on each page. This may cause seemingly oddly placed stray plots. All x axes are time in kyBP and only go from 0 to 30 kyBP, spanning just the eras of interest in this work and even though data going further back may have been compiled. All y axes are $\delta^{18}\text{O}$ in permil PDB, span the maximum range resulting from including all cores in all grid boxes, and are inverted to be reminiscent of the global mean temperature increase from the LGM to PD. See Chapter 5 for a description of the data, its averaging, and caveats.

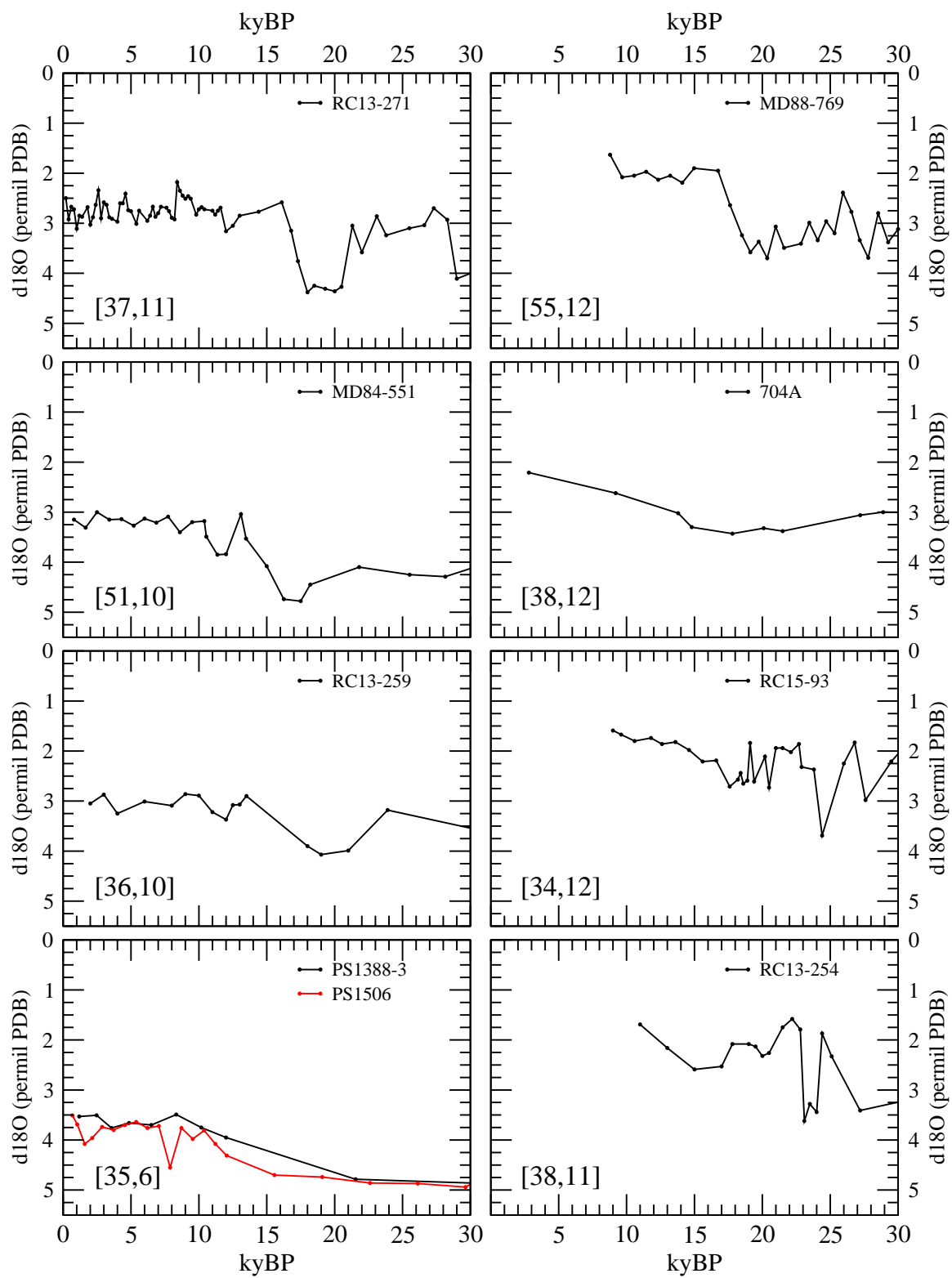


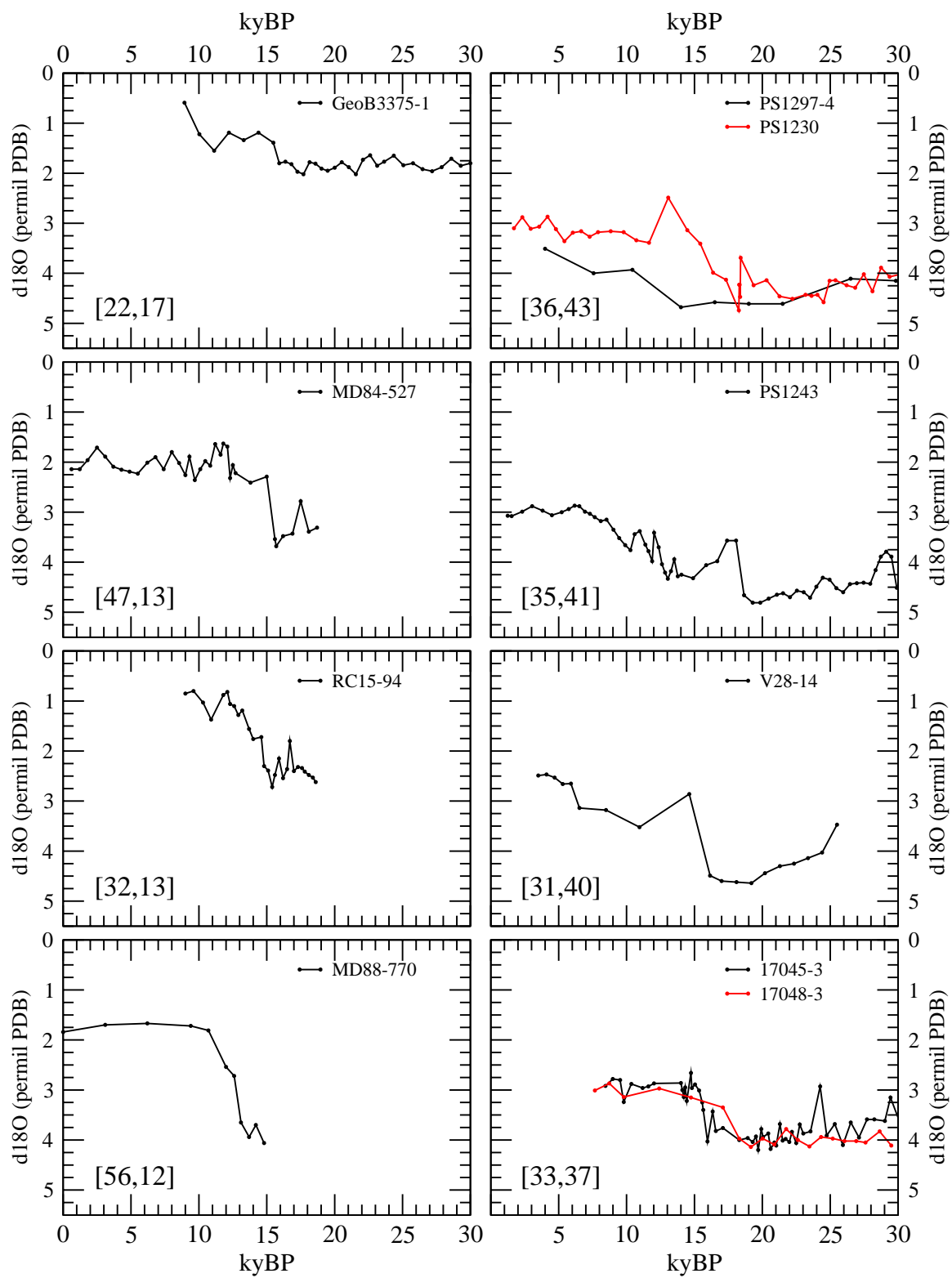


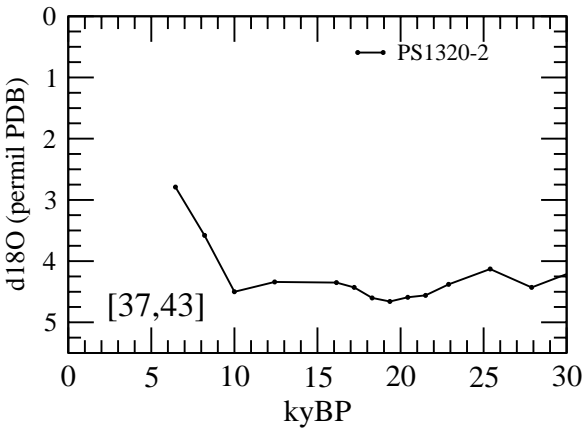


B.6 Downcore $\delta^{18}\text{O}$ Time Series Plots for *Neoglobobulimina papyroderma* (sinistral)

Each plot corresponds to a $5^\circ \times 4^\circ$ CGCM grid box and includes the downcore $\delta^{18}\text{O}$ time series of all the cores whose locations are encompassed by that grid box. The [lon#,lat#] of the CGCM grid box is in the lower left corner of each plot. See any of the CGCM grid box maps in this work to locate it on a world map. The plots are arranged in order of increasing latitude starting from lower left and proceeding in an “N” on each page. This may cause seemingly oddly placed stray plots. All x axes are time in kyBP and only go from 0 to 30 kyBP, spanning just the eras of interest in this work and even though data going further back may have been compiled. All y axes are $\delta^{18}\text{O}$ in permil PDB, span the maximum range resulting from including all cores in all grid boxes, and are inverted to be reminiscent of the global mean temperature increase from the LGM to PD. See Chapter 5 for a description of the data, its averaging, and caveats.

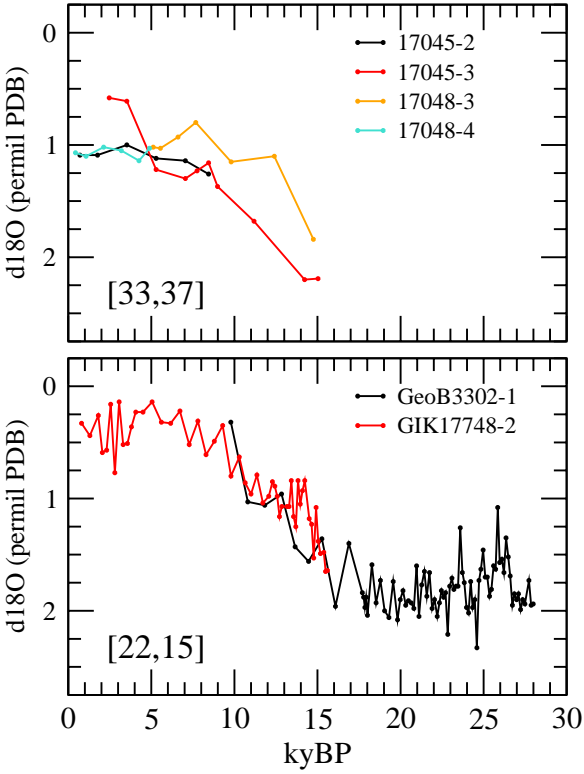






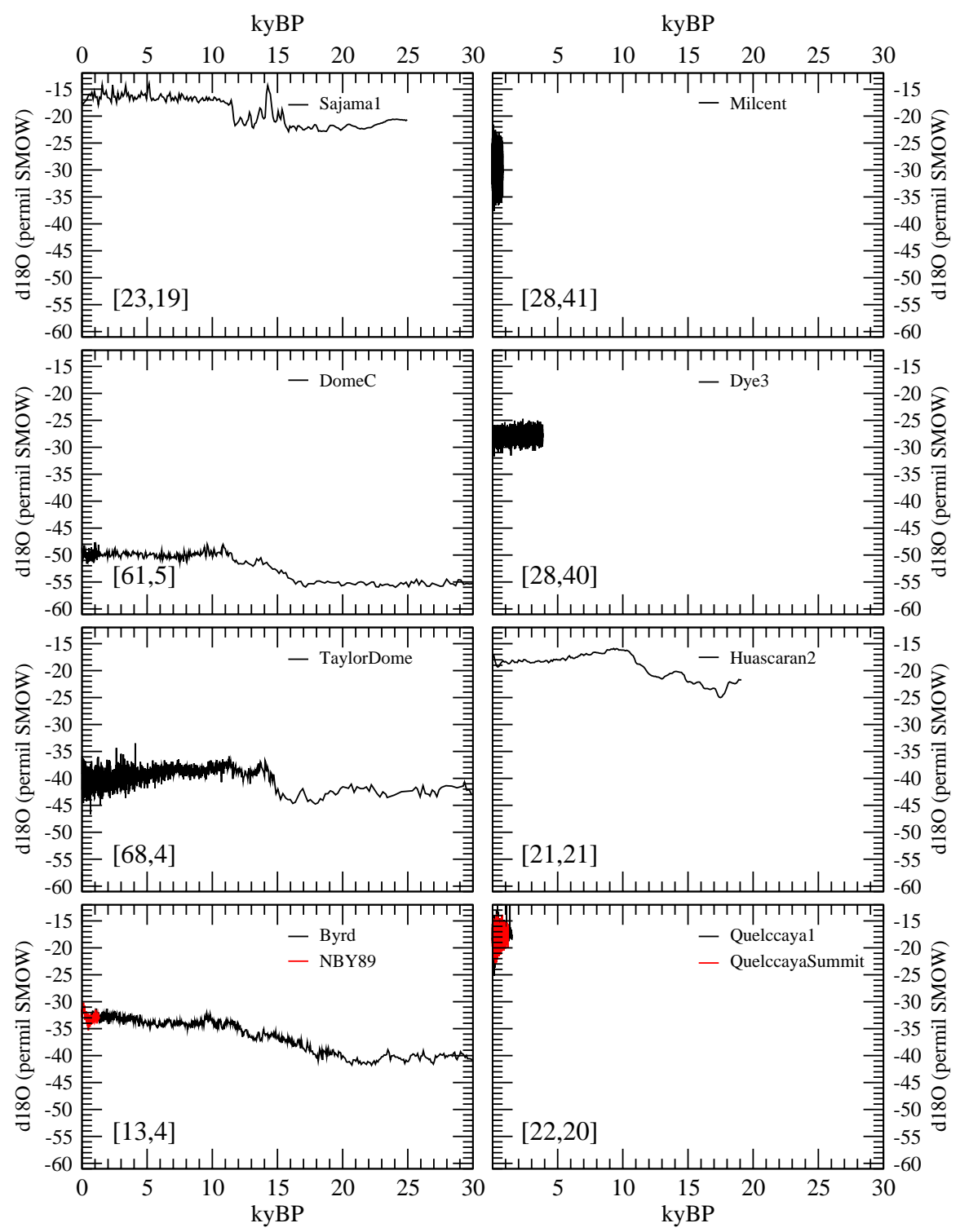
B.7 Downcore $\delta^{18}\text{O}$ Time Series Plots for *Neoglobobulimina papyroderma* (dextral)

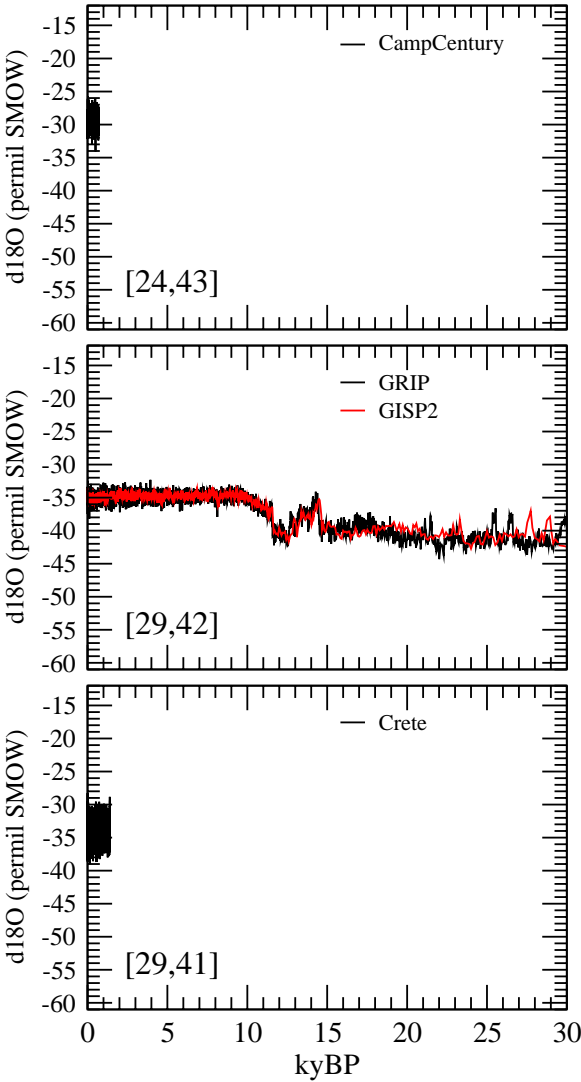
Each plot corresponds to a $5^\circ \times 4^\circ$ CGCM grid box and includes the downcore $\delta^{18}\text{O}$ time series of all the cores whose locations are encompassed by that grid box. The [lon#,lat#] of the CGCM grid box is in the lower left corner of each plot. See any of the CGCM grid box maps in this work to locate it on a world map. The plots are arranged in order of increasing latitude starting from lower left and proceeding in an “N” on each page. This may cause seemingly oddly placed stray plots. All x axes are time in kyBP and only go from 0 to 30 kyBP, spanning just the eras of interest in this work and even though data going further back may have been compiled. All y axes are $\delta^{18}\text{O}$ in permil PDB, span the maximum range resulting from including all cores in all grid boxes, and are inverted to be reminiscent of the global mean temperature increase from the LGM to PD. See Chapter 5 for a description of the data, its averaging, and caveats.



B.8 Downcore $\delta^{18}\text{O}$ Time Series Plots for Glacier Ice H_2O

Each plot corresponds to a $5^\circ \times 4^\circ$ CGCM grid box and includes the downcore $\delta^{18}\text{O}$ time series of all the cores whose locations are encompassed by that grid box. The [lon#,lat#] of the CGCM grid box is in the lower left corner of each plot. See any of the CGCM grid box maps in this work to locate it on a world map. The plots are arranged in order of increasing latitude starting from lower left and proceeding in an “N” on each page. This may cause seemingly oddly placed stray plots. All x axes are time in kyBP and only go from 0 to 30 kyBP, spanning just the eras of interest in this work and even though data going further back may have been compiled. All y axes are $\delta^{18}\text{O}$ in permil SMOW and span the maximum range resulting from including all cores in all grid boxes. See Chapter 5 for a description of the data, its averaging, and caveats.





Appendix C

Downcore $U_{37}^{K'}$ SST Time Series

Core Information

Cores are listed numerically and alphabetically by core name.

Core: BOFS31K **Lat:** 19° 0' **Lon:** -20° 10' **Depth:** 3300 m **References:** Chapman et al. 1996 **Age Model:** A detailed $\delta^{18}\text{O}$ stratigraphy obtained from measurements of the planktonic species *G. bulloides* provides the basis; chronology obtained by attributing ages to key stratigraphic events, which had been identified in other cores from North Atlantic with detailed ^{14}C chronologies, and interpolating between these age control points; prior to interpolation the ^{14}C ages converted to calendar years using the calibration of Bard et al. 1993. **Notes:** Core name is from reference; known as BOFS31/1K in dataset. Age values typed in from reference Table 1. $U_{37}^{K'}$ values not available. Prahl et al. 1988 SST($U_{37}^{K'}$) calibration. **Dataset Sources:** http://www.pangaea.de/ddi/BOFS31-1K_d18O_SST.tab?datasetid=52726&login=0

Core: GIK17748-2 **Lat:** -32° 45' **Lon:** -72° 2' **Depth:** 2545 m **References:** Kim et al. 2002, Lamy et al. 1999 **Age Model:** Based on six AMS ^{14}C dates that were corrected for ^{13}C and for a reservoir age of 400 years and that were converted to calendar years after the method of Bard et al. 1993; linear interpolation between these age control points using a zero-age depth of -.13 m (since core top missing) and a core bottom age of 15.6 kyr; all as specified in second reference. **Notes:** Müller et al. 1998 SST($U_{37}^{K'}$) calibration (identical within error limits to Prahl et al. 1988). **Dataset Sources:** http://www.pangaea.de/ddi/GIK17748-2_Age_SR_UK37_SST.tab?datasetid=66806&login=0

Core: GeoB1008-3 **Lat:** -6° 34.9' **Lon:** 10° 19.1' **Depth:** 3124 m **References:** Schneider et al. 1995, Schneider et al. 1994 **Age Model:** Obtained $\delta^{18}\text{O}$ records

from handpicked samples of planktonic foraminiferal species *G. ruber* and *G. bulloides*; comparison against the SPECMAP stacked record of Imbrie et al. 1984; dataset implies ages are ^{14}C but references indicate they are calendar. **Notes:** Lat minutes and Lon minutes are from first reference; those in dataset are 34.54 and 19.06. Prahl et al. 1988 SST($U_{37}^{K'}$) calibration. **Dataset Sources:** ftp://ftp.ngdc.noaa.gov/paleo/paleocean/sediment_files/complete/gb10083-tab.txt

Core: GeoB1016-3 **Lat:** $-11^{\circ} 46.2'$ **Lon:** $11^{\circ} 40.9'$ **Depth:** 3411 m **References:** Schneider et al. 1995 **Age Model:** Comparison of the $\delta^{18}\text{O}$ records against the SPECMAP stacked record of Imbrie et al. 1984; dataset implies ages are ^{14}C but references indicate they are calendar. **Notes:** Lat minutes and Lon minutes are from reference; those in dataset are 46.02 and 40.54. Prahl et al. 1988 SST($U_{37}^{K'}$) calibration. **Dataset Sources:** ftp://ftp.ngdc.noaa.gov/paleo/paleocean/sediment_files/complete/gb10163-tab.txt

Core: GeoB1023-5 **Lat:** $-17^{\circ} 9.5'$ **Lon:** $11^{\circ} .5'$ **Depth:** 1978 m **References:** Kim et al. 2002b, Kim et al. 2002a **Age Model:** Established by seven AMS ^{14}C determinations on *G. inflata* or on mixed samples containing planktonic foraminiferal tests of *G. inflata* and *G. bulloides* and two conventional ^{14}C dates on TOC from the late Holocene section of a second core (GeoB1023-4) from the same site (correlation between the two cores was based on their CaCO_3 records); a continuous time scale was obtained by linear interpolation between the nine age control points, after converting the ^{14}C ages into calendar years using the CALIB 4.3 algorithm, with no correction for a regional ^{14}C reservoir age (ΔR = the deviation from the surface ocean average of 400 years). **Notes:** Lat minutes and Lon minutes are from references; given as 9.4 and .7 in dataset. Müller et al. 1998 SST($U_{37}^{K'}$) calibration (identical within error limits to Prahl et al. 1988). **Dataset Sources:** http://www.pangaea.de/ddi/GeoB1023-5_Age_SR_UK37_SST.tab?datasetid=88346&login=0

Core: GeoB1028-5 **Lat:** $-20^{\circ} 6.2'$ **Lon:** $9^{\circ} 11.1'$ **Depth:** 2209 m **References:** Schneider et al. 1995, Wefer et al. 1996 **Age Model:** See Core GeoB1016-3. **Notes:** Lat minutes and Lon minutes are from first reference; those in dataset are 6.12 and 11.06. Second reference gives ocean depth as 2215 m. Prahl et al. 1988 SST($U_{37}^{K'}$) calibration. **Dataset Sources:** ftp://ftp.ngdc.noaa.gov/paleo/paleocean/sediment_files/complete/gb10285-tab.txt

Core: GeoB1105-3 **Lat:** $-1^{\circ} 39.9'$ **Lon:** $-12^{\circ} 25.7'$ **Depth:** 3225 m **References:** Müller et al. 1998, Bickert and Wefer 1996, Wefer et al. 1996 **Age Model:** Graphic correlation of the oxygen isotope record to the Imbrie et al. 1984 SPECMAP standard record. **Notes:** Ocean depth above is that given in second/third references for GeoB1105-3/4; that in first reference is 3232 m; that in datasets for this core is 3231 m. Core's depth/age data from first dataset applied to its $U_{37}^{K'}$ data from second dataset. SST($U_{37}^{K'}$) calibration is from first reference but is identical within error limits to Prahl et al. 1988. **Dataset Sources:** http://www.pangaea.de/ddi/GeoB1105_age_isotopes_CaCO3_TOC.tab?datasetid=58768&login=0, <http://www.pangaea.de/ddi/>

SST_UK37.tab?datasetid=54788&login=0

Core: GeoB1105-4 **Lat:** -1° 39.9' **Lon:** -12° 25.7' **Depth:** 3225 m **References:** Schneider et al. 1996, Bickert and Wefer 1996, Wefer et al. 1996 **Age Model:** Oxygen isotope analyses of *G. ruber*; graphic correlation of $\delta^{18}\text{O}$ records with Imbrie et al. 1984 SPECMAP standard record. **Notes:** Core's depth/age data from first dataset applied to its $\text{U}_{37}^{K'}$ data from second dataset. Prah et al. 1988 SST($\text{U}_{37}^{K'}$) calibration. **Dataset Sources:** http://www.pangaea.de/ddi/GeoB1105_age_isotopes_CaCO3_TOC.tab?datasetid=58768&login=0, http://www.pangaea.de/ddi/GeoB1105-4_d18O_ruber_TOC_UK37_SST.tab?datasetid=54864&login=0

Core: GeoB1710-3 **Lat:** -23° 25.8' **Lon:** 11° 42' **Depth:** 2987 m **References:** Kirst et al. 1999 **Age Model:** Visually correlated with the normalized SPECMAP standard record of Imbrie et al. 1984; twenty-six isotopic events were identified between 6000 and 245,000 yr ago; dataset implies ages are ^{14}C but reference indicates they are calendar. **Notes:** Prah et al. 1988 SST($\text{U}_{37}^{K'}$) calibration. **Dataset Sources:** http://www.pangaea.de/ddi/GeoB1710-3_TOC_Alkenones_SST.tab?datasetid=58041&login=0

Core: GeoB3302-1 **Lat:** -33° 13' **Lon:** -72° 6' **Depth:** 1498 m **References:** Kim et al. 2002, Lamy et al. 1999 **Age Model:** Principally based on seven AMS ^{14}C dates that were corrected for ^{13}C and for a reservoir age of 400 years and that were converted to calendar years after the method of Bard et al. 1993; linear interpolation applied between these control points; additionally, for the uppermost sample, the oxygen isotope record was correlated with that for core GIK17748-2. **Notes:** Lat minutes and Lon minutes are from references; given as 13.1 and 5.4 in dataset. Müller et al. 1998 SST($\text{U}_{37}^{K'}$) calibration (identical within error limits to Prah et al. 1988). **Dataset Sources:** http://www.pangaea.de/ddi/GeoB3302-1_Age_SR_UK37_SST.tab?datasetid=66805&login=0

Core: M35003-4 **Lat:** 12° 5' **Lon:** -61° 15' **Depth:** 1299 m **References:** Rühlmann et al. 1999 **Age Model:** Nine ^{14}C ages were determined on monospecific samples of *G. ruber* (white) and four ages on a mixture of *G. ruber* (white and pink), *G. sacculifer* and *O. universa*. The ^{14}C ages were corrected for a reservoir age of 400 years (Hughen 1998); they were then converted to calendar ages using the program CALIB 3.0.3c (Stuiver and Reimer 1993) for ages < 20,000 yr and using the equation given in the caption of Figure 3 of Bard et al. 1997 for ages > 20,000 yr. For the deglacial, conservatively estimated the calendar year chronology to be good within ± 500 yr. Before about 25 cal. kyr BP there are only a limited number of calibration points, thus the assumed correction has an uncertainty within at least $\pm 1,500$ yr. **Notes:** Dataset is from GeoB of Institute part of Pangaea; the associated dataset in the core data part (DataSet ID 55923) does not have the ages interpolated (linearly?) between the corrected/calibrated ^{14}C ages; $\text{U}_{37}^{K'}$ had to be calculated from dataset as $\text{C37:2}/(\text{C37:3}+\text{C37:2})$. Müller et al. 1998 SST($\text{U}_{37}^{K'}$) calibration (identical within error limits to Prah et al. 1988). **Dataset Sources:** <http://www.pangaea.de/ddi?retr=/>

Institutes/GeoB/CRuehlemann/Nature_1999.retr&conf=/Projects/GeoB/CRuehlemann/Nature_1999.2.conf&format=textfile

Core: MD79257 **Lat:** -20° 24' **Lon:** 36° 20' **Depth:** 1260 m **References:** Bard et al. 1997, Sonzogni et al. 1998 **Age Model:** Based on AMS ^{14}C dating of *G. ruber*; calibrated to calendar years back to 42 kyr using equation based on U-Th dating of corals; final timescale obtained by fifth-order polynomial fitting through these ages. **Notes:** $\text{U}_{37}^{K'}$ values typed in from second reference Table 4, with swapped digits of value at 812 cm depth corrected. Prahl et al. 1988 SST($\text{U}_{37}^{K'}$) calibration. **Dataset Sources:** ftp://ftp.ngdc.noaa.gov/paleo/paleocean/by_contributor/bard1997/bard1997.txt

Core: MD85668 **Lat:** -0° 1' **Lon:** 46° 2' **Depth:** 4020 m **References:** Bard et al. 1997 **Age Model:** Based on matching $\delta^{18}\text{O}$ record with SPECMAP timescale. **Notes:** Lat degrees is from reference; that from dataset is 0 (i.e., N not S). $\text{U}_{37}^{K'}$ values not available. Prahl et al. 1988 SST($\text{U}_{37}^{K'}$) calibration. **Dataset Sources:** ftp://ftp.ngdc.noaa.gov/paleo/paleocean/by_contributor/bard1997/bard1997.txt

Core: MD85674 **Lat:** 3° 11' **Lon:** 50° 26' **Depth:** 4875 m **References:** Bard et al. 1997 **Age Model:** See Core MD85668. **Notes:** $\text{U}_{37}^{K'}$ values not available. Prahl et al. 1988 SST($\text{U}_{37}^{K'}$) calibration. **Dataset Sources:** ftp://ftp.ngdc.noaa.gov/paleo/paleocean/by_contributor/bard1997/bard1997.txt

Core: MD900963 **Lat:** 5° 4' **Lon:** 73° 53' **Depth:** 2450 m **References:** Rostek et al. 1993, Rostek et al. 1997 **Age Model:** Detailed $\delta^{18}\text{O}$ stratigraphy established on surface dwelling planktonic foraminifer *G. ruber* (white); timescale obtained by tuning $\delta^{18}\text{O}$ record to SPECMAP record of Imbrie et al. 1984. **Notes:** Core name is from references; known as MD90-963 in first dataset and MD90963 in second dataset. Lat minutes and Lon minutes are from references and second dataset; first dataset incorrectly has these values as decimal parts. Ages from second dataset applied to $\text{U}_{37}^{K'}$ values and more-precise SSTs from first dataset; first SST from both datasets indicated in first reference to actually be from climatology due to missing coretop so removed here; last three from second dataset don't match first dataset so not used here; first dataset has more than second so remainder not used here. Prahl et al. 1988 SST($\text{U}_{37}^{K'}$) calibration. **Dataset Sources:** http://www.pangaea.de/ddi/MD90-963_UKs37_SST.tab?datasetid=55875&login=0, ftp://ftp.ngdc.noaa.gov/paleo/paleocean/by_contributor/bard1997/bard1997.txt

Core: MD952040 **Lat:** 40° 35' **Lon:** -9° 52' **Depth:** 2465 m **References:** Pailler and Bard 2002 **Age Model:** Established by fitting its CaCO_3 profile to the equivalent for core MD952042. **Notes:** Known as MD95-2040 in dataset. Prahl et al. 1988 SST($\text{U}_{37}^{K'}$) calibration. **Dataset Sources:** http://www.pangaea.de/ddi/MD95-2040_geochemistry.tab?datasetid=96865&login=0

Core: MD952042 **Lat:** 37° 45' **Lon:** -10° 10' **Depth:** 3146 m **References:**

Pailler and Bard 2002, Cayre et al. 1999 **Age Model:** Oxygen isotopic composition of planktonic foraminifer *G. bulloides*; MIS 6-4 were identified, and ages given to their boundaries, by comparison with the stacked isotopic record of Martinson et al. 1987; for the Holocene and last deglaciation, ages of nearby core SU8118, derived from more than 22 AMS ^{14}C ages converted to calendar ages via Bard et al. 1987/1996, were used. **Notes:** Known as MD95-2042 in third reference and dataset. Lat minutes is from first reference; that in other references and dataset is 48. Pahl et al. 1988 SST($U_{37}^{K'}$) calibration. **Dataset Sources:** <http://www.pangaea.de/ddi/MD95-2042-geochemistry.tab?datasetid=96864&login=0>

Core: SU8118 **Lat:** 37° 46' **Lon:** -10° 11' **Depth:** 3135 m **References:** Bard et al. 2000 **Age Model:** Based on translating the original AMS ^{14}C ages into calendar ages by means of the most recent ^{14}C calibration; beyond 20,000 cal yr B.P. also used the ^{14}C ages measure on a nearby core, MD952039, which is precisely tied to SU8118 through correlation of magnetic properties records. **Notes:** Pahl et al. 1988/Müller et al. 1998 SST($U_{37}^{K'}$) calibration (#1 T $U_{37}^{K'}$ in dataset). **Dataset Sources:** <http://www.sciencemag.org/feature/data/1050685.shl>

Core: TY93-929/P **Lat:** 13° 42' **Lon:** 53° 15' **Depth:** 2490 m **References:** Rostek et al. 1997 **Age Model:** An oxygen isotope stratigraphy established on the subsurface dwelling planktonic foraminifera *N. dutertrei*; correlation with the SPECMAP standard time scale of Imbrie et al. 1984 and Martinson et al. 1987. **Notes:** Core name is from reference; known as TY93929/P in dataset. $U_{37}^{K'}$ values not available. Pahl et al. 1988 SST($U_{37}^{K'}$) calibration. **Dataset Sources:** ftp://ftp.ngdc.noaa.gov/paleo/paleocean/by_contributor/bard1997/bard1997.txt

Core: W8402A-14GC **Lat:** 0° 57.2' **Lon:** -138° 57.3' **Depth:** 4287 m **References:** Pahl et al. 1989 **Age Model:** Based on cross correlation of the $\delta^{18}\text{O}$ stratigraphy obtained for the planktonic foraminifera *G. tumida* with the SPECMAP stack of Imbrie et al. 1984. **Notes:** Core name is from reference; known as W8402A-14 in dataset. Age values typed in from reference TABLE 1, with 7.4 and 24.4 kyr added here by linear interpolation to match extra $U_{37}^{K'}$ /SST data in dataset below .455 m core depth. Pahl et al. 1988 SST($U_{37}^{K'}$) calibration. **Dataset Sources:** <http://www.pangaea.de/ddi?datasetid=51936&login=0>

Core: W8709A-8PC **Lat:** 42° 15.7' **Lon:** -127° 40.7' **Depth:** 3111 m **References:** Pahl et al. 1995, Lyle et al. 1992 **Age Model:** From second reference; based on a combination of AMS ^{14}C dates and $\delta^{18}\text{O}$ stratigraphy on benthic foraminifera; the former for the last 23 kyr and the latter throughout the core; the ^{14}C dates were corrected to a calendar age assuming that subarctic surface waters have a reservoir age of 717 ± 47 years and using a linear correction of ^{14}C age to ^{230}Th age; the $\delta^{18}\text{O}$ stratigraphy was matched to the high-resolution isotope stack and linked to the ^{14}C -based time scale by minor adjustments. **Notes:** Known as W8709A-8 in dataset. Lat minutes is from second reference and dataset; that in first reference is 32.5. Pahl et al. 1988 SST($U_{37}^{K'}$) calibration. **Dataset Sources:** <http://www.pangaea.de/ddi?>

datasetid=52696&login=0

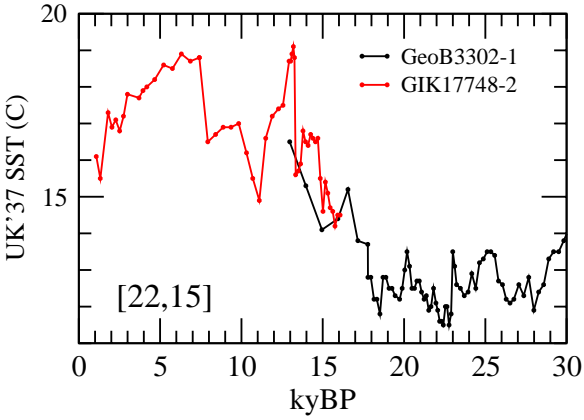
Core: W8709A-8TC **Lat:** 42° 15.7' **Lon:** -127° 40.7' **Depth:** 3111 m **References:** Prahl et al. 1995, Lyle et al. 1992 **Age Model:** See Core W8709A-8PC. **Notes:** Lat minutes is from second reference and dataset; that in first reference is 32.5. Prahl et al. 1988 SST($U_{37}^{K'}$) calibration. **Dataset Sources:** <http://www.pangaea.de/ddi?datasetid=52696&login=0>

Appendix D

Downcore $U_{37}^{K'}$ SST Time Series Plots

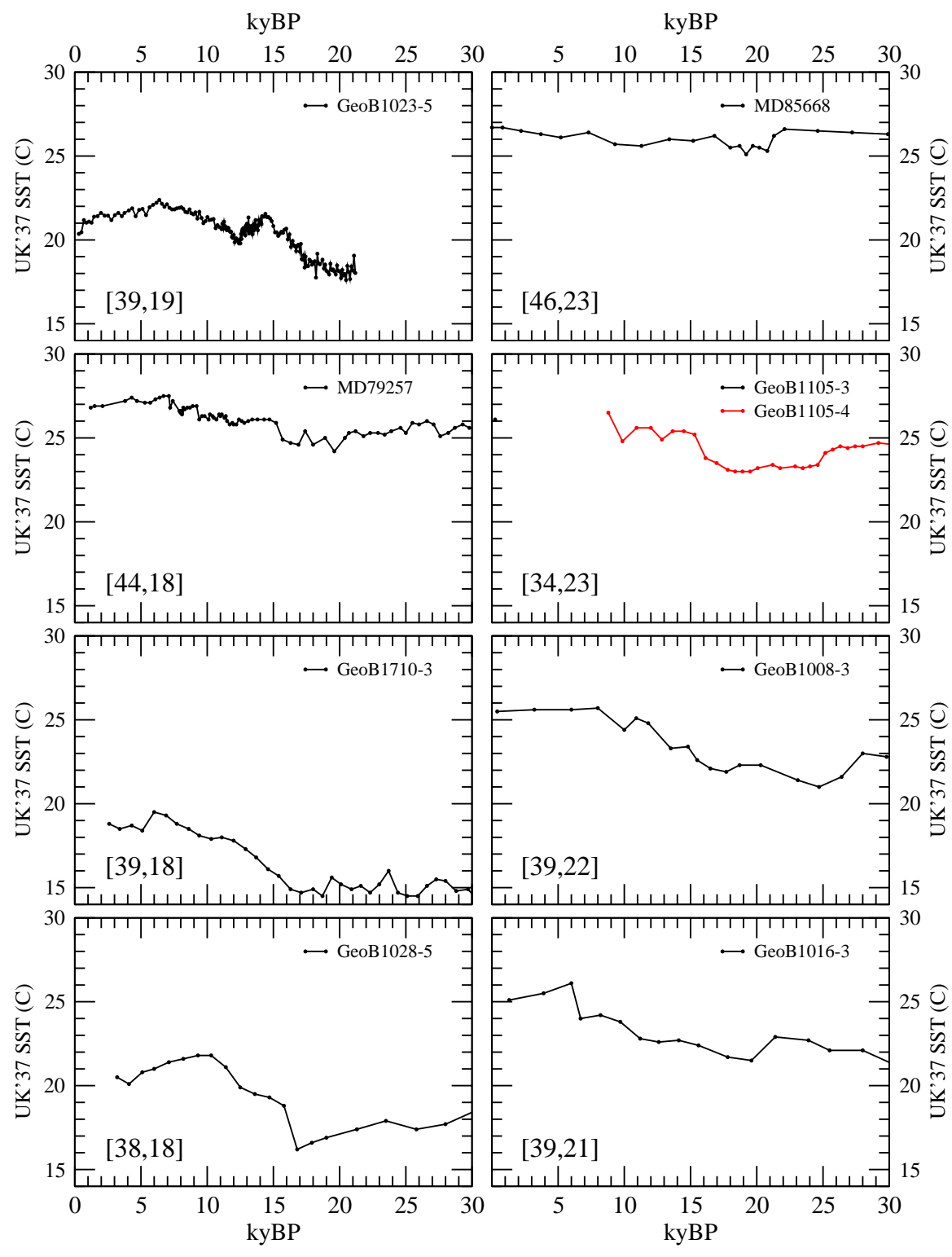
D.1 Downcore $U_{37}^{K'}$ SST Time Series Plots for the Southern Extra-Tropics

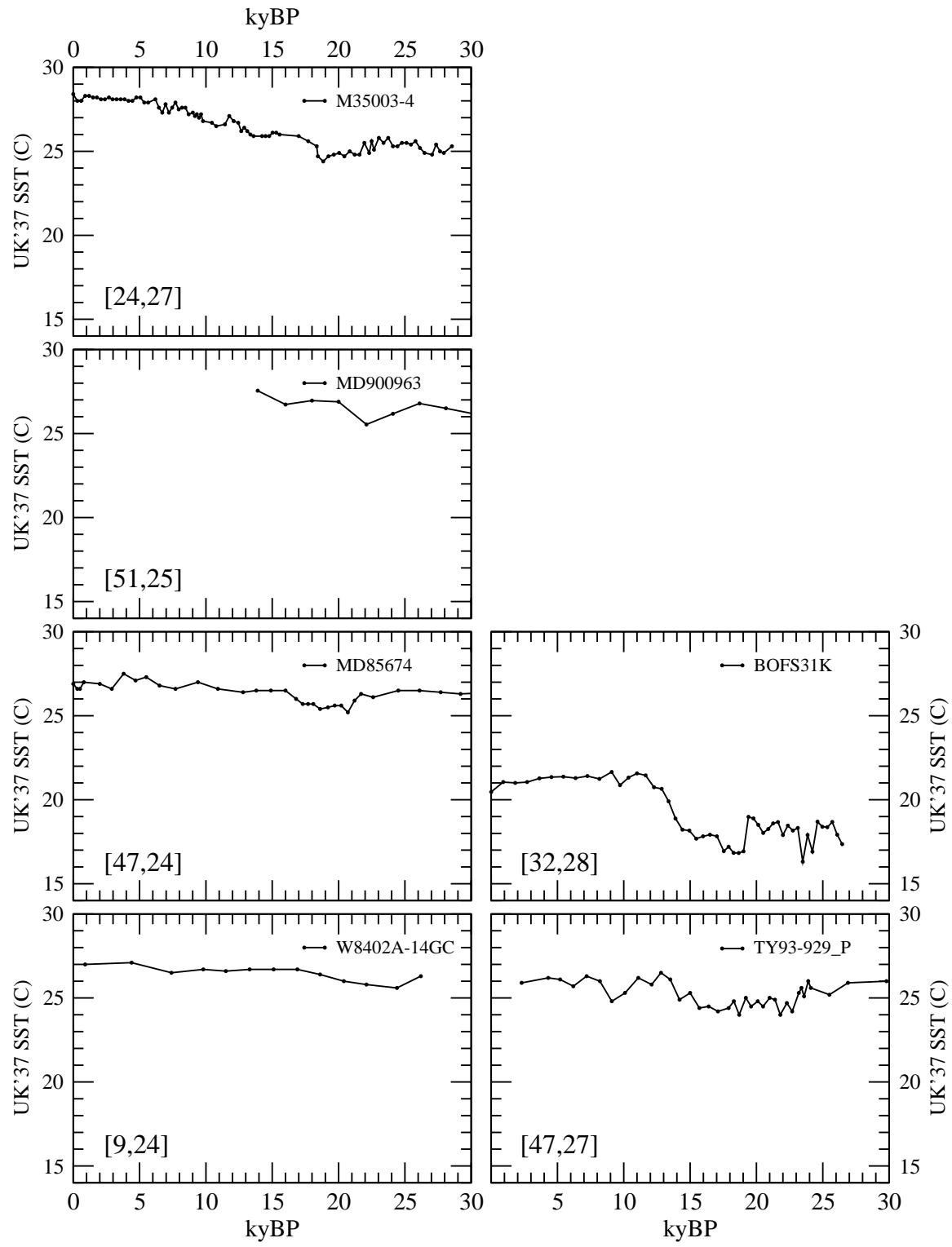
Each plot corresponds to a $5^\circ \times 4^\circ$ CGCM grid box and includes the downcore $U_{37}^{K'}$ SST (sea surface temperature) time series of all the cores whose locations are encompassed by that grid box. The [lon#,lat#] of the CGCM grid box is in the lower left corner of each plot. See any of the CGCM grid box maps in this work to locate it on a world map. The plots are arranged in order of increasing latitude starting from lower left and proceeding in an “N” on each page. This may cause seemingly oddly placed stray plots. All x axes are time in kyBP and only go from 0 to 30 kyBP, spanning just the eras of interest in this work and even though data going further back may have been compiled. All y axes are $U_{37}^{K'}$ SST in Celsius and span the maximum range resulting from including all cores in all grid boxes. See Section 7.2.2 for a description of the data, its averaging, and caveats.



D.2 Downcore $U_{37}^{K'}$ SST Time Series Plots for the Tropics

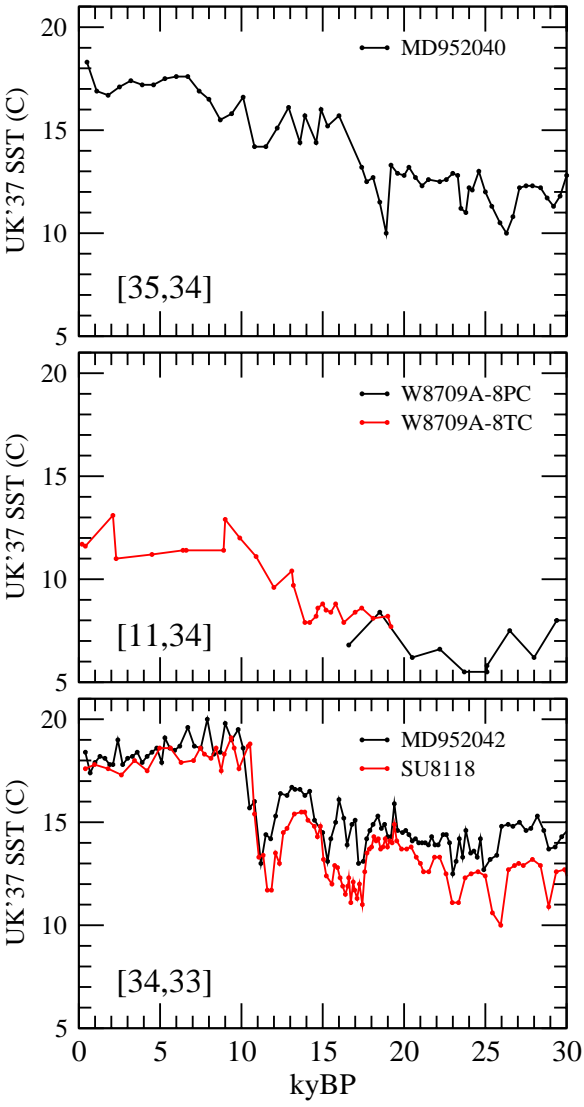
Each plot corresponds to a $5^\circ \times 4^\circ$ CGCM grid box and includes the downcore $U_{37}^{K'}$ SST (sea surface temperature) time series of all the cores whose locations are encompassed by that grid box. The [lon#,lat#] of the CGCM grid box is in the lower left corner of each plot. See any of the CGCM grid box maps in this work to locate it on a world map. The plots are arranged in order of increasing latitude starting from lower left and proceeding in an “N” on each page. This may cause seemingly oddly placed stray plots. All x axes are time in kyBP and only go from 0 to 30 kyBP, spanning just the eras of interest in this work and even though data going further back may have been compiled. All y axes are $U_{37}^{K'}$ SST in Celsius and span the maximum range resulting from including all cores in all grid boxes. See Section 7.2.2 for a description of the data, its averaging, and caveats.





D.3 Downcore $U_{37}^{K'}$ SST Time Series Plots for the Northern Extra-Tropics

Each plot corresponds to a $5^\circ \times 4^\circ$ CGCM grid box and includes the downcore $U_{37}^{K'}$ SST (sea surface temperature) time series of all the cores whose locations are encompassed by that grid box. The [lon#,lat#] of the CGCM grid box is in the lower left corner of each plot. See any of the CGCM grid box maps in this work to locate it on a world map. The plots are arranged in order of increasing latitude starting from lower left and proceeding in an “N” on each page. This may cause seemingly oddly placed stray plots. All x axes are time in kyBP and only go from 0 to 30 kyBP, spanning just the eras of interest in this work and even though data going further back may have been compiled. All y axes are $U_{37}^{K'}$ SST in Celsius and span the maximum range resulting from including all cores in all grid boxes. See Section 7.2.2 for a description of the data, its averaging, and caveats.



Appendix E

Downcore Mg/Ca SST Time Series Core Information

Cores are listed numerically and alphabetically by core name.

Core: CP6001-4PC,TC **Lat:** 14° 55' **Lon:** -71° 50' **Depth:** 3645 m **Mg/Ca Sources:** *Globigerinoides sacculifer* **References:** Hastings et al. 1998 **Age Model:** Ages estimated by assigning isotope stage 1/2 boundary to core depth at which *G. menardii* appears and assuming a constant sedimentation rate through stage 1; LGM assigned to a specific core depth on the basis of $\delta^{18}\text{O}$ values; ages for stage 2 and early stage 3 estimated on basis of constant sedimentation rate; ages for deepest samples based on assigning stage 5e (123.8 ka) at a specific core depth and a constant sedimentation rate for stages 3-6. **Notes:** A composite of piston (PC) and trigger (TC). Data typed in from reference Table 2. **Dataset Sources:** Reference

Core: E11-2 **Lat:** -56° 4' **Lon:** -115° 5' **Depth:** 3094 m **Mg/Ca Sources:** *Neogloboquadrina pachyderma (sinistral)* **References:** Mashiotta et al. 1999, Nin-nemann and Charles 1997 **Age Model:** Correlation of planktonic $\delta^{18}\text{O}$ record with counterparts in benchmark cores with existing well established age models; specific isotopic events assigned ages based on this correlation and an interpolation curve applied to generate ages between control points; for 40 kyr to present a chronology for reference core RC11-83, constrained by 14 AMS ^{14}C dates, was used that was slightly different from the SPECMAP orbitally tuned chronology because of conversion of ^{14}C dates to calendar ages; for 300 kyr to 40 kyr $\delta^{18}\text{O}$ series tied to planktonic $\delta^{18}\text{O}$ of Sub-antarctic reference core RC11-120 by using Martinson et al. 1987; for older than 300 kyr, the SPECMAP chronology of Imbrie et al. 1984 used. **Dataset Sources:** ftp://ftp.ngdc.noaa.gov/paleo/contributions_by_author/mashiotta1999/mashiotta1999.txt

Core: EN066-17GGC **Lat:** 5° 22' **Lon:** -21° 5' **Depth:** 3050 m **Mg/Ca Sources:** *Globigerinoides sacculifer* **References:** Hastings et al. 1998 **Age Model:** Based on $\delta^{18}\text{O}$ measurements on *C. wuellerstorfi*; isotope stage boundaries located at midpoint between $\delta^{18}\text{O}$ maxima and minima; ages associated with these boundaries from the stacked SPECMAP curve of Imbrie et al. 1984 and Martinson et al. 1987; all ages in calendar years using a multilinear algorithm based on the original linear equation. **Notes:** Data typed in from reference Table 1. **Dataset Sources:** Reference

Core: GeoB1105 **Lat:** -1° 39.9' **Lon:** -12° 25.7' **Depth:** 3225 m **Mg/Ca Sources:** *Globigerinoides sacculifer* **References:** Nürnberg et al. 2000, Bickert and Wefer 1996 **Age Model:** Based on graphic correlation of *C. wuellerstorfi* $\delta^{18}\text{O}$ records to the $\delta^{18}\text{O}$ standard record of Martinson et al. 1987. **Notes:** Briefly referred to as GeoB 1105-3/4 in first reference. **Dataset Sources:** ftp://ftp.ngdc.noaa.gov/paleo/contributions_by_author/nuernberg2000/1105_mg-data.txt

Core: GeoB1112 **Lat:** -5° 46.2' **Lon:** -10° 44.7' **Depth:** 3122 m **Mg/Ca Sources:** *Globigerinoides sacculifer* **References:** Nürnberg et al. 2000, Bickert and Wefer 1996 **Age Model:** See Core GeoB1105. **Notes:** Briefly referred to as GeoB 1112-3/4 in first reference. **Dataset Sources:** ftp://ftp.ngdc.noaa.gov/paleo/contributions_by_author/nuernberg2000/1112_mg-data.txt

Core: PL07-39PC **Lat:** 10° 42' **Lon:** -64° 56.5' **Depth:** 790 m **Mg/Ca Sources:** *Globigerinoides ruber (white)* **References:** Lea et al. 2003 **Age Model:** From available ^{14}C dates calibrated to calendar ages using Calib v. 4.4 assuming a reservoir age of 420 years ($\Delta R = 0?$; age is median probability age?) and grayscale wiggle matching with another core that had been placed on a varve chronology. **Notes:** See supporting online material of reference at <http://www.sciencemag.org/cgi/content/full/301/5638/1361/DC1> **Dataset Sources:** ftp://ftp.ngdc.noaa.gov/paleo/contributions_by_author/lea2003/cariaco_2003.txt

Core: RC11-120 **Lat:** -43° 31' **Lon:** 79° 52' **Depth:** 3135 m **Mg/Ca Sources:** *Globigerina bulloides* **References:** Mashiotta et al. 1999, Martinson et al. 1987 **Age Model:** SPECMAP, based on Martinson et al. 1987. **Dataset Sources:** ftp://ftp.ngdc.noaa.gov/paleo/contributions_by_author/mashiotta1999/mashiotta1999.txt

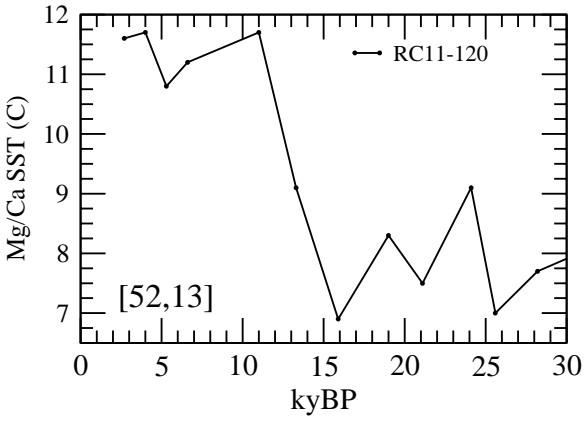
Core: TT9108-1GC **Lat:** 11° 39.83' **Lon:** -79° 35.52' **Depth:** 2540 m **References:** Hastings et al. 1998 **Mg/Ca Sources:** *Globigerinoides sacculifer* **Age Model:** Developed by assigning the stage 1/2 boundary to a specific core depth and the $\delta^{18}\text{O}$ minimum at a specific core depth to the LGM (the ages associated with these boundaries are from the stacked SPECMAP curve of Imbrie et al. 1984 and Martinson et al. 1987?); below the latter a constant sedimentation rate was assumed. **Notes:** Data typed in from reference Table 2. **Dataset Sources:** Reference

Appendix F

Downcore Mg/Ca SST Time Series Plots

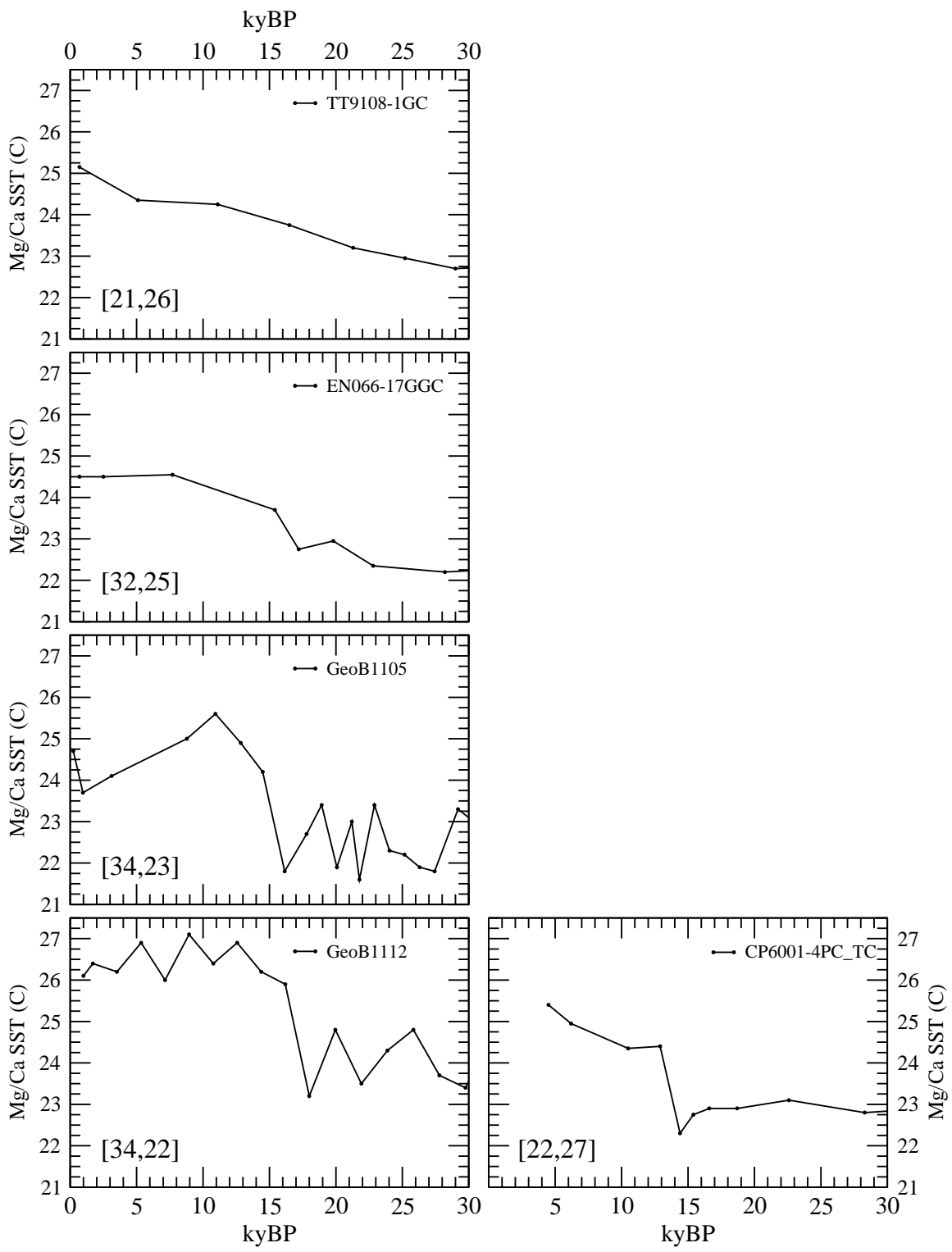
F.1 Downcore Mg/Ca SST Time Series Plots for *Globigerina bulloides*

Each plot corresponds to a 5° x 4° CGCM grid box and includes the downcore Mg/Ca SST (sea surface temperature) time series of all the cores whose locations are encompassed by that grid box. The [lon#,lat#] of the CGCM grid box is in the lower left corner of each plot. See any of the CGCM grid box maps in this work to locate it on a world map. The plots are arranged in order of increasing latitude starting from lower left and proceeding in an “N” on each page. This may cause seemingly oddly placed stray plots. All x axes are time in kyBP and only go from 0 to 30 kyBP, spanning just the eras of interest in this work and even though data going further back may have been compiled. All y axes are Mg/Ca SST in Celsius and span the maximum range resulting from including all cores in all grid boxes. See Section 7.2.3 for a description of the data, its averaging, and caveats.



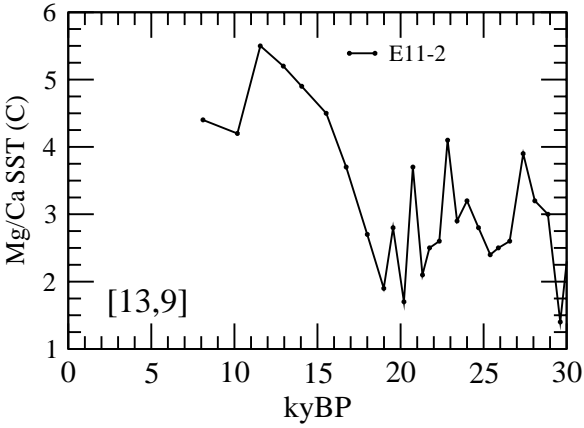
F.2 Downcore Mg/Ca SST Time Series Plots for *Globigerinoides sacculifer*

Each plot corresponds to a 5° x 4° CGCM grid box and includes the downcore Mg/Ca SST (sea surface temperature) time series of all the cores whose locations are encompassed by that grid box. The [lon#,lat#] of the CGCM grid box is in the lower left corner of each plot. See any of the CGCM grid box maps in this work to locate it on a world map. The plots are arranged in order of increasing latitude starting from lower left and proceeding in an “N” on each page. This may cause seemingly oddly placed stray plots. All x axes are time in kyBP and only go from 0 to 30 kyBP, spanning just the eras of interest in this work and even though data going further back may have been compiled. All y axes are Mg/Ca SST in Celsius and span the maximum range resulting from including all cores in all grid boxes. See Section 7.2.3 for a description of the data, its averaging, and caveats.



F.3 Downcore Mg/Ca SST Time Series Plots for *Neogloboquadrina pachyderma* (sinistral)

Each plot corresponds to a 5° x 4° CGCM grid box and includes the downcore Mg/Ca SST (sea surface temperature) time series of all the cores whose locations are encompassed by that grid box. The [lon#,lat#] of the CGCM grid box is in the lower left corner of each plot. See any of the CGCM grid box maps in this work to locate it on a world map. The plots are arranged in order of increasing latitude starting from lower left and proceeding in an “N” on each page. This may cause seemingly oddly placed stray plots. All x axes are time in kyBP and only go from 0 to 30 kyBP, spanning just the eras of interest in this work and even though data going further back may have been compiled. All y axes are Mg/Ca SST in Celsius and span the maximum range resulting from including all cores in all grid boxes. See Section 7.2.3 for a description of the data, its averaging, and caveats.



F.4 Downcore Mg/Ca SST Time Series Plots for *Globigerinoides ruber* (white)

Each plot corresponds to a 5° x 4° CGCM grid box and includes the downcore Mg/Ca SST (sea surface temperature) time series of all the cores whose locations are encompassed by that grid box. The [lon#,lat#] of the CGCM grid box is in the lower left corner of each plot. See any of the CGCM grid box maps in this work to locate it on a world map. The plots are arranged in order of increasing latitude starting from lower left and proceeding in an “N” on each page. This may cause seemingly oddly placed stray plots. All x axes are time in kyBP and only go from 0 to 30 kyBP, spanning just the eras of interest in this work and even though data going further back may have been compiled. All y axes are Mg/Ca SST in Celsius and span the maximum range resulting from including all cores in all grid boxes. See Section 7.2.3 for a description of the data, its averaging, and caveats.

